2007

An experimental study on buckling of vanadium steel members with single or double angle cross-sections

Ali Bedii Candas
Lehigh University

Candas, Ali Bedii

An Experimental Study on Buckling of Vanadium Steel Members With Single or Double Angle...

September 2007

AN EXPERIMENTAL STUDY ON BUCKLING OF VANADIUM STEEL MEMBERS WITH SINGLE OR DOUBLE ANGLE CROSS-SECTIONS

by

Ali Bedii Candas

A Thesis

Presented to the Graduate and Research Committee

of Lehigh University

in Candidacy for the Degree of

Master of Science

in

Civil Engineering

Lehigh University

July 2007

This thesis is accepted and approved in partial fulfillment of the requirements for the Master of Science.

July 9, 2007
Date

Dr. Richard Sause, Thesis Advisor

Dr. James M. Ricles, Thesis Advisor

Dr. Stephen Kessiki, Department Chairperson

Acknowledgements

First and foremost, I would like to thank my family and friends for they have provided me with the patience, confidence, faith and strength. I owe them my heartfelt gratitude for being there all along the road.

I would like to thank my research advisors Dr. Richard Sause and Dr. James Ricles for their patience, encouragement, and guidance in building everlasting experience in the last two years.

This research was funded by a research contract to the ATLSS Center from SGH, Inc. In addition, Ronald O. Hamburger, Ronald L. Mayes, and Mark Webster, of SGH, Inc. provided substantial technical input, including the design of the test specimens, with input from the ATLSS research team. The truss test specimens and some of the isolated compression members were fabricated by Canam Group Inc.

Finally, I would like to thank the staff of the ATLSS facility including Dr. Eric Kaufmann, Mr. Frank Stokes, Mr. John Hoffner, Mr. Todd Anthony, and Mr. Russ Longenbach for their dedicated work during my experimental studies.

Table of Contents

List of Tables

List of Figures

ABSTRACT

This thesis presents experimental research on the buckling behavior of compression members with angle-shaped cross-sections made from Vanadium steel, which is a microalloyed high strength steel, having a nominal yield stress of 80 ksi. Members with single or double angle cross-sections are often used in trusses and joists that support roof and floor support systems. The thesis focuses on Vanadium steel single and double angle members that would be used in these trusses and joists.

A selected series of single angle specimens, double angle specimens, and single angle specimens with crimped ends were tested as isolated members under concentrically-applied axial compression. Truss subassemblies consisting of only double angle members were also tested. The tests of the truss subassemblies investigated the behavior of double angle members as chord or web members within the trusses. The results of these tests were compared with the behavior expected from the AISC (2005) specification.

Based on the experimental study, it is found that the AISC (2005) specification provisions for compression members with single or double angle cross-sections are conservative for single or double angle compression members made from Vanadium steel. These specification provisions underestimate the experimental capacity of these members, especially when the cross-section is considered slender with respect to the width-to-thickness ratio of the angle legs. The test results for single angle specimens with crimped ends showed that the simple application of the AISC (2005) specification provisions for single angle compression members to angles with crimped

ends, without considering the reduced flexural stiffness and strength of the crimped ends, is not conservative and is not recommended. Finally, the results of the truss tests show that it is appropriate to use an effective length factor, K, equal to 1.0 to predict the buckling capacity of double angle Vanadium steel truss members in compression.

Chapter 1 Introduction

1.0 General

The study presented in this thesis was conducted at the Advanced Technology for Large Structural Systems (ATLSS) Center at Lehigh University in Bethlehem, Pennsylvania.

The thesis presents experimental research on the buckling behavior of compression members with angle-shaped cross-sections made from Vanadium steel. Vanadium steel is a microalloyed high strength steel with chemical composition that is somewhat similar to ASTM A572 steel. A higher strength is achieved for Vanadium steel by increasing nitrogen, carbon, manganese, and vanadium above the typical levels in A572 Grade 50 compositions, as shown in Table 1.1. The nominal yield stress value for Vanadium steel is 80 ksi.

Angle cross-sections are used in a wide variety of applications in structural systems because of their easy connection to other structural members. As shown in Figure 1.1, angles are often used in trusses and joists that support roof and floor systems. In these systems, either single angles or double angles are utilized as truss and joist members. Single and double angle truss and joist compression members made of Vanadium steel are the focus of this study. When a single angle (tension or compression) member is connected to other members by one of the legs of the angle, the angle is loaded eccentric to its centroid. However, the symmetric shape of double angle members allows them to be concentrically loaded. For joists in roof and floor

systems, the ends of single angle members used as diagonal web members in the joist can be crimped to reduce the eccentricity in loading. Crimped end single angle compression members are considered in this study.

1.1 Research Objectives

The overall objective of this research is to understand the buckling behavior of Vanadium steel angle cross-section members that represent compression members in trusses and joists. In order to achieve this overall objective, more specific research objectives were formulated:

1. To determine the mechanical (stress-strain) properties of the Vanadium steel angles.
2. To experimentally evaluate the buckling behavior of isolated single angle members, double angle members, and single angle members with crimped ends under concentrically-applied axial compression.
3. To experimentally evaluate the buckling behavior of double angle members in trusses.
4. To compare the experimental behavior of isolated angle members in trusses with the behavior anticipated by the American Institute of Steel Construction "Specification for Structural Steel Buildings" (AISC, 2005).

1.2 Research Scope

To achieve these objectives, the following research was conducted. First, tensile coupon test specimens were prepared from different size Vanadium steel angles and

tested to find the yield stress and ultimate stress of Vanadium steel. Then, a selected series of single angle specimens, double angle specimens, and crimped angle specimens were tested under concentrically-applied axial compression. The results of these isolated member tests were compared with the behavior expected from the AISC (2005) specification.

Finally, trusses consisting of only double angle members were tested. In these tests, the behavior of Vanadium steel truss compression chord members near mid-span where the overall moment reaches its maximum value and the shear is small, and the behavior of Vanadium steel truss web members in regions of combined overall shear and moment were evaluated. Again, the results of these tests were compared with the behavior expected from the AISC (2005) specification.

1.3 Organization of Thesis

The remainder of this thesis consists of following chapters. In Chapter 2, background on angle members under axial compression is introduced with an overview of the related parts of the AISC (2005) specification. Chapter 3 presents the mechanical properties of Vanadium steel angles. Chapter 4 presents experiments on single angle compression members. The experimental results are compared with predictions based on the AISC (2005) specification. Chapter 5 presents an experimental study of double angle compression members. Again, the experimental results are compared with predictions based on the AISC (2005) specification. Chapter 6 presents an experimental study on single angle members with crimped ends. In Chapter 7, an experimental study of double angle compression members in truss

subassemblies is presented. Chapter 8 presents a summary and conclusions regarding the buckling behavior of Vanadium steel angle compression members and recommends future work on the subject.

Table 1.1 Chemical Composition of Vanadium Steel Compared to ASTM A572 Grade 50 Steel

	C	Mn	P	S	Si	Ni	Cr	Mo	V	Nb	Cu	Sn	N
Vanadium steel	0.2	1.16	0.014	0.033	0.26	0.094	0.084	0.031	0.08	0.001	0.29	0.011	0.012
ASTM A572 Grade 50	0.23 max.	1.35 max.	0.04 max.	0.05 max.	0.40 max.				0.01-0.15	0.005-0.05			0.003-0.015

Note: contents expressed in percent

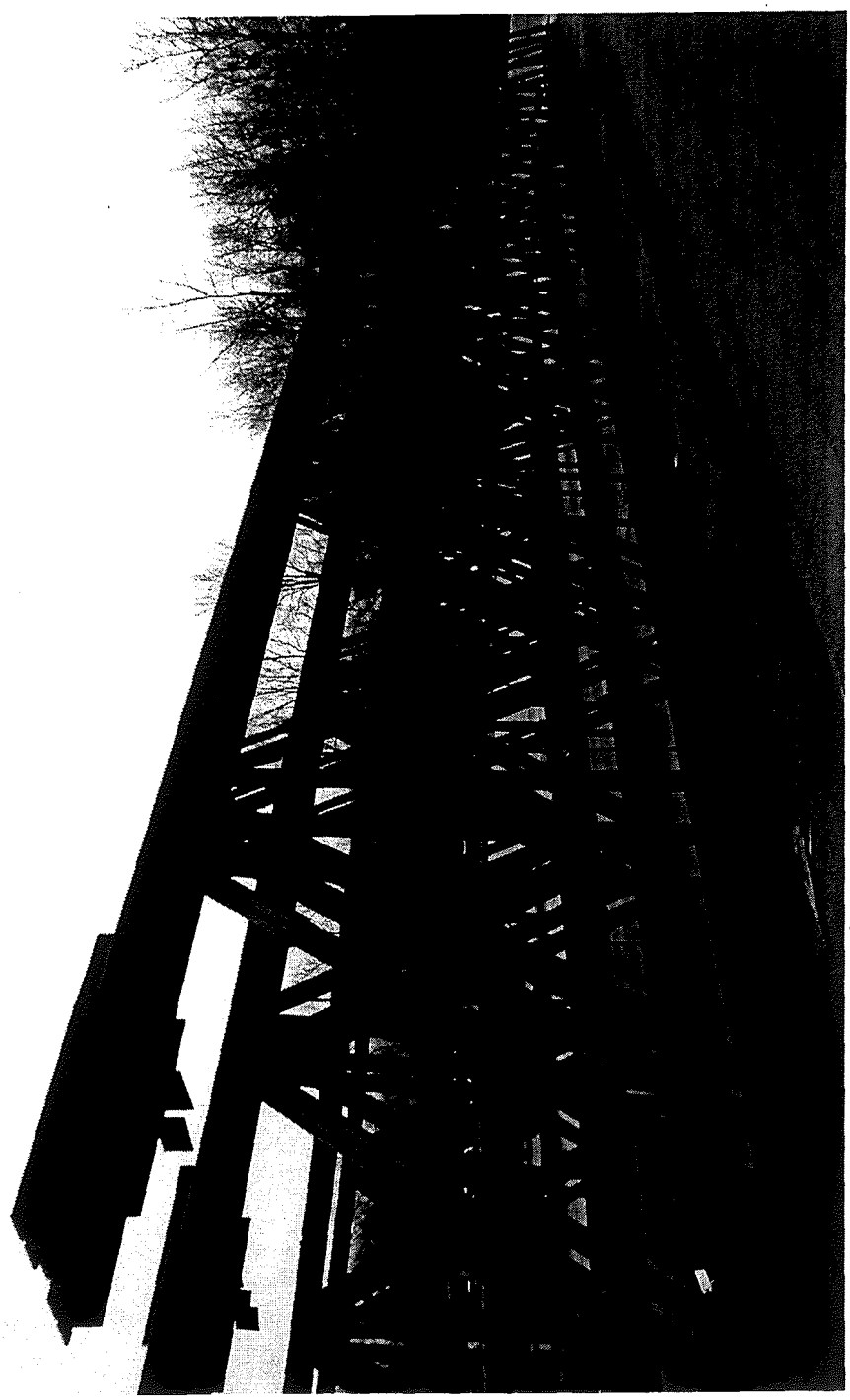

Figure 1.1 Angle Cross-sections Used in Roof Trusses

Chapter 2 Buckling Analysis of Single Angle and Double Angle Members

2.0 General

This chapter addresses the theoretical buckling analysis of members with angle shaped cross-sections. The cross-sections of the members studied in this project consist of single angle and double angles where the angles have equal legs. These cross-sections are examined under concentrically applied compressive axial load. Elastic buckling of members with these cross-sections are covered first in the chapter, and then inelastic buckling is covered. At the end of the chapter, related provisions for single and double angle members under compression from the Specification for Structural Steel Buildings (AISC, 2005) will be briefly reviewed.

2.1 Theory

Columns are structural members that transmit compressive axial load along their centroidal axis. The buckling load of a column is defined as the maximum compressive load that it carries. The buckling load is called the "critical load" throughout the following discussion.

Member buckling and local buckling are two types of buckling that can occur for an axially loaded column. Figure 2.1 shows the coordinate system and degrees of freedom used to explain the following analyses of these two types of buckling.

2.1.1 Member Buckling

Depending on the deformation pattern at the critical load, member buckling is classified as either flexural buckling, torsional buckling, or coupled flexural-torsional buckling.

2.1.1.1 Flexural Buckling

During flexural buckling, a column has a deflection in the minor principle axis (weak axis) or the major principle axis (strong axis) directions caused by bending. For a pin-ended member, the expected flexural buckling shape is a half sine wave over the member length and therefore flexural buckling results in a maximum deflection at the mid-height cross-section.

The cross-sections of the members studied in this project have one axis of symmetry, which is the strong axis of the member. This strong axis is the y_c axis for these cross-sections as shown in Figure 2.2. Flexural buckling occurs about the principal axis with the largest slenderness ratio KL/r: where K is the effective length factor, L is the length of the member, and r is the radius of gyration of the cross-section about the principal axis. For the cross-sections shown in Figure 2.2, the weak axis (i.e., the x_c axis) has the largest slenderness ratio when K_x equals K_y. The effective length concept will be discussed later in the chapter.

2.1.1.2 Torsional Buckling

During torsional buckling, a column has a torsional deformation about a longitudinal axis passing through the shear center. The shear center is the point

through which the cross-section shear force must act to avoid inducing torsion on the section. As shown in Figure 2.2, the shear center is eccentric to the centroid of a cross-section which is singly symmetric about one principal axis.

Under applied torsional moment, total torsional resistance of a cross-section is the summation of the pure torsional resistance (i.e., St. the Venant torsional resistance) and the warping torsional resistance:

$$T = T_{St.Venant} + T_{warping}$$
$$T_{St.Venant} = G \times J \times \theta^{i}$$
$$T_{warping} = -E \times C_w \times \theta^{iii} \qquad \textbf{(2.1)}$$

where

T : the total torsional resistance

$T_{St.Venant}$: the St. Venant torsional resistance

$T_{warping}$: the warping torsional resistance

G : the shear modulus of elasticity of steel

J : the torsional constant of the cross-section

E : the elastic modulus of steel

C_w : the warping constant

θ : the angle of twist (the rotation of the cross-section about the longitudinal axis passing through the shear center). Note that the notation ^{i} indicates the 1st derivative with respect to the length axis z and the notation ^{iii} indicates the 3rd derivative.

When the warping is unrestrained, only pure torsional stresses develop (i.e., only the St. Venant torsional resistance develops). On the other hand, when the warping is restrained, then additional stresses develop due to warping. The warping stiffness of a cross-section composed of angles is rather small, so that the contribution of warping torsion to the torsional buckling capacity is assumed to be negligible for these cross-sections in the AISC (2005) specification.

2.1.1.3 Flexural-torsional Buckling

During flexural-torsional buckling, a column has simultaneous flexural and torsional deformation. This mode of buckling is a coupled mode of buckling that includes both the flexural buckling mode and the torsional buckling mode.

2.1.2 Local Buckling

Another possible failure mode for a member under axial load is local buckling. During local buckling, the plate elements of the member cross-section buckle before the critical load for the entire member is reached. Local buckling occurs with local bending of the plate elements of the cross-section. The regions of the plate with the largest out-of-plane deformation carry a reduced level of compressive normal stress.

The nonuniform normal stress pattern on the cross-section caused by local buckling may result in a reduction in the compressive strength of the member. In order

to account for the effects of local plate buckling on the compressive strength of a member, the reduction factor Q is introduced into the predicted buckling capacity calculations by the AISC (2005) specification. This factor will be discussed later in the chapter.

2.1.3 Elastic Analysis of Member Buckling

Differential equations of equilibrium are given below. To develop these equations, several important assumptions are made:

- The material is elastic, isotropic, and homogeneous.
- The member is perfectly straight and prismatic.
- The axial compressive load is applied concentrically (i.e., at the centroid of the cross-section).
- The ends of the members are ideally pin-ended, and no bending moment is applied to the ends.
- Sections that are plane before loading remain plane after loading.
- Strains and deflections are relatively small.

2.1.3.1 Differential Equations of Equilibrium

A second order equilibrium analysis of a member under axial load will lead to the three differential equations (Galambos, 1978) given below. These equations are linear with respect to the displacements u and v, which are in the x_c axis and y_c axis directions respectively, and with respect to θ, which is the twist about the shear center.

These equations are not independent. The solution of these equations leads to an eigenvalue problem, and the characteristic equation has three roots, which are related critical loads. The lowest of the critical loads will determine elastic buckling strength of the member, which is the axial load at buckling.

$$EI_x v^{iv} + Pv^{ii} - Px_0\theta^{ii} = 0 \tag{2.2}$$

$$EI_y u^{iv} + Pu^{ii} + Py_0\theta^{ii} = 0 \tag{2.3}$$

$$EC_w\theta^{iv} + (P\overline{r_0}^2 - GJ)\theta^{ii} + Py_0u^{ii} - Px_0v^{ii} = 0 \tag{2.4}$$

where

I_x, I_y : the moment of inertia about the principal axes

P : the axial load

x_0 : the distance between the shear center and the centroid of the cross-section in the x_c axis direction

y_0 : the distance between the shear center and the centroid of the cross-section in the y_c axis direction

$\overline{r_0}$: the polar radius of gyration about the shear center

$$\overline{r_0}^2 = x_0^2 + y_0^2 + \frac{I_x + I_y}{A}$$

(2.5)

The roman numerals as subscripts to the displacements u, v and θ, represent derivatives of the displacements with respect to the length axis z.

For members with cross-sections that have one axis of symmetry, in this case the y_c axis, x_0 equals zero. Then, the three differential equations simplify to:

$$EI_x v^{iv} + Pv^{ii} = 0$$

(2.6)

$$EI_y u^{iv} + Pu^{ii} + Py_0\theta^{ii} = 0$$

(2.7)

$$Ec_w\theta^{iv} + (P\overline{r_0}^2 - GJ)\theta^{ii} + Py_0u^{ii} = 0$$

(2.8)

To solve this system of equations, simply supported end conditions are assumed resulting in displacements u, v and θ with the form of a half sine over the length of the member.

Equation (2.6) is an uncoupled equation. The solution of this equation provides the critical load for flexural buckling about the x_c axis of the member:

$$P_{cr-x} = \frac{\pi^2 EI_x}{L^2}$$

(2.9)

Equations (2.7) and (2.8) are coupled and the solution of this system of equations provides the critical load for flexural-torsional buckling involving flexural buckling about the y_c axis combined with torsional buckling. The solution of this system of equations has two roots:

$$P_{cr-ft} = \frac{P_{cr-y} + P_{cr-z}}{2H}\left[1 \pm \sqrt{1 - \frac{4HP_{cr-y}P_{cr-z}}{\left(P_{cr-y} + P_{cr-z}\right)^2}}\right] \tag{2.10}$$

where

P_{cr-y} : the critical load for flexural buckling about the y_c axis of the member

$$P_{cr-y} = \frac{\pi^2 EI_y}{L^2} \tag{2.11}$$

P_{cr-z} : the critical load for torsional buckling about the longitudinal axis passing through the shear center of the cross-section

$$P_{cr-z} = \left[\frac{\pi^2 EC_w}{L^2} + GJ\right]\frac{1}{\bar{r}_0^2} \tag{2.12}$$

H : a constant

$$H = 1 - \frac{x_0^2 + y_0^2}{\bar{r}_0^2} \tag{2.13}$$

Since $x_0 = 0$, Equations (2.5) and (2.13) simplify to:

$$\bar{r}_0^2 = y_0^2 + \frac{I_x + I_y}{A}$$

(2.14)

$$H = 1 - \frac{y_0^2}{\bar{r}_0^2}$$

(2.15)

Since the warping contribution to the torsional resistance for single angle and double angle members is small and can be neglected, Equation (2.12) simplifies to:

$$P_{cr-z} = \frac{GJ}{\bar{r}_0^2}$$

(2.16)

2.1.4 Major Factors Affecting the Actual Compressive Strength of Columns

2.1.4.1 Residual Stress Effect

Steel and other metal members develop residual normal stresses on the cross-section for many reasons, such as uneven cooling after hot rolling or after welding. The distribution and magnitude of residual normal stresses depend on the cross-section shape, rolling temperatures, material properties, cooling conditions, and straightening that may be applied after cooling. Compressive residual stresses are expected at the tip of the legs of angle cross-sections due to the fact that the tips cool faster after rolling.

Due to compressive residual stress, σ_{rc} at the tips of the legs of the angle, this part of the cross-section will yield when the average stress applied to the specimen reaches a value of $\sigma_{applied} = \sigma_y - \sigma_{rc}$, where σ_y is the yield stress of the material without

residual stress. Thus, residual stresses start the process of yielding of the cross-section before the yield load is reached. A partially yielded cross-section has less flexural stiffness and torsional stiffness, and under such partially-yielded conditions, flexural or torsional buckling could be expected at a load less than the elastic buckling load described earlier (Galambos, 1978).

2.1.4.2 Initial Out-of-straightness

A column member is expected to have initial curvature (sweep or camber) before being loaded, known as the initial out-of-straightness. A mean value for the maximum out-of-straightness along the length of a column member equal to 1/1470 of the length of the member was determined by Bjorhovde (1972).

Initial out-of-straightness will result in increasing lateral deflections under increasing axial load. The effect of the out-of-straightness reduces the load carried by the column to less than the theoretical elastic buckling load.

2.1.4.3 End Restraint Effect

If the ends of a column member are not ideal pin ends, then the restraint of the end rotation will increase the buckling capacity. This effect is often modeled using the effective length concept. The effective length is defined as the portion of length of the member between the zero curvature points (points of inflection) in its buckled shape. For instance, for a pin-ended member the effective length is equal to the actual length of the member. Assuming that the ends of the member do not displace, for a member

with end restraint will have an effective length that is shorter than the actual length, as points of inflection will occur within the actual length.

The effective length is often represented with an effective length factor, K. The effective length, L_{eff}, equals KL where L is the actual length. For an ideally pin-ended member, the effective length factor K is equal to 1.0. For a member with end restraint K will be less than 1.0.

2.1.5 Inelastic Buckling

The strength of columns with a partially yielded cross-section due to residual stresses is approximated by "column strength curves". Bjorhovde (1972) conducted a thorough numerical study of the capacity of column members with a wide range of residual stress and initial imperfections (Galambos, 1998). Bjorhovde (1972) produced a wide variety of column strength curves, and then categorized these curves into three groups, which are now known as Structural Stability Research Council (SSRC) column strength curves 1, 2, and 3 (Galambos, 1998). In the development of these curves, the initial out-of straightness was taken as 1/1000 of the length of the member, where 1/1000 of the length is considered acceptable for column members in practice. Bjorhovde (1972) also developed a second set of curves for an initial out-of-straightness that was taken to be 1/1470 of the length of the member, where 1/1470 of the length is considered to be a mean value for columns in practice. These curves are known as SSRC 1P, 2P, and 3P.

The SSRC 2P curve, shown in Figure 2.3 was adapted by the AISC (2005) specification as the curve that represents column strength. Figure 2.3 shows that the suggested column strength curve suggested provides a large margin of safety to account for the effects of residual stresses and the initial out-of-straightness. When this column strength curve was adapted into the AISC specification (AISC, 1993) it was defined with following equations:

for $\lambda_c \leq 1.5$

$$\frac{F_{cr}}{F_y} = 0.658^{\lambda_c^2} \tag{2.17}$$

where F_y is the yield stress of the material and λ_c is the non-dimensional slenderness parameter

$$\lambda_c = \frac{1}{\pi}\frac{L}{r}\sqrt{\frac{F_y}{E}} \tag{2.18}$$

for $\lambda_c > 1.5$

$$\frac{F_{cr}}{F_y} = \frac{0.877}{\lambda_c^{\,2}} \tag{2.19}$$

As seen from the above equations, $\lambda_c = 1.5$ ($F_{cr} = 0.44F_y$) limit is the transition from elastic buckling to inelastic buckling column strength.

2.2 Relevant Prior Research

There is a little prior research on the inelastic buckling behavior of columns composed of angle cross-sections. Kitipornchai and Lee (1986) used finite element analyses and tests to study inelastic buckling of angle members. In this research, concentrically-loaded pin-ended single angle and double angle members were tested to determine the inelastic flexural and flexural-torsional buckling capacities. 26 single angle and 16 double angle specimens were tested. In the test setup, rotation of the ends about each principal axis direction was unrestrained, but twist about the longitudinal axis was restrained at the ends. In the analyses, an idealized pattern of residual stresses on the cross-section of the members was utilized. The report concluded that the flexural buckling is the observed failure mode for most of the members. The report suggested that for the singly symmetric cross-sections, flexural-torsional buckling occurs when r_x (the radius of gyration for the minor principle axis direction) is larger than r_y (the radius of gyration for the major principle axis direction). SSRC Curve 2 was suggested as a representative column strength curve for both single and double angle members.

Adluri and Madugula (1996) tested 26 single angle members. They noted that flexural buckling was the basic failure mode considered by the design codes at the time their work was published. They also suggested that the other failure modes, such as flexural-torsional buckling or local buckling, are possible for single angle members. The buckling capacities for these other types of failures could be related to the basic flexural buckling capacity formulas, so Adluri and Madugula focused on the flexural

buckling capacity of single angle members. Their test matrix included members with slenderness ratios between 68 and 188. The members were tested under concentrically-applied axial load. The end conditions were pin-ended. In the experimental study, the residual stress pattern and the initial out-of-straightness were measured. The results suggested that the maximum residual stress in the angle legs does not exceed the 25% of the yield stress, and that the suggested value for initial out-of-straightness, approximately $L/1500$, is appropriate for single angle members.

Lu et al. (1983) studied the inelastic behavior of members having initial out-of-straightness. The analytical study focused on the flexural and flexural-torsional buckling of single angle members under either concentrically or eccentrically applied load. As part of the analytical study, four single angle members were studied. Two of the angles had legs with equal size, while the other angles had legs with unequal width. The end conditions were pin-ended. Lu et al. suggested that a single angle member with a non-zero initial out-of-straightness in the major principal axis direction would fail in the flexural-torsional buckling mode when it is loaded concentrically. The effect of initial out-of-straightness was found to be considerable when the non-dimensional slenderness parameter (see Equation (2.18)) is less than approximately 1.5. The writers concluded that the initial out-of-straightness is a significant factor that influences the buckling capacity of angle members.

2.3 AISC (2005) Specification

In this section, the calculation of the nominal compressive strength P_n of a column according to the AISC (2005) specification is discussed.

The limiting width to thickness ratio is used to classify the member for local buckling. For members under uniform axial compression, sections are classified as;

Noncompact if $\frac{b}{t} < \lambda_r$

Slender if $\frac{b}{t} > \lambda_r$

where b is the width and t is the thickness of an outstanding flange or leg of the cross-section. For angles, b and t are the width and thickness of a leg of the angle.

In this research, all the sections that were studied are slender sections. Thus only λ_r limit is of interest. λ_r for uniform compression of single angles and the legs of double angles is:

$$\lambda_r = 0.45\sqrt{\frac{E}{F_y}} \tag{2.20}$$

2.3.1.1.1 Flexural Buckling Capacity of Slender Members

The nominal compressive strength based on the limit state of flexural buckling is:

$$P_n = F_{cr} A_g \tag{2.21}$$

where A_g is the cross-sectional area of the member. The flexural buckling stress, F_{cr}, is determined as follows:

for $F_e \geq 0.44QF_y$

$$F_{cr} = Q\left[0.658^{\frac{QFy}{Fe}}\right]F_y$$

(2.22)

where Q is the reduction factor for slender cross-sections to consider local buckling effects and F_e is the elastic critical buckling stress. The Q reduction factor is explained later.

For $F_e < 0.44QF_y$

$$F_{cr} = 0.877F_e$$

(2.23)

where F_e is determined as follows:

$$F_e = \frac{\pi^2 E}{\left(\frac{KL}{r}\right)^2}$$

(2.24)

where K is the effective length factor, L is the length of the member, and r is the radius of gyration.

The elastic critical buckling stress and the critical flexural buckling stress about the principal axes are represented with the appropriate subscripts and the relative cross-sectional properties as follows:

$F_{e\text{-}x}$: is the elastic critical buckling stress about the minor principle axis (weak axis) and is a function of K_x and r_x.

$F_{e\text{-}y}$: is the elastic critical buckling stress about the major principle axis (strong axis) and is a function of K_y and r_y.

$F_{cr\text{-}x}$: is the critical flexural buckling stress about the minor principle axis.

$F_{cr\text{-}y}$: is the critical flexural buckling stress about the major principle axis.

The Q reduction factor is the ratio of the plate local buckling stress of a member to its yield stress. This factor is introduced into the buckling equations for the slender members (i.e., members with slender elements). The Q reduction factor is determined as follows:

$$Q = Q_s Q_a \tag{2.25}$$

where Q_s represents the reduction factor for slender unstiffened compression elements and Q_a represents the reduction factor for slender stiffened compression elements. A stiffened element has stiffening elements along both edges, for example, the web of a channel section, which is stiffened by the two flanges. An unstiffened element has one free edge, for example, the flange of a channel section.

For cross sections composed of only unstiffened elements such as single and double angle sections Q_a = 1.0. For members with cross-sections composed of one or more angles, Q_s is determined as follows (other formulas are given (AISC, 2005) for members with other cross-sections):

$$\text{when } \frac{b}{t} \le 0.45\sqrt{\frac{E}{F_y}}$$

$$Q_s = 1.0 \tag{2.26}$$

when $0.45\sqrt{\frac{E}{F_y}} \le \frac{b}{t} \le 0.91\sqrt{\frac{E}{F_y}}$

$$Q_s = 1.34 - 0.76\left(\frac{b}{t}\right)\sqrt{\frac{F_y}{E}} \tag{2.27}$$

when $\frac{b}{t} > 0.91\sqrt{\frac{E}{F_y}}$

$$Q_s = \frac{0.53E}{F_y\left(\frac{b}{t}\right)^2} \tag{2.28}$$

2.3.1.1.2 Flexural-torsional Buckling Capacity

The nominal compressive strength based on the limit state of flexural-torsional buckling is calculated as follows:

$$P_n = F_{cr-ft} A_g \tag{2.29}$$

For compression members with cross-sections having a single axis of symmetry, F_{cr-ft}, is found by the following equations:

for $F_{e-ft} \ge 0.44QF_y$

$$F_{cr-ft} = Q\left[0.658^{\frac{QF_y}{F_{e-ft}}}\right]F_y \tag{2.30}$$

for $F_{e-ft} < 0.44QF_y$

$$F_{cr-ft} = 0.877F_{e-ft} \tag{2.31}$$

where F_{e-ft} is the elastic critical flexural-torsional buckling stress, which is determined as follows:

$$F_{e-ft} = \left(\frac{F_{e-y} + F_{e-z}}{2H}\right)\left[1 - \sqrt{1 - \frac{4F_{e-y}F_{e-z}H}{\left(F_{e-y} + F_{e-z}\right)^2}}\right] \tag{2.32}$$

where

$$F_{e-y} = \frac{\pi^2 E}{\left(\frac{K_y L}{r_y}\right)^2} \tag{2.33}$$

$$F_{e-z} = \frac{GJ}{A_g \overline{r_o}^2} \tag{2.34}$$

The AISC (2005) specification gives specific provisions for built-up members made by connecting cross-section components (such as angles) together with connecting elements (such as welded spacers) along their length. Applying these provisions to double angle members, the strong axis elastic flexural buckling capacity F_{e-y} is calculated (and then used in Equation (2.32)) by using the modified slenderness ratio $\left(\frac{KL}{r}\right)_m$ in place of $\left(\frac{K_y L}{r_y}\right)$, where

$$\left(\frac{KL}{r}\right)_m = \sqrt{\left(\frac{KL}{r}\right)_o^2 + 0.82\frac{\alpha^2}{1+\alpha^2}\left(\frac{a}{r_{ib}}\right)^2}$$

(2.35)

where

$\left(\frac{KL}{r}\right)_m$: the modified column slenderness for a built-up member

$\left(\frac{KL}{r}\right)_o$: the column slenderness of a built-up member with the cross-section components acting compositely as an ideal cross-section (i.e., with plane sections remain plane)

α : the separation ratio

$$\alpha = \frac{h}{2r_{ib}}$$

(2.36)

where

r_{ib} : the radius of gyration of an individual cross-section component

h : the distance between the centroids of the individual components perpendicular to the member axis of buckling

a : the spacing between connectors

An alternative method for the capacity calculations of double angle members is provided by the AISC (2005) specification for non-slender members. Here, this

method is extended to slender members by inserting the Q reduction factor into the formulas, however, the resulting formulas are not part of the AISC (2005) specification:

$$P_n = F_{cr-ft} A_g \tag{2.37}$$

where F_{cr-ft} is determined from:

$$F_{cr-ft} = \left(\frac{F_{cr-y} + F_{cr-z}}{2H} \right) \left[1 - \sqrt{1 - \frac{4 F_{cr-y} F_{cr-z} H}{\left(F_{cr-y} + F_{cr-z} \right)^2}} \right] \tag{2.38}$$

where

$$F_{cr-z} = \frac{GJ}{A_g \overline{r_o}^2} \tag{2.39}$$

and F_{cr-y} is found as follows:

for $F_{e-y} \geq 0.44 Q F_y$

$$F_{cr-y} = Q \left[0.658^{\frac{Q F_y}{F_{e-y}}} \right] F_y \tag{2.40}$$

for $F_{e-y} < 0.44 Q F_y$

$$F_{cr-y} = 0.877 F_{e-y} \tag{2.41}$$

where F_{e-y} is determined as follows:

$$F_{e-y} = \frac{\pi^2 E}{\left(\frac{KL}{r}\right)_m^2}$$

(2.42)

The main difference between these two approaches (the first approach based on Equations (2.33), (2.34), (2.35), (2.36), and (2.37), and the second approach based on Equations (2.40), (2.41), (2.42), (2.43), and (2.44)) is that the torsional resistance (from GJ, the shear modulus of steel times the St. Venant torsional constant) is not subjected to an inelastic reduction or local buckling reduction in the second approach, while, the torsional resistance in the first approach is subjected to these reductions as shown in Equations (2.33) or (2.34).

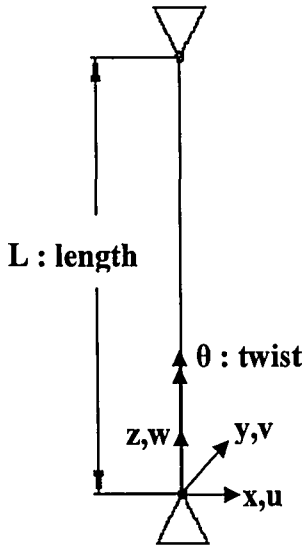

(a) Coordinate System

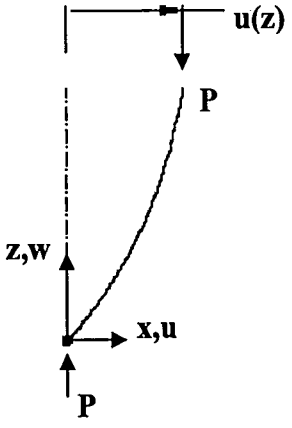

(b) Displacement in x axis Direction

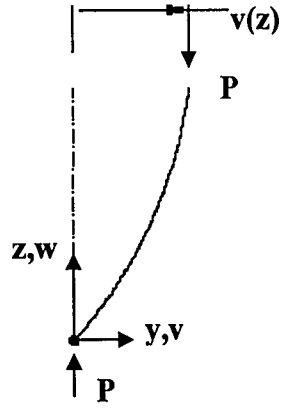

(c) Displacement in y axis Direction

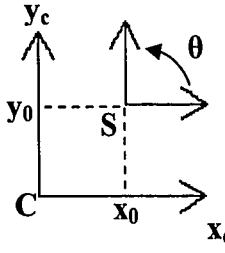

(d) Location of Shear Center (S) and Centroid (C) of Cross-section

Figure 2.1 Coordinate System and Degrees of Freedom

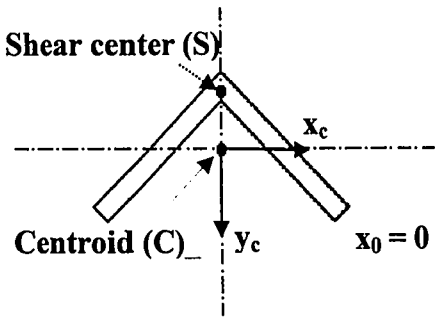

(a) Cross-section and Coordinate System for Single Angle

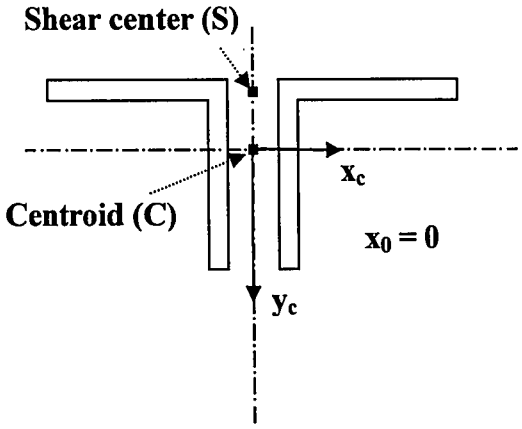

(b) Cross-section and Coordinate System for Double Angles

Figure 2.2 Cross-sections and Coordinate Systems for Single Angle and Double Angles

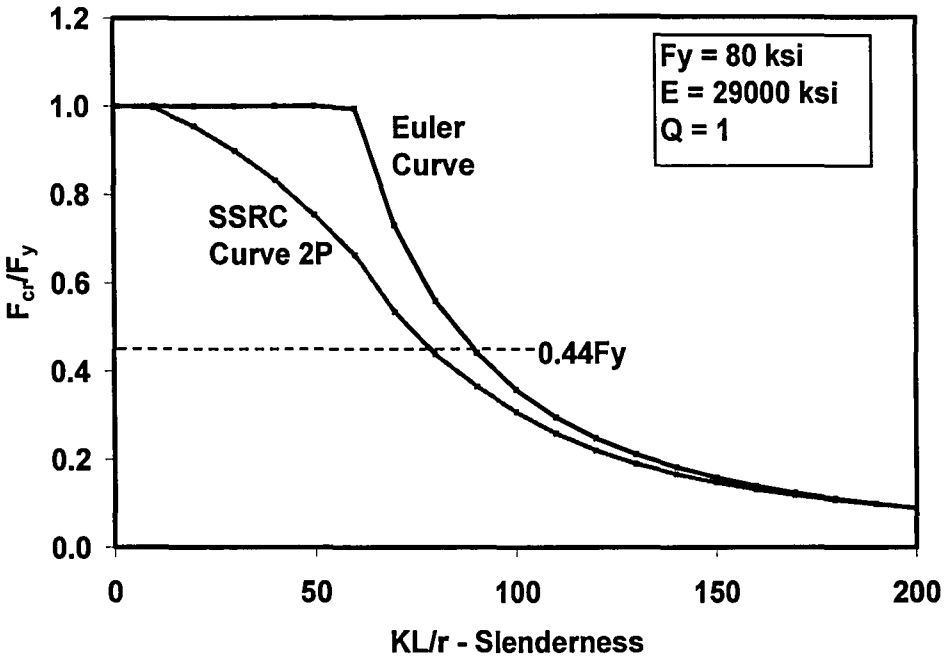

Figure 2.3 SSRC 2P Column Strength Curve

Chapter 3 Material Stress-Strain Properties

3.0 General

This chapter presents the material stress-strain properties of the Vanadium steel specimens studied in this project. The material property tests followed ASTM Standard E8 (ASTM, 2001) with modifications described in SSRC Technical Memorandum No. 7 (Galambos, 1998). This chapter is organized as follows. First, the test matrix is introduced. Then, the test equipment and the instrumentation that were utilized in the testing are presented. Then, the test procedure is presented. Finally, the test results are presented.

3.1 Test Matrix

The test specimens used to determine the material stress-strain properties are referred to as coupons in the following discussions. ASTM E8 Standard Test Methods and Definitions for Mechanical Testing of Steel Products (ASTM, 2001) defines the size of the coupons. The coupons were cut from the angle stock used in the project, and the nominal thickness of the angles is the critical parameter that determines dimensions of the coupons. Coupons were prepared according to ASTM Standard E8, and their dimensions are described in Figure 3.1 and Figure 3.2. The nominal dimensions of the coupons are listed in Table 3.1. These coupons were cut from the angle stock as shown in Figure 3.3. The 1/8 in. and some of the 3/16 in. thick coupons are sheet-type coupons (Figure 3.1) and the 3/8 in., 1/2 in., and some of the 3/16 in. thick coupons are plate-type coupons (Figure 3.2) based on ASTM E8.

Note that the test specimens include both Vanadium steel and Grade 50 steel (ASTM A572) coupons.

3.2 Equipment and Instrumentation

This section describes the equipment and instrumentation used in the tensile tests of the coupons.

3.2.1 Universal Testing Machine

The universal testing machine used to test the coupons is referred to as the SATEC machine, which is the manufacturer of the machine. The SATEC machine is located at the ATLSS Center. It has a 600 kip loading capacity. The coupons are placed in grips in the two cross-heads of the machine as shown in Figure 3.4. Two of the machine columns are stationary throughout a test and the other two, which are attached to the top cross-head, are displaced in the vertical direction. In the tensile tests, these latter columns move the top cross-head so that the distance between the two cross-heads increases and a tensile load is applied to the coupons. The ends of the coupons are held by the grips of the machine, shown in Figure 3.5, firmly enough so that the coupons do not slip under the applied tensile load.

3.2.2 Data Acquisition System

Data were acquired using two different data acquisition systems. The data from the load cell of the SATEC machine and from the transducer that measures the travel of the cross-heads of the machine were recorded by the SATEC Controller (Figure 3.6). For the sheet-type coupons, data from the extensometer used to measure strain (the

KSM 1125) was also recorded by the SATEC Controller. For the plate-type coupons, an external data acquisition system was used to collect data for the strain measurements, while the data for the load and cross-head displacement was recorded by both the SATEC Controller and the external data acquisition system for comparison purposes.

3.2.3 Extensometer

Two types of extensometers were used. They both have the same working principle. For the plate-type coupons, the extensometer is shown in Figure 3.7. This extensometer has two longitudinal displacement transducers placed parallel to the length of the coupon. These transducers are placed one on each side of a coupon and are attached to the coupon with two plates which grab the coupon. These two plates displace relative to each other as the tension deformation is applied to the coupon, and the change in the distance between these plates is measured by the attached transducers. The two plates are attached to the coupon so they initially have a gage length of 8 inches between them.

The second type of extensometer used for the sheet-type coupons is shown in Figure 3.8. This extensometer, referred to by its model number KSM1125, has two teeth grips that are separated 2 inches from each other. These grips are adjusted to the thickness of a coupon.

3.3 Test Procedure

The coupons were manufactured and shipped to the ATLSS Center at Lehigh

University. They were manufactured longer than shown in Figure 3.1 and Figure 3.2 so that the ends of the coupons could be used for hardness tests. The extra lengths of the coupons were cut off, and after removing the mill scale, they were subjected to a hardness test. The Rockwell hardness scale was used and the obtained ultimate strength estimates were compared to the tension test results.

The coupons were punched with a punch marker as shown in Figure 3.1 and Figure 3.2. The marked points are used as a reference to determine the elongation of the coupons. Then the initial width and thickness at the middle cross-section of the coupon were measured and recorded.

To begin a test, each end of the coupon is placed between the cross-heads of the SATEC machine, and clamped into the bottom grip of the machine. The top cross-head is then lowered and the coupon is clamped to the top grip of the machine. After an alignment check, the extensometer is placed on the coupon.

For the sheet-type coupons, the loading was first controlled by stress with a value of 10 ksi per minute. After half of the expected yield stress was reached, the loading control was changed to displacement control with a value of 0.02 in. per minute. This loading rate was continued until the strain hardening portion of the stress-strain curve was reached. When yielding was observed, three static yield stress values were obtained by literally stopping the loading (in displacement control) and holding the displacement until the reduction in stress stopped. These stress values were recorded and are called the static yield stress of the coupons.

After strain hardening begins, the loading rate was increased to a value of 0.20 in. per minute until fracture occurred.

The test procedure for the plate-type coupons was essentially the same, and the differences in the procedure are as follows. For these coupons, the larger extensometer shown in Figure 3.7 was used. After performing hardness test and punching the points shown in Figure 3.2, pretest width and thickness measurements were taken at the middle cross-section of the coupon and recorded. Before placing the coupon into the machine grips, the extensometer was mounted on the coupon. Until the strain hardening portion of the stress-strain curve, the loading was controlled by displacement control with a value of 0.10 in. per minute. After strain hardening was reached, the speed of loading was increased to 0.50 in. per minute until fracture occurred.

After fracture occurred, the coupons were removed from the machine for final measurements. The width and thickness of the fracture area were measured in addition to the final length between the punch marks.

3.4 Results

The complete results from each tensile test are presented in Appendix A. The yield stress was determined by taking the average of the stress values on the yield plateau. For some of the coupons, three static yield stress readings were acquired, and average of these readings are presented in Table 3.2. These static yield stress readings were obtained on the yield plateau by holding the displacement until the reduction in stress

stopped. Ultimate tensile strength was determined by dividing the maximum load by the measured initial cross-sectional area.

Figure 3.9 and Figure 3.10 presents examples of the behavior of sheet-type and plate-type coupons, respectively.

The yield stress and ultimate tensile strength results are shown in Table 3.2. The results are averaged and presented in Table 3.3.

Table 3.1 Coupon Dimensions

Specimen ID	Coupon Type	Gage Length	Width	Thickness
		in.	in.	in.
L 1.75x1.75x1/8	Sheet	2	0.5	0.125
L 2x2x3/16	Sheet	2	0.5	0.1875
L 3x3x3/16	Plate	8	1.5	0.1875
L 3.5x3.5x3/8	Plate	8	1.5	0.375
L 4x4x1/2	Plate	8	1.5	0.5

Table 3.2 Tensile Coupon Test Results

Specimen ID*	Steel Type	Nominal Yield Stress	Measured Yield Stress	Ultimate Tensile Strength	Static Yield Stress
		ksi	ksi	ksi	ksi
1.75x1.75x1/8-A1	Vanadium	80.0	77.5	99.9	
1.75x1.75x1/8-A3	Vanadium	80.0	79.1	98.9	71.6
1.75x1.75x1/8-B1	Vanadium	80.0	79.2	102.0	
1.75x1.75x1/8-B2	Vanadium	80.0	79.9	103.3	
1.75x1.75x1/8-B3	Vanadium	80.0	79.6	99.5	72.1
1.75x1.75x1/8-1	Vanadium	80.0	76.0	98.0	
1.75x1.75x1/8-3	Vanadium	80.0	78.0	100.0	
2x2x3/16-A1	Vanadium	80.0	74.8	99.1	
2x2x3/16-A2	Vanadium	80.0	75.9	99.6	
2x2x3/16-A3	Vanadium	80.0	78.0	99.9	72.5
2x2x3/16-B2	Vanadium	80.0	78.7	102.8	
2x2x3/16-B3	Vanadium	80.0	77.9	99.4	71.6
2x2x3/16-3	Vanadium	80.0	76.0	100.0	
3x3x3/16-A2	Vanadium	80.0	78.3	99.7	
3x3x3/16-A3	Vanadium	80.0	77.9	98.7	
3x3x3/16-B2	Vanadium	80.0	76.3	96.6	
3x3x3/16-B3	Vanadium	80.0	76.2	96.3	
3x3x3/16-1	Vanadium	80.0	78.0	96.0	67.1
3x3x3/16-2	Vanadium	80.0	77.0	95.0	70.0
3x3x3/16-3	Vanadium	80.0	79.0	98.0	70.0
3.5x3.5x3/8-A2	Vanadium	80.0	75.1	99.5	
3.5x3.5x3/8-A3	Vanadium	80.0	74.9	98.5	
3.5x3.5x3/8-B2	Vanadium	80.0	72.8	95.9	
3.5x3.5x3/8-B3	Vanadium	80.0	72.1	96.1	
3.5x3.5x3/8-1	Vanadium	80.0	73.0	96.0	66.7
3.5x3.5x3/8-2	Vanadium	80.0	74.0	98.0	70.9
3.5x3.5x3/8-3	Vanadium	80.0	74.0	98.0	67.7
4x4x1/2-A1	Vanadium	80.0	71.1	95.9	
4x4x1/2-A2	Vanadium	80.0	71.7	95.3	
4x4x1/2-B1	Vanadium	80.0	71.3	95.0	
4x4x1/2-B2	Vanadium	80.0	70.8	94.7	
4x4x1/2-1	Vanadium	80.0	71.0	95.0	66.6
4x4x1/2-2	Vanadium	80.0	70.0	96.0	66.4
4x4x1/2-3	Vanadium	80.0	71.0	96.0	66.0
3.5x3.5x3/8-A3	Grade 50	50.0	64.7	86.6	
3.5x3.5x3/8-B3	Grade 50	50.0	65.3	87.3	
3x3x3/16-A3	Grade 50	50.0	60.2	83.2	
3x3x3/16-B3	Grade 50	50.0	60.2	83.5	

*A,B identify a different leg of the angle stock, 1,2, 3 are the coupon numbers

Table 3.3 Average Tensile Coupon Results

Angle Stock	Steel Type	Nominal Yield Stress	Ultimate Strength from Rockwell Hardness	Yield Stress	Static Yield Stress	Ultimate Strength from Tensile Test
		ksi	ksi	ksi	ksi	ksi
1.75x1.75x1/8	Vanadium	80.0	102.0	78.5	71.9	100.7
2x2x3/16	Vanadium	80.0	100.0	76.9	72.1	100.2
3x3x3/16	Vanadium	80.0	100.0	77.5	69.0	97.8
3.5x3.5x3/8	Vanadium	80.0	100.0	73.7	68.4	97.5
4x4x1/2	Vanadium	80.0	100.0	71.0	66.3	95.2
3x3x3/16	Grade 50	50.0	89.0	60.2	n/a*	83.4
3.5x3.5x3/8	Grade 50	50.0	86.0	65.0	n/a*	87.0

* For 50 ksi material no static yield data was acquired

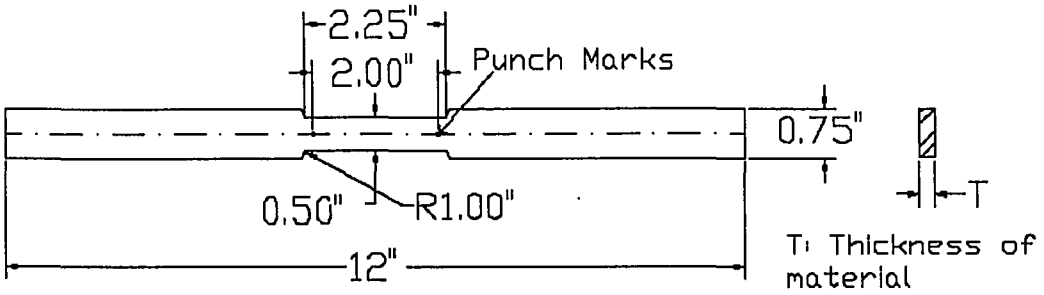

Figure 3.1 Sheet-type Tensile Coupon Dimensions used for 1/8 in. and 3/8 in. Thick Angle Stock (1" = 1 in.)

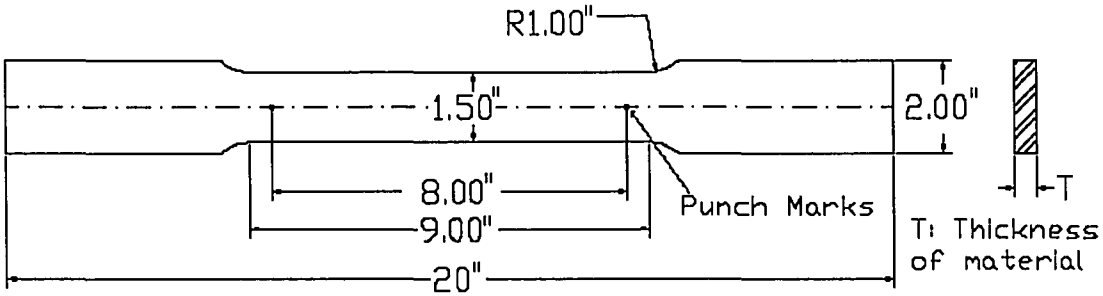

Figure 3.2 Plate-type Tensile Coupon Dimensions used for 3/16 in., 3/8 in., and 1/2 in. Thick Angle Stock (1" = 1 in.)

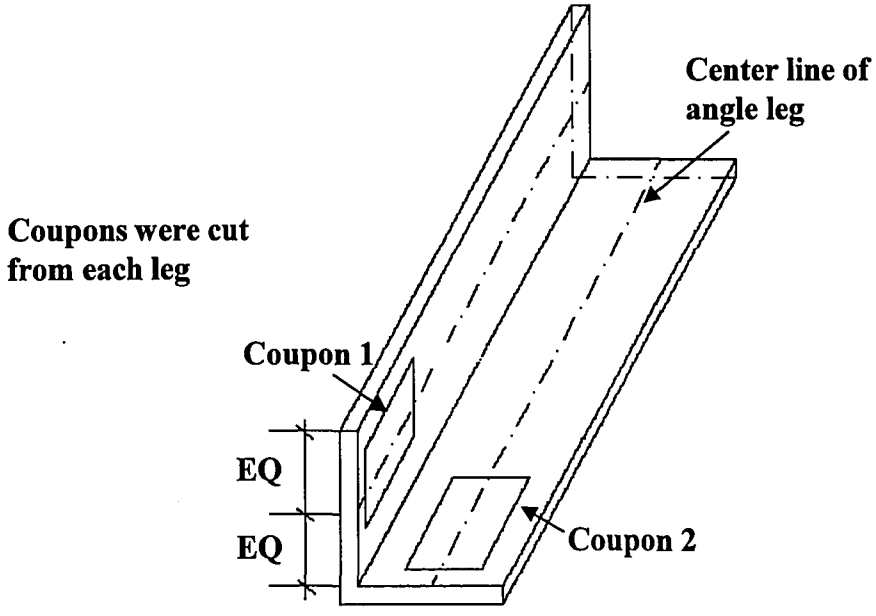

Figure 3.3 Locations of Coupons from Angle Stock

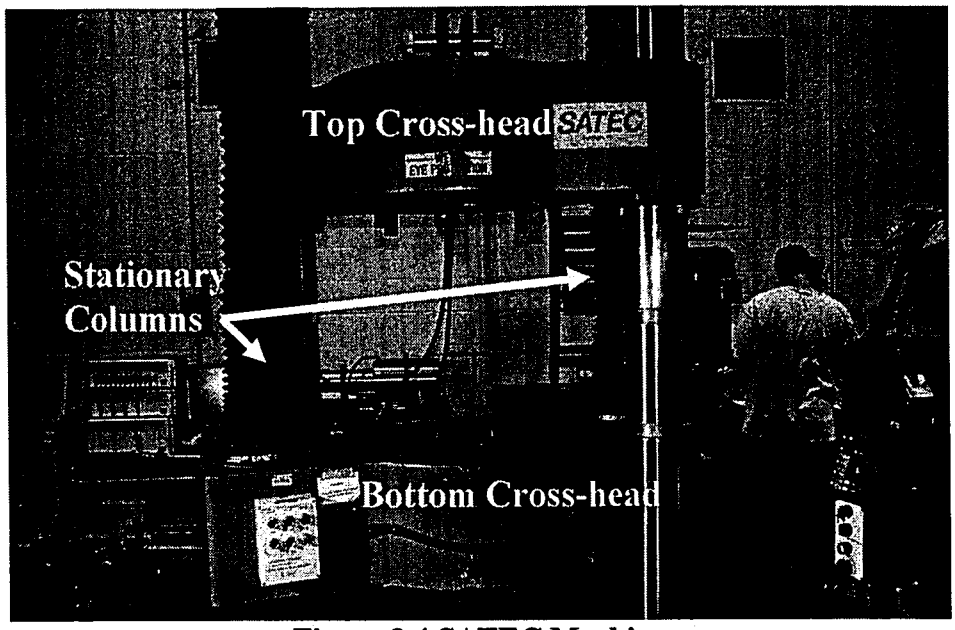

Figure 3.4 SATEC Machine

(a) Top Cross-head Grip

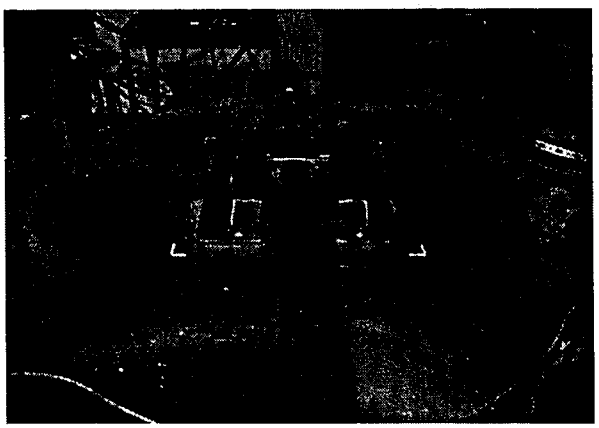

(b) Bottom Cross-head Grip

Figure 3.5 Grips of SATEC Machine

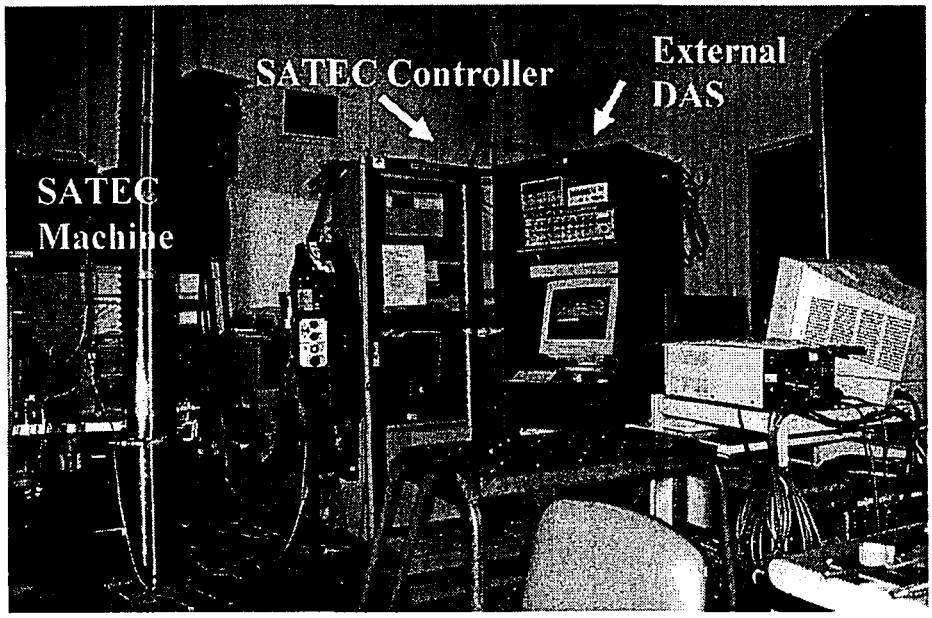

Figure 3.6 Data Acquisition System (DAS) and SATEC Machine

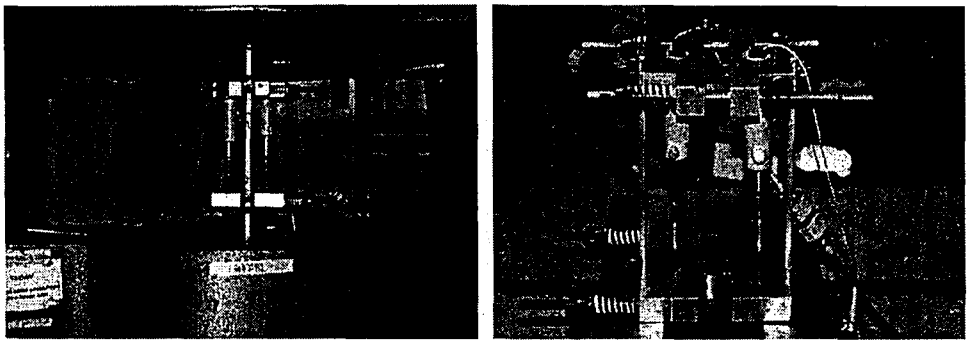

Figure 3.7 Extensometer Used for Plate-type Coupon Specimens

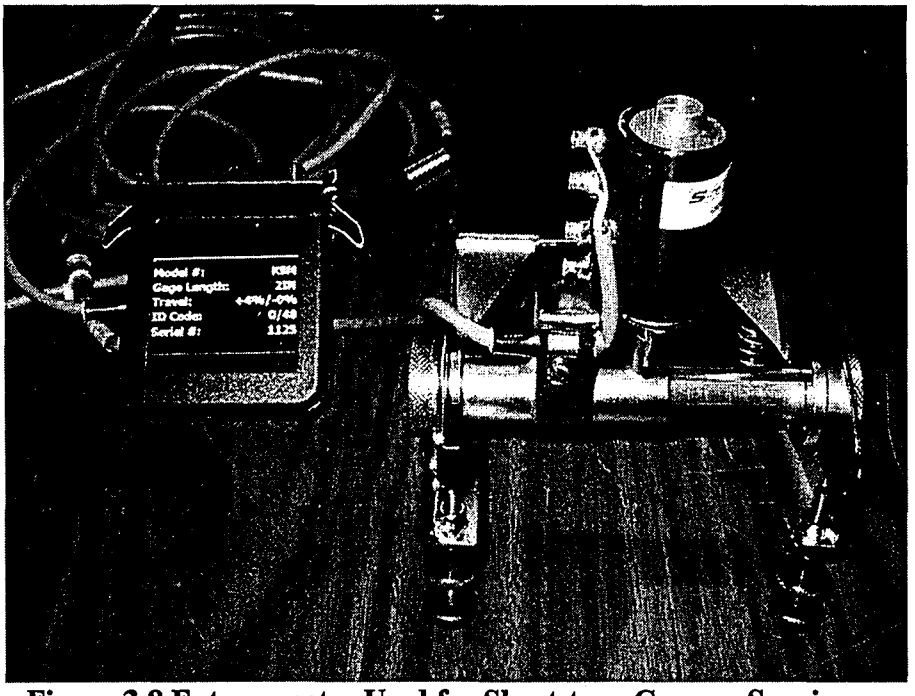

Figure 3.8 Extensometer Used for Sheet-type Coupon Specimens

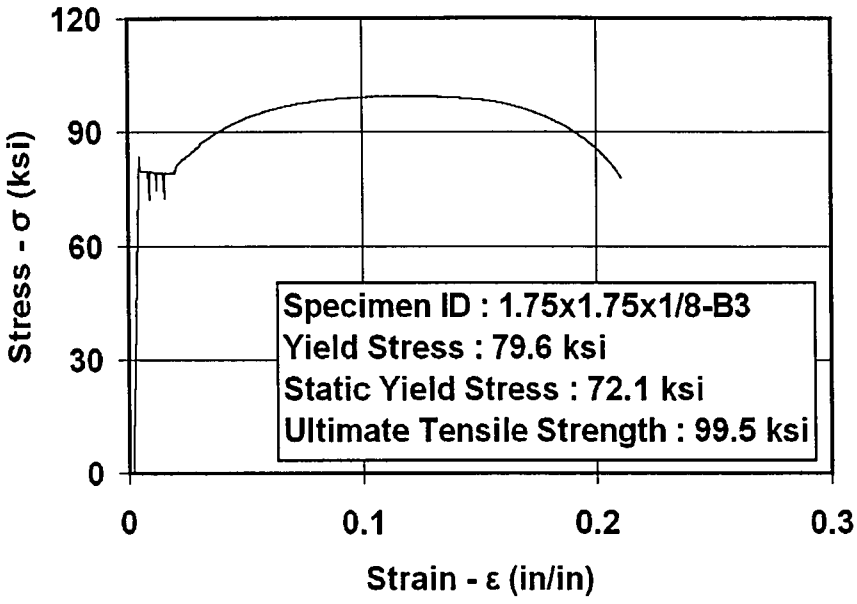

Figure 3.9 Tensile Coupon Test Result for a Sheet-Type Coupon Coupon 1.75x1.75x1/8-B3

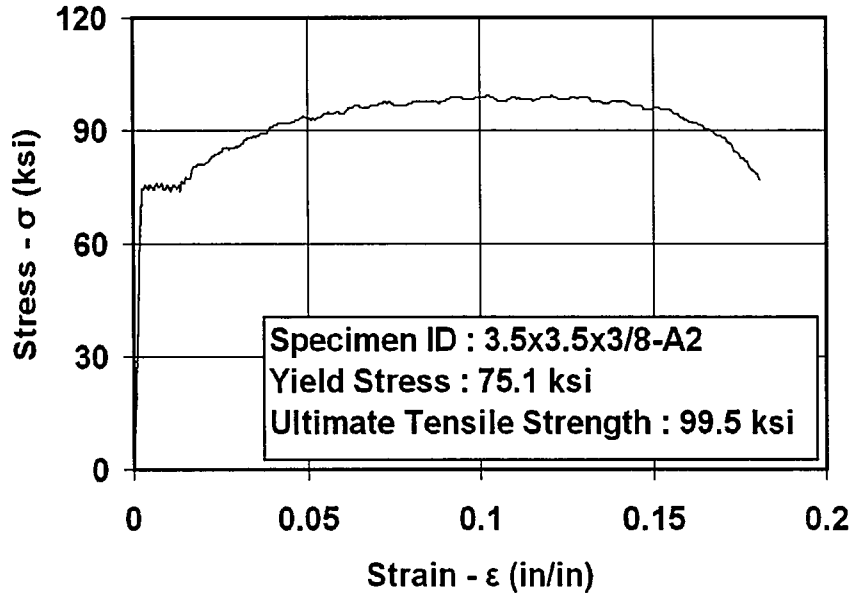

Figure 3.10 Tensile Coupon Test Result for a Plate-Type Coupon Coupon 3.5x3.5x3/8-A2

Chapter 4 Buckling Tests of Single Angle Specimens

4.0 General

This chapter addresses the experiments on the single angle specimens. First, the test matrix of specimens is presented. Then, the test set-up and related equipment are discussed. Then, the preparation of the test specimens, the initial out-of-straightness measurements of the specimens, and the instrumentation of the specimens are discussed, along with the test procedure. Then, the theoretical buckling capacities are presented. Finally, the test results are discussed.

4.1 Test Matrix

Single angle compression members are expected to fail in one of the following buckling mode shapes: flexural buckling about the weak axis; or flexural-torsional buckling involving flexural buckling about the strong axis and torsional buckling. These buckling modes are discussed in Chapter 2. The coordinate systems used to discuss the single angle specimens are presented in Figure 4.1. The predicted buckling capacities are calculated according to Chapter E of the AISC (2005) specification as described later.

The test specimens are identified in Table 4.1, along with the steel type and related parameters such as the length of the specimen. The yield stress values are also presented in this table. The yield stress values were determined from tensile coupon tests as described in Chapter 3. In Table 4.1, the rated load capacities of the bearings used for the test specimens are also presented. The bearings are referred to by their

rated load capacities. The 500 kip bearings were used for all the single angle specimens.

4.2 Test Setup

4.2.1 Test Machine

The SATEC universal testing machine at the ATLSS Center that was used for the tensile coupon tests was also used for the compression specimen tests. The machine has a 600 kip loading capacity. The SATEC load frame and controller unit are shown in Figure 4.2. The SATEC load frame consists of a cross-head, columns, and a platen which displaces when hydraulic pressure is introduced from underneath. For compression testing, the test specimen and cylindrical bearings are placed between the cross-head and the platen as shown in Figure 4.2. The SATEC controller unit includes software with built-in features such as simultaneous display of test data plots and data. The software permits automatic control and manual control during testing.

4.2.2 Cylindrical Bearings

A key parameter in the compressive strength of a column is the slenderness ratio, KL/r. The governing slenderness ratio is the slenderness ratio for buckling about the principal axis of the specimen which provides the lowest buckling strength. The compressive strength of a column is inversely related to KL/r, thus the compressive strength is controlled by the largest slenderness ratio.

The slenderness ratio includes the effective length factor, K, which depends on the end conditions of the specimen. When the ends of the column are restrained against

displacement, the K factor varies from 0.5 to 1.0. The K factor equals 1.0 when the end rotations are unrestrained (pinned-pinned conditions) and the K factor equals to 0.5 when the end rotations are fully restrained (fixed-fixed conditions). One advantage of pinned-pinned conditions is the specimen length needed to provide a given slenderness ratio is half that needed for fixed-fixed end conditions. When pinned-pinned end conditions are utilized at the ends of a specimen, the specimen will be free to rotate about one axis; however, the rotation about the perpendicular axis can be restrained. For the single angle specimens in this study, the restrained direction of rotation was the rotation about the minor principle axis of the specimens about which pure flexural buckling would occur (i.e., rotation about the x axis or weak axis, shown in Figure 4.1, is restrained).

In order to create pinned-pinned end conditions, the specimens were tested with cylindrical bearings placed at both ends of the specimens, as shown in Figure 4.3. The sign convention for rotations of the bearings is presented in Figure 4.3(b). This type of bearing was used previously in tests at Fritz Engineering Laboratory at Lehigh University. The details of the bearings are presented by Huber (1958). These bearings provide an effective column length equal to the specimen length. Figure 4.4 shows that the axial load is always applied through the instantaneous center of rotation of each bearing at the contact point of the bearing with the surface of the bearing plate attached to the cross-head or the platen. Figure 4.4 shows that the line of action of the applied load passes along a radial line through the center of the bearing. When the center of the bearing is aligned with the centroid of the end cross-section, no moment

develops at the end of the specimen (i.e., the end of the specimen is a point of zero moment). Therefore, the effective length equals the actual length of the specimen.

4.3 Test Preparation, Instrumentation, and Procedure

A procedure for column testing, which is suggested by SSRC (Galambos, 1998), was followed during the tests. This procedure is described in Technical Memorandum B4: Procedure for Testing Centrally Loaded Columns (Galambos, 1998). The memorandum suggests that some of the key factors affecting the compressive strength of a column specimen are eccentric loading, the geometric imperfections of the specimen, the residual stresses, the imperfections in the end conditions, and the method of loading. In particular, the imperfections in the end conditions were eliminated by following the procedure in the memorandum as explained in the following discussion.

4.3.1 Preparation of Test Specimens

The test specimens were cut from the same angle stock. The ends of the specimens were saw-cut square and de-burred with a grinder to maintain flatness of the end cross-sections that bear against the bearings.

4.3.2 Initial Out-of-Straightness and Other Pretest Measurements

The purpose of the pretest measurements is to measure the initial camber and initial sweep along the length of each specimen, as well as the width and thickness. Camber refers to the strong axis out-of-straightness (deflection) and sweep refers to the weak axis out-of-straightness (deflection). These deflection measurements are

usually defined for the centroid of the cross-section. Since the centroid of a single angle is not located on the legs of the cross-section of the single angle, the camber and sweep were measured at the heel of the cross-section. The procedure that was followed during the pretest measurements of the single angle specimen is described below.

As shown in Figure 4.5, measurements of the location of the angle cross-section for camber, sweep, and width were taken at 6 locations on a cross-section in the x_h' axis and y_h' axis directions, respectively. These measurements were repeated at the ends and at each quarter length of the specimen.

The devices that were used for the pretest measurements are a dial gage stand with a precision of 0.001 inches, and a caliper with a precision of 0.001 inches.

As shown in Figure 4.6, a wide flange beam with a machined surface was used to provide a reference surface for the measurements. A 1 in. thick bar with a machined edge was clamped to the beam and two 3 in. long spacer blocks were used to provide a reference for the measurements to the upstanding leg of the specimen (i.e., the bar is used for the measurements in y_h' axis direction). These spacer blocks are bearing against both the 1 in. thick bar and the ends of the specimen as shown in Figure 4.6.

For the measurements in x_h' axis direction, three spacer blocks were utilized such that by locating these blocks underneath the specimen, measurements could be taken with reference to the surface of the beam as shown in Figure 4.6. Two of these spacer blocks were placed under the end cross-sections of the specimen, and the third block

was placed in between. Because of this arrangement of three spacer blocks, for some of the test specimens, a chord drawn between the two end cross-sections was not parallel to the machined beam surface. This issue was resolved by a linear adjustment of the measurements relative to a chord drawn to the end cross-sections.

All thickness and width measurements of legs were directly taken by calipers. Three thickness measurements were taken from each leg of the end cross-sections of the single angle specimen, as shown in Figure 4.5. The average of these three measurements for a leg is reported as the thickness of that leg. The pretest measurements of the width and thickness of the specimens, and the corresponding cross-section parameters are presented in Table 4.2. The cross-section parameters were also calculated from the nominal width and thickness and are presented in Table 4.3.

After the measurements were taken, deflections in x_h' axis and y_h' axis directions were transformed into x_h axis and y_h axis direction deflections and reported as the initial out-of-straightness measurements, Δx_{h0} and Δy_{h0}. These measurements are reported in Table 4.4, where Δx_{h0} is the sweep measurement and Δy_{h0} is the camber measurement. Bjorhovde (1972) suggests a model for the initial out-of-straightness that is a half sine wave over the length of a column with a maximum initial out-of-straightness value of 1/1470 of the length of the column at the mid-height cross-section.

In Table 4.4 the initial out-of-straightness measurements are both presented at the mid-height cross-section and at the cross-section where these measurements reach their maximum values. It is noted that only the slender specimens, SA2 and SB2, have a maximum initial out-of-straightness values in the y_h axis direction that is larger than the suggested value of L/1470. The initial out-of-straightness measurements in both the x_h axis and the y_h axis directions along the length of the other single angle specimens are presented in the test results sections for each specimen.

4.3.3 Instrumentation

According to Technical Memorandum B4 (Galambos, 1998), the test data should include the applied load, the lateral deflection, the twist of the critical cross-section, the axial shortening, and strain data. The applied load and the cross-head displacement of the SATEC test machine were determined from the SATEC test machine output. Appendix B explains how the axial shortening of the specimens was determined from the cross-head displacement. The other measurements were acquired using an external data acquisition system.

For pin ended columns, the mid-height cross-section is assumed to be the critical section, thus deflection measurements are taken at this cross-section as shown in Figure 4.7. As shown in Figure 4.3, an inclinometer was placed on each bearing to measure the rotation of the bearing.

Seven strain gages were placed near the mid-height cross-section as shown in Figure 4.8. The strain gages were generally placed back-to-back to account for local

bending of the cross-section as shown in Figure 4.8. For example, SG-5 and SG-6 are back-to-back.

LVDTs were attached to the mid-height cross-section using four 1/16 in. diameter holes that were drilled at the locations shown in Figure 4.9. The wire of each LVDT passed through one of these holes, and was attached to a small nut on the far side of the angle leg so that the wire stays attached throughout the test.

Four LVDTs were used to measure the lateral deflection at the mid-height cross-section. The lateral deflection is measured and reported as the deflection of the heel of the single angle specimens. The reported deflections are in x_h axis and y_h axis directions. Figure 4.9 shows the pattern of the LVDTs. As this figure shows, LVDT2 and LVDT4 were used to take measurements at 1/8 in. plus the thickness of a leg from the heel of the cross-section. The length of the LVDTs was intentionally made long enough so that the measurements acquired from these two LVDTs could be assumed to be taken at the heel of the cross-section.

In order to calculate the lateral deflections, the Law of Sines and the Law of Cosines are utilized. The displaced position of the heel from the initial position of the heel was found using the data from LVDT2 and LVDT4 and utilizing the following equations which refer to Figure 4.10.

The Law of Cosines states that:

$$L_{2-4}{}^2 = (L2+\Delta 2)^2 + (L4+\Delta 4)^2 - 2\times(L2+\Delta 2)\times(L4+\Delta 4)\times COS(\theta 3') \quad (4.1)$$

where

$L_{2\text{-}4}$: the distance between the attachment points of LVDT2 and LVDT4

L2 : the initial distance between the attachment points of LVDT2

Δ2 : the length change measured by LVDT2 at a displaced position of the cross-section

L4 : the initial distance between the attachment points of LVDT4

Δ4 : the length change measured by LVDT4 at a displaced position of the cross-section

θ3' : the angle between LVDT2 and LVDT4 wires at their attachments to the cross-section, where θ3 is the initial angle

The Law of Sines states that;

$$\frac{(L4+\Delta 4)}{SIN(\theta 4')} = \frac{(L2+\Delta 2)}{SIN(\theta 2')} = \frac{L_{2\text{-}4}}{SIN(\theta 3')} \qquad \textbf{(4.2)}$$

θ2' : the angle between LVDT2 and the line connecting LVDT2 and LVDT4 at a displaced position of the cross-section, where θ2 is the initial angle

θ4' : the angle between LVDT4 and the line connecting LVDT4 and LVDT2 at a displaced position of the cross-section, where θ4 is the initial angle

By utilizing Equations (4.1) and (4.2), one can find angle θ2' (or angle θ4') as the cross-section displaces. Then, the lateral deflections are obtained as follows:

$$X_{h0} = (L2) \times COS(\theta 4)$$
$$Y_{h0} = (L2) \times SIN(\theta 4)$$
$$X_{hi} = (L2 + \Delta 2) \times COS(\theta 4')$$
$$Y_{hi} = (L2 + \Delta 2) \times SIN(\theta 4')$$
$$\Delta X_h = X_{hi} - X_{h0}$$
$$\Delta Y_h = Y_{hi} - Y_{h0}$$
$$\Delta x_h = \Delta X_h$$
$$\Delta y_h = \Delta Y_h$$

(4.3)

where ΔX_h and ΔY_h are the relative lateral deflections of the heel relative to the initial position of the heel (X_{ho}, Y_{ho}), in the (X,Y) coordinate system defined in Figure 4.10.

The twist of the mid-height cross-section, θ_z, was found using the data from LVDT1 and LVDT3 and utilizing the following equations which refer to Figure 4.11.

As seen in Figure 4.11, the center line of each leg was taken to represent the leg. The rotations of both legs were utilized in the twist calculations as follows:

$$\theta_1 = \frac{\sqrt{(L1 - \Delta x_h')^2 + (\Delta y_h')^2} - (L1 + \Delta 1)}{L_1}$$
$$\theta_2 = \frac{(L3 + \Delta 3) - \sqrt{(L3 - \Delta y_h')^2 + (\Delta x_h')^2}}{L_3}$$

(4.4)

Equation (4.4) is derived using Pythagorean theorem, where

L_1 : the distance between the heel and the attachment point of LVDT1

L_3 : the distance between the heel and the attachment point of LVDT3

L1 : the initial distance between the attachment points of LVDT1

L3 : the initial distance between the attachment points of LVDT3

$\Delta 1$: the length change measured by LVDT1 at a displaced position of the cross-section

$\Delta 3$: the length change measured by LVDT3 at a displaced position of the cross-section

θ_1 : the rotation of the left leg on Figure 4.11

θ_2 : the rotation of the right leg on Figure 4.11

$\Delta x_h'$: the lateral deflection of the heel in the x_h' axis direction at a displaced position of the cross-section

$\Delta y_h'$: the lateral deflection of the heel in the y_h' axis direction at a displaced position of the cross-section

Then the twist of the cross-section is found by following equation:

$$\theta_z = \frac{\theta_1 + \theta_2}{2} \tag{4.5}$$

It should be noted that this method is not accurate as the twist becomes large. Table 4.5 provides a summary of the instrumentation used to acquire data for the single angle specimens.

4.4 Test Procedure

After each specimen was placed between the bearings, a small initial load was applied while the specimen was aligned. The initial load was gradually increased to approximately 1/20 of the predicted load capacity of the specimen. Then the data acquisition was initiated and further loading was applied to the specimen. In the first (linear elastic) phase of loading, the load was controlled by nominal stress (load divided by area) per unit time and the value of the loading rate was approximately 3 ksi/min. After the applied load reached half of the predicted buckling load, further loading was controlled by a nominal strain (cross-head displacement divided by specimen length) rate that corresponds very approximately to the initial stress loading rate during the linear elastic range. This loading rate was 0.01 in/min and was kept constant until the end of the test.

4.5 Predicted Buckling Capacities of the Single Angle Specimens

The predicted buckling capacities, which are based on the measured and also the nominal width and thickness measurements, are presented in Table 4.6. A comparison of these results in Table 4.7 shows that the predicted buckling capacities based on the measured dimensions are within a few percent of the predicted capacities based on the nominal dimensions. In Table 4.8, the predicted buckling capacities are presented along with the Q reduction factor and the slenderness ratios for the principle axes. P_Y in Table 4.8 is the yield strength of the specimen, found by multiplying the measured yield stress value from the tensile coupon tests (Chapter 3) with the cross-sectional area. The measured yield stress values were used for all the calculated results in Table

4.8. For all the calculated results given in Table 4.8, the measured cross-sectional dimensions were utilized.

In order to find the predicted flexural buckling capacity about the strong axis (i.e., the y axis) the following steps are followed: (1) the elastic critical buckling stress about the strong axis, $F_{e\text{-}y}$, was found from Equation E4-10 of the AISC (2005) specification (Equation 2-24 in Chapter 2); (2) the flexural buckling stress about strong axis, $F_{cr\text{-}y}$, was found from Section E7 and Equations E7-2 (Equation 2-22) and E7-3 (Equation 2-23); (3) the flexural buckling stress value was multiplied by the cross-sectional area of the specimen to determine the nominal compressive strength based on the limit state of flexural buckling about the strong axis, $P_{cr\text{-}y}$. In this study, $P_{cr\text{-}y}$ is referred to as the predicted flexural buckling capacity about the strong axis. Similar steps were used to find the predicted buckling capacity about the weak axis (i.e., the x axis), $P_{cr\text{-}x}$.

In order to find the predicted flexural-torsional buckling capacity the following steps are followed: (1) the elastic critical buckling stress about the strong axis, $F_{e\text{-}y}$, was found from Equation E4-10 (Equation 2-33) and the elastic critical buckling stress about the z axis, $F_{e\text{-}z}$, was found from Equation E4-11 (Equation 2-34) of the AISC (2005) specification; (2) the flexural-torsional elastic buckling stress, $F_{e\text{-}ft}$ was found from Equation E4-5 (Equation 2-32); (3) the flexural-torsional buckling stress, $F_{cr\text{-}ft}$, was found from Section E7 and Equations E7-2 (Equation 2-30) and E7-3 (Equation 2-31); (4) the flexural-torsional buckling stress, $F_{cr\text{-}ft}$, value found in previous step was

multiplied by the cross-sectional area of the specimen to determine the flexural-torsional buckling capacity, $P_{cr\text{-}ft}$.

As seen from Table 4.8, the slenderness values for the principal axes directions are very close to each other. Thus, the predicted flexural buckling capacities about the x axis and the y axis are very close.

On the other hand, the predicted flexural-torsional buckling capacity is smaller than either of the predicted flexural buckling capacities (i.e., about the weak axis or the strong axis). As a result, the single angle specimens are expected to buckle in the flexural-torsional buckling mode.

4.6 Test Results

4.6.1 Specimen SA1

The load vs. the cross-head displacement is shown in Figure 4.12. The maximum experimental load, P_{EXP}, is higher than both the predicted flexural-torsional buckling capacity, $P_{cr\text{-}ft}$, and the predicted flexural buckling capacity about the strong axis, $P_{cr\text{-}y}$. The experimental load is also higher than the yield load, P_Y. Thus, the P_{EXP}/P_Y ratio is greater than 1.0 which is an indication of plastic buckling.

Figure 4.13 presents the graph of the load vs. the specimen shortening. The specimen shortening was determined from the cross-head displacement as described in Appendix B.

Twist of the mid-height cross-section is shown in Figure 4.14. This figure indicates there is no apparent torsional deformation before the peak load level,

however, the deformation starts at peak load and continues to grow in the post-peak region. Figure 4.15 shows the load vs. the rotation of the bearings. This figure shows that there is no observable rotation before the peak load level. As Figure 4.16 shows, the x_h axis lateral deflection is much larger than the y_h axis lateral deflection at the mid-height cross-section in the post-peak region. There is no noticeable deflection observed before the peak load level.

Figure 4.17 shows the load vs. the strain separation data acquired near the mid-height cross-section. As seen from this figure, there isn't any apparent separation of strain measurements between the back-to-back strain gages before the peak load level. This indicates that local plate buckling was not observed at the mid-height cross-section, where the strain gages were placed, before the peak load level was reached. This indication is consistent with visual observations.

Compared to the other single angle specimens, Specimen SA1 has the lowest value of the maximum initial out-of-straightness in the strong axis direction, Δy_{h0}, as shown in Table 4.4. The initial out-of-straightness along the length of the specimen is shown in Figure 4.18.

The torsional deformation and the lateral deflection in the x_h axis direction, Δx_h, at the mid-height cross-section both grow simultaneously in the post-peak region, which is an indication of the flexural-torsional buckling mode. Thus, the specimen buckled in the expected mode shape. The buckled shape of the specimen after peak load is shown in Figure 4.19. The twist and lateral deflection at the mid-height of the specimen can

be seen in this figure.

4.6.2 Specimen SA2

The load vs. the cross-head displacement is shown in Figure 4.20. The maximum experimental load, P_{EXP}, is higher than both the predicted flexural-torsional buckling capacity, $P_{cr\text{-}ft}$, and the predicted flexural buckling capacity about the strong axis, $P_{cr\text{-}y}$.

Figure 4.21 presents the graph of the load vs. the specimen shortening, which was determined from the cross-head displacement as described in Appendix B.

Twist of the mid-height cross-section is shown in Figure 4.22. As seen from this figure there is some noticeable torsional deformation observed before the peak load level, which continues to grow in the post-peak region. Figure 4.23 shows the load vs. the rotation of the bearings. This figure indicates that the bearing rotations start very early in the test and continue to grow throughout the test. As Figure 4.24 indicates, there is some observable lateral deflection observed in both the weak axis, x_h, and the strong axis, y_h, directions. As seen in Table 4.4, the initial out-of-straightness value for the strong axis (y_h) direction is the largest compared to the other single angle specimens, and it has a value that is almost twice the value for the weak axis direction. The large initial out-of-straightness may be the reason for the significant y_h axis deflection during the test.

Figure 4.25 shows the load vs. the strain separation data acquired near the mid-height cross-section. As seen from this figure, a separation of strain measurements between the back-to-back strain gages SG 5&6 initiates before the peak load is

reached. This shows that local plate bending occurred at the mid-height cross-section before the peak load.

The initial out-of-straightness along the length of the Specimen SA2 is shown in Figure 4.26. This figure shows that the maximum initial out-of-straightness for both directions is at a cross-section other than the mid-height cross-section.

The torsional deformation and the lateral deflection in the x_h axis direction at the mid-height cross-section grow simultaneously throughout the test which is an indication of the flexural-torsional buckling mode. On the other hand, there is some noticeable lateral deflection in the strong axis direction. The specimen appears to have buckled in the expected mode shape accompanied by lateral deflection in the strong axis direction. There is no available photo for this test specimen.

4.6.3 Specimen SA3

The load vs. the cross-head displacement is shown in Figure 4.27. The maximum experimental load, P_{EXP}, is higher than the predicted flexural-torsional buckling capacity, $P_{cr\text{-}ft}$, and 1% less than the predicted flexural buckling capacity about the strong axis, $P_{cr\text{-}y}$.

Figure 4.28 presents the graph of the load vs. the specimen shortening, which was determined from the cross-head displacement as described in Appendix B.

Twist of the mid-height cross-section is shown in Figure 4.29. This figure indicates that the torsional deformation starts just before the peak load and continue to grow in the post-peak region. Figure 4.30 indicates the load vs. the rotation of the

bearings. As seen from this figure, the bearing rotations start before the peak load and continue to grow in the post-peak region. As Figure 4.31 shows that there is very little lateral deflection in the y_h axis direction in the post-peak region, while the x_h axis lateral deflection starts to grow at the peak load level and is much larger than the y_h axis lateral deflection in the post-peak region. As seen in Figure 4.31, there is no observable lateral deflection occur before the peak load level.

Figure 4.32 shows the load vs. the strain separation data acquired near the mid-height cross-section. As seen from this figure, there is a separation of strain measurements between the back-to-back strain gages SG 5&6 and SG 2&3 before the peak load. This shows that local plate bending occurred at the mid-height cross-section before the peak load.

The initial out-of-straightness along the length of the specimen SA3 is shown in Figure 4.33. The maximum initial out-of-straightness for both directions is at a cross-section other than the mid-height cross-section.

During the tests the torsional deformation starts just before the peak load level is reached when there is no apparent lateral deflection. On the other hand, the torsional deformation is accompanied by lateral deflection in the x_h axis direction in the post-peak region where both deformations grow simultaneously, which is an indication of the flexural-torsional buckling mode. Thus, the specimen buckled in the expected mode shape. The buckled shape of the specimen after peak load is shown in Figure 4.34.

4.6.4 Specimen SB1

The load vs. the cross-head displacement is shown in Figure 4.35. The maximum experimental load, P_{EXP}, is higher than both the predicted flexural-torsional buckling capacity, $P_{cr\text{-}ft}$, and predicted flexural buckling capacity about the strong axis, $P_{cr\text{-}y}$.

Figure 4.36 presents the graph of the load vs. the specimen shortening, which was determined from the cross-head displacement as described in Appendix B.

Twist of the mid-height cross-section is shown in Figure 4.37. As seen from this figure, there is a large torsional deformation observed before the peak load level. Figure 4.38 shows the load vs. the rotation of the bearings. The bearing rotations start before the peak load level and continue to grow in the post-peak region. As Figure 4.39 shows, there is no apparent lateral deflection in the y_h axis direction before the peak load, while, there is some deflection is observed in the x_h axis direction before the peak load level. The x_h axis lateral deflection is larger than the y_h axis lateral deflection in the post-peak region.

Figure 4.40 shows the load vs. the strain separation data acquired near the mid-height cross-section. As seen from this figure, there is a noticeable separation of strain measurements between all the back-to-back strain gages SG 1&4, SG 2&3, and SG 5&6 before the peak load. This shows that local plate bending occurred at the mid-height cross-section before the peak load. Figure 4.42 shows that there is a noticeable local plate bending occurred at a cross-section near the mid-height cross-section.

The initial out-of-straightness along the length of the specimen is shown in Figure

4.41. Table 4.4 shows that the out-of-straightness for this specimen was rather small.

During the test the torsional deformation was accompanied by lateral deflection in the x_h axis direction and started before the peak load was reached and continued in the post-peak region. These deformations are an indication of the flexural-torsional buckling mode. Thus, the specimen buckled in the expected mode shape with an observable local plate bending near the mid-height cross-section. The buckled shape of the specimen after peak load is shown in Figure 4.42.

4.6.5 Specimen SB2

The load vs. the cross-head displacement is shown in Figure 4.43. The maximum experimental load, P_{EXP}, is higher than both the predicted flexural-torsional buckling capacity, $P_{cr\text{-}ft}$, and the predicted flexural buckling capacity about the strong axis, $P_{cr\text{-}y}$.

Figure 4.44 presents the graph of the load vs. the specimen shortening, which was determined from the cross-head displacement as described in Appendix B.

Twist of the mid-height cross-section is shown in Figure 4.45. This figure indicates that a large torsional deformation occurred near the peak load level. Figure 4.46 shows the load vs. the rotation of the bearings. There are some noticeable bearing rotations observed before the peak load level. As Figure 4.47 indicates, there is some lateral deflection in the x_h axis direction near the peak load level, which continues to increase in the post-peak region. On the other hand, there is only a small lateral deflection in the y_h axis direction before the peak load level.

Figure 4.48 shows the load vs. the strain separation data acquired near the mid-

height cross-section. As seen from this figure, a separation of strain measurements between the back-to-back strain gages SG 2&3 initiated close to the peak load.

The initial out-of-straightness along the length of the specimen is shown in Figure 4.49. In the strong axis direction, the maximum initial out-of-straightness is at a cross-section other than the mid-height cross-section.

During the tests, the torsional deformation and the lateral deflection in the x_h axis direction at the mid-height cross-section both grow simultaneously near the peak load level, and they both continue to increase in the post-peak region, which is an indication of the flexural-torsional buckling mode. Thus, the specimen appears to have buckled in the expected mode shape. The buckled shape of the specimen after peak load is shown in Figure 4.50.

4.6.6 Specimen SB3

The load vs. the cross-head displacement for Specimen SB3 is shown in Figure 4.51. The maximum experimental load, P_{EXP}, is higher than both the predicted flexural-torsional buckling capacity, $P_{cr\text{-}ft}$, and the predicted flexural buckling capacity about the strong axis, $P_{cr\text{-}y}$.

Figure 4.52 presents the graph of the load vs. the specimen shortening, which was determined from the cross-head displacement as described in Appendix B.

Twist of the mid-height cross-section is shown in Figure 4.53. This figure shows that there is no apparent torsional deformation before the peak load level. Torsional deformation occurred at the peak load level and continued to grow in the post-peak

region. Figure 4.54 shows the load vs. the rotation of the bearings. This figure shows no observable bearing rotations occurred before the peak load level. Figure 4.55 indicates that the lateral deflection at the mid-height cross-section is not observed for both directions before the peak load is reached. On the other hand, in the post-peak region, some lateral deflection observed. The x_h axis lateral deflection is much larger than the y_h axis lateral deflection in the post-peak region.

Figure 4.56 shows the load vs. the strain separation data acquired near the mid-height cross-section. As seen from this figure, there is no apparent separation of strain measurements between the back-to-back strain gages before the peak load. Therefore, local plate bending was not observed at the mid-height cross-section before the peak load. For this particular specimen, local plate bending occurred at a cross-section other than the mid-height cross-section, as shown in Figure 4.58.

The initial out-of-straightness along the length of the specimen is shown in Figure 4.57. This figure indicates that the maximum initial out-of-straightness in both axis directions occur at the mid-height cross-section.

The buckled shape of the specimen after peak load is shown in Figure 4.58. During the test, the torsional deformation and lateral deflection in the x_h axis direction both grow simultaneously in the post-peak region, which is an indication of the flexural-torsional buckling mode. Thus, the specimen buckled in the expected mode shape with an apparent local plate bending near the mid-height cross-section.

4.7 Discussion of Results

In Table 4.9, the test results are compared with the predicted flexural buckling capacity about the strong axis, P_{cr-y}, and the predicted flexural-torsional buckling capacity, P_{cr-ft}, based on the measured dimensions. As seen in this table, the test results, P_{EXP}, have better agreement with the predicted capacity P_{cr-y}. The average ratio of P_{EXP} to P_{cr-y} was found to be 1.08 with a standard deviation of 0.04, while the average ratio of P_{EXP} to P_{cr-ft} is 1.45 with a standard deviation of 0.21.

The test results are compared to P_{cr-y} and P_{cr-ft} in Figure 4.59. This figure shows that the AISC specification provisions for the flexural-torsional capacity, P_{cr-ft}, of single angle columns are conservative for both the Vanadium and Grade 50 steel specimens. In the same figure, it can be observed that test results are very close to the predicted flexural buckling capacity about the strong axis, P_{cr-y}, even though the observed buckling mode for all the single angle specimens was the flexural-torsional buckling mode.

The ratio of P_{EXP} to P_{cr-ft} vs. the Q reduction factor is shown in Figure 4.60. It can be seen from this figure that as the Q reduction factor is smaller; the P_{EXP}/P_{cr-ft} ratio is greater, which shows that the provisions in the AISC specification are increasingly conservative as the cross-section slenderness increases.

In Figure 4.61 and Figure 4.62, the test results are compared with the predicted buckling stresses F_{cr-y} and F_{cr-ft} for the Vanadium steel specimens, in addition to the yield stress, F_Y, the yield stress multiplied by the Q reduction factor, QF_Y, and the

elastic flexural-torsional buckling stress, $F_{e\text{-}ft}$.

A comparison of P_{EXP} vs. the axial yield strength, P_Y, the yield capacity multiplied by the Q reduction factor, QP_Y, and the elastic flexural-torsional buckling capacity, $P_{e\text{-}ft}$, for each of the specimens is also included in Table 4.9. Figures 4.61 and 4.62 show that the AISC (2005) specification provisions for the flexural-torsional buckling stress $F_{cr\text{-}ft}$ govern and that the test results are consistently well above this predicted capacity.

For the cases with the smaller KL/r value (SA1 and SB1), the test results exceed the product QF_y. For the SB cases, with the smaller values of Q, the test results are well above the predicted flexural-torsional buckling capacity $F_{cr\text{-}ft}$.

Table 4.1 Test Matrix for Single Angle Specimens

Specimen ID	Steel Type	Specimen Size	Bearing Capacity	Measured Yield Stress	Length
		in.×in.× in.	kips	ksi	in.
SA1	Vanadium	L3.5x3.5x3/8	500	73.7	24
SA2	Vanadium	L3.5x3.5x3/8	500	73.7	60
SA3	Grade 50	L3.5x3.5x3/8	500	65.0	24
SB1	Vanadium	L3x3x3/16	500	77.5	24
SB2	Vanadium	L3x3x3/16	500	77.5	48
SB3	Grade 50	L3x3x3/16	500	60.2	24

Table 4.2 Cross-sectional Properties Based on Measured Dimensions for Width and Thickness

Specimen ID	b_1	b_2	t_1	t_2	F_y	L	A_g	tan(α)	I_x	I_y	r_x	r_y	r_z	C_w	J	y_o	r_o^2	H
	in.	in.	in.	in.	ksi	in.	in^2		in^4	in^4	in.	in.	in.	in^6	in^4	in.	in^2	
SA1	3.487	3.570	0.377	0.372	73.7	23.94	2.50	0.96	1.20	4.67	0.69	1.37	0.69	0.109	0.117	1.18	3.74	0.628
SA2	3.495	3.581	0.379	0.372	73.7	59.97	2.52	0.96	1.21	4.72	0.69	1.37	0.69	0.111	0.118	1.18	3.75	0.628
SA3	3.506	3.610	0.378	0.375	65.0	24.97	2.54	0.94	1.24	4.82	0.70	1.38	0.70	0.113	0.120	1.19	3.80	0.628
SB1	2.979	2.961	0.196	0.191	77.5	23.97	1.11	0.98	0.39	1.53	0.59	1.17	0.59	0.010	0.014	1.02	2.76	0.626
SB2	2.969	2.990	0.186	0.192	77.5	47.95	1.09	0.97	0.38	1.51	0.59	1.18	0.59	0.009	0.013	1.02	2.78	0.626
SB3	3.021	3.003	0.189	0.188	60.2	23.94	1.10	0.99	0.39	1.56	0.60	1.19	0.60	0.009	0.013	1.03	2.84	0.626

Table 4.3 Cross-sectional Properties Based on Nominal Dimensions for Width and Thickness

Specimen ID	b_1	b_2	t_1	t_2	F_y	L	A_g*	tan(α)*	I_x**	I_y**	r_x**	r_y**	r_z*	C_w*	J*	y_o**	r_o^2**	H**
	in.	in.	in.	in.	ksi	in.	in^2		in^4	in^4	in.	in.	in.	in^6	in^4	in.	in^2	
SA1	3.500	3.500	0.375	0.375	73.7	24.00	2.48	1.00	1.17	4.55	0.69	1.35	0.68	0.106	0.116	1.15	3.67	0.629
SA2	3.500	3.500	0.375	0.375	73.7	60.00	2.48	1.00	1.17	4.55	0.69	1.35	0.68	0.106	0.116	1.15	3.67	0.629
SA3	3.500	3.500	0.375	0.375	65.0	24.00	2.48	1.00	1.17	4.55	0.69	1.35	0.68	0.106	0.116	1.15	3.67	0.629
SB1	3.000	3.000	0.1875	0.1875	77.5	24.00	1.09	1.00	0.37	1.37	0.59	1.12	0.59	0.009	0.013	1.02	2.82	0.626
SB2	3.000	3.000	0.1875	0.1875	77.5	48.00	1.09	1.00	0.37	1.37	0.59	1.12	0.59	0.009	0.013	1.02	2.82	0.626
SB3	3.000	3.000	0.1875	0.1875	60.2	24.00	1.09	1.00	0.37	1.37	0.59	1.12	0.59	0.009	0.013	1.02	2.82	0.626

* tabulated value in AISC Manual (LRFD, 2005)

** calculated by using nominal dimensions

Table 4.4 Initial Imperfection in Principal Axis Directions

Specimen ID	L/1470	Mid-height out-of-straightness		Maximum out-of-straightness	
		Δx_{h0} (in.)	Δy_{h0} (in.)	Δx_{h0} (in.)	Δy_{h0} (in.)
SA1	0.0163	0.0011	0.0117	0.0012	0.0117
SA2	0.0408	-0.0163	0.0346	0.0219	0.0424
SA3	0.0163	0.0053	0.0060	0.0083	0.0060
SB1	0.0163	-0.0007	0.0035	0.0018	0.0035
SB2	0.0327	0.0067	0.0258	0.0067	0.0331
SB3	0.0163	0.0057	0.0099	0.0057	0.0099

Table 4.5 Instrumentation and Measurements

Data	Unit	Instrumentation	Notes : Measurement / Placement
P	kips	SATEC	Axial load
δ	in	SATEC	Cross-head displacement
Δ_1	in	LVDT	Displacement at mid-height cross-section
Δ_2	in	LVDT	Displacement at mid-height cross-section
Δ_3	in	LVDT	Displacement at mid-height cross-section
Δ_4	in	LVDT	Displacement at mid-height cross-section
θ_1	degree	Inclinometer	Top bearing rotation
θ_2	degree	Inclinometer	Bottom bearing rotation
ε_1	microstrain	Strain Gage	Strain at mid-height cross-section
ε_2	microstrain	Strain Gage	Strain at mid-height cross-section
ε_3	microstrain	Strain Gage	Strain at mid-height cross-section
ε_4	microstrain	Strain Gage	Strain at mid-height cross-section

Table 4.6 Predicted Capacities Based on Measured vs. Nominal Cross-sectional Properties

Specimen ID	$P_Y^{[1]}$	$P_{cr\text{-}x}^{[1]}$	$P_{cr\text{-}y}^{[1]}$	$P_{cr\text{-}ft}^{[1]}$	$P_{e\text{-}ft}^{[1]}$	$P_Y^{[2]}$	$P_{cr\text{-}x}^{[2]}$	$P_{cr\text{-}y}^{[2]}$	$P_{cr\text{-}ft}^{[2]}$	$P_{e\text{-}ft}^{[2]}$
	kips	kips	kips	kips	kips	kips	kips	kips	kips	kips
SA1	184.4	175.5	175.4	144.8	338.8	182.8	174.2	174.0	144.4	342.3
SA2	185.4	149.5	148.7	130.6	229.1	182.8	147.0	146.1	128.9	226.0
SA3	164.9	160.4	160.2	134.8	341.7	161.2	156.9	156.7	132.6	342.3
SB1	86.2	59.3	59.3	38.9	56.3	84.5	58.2	58.1	36.6	50.8
SB2	84.5	52.7	52.6	35.5	47.7	84.5	52.7	52.7	35.0	46.5
SB3	66.1	50.6	50.6	34.1	51.4	65.6	50.1	50.1	33.7	50.8

[1]: capacities based on measured cross-sectional properties
[2]: capacities based on nominal cross-sectional properties

Table 4.7 Comparison of Predicted Capacities Based on Measured and Nominal Cross-sectional Properties

Specimen ID	$P_Y^{[1]}/P_Y^{[2]}$	$P_{cr\text{-}x}^{[1]}/P_{cr\text{-}x}^{[2]}$	$P_{cr\text{-}y}^{[1]}/P_{cr\text{-}y}^{[2]}$	$P_{cr\text{-}ft}^{[1]}/P_{cr\text{-}ft}^{[2]}$	$P_{e\text{-}ft}^{[1]}/P_{e\text{-}ft}^{[2]}$
SA1	1.01	1.01	1.01	1.00	0.99
SA2	1.01	1.02	1.02	1.01	1.01
SA3	1.02	1.02	1.02	1.02	1.00
SB1	1.02	1.02	1.02	1.06	1.11
SB2	1.00	1.00	1.00	1.01	1.03
SB3	1.01	1.01	1.01	1.01	1.01

[1]: capacities based on measured cross-sectional properties
[2]: capacities based on nominal cross-sectional properties

Table 4.8 Predicted Buckling Capacities

Specimen ID	K_x	K_y	$(KL/r)_x$	$(KL/r)_y$	Q	P_Y*	P_{cr-x}*	P_{cr-y}*	P_{cr-ft}*	P_{e-ft}*
						kips	kips	kips	kips	kips
SA1	0.5	1.0	17.3	17.6	0.98	184.4	175.5	175.4	144.8	338.8
SA2	0.5	1.0	43.2	43.8	0.98	185.4	149.5	148.7	130.6	229.1
SA3	0.5	1.0	17.2	17.4	1.00	164.9	160.4	160.2	134.8	341.7
SB1	0.5	1.0	20.3	20.4	0.71	86.2	59.3	59.3	38.9	56.3
SB2	0.5	1.0	40.5	40.7	0.71	84.5	52.7	52.6	35.5	47.7
SB3	0.5	1.0	20.1	20.2	0.79	66.1	50.6	50.6	34.1	51.4

* capacities based on measured cross-sectional properties

Table 4.9 Experimental Test Results vs. Predicted Buckling Capacities

Specimen ID	P_{EXP}	P_{EXP}/P_{cr-y}	P_{EXP}/P_{cr-ft}	P_{EXP}/P_Y	P_{EXP}/QP_Y	P_{EXP}/P_{e-ft}
	kips	kips	kips	kips	kips	kips
SA1	187.9	1.07	1.30	1.02	1.04	0.55
SA2	162.1	1.09	1.24	0.87	0.89	0.71
SA3	159.1	0.99	1.18	0.96	0.96	0.47
SB1	67.5	1.14	1.74	0.78	1.10	1.20
SB2	56.7	1.08	1.60	0.67	0.95	1.19
SB3	55.5	1.10	1.63	0.84	1.06	1.08
Average		1.08	1.45	0.86	1.00	0.87
Standard Deviation		0.04	0.21	0.11	0.07	0.30

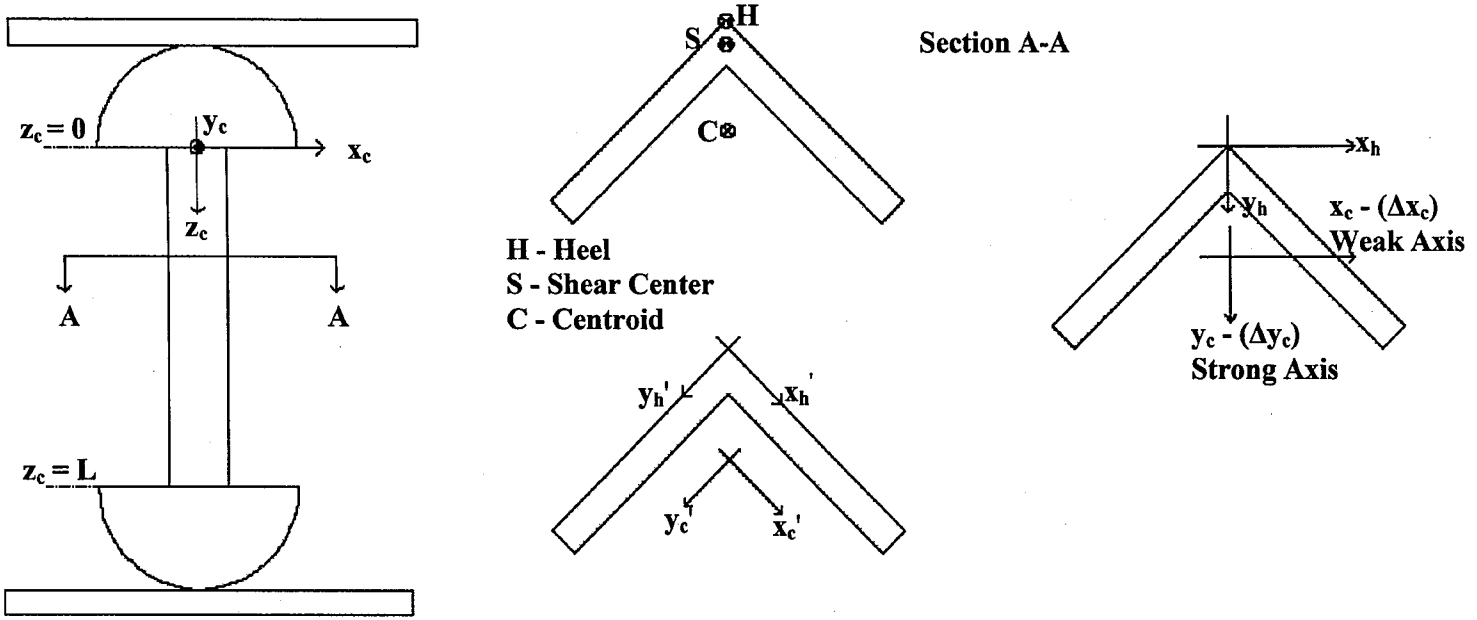

Figure 4.1 Coordinate Axis Systems

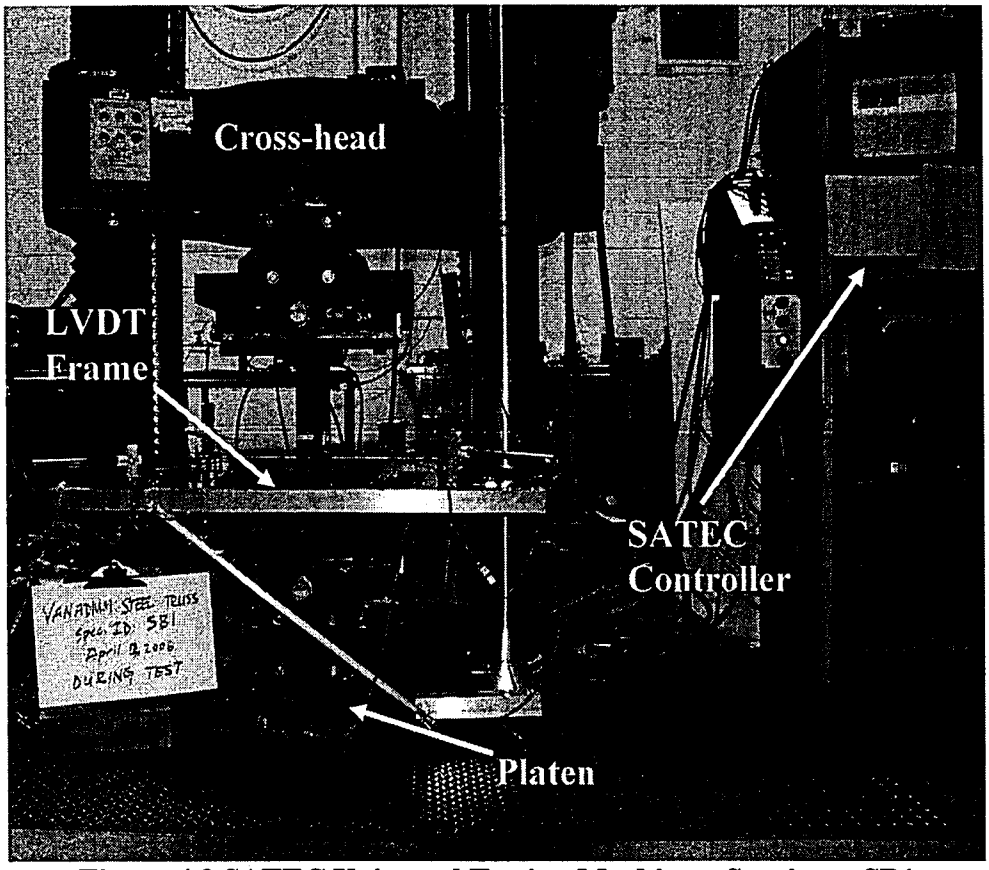

Figure 4.2 SATEC Universal Testing Machine – Specimen SB1

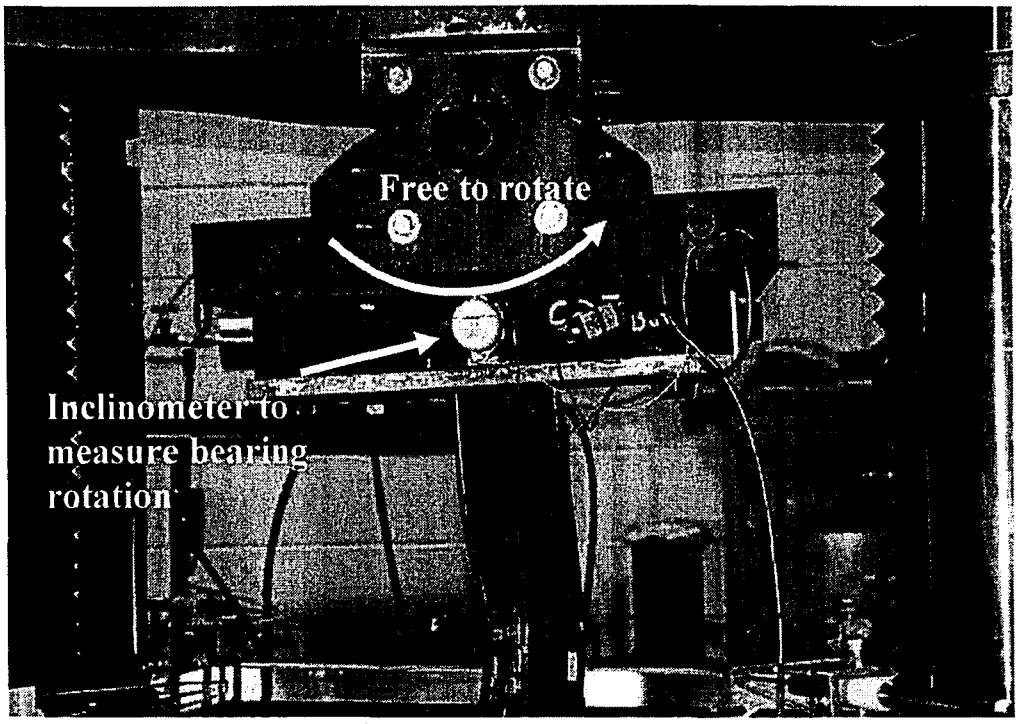

(a) Cylindrical Bearing

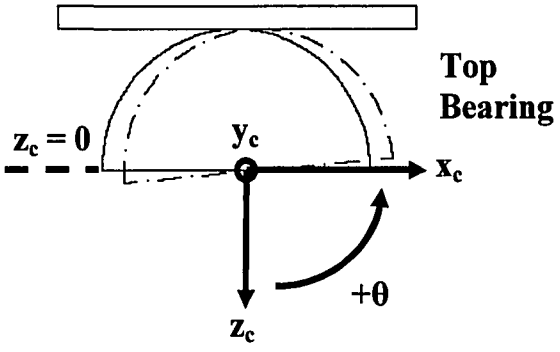

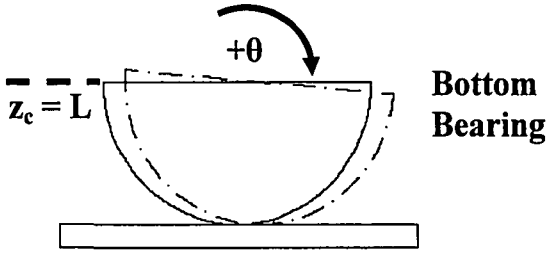

(b) Bearing Sign Convention

Figure 4.3 Cylindrical Bearings and Sign Convention

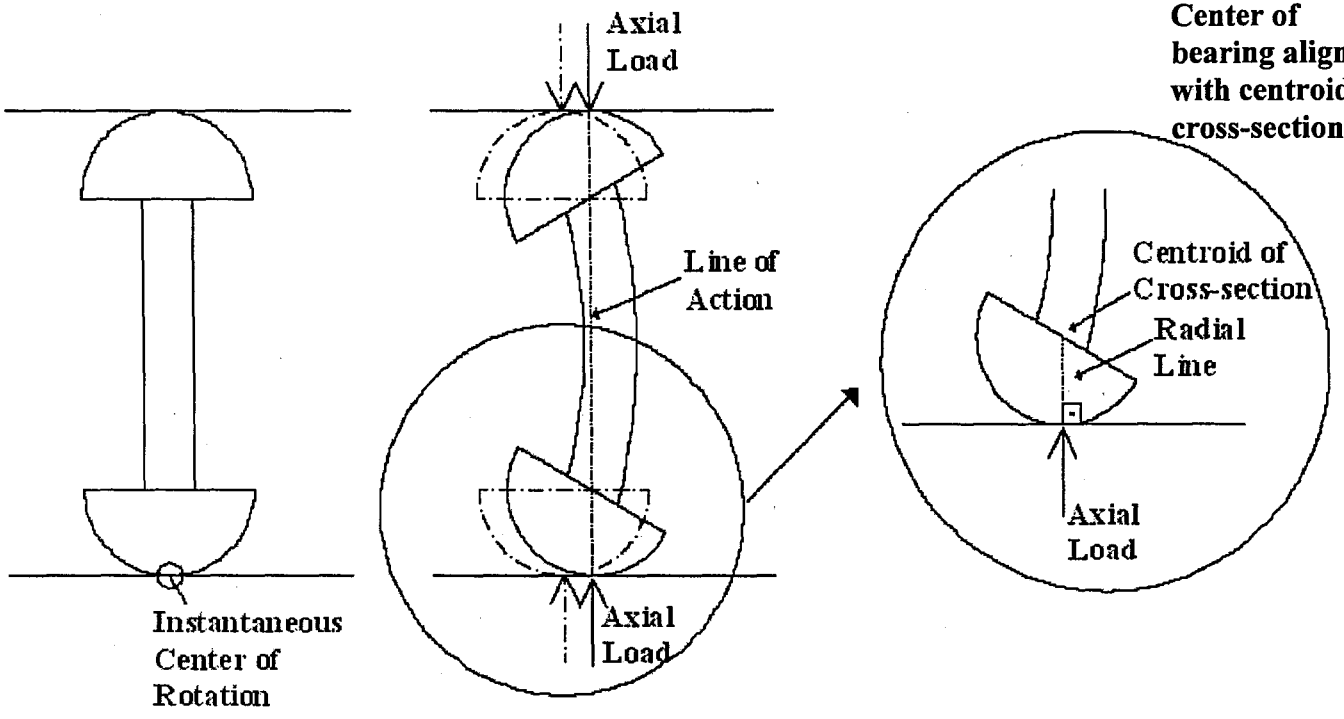

Figure 4.4 Effective Buckling Length

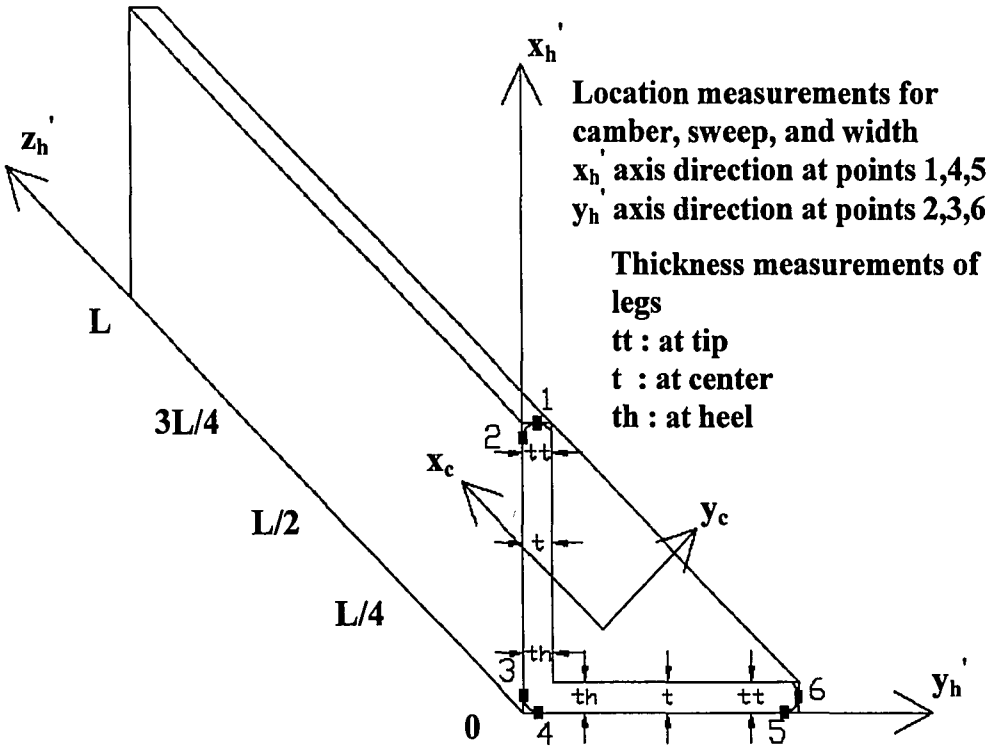

Figure 4.5 Cross-section Measurements

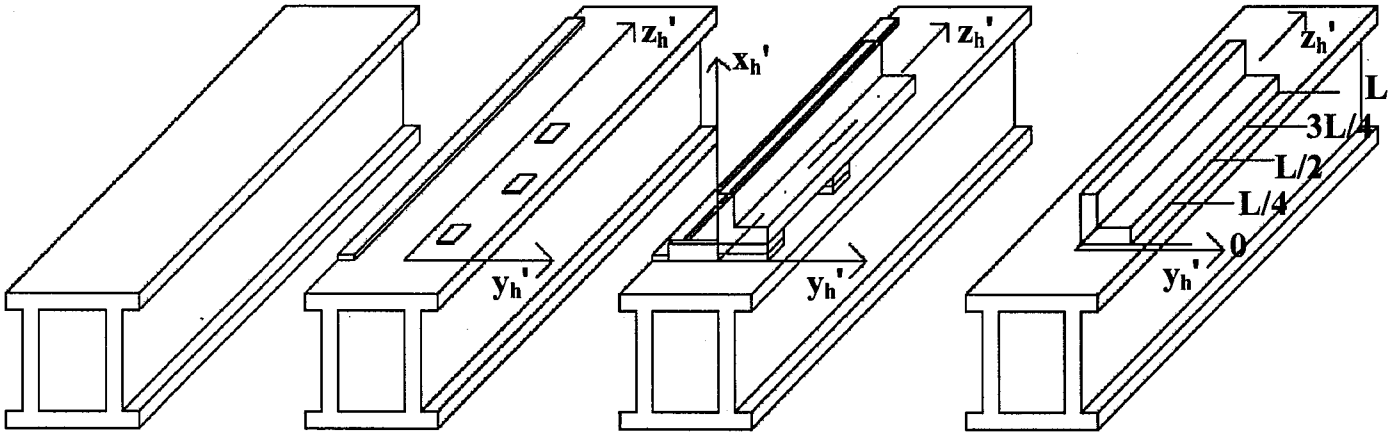

- Top surface of the beam is machined

- Global reference coordinate system
- Bar with a machined surface parallel to z_h'

- Three 1 in. thick spacer blocks placed under the specimen
- Two 3 in. long spacer blocks between the specimen and the bar

- Position of the specimen in the x_h' and y_h' direction are measured at 5 locations along the z_h' axis

Figure 4.6 Pretest Measurements

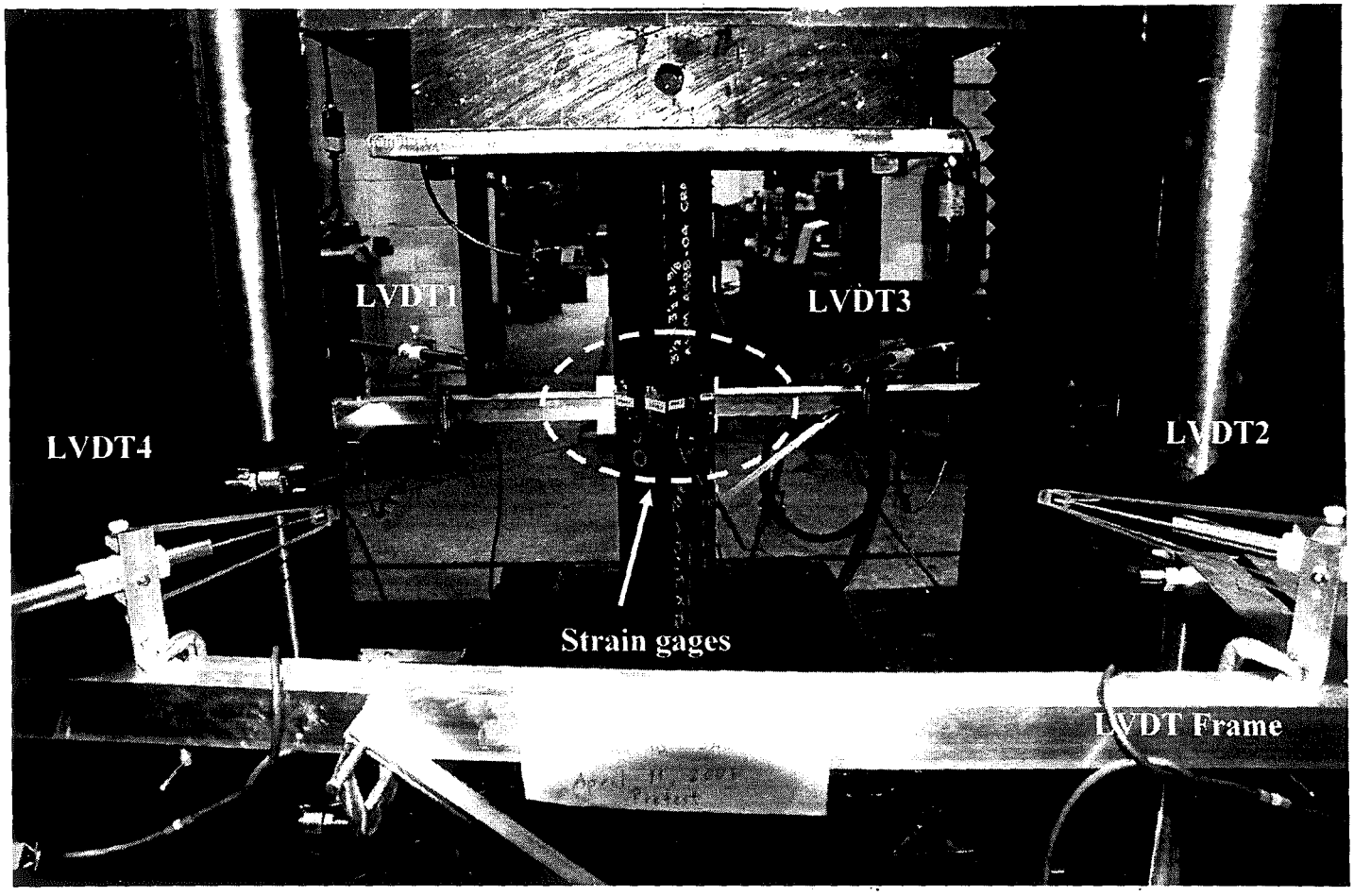

Figure 4.7 Instrumentation for Single Angle Specimens

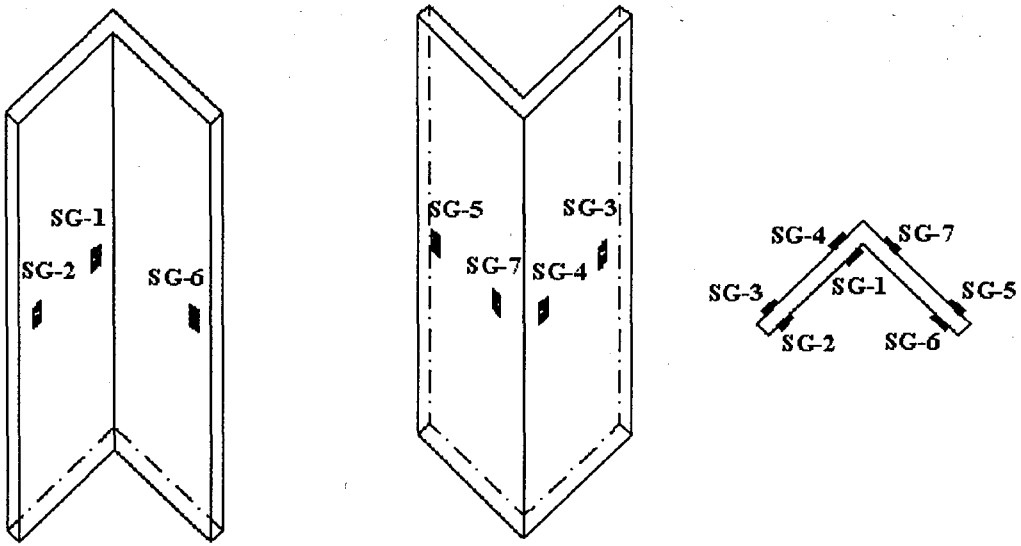

Figure 4.8 Strain Gages

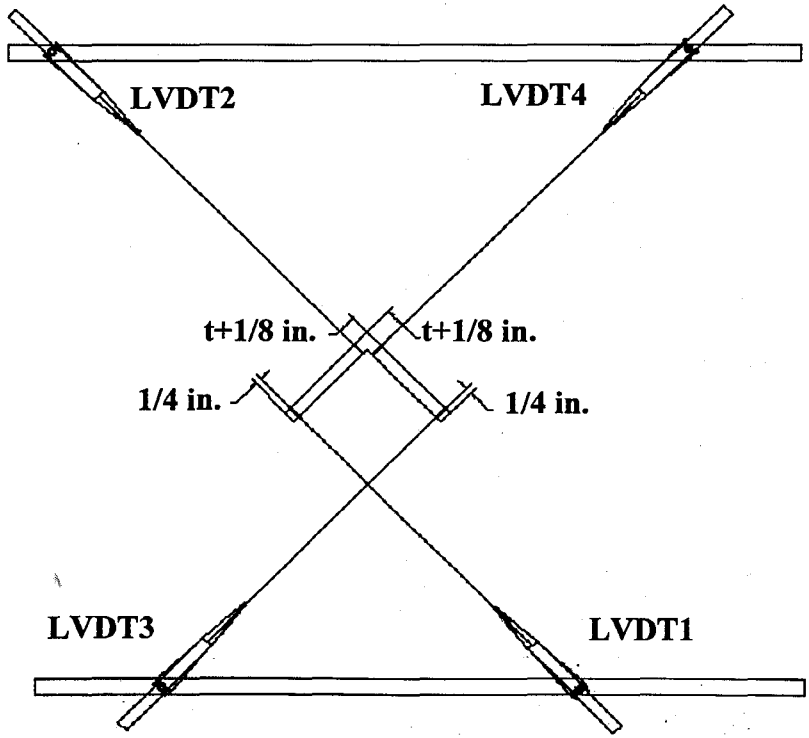

Figure 4.9 LVDT Attachments at Mid-height Cross-section

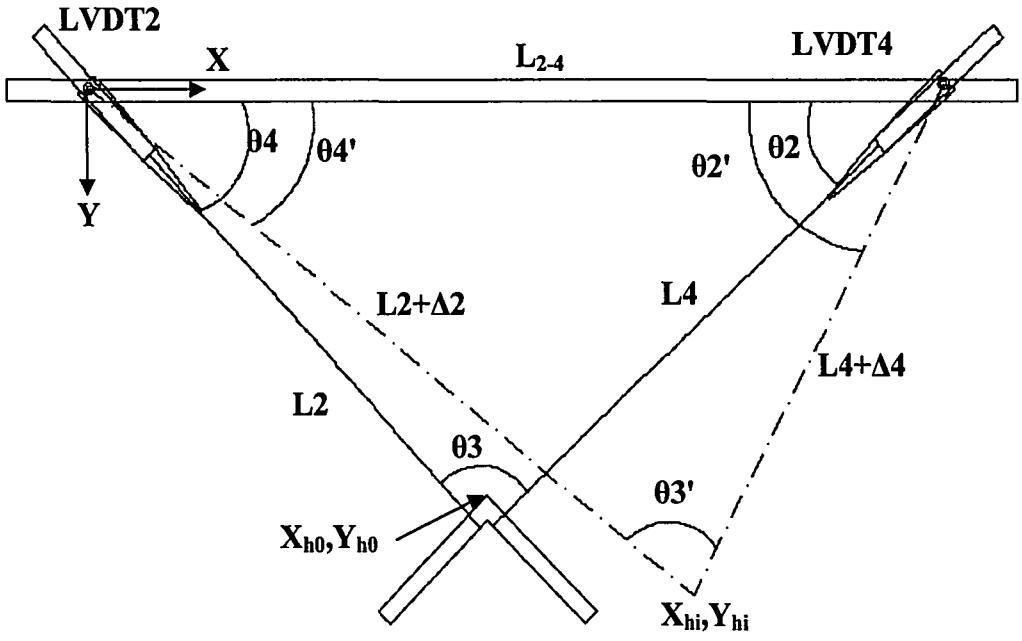

Figure 4.10 Parameters Used for Heel Lateral Deflection Calculations

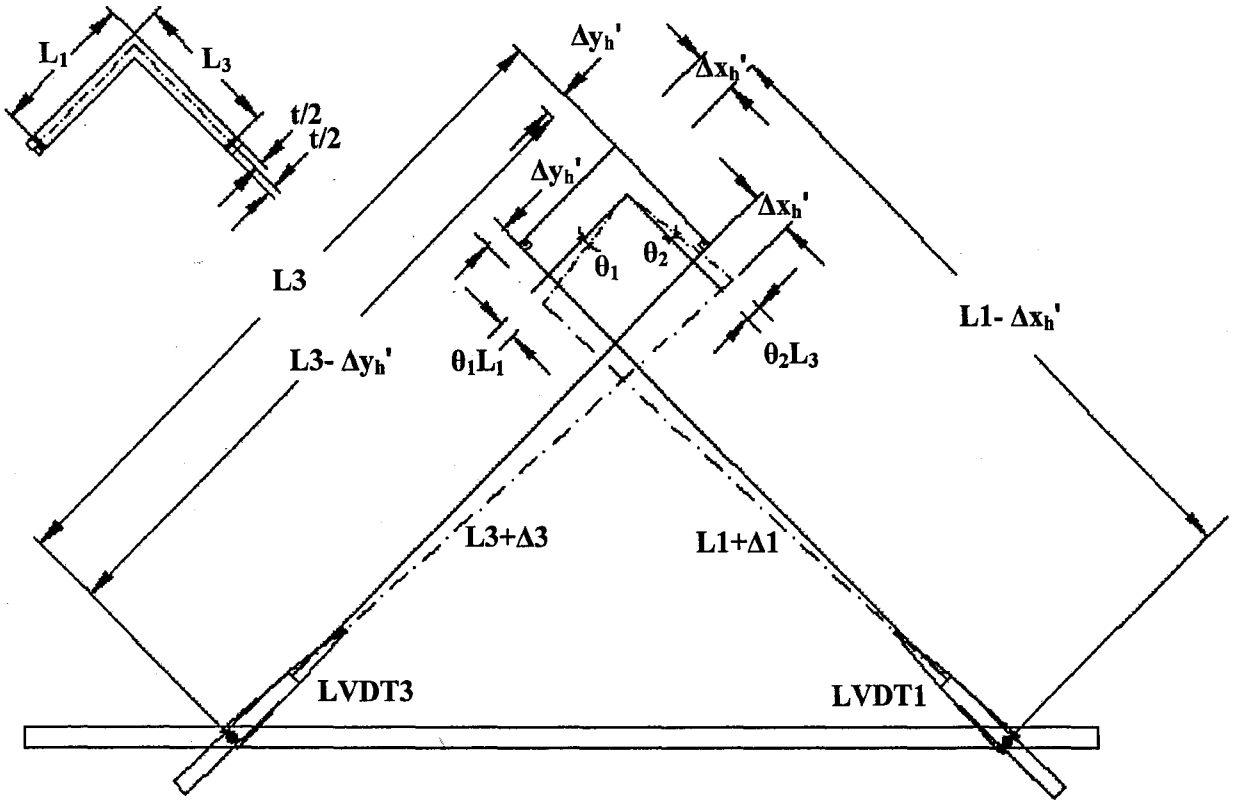

Figure 4.11 Parameters Used for Twist Calculations

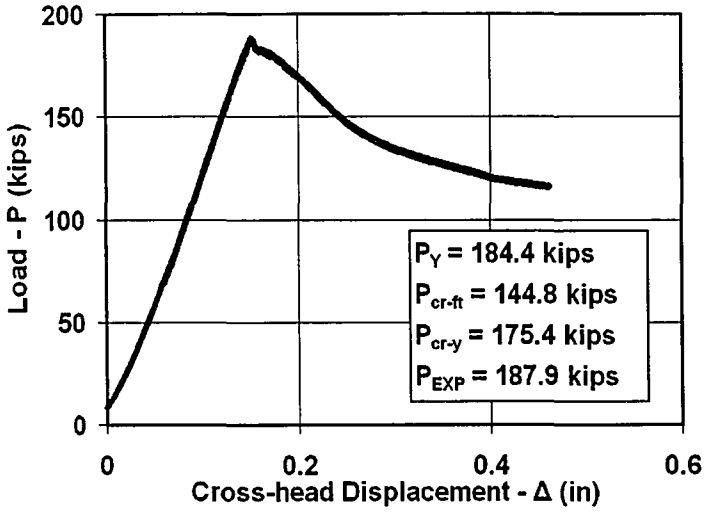

Figure 4.12 SA1 Specimen Load vs. Cross-head Displacement

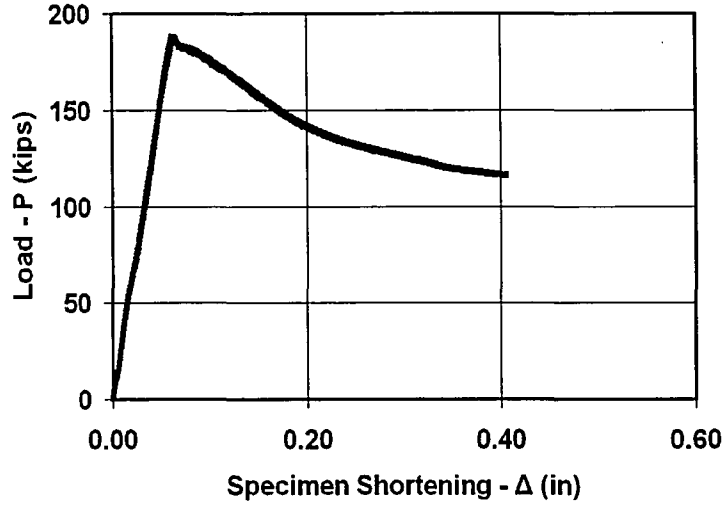

Figure 4.13 SA1 Specimen Load vs. Specimen Shortening

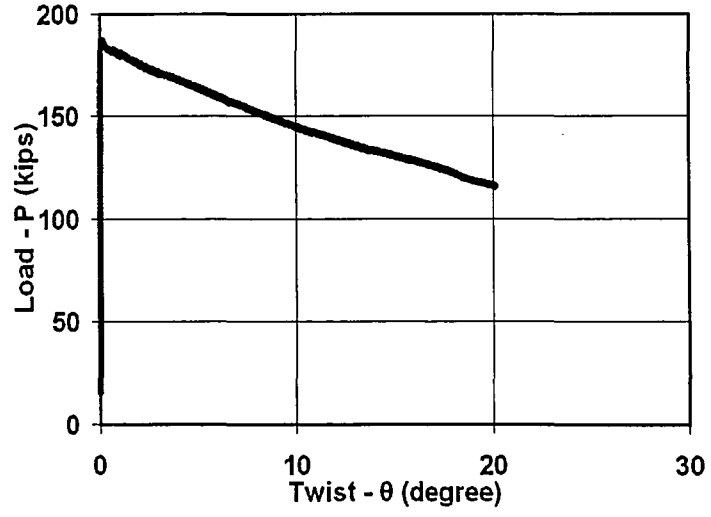

Figure 4.14 SA1 Specimen Load vs. Twist

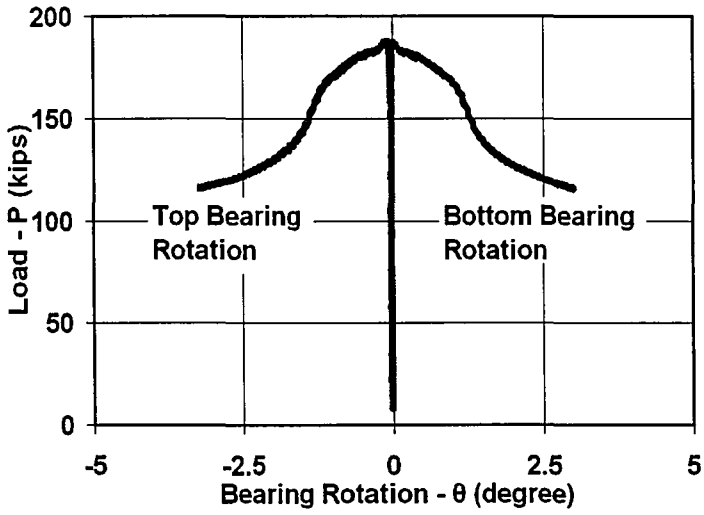

Figure 4.15 SA1 Specimen Load vs. Bearing Rotation

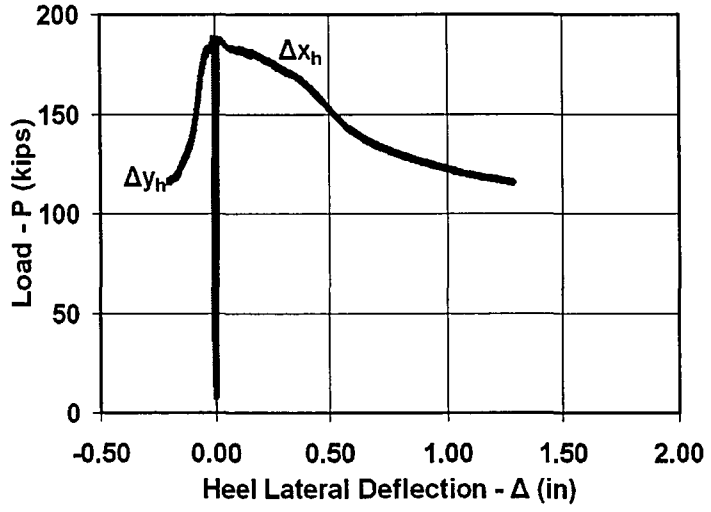

Figure 4.16 SA1 Specimen Load vs. Heel Lateral Deflection

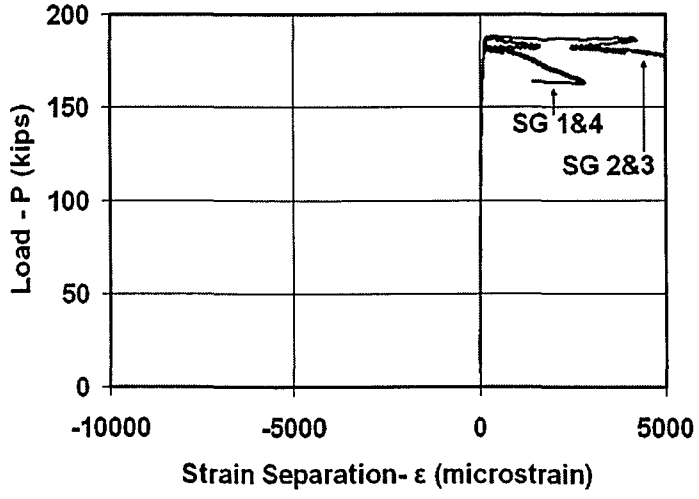

Figure 4.17 SA1 Specimen Load vs. Strain Separation

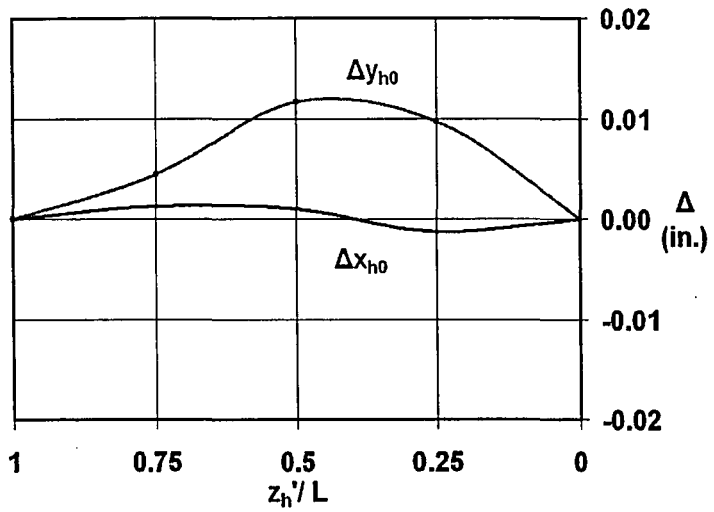

Figure 4.18 SA1 Specimen Initial Out-of-Straightness

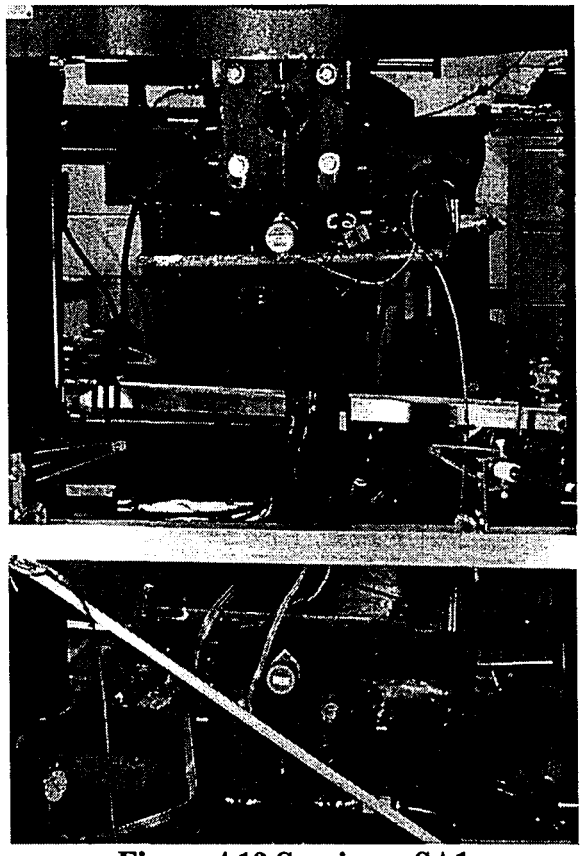

Figure 4.19 Specimen SA1

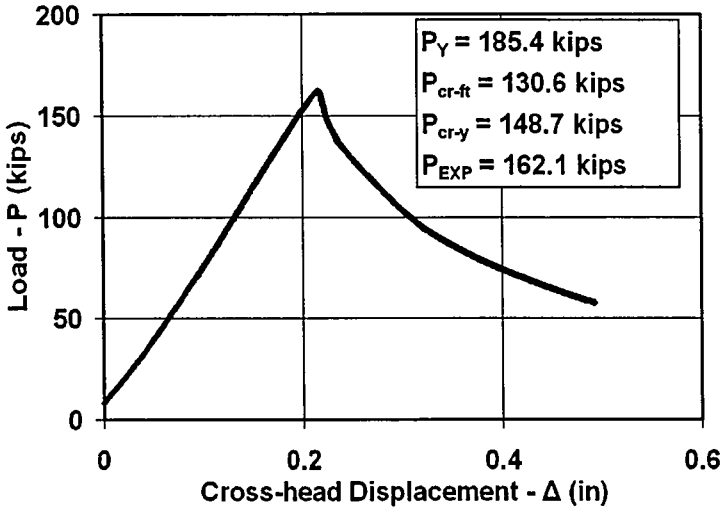

Figure 4.20 SA2 Specimen Load vs. Cross-head Displacement

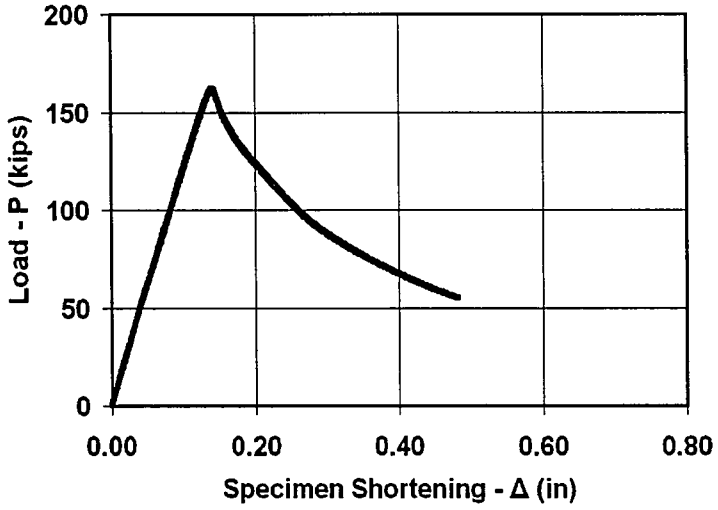

Figure 4.21 SA2 Specimen Load vs. Specimen Shortening

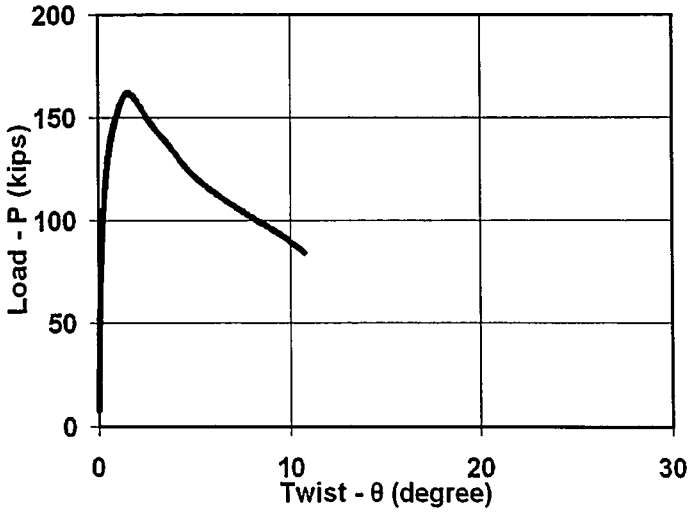

Figure 4.22 SA2 Specimen Load vs. Twist

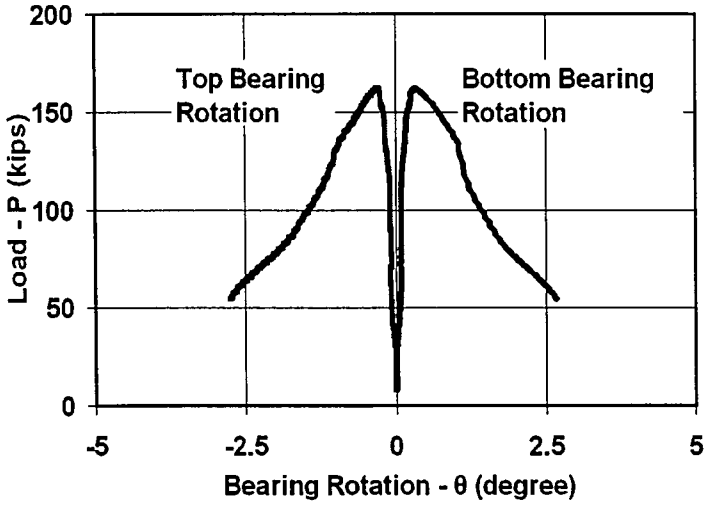

Figure 4.23 SA2 Specimen Load vs. Bearing Rotation

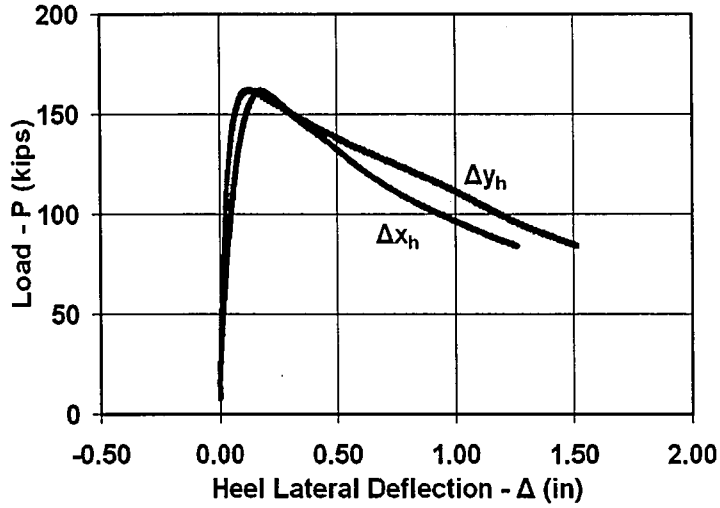

Figure 4.24 SA2 Specimen Load vs. Heel Lateral Deflection

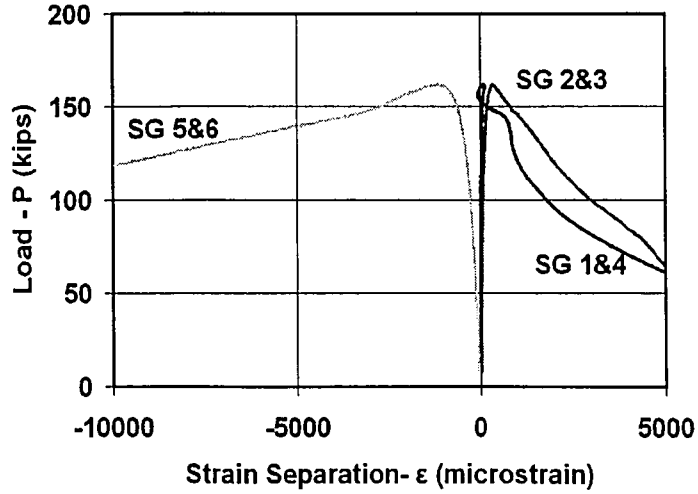

Figure 4.25 SA2 Specimen Load vs. Strain Separation

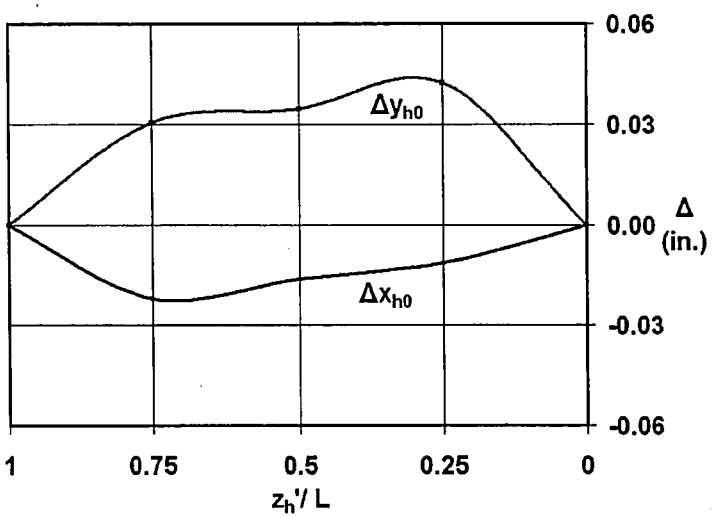

Figure 4.26 SA2 Specimen Initial Out-of-Straightness

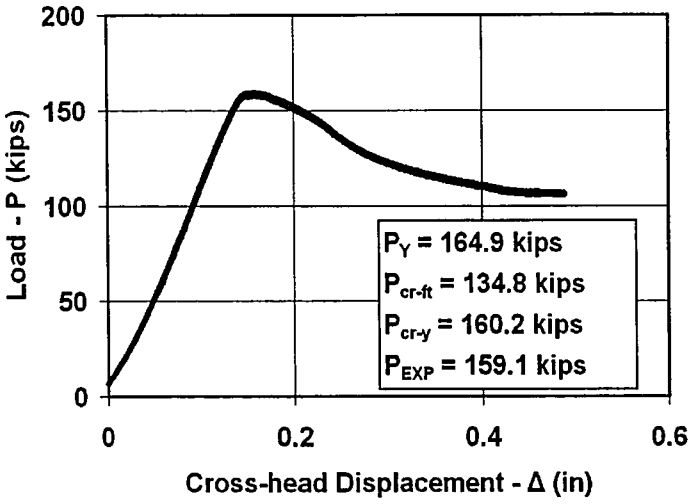

Figure 4.27 SA3 Specimen Load vs. Cross-head Displacement

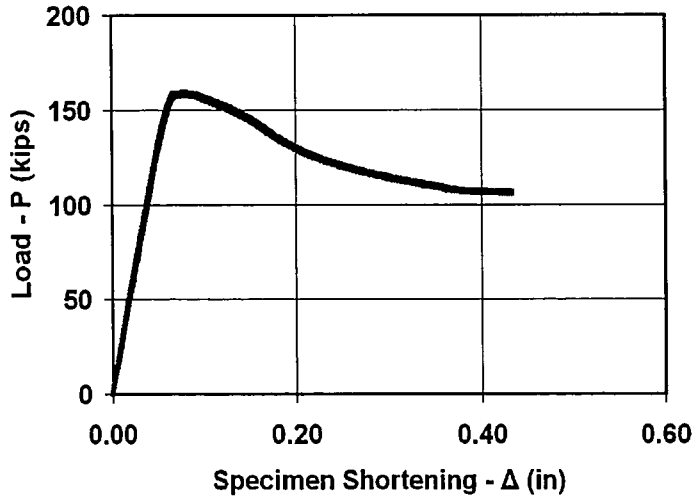

Figure 4.28 SA3 Specimen Load vs. Specimen Shortening

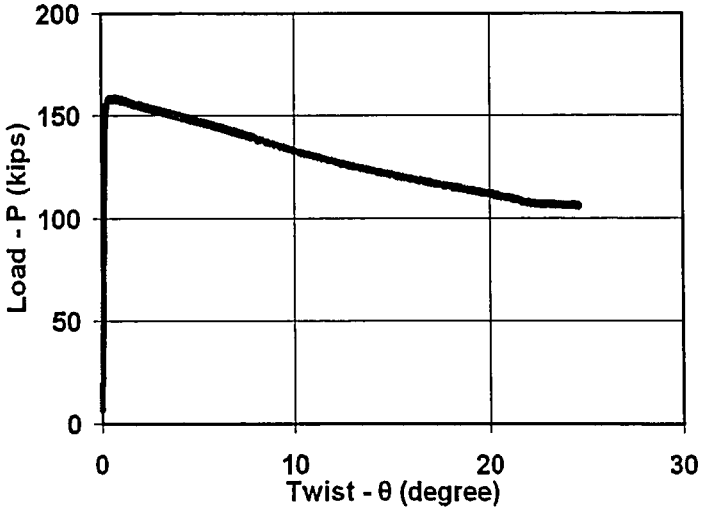

Figure 4.29 SA3 Specimen Load vs. Twist

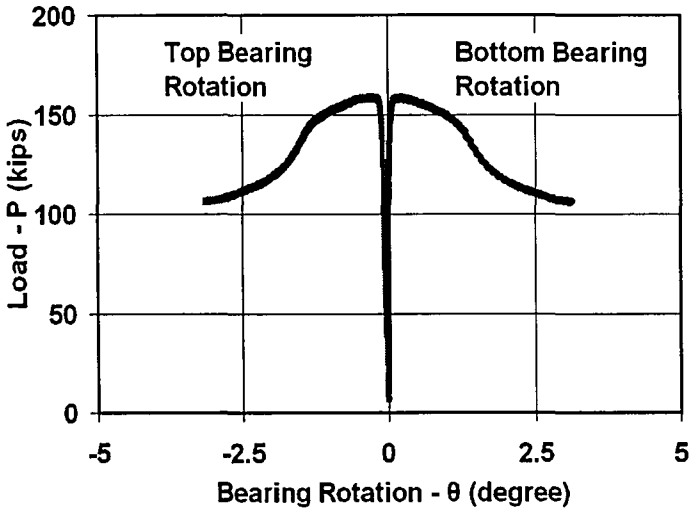

Figure 4.30 SA3 Specimen Load vs. Bearing Rotation

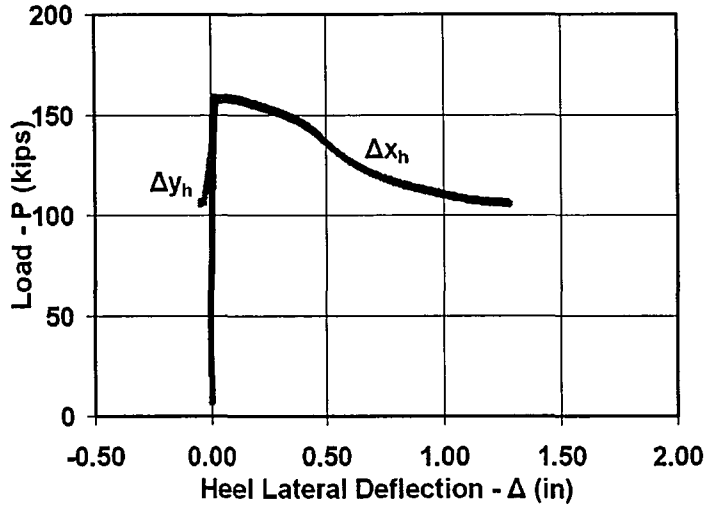

Figure 4.31 SA3 Specimen Load vs. Heel Lateral Deflection

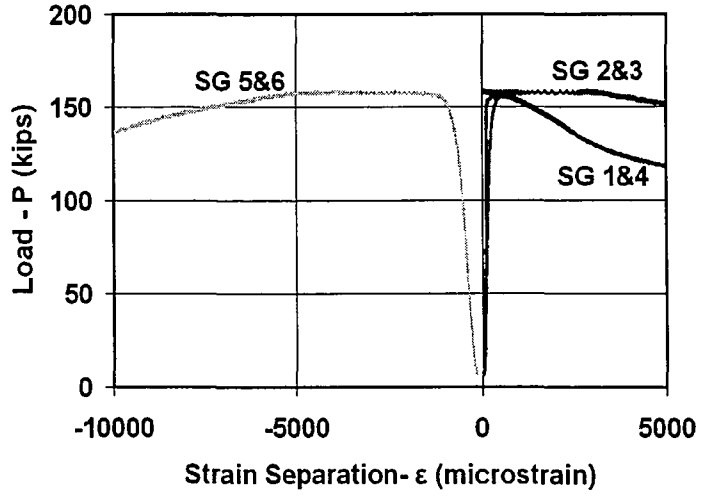

Figure 4.32 SA3 Specimen Load vs. Strain Separation

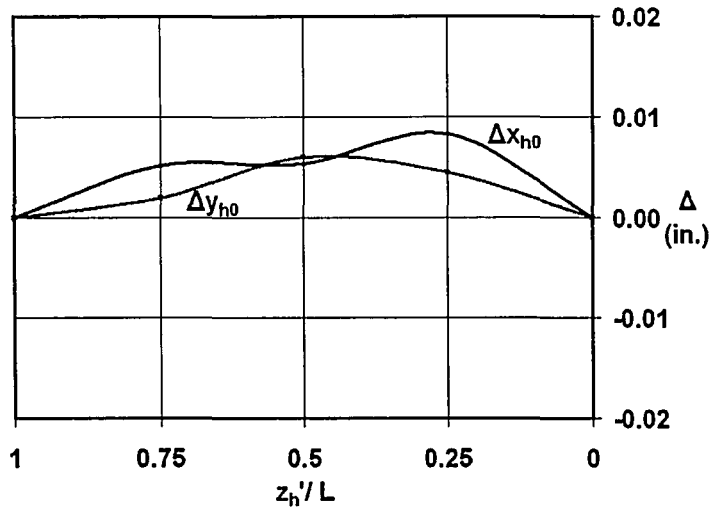

Figure 4.33 SA3 Specimen Initial Out-of-Straightness

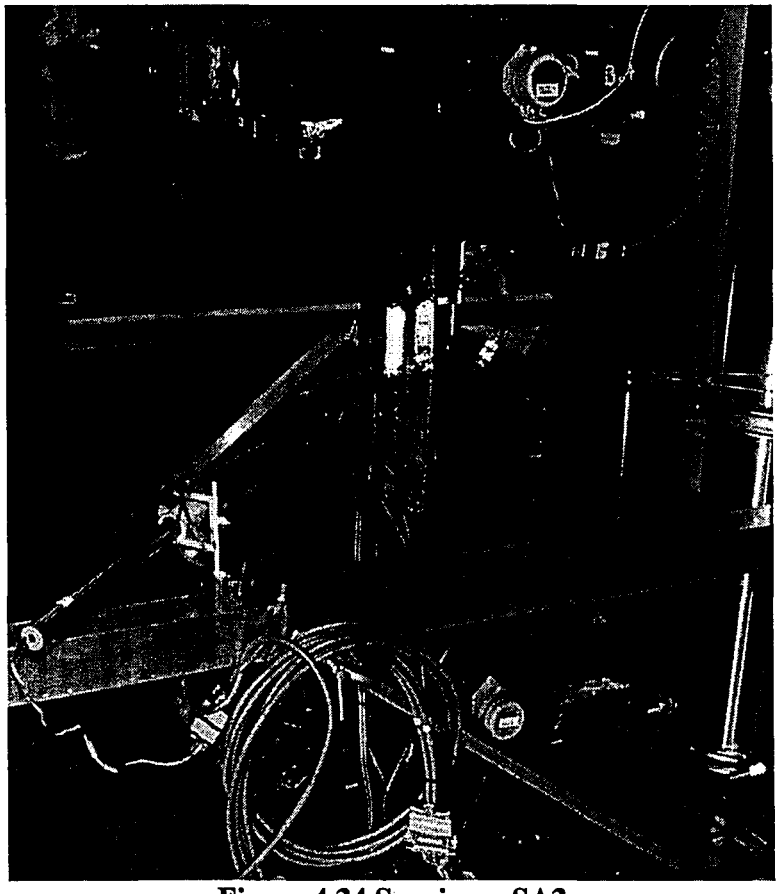

Figure 4.34 Specimen SA3

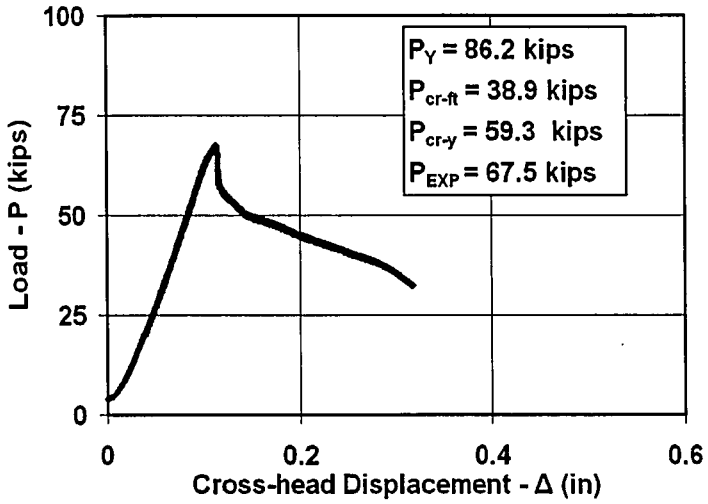

Figure 4.35 SB1 Specimen Load vs. Cross-head Displacement

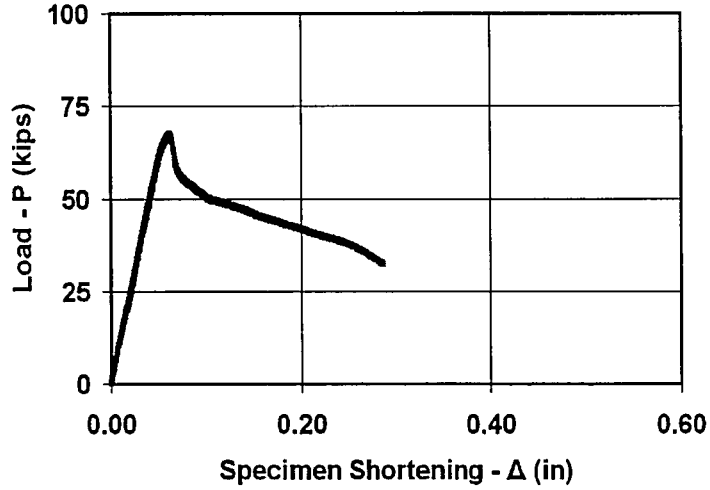

Figure 4.36 SB1 Specimen Load vs. Specimen Shortening

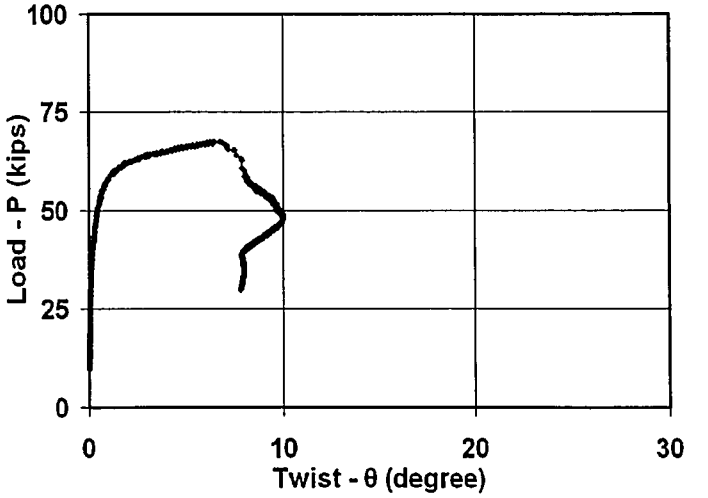

Figure 4.37 SB1 Specimen Load vs. Twist

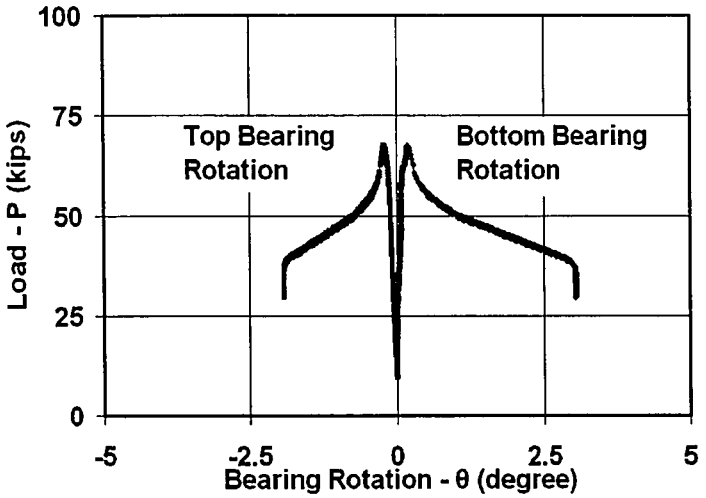

Figure 4.38 SB1 Specimen Load vs. Bearing Rotation

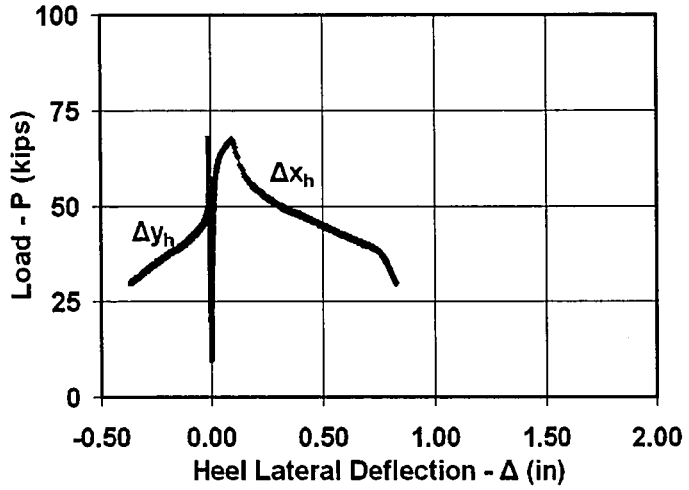

Figure 4.39 SB1 Specimen Load vs. Heel Lateral Deflection

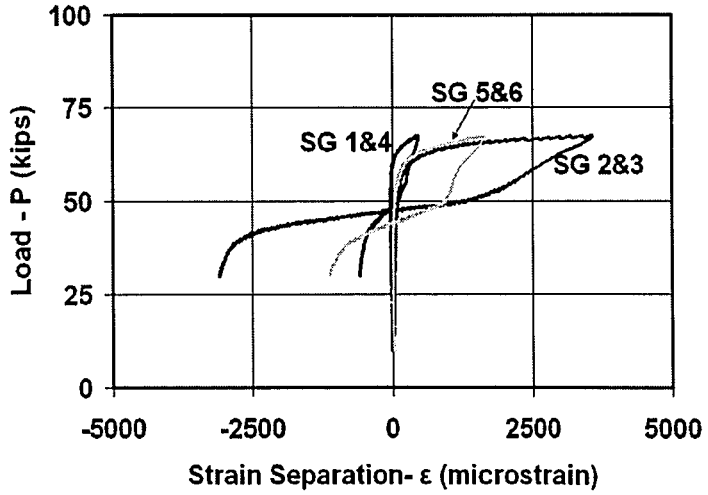

Figure 4.40 SB1 Specimen Load vs. Strain Separation

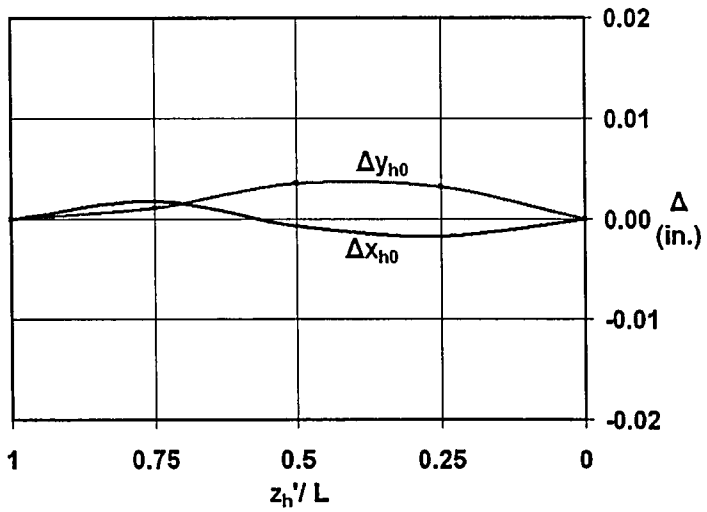

Figure 4.41 SB1 Specimen Initial Out-of-Straightness

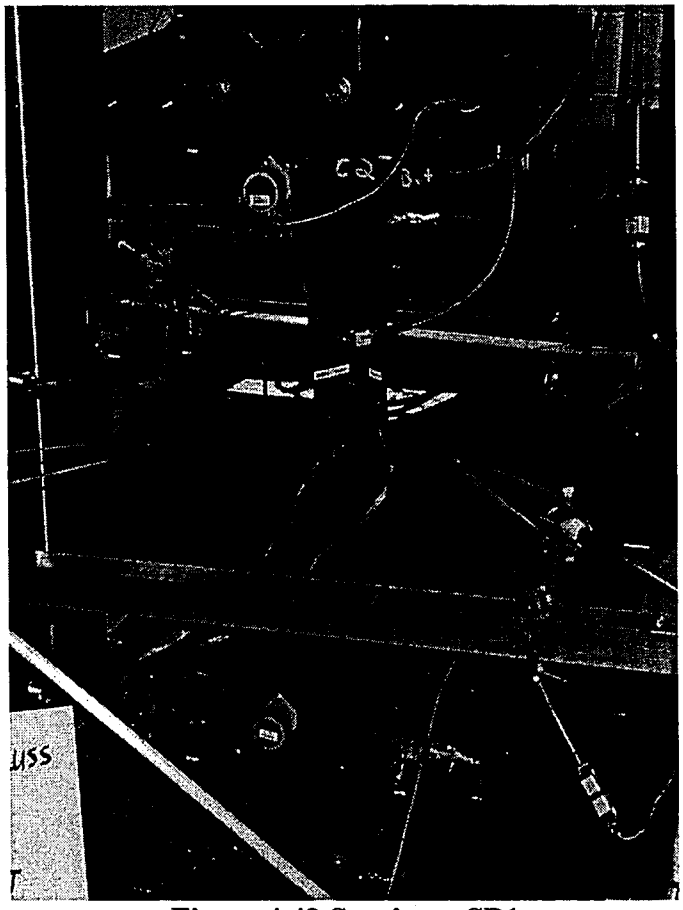

Figure 4.42 Specimen SB1

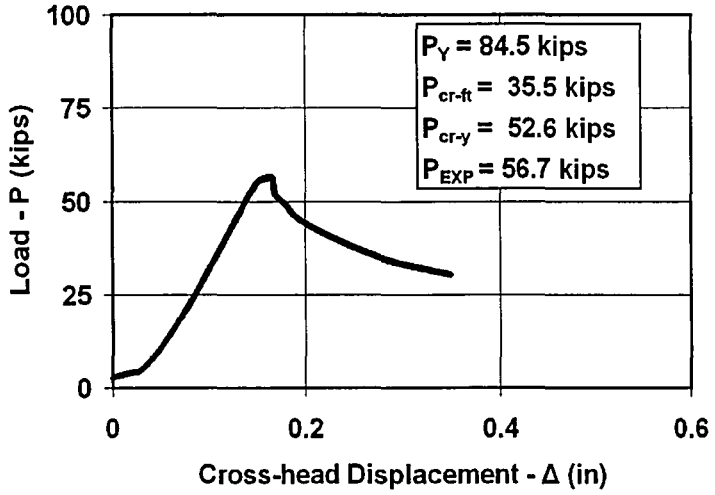

Figure 4.43 SB2 Specimen Load vs. Cross-head Displacement

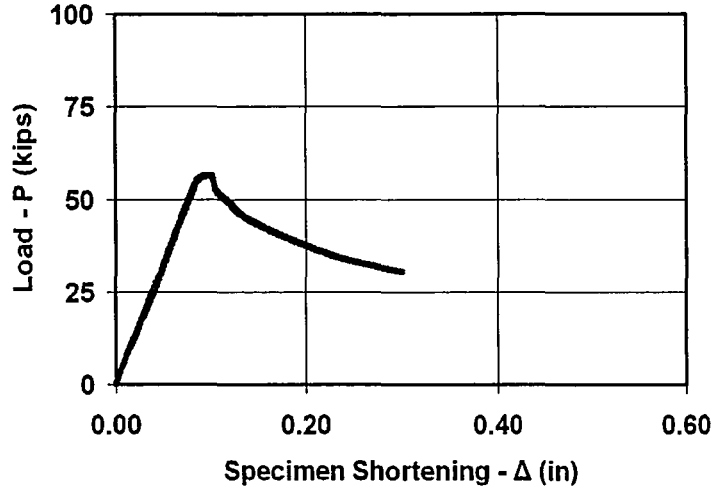

Figure 4.44 SB2 Specimen Load vs. Specimen Shortening

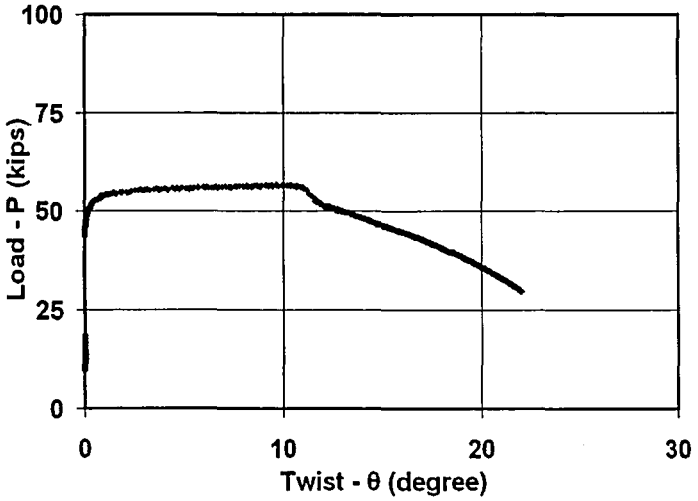

Figure 4.45 SB2 Specimen Load vs. Twist

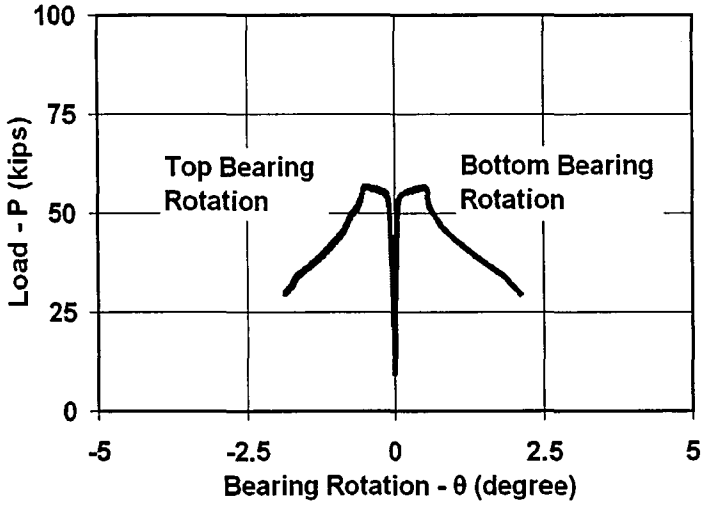

Figure 4.46 SB2 Specimen Load vs. Bearing Rotation

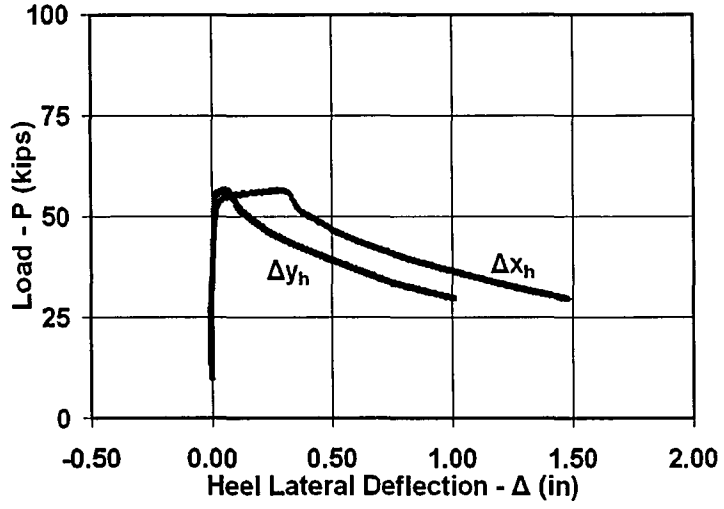

Figure 4.47 SB2 Specimen Load vs. Heel Lateral Deflection

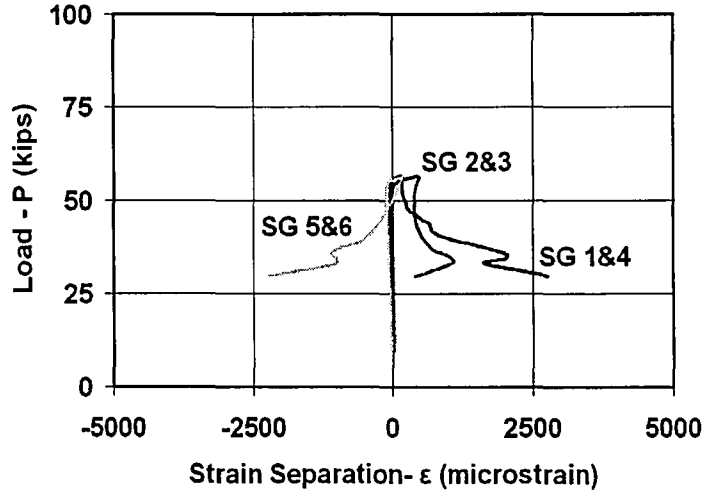

Figure 4.48 SB2 Specimen Load vs. Strain Separation

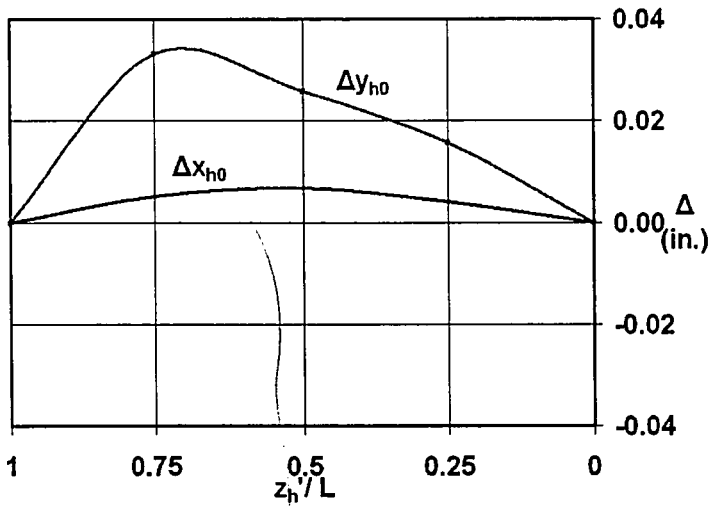

Figure 4.49 SB2 Specimen Initial Out-of-Straightness

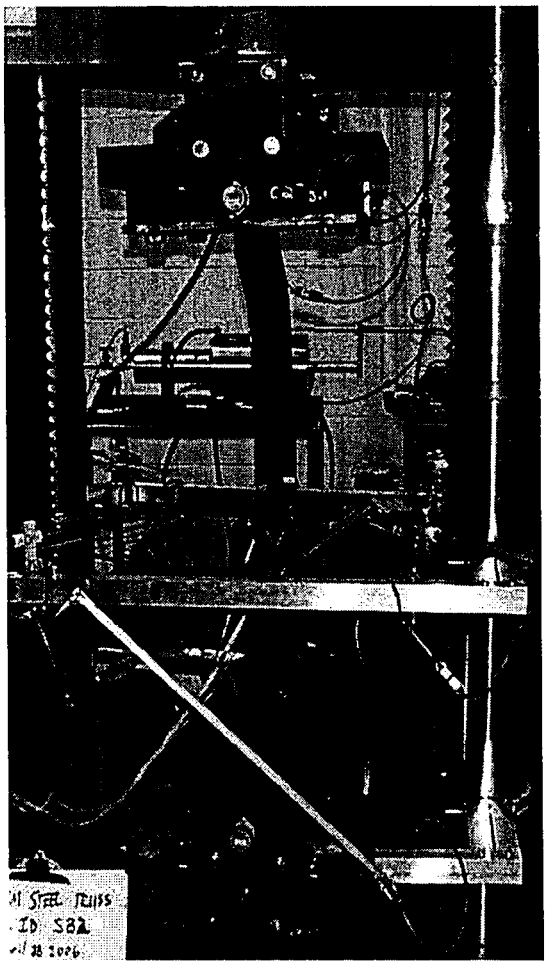

Figure 4.50 Specimen SB2

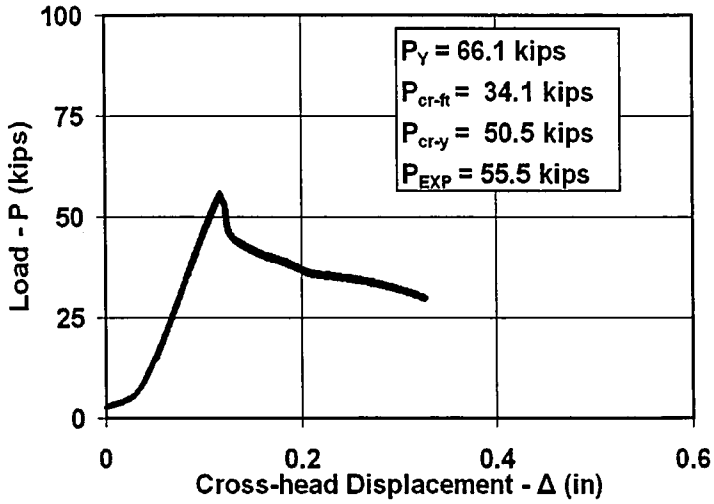

Figure 4.51 SB3 Specimen Load vs. Cross-head Displacement

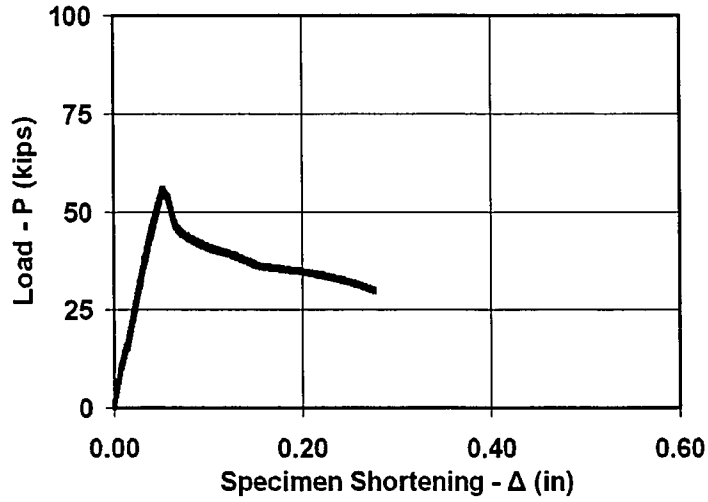

Figure 4.52 SB3 Specimen Load vs. Specimen Shortening

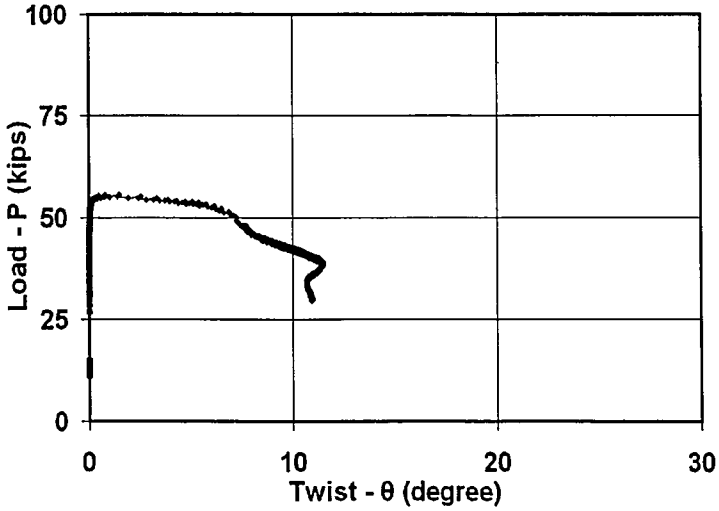

Figure 4.53 SB3 Specimen Load vs. Twist

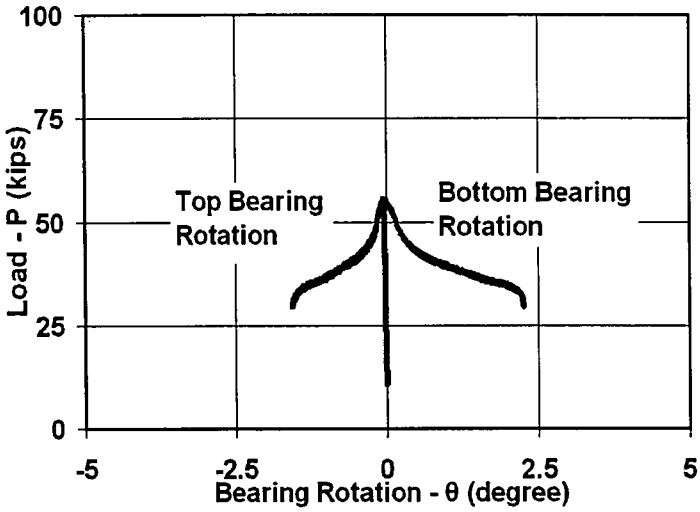

Figure 4.54 SB3 Specimen Load vs. Bearing Rotation

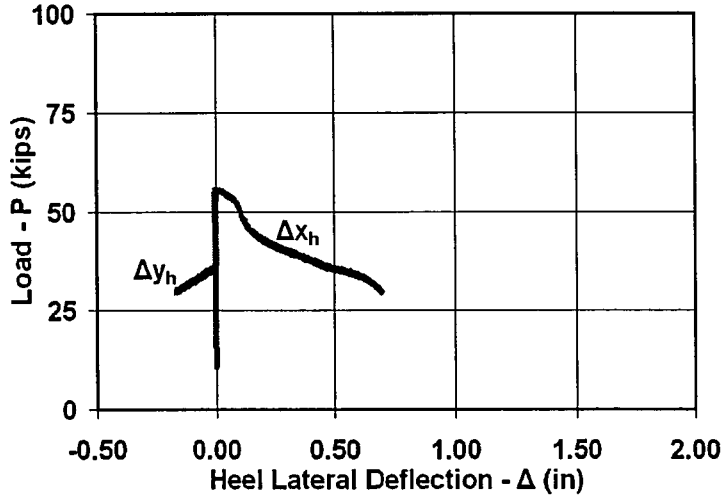

Figure 4.55 SB3 Specimen Load vs. Heel Lateral Deflection

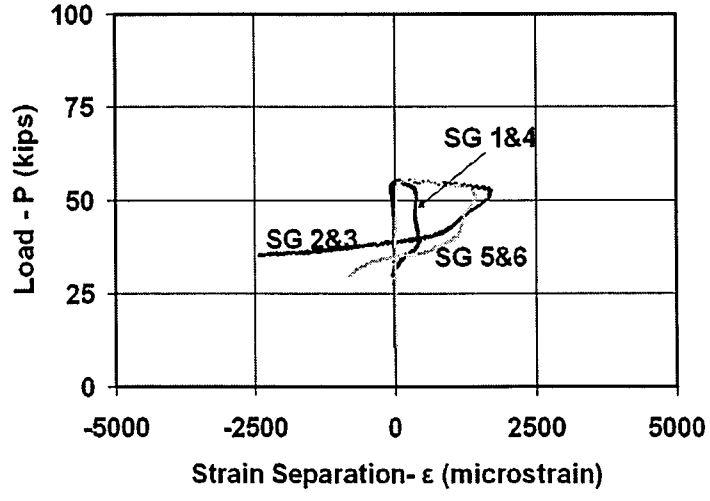

Figure 4.56 SB3 Specimen Load vs. Strain Separation

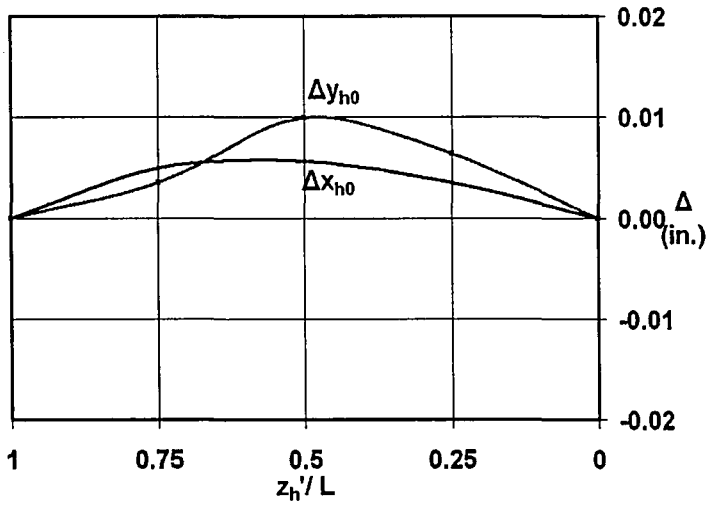

Figure 4.57 SB3 Specimen Initial Out-of-Straightness

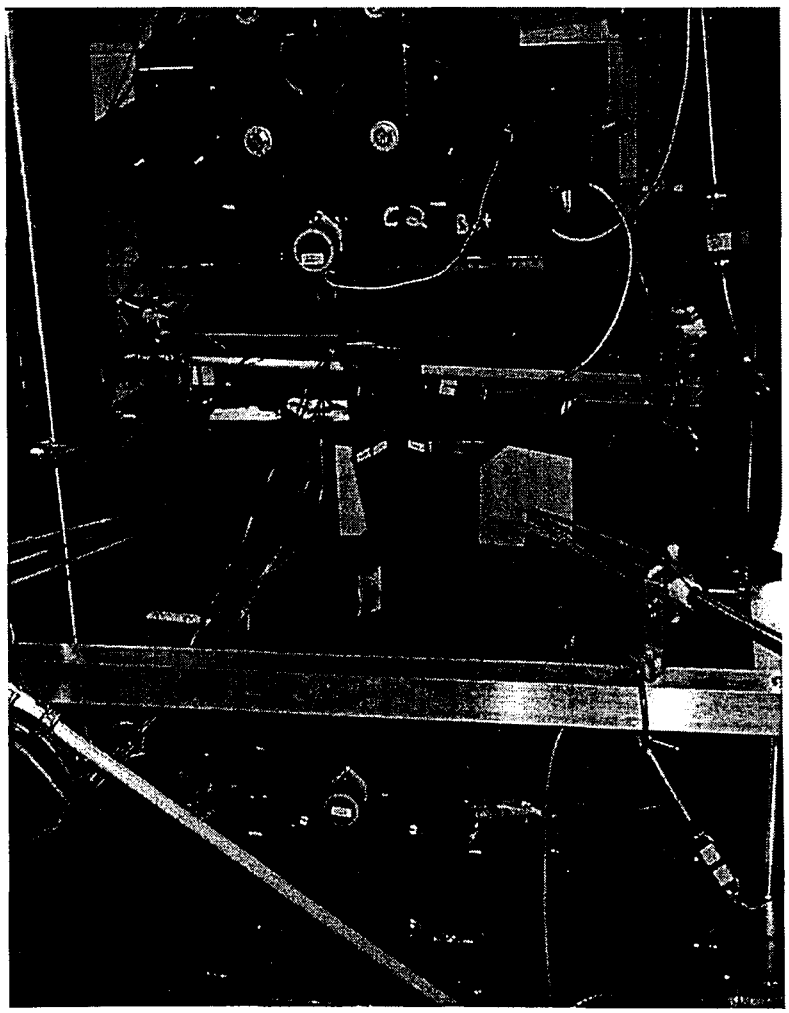

Figure 4.58 Specimen SB3

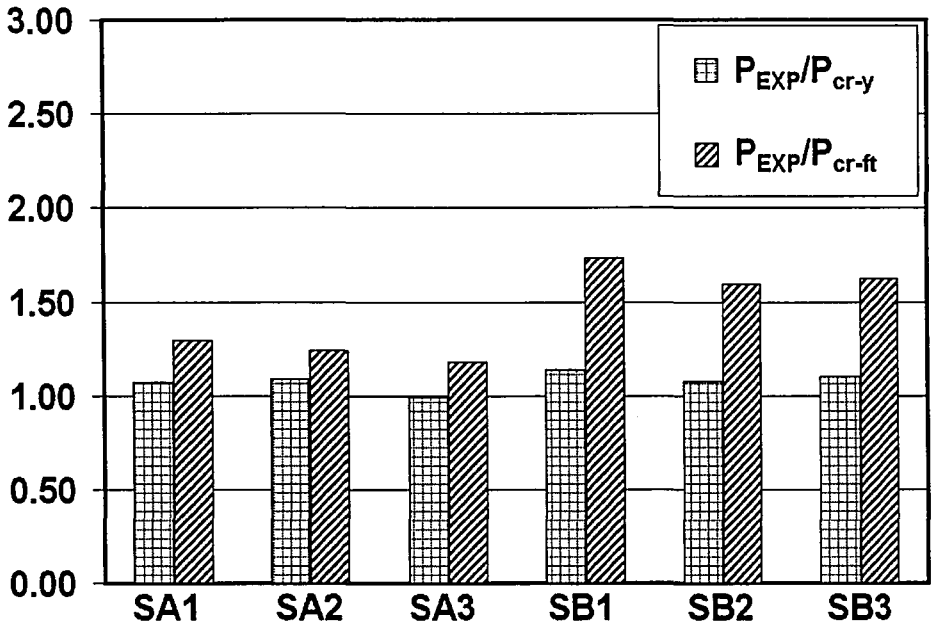

Figure 4.59 Predicted vs. Experimental Results

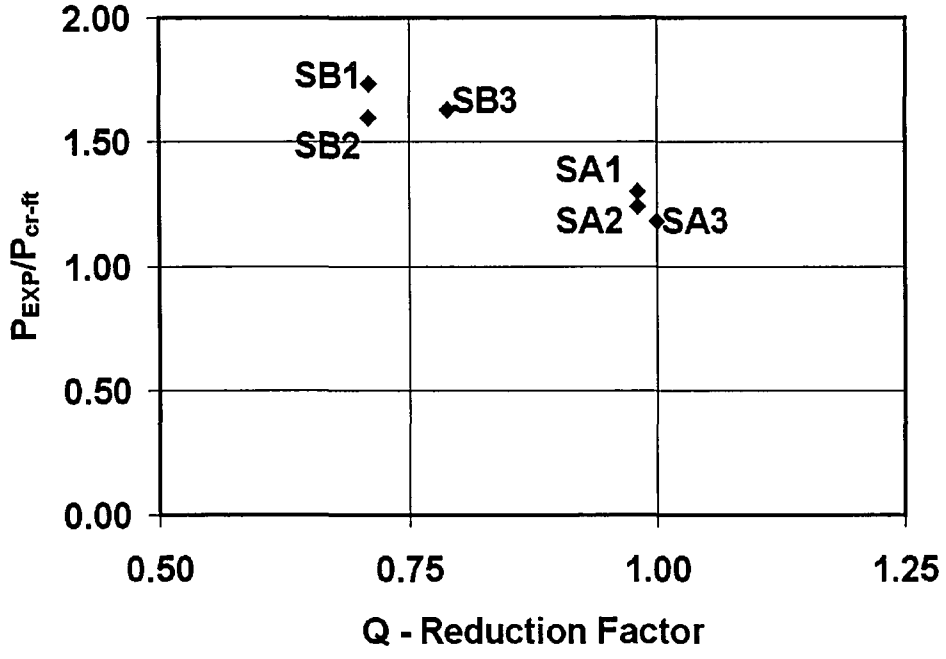

Figure 4.60 Experimental Results vs. Q Reduction Factor

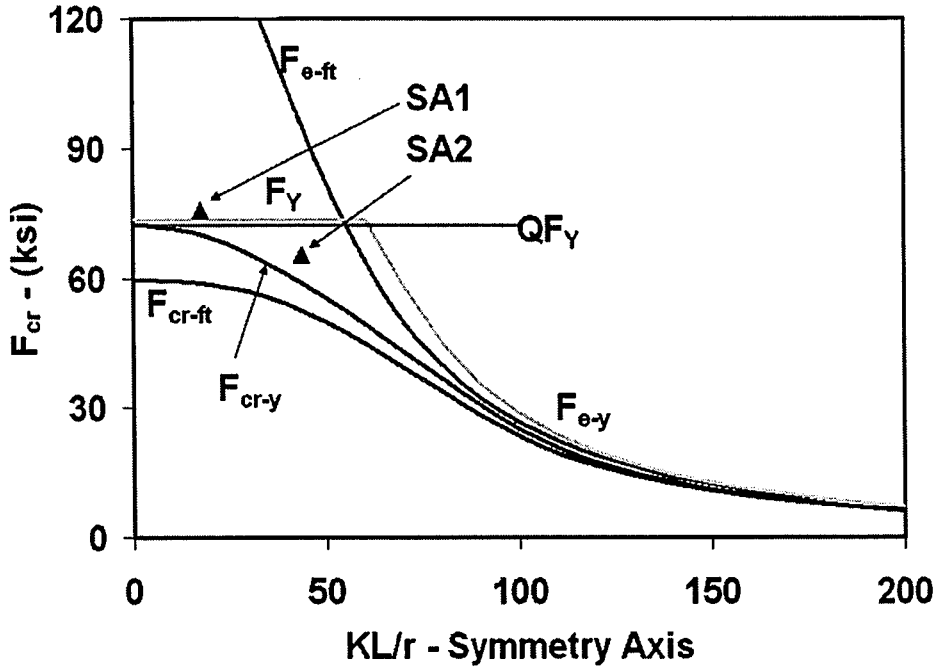

Figure 4.61 Comparison of Experimental Results with Predicted Results for SA1 and SA2 (Vanadium Steel) Specimens

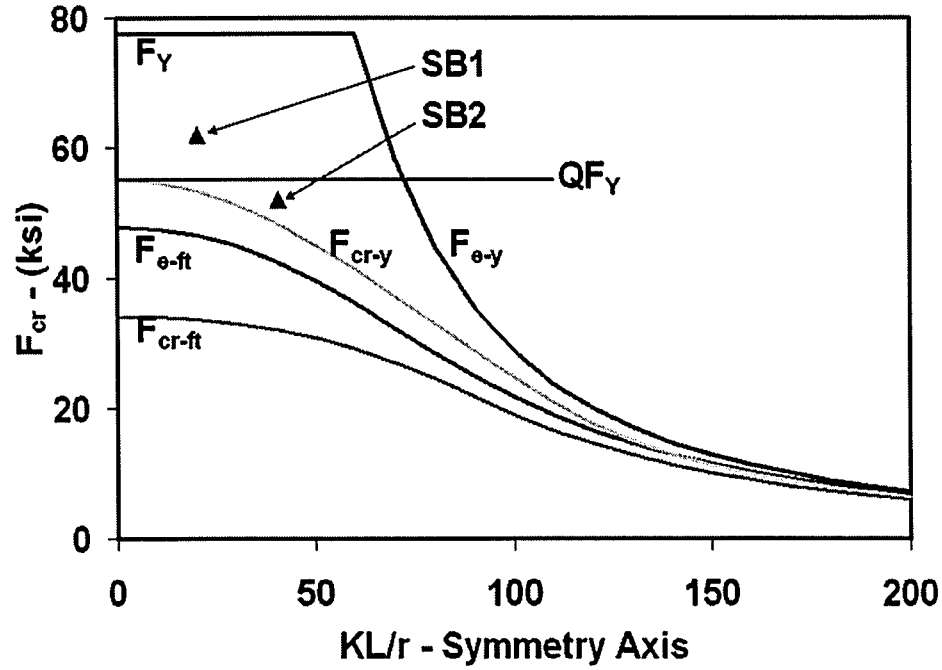

Figure 4.62 Comparison of Experimental Results with Predicted Results for SB1 and SB2 (Vanadium Steel) Specimens

Chapter 5 Buckling Tests of Double Angle Specimens

5.0 General

This chapter addresses the experiments on the double angle specimens. First, the test matrix of specimens is presented. The test setup and related equipment are discussed next. Then the preparation of the test specimens, the initial out-of-straightness measurements of the specimens, and the instrumentation of the specimens are discussed, along with the test procedure. This is followed by a presentation of the theoretical buckling capacities. Finally, the test results are presented and discussed.

5.1 Test Matrix

The double angle specimens have singly symmetric cross-sections. Each angle has equal legs. Double angle compression members are expected to fail in one of the following buckling mode shapes: either flexural buckling about the weak axis, flexural-torsional buckling involving flexural buckling about the strong axis and torsional buckling. These buckling modes are discussed in Chapter 2. The coordinate systems used to discuss the double angle specimens are presented in Figure 5.1. The predicted buckling capacities are calculated according to Chapter E of the AISC (2005) specification as described later.

The test specimens are identified in Table 5.1, along with the steel type and the related parameters such as the length of the specimen. The measured yield stress values are also presented in this table. The yield stress values were determined from tensile coupon tests discussed in Chapter 3. In Table 5.1, the rated load capacities of

the bearings used for these test specimens are also presented. The bearings are referred to by their rated load capacities. The bearings were chosen according to the cross-sectional dimensions of the specimen and the predicted buckling capacity of the specimen. The bearings are discussed further in Section 5.2.2. The 500 kip bearings were used for the DA and DB series specimens, and the 100 kip bearings were used for the DC series specimens.

The test matrix also includes information about the number of mid-spacers and the spacing between the back-to-back angles of the specimens. This information is used to find the modified slenderness of the double angle specimens. The modified slenderness concept is utilized in Section E6 of the AISC (2005) specification, as described in Section 2.3.1.1.2.

5.2 Test Setup

5.2.1 Test Machine

The SATEC universal testing machine at the ATLSS Center was used for the double angle specimen compression tests. The load frame and controller unit of the SATEC machine are shown in Figure 5.2. More detail about the SATEC machine can be found in Section 4.2.1.

5.2.2 Cylindrical Bearings

In order to create pinned-pinned end conditions, the double angle specimens were tested with cylindrical bearings placed at both ends of the specimens, as shown in Figure 5.3. The two types of bearings, shown in Figure 5.3, have the same working

principles, which are explained in Section 4.2.2.

The flat surface of the 500 kip bearing, shown in Figure 5.3(a), is large enough to cover the cross-section of each double angle specimen. On the other hand, the flat surface of the 100 kip bearing, shown in Figure 5.3(b), can cover the cross-section of only the DC series test specimens (see Table 5.1). The predicted buckling capacities for the DA and DB series test specimens are greater than 100 kips, thus these specimens were tested with the 500 kip bearings. On the other hand, the predicted buckling capacities for the DC series test specimens are less than 100 kips. Thus, only the DC series test specimens were tested with the 100 kip bearings.

For the double angle specimen tests, the bearings restrained the rotation about the minor principle axis (i.e., weak axis, see Figure 5.1) of the specimens about which pure flexural buckling would occur (i.e., rotation about the weak axis, shown in Figure 5.1, is restrained). Rotation about the major principle axis (i.e., the strong axis), however, was unrestrained by the bearings.

5.3 Test Preparation, Instrumentation, and Procedure

A procedure on column testing, which is suggested by SSRC (Galambos, 1998), was followed during the tests. This procedure is referred to as Technical Memorandum B4: Procedure for Testing Centrally Loaded Columns (Galambos, 1998).

5.3.1 Preparation of Test Specimens

The double angle specimens were fabricated at the ATLSS Center. The test specimen material was shipped to the ATLSS Center as single angle stock. First, two

single angles were cut to the length of a double angle test specimen. Then, the ends of the single angles were saw cut square and de-burred with a grinder to maintain flatness of the end cross-sections that bear against bearings. Then, using the number of mid-spacers and the spacing between the angles shown in Table 5.1, each double angle specimen was made by welding the mid-spacers to the angles.

The locations of the mid-spacers along the specimen length depend on the number of mid-spacers used for a specimen. The mid-spacers were distributed at equal distances along the length of a specimen. For instance, for the specimens with one mid-spacer, the mid-spacer was placed at the mid-height cross-section of the built-up double angle specimen.

The types of mid-spacers and the welds used to attach them to the angles are shown in Figure 5.4. The type of mid-spacer was determined by the type of truss member that was simulated by the test specimen. For instance, the DA series test specimens simulated typical chord members in trusses. A round bar welded between the closest legs of the two angles was used as the mid-spacer for these members (Figure 5.4(a)). The diameter of the round bar mid-spacer is equal to the back-to-back spacing of the angles of the built-up member. The DB and DC series test specimens simulated typical web members in trusses. A piece of light-weight angle (L1x1x1/8) welded to the outstanding legs of the two angles was used as the mid-spacer for these members (Figure 5.4 (b)).

5.3.2 Initial Out-of-Straightness and Other Pretest Measurements

The purpose of the pretest measurements is to measure the initial camber and initial sweep along the length of each specimen, as well as the width and thickness of the angles. Camber refers to the strong axis out-of-straightness (deflection) and sweep refers to the weak axis out-of-straightness (deflection). These deflection measurements are usually defined for the centroid of the cross-section. Since the centroid of the double angle member is not on the legs of either of the angles, the camber and the sweep were measured at the heels of the angles.

The camber and sweep of the double angle specimens were estimated by taking the average of the camber and sweep measurements for the heel of each angle in the cross-section. The procedure that was followed during the pretest measurements of the double angle specimens is as follows.

As shown in Figure 5.5, measurements of the locations of the angle cross-sections for camber and sweep were taken at 12 locations on the two angle cross-sections in the x_h axis and y_h axis directions. These measurements were repeated at the ends and at each quarter length of the specimen.

The devices that were used for the pretest measurements are a dial gage stand with a precision of 0.001 inches, and a caliper with a precision of 0.001 inches.

As it is shown in Figure 5.6, a wide flange beam with a machined surface was used to provide a second reference surface for the measurements. A 1 in. thick bar with a machined edge was clamped to the beam to provide a reference for the measurements.

Two 3 in. long spacer blocks were used to provide a reference for the measurements to the upstanding legs of the specimen (i.e., the bar is used for the measurements in x_h axis direction). These spacer blocks were bearing against both the 1 in. thick bar and the ends of the specimen as shown in Figure 5.6(c).

For the measurements in y_h axis direction, four 1 in. spacer blocks were located underneath the specimen, so measurements could be taken with reference to the surface of the beam as shown in Figure 5.6(b). Two of these spacer blocks were placed under the end cross-sections of the specimen, and the other two blocks were placed in between. Because of this arrangement of the four spacer blocks, for some of the test specimens, a chord drawn between the two end cross-sections was not parallel to the machined beam surface. This issue was resolved by a linear adjustment of the measurements relative to a chord drawn to the end cross-sections made after the measurements were taken.

All thickness and width measurements of legs were directly taken by calipers. Three thickness measurements were taken for each leg of the end cross-sections of the double angle specimen, as shown in Figure 5.5. The average of these three measurements for a leg is reported as the thickness of that leg.

The pretest measurements of the width and thickness of the specimens, and the corresponding cross-section parameters are presented in Table 5.2. The cross-section parameters were also calculated from the nominal width and thickness and are presented in Table 5.3. A comparison of the measured versus the nominal dimensions

and cross-sectional properties based on these dimensions is given later.

The initial out-of-straightness measurements in both the x_h axis and the y_h axis are reported in Table 5.4, where Δx_{h0} is the sweep measurement and Δy_{h0} is the camber measurement.

Bjorhovde (1972) suggests a model for the initial out-of-straightness that is a half sine wave over the length L of a column with a maximum initial out-of-straightness value of 1/1470 of the length of the column at the mid-height cross-section.

In Table 5.4 the initial out-of-straightness measurements are both presented at the mid-height cross-section and at the cross-section where these measurements reach their maximum values. As seen in this table, the initial imperfection measurements are generally smaller than the value of L/1470.

Table 5.4 indicates that specimen DA42 has a maximum initial out-of-straightness value in the x_h axis direction that is greater than the value of L/1470. This table also shows that specimens DC2, DC3, DC32, and DC4 have a maximum initial out-of-straightness value in the y_h axis direction that is greater than the suggested limit than L/1470. For these specimens the maximum initial out-of-straightness in the y_h axis direction occurred at the mid-height. The initial out-of-straightness measurements along the length of these test specimens and the other double angle specimens are presented with the test results for the test specimens.

5.3.3 Instrumentation

According to Technical Memorandum B4 (Galambos, 1998), the test data should include the applied load, the lateral deflection, the twist of the critical cross-section, the axial shortening, and strain data. The applied load and the cross-head displacement were determined from the SATEC test machine output. The axial shortening was determined from the cross-head displacement using the procedure presented in Appendix B. The other measurements were acquired using an external data acquisition system.

For pin-ended columns, the mid-height cross-section is assumed to be the critical section, thus deflection and strain measurements are taken at this cross-section as shown in Figure 5.7. As it is shown in Figure 5.3, an inclinometer was placed on each bearing to measure the rotation of the bearing.

Seven LVDTs were used to measure the lateral deflection at the mid-height cross-section. The twist of the mid-height cross-section, θ_z, was calculated from the LVDT data. For LVDT attachment to the mid-height cross-section, seven 1/16 in. diameter holes were drilled at the locations shown in Figure 5.8. The wire of each LVDT passed through one of these holes and was attached to a small nut on the far side of the angle leg so that the wire stays attached throughout the test.

The lateral deflection was measured in x_h axis and y_h axis directions. Figure 5.8 shows the parameters used to calculate the lateral deflection of the "heel" of the double angle specimens.

As Figure 5.8 shows, LVDT2 and LVDT3 were used to take measurements at 1/8 in. plus the thickness of a leg from the heels of the angles. The length of these LVDTs was intentionally made long enough so that the measurements acquired from these two LVDTs could be assumed to be taken at the heel of the angles.

In order to calculate the lateral deflections, the Law of Sines and the Law of Cosines are utilized. The displaced position of the "heel" shown in Figure 5.1 from the initial position of the heel was found using the data from LVDT2, LVDT3 and LVDT5 and utilizing the equations below, which refer to Figure 5.9. Note that the "heel" deflection is an approximate deflection of the point between the heels of the two angles in the cross-section shown in Figure 5.1.

The measurements acquired from LVDT2 and LVDT3 were averaged and referred to as the measurements from an imaginary LVDT23, as shown in Figure 5.9. The error introduced by this assumption is negligible due to the fact that the spacing between the angles is small enough compared to the length of the two LVDTs. The following equations use the data from LVDT23 and LVDT5 as follows:

The Law of Cosines states that;

$$L_{23\text{-}5}{}^2 = (L23 + \Delta 23)^2 + (L5 + \Delta 5)^2 - 2 \times (L23 + \Delta 23) \times (L5 + \Delta 5) \times COS(\theta 3') \quad \textbf{(5.1)}$$

where

$L_{23\text{-}5}$: the distance between the attachment points of LVDT5 and LVDT23

L23 : the initial distance between the attachment points of LVDT23

Δ23 : the length change measured by LVDT23 at a displaced position of the cross-section

L5 : the initial distance between the attachment points of LVDT5

Δ5 : the length change measured by LVDT5 at a displaced position of the cross-section

θ3' : the angle between LVDT23 and LVDT5 wires at their attachments to the cross-section, where θ3 is the initial angle

The Law of Sines states that;

$$\frac{(L5+\Delta 5)}{SIN(\theta 5')} = \frac{(L23+\Delta 23)}{SIN(\theta 23')} = \frac{L_{23-5}}{SIN(\theta 3')} \tag{5.2}$$

θ23' : the angle between LVDT23 and the line connecting LVDT23 and LVDT5 at a displaced position of the cross-section, where θ23 is the initial angle

θ5' : the angle between LVDT5 and the line connecting LVDT5 and LVDT23 at a displaced position of the cross-section, where θ5 is the initial angle

By utilizing Equations (5.1) and (5.2), one can find angle θ23' (or θ5'), as the cross-section displaces. Then, the lateral deflections are obtained as follows:

$$X_{h0} = (L23) \times COS(\theta 5)$$
$$Y_{h0} = (L23) \times SIN(\theta 5)$$
$$X_{hi} = (L23 + \Delta 23) \times COS(\theta 5')$$
$$Y_{hi} = (L23 + \Delta 23) \times SIN(\theta 5')$$
$$\Delta X_h = X_{hi} - X_{h0}$$
$$\Delta Y_h = Y_{hi} - Y_{h0}$$
$$\Delta x_h = \Delta X_h$$
$$\Delta y_h = \Delta Y_h$$

(5.3)

where ΔX_h and ΔY_h are the relative lateral deflections of the heel, from the initial position of the heel (X_{ho}, Y_{ho}), in the (X,Y) coordinate system defined in Figure 5.9.

The twist of the mid-height cross-section, θ_z, was found using the data from LVDTs 1, 4, 6, and 7 and utilizing the following equations which refer to Figure 5.10.

As seen in Figure 5.10, the center line of each leg was taken to represent the leg. The rotations of each leg of the angles of double angle cross-section were utilized in the twist calculations as follows:

$$\theta_{11} = \frac{\sqrt{(L4 + \Delta y_h)^2 + (\Delta x_h)^2} - (L4 + \Delta 4)}{L_{11}}$$
$$\theta_{12} = \frac{\sqrt{(L7 + \Delta x_h)^2 + (\Delta y_h)^2} - (L7 + \Delta 7)}{L_{12}}$$
$$\theta_{21} = \frac{(L6 + \Delta 6) - \sqrt{(L6 - \Delta x_h)^2 + (\Delta y_h)^2}}{L_{21}}$$
$$\theta_{22} = \frac{(L1 + \Delta 1) - \sqrt{(L1 + \Delta y_h)^2 + (\Delta x_h)^2}}{L_{22}}$$

(5.4)

where

L_{11} : the distance between the heel and the attachment point of LVDT4

L_{12} : the distance between the heel and the attachment point of LVDT7

L_{21} : the distance between the heel and the attachment point of LVDT6

L_{22} : the distance between the heel and the attachment point of LVDT1

L1 : the initial distance between the attachment points of LVDT1

L4 : the initial distance between the attachment points of LVDT4

L6 : the initial distance between the attachment points of LVDT6

L7 : the initial distance between the attachment points of LVDT7

$\Delta 1$: the length change measured by LVDT1 at a displaced position of the cross-section

$\Delta 4$: the length change measured by LVDT4 at a displaced position of the cross-section

$\Delta 6$: the length change measured by LVDT6 at a displaced position of the cross-section

$\Delta 7$: the length change measured by LVDT7 at a displaced position of the cross-section

θ_{11} : the rotation of the leg measuring the length L_{11}

θ_{12} : the rotation of the leg measuring the length L_{12}

θ_{21} : the rotation of the leg measuring the length L_{21}

θ_{22} : the rotation of the leg measuring the length L_{22}

Δx_h : the lateral deflection of the "heel" in the x_h axis direction at a displaced position of the cross-section

Δy_h : the lateral deflection of the "heel" in the y_h axis direction at a displaced position of the cross-section

Then the twist of the cross-section is found by following equation:

$$\theta_z = \frac{\theta_{11} + \theta_{12} + \theta_{21} + \theta_{22}}{4} \tag{5.5}$$

It should be noted that this method is not accurate as the twist becomes large.

Eight strain gages were placed near the mid-height cross-section as shown in Figure 5.11. The strain gages were generally placed back-to-back to account for local bending of the cross-section as shown in Figure 5.11. For example, SG-1 and SG-2 are back-to-back.

Table 5.5 provides a summary of the instrumentation used to acquire data for the double angle specimens.

5.3.4 Test Procedure

After each specimen was placed between the bearings, a small initial load was applied while the specimen was aligned. The initial load was gradually increased to approximately 1/20 of the predicted buckling load of the specimen. Then the data

acquisition system was initiated and further loading was applied to the specimen. In the first phase of loading, the load was controlled by nominal stress (load divided by area) per unit time, and the value of the loading rate was approximately 3 ksi/min. After the applied load reached half of the predicted buckling load, further loading was controlled by a nominal strain (cross-head displacement divided by specimen length) that corresponds very approximately to the initial stress loading rate in the linear elastic range. This loading rate was 0.01 in/min and was kept constant until the end of the test.

5.4 Predicted Buckling Capacities of the Double Angle Specimens

The predicted buckling capacities, which are based on the measured and also the nominal width and thickness measurements, are presented in Table 5.6. The comparison of these results in Table 5.7 shows that the predicted buckling capacities based on the measured dimensions are generally within a few percent and always within 10% of the predicted capacities based on the nominal dimensions.

In Table 5.8, the predicted buckling capacities are presented along with the Q reduction factor and the slenderness ratios for the principle axes. For the calculated results given in this table, the measured cross-sectional dimensions were utilized.

In order to calculate the predicted flexural buckling capacity about the strong axis, $P_{cr\text{-}y}$, the steps are as follows: (1) the strong axis slenderness ratio, $(KL/r)_y$, was modified according to Section E6 of the AISC (2005) specification, using Equation E6-2 (Equation 2-35) and the modified slenderness ratio is referred to as $(KL/r)_m$; (2)

the elastic critical buckling stress about the strong axis, $F_{e\text{-}y}$, was found from Equation E4-10 of the AISC (2005) specification (Equation 2-24 in Chapter 2); (3) the flexural buckling stress about the strong axis, $F_{cr\text{-}y}$, was found from Section E7 and Equation E7-2 (Equation 2-22) or Equation E7-3 (Equation 2-23); (4) the flexural buckling stress value was multiplied by the cross-sectional area of the specimen to determine the nominal compressive strength based on the limit state of flexural buckling about the strong axis, $P_{cr\text{-}y}$. $P_{cr\text{-}y}$ is referred to as the predicted flexural buckling capacity about the strong axis. Similar steps were used to find the predicted buckling capacity about the weak axis (i.e., the x axis), $P_{cr\text{-}x}$, except that $(KL/r)_x$ is not modified (i.e., $(KL/r)_m$ is not calculated for x axis) because for flexural buckling about the weak axis, the capacity of the built-up double angle member does not depend on force transfer between the connecting elements.

The double angle members have the potential to buckle as individual angle members with the buckled length equal to the distance between the connecting elements (the spacers). The single angle buckling capacity of the built-up double angle members, $2xP_{cr\text{-}SA}$, was calculated using the following steps: (1) the elastic critical buckling stress about the weak axis, $F_{e\text{-}SA}$, was found from Equation E4-10 of the AISC (2005) specification (Equation 2-24 in Chapter 2), where length of the member is calculated by dividing the length of the built-up member by n+1 where n is the number of mid-spacers; (2) the flexural buckling stress about weak axis, $F_{cr\text{-}SA}$, was found from Section E7 and Equations E7-2 (Equation 2-22) and E7-3 (Equation 2-23); (3) the flexural buckling stress value was multiplied by twice the cross-sectional area

of the single angle member to determine the nominal compressive strength based on single angle flexural buckling about the weak axis, $2xP_{cr\text{-}SA}$. As seen in Table 5.8, the capacities calculated for the single angle buckling behavior of the built-up double angle specimens are always higher than both the flexural buckling and flexural-torsional buckling capacities of the double angle specimens.

In order to find the predicted flexural-torsional buckling capacity of the double angle specimens, $P_{cr\text{-}ft}$, the steps are as follows: (1) the strong axis slenderness ratio, $(KL/r)_y$, was modified according to Section E6 of the AISC (2005) specification, using Equation E6-2 (Equation 2-35), and the modified slenderness ratio is referred to as $(KL/r)_m$; (2) the elastic critical buckling stress about the strong axis, $F_{e\text{-}y}$, was found from Equation E4-10 (Equation 2-33) and the elastic critical buckling stress about the z axis, $F_{e\text{-}z}$, was found from Equation E4-11 (Equation 2-34) of the AISC (2005) specification; (3) the elastic flexural-torsional buckling stress, $F_{e\text{-}ft}$ was found from Equation E4-5 (Equation 2-32); (4) the flexural-torsional buckling stress, $F_{cr\text{-}ft}$, was found from Section E7 and Equation E7-2 (Equation 2-30) or Equation E7-3 (Equation 2-31); (5) the flexural-torsional buckling stress value was multiplied by cross-sectional area of the specimen to determine the nominal compressive strength based on the limit state of flexural-torsional buckling, $P_{cr\text{-}ft}$.

The predicted buckling capacities found by using the measured width and thickness measurements are presented in Table 5.8. This table shows that the predicted flexural-torsional buckling capacity is smaller than either the predicted flexural buckling capacity about the weak axis (x axis) or the predicted flexural buckling

capacity about the strong axis (y axis). As a result, the double angle specimens are expected to buckle in the flexural-torsional buckling mode.

5.5 Test Results

The following discussions are based on test data that is arranged to include the applied load, the cross-head displacement, the specimen shortening, the lateral deflection of the heel at the mid-height cross-section, the twist of the mid-height cross-section. The test data also include strain data for a few specimens. In the presentation of the test data, zero relative measurement was assumed at the beginning of the test when there is a small initial load.

It should be noted at this point that the instrumentation were only placed on the mid-height cross-section and on the bearings. Thus, a limited amount of data was available to evaluate the behavior of the entire of the specimen.

5.5.1 Specimen DA1

The load vs. the cross-head displacement is shown in Figure 5.12. The maximum experimental load, P_{EXP}, is higher than both the predicted flexural-torsional buckling capacity, $P_{cr\text{-}ft}$, and the predicted flexural buckling capacity about the strong axis, $P_{cr\text{-}y}$.

Figure 5.13 presents the graph of the load vs. the specimen shortening. The specimen shortening was determined from the cross-head displacement as described in Appendix B. The small offset in the load vs. the specimen shortening curve at a load of 180 kips (P_{LL}, which is the lower load limit that was considered to be end of seating of the specimen that is observed from load vs. cross-head displacement curve, is equal

to 180 kips for the DA series specimens, see Appendix B) is caused by error introduced by the approximations described in Appendix B.

The load vs. the twist of the mid-height cross-section is shown in Figure 5.14. This figure indicates a small torsional deformation occurred in the post-peak region. Figure 5.15 shows the load vs. the rotation of the bearings. The seating of the specimen is presumed to be the cause of the initial bearing rotations. Larger rotations of the bearings begin to develop just before the peak load and continue to grow in the post-peak region. As Figure 5.16 shows, x_h axis lateral deflection of the mid-height cross-section is observed in the post-peak region but very little x_h axis deflection occurs before the peak load is reached. There is no measurable y_h axis lateral deflection as shown in this figure.

The initial out-of-straightness along the length of the specimen is shown in Figure 5.17. This figure shows that the maximum initial out-of-straightness in both the x_h axis and the y_h axis directions were measured at a cross-section close to the bottom bearing.

Twist, θ_z, and lateral deflection, Δx_h, both occurred at the mid-height cross-section in the post-peak region which is an indication of the flexural-torsional buckling mode, although the x_h axis lateral deflection continued to grow while the twist remained constant after the load decreased by about 10% of the peak load. The buckled shape of the specimen after peak load is shown in Figure 5.18. This figure shows that local plate bending occurred at a cross-section near the bottom of the specimen, which may

have influenced the buckling capacity of the specimen.

5.5.2 Specimen DA12

This test specimen is a repetition of the first test specimen, specimen DA1. The load vs. the cross-head displacement is shown in Figure 5.19. The maximum experimental load, P_{EXP}, is approximately same as the result for specimen DA1, and P_{EXP} is higher than both the predicted flexural-torsional buckling capacity, $P_{cr\text{-}ft}$, and the predicted flexural buckling capacity about the strong axis, $P_{cr\text{-}y}$.

Figure 5.20 presents the graph of the load vs. the specimen shortening, determined from the cross-head displacement as described in Appendix B.

The load vs. the twist of the mid-height cross-section is shown in Figure 5.21. This figure indicates a small torsional deformation early in the post-peak region. Figure 5.22 shows the load vs. the rotation of the bearings. The bearing rotations began to grow just before the peak load and continue to grow in the post-peak region. Figure 5.23 shows that the x_h axis lateral deflection at the mid-height cross-section is noticeable in the post-peak region. On the other hand, the y_h axis deflection is small as shown by the figure. The twist, the bearing rotations, and the lateral deflection data acquired for specimen DA12 resemble very much the data acquired for specimen DA1.

The initial out-of-straightness along the length of the specimen is shown in Figure 5.24. This figure shows that the maximum initial out-of-straightness in both the x_h axis and the y_h axis direction were near the mid-height cross-section.

The lateral deflection, Δx_h, at the mid-height cross-section is accompanied by a small twist, θ_z,(see Figure 5.21) in the post-peak region, which suggests that flexural-torsional buckling occurred, although the twist remains nearly constant (and even reduces slightly) after approximately 10% load drop from the peak load. The buckled shape of the specimen after peak load is shown in Figure 5.25. This figure shows that local plate bending occurred at a cross-section near the top of the specimen which may have influenced the buckling capacity of the specimen.

5.5.3 Specimen DA2

The load vs. the cross-head displacement is shown in Figure 5.26. The maximum experimental load, P_{EXP}, is higher than both the predicted flexural-torsional buckling capacity, $P_{cr\text{-}ft}$, and the predicted flexural buckling capacity about the strong axis, $P_{cr\text{-}y}$.

Figure 5.27 shows the load vs. the specimen shortening, determined from the cross-head displacement as described in Appendix B.

The load vs. the twist of the mid-height cross-section is shown in Figure 5.28. This figure indicates that the torsional deformation initiates just before the peak load and continues to grow in the post-peak region. Figure 5.29 pres ents the load vs. the rotation of the bearings. The bearing rotations begin to grow just before the peak load. As Figure 5.30 shows, lateral deflection of the mid-height cross-section is observed in the post-peak region. The x_h axis lateral deflection is larger than the y_h axis lateral deflection, but some y_h axis deflection was observed as shown in the figure.

Figure 5.31 shows the load vs. the strain separation data acquired near the mid-

height cross-section. As seen from this figure, back-to-back strain separation data is only available for SG 3&4 and SG7&8. There is no apparent strain data separation observed for these gage locations prior to reaching the peak load. Thus, there is no apparent local plate bending occurred at the mid-height cross-section before the peak load is reached.

The initial out-of-straightness along the length of the specimen is shown in Figure 5.32. The maximum initial out-of-straightness measurements in both the x_h axis and the y_h axis directions are observed in cross-sections other than the mid-height cross-section.

Twist, θ_z, and lateral deflection, Δx_h, both occurred at the mid-height cross-section in the post-peak region which is an indication of the flexural-torsional buckling mode. The buckled shape of the specimen in the post-peak region is shown in Figure 5.33.

5.5.4 Specimen DA22

This specimen is similar to specimen DA2, but has one more mid-spacer with a closer spacing of the two angles (see Table 5.1). The load vs. the cross-head displacement is shown in Figure 5.34. The maximum experimental load, P_{EXP}, is higher than both the predicted flexural-torsional buckling capacity, $P_{cr\text{-}ft}$, and the predicted flexural buckling capacity about the strong axis, $P_{cr\text{-}y}$.

Figure 5.35 presents the graph of the load vs. the specimen shortening. The specimen shortening was calculated from the cross-head displacement (see Appendix B), and the small offset in the load vs. the specimen shortening curve at a load of 180

kips is from the approximations introduced by these calculations.

The load vs. the twist of the mid-height cross-section is shown in Figure 5.36. This figure shows that the torsional deformation initiates at the peak load and continues to grow in the post-peak region. Figure 5.37 shows the load vs. the rotation of the bearings. As seen in this figure, a very little bearing rotation is observed before the peak load level and the rotations begin to grow in the post-peak region. Figure 5.38 shows that lateral deflections in both the x_h axis and the y_h axis directions at the mid-height cross-section begin to grow at the peak load. The x_h axis lateral deflection is much larger than the y_h axis lateral deflection in the post-peak region.

The initial out-of-straightness along the length of the specimen is shown in Figure 5.39. This figure indicates that the maximum initial out-of-straightness in the x_h axis direction is at a cross-section near the bottom bearing where it is much larger than the maximum initial out-of-straightness in the y_h axis direction.

Twist, θ_z, and lateral deflection, Δx_h, at the mid-height cross-section grow simultaneously in the post-peak region which indicates that the specimen buckled in the expected flexural-torsional mode. The buckled shape of the specimen after the peak load is shown in Figure 5.40. This figure shows that local plate bending occurred near the mid-height cross-section, which may have influenced the flexural-torsional buckling behavior.

5.5.5 Specimen DA3

The load vs. the cross-head displacement is shown in Figure 5.41. The maximum

experimental load, P_{EXP}, is higher than both the predicted flexural-torsional buckling capacity, $P_{cr\text{-}ft}$, and the predicted flexural buckling capacity about the strong axis, $P_{cr\text{-}y}$.

Figure 5.42 presents the graph of the load vs. the specimen shortening, determined from the cross-head displacement as described in Appendix B.

The load vs. the twist of the mid-height cross-section is shown in Figure 5.43. This figure indicates the torsional deformation starts at the peak load and continues to grow in the post-peak region. Figure 5.44 shows the load vs. the rotation of the bearings. As seen from this figure, the bearing rotations start at the peak load level. As Figure 5.45 shows, the lateral deflections in both the x_h axis and y_h axis directions begin at the peak load level, and then these deflections increase in the post-peak region. The x_h axis lateral deflection is much larger than the y_h axis lateral deflection in the post-peak region.

The initial out-of-straightness along the length of the specimen is shown in Figure 5.46. The maximum x_h axis initial out-of-straightness is measured at a cross-section near the top bearing where it is much larger than the y_h axis initial out-of-straightness measurement. The maximum y_h axis initial out-of-straightness is measured is near mid-height.

Twist, θ_z, and lateral deflection, Δx_h, at the mid-height cross-section grow simultaneously in the post-peak region which indicates that the specimen buckled in the expected flexural-torsional buckling mode. The buckled shape of the specimen after the peak load is shown in Figure 5.47.

5.5.6 Specimen DA4

The load vs. the cross-head displacement is shown in Figure 5.48. There is a rapid drop of load observed when the load level reached to the peak load. Loading was stopped by using the manual control option of the SATEC machine immediately after failure was observed. Thus, limited data was acquired in the post-peak region. The maximum experimental load, P_{EXP}, is higher than both the predicted flexural-torsional buckling capacity, $P_{cr\text{-}ft}$, and the predicted flexural buckling capacity about the strong axis, $P_{cr\text{-}y}$.

Figure 5.49 presents the graph of the load vs. the specimen shortening, determined from the cross-head displacement. The small offset in the load vs. the specimen shortening curve at a load of 180 kips is caused by error introduced by the approximations described in Appendix B.

The load vs. the twist of the mid-height cross-section is shown in Figure 5.50. This figure indicates that there is no apparent torsional deformation before the peak load level. Figure 5.50 indicates a large torsional deformation immediately after the peak load is reached. Figure 5.51 shows the load vs. the rotation of the bearings. This figure indicates that at peak load, the bearing rotations increased while the load stayed constant until the specimen failed. Then a rapid drop in load is observed accompanied by more rotation of the bearings. As Figure 5.52 shows, there is a very little lateral deflection at the mid-height cross-section before the peak load level. In the post-peak region, the x_h axis and the y_h axis lateral deflection occur as the load drops rapidly. The x_h axis lateral deflection becomes much larger than the y_h axis lateral deflection as

the load decreased.

The initial out-of-straightness along the length of the specimen is shown in Figure 5.53. The maximum initial out-of-straightness in x_h axis direction was close to the top bearing, while, the maximum initial out-of-straightness in y_h axis direction was near the mid-height cross-section.

The specimen was expected to buckle in the flexural-torsional buckling mode. The buckled shape of the specimen after the peak load is shown in Figure 5.54. As seen from this figure, the built-up member was controlled by single angle behavior. The single angle section on the right of this figure failed at the peak load and then contacted with the left single angle and compelled it to displace in the x_h axis direction, which resulted in a large x_h axis lateral deflection (see Figure 5.52). Even though this single angle buckling behavior was observed, the experimental load was larger than the predicted double angle flexural-torsional and flexural buckling capacities.

5.5.7 Specimen DA42

Specimen DA42 was similar to specimen DA4, except that specimen DA42 has 1 mid-spacer while specimen DA4 has 2 mid-spacers. The load vs. the cross-head displacement is shown in Figure 5.55. The maximum experimental load, P_{EXP}, is higher than both the predicted flexural-torsional buckling capacity, $P_{cr\text{-}ft}$, and the predicted flexural buckling capacity about the strong axis, $P_{cr\text{-}y}$.

Figure 5.56 presents the graph of the load vs. the specimen shortening, determined

from the cross-head displacement. The small offset in the load vs. the specimen shortening curve at a load of 180 kips is caused by error introduced by the approximations described in Appendix B.

The load vs. the twist of the mid-height cross-section is shown in Figure 5.57. There is no apparent torsional deformation observed until the peak load level. The twist initiates close to the peak load and reverses direction as the specimen fails. Figure 5.58 shows the load vs. the rotation of the bearings. The bearing rotations grow throughout the test. At the peak load, the rotations increase while the load stays constant.

As Figure 5.59 shows, very little x_h axis lateral deflection at the mid-height cross-section is observed before the peak load level. In the post-peak region, the x_h axis lateral deflection grows, becoming much larger than the y_h axis lateral deflection. The rotations of the bearings and the lateral deflection measurements resemble the measurements observed for the specimen DA4, while the twist in the post-peak region for specimen DA42 is smaller than for specimen DA4.

The initial out-of-straightness along the length of the specimen is shown in Figure 5.60. The maximum initial out-of-straightness in both x_h axis and y_h axis directions occurs near the top bearing. The maximum initial out-of-straightness in the x_h axis direction is higher than the initial out-of-straightness value of L/1470 discussed in Chapter 2 (Bjorhovde, 1972).

Specimen DA42 was expected to buckle in the flexural-torsional buckling mode.

The buckled shape of the specimen after the peak load is shown in Figure 5.61. It is observed that single angle buckling behavior controlled the behavior of specimen DA42 as it did for specimen DA4.

The built-up members designed according to the Section E6 of the AISC (2005) specification must fulfill the following requirement. The slenderness ratio of the double angle member should be larger than the 4/3 of the slenderness ratio of the single angles that are used to build up the member. According to this requirement, specimen DA42 should have at least 2 mid-spacers, while, only 1 mid-spacer was present in this specimen. Thus, the single angle buckling behavior can be explained by the failure to fulfill this requirement. Nonetheless, the experimental capacity at specimen DA42 exceeded the predicted double angle capacities.

5.5.8 Specimen DA5

The load vs. the cross-head displacement is shown in Figure 5.62. The maximum experimental load, P_{EXP}, is higher than both the predicted flexural-torsional buckling capacity, $P_{cr\text{-}ft}$, and the predicted flexural buckling capacity about the strong axis, $P_{cr\text{-}y}$.

Figure 5.63 presents the graph of the load vs. the specimen shortening, determined from the cross-head displacement as described in Appendix B.

The load vs. the twist of the mid-height cross-section is shown in Figure 5.64. This figure indicates a very small torsional deformation before the peak load, and twist data changes direction after a slight drop of load in the post-peak region. Figure 5.65 shows the load vs. the rotation of the bearings. The initial rotations of the bearings, caused by

the seating effect (see Section 5.4.1) do not grow before the peak load is reached, however, the rotations grow in the post-peak region. As Figure 5.66 shows, x_h axis lateral deflection at the mid-height cross-section is observed in the post-peak region. There is no apparent y_h axis lateral deflection observed throughout the test.

The initial out-of-straightness along the length of the specimen is shown in Figure 5.67. The maximum initial out-of-straightness for both axis directions occurs close to the mid-height cross-section.

Twist, θ_z, and lateral deflection, Δx_h, at the mid-height cross-section both initiate in the post-peak region. The twist, however, reverses direction after an approximately 10% decrease in load after the peak load level. The buckled shape of the specimen after the peak load is shown in Figure 5.68. In this figure, some single angle buckling behavior is apparent in the buckling shape of the single angle on the right of this figure, but in addition, this angle exhibits substantial local plate bending. The fact that the twist data reverses direction after a load drop from the peak load suggests that the single angle behavior and plate bending occurred after the peak load was reached. The initial decrease in load from the peak load may have been from buckling in the flexural-torsional mode.

5.5.9 Specimen DB1

The load vs. the cross-head displacement is shown in Figure 5.69. The maximum experimental load, P_{EXP}, is higher than both the predicted flexural-torsional buckling capacity, $P_{cr\text{-}ft}$, and the predicted flexural buckling capacity about the strong axis, $P_{cr\text{-}y}$.

After the load reached the peak load, it dropped rapidly and continued to decrease.

Figure 5.70 presents the graph of the load vs. the specimen shortening, determined from the cross-head displacement as described in Appendix B.

The load vs. the twist of the mid-height cross-section is shown in Figure 5.71. This figure indicates some torsional deformation occurred before the peak load level. The rapid drop in the load occurred as the twist at the mid-height cross-section vanished; however, as the load decreased in the post-peak region, the twist at the mid-height cross-section increased. Figure 5.72 shows the load vs. the rotation of the bearings. There was no observable rotation in the bearings before reaching the peak load. As Figure 5.73 shows, there is some x_h axis lateral deflection at the mid-height cross-section observed in the post-peak region, but no apparent y_h axis lateral deflection is observed.

The initial out-of-straightness along the length of the specimen is shown in Figure 5.74. The maximum initial out-of-straightness for both the x_h axis and the y_h axis directions are negligible as seen in Table 5.4.

The specimen was expected to buckle in the flexural-torsional buckling mode. However, both the lateral deflection and the twist were quite small. The deformed shape of the specimen after the peak load is shown in Figure 5.75. As seen from this figure, it appears that local plate buckling occurred near the mid-height cross-section.

As shown in Figure 5.75, strain gages were placed on the mid-height cross-section, however, due to difficulties with the data acquisition system, strain gage data were not

acquired.

5.5.10 Specimen DB2

The load vs. the cross-head displacement is shown in Figure 5.76. The maximum experimental load, P_{EXP}, is higher than both the predicted flexural-torsional buckling capacity, $P_{cr\text{-}ft}$, and the predicted flexural buckling capacity about the strong axis, $P_{cr\text{-}y}$. As shown in Figure 5.76, the load dropped rapidly after it reached the peak load level.

Figure 5.77 presents the graph of the load vs. the specimen shortening, determined from the cross-head displacement as described in Appendix B.

The load vs. the twist of the mid-height cross-section is shown in Figure 5.78. This figure shows that some torsional deformation occurred before the peak load level was reached. As the load dropped, this twist decreased. Figure 5.79 shows the load vs. the rotation of the bearings. There was no observable rotation in the bearings before the peak load is reached and the bearing rotations begin to grow at the peak load level while the load stays constant until failure occurs. As Figure 5.80 shows, no apparent lateral deflection at the mid-height cross-section is observed before reaching the peak load level. The x_h axis lateral deflection is larger than the y_h axis lateral deflection in the post-peak region, as shown in this figure.

The initial out-of-straightness along the length of the specimen is shown in Figure 5.81. The maximum initial out-of-straightness for both the x_h axis and the y_h axis directions are small as seen in Table 5.4.

This specimen was expected to fail in the flexural-torsional buckling mode. Some

twist occurred before the peak load was reached but there was little lateral deflection before the peak load. After the peak, there was some lateral deflection, but no significant twist. The deformed shape of the specimen after the peak load is shown in Figure 5.82. It appears from this figure that the failure behavior of the member was local plate buckling near the mid-height cross-section.

5.5.11 Specimen DB3

The load vs. the cross-head displacement is shown in Figure 5.83. The maximum experimental load, P_{EXP}, is higher than both the predicted flexural-torsional buckling capacity, $P_{cr\text{-}ft}$, and the predicted flexural buckling capacity about the strong axis, $P_{cr\text{-}y}$. A rapid drop of load is observed at the peak load level. As seen in Figure 5.83, the load droped rapidly when the specimen failed.

Figure 5.84 presents the graph of the load vs. the specimen shortening, determined from the cross-head displacement as described in Appendix B.

The load vs. the twist of the mid-height cross-section is shown in Figure 5.85. As seen in this figure, a large torsional deformation is observed before the peak load is reached, and the deformation continues to grow after the load drop. Figure 5.86 shows the load vs. the rotation of the bearings. This figure indicates that the bearing rotations initiate at a load level that is close to the peak load, and continues to grow at the peak load. The increase in the rotations of the bearings continues after a drop of load is observed.

As Figure 5.87 shows, lateral deflection in the x_h axis direction is observed at the

peak load level in the x_h axis direction. The x_h axis lateral deflection continues to grow in the post-peak region, while, there is a very little y_h axis lateral deflection observed throughout the test.

Figure 5.88 shows the load vs. the strain separation data acquired near the mid-height cross-section. As seen from this figure, there is an apparent separation of strain measurements between the back-to-back strain gages SG 1&2 and SG 5&6 before the peak load is reached. This indicates that local plate bending occurred at the mid-height cross-section, where the strain gages were placed, before the peak load.

The initial out-of-straightness along the length of the specimen is shown in Figure 5.89. The maximum initial out-of-straightness in both axis directions occurs close to the top bearing.

The large torsional deformation near the peak load level is accompanied by a relatively small amount of lateral deflection in the x_h axis direction. This specimen was expected to fail in the flexural-torsional buckling mode. The deformed shape of the specimen after the peak load is shown in Figure 5.90. As seen from this figure, substantial local plate bending occurred between the middle and upper mid-spacers. The strain separation data, as shown in Figure 5.88, shows that local plate bending occurred near the mid-height cross-section before the peak load is reached. The specimen appears to have failed from flexural-torsional buckling with substantial local plate bending.

5.5.12 Specimen DB4

The load vs. the cross-head displacement is shown in Figure 5.91. The maximum experimental load, P_{EXP}, is higher than both the predicted flexural-torsional buckling capacity, $P_{cr\text{-}ft}$, and the predicted flexural buckling capacity about the strong axis, $P_{cr\text{-}y}$. A drop in the load was observed right after the peak load was reached.

Figure 5.92 presents the graph of the load vs. the specimen shortening, determined from the cross-head displacement as described in Appendix B.

The load vs. the twist of the mid-height cross-section is shown in Figure 5.93. This figure shows that some torsional deformation occurred before the peak load level and the deformation continued to grow in the post-peak region. Figure 5.94 indicates the load vs. the rotation of the bearings. It is observed from this figure that the bottom bearing rotation begin to increase before the peak load level whereas there is no apparent rotation in the top bearing. The bearing rotations grow throughout the rest of the test. As Figure 5.95 shows, there is apparent lateral deflection at the mid-height cross-section observed before the peak load level. In the post-peak region, the increase in the x_h axis lateral deflection is much larger than the y_h axis lateral deflection.

The initial out-of-straightness along the length of the specimen is shown in Figure 5.96. The maximum initial out-of-straightness in both axis directions occurs close to the top bearing.

The specimen was expected to buckle in the flexural-torsional buckling mode. The deformed shape of the specimen after the peak load is shown in Figure 5.97 suggests

that the built-up member failed in a single angle mode, with substantial local plate bending. Although the single angle behavior was observed, the experimental capacity was larger than the predicted double angle buckling capacities. It is also observed that the lateral deflection in both the x_h and the y_h axis directions at the mid-height cross-section was accompanied by a noticeable torsional deformation before the peak load was reached.

5.5.13 Specimen DB5

The load vs. the cross-head displacement is shown in Figure 5.98. The maximum experimental load, P_{EXP}, is higher than both the predicted flexural-torsional buckling capacity, $P_{cr\text{-}ft}$, and the predicted flexural buckling capacity about the strong axis, $P_{cr\text{-}y}$. The load dropped rapidly after the peak load was reached.

Figure 5.99 presents the graph of the load vs. the specimen shortening, determined from the cross-head displacement as described in Appendix B.

The load vs. the twist of the mid-height cross-section is shown in Figure 5.100. This figure indicates that a noticeable torsional deformation starts with the initial loading and continues to grow throughout the test. Figure 5.101 shows the load vs. the rotation of the bearings. There are no apparent bearing rotations before the peak load is reached. However, at the peak load level, the rotations begin to grow. As Figure 5.102 shows, there is no apparent lateral deflection at the mid-height cross-section observed before the peak load. The x_h axis lateral deflection increases in the post-peak region and it is much larger than the y_h axis lateral deflection.

The initial out-of-straightness along the length of the specimen is shown in Figure 5.103. The maximum initial out-of-straightness in both directions is near the mid-height cross-section.

The specimen was expected to buckle in flexural-torsional buckling mode. The deformed shape of the specimen after peak load is shown in Figure 5.104. Single angle behavior appears to have affected the failure mode of the member. As it is seen from this figure, local buckling occurred in one of the angles. The experimental capacity was larger than the predicted buckling capacities, even though the failure mode differed from the expected mode.

5.5.14 Specimen DC1

The load vs. the cross-head displacement is shown in Figure 5.105. The maximum experimental load, P_{EXP}, is higher than both the predicted flexural-torsional buckling capacity, $P_{cr\text{-}ft}$, and the predicted flexural buckling capacity about the strong axis, $P_{cr\text{-}y}$. A rapid drop of load was observed right after the peak load was reached.

Figure 5.106 presents the graph of the load vs. the specimen shortening, determined from the cross-head displacement as described in Appendix B.

The load vs. the twist of the mid-height cross-section is shown in Figure 5.107. As seen from this figure there is a very little twist occurs before the peak load and the twist does not grow in the post-peak region.. Figure 5.108 shows the load vs. the rotation of the bearings. Before the peak load the bearing rotations are small, but they increase at the peak load level. As Figure 5.109 shows, there is no lateral deflection

observed before the peak load level. A small x_h axis lateral deflection at the mid-height cross-section is observed in the post-peak region, while, the y_h axis deflection is essentially zero.

The initial out-of-straightness along the length of the specimen is shown in Figure 5.110. The maximum initial out-of-straightness for both directions occurs near the mid-height cross-section.

The specimen was expected to buckle in the flexural-torsional buckling mode. The deformed shape of the specimen after peak load is shown in Figure 5.111. As seen from this figure, local plate buckling occurred between the middle and upper mid-spacers. Even though the failure mode is differed from the expected flexural-torsional buckling mode, the experimental capacity was much higher than the predicted buckling capacities.

5.5.15 Specimen DC2

The load vs. the cross-head displacement is shown in Figure 5.112. The maximum experimental load, P_{EXP}, is higher than both the predicted flexural-torsional buckling capacity, $P_{cr\text{-}ft}$, and the predicted flexural buckling capacity about the strong axis, $P_{cr\text{-}y}$. A rapid drop of load was observed at the peak load was reached.

Figure 5.113 presents the graph of the load vs. the specimen shortening, determined from the cross-head displacement as described in Appendix B.

The load vs. the twist of the mid-height cross-section is shown in Figure 5.114. This figure indicates that some torsional deformation occurred before the peak load

level and torsional deformation continues to grow in the post-peak region. Figure 5.115 shows the load vs. the rotation of the bearings. As seen from this figure, the bearing rotations start early in the test, and continue to grow throughout the test. As Figure 5.116 shows, there is no significant lateral deflection at the mid-height cross-section before the peak load level. The x_h axis lateral deflection and the y_h axis lateral deflection develop in the post-peak region. The x_h axis lateral deflection is larger than the y_h axis lateral deflection.

The initial out-of-straightness along the length of the specimen is shown in Figure 5.117. The maximum initial out-of-straightness in the y_h axis direction occurs near the mid-height cross-section and it is larger than the maximum initial out-of-straightness in the x_h axis direction at this cross-section. The maximum initial out-of-straightness in the y_h axis direction (Table 5.4) is higher than the initial out-of-straightness value of L/1470 suggested by Bjorhovde (1972).

The deformed shape of the specimen after the peak load is shown in Figure 5.118. As seen from this figure, local plate bending occurred between the middle and upper mid-spacers which may have influenced the buckling capacity of the member. Even though the failure mode differs from the expected flexural-torsional buckling mode, the experimental capacity is much higher than the predicted buckling capacities.

5.5.16 Specimen DC3

The load vs. the cross-head displacement is shown in Figure 5.119. The maximum experimental load, P_{EXP}, is higher than both the predicted flexural-torsional buckling

capacity, $P_{cr\text{-}ft}$, and the predicted flexural buckling capacity about the strong axis, $P_{cr\text{-}y}$. The load rapidly dropped from the peak load and continued to decrease, during the test.

Figure 5.120 presents the graph of the load vs. the specimen shortening, determined from the cross-head displacement as described in Appendix B. The small offset in the load vs. the specimen shortening curve at a load of 25 kips (which is the lower load limit, P_{LL}, for the DC series specimens) is caused by error introduced by the approximations described in Appendix B.

The load vs. the twist of the mid-height cross-section is shown in Figure 5.121. This figure indicates that torsional deformation started early in the test and the torsional deformation continued to grow in the post-peak region. Figure 5.122 indicates the load vs. the rotation of the bearings. There are noticeable bearing rotations before the peak load is reached, which continued in the post-peak region As Figure 5.123 shows, the lateral deflection at the mid-height cross-section occurred in both directions before the peak load was reached. The x_h axis lateral deflection is larger than the y_h axis lateral deflection in the post-peak region, as shown in this figure.

The initial out-of-straightness along the length of the specimen is shown in Figure 5.124. The maximum initial out-of-straightness in the y_h axis direction occurs near the mid-height cross-section and is higher than the initial out-of-straightness value of L/1470 by 20%, as seen in Table 5.4.

The twist and the lateral deflection in x_h axis direction at the mid-height cross-section grow simultaneously before and after the peak load level which is an indication of the flexural-torsional buckling mode. The deformed shape of the specimen after peak load is shown in Figure 5.125. The specimen appears to have buckled in the expected flexural-torsional buckling mode accompanied by local plate bending close to the mid-height cross-section.

5.5.17 Specimen DC32

The load vs. the cross-head displacement is shown in Figure 5.126. The maximum experimental load, P_{EXP}, is higher than both the predicted flexural-torsional buckling capacity, $P_{cr\text{-}ft}$, and the predicted flexural buckling capacity about the strong axis, $P_{cr\text{-}y}$. A rapid drop of load is observed after the peak load is reached, as seen in Figure 5.126.

Figure 5.127 presents the graph of the load vs. the specimen shortening. The specimen shortening was calculated from the cross-head displacement (see Appendix B), and the small offset in the load vs. the specimen shortening curve at a load of 25 kips is from the approximations introduced by these calculations.

The load vs. the twist of the mid-height cross-section is shown in Figure 5.128. As seen from this figure, a noticeable torsional deformation is observed before the peak load and this torsional deformation continues to grow in the post-peak region. Figure 5.129 shows the load vs. the rotation of the bearings. The top bearing has some rotation before the peak load is reached, while, there is no observable rotation in the

bottom bearing before the peak load. After the peak, the direction of bearing rotation reverses for both bearings, and both bearing rotations increase in the post-peak region. As Figure 5.130 shows, there are small lateral deflections at the mid-height cross-section observed before the peak load level. The x_h axis lateral deflection reverses direction at the peak load and becomes larger than the y_h axis lateral deflection in the post-peak region.

The initial out-of-straightness along the length of the specimen is shown in Figure 5.131. The maximum initial out-of-straightness for both directions occurs near the mid-height cross-section. The maximum Δy_{h0} axis is higher than the initial out-of-straightness value of L/1470.

The expected failure mode is the flexural-torsional buckling mode. The deformed shape of the specimen after the peak load is shown in Figure 5.132. The member sustained a large torsional deformation, but the lateral deflections in both the x_h and y_h axis directions were relatively very small. Significant local plate bending occurred at the base of one of the angles, as shown in Figure 5.132.

5.5.18 Specimen DC4

The load vs. the cross-head displacement is shown in Figure 5.133. The maximum experimental load, P_{EXP}, is higher than both the predicted flexural-torsional buckling capacity, $P_{cr\text{-}ft}$, and the predicted flexural buckling capacity about the strong axis, $P_{cr\text{-}y}$.

Figure 5.134 presents the graph of the load vs. the specimen shortening, determined from the cross-head displacement as described in Appendix B.

The load vs. the twist of the mid-height cross-section is shown in Figure 5.135. This figure indicates that the torsional deformation starts just before the peak load level and the torsional deformation gradually increases in the post-peak region. Figure 5.136 shows the load vs. the rotation of the bearings. The bearing rotations start to grow just before the peak load level. As Figure 5.137 shows, there is a noticeable lateral deflection at the mid-height cross-section observed in both the x_h axis and the y_h axis directions before and after the peak load level. The x_h axis lateral deflection in the post-peak region is larger than the y_h axis lateral deflection.

The initial out-of-straightness along the length of the specimen is shown in Figure 5.138. The maximum initial out-of-straightness for both directions occurs near the mid-height cross-section. The maximum initial out-of-straightness y axis direction is approximately 25% higher than the maximum initial out-of-straightness value of L/1470, as seen in Table 5.4.

The expected failure mode is the flexural-torsional buckling mode. The deformed shape of the specimen after the peak load is shown in Figure 5.139. As seen from this figure the member has both lateral and torsional deformation. At the ends of the member, and at the mid-height cross-section, local plate bending is observed which might have influenced the buckling behavior of the specimen, however, the experimental capacity was much higher than the predicted buckling capacities.

5.5.19 Specimen DC42

The load vs. the cross-head displacement is shown in Figure 5.140. The maximum

experimental load, P_{EXP}, is higher than both the predicted flexural-torsional buckling capacity, $P_{cr\text{-}ft}$, and the predicted flexural buckling capacity about the strong axis, $P_{cr\text{-}y}$. The load dropped rapidly from the peak load, as seen in Figure 5.140.

Figure 5.141 presents the graph of the load vs. the specimen shortening, determined from the cross-head displacement as described in Appendix B. The small offset in the load vs. the specimen shortening curve at a load of 25 kips is caused by error introduced by the approximations described in Appendix B.

The load vs. the twist of the mid-height cross-section is shown in Figure 5.142. This figure indicates that torsional deformation initiates at the beginning of the test, is quite noticeable before the peak load level, and continues to grow in the post-peak region. Figure 5.143 shows the load vs. the rotation of the bearings. The bearing rotations are very small before the peak load is reached, but the rotations grow after the peak load level. As Figure 5.144 shows, there is noticeable lateral deflection at the mid-height cross-section in both axis direction observed before reaching the peak load level. After the peak load, the x_h axis lateral deflection reverses. The x_h axis lateral deflection is larger than the y_h axis lateral deflection in the post-peak region.

The initial out-of-straightness along the length of the specimen is shown in Figure 5.145. The maximum initial out-of-straightness in the y_h axis direction occurs near the mid-height cross-section and it is much larger than the maximum initial out-of-straightness in the x_h axis direction at this cross-section.

The deformed shape of the specimen after peak load is shown in Figure 5.146. The

twist and the lateral deflection in the x_h axis direction at the mid-height cross-section both grow simultaneously before the peak load level and in the post-peak region which is an indication of the flexural-torsional buckling mode. Thus, the specimen appears to have buckled in the expected mode shape. Significant local plate bending occurred at the base of one of the angles, as shown in Figure 5.146.

5.6 Discussion of Results

In Table 5.9 the test results are compared with the predicted flexural buckling capacity about the strong axis, $P_{cr\text{-}y}$, and the predicted flexural-torsional buckling capacity, $P_{cr\text{-}ft}$, based on the measured dimensions. As seen in this table, the test results, P_{EXP}, have better agreement with the predicted flexural buckling capacity $P_{cr\text{-}y}$. The average ratio of P_{EXP} to $P_{cr\text{-}y}$ was found to be 1.11 with a standard deviation of 0.07, while the average ratio of P_{EXP} to $P_{cr\text{-}ft}$ is 1.92 with a standard deviation of 0.58.

The test results are compared to $P_{cr\text{-}y}$ and $P_{cr\text{-}ft}$ in Figure 5.147. This figure shows that the AISC (2005) specification provisions for the flexural-torsional capacity, $P_{cr\text{-}ft}$, of double angle columns are conservative for both the Vanadium and Grade 50 steel specimens. In the same figure, it can be observed that test results are very close to the predicted flexural buckling capacity about the strong axis, $P_{cr\text{-}y}$.

In Table 5.10, the flexural-torsional buckling capacities calculated using Equation E4-2 (Equation 2-38) of the AISC (2005) specification are compared with the flexural-torsional buckling capacities calculated using Equation E4-5(Equation 2-32), with Equations E7-2 or E7-3 of the AISC (2005) specification. The AISC (2005)

specification suggests using Equation E4-2 for non-slender double angle compression members. However, the double angle specimens tested in this study are categorized as slender members and therefore the capacities reported previously were calculated using Equation E4-5, with Equations E7-2 or E7-3. The Q reduction factor (Equation 2-25) is introduced into the buckling equations for the slender members to account for an inelastic or local buckling reduction.

The main difference between these two approaches is that torsional resistance (from GJ, the shear modulus times the St. Venant torsional constant) is not subjected to an inelastic reduction or local buckling reduction in Equation E4-2, but the flexural buckling resistance is subjected to these reductions in Equations E7-2 or E7-3, which should account for the effects of residual stresses and local plate buckling. As seen in Table 5.10, Equation E4-5 with Equations E7-2 or E7-3 produces buckling capacities up to 10% lower than the capacities predicted using Equation E4-2, and the test results are generally in closer agreement with the results from Equation E4-2. The average ratio of P_{EXP} to the flexural-torsional buckling capacity based on Equation E4-5 was found to be 1.92 with a standard deviation of 0.58, while the average ratio of P_{EXP} to the flexural-torsional buckling capacity based on Equation E4-2 is 1.81 with a standard deviation of 0.53.

The ratio of P_{EXP} to $P_{cr\text{-}ft}$ vs. the Q reduction factor is shown in Figure 5.148. It can be seen from this figure that as the Q reduction factor is smaller; the $P_{EXP}/P_{cr\text{-}ft}$ ratio is greater, which indicates that the provisions in the AISC (2005) specification are increasingly conservative for angles with more slender cross-sections, and they are

very conservative when Q is approximately 0.75.

The ratio of P_{EXP} to $P_{cr\text{-}ft}$ vs. the modified effective slenderness factor, K_m, is shown in Figure 5.149. It can be seen from this figure that the conservatism in the calculated buckling capacities does not correlate with K_m.

In Figures 5.150, 5.151, and 5.152, the test results are compared with the predicted buckling stresses $F_{cr\text{-}y}$ and $F_{cr\text{-}ft}$ for the Vanadium steel specimens, in addition to the yield stress, F_Y, the yield stress multiplied by the Q reduction factor, QF_Y, and the elastic flexural-torsional buckling stress, $F_{e\text{-}ft}$. A comparison of P_{EXP} vs. the axial yield strength, P_Y, the yield capacity multiplied by the Q reduction factor, QP_Y, and the elastic flexural-torsional buckling capacity, $P_{e\text{-}ft}$, for each of the specimens is also included in Table 5.9. For Vanadium steel specimens, it is evident from these three figures that the AISC (2005) specification provisions for the flexural-torsional buckling stress $F_{cr\text{-}ft}$ govern and that the test results are consistently well above this predicted capacity. Figure 5.151 and Figure 5.152 show that the flexural-torsional buckling capacity predictions including the Q reduction factor fall well below the test results for the DB and DC series specimens with smaller slenderness values.

In Figure 5.151 and Figure 5.152, the transition from the predicted flexural-torsional buckling capacity curve to predicted flexural buckling capacity curve is observed to occur at high slenderness ratio values for the specimens (the DB and DC series specimens) with the lower Q reduction factors.

Table 5.1 Test Matrix for Double Angle Specimens

Specimen ID	Steel Type	Specimen Size	Bearing Capacity	No. of Mid-Spacers	Back-to-back spacing	Measured Yield Stress	Length
		in.×in.× in.	kips		in.	ksi	in.
DA1	Vanadium	LL3.5x3.5x3/8	500	1	1	73.7	30
DA12	Vanadium	LL3.5x3.5x3/8	500	1	1	73.7	30
DA2	Vanadium	LL3.5x3.5x3/8	500	1	1	73.7	48
DA22	Vanadium	LL3.5x3.5x3/8	500	2	0.75	73.7	48
DA3	Vanadium	LL3.5x3.5x3/8	500	1	1	73.7	66
DA4	Vanadium	LL3.5x3.5x3/8	500	2	1	73.7	84
DA42	Vanadium	LL3.5x3.5x3/8	500	1	1	73.7	84
DA5	Grade 50	LL3.5x3.5x3/8	500	1	1	65.0	48
DB1	Vanadium	LL3x3x3/16	500	1	1.5	77.5	24
DB2	Vanadium	LL3x3x3/16	500	1	1.5	77.5	48
DB3	Vanadium	LL3x3x3/16	500	3	1.5	77.5	72
DB4	Vanadium	LL3x3x3/16	500	1	1.5	77.5	96
DB5	Grade 50	LL3x3x3/16	500	1	1.5	60.2	48
DC1	Vanadium	LL1.75x1.75x1/8	100	3	1.5	78.5	24
DC2	Vanadium	LL1.75x1.75x1/8	100	3	1.5	78.5	33
DC3	Vanadium	LL1.75x1.75x1/8	100	3	1.5	78.5	42
DC32	Vanadium	LL1.75x1.75x1/8	100	1	1.5	78.5	42
DC4	Vanadium	LL1.75x1.75x1/8	100	3	1.5	78.5	51
DC42	Vanadium	LL1.75x1.75x1/8	100	1	1.5	78.5	51

Table 5.2 Cross-sectional Properties Based on Measured Dimensions for Width and Thickness

Specimen ID	b_{11}	b_{12}	b_{21}	b_{22}	t_{11}	t_{12}	t_{21}	t_{22}	F_y	L	A_g	# of mid-spacers	distance between angles
	in.	in.	in.	in.	in.	in.	in.	in.	ksi	in.	in^2		in.
DA1	3.479	3.546	3.473	3.546	0.381	0.371	0.378	0.371	73.7	30.00	4.99	1	0.993
DA12	3.561	3.456	3.540	3.469	0.373	0.378	0.373	0.380	73.7	30.00	4.99	1	0.978
DA2	3.472	3.537	3.462	3.536	0.373	0.367	0.373	0.365	73.7	48.00	4.90	1	0.989
DA22	3.551	3.488	3.561	3.477	0.367	0.379	0.368	0.383	73.7	48.00	4.99	2	0.755
DA3	3.560	3.468	3.438	3.536	0.370	0.379	0.376	0.370	73.7	66.00	4.95	1	1.001
DA4	3.479	3.527	3.525	3.424	0.380	0.369	0.368	0.377	73.7	84.00	4.93	2	0.978
DA42	3.471	3.535	3.499	3.491	0.378	0.372	0.368	0.384	73.7	84.00	4.97	1	1.019
DA5	3.539	3.510	3.458	3.534	0.370	0.380	0.369	0.381	65.0	48.00	4.98	1	0.987
DB1	2.982	2.947	2.979	2.951	0.193	0.190	0.192	0.193	77.5	24.00	2.20	1	1.539
DB2	2.961	2.964	2.949	2.968	0.189	0.196	0.190	0.195	77.5	48.00	2.21	1	1.529
DB3	2.955	2.973	2.984	2.972	0.189	0.194	0.187	0.195	77.5	72.00	2.20	3	1.566
DB4	2.981	2.863	2.935	2.916	0.197	0.191	0.192	0.196	77.5	96.00	2.19	1	1.517
DB5	3.005	3.020	3.010	3.001	0.185	0.185	0.185	0.186	60.2	48.00	2.16	1	1.552
DC1	1.721	1.731	1.708	1.726	0.129	0.130	0.128	0.130	78.5	24.00	0.86	3	1.539
DC2	1.717	1.723	1.711	1.717	0.128	0.130	0.126	0.128	78.5	33.00	0.85	3	1.531
DC3	1.714	1.725	1.717	1.706	0.126	0.131	0.124	0.128	78.5	42.00	0.84	3	1.532
DC32	1.714	1.732	1.711	1.724	0.126	0.128	0.126	0.128	78.5	42.00	0.84	1	1.488
DC4	1.715	1.720	1.716	1.714	0.126	0.129	0.125	0.130	78.5	51.00	0.84	3	1.528
DC42	1.716	1.748	1.727	1.715	0.128	0.131	0.130	0.128	78.5	51.00	0.86	1	1.510

Table 5.2 Cross-sectional Properties Based on Measured Dimensions for Width and Thickness (continued)

Specimen ID	I_x	I_y	r_x	r_y	r_z	C_w	J	y_o	r_o^2	H
	in^4	in^4	in.	in.	in.	in^6	in^4	in.	in^2	
DA1	5.90	16.95	1.09	1.84	0.69	0.215	0.234	0.84	5.28	0.868
DA12	5.62	17.47	1.06	1.87	0.69	0.216	0.235	0.81	5.29	0.875
DA2	5.78	16.52	1.09	1.84	0.69	0.205	0.223	0.84	5.25	0.867
DA22	5.72	15.69	1.07	1.77	0.69	0.215	0.233	0.83	4.98	0.862
DA3	5.73	17.01	1.08	1.85	0.69	0.211	0.231	0.83	5.28	0.870
DA4	5.60	16.90	1.07	1.85	0.69	0.208	0.229	0.82	5.23	0.873
DA42	5.81	17.00	1.08	1.85	0.69	0.214	0.234	0.84	5.29	0.867
DA5	5.88	16.79	1.09	1.84	0.69	0.215	0.234	0.85	5.27	0.863
DB1	1.87	7.50	0.92	1.85	0.60	0.019	0.027	0.71	4.75	0.895
DB2	1.91	7.25	0.93	1.81	0.60	0.019	0.027	0.73	4.69	0.886
DB3	1.92	7.40	0.93	1.83	0.60	0.018	0.027	0.73	4.77	0.888
DB4	1.78	7.37	0.90	1.83	0.60	0.018	0.028	0.69	4.64	0.898
DB5	1.92	7.42	0.94	1.85	0.60	0.018	0.025	0.73	4.86	0.890
DC1	0.25	1.56	0.54	1.35	0.35	0.001	0.005	0.42	2.29	0.923
DC2	0.24	1.54	0.54	1.35	0.35	0.001	0.005	0.42	2.28	0.923
DC3	0.24	1.52	0.54	1.34	0.35	0.001	0.005	0.42	2.27	0.922
DC32	0.25	1.48	0.54	1.33	0.35	0.001	0.005	0.42	2.23	0.920
DC4	0.24	1.52	0.54	1.34	0.35	0.001	0.005	0.42	2.27	0.922
DC42	0.25	1.55	0.54	1.34	0.35	0.001	0.005	0.42	2.27	0.923

Table 5.3 Cross-sectional Properties Based on Nominal Dimensions for Width and Thickness

Specimen ID	b_{11}	b_{12}	b_{21}	b_{22}	t_{11}	t_{12}	t_{21}	t_{22}	F_y	L	A_g**	# of mid-spacers	distance between angles
	in.	in.	in.	in.	in.	in.	in.	in.	ksi	in.	in^2		in.
DA1	3.500	3.500	3.500	3.500	0.375	0.375	0.375	0.375	73.7	30.00	5.00	1	1.000
DA12	3.500	3.500	3.500	3.500	0.375	0.375	0.375	0.375	73.7	30.00	5.00	1	1.000
DA2	3.500	3.500	3.500	3.500	0.375	0.375	0.375	0.375	73.7	48.00	5.00	1	1.000
DA22	3.500	3.500	3.500	3.500	0.375	0.375	0.375	0.375	73.7	48.00	5.00	2	0.750
DA3	3.500	3.500	3.500	3.500	0.375	0.375	0.375	0.375	73.7	66.00	5.00	1	1.000
DA4	3.500	3.500	3.500	3.500	0.375	0.375	0.375	0.375	73.7	84.00	5.00	2	1.000
DA42	3.500	3.500	3.500	3.500	0.375	0.375	0.375	0.375	73.7	84.00	5.00	1	1.000
DA5	3.500	3.500	3.500	3.500	0.375	0.375	0.375	0.375	65.0	48.00	5.00	1	1.000
DB1	3.000	3.000	3.000	3.000	0.1875	0.1875	0.1875	0.1875	77.5	24.00	2.18	1	1.500
DB2	3.000	3.000	3.000	3.000	0.1875	0.1875	0.1875	0.1875	77.5	48.00	2.18	1	1.500
DB3	3.000	3.000	3.000	3.000	0.1875	0.1875	0.1875	0.1875	77.5	72.00	2.18	3	1.500
DB4	3.000	3.000	3.000	3.000	0.1875	0.1875	0.1875	0.1875	77.5	96.00	2.18	1	1.500
DB5	3.000	3.000	3.000	3.000	0.1875	0.1875	0.1875	0.1875	60.2	48.00	2.18	1	1.500
DC1	1.750	1.750	1.750	1.750	0.125	0.125	0.125	0.125	78.5	24.00	0.84	3	1.500
DC2	1.750	1.750	1.750	1.750	0.125	0.125	0.125	0.125	78.5	33.00	0.84	3	1.500
DC3	1.750	1.750	1.750	1.750	0.125	0.125	0.125	0.125	78.5	42.00	0.84	3	1.500
DC32	1.750	1.750	1.750	1.750	0.125	0.125	0.125	0.125	78.5	42.00	0.84	1	1.500
DC4	1.750	1.750	1.750	1.750	0.125	0.125	0.125	0.125	78.5	51.00	0.84	3	1.500
DC42	1.750	1.750	1.750	1.750	0.125	0.125	0.125	0.125	78.5	51.00	0.84	1	1.500

Table 5.3 Cross-sectional Properties Based on Nominal Dimensions for Width and Thickness (Continued)

Specimen ID	I_x**	I_y**	r_x**	r_y**	r_z*	C_w*	J*	y_o**	r_o^2**	H**
	in^4	in^4	in.	in.	in.	in^6	in^4	in.	in^2	
DA1	5.73	17.10	1.07	1.86	0.68	0.213	0.233	0.83	5.28	0.871
DA12	5.73	17.10	1.07	1.86	0.68	0.213	0.233	0.83	5.28	0.871
DA2	5.73	17.10	1.07	1.86	0.68	0.213	0.233	0.83	5.28	0.871
DA22	5.73	15.30	1.07	1.76	0.68	0.213	0.233	0.83	4.91	0.861
DA3	5.73	17.10	1.07	1.86	0.68	0.213	0.233	0.83	5.28	0.871
DA4	5.73	17.10	1.07	1.86	0.68	0.213	0.233	0.83	5.28	0.871
DA42	5.73	17.10	1.07	1.86	0.68	0.213	0.233	0.83	5.28	0.871
DA5	5.73	17.10	1.07	1.86	0.68	0.213	0.233	0.83	5.28	0.871
DB1	1.92	7.29	0.94	1.83	0.60	0.018	0.026	0.73	4.76	0.889
DB2	1.92	7.29	0.94	1.83	0.60	0.018	0.026	0.73	4.76	0.889
DB3	1.92	7.29	0.94	1.83	0.60	0.018	0.026	0.73	4.76	0.889
DB4	1.92	7.29	0.94	1.83	0.60	0.018	0.026	0.73	4.76	0.889
DB5	1.92	7.29	0.94	1.83	0.60	0.018	0.026	0.73	4.76	0.889
DC1	0.25	1.54	0.55	1.35	0.35	0.001	0.004	0.42	2.30	0.923
DC2	0.25	1.54	0.55	1.35	0.35	0.001	0.004	0.42	2.30	0.923
DC3	0.25	1.54	0.55	1.35	0.35	0.001	0.004	0.42	2.30	0.923
DC32	0.25	1.54	0.55	1.35	0.35	0.001	0.004	0.42	2.30	0.923
DC4	0.25	1.54	0.55	1.35	0.35	0.001	0.004	0.42	2.30	0.923
DC42	0.25	1.54	0.55	1.35	0.35	0.001	0.004	0.42	2.30	0.923

* tabulated value in AISC Manual (LRFD, 2005)
**based on nominal dimensions

Table 5.4 Initial Imperfection in Principal Axis Directions

Specimen ID	L/1470	Mid-height out-of-straightness		Maximum out-of-straightness	
		Δx_{h0} (in.)	Δy_{h0} (in.)	Δx_{h0} (in.)	Δy_{h0} (in.)
DA1	0.0204	-0.002	0.014	-0.009	0.017
DA12	0.0204	0.015	0.010	0.015	0.010
DA2	0.0327	0.003	0.006	0.012	0.009
DA22	0.0327	-0.011	-0.002	-0.017	0.003
DA3	0.0449	0.010	0.005	0.014	0.005
DA4	0.0571	0.022	-0.021	0.029	-0.021
DA42	0.0571	0.020	0.028	0.059	0.032
DA5	0.0327	0.018	-0.017	0.018	-0.017
DB1	0.0163	0.002	0.001	0.014	-0.007
DB2	0.0327	-0.008	-0.004	-0.008	-0.007
DB3	0.0490	-0.030	0.031	-0.040	0.034
DB4	0.0653	0.004	0.037	0.018	0.047
DB5	0.0327	-0.012	0.025	-0.012	0.025
DC1	0.0163	-0.002	0.007	-0.003	0.007
DC2	0.0224	-0.007	0.026	0.008	0.026
DC3	0.0286	0.004	0.036	0.015	0.036
DC32	0.0286	0.014	0.038	0.014	0.038
DC4	0.0347	0.020	0.048	0.019	0.048
DC42	0.0347	-0.009	0.028	-0.009	0.028

Table 5.5 Instrumentation and Measurements

Data	Unit	Instrumentation	Notes
P	kips	SATEC	Axial load
δ	in	SATEC	Cross-head displacement
Δ_1	in	LVDT	Displacement at mid-height cross-section
Δ_2	in	LVDT	Displacement at mid-height cross-section
Δ_3	in	LVDT	Displacement at mid-height cross-section
Δ_4	in	LVDT	Displacement at mid-height cross-section
Δ_5	in	LVDT	Displacement at mid-height cross-section
Δ_6	in	LVDT	Displacement at mid-height cross-section
Δ_7	in	LVDT	Displacement at mid-height cross-section
θ_1	degree	Inclinometer	Top bearing rotation
θ_2	degree	Inclinometer	Bottom bearing rotation
ε_1	microstrain	Strain Gage	Strain at mid-height cross-section
ε_2	microstrain	Strain Gage	Strain at mid-height cross-section
ε_3	microstrain	Strain Gage	Strain at mid-height cross-section
ε_4	microstrain	Strain Gage	Strain at mid-height cross-section
ε_5	microstrain	Strain Gage	Strain at mid-height cross-section
ε_6	microstrain	Strain Gage	Strain at mid-height cross-section
ε_7	microstrain	Strain Gage	Strain at mid-height cross-section
ε_8	microstrain	Strain Gage	Strain at mid-height cross-section

Table 5.6 Predicted Buckling Capacities Based on Measured and Nominal Cross-sectional Properties

Specimen ID	P_Y[1]	P_{cr-x}[1]	P_{cr-y}[1]	P_{cr-ft}[1]	P_{e-ft}[1]	$2xP_{cr-SA}$[1]	P_Y[2]	P_{cr-x}[2]	P_{cr-y}[2]	P_{cr-ft}[2]	P_{e-ft}[2]	$2xP_{cr-SA}$[2]
	kips	kips	kips	kips	kips	kips	kips	kips	kips	kips	kips	kips
DA1	367.6	353.9	347.2	267.0	500.2	359.3	368.5	352.4	346.0	265.9	498.1	355.2
DA12	367.8	353.8	347.7	267.4	502.4	359.4	368.5	352.4	346.0	265.9	498.1	355.2
DA2	361.3	337.0	320.8	257.1	461.0	350.4	368.5	341.2	325.6	262.7	478.9	348.3
DA22	367.6	342.4	330.1	268.1	507.9	359.0	368.5	341.2	328.4	268.2	512.9	354.6
DA3	365.1	324.6	296.9	253.9	434.4	349.8	368.5	325.5	297.9	255.2	438.6	338.4
DA4	363.5	302.9	276.2	245.0	396.7	350.7	368.5	306.0	278.4	246.6	398.8	344.3
DA42	366.5	306.9	264.8	238.5	365.9	346.0	368.5	306.0	265.1	238.9	367.9	325.9
DA5	324.0	309.3	295.9	244.2	479.6	320.3	325.0	308.0	295.3	243.5	478.9	313.7
DB1	170.8	119.8	118.9	55.8	65.3	121.1	169.0	118.6	117.6	53.1	61.6	119.2
DB2	170.9	115.3	111.3	56.2	65.9	120.0	169.0	114.0	110.1	52.7	61.0	116.3
DB3	170.5	107.6	105.2	54.3	63.1	120.4	169.0	106.8	104.2	52.3	60.4	118.0
DB4	170.0	96.2	85.3	54.3	63.3	114.2	169.0	97.4	84.8	50.1	57.5	105.5
DB5	130.1	97.8	95.0	48.8	57.8	101.1	131.2	98.6	95.7	50.8	61.0	100.3
DC1	67.2	50.6	51.0	20.9	23.9	52.7	65.9	49.9	50.2	19.3	22.0	51.7
DC2	66.4	48.0	48.8	20.4	23.2	52.0	65.9	48.0	48.7	19.2	21.9	51.4
DC3	66.0	45.3	46.4	20.3	22.8	51.5	65.9	45.6	46.6	19.1	21.8	51.0
DC32	66.1	45.3	43.3	20.1	23.0	51.5	65.9	45.6	43.5	19.0	21.7	48.0
DC4	66.2	42.4	44.2	20.0	22.8	50.2	65.9	42.8	44.3	19.0	21.7	50.5
DC42	67.5	43.4	40.7	20.7	23.6	50.4	65.9	42.8	40.0	18.8	21.4	46.1

[1]: capacities based on measured cross-sectional properties
[2]: capacities based on nominal cross-sectional properties

Table 5.7 Comparison of Predicted Capacities Based on Measured and Nominal Cross-sectional Properties

Specimen ID	$P_Y^{[1]}/P_Y^{[2]}$	$P_{cr\text{-}x}^{[1]}/P_{cr\text{-}x}^{[2]}$	$P_{cr\text{-}y}^{[1]}/P_{cr\text{-}y}^{[2]}$	$P_{cr\text{-}ft}^{[1]}/P_{cr\text{-}ft}^{[2]}$	$P_{e\text{-}ft}^{[1]}/P_{e\text{-}ft}^{[2]}$	$2xP_{cr\text{-}SA}^{[1]}/\ 2xP_{cr\text{-}SA}^{[2]}$
DA1	1.00	1.00	1.00	1.00	1.00	1.01
DA12	1.00	1.00	1.00	1.01	1.01	1.01
DA2	0.98	0.99	0.99	0.98	0.96	1.01
DA22	1.00	1.00	1.01	1.00	0.99	1.01
DA3	0.99	1.00	1.00	0.99	0.99	1.03
DA4	0.99	0.99	0.99	0.99	0.99	1.02
DA42	0.99	1.00	1.00	1.00	0.99	1.06
DA5	1.00	1.00	1.00	1.00	1.00	1.02
DB1	1.01	1.01	1.01	1.05	1.06	1.02
DB2	1.01	1.01	1.01	1.07	1.08	1.03
DB3	1.01	1.01	1.01	1.04	1.04	1.02
DB4	1.01	0.99	1.01	1.08	1.10	1.08
DB5	0.99	0.99	0.99	0.96	0.95	1.01
DC1	1.02	1.01	1.02	1.09	1.09	1.02
DC2	1.01	1.00	1.00	1.06	1.06	1.01
DC3	1.00	0.99	0.99	1.06	1.05	1.01
DC32	1.00	0.99	1.00	1.06	1.06	1.07
DC4	1.00	0.99	1.00	1.05	1.05	0.99
DC42	1.02	1.01	1.02	1.10	1.10	1.09

[1]: capacities based on measured cross-sectional properties
[2]: capacities based on nominal cross-sectional properties

Table 5.8 Predicted Buckling Capacities

Specimen ID	K_x	K_y	$(KL/r)_x$	$(KL/r)_y$	$(KL/r)_m$	K_m	Q	P_Y*	P_{cr-x}*	P_{cr-y}*	P_{cr-ft}*	P_{e-ft}*	$2xP_{cr-SA}$*
								kips	kips	kips	kips	kips	kips
DA1	0.5	1	13.8	16.3	19.2	1.18	0.98	367.6	353.9	347.2	267.0	500.2	359.3
DA12	0.5	1	14.1	16.0	19.1	1.19	0.98	367.8	353.8	347.7	267.4	502.4	359.4
DA2	0.5	1	22.1	26.1	30.9	1.18	0.98	361.3	337.0	320.8	257.1	461.0	350.4
DA22	0.5	1	22.4	27.1	29.1	1.08	0.98	367.6	342.4	330.1	268.1	507.9	359.0
DA3	0.5	1	30.7	35.6	42.2	1.19	0.98	365.1	324.6	296.9	253.9	434.4	349.8
DA4	0.5	1	39.4	45.4	49.3	1.09	0.98	363.5	302.9	276.2	245.0	396.7	350.7
DA42	0.5	1	38.9	45.4	53.9	1.19	0.98	366.5	306.9	264.8	238.5	365.9	346.0
DA5	0.5	1	22.1	26.1	30.9	1.18	1.00	324.0	309.3	295.9	244.2	479.6	320.3
DB1	0.5	1	13.0	13.0	16.4	1.26	0.71	170.8	119.8	118.9	55.8	65.3	121.1
DB2	0.5	1	25.8	26.5	33.1	1.25	0.71	170.9	115.3	111.3	56.2	65.9	120.0
DB3	0.5	1	38.6	39.2	42.0	1.07	0.71	170.5	107.6	105.2	54.3	63.1	120.4
DB4	0.5	1	53.3	52.4	65.8	1.26	0.71	170.0	96.2	85.3	54.3	63.3	114.2
DB5	0.5	1	25.4	25.9	32.7	1.26	0.79	130.1	97.8	95.0	48.8	57.8	101.1
DC1	0.5	1	22.2	17.8	20.0	1.13	0.79	67.2	50.6	51.0	20.9	23.9	52.7
DC2	0.5	1	30.7	24.5	27.5	1.12	0.79	66.4	48.0	48.8	20.4	23.2	52.0
DC3	0.5	1	39.1	31.2	35.5	1.14	0.79	66.0	45.3	46.4	20.3	22.8	51.5
DC32	0.5	1	38.9	31.7	44.9	1.42	0.79	66.1	45.3	43.3	20.1	23.0	51.5
DC4	0.5	1	47.5	38.0	42.6	1.12	0.79	66.2	42.4	44.2	20.0	22.8	50.2
DC42	0.5	1	47.2	38.0	54.2	1.43	0.79	67.5	43.4	40.7	20.7	23.6	50.4

* buckling capacities based on measured cross-sectional properties

Table 5.9 Experimental Results vs. Predicted Buckling Capacities

Specimen ID	P_{EXP}	P_{EXP}/P_{cr-y}	P_{EXP}/P_{cr-ft}	P_{EXP}/P_Y	P_{EXP}/QP_Y	P_{EXP}/P_{e-ft}
DA1	360.9	1.04	1.35	0.98	1.00	0.72
DA12	359.7	1.03	1.35	0.98	1.00	0.72
DA2	343.7	1.07	1.34	0.95	0.97	0.75
DA22	361.8	1.10	1.35	0.98	1.00	0.71
DA3	341.1	1.15	1.34	0.93	0.95	0.79
DA4	338.4	1.23	1.38	0.93	0.95	0.85
DA42	300.9	1.14	1.26	0.82	0.84	0.82
DA5	313.9	1.06	1.29	0.97	0.97	0.65
DB1	143.2	1.20	2.57	0.84	1.18	2.19
DB2	126.4	1.14	2.25	0.74	1.04	1.92
DB3	117.2	1.11	2.16	0.69	0.97	1.86
DB4	86.0	1.01	1.58	0.51	0.71	1.36
DB5	98.7	1.04	2.02	0.76	0.97	1.71
DC1	63.5	1.25	3.04	0.94	1.20	2.66
DC2	58.2	1.19	2.85	0.88	1.11	2.51
DC3	52.1	1.12	2.57	0.79	1.00	2.29
DC32	47.2	1.09	2.35	0.71	0.91	2.05
DC4	47.9	1.08	2.40	0.72	0.92	2.10
DC42	42.4	1.04	2.05	0.63	0.80	1.80
Average		1.11	1.92	0.83	0.97	1.50
Standard Deviation		0.07	0.58	0.13	0.11	0.69

Table 5.10 Predicted Flexural-Torsional Buckling Capacities Using Equations E4-2 and E4-5

Specimen ID	$P_{cr\text{-}ft}$[a]	$P_{cr\text{-}ft}$[b]	P_{EXP}	$P_{EXP}/P_{cr\text{-}ft}$[a]	$P_{EXP}/P_{cr\text{-}ft}$[b]	$P_{EXP}/P_{cr\text{-}ft}$[a]-$P_{EXP}/P_{cr\text{-}ft}$[b]
	kips	kips	kips			
DA1	267.0	294.2	360.9	1.35	1.23	0.12
DA12	267.4	296.6	359.7	1.35	1.21	0.13
DA2	257.1	274.2	343.7	1.34	1.25	0.08
DA22	268.1	285.6	361.8	1.35	1.27	0.08
DA3	253.9	260.5	341.1	1.34	1.31	0.03
DA4	245.0	246.3	338.4	1.38	1.37	0.01
DA42	238.5	237.3	300.9	1.26	1.27	-0.01
DA5	244.2	259.3	313.9	1.29	1.21	0.07
DB1	55.8	59.3	143.2	2.57	2.41	0.15
DB2	56.2	59.2	126.4	2.25	2.14	0.11
DB3	54.3	57.1	117.2	2.16	2.05	0.11
DB4	54.3	56.8	86.0	1.58	1.51	0.07
DB5	48.8	51.7	98.7	2.02	1.91	0.11
DC1	20.9	22.6	63.5	3.04	2.81	0.23
DC2	20.4	22.0	58.2	2.85	2.65	0.21
DC3	20.3	21.8	52.1	2.57	2.39	0.18
DC32	20.1	21.7	47.2	2.35	2.18	0.17
DC4	20.0	21.6	47.9	2.40	2.22	0.18
DC42	20.7	22.2	42.4	2.05	1.91	0.14
Average				1.92	1.81	0.12
Standard Deviation				0.58	0.53	0.06

[a]: Pcr-ft calculated based on Equation E4-5, AISC (2005)
[b]: Pcr-ft calculated based on Equation E4-2, AISC (2005)

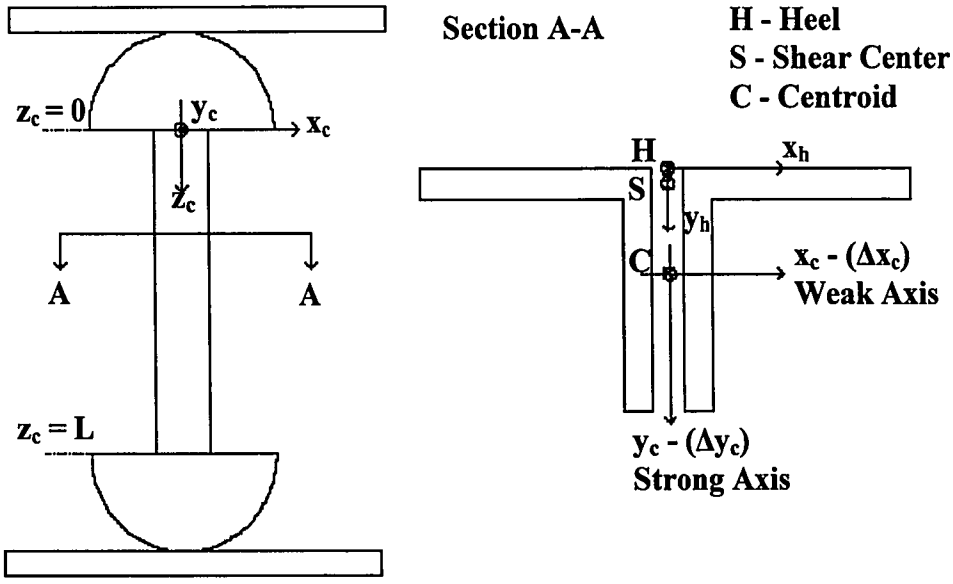

Figure 5.1 Coordinate Axis Systems

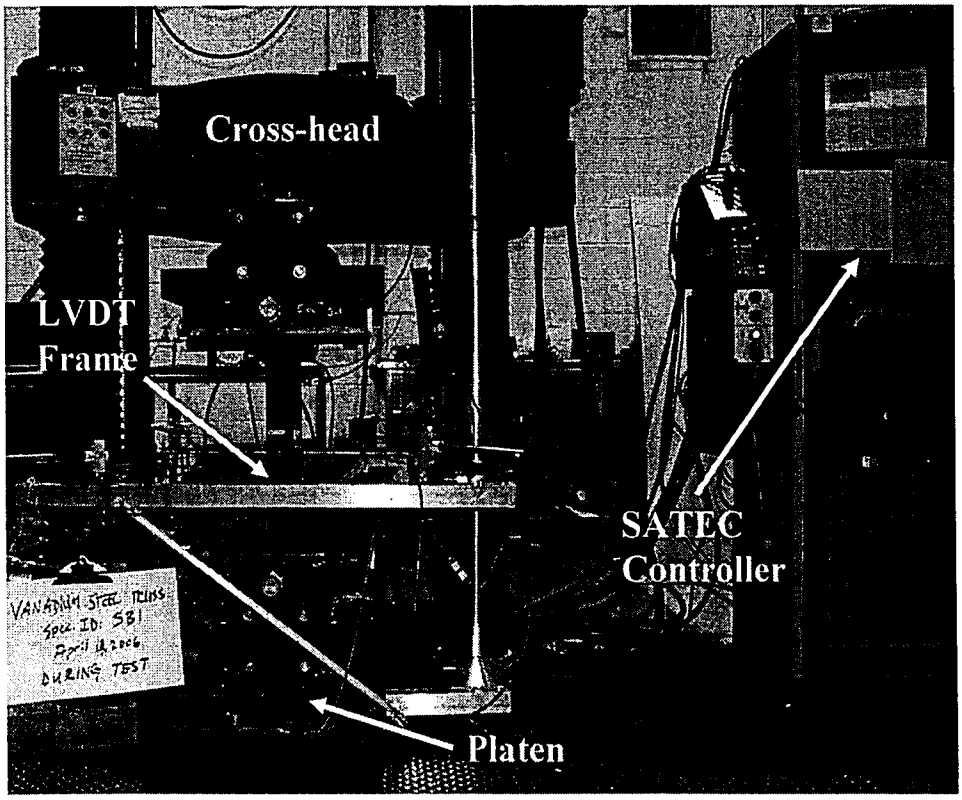

Figure 5.2 SATEC Universal Testing Machine

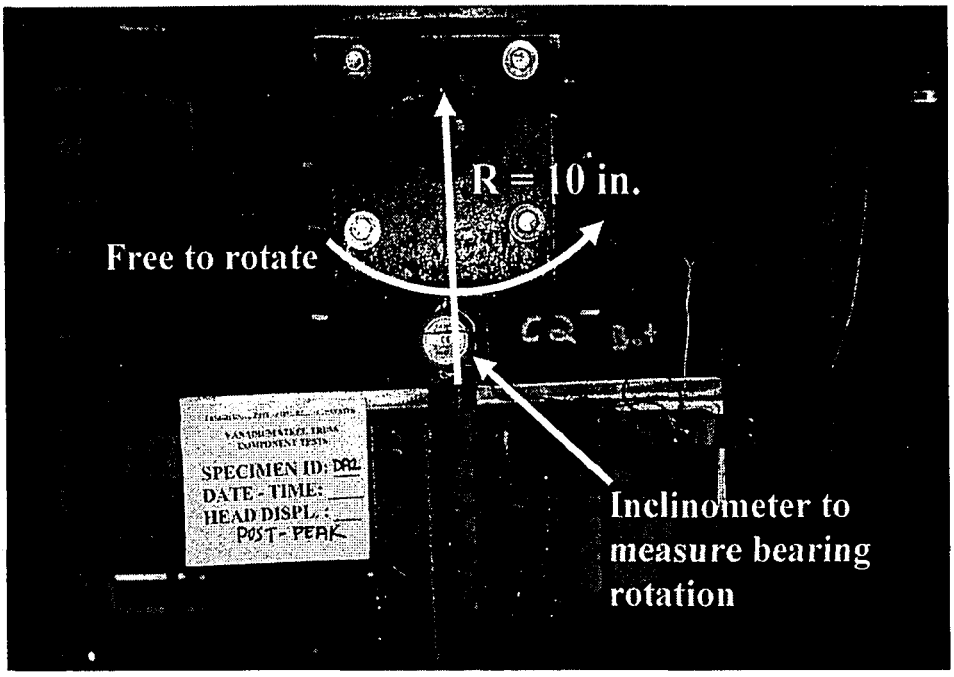

(a) 500 kip Cylindrical Bearing

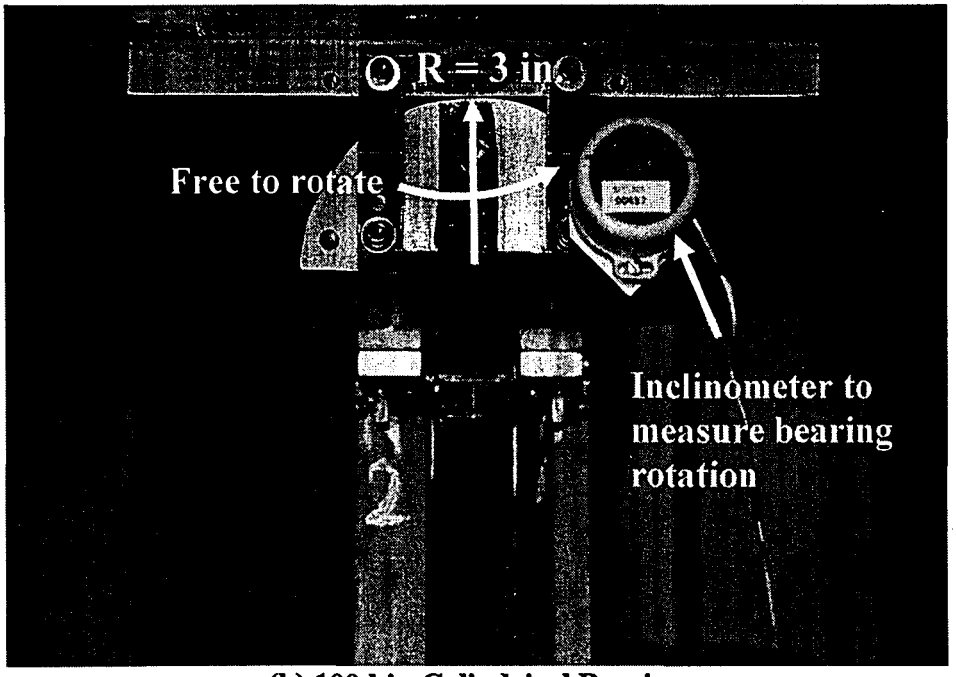

(b) 100 kip Cylindrical Bearing

Figure 5.3 Cylindrical Bearings

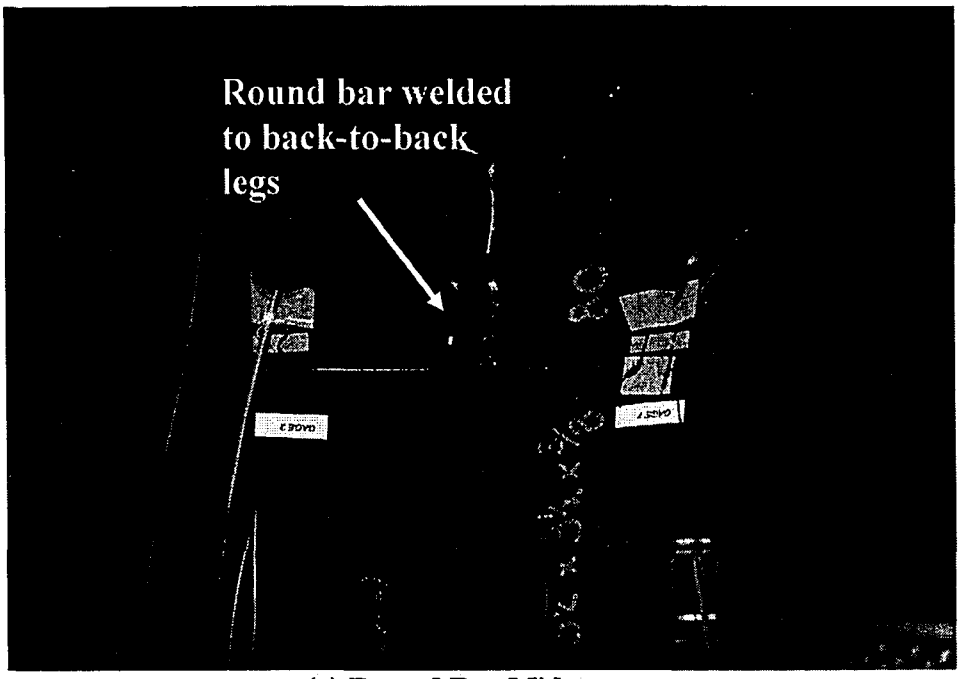

(a) Round Bar Mid-spacer

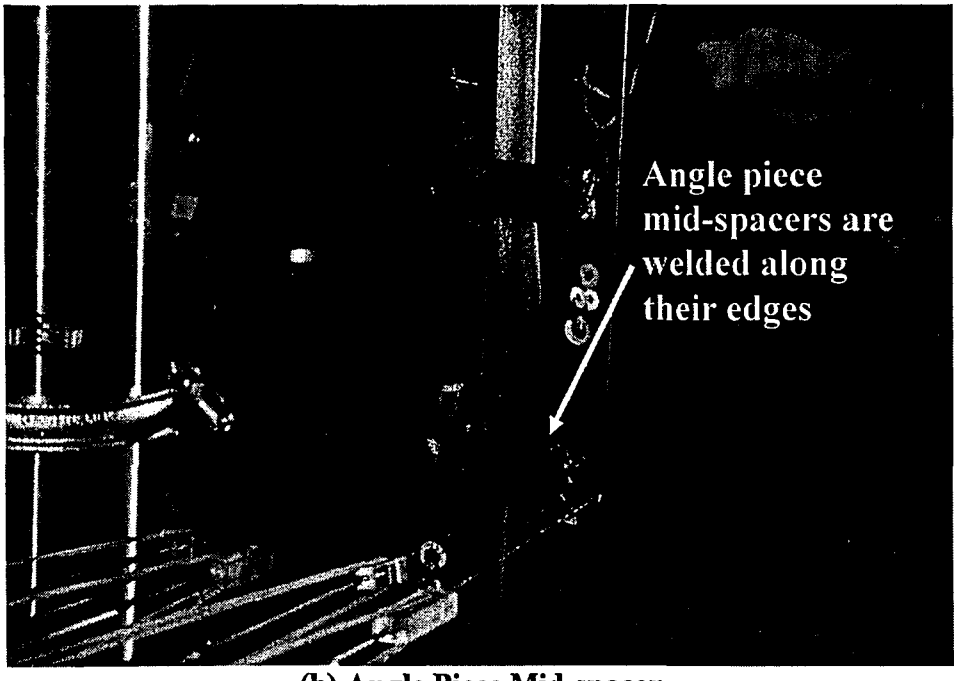

(b) Angle Piece Mid-spacer

Figure 5.4 Types of Mid-spacers

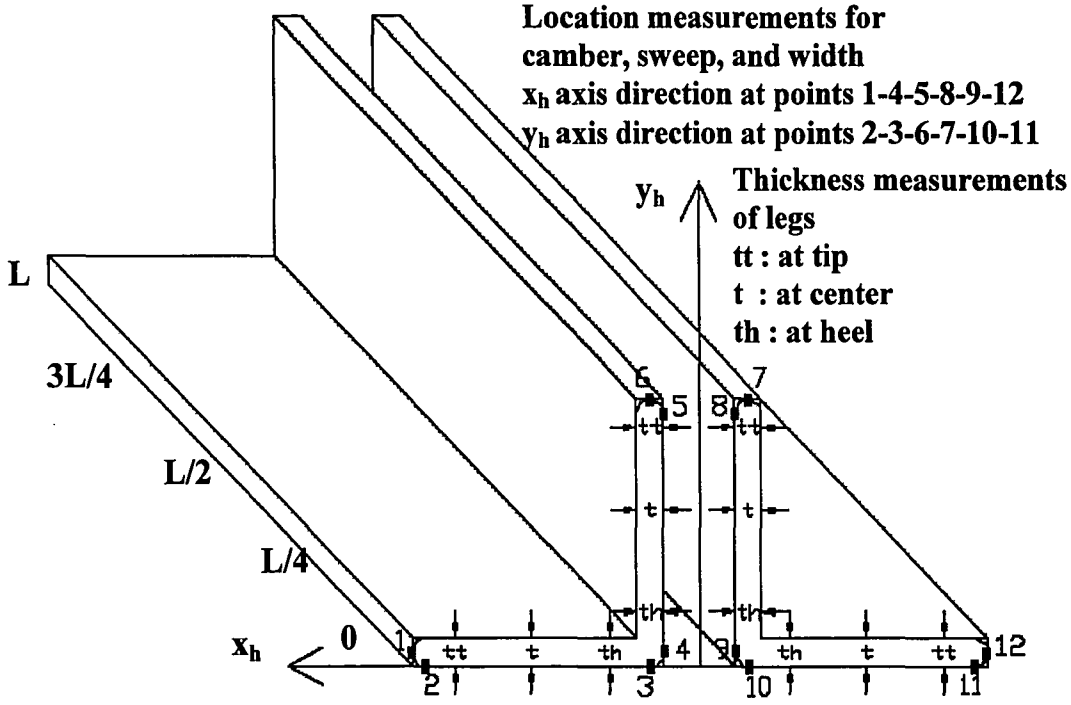

Figure 5.5 Cross-sectional Measurements

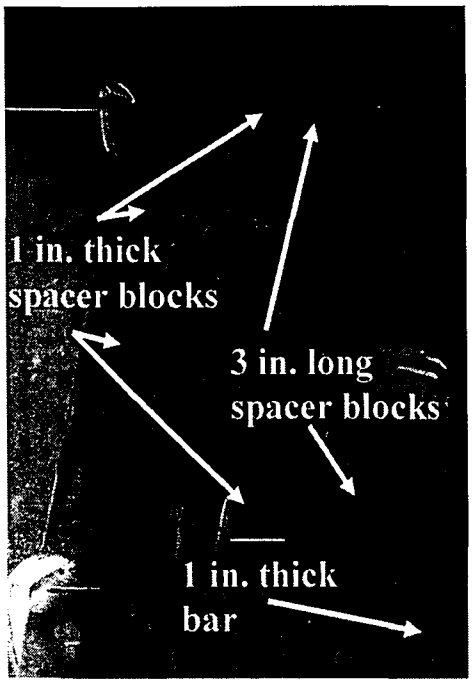

(a) Spacer Blocks

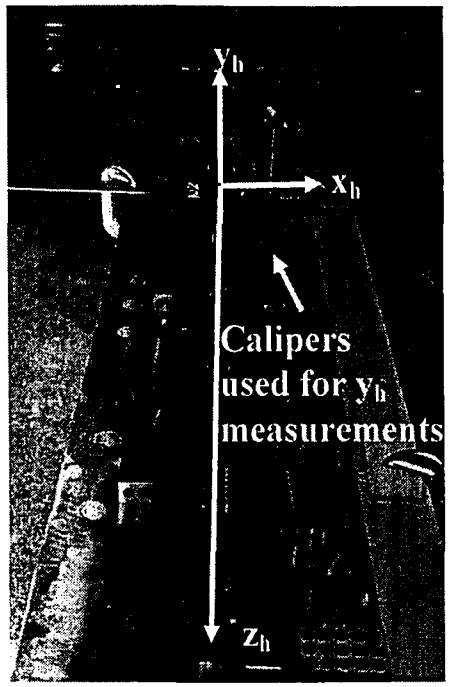

(b) Coordinate Axis System and Calipers

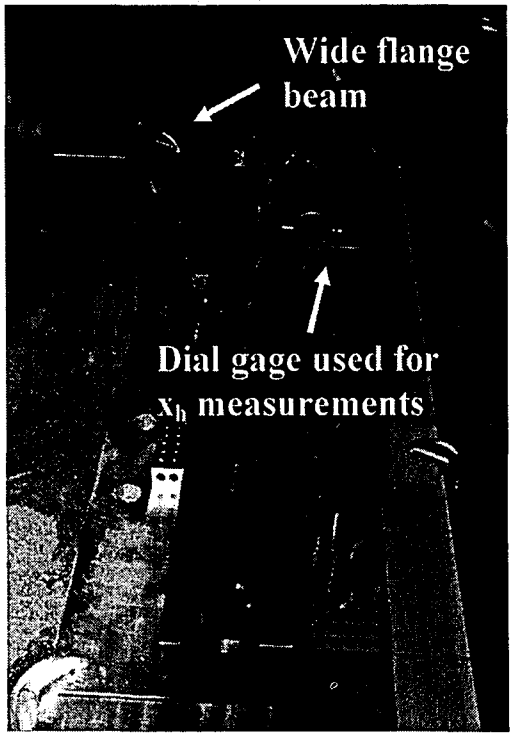

(c) Measurement Rig

Figure 5.6 Initial Measurement Devices and Measurement Rig

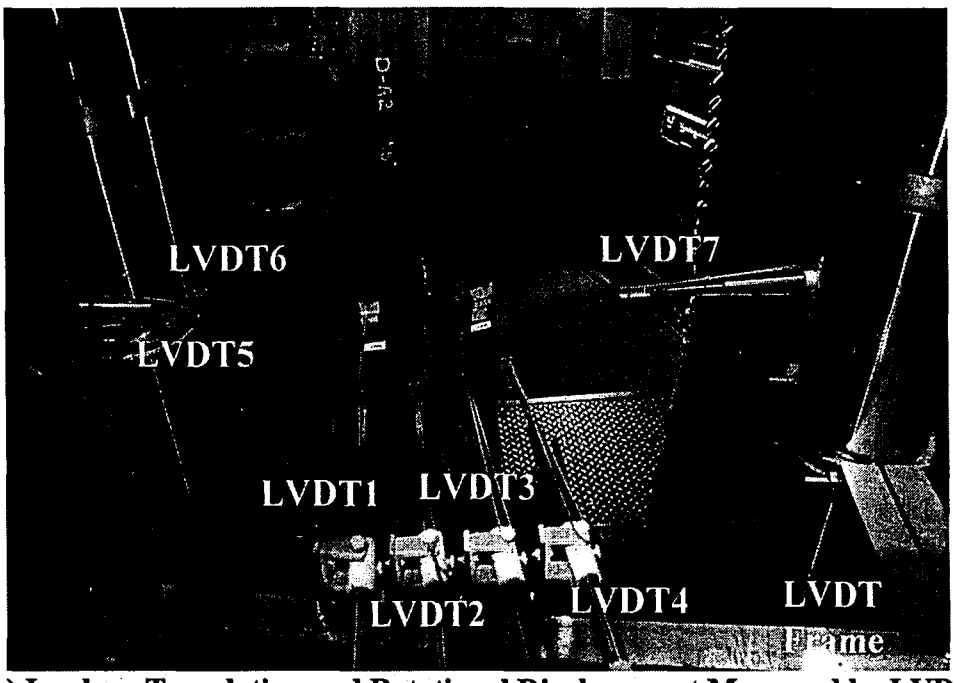

(a) In-plane Translation and Rotational Displacement Measured by LVDT

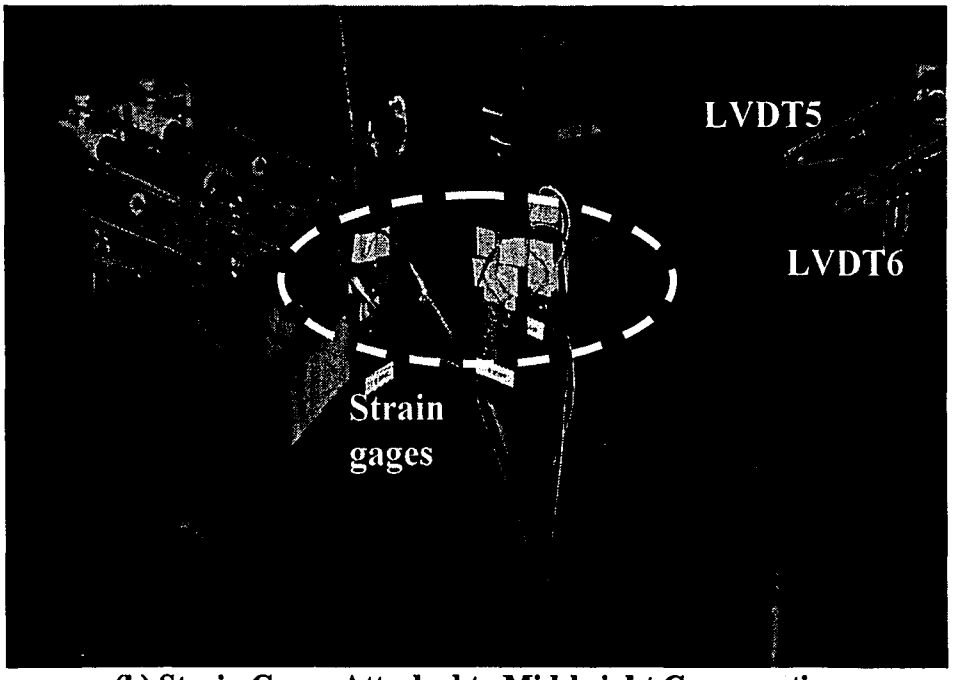

(b) Strain Gages Attached to Mid-height Cross-section

Figure 5.7 Instrumentation for Double Angle Specimens

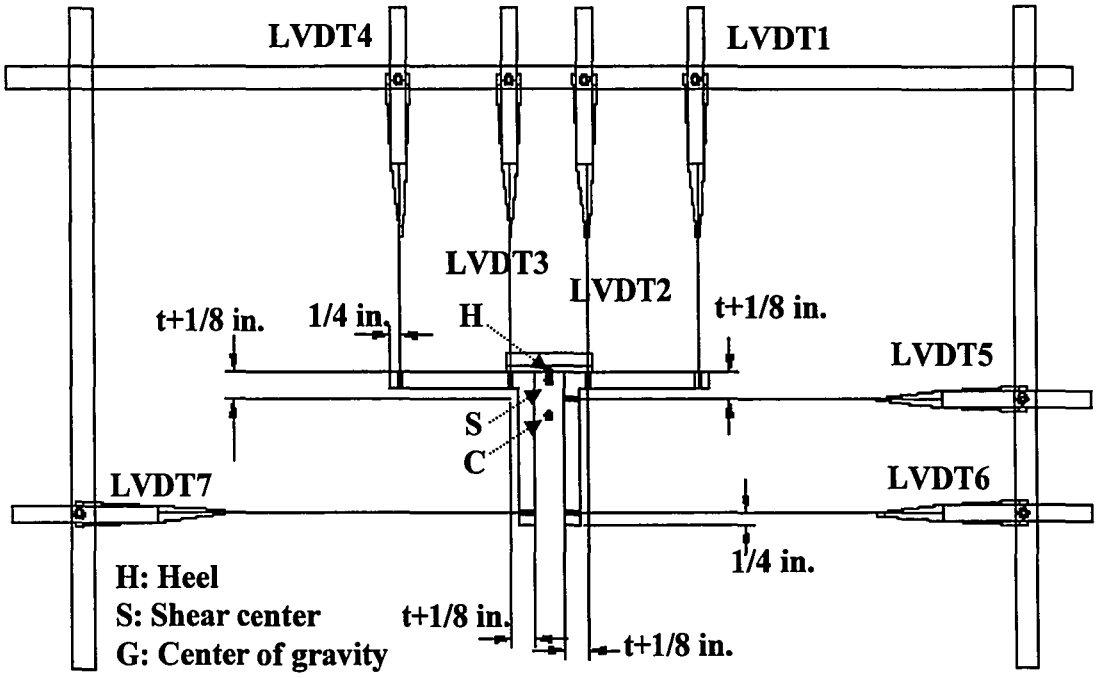

Figure 5.8 LVDT Attachment Pattern

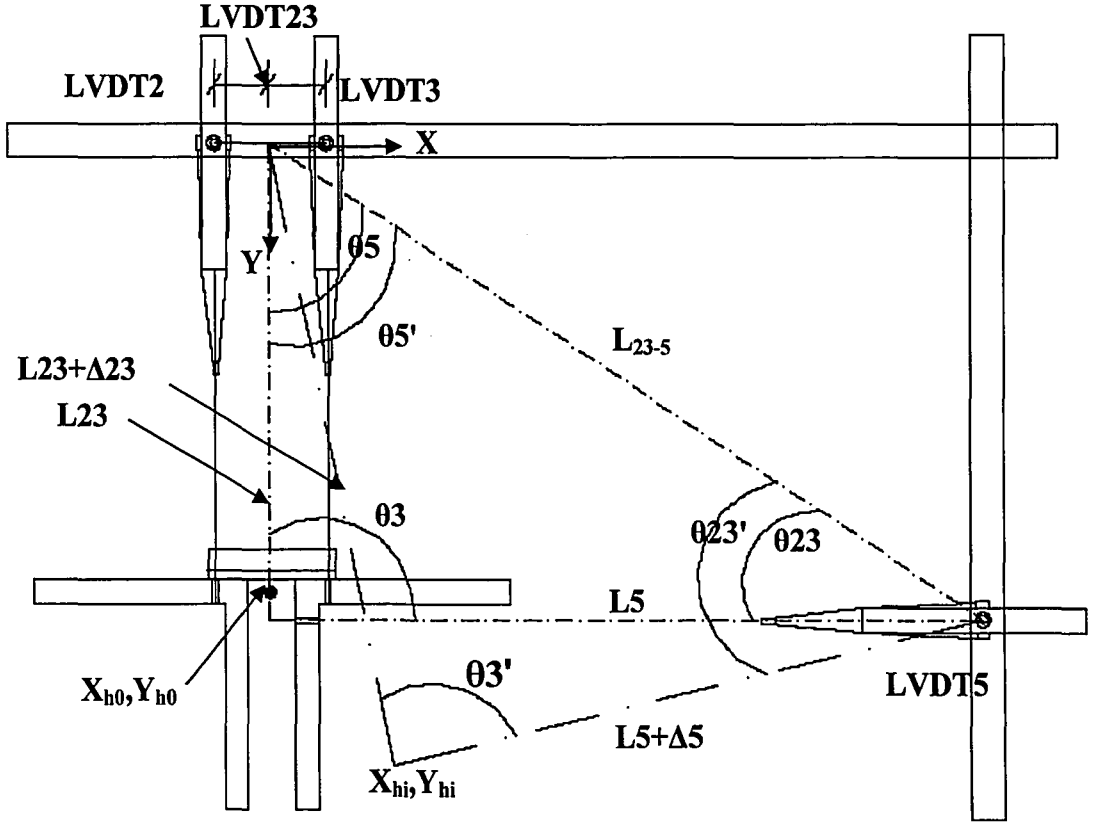

Figure 5.9 Parameters Used for Heel Lateral Deflection Calculations

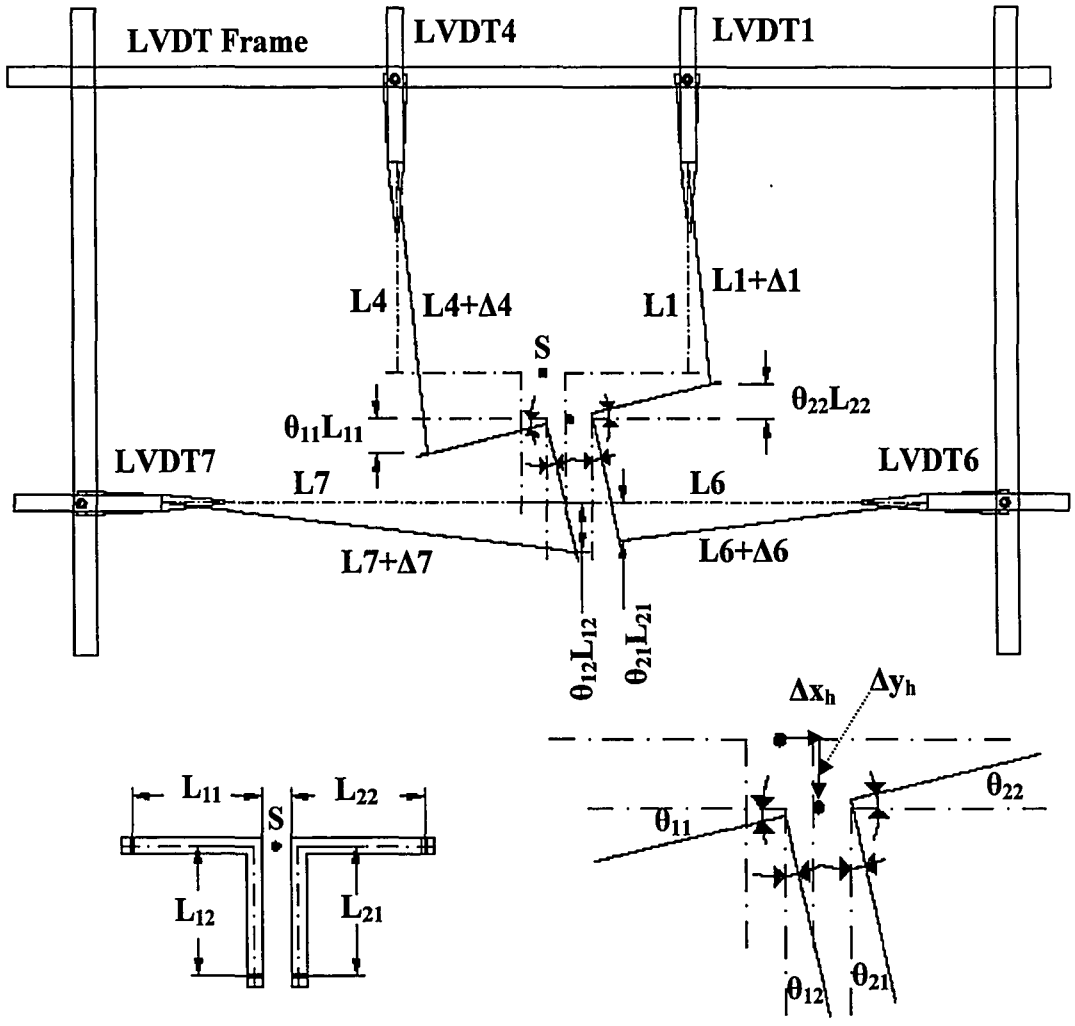

Figure 5.10 Parameters Used for Twist Calculations

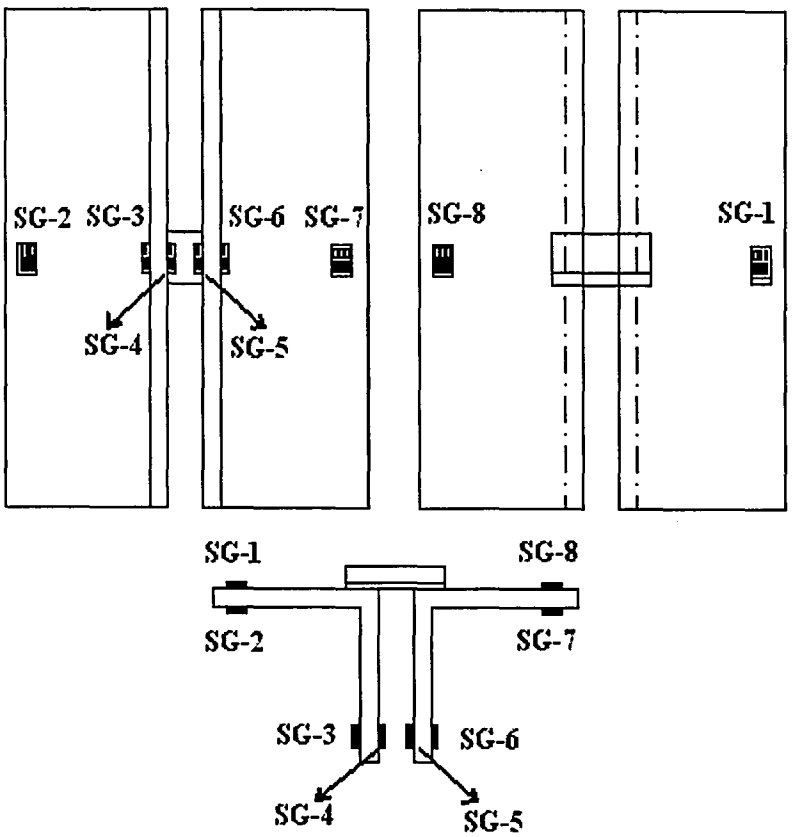

Figure 5.11 Strain Gages (SG) on Mid-height Cross-section

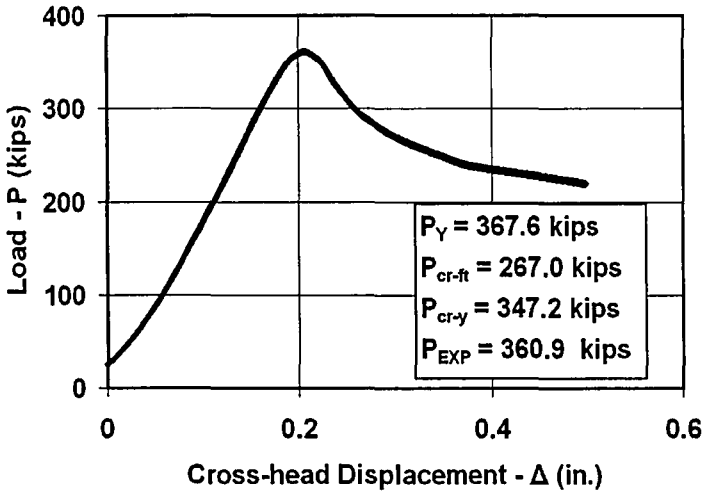

Figure 5.12 DA1 Specimen Load vs. Cross-head Displacement

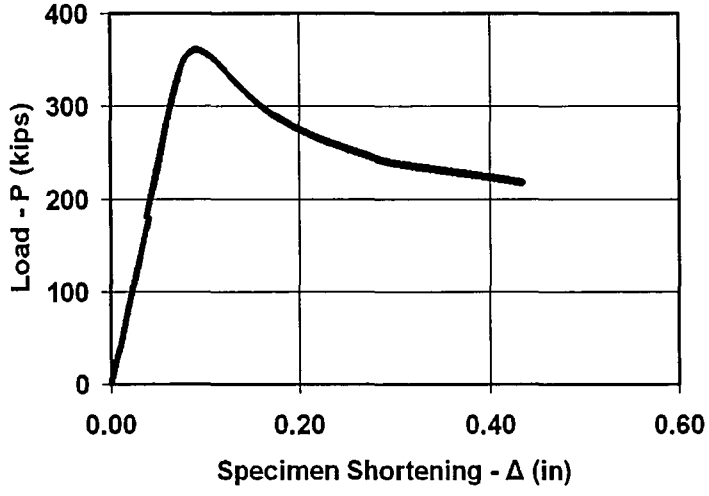

Figure 5.13 DA1 Specimen Load vs. Specimen Shortening

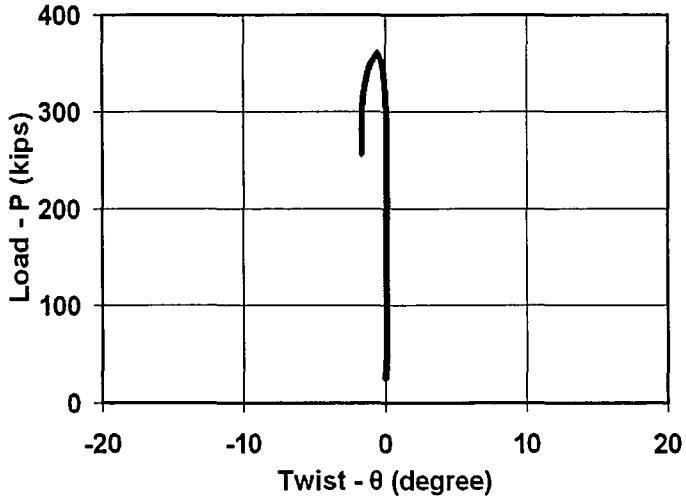

Figure 5.14 DA1 Specimen Load vs. Twist

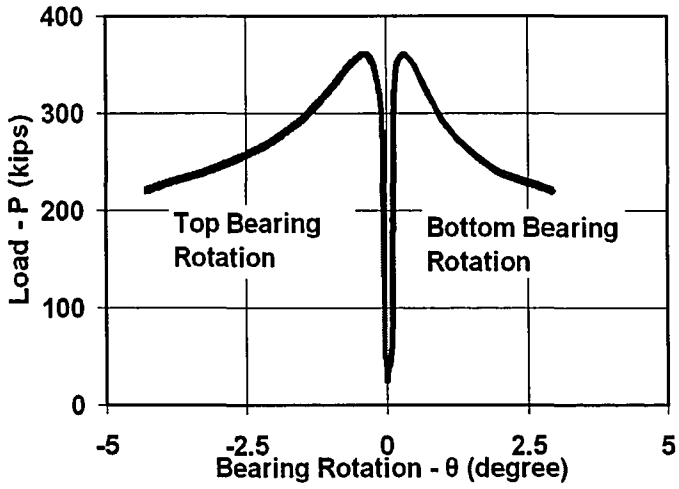

Figure 5.15 DA1 Specimen Load vs. Bearing Rotation

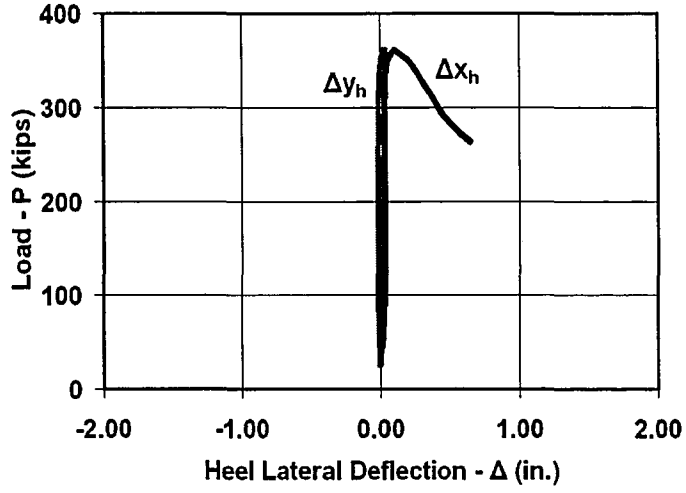

Figure 5.16 DA1 Specimen Load vs. Heel Lateral Deflection

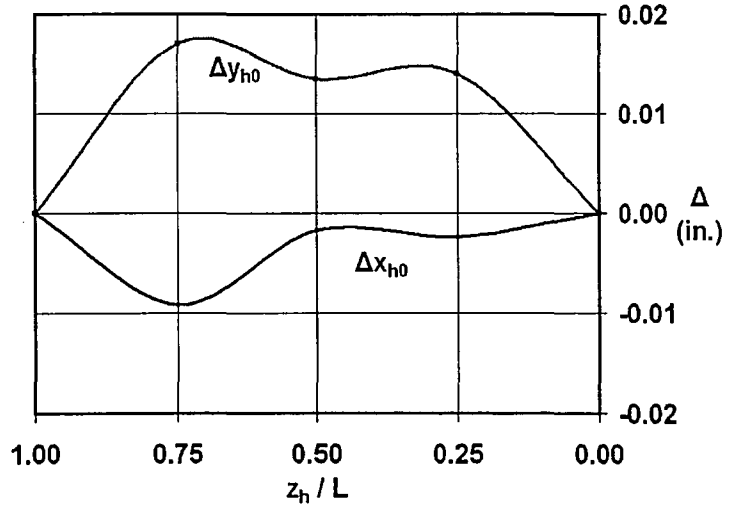

Figure 5.17 DA1 Specimen Initial Out-of-Straightness

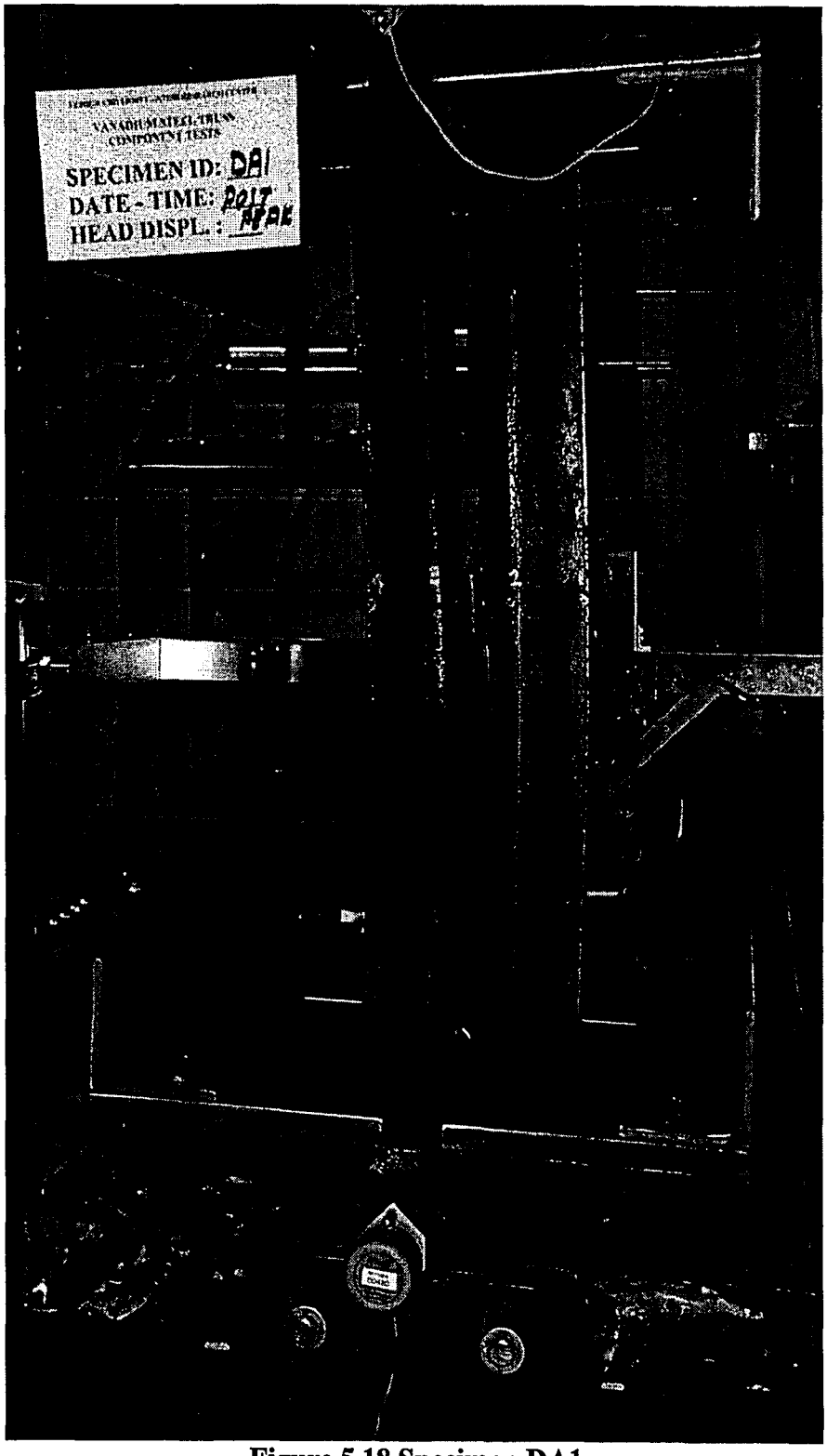

Figure 5.18 Specimen DA1

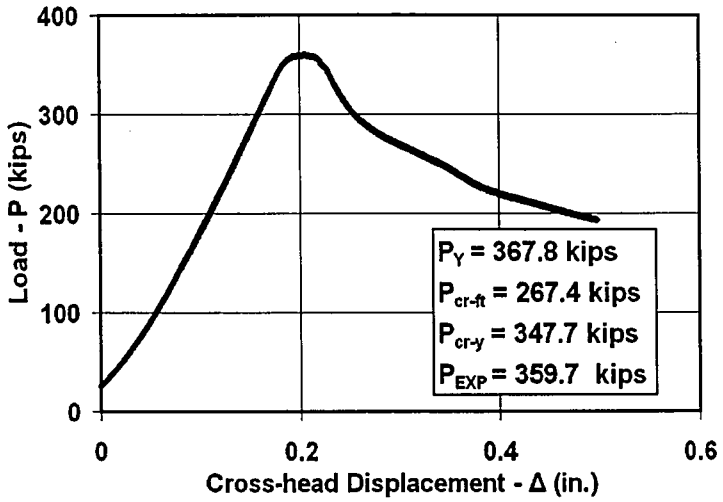

Figure 5.19 DA12 Specimen Load vs. Cross-head Displacement

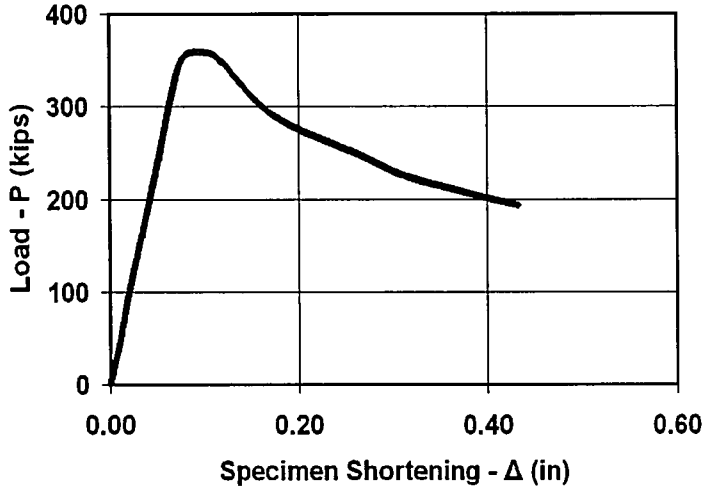

Figure 5.20 DA12 Specimen Load vs. Specimen Shortening

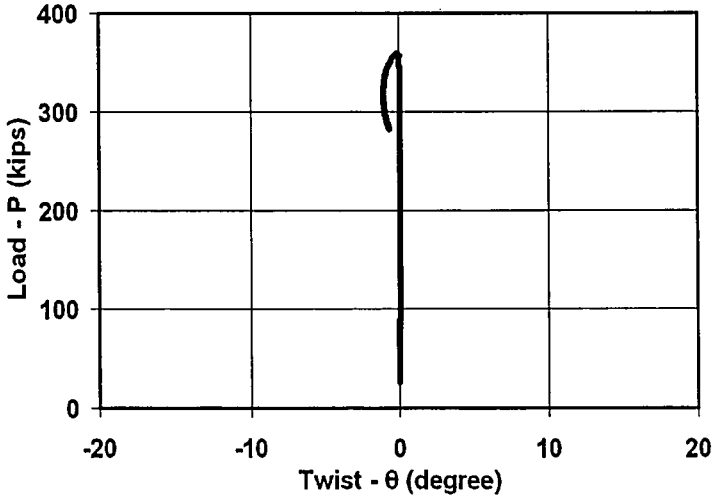

Figure 5.21 DA12 Specimen Load vs. Twist

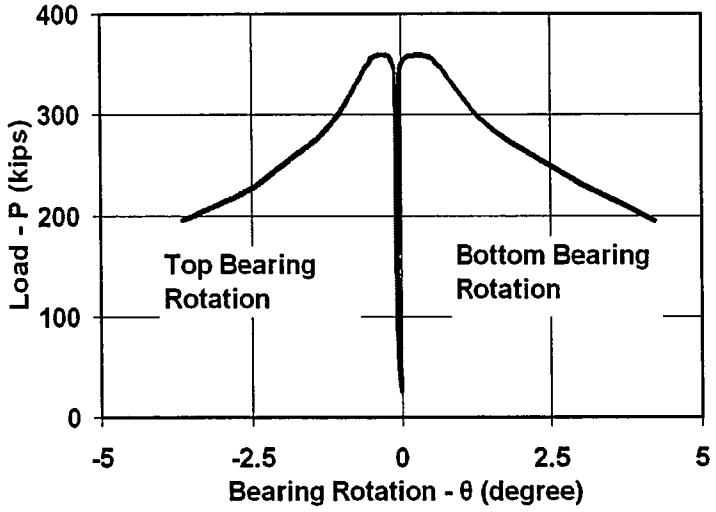

Figure 5.22 DA12 Specimen Load vs. Bearing Rotation

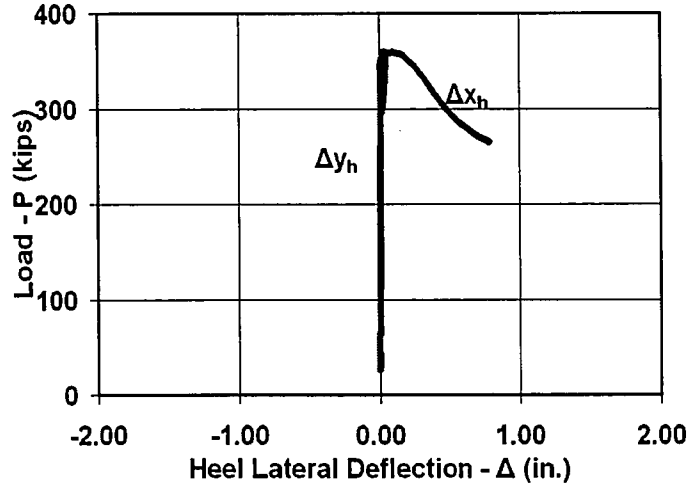

Figure 5.23 DA12 Specimen Load vs. Heel Lateral Deflection

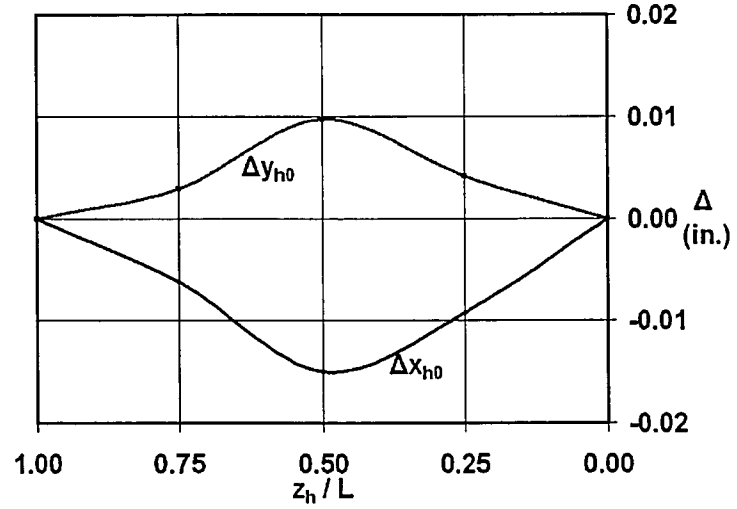

Figure 5.24 DA12 Specimen Initial Out-of-Straightness

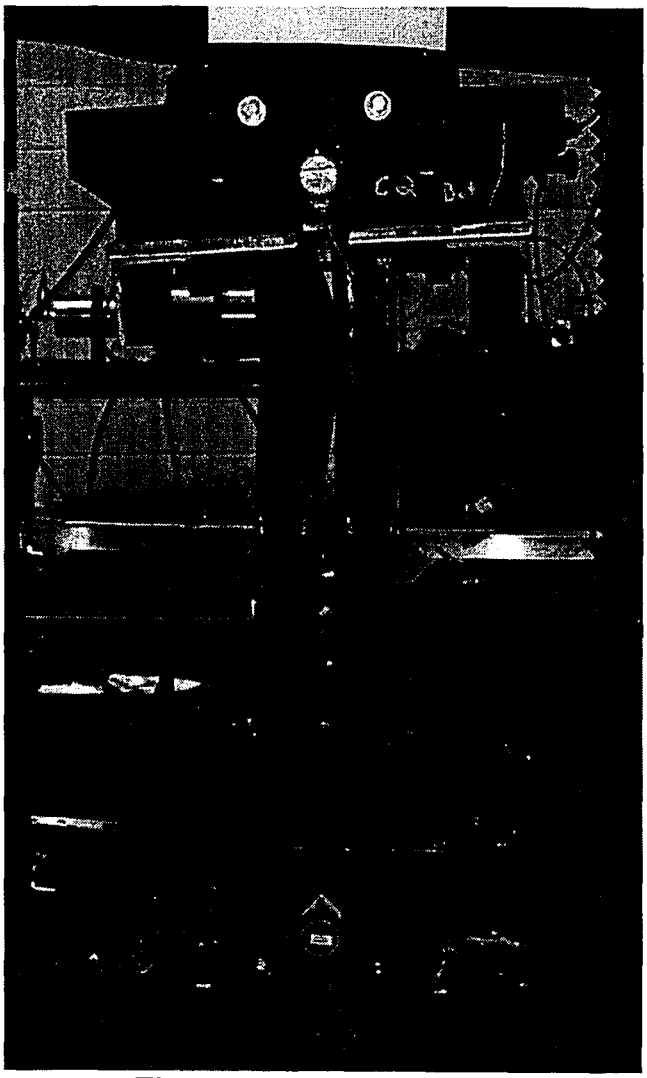

Figure 5.25 Specimen DA12

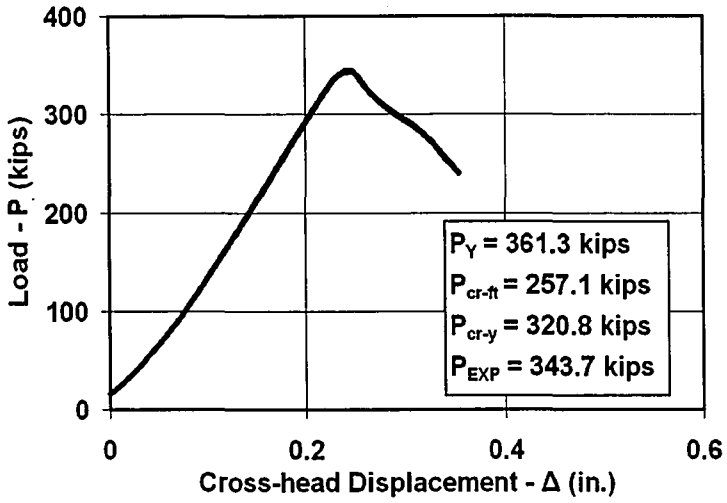

Figure 5.26 DA2 Specimen Load vs. Cross-head Displacement

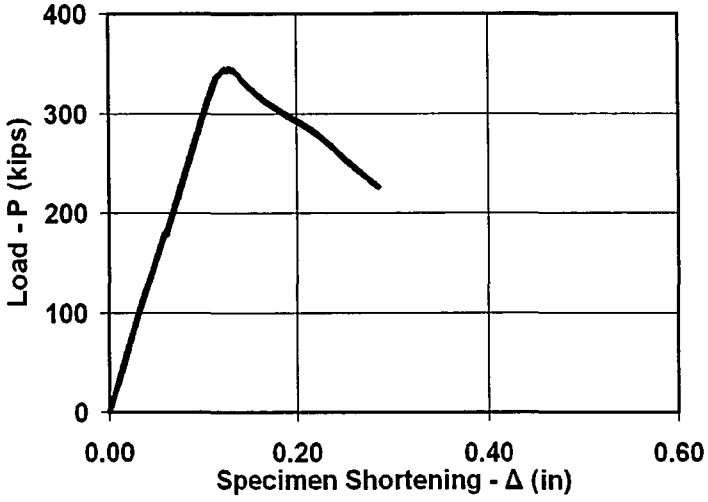

Figure 5.27 DA2 Specimen Load vs. Specimen Shortening

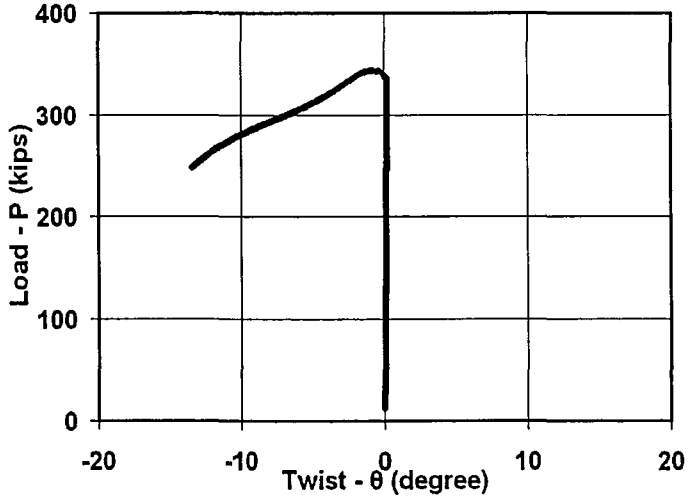

Figure 5.28 DA2 Specimen Load vs. Twist

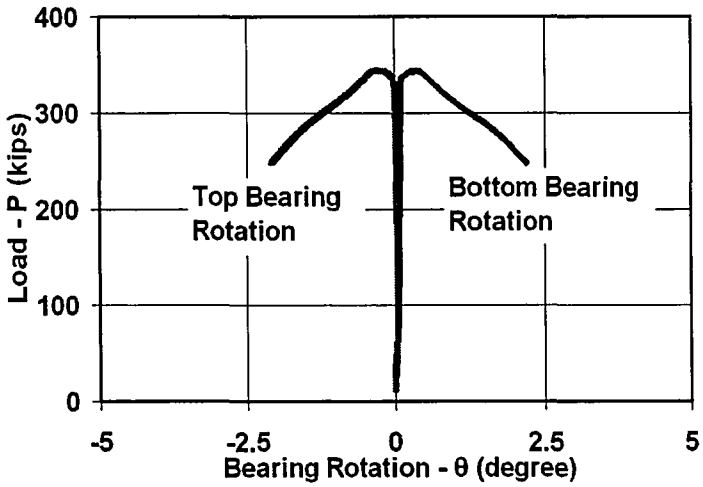

Figure 5.29 DA2 Specimen Load vs. Bearing Rotation

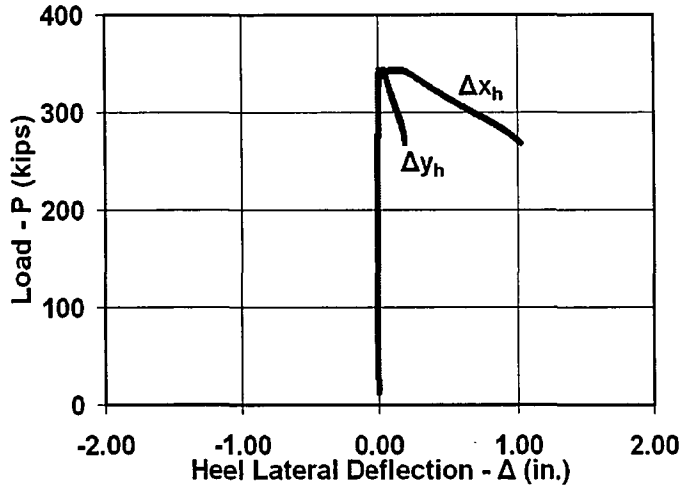

Figure 5.30 DA2 Specimen Load vs. Heel Lateral Deflection

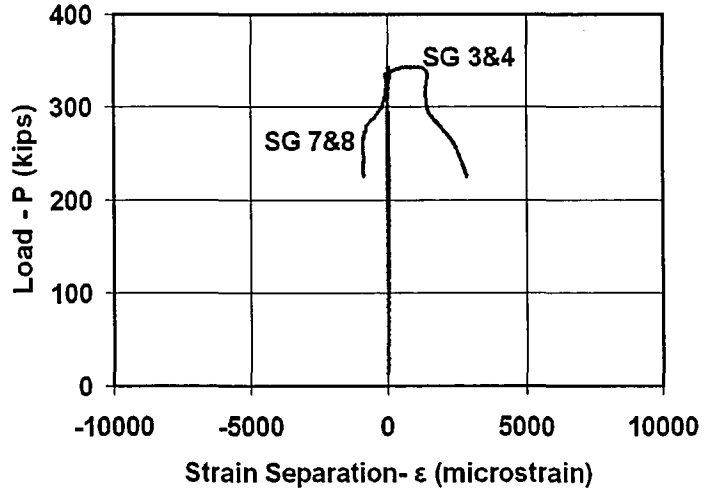

Figure 5.31 DA2 Specimen Load vs. Strain Separation

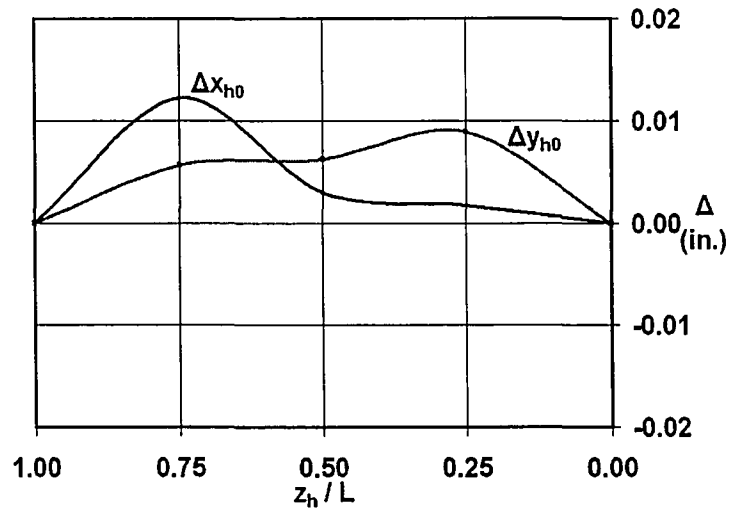

Figure 5.32 DA2 Specimen Initial Out-of-Straightness

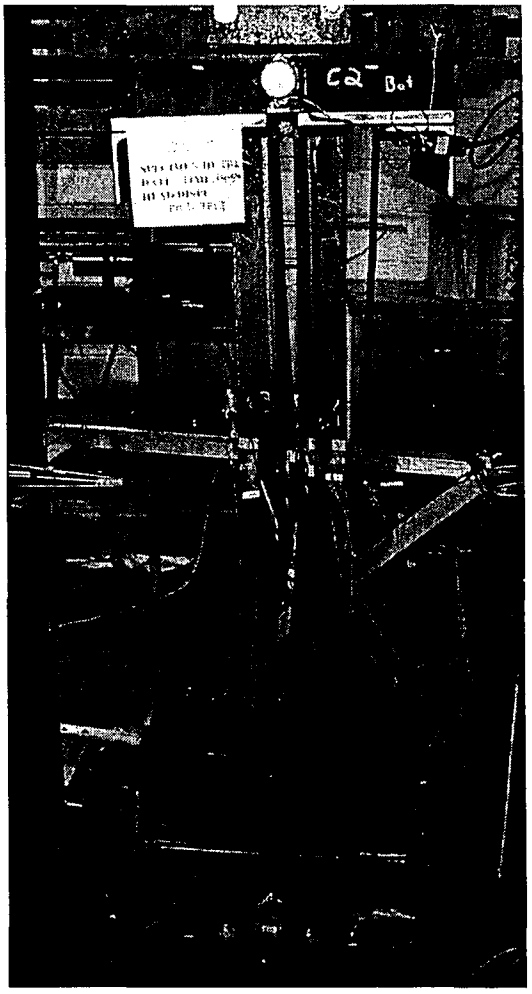

Figure 5.33 Specimen DA2

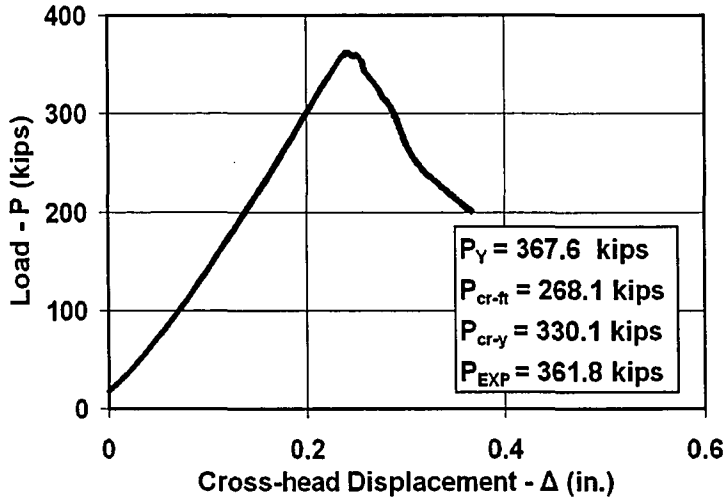

Figure 5.34 DA22 Specimen Load vs. Cross-head Displacement

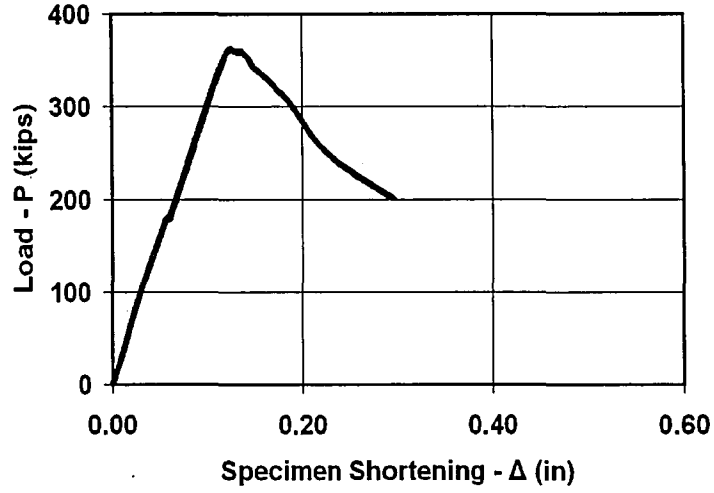

Figure 5.35 DA22 Specimen Load vs. Specimen Shortening

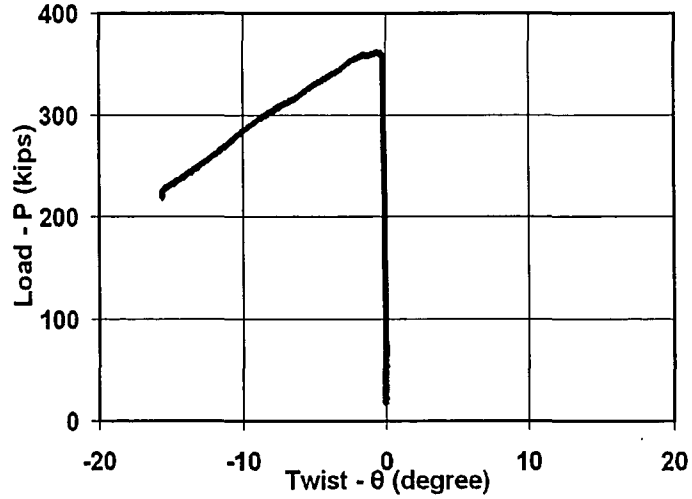

Figure 5.36 DA22 Specimen Load vs. Twist

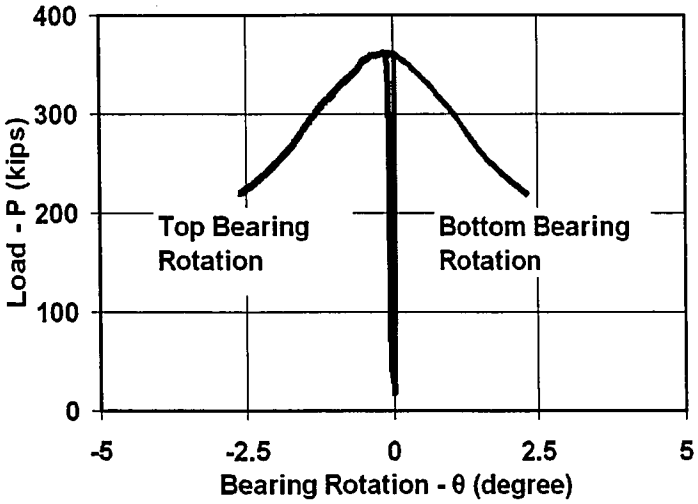

Figure 5.37 DA22 Specimen Load vs. Bearing Rotation

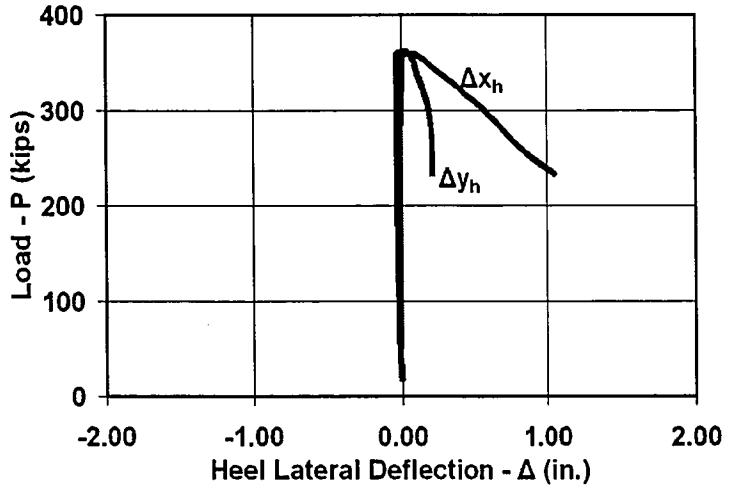

Figure 5.38 DA22 Specimen Load vs. Heel Lateral Deflection

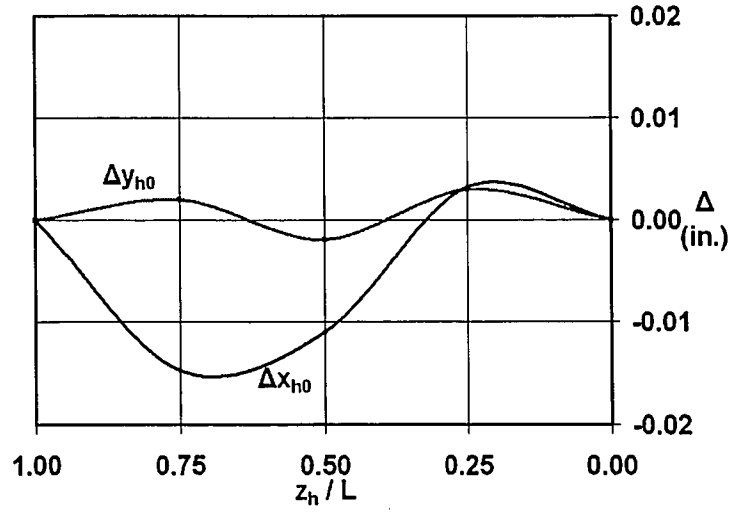

Figure 5.39 DA22 Specimen Initial Out-of-Straightness

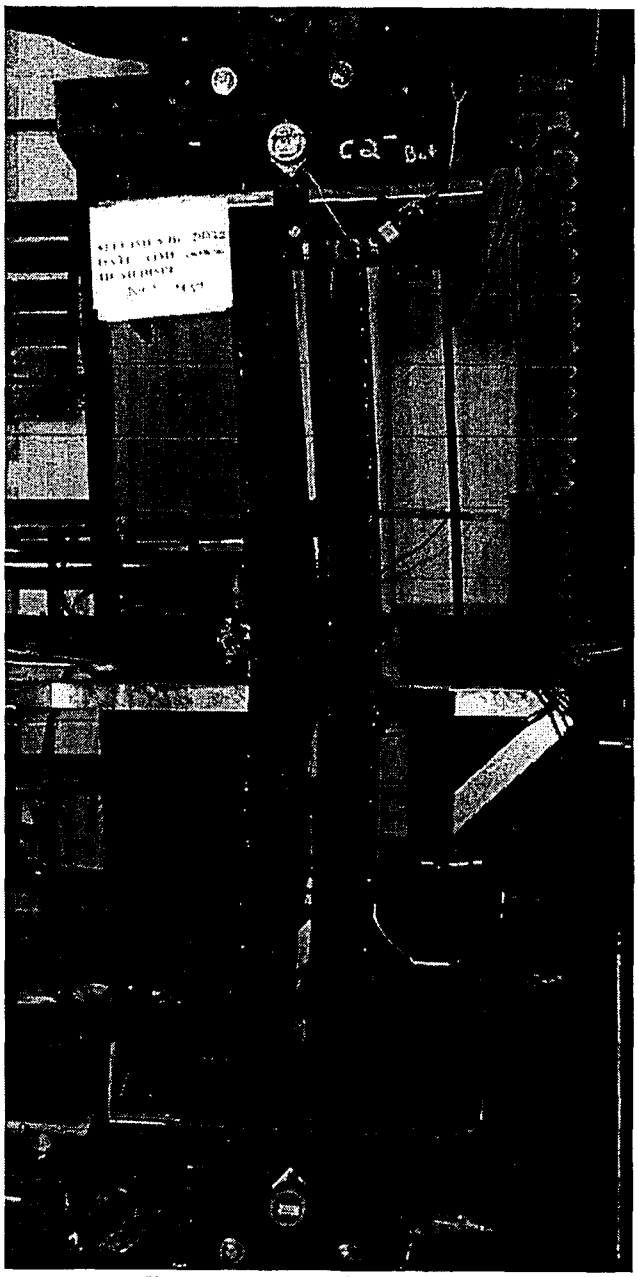

Figure 5.40 Specimen DA22

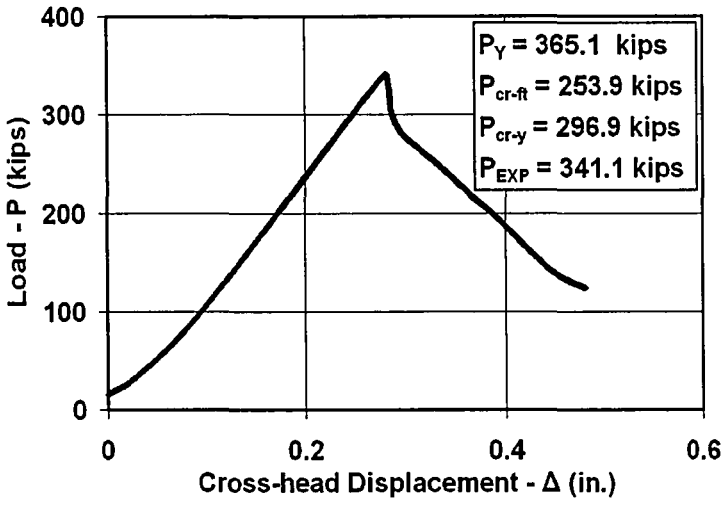

Figure 5.41 DA3 Specimen Load vs. Cross-head Displacement

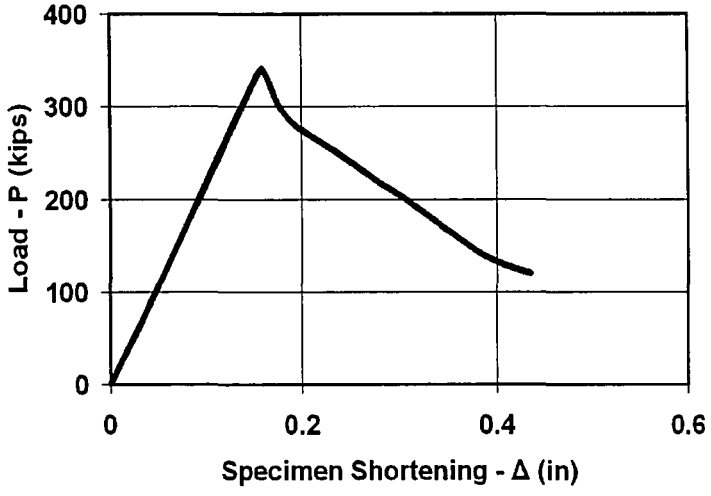

Figure 5.42 DA3 Specimen Load vs. Specimen Shortening

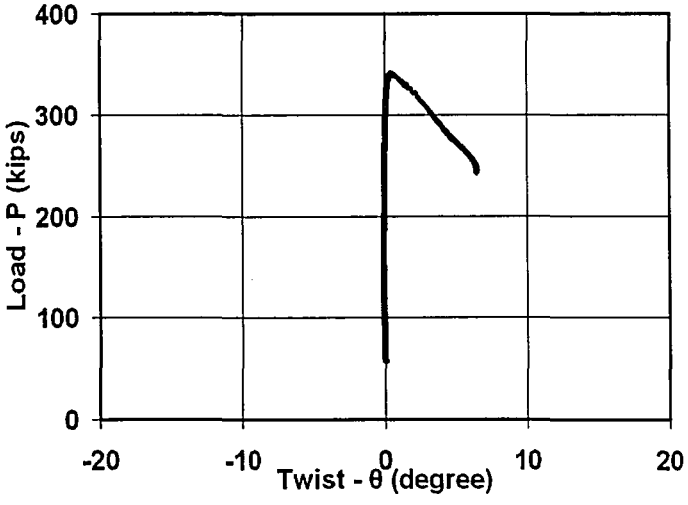

Figure 5.43 DA3 Specimen Load vs. Twist

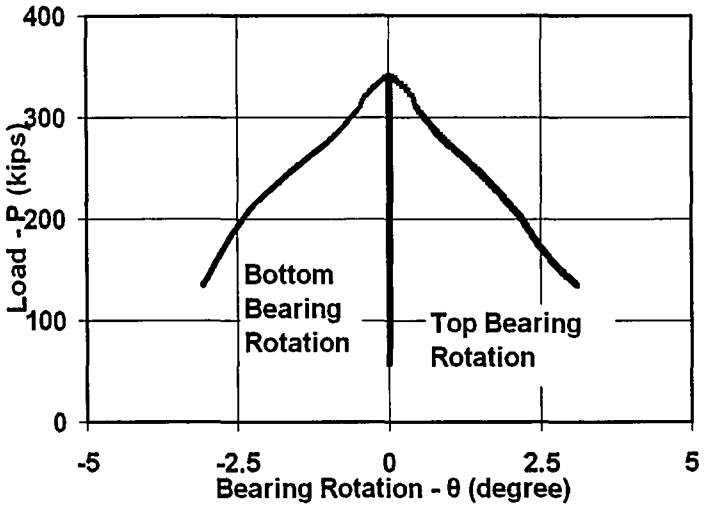

Figure 5.44 DA3 Specimen Load vs. Bearing Rotation

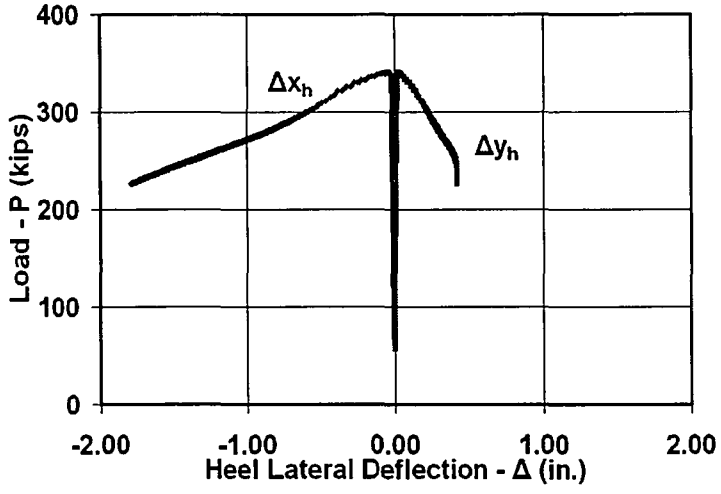

Figure 5.45 DA3 Specimen Load vs. Heel Lateral Deflection

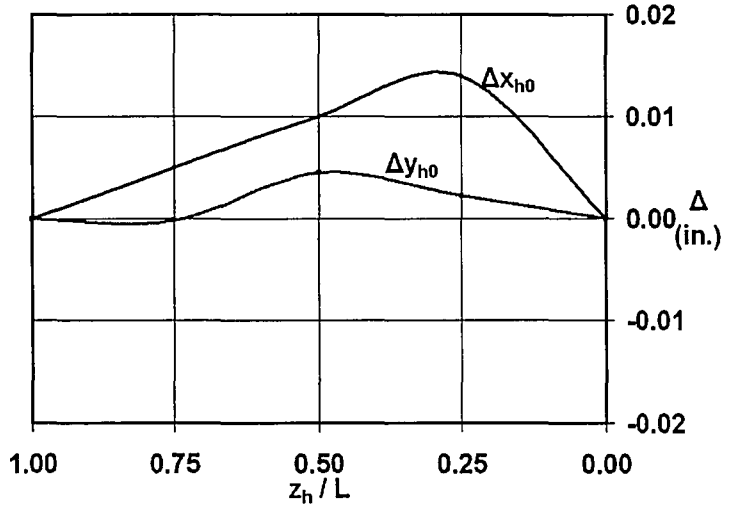

Figure 5.46 DA3 Specimen Initial Out-of-Straightness

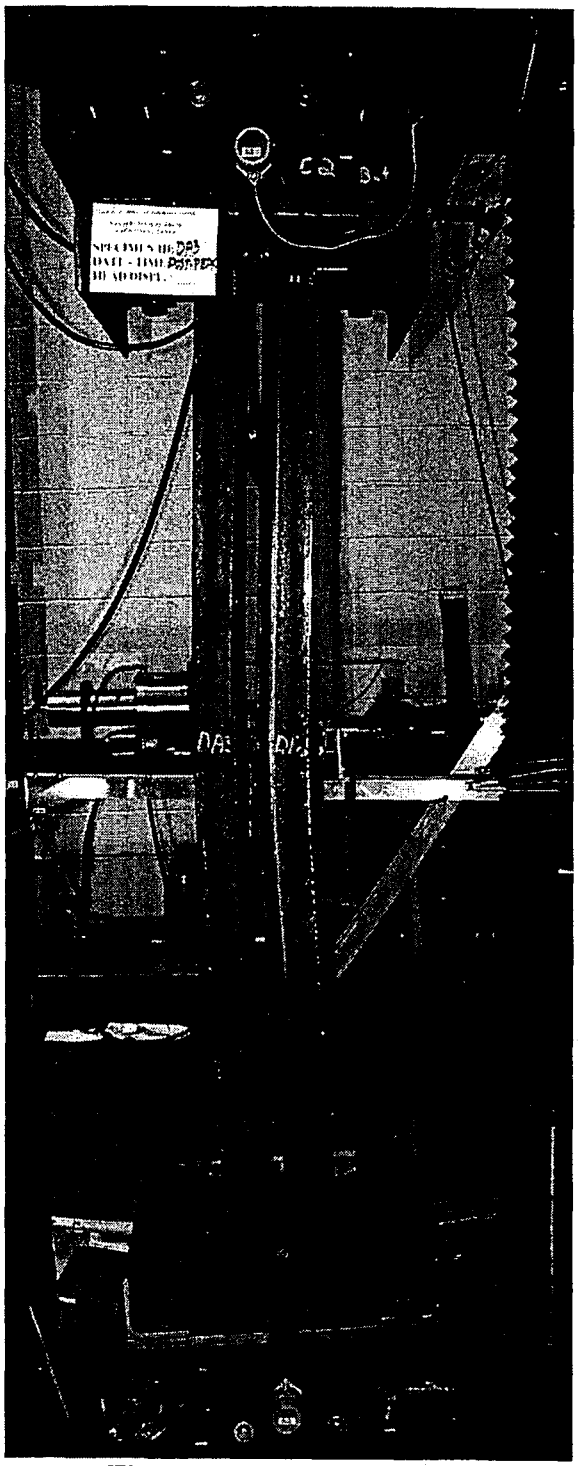

Figure 5.47 Specimen DA3

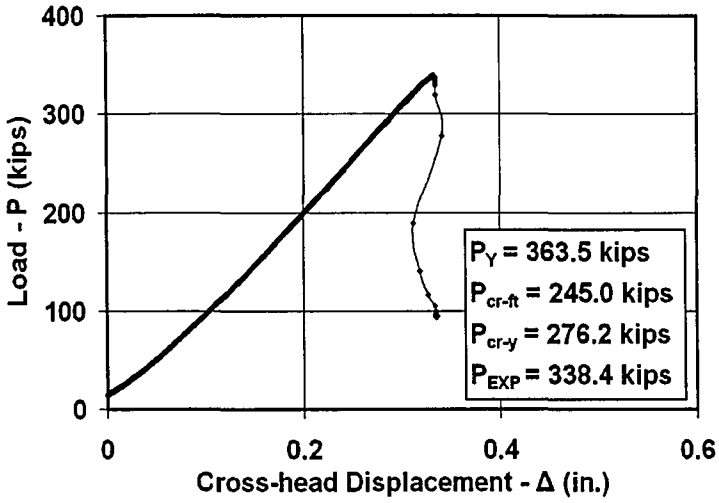

Figure 5.48 DA4 Specimen Load vs. Cross-head Displacement

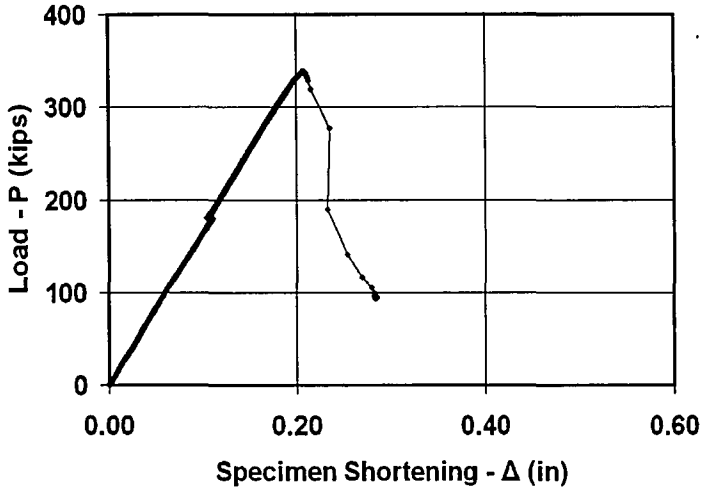

Figure 5.49 DA4 Specimen Load vs. Specimen Shortening

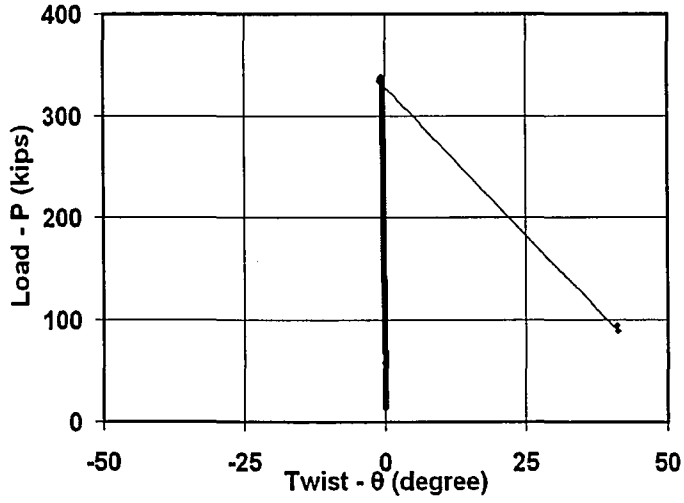

Figure 5.50 DA4 Specimen Load vs. Twist

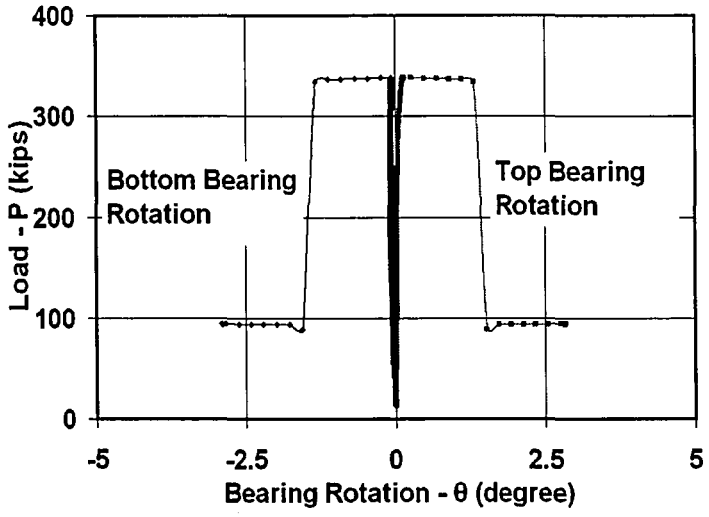

Figure 5.51 DA4 Specimen Load vs. Bearing Rotation

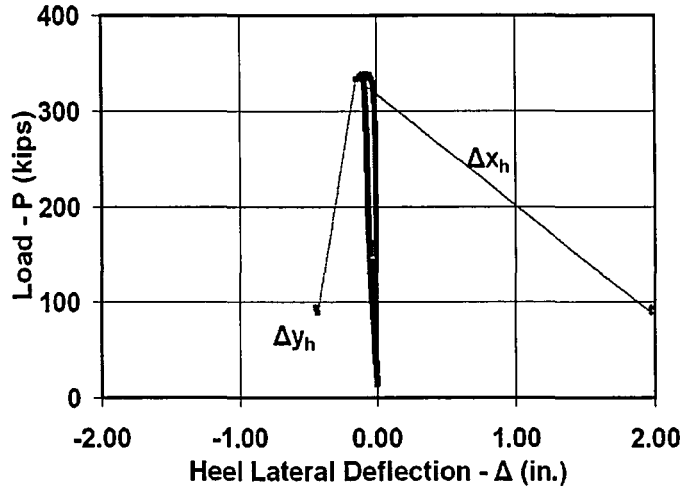

Figure 5.52 DA4 Specimen Load vs. Heel Lateral Deflection

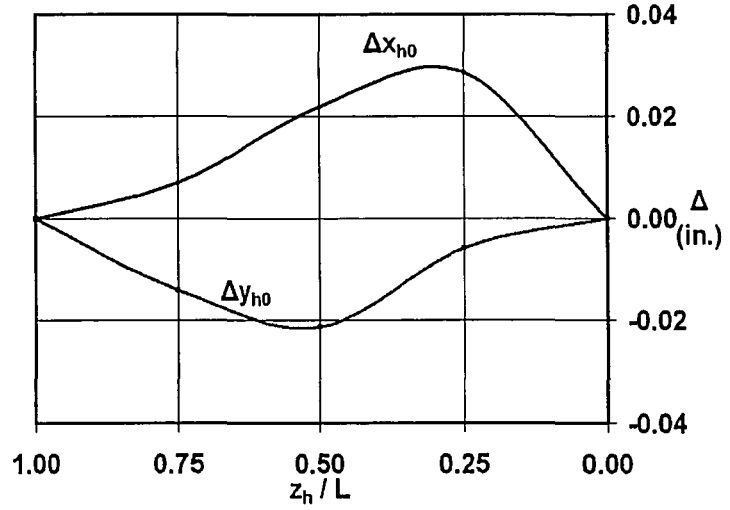

Figure 5.53 DA4 Specimen Initial Out-of-Straightness

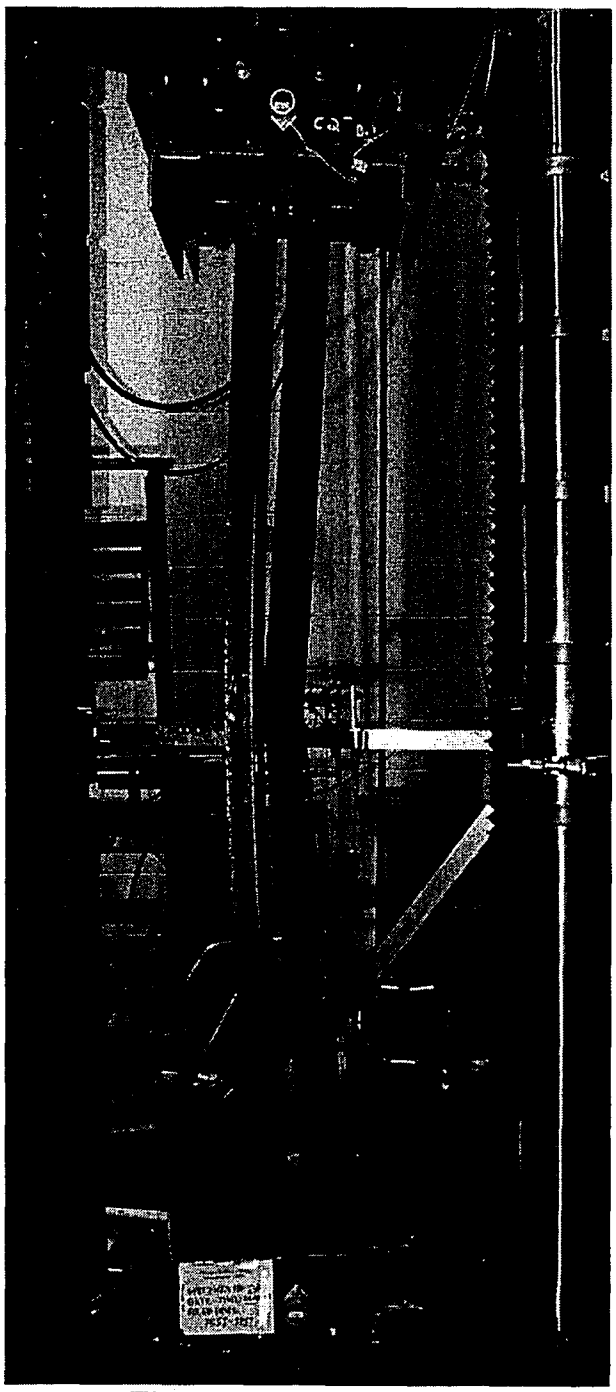

Figure 5.54 Specimen DA4

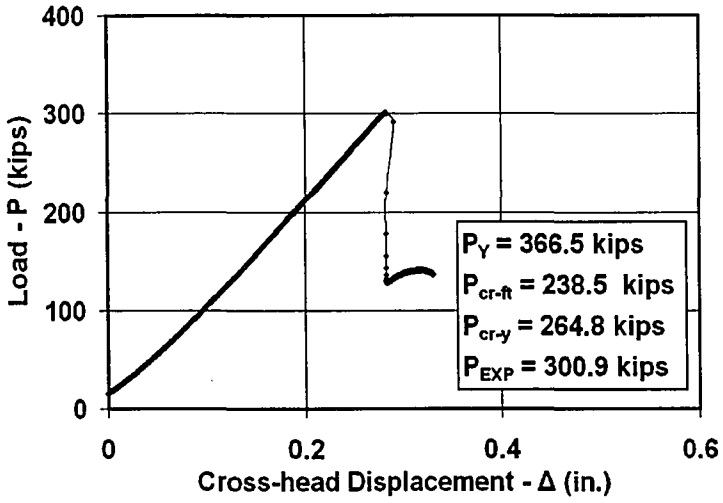

Figure 5.55 DA42 Specimen Load vs. Cross-head Displacement

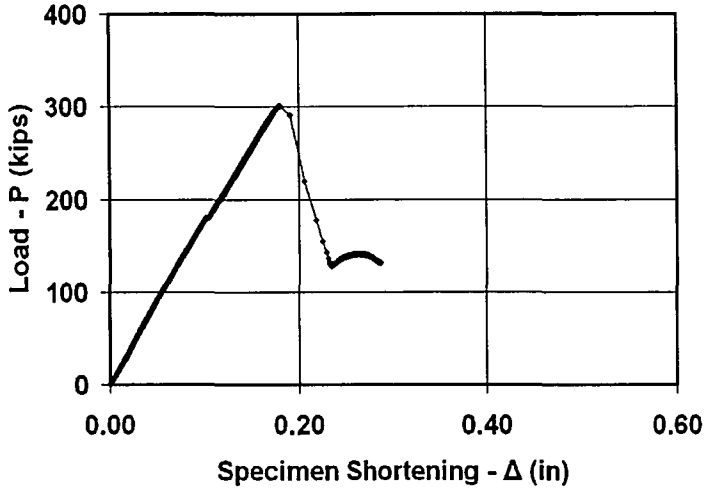

Figure 5.56 DA42 Specimen Load vs. Specimen Shortening

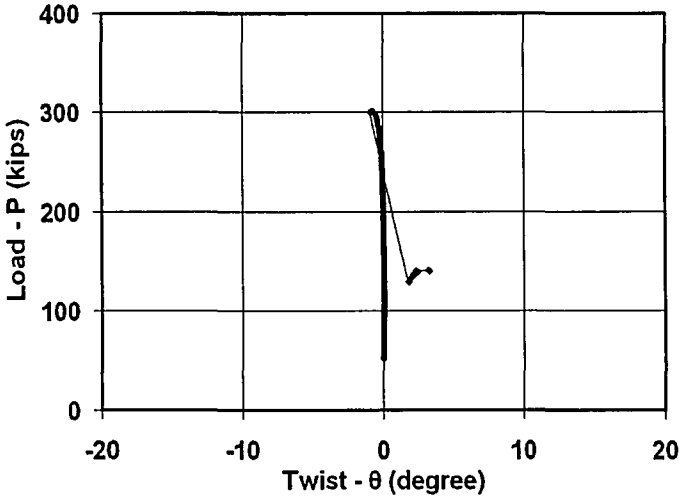

Figure 5.57 DA42 Specimen Load vs. Twist

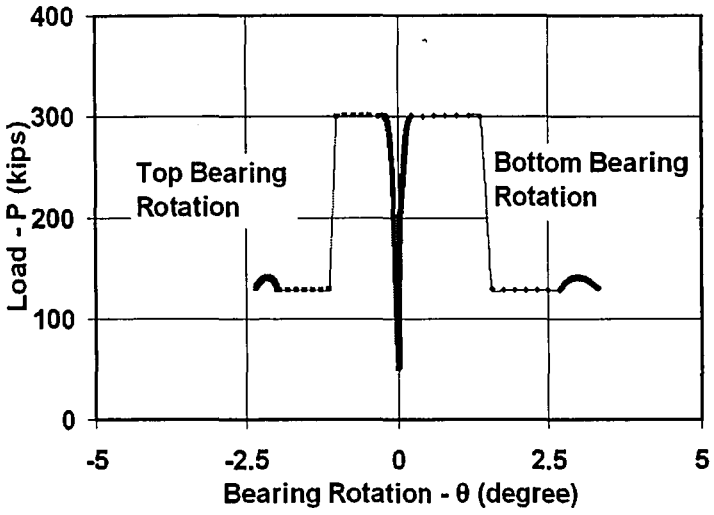

Figure 5.58 DA42 Specimen Load vs. Bearing Rotation

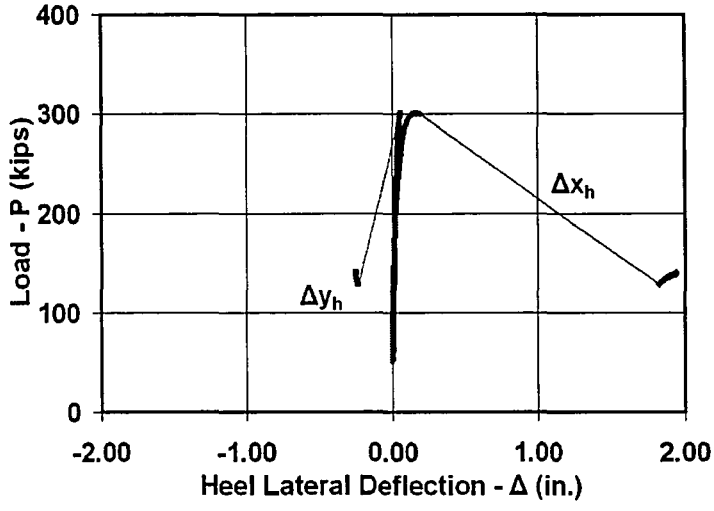

Figure 5.59 DA42 Specimen Load vs. Heel Lateral Deflection

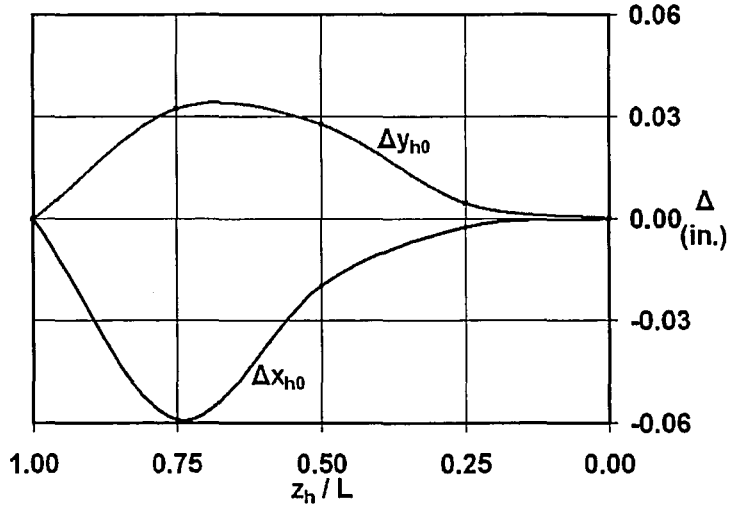

Figure 5.60 DA42 Specimen Initial Out-of-Straightness

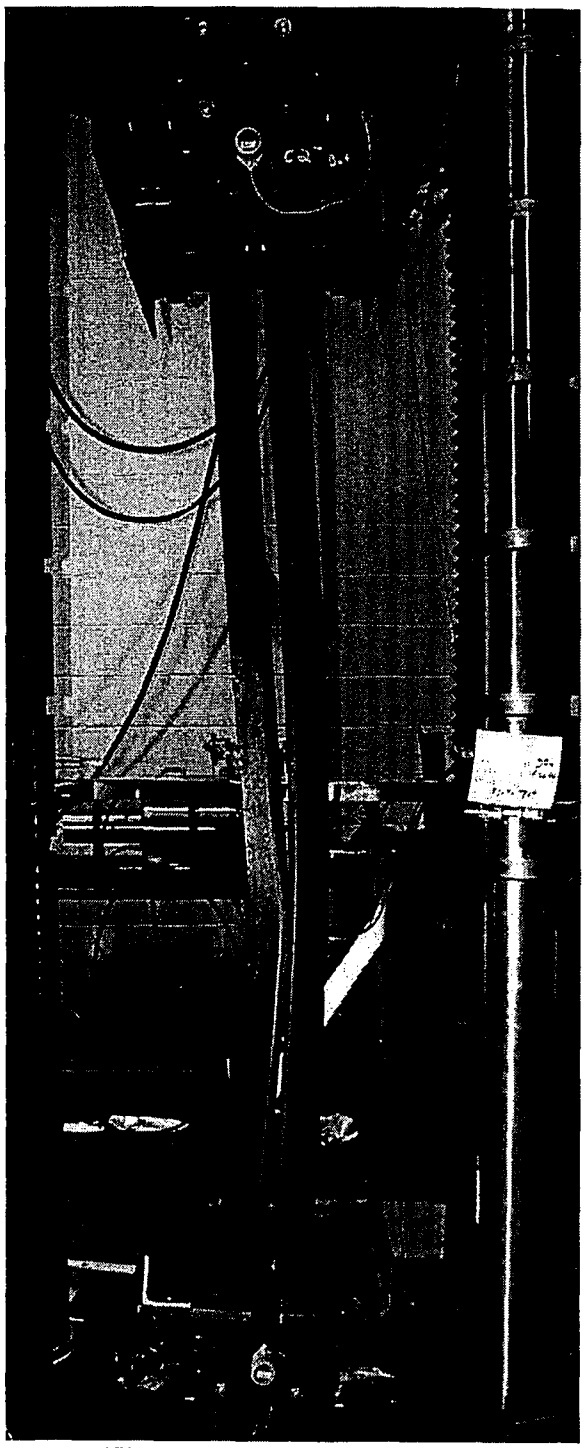

Figure 5.61 Specimen DA42

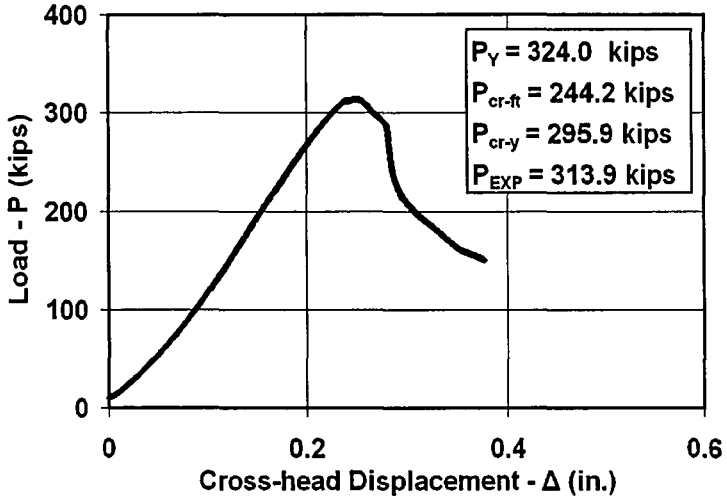

Figure 5.62 DA5 Specimen Load vs. Cross-head Displacement

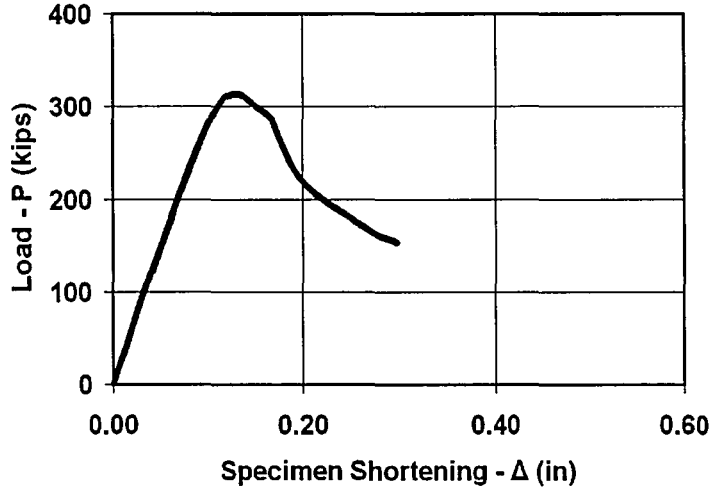

Figure 5.63 DA5 Specimen Load vs. Specimen Shortening

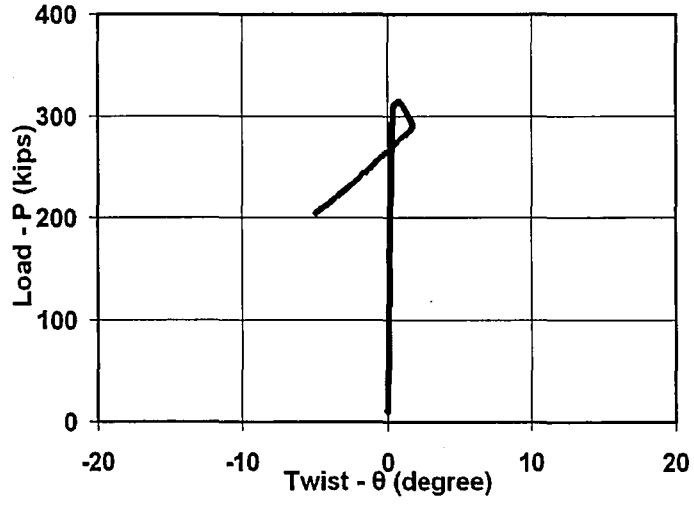

Figure 5.64 DA5 Specimen Load vs. Twist

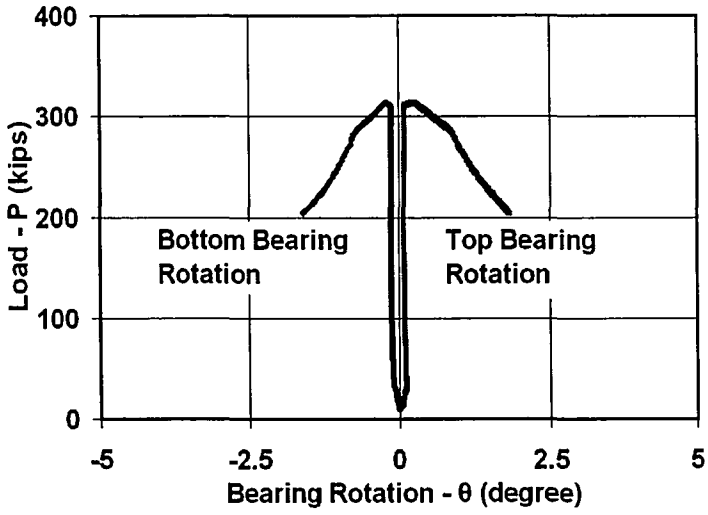

Figure 5.65 DA5 Specimen Load vs. Bearing Rotation

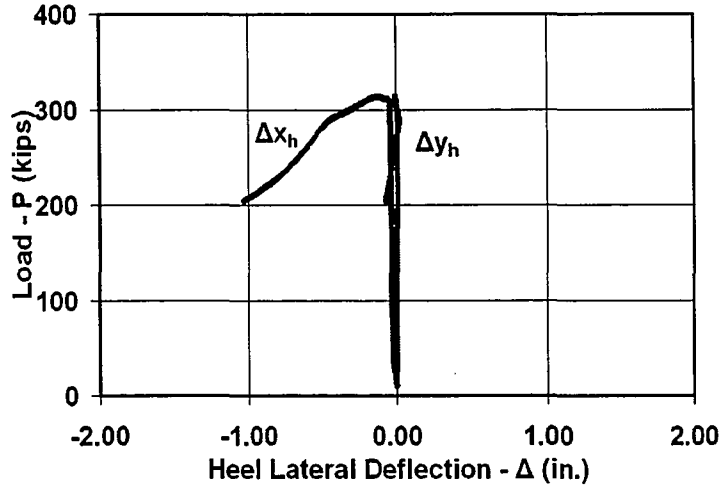

Figure 5.66 DA5 Specimen Load vs. Heel Lateral Deflection

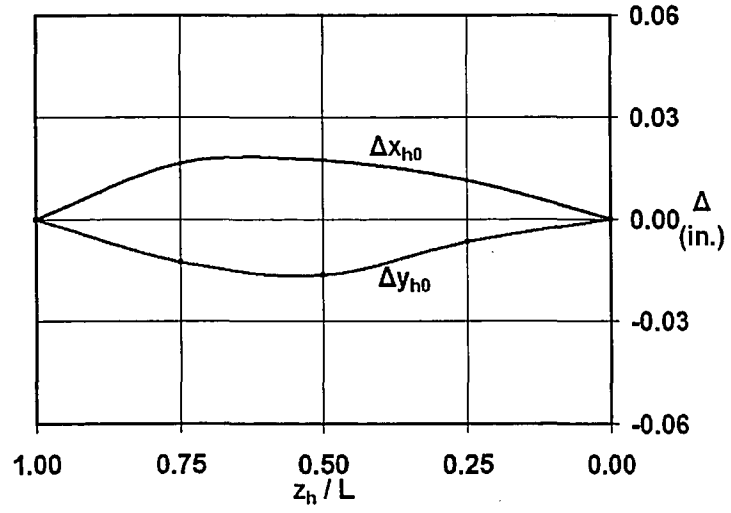

Figure 5.67 DA5 Specimen Initial Out-of-Straightness

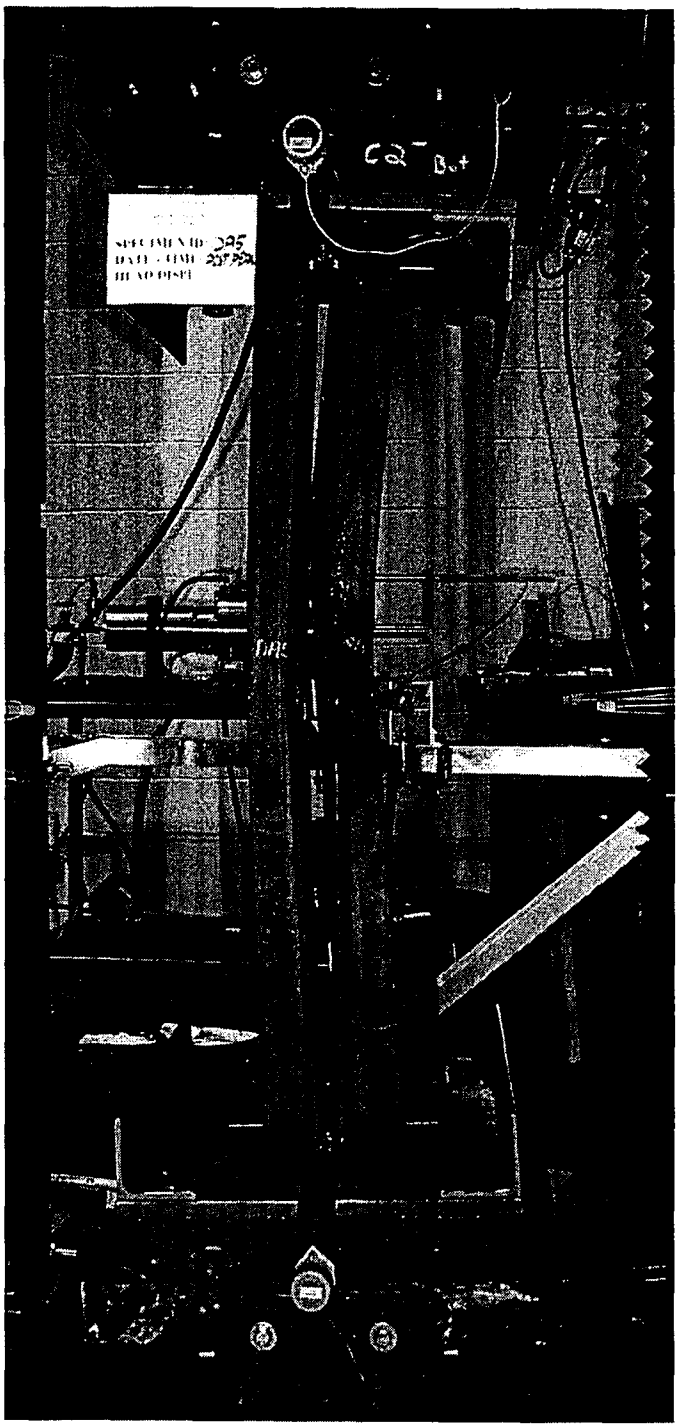

Figure 5.68 Specimen DA5

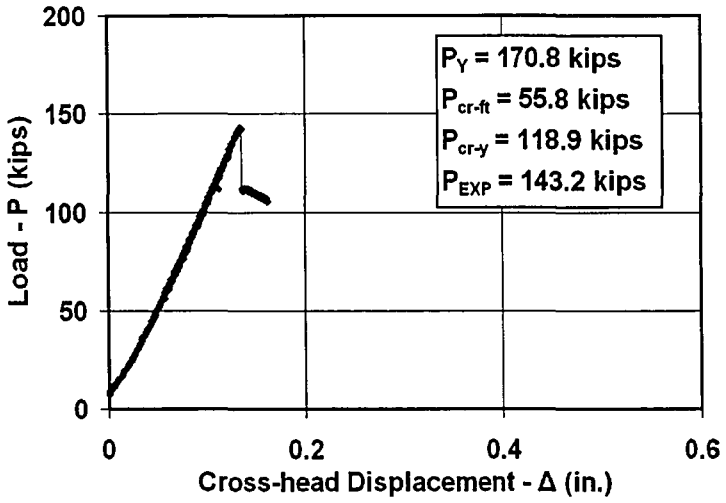

Figure 5.69 DB1 Specimen Load vs. Cross-head Displacement

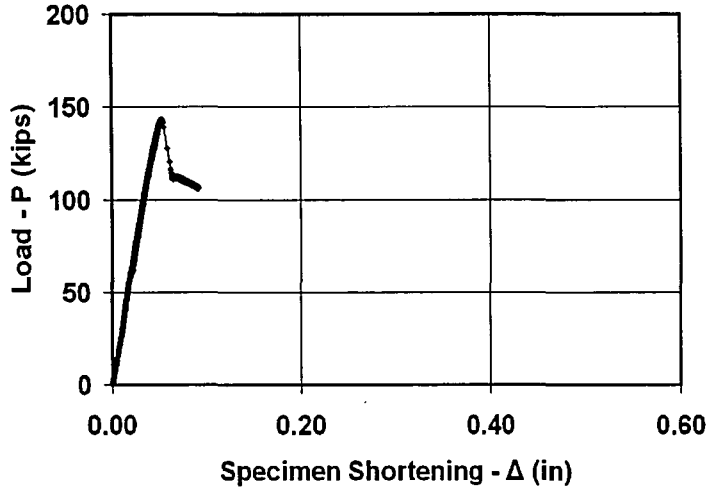

Figure 5.70 DB1 Specimen Load vs. Specimen Shortening

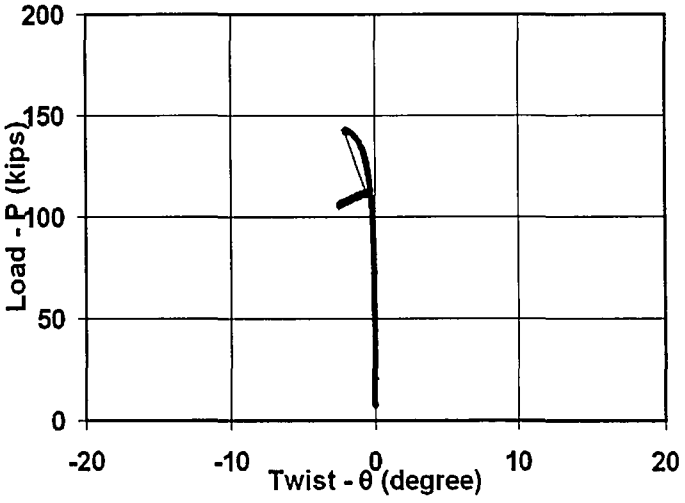

Figure 5.71 DB1 Specimen Load vs. Twist

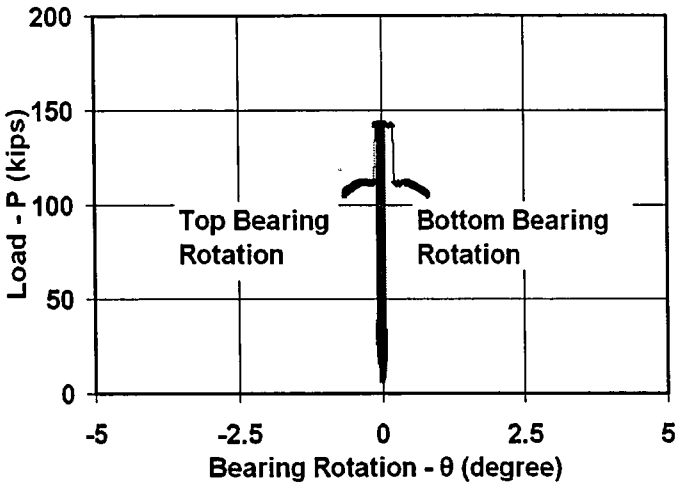

Figure 5.72 DB1 Specimen Load vs. Bearing Rotation

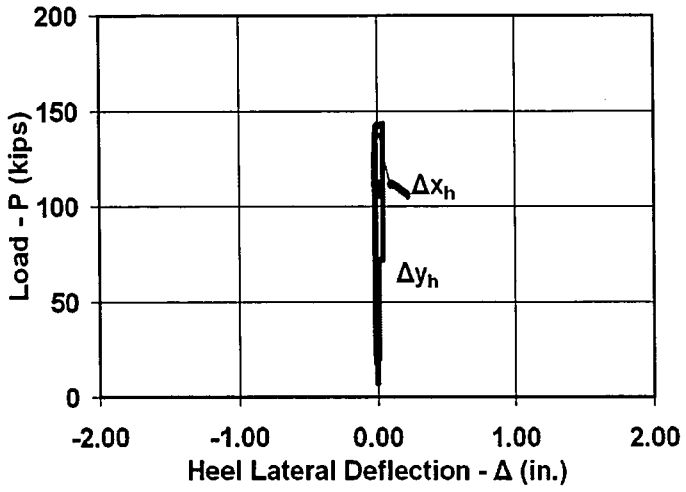

Figure 5.73 DB1 Specimen Load vs. Heel Lateral Deflection

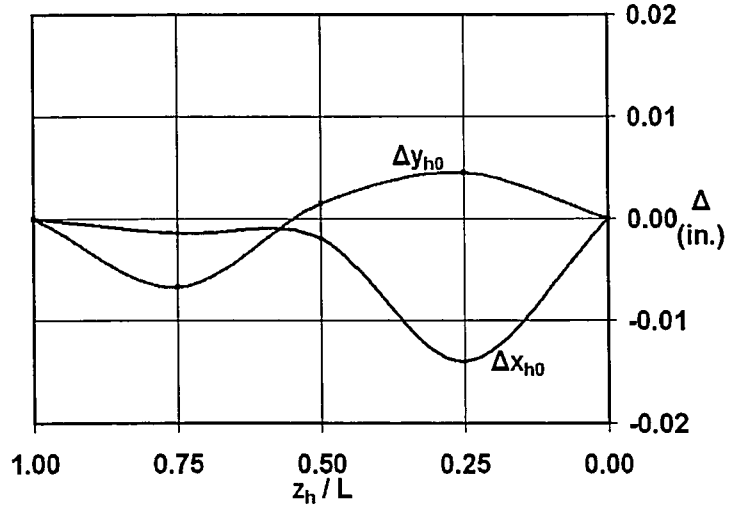

Figure 5.74 DB1 Specimen Initial Out-of-Straightness

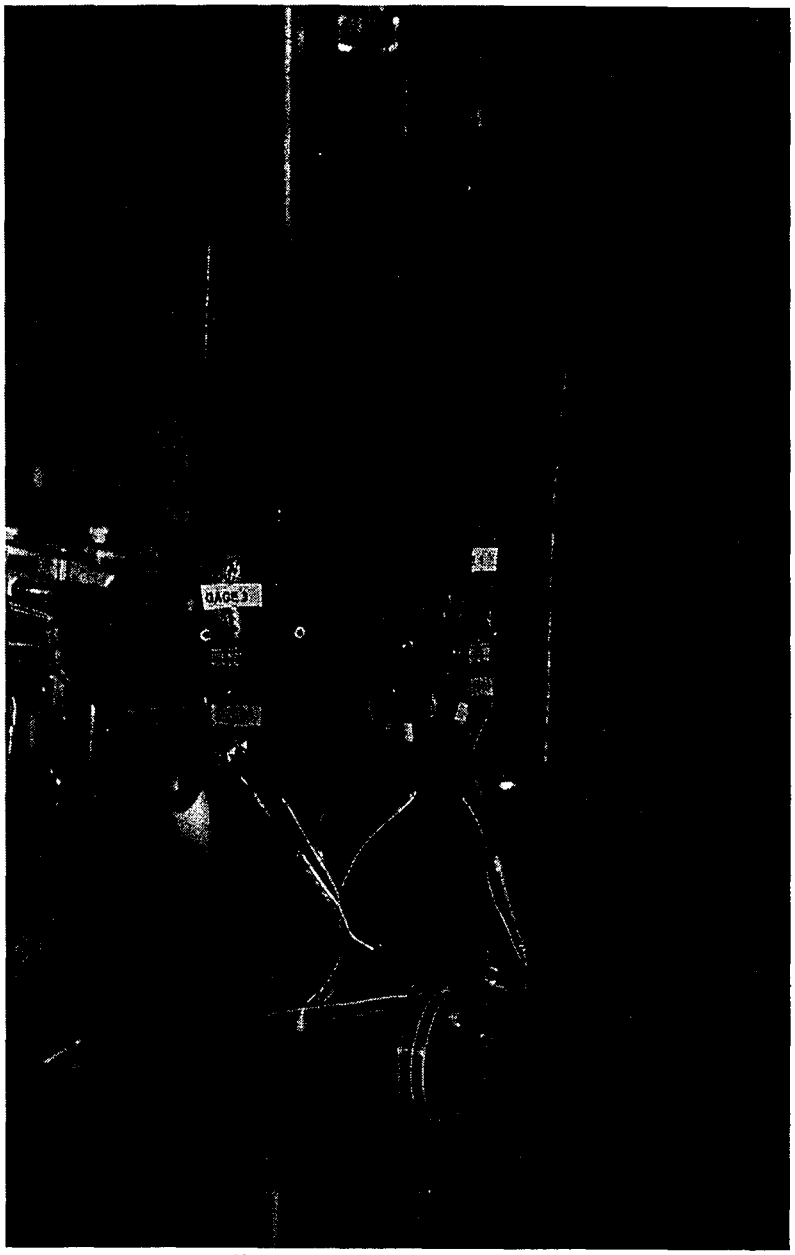

Figure 5.75 Specimen DB1

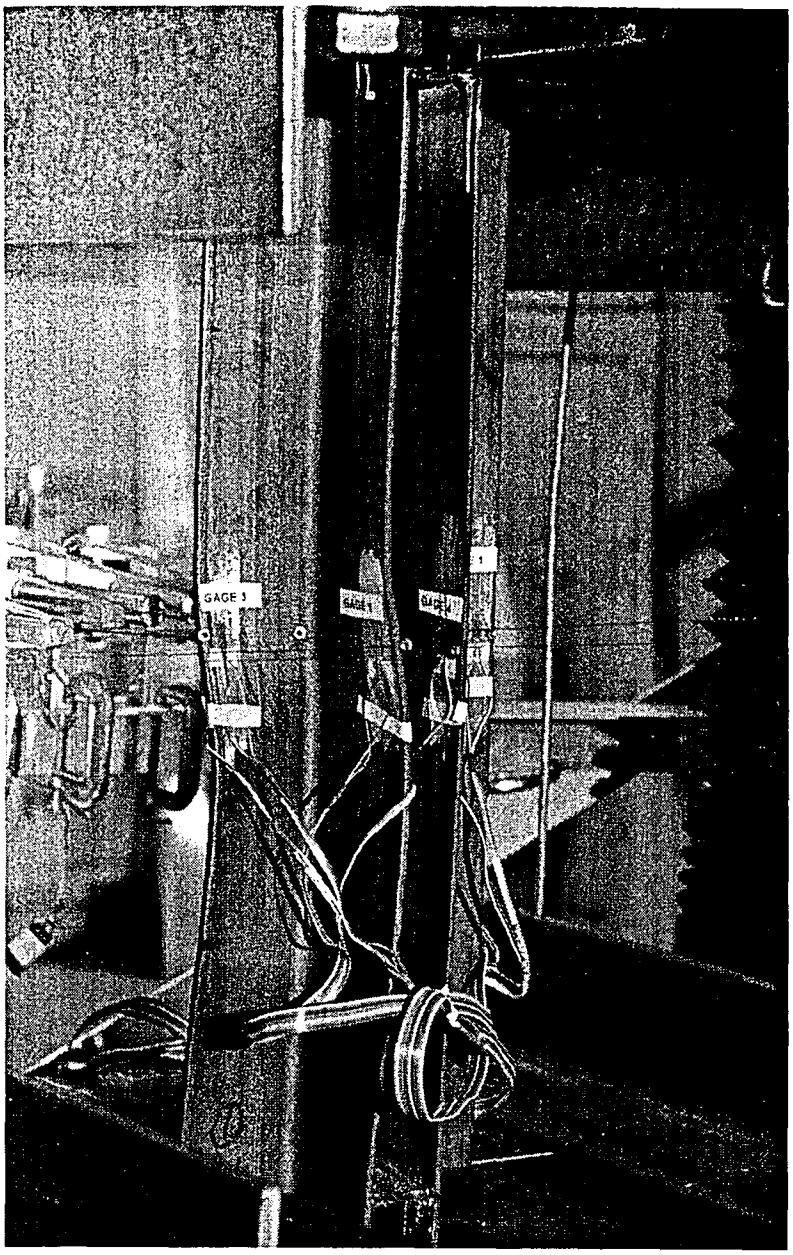

Figure 5.75 Specimen DB1

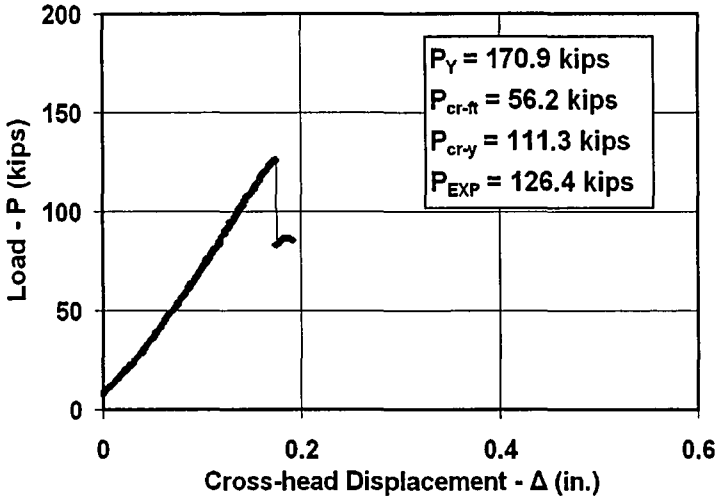

Figure 5.76 DB2 Specimen Load vs. Cross-head Displacement

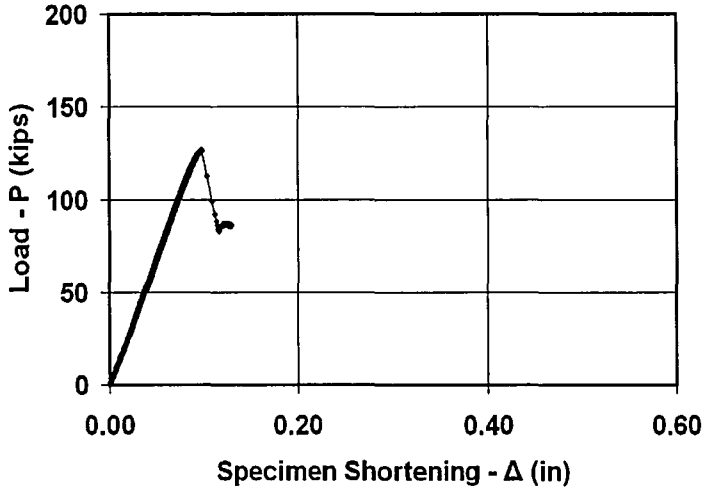

Figure 5.77 DB2 Specimen Load vs. Specimen Shortening

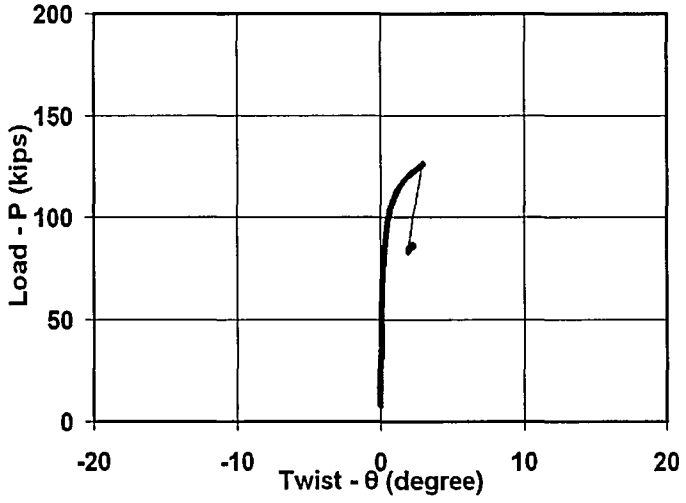

Figure 5.78 DB2 Specimen Load vs. Twist

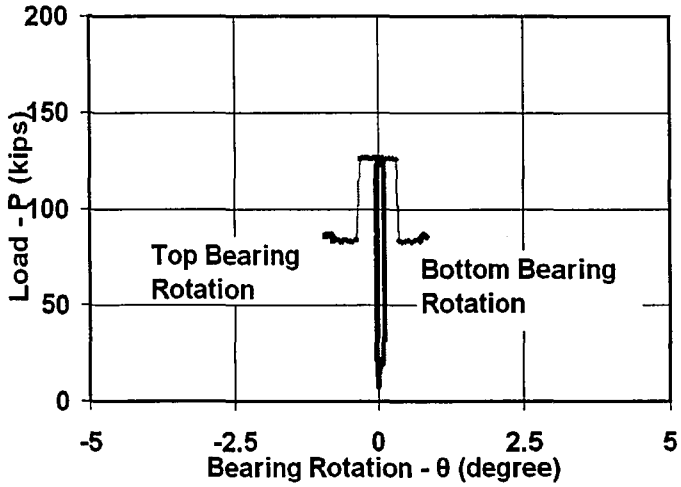

Figure 5.79 DB2 Specimen Load vs. Bearing Rotation

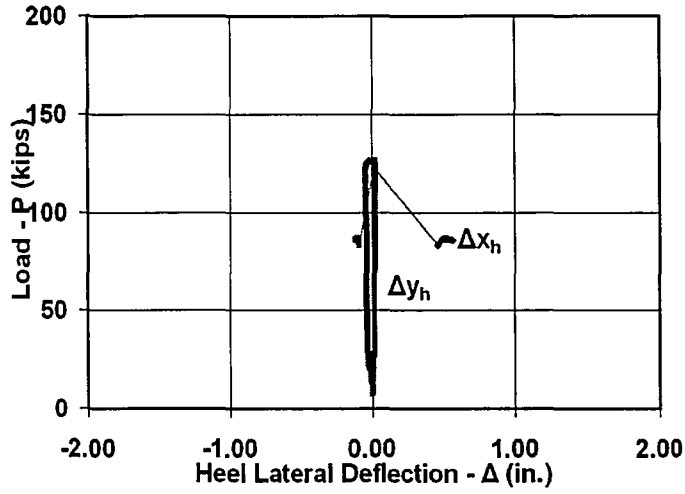

Figure 5.80 DB2 Specimen Load vs. Heel Lateral Deflection

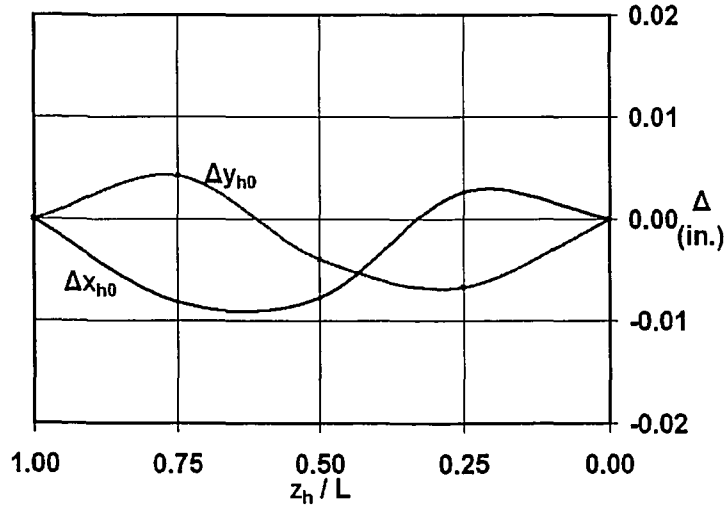

Figure 5.81 DB2 Specimen Initial Out-of-Straightness

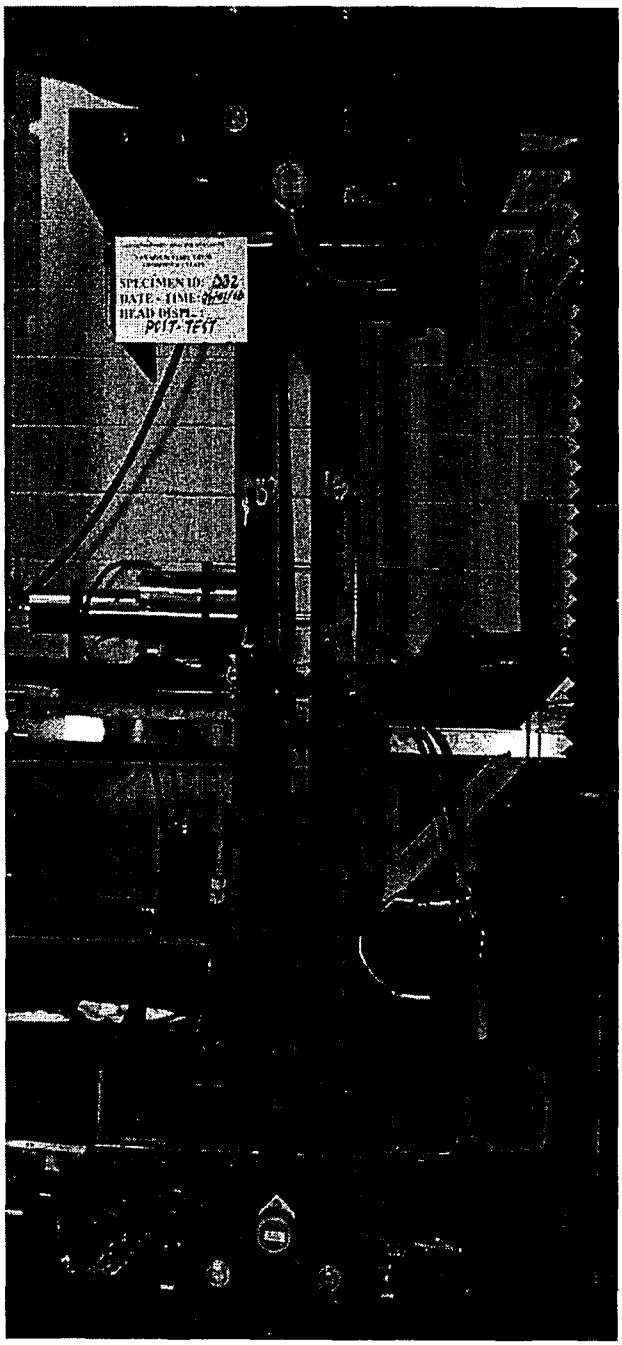

Figure 5.82 Specimen DB2

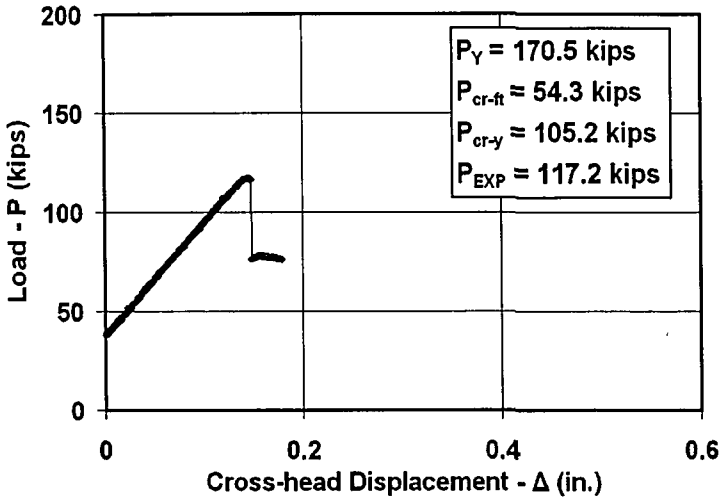

Figure 5.83 DB3 Specimen Load vs. Cross-head Displacement

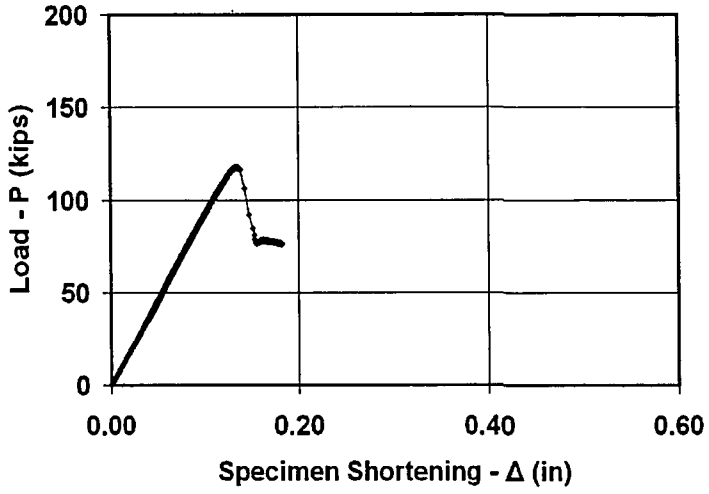

Figure 5.84 DB3 Specimen Load vs. Specimen Shortening

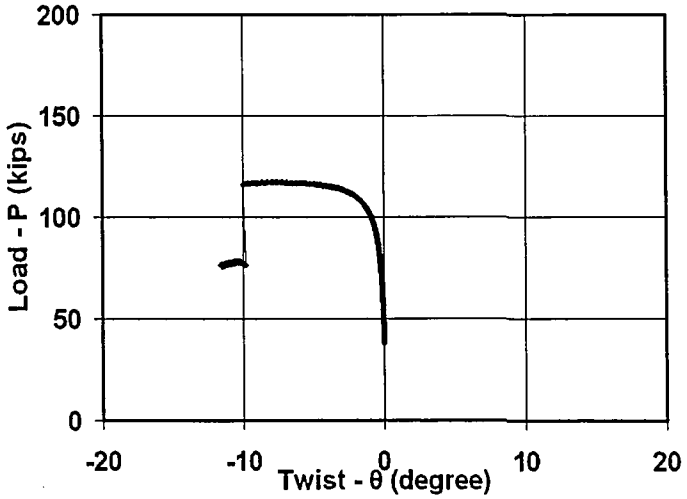

Figure 5.85 DB3 Specimen Load vs. Twist

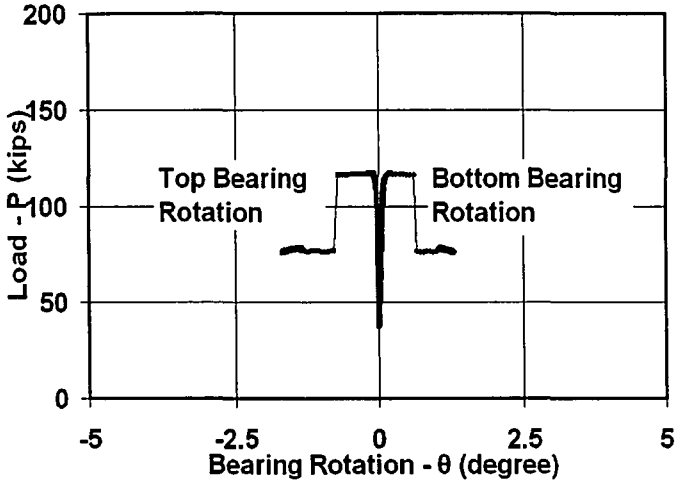

Figure 5.86 DB3 Specimen Load vs. Bearing Rotation

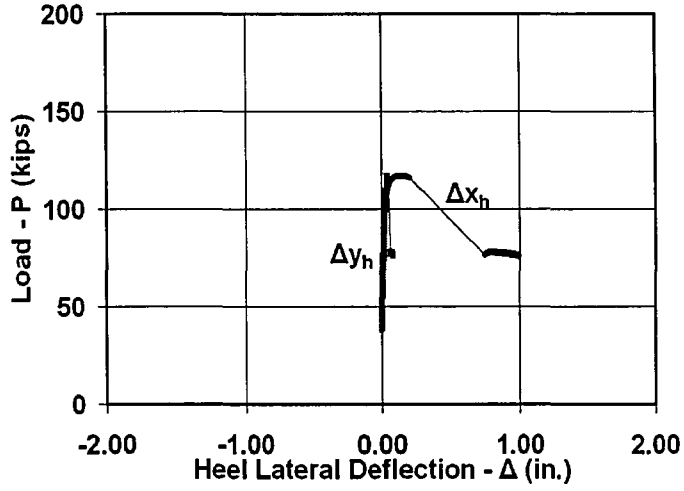

Figure 5.87 DB3 Specimen Load vs. Heel Lateral Deflection

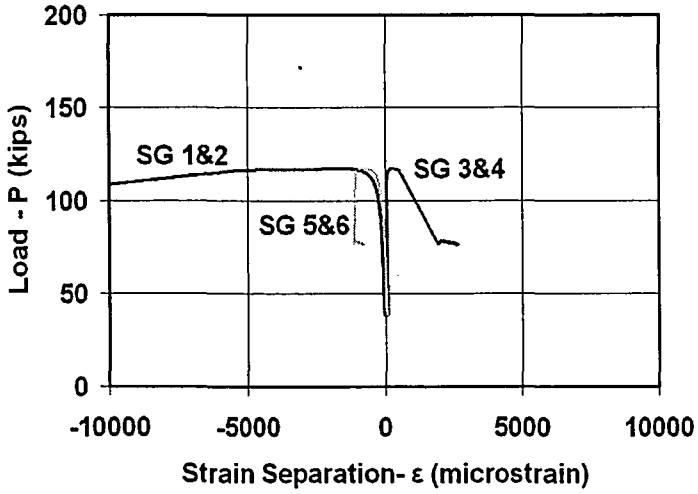

Figure 5.88 DB3 Specimen Load vs. Strain Separation

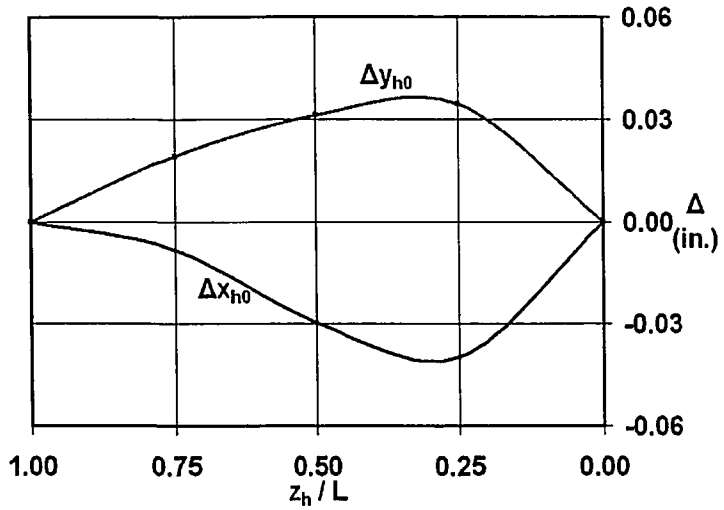

Figure 5.89 DB3 Specimen Initial Out-of-Straightness

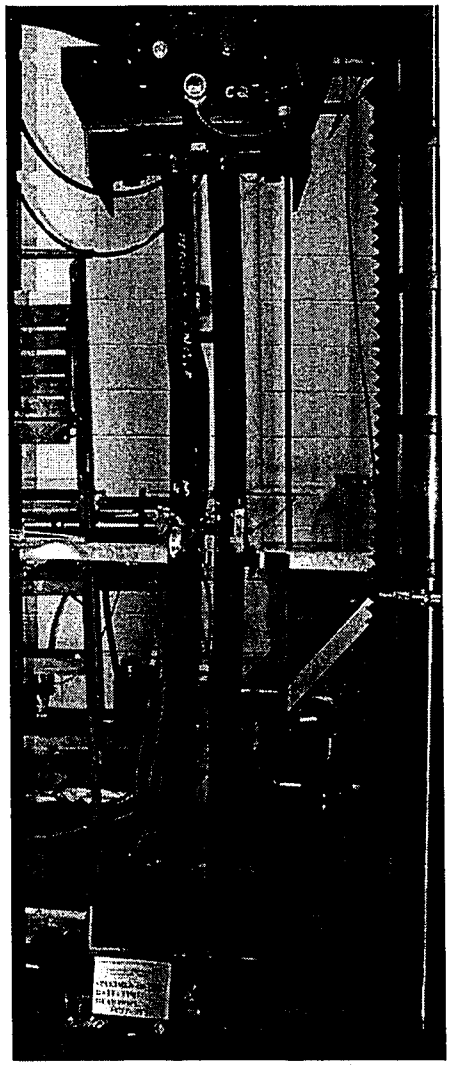

Figure 5.90 Specimen DB3

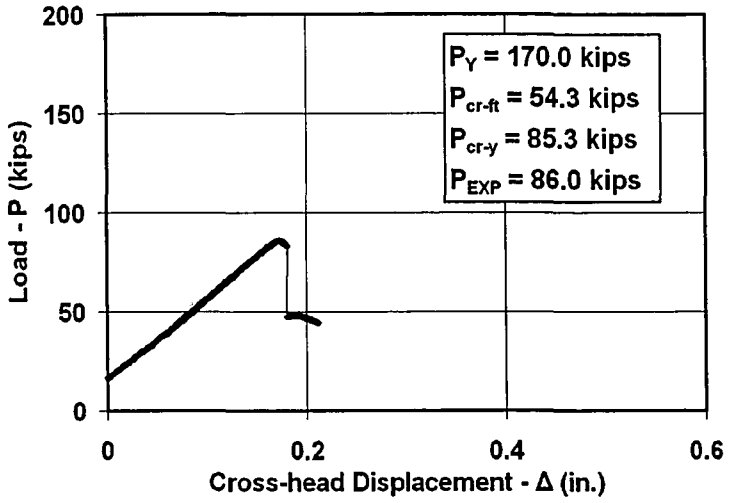

Figure 5.91 DB4 Specimen Load vs. Cross-head Displacement

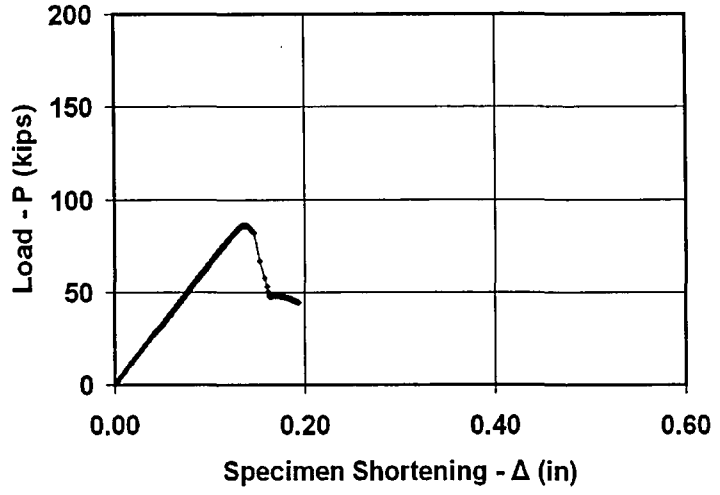

Figure 5.92 DB4 Specimen Load vs. Specimen Shortening

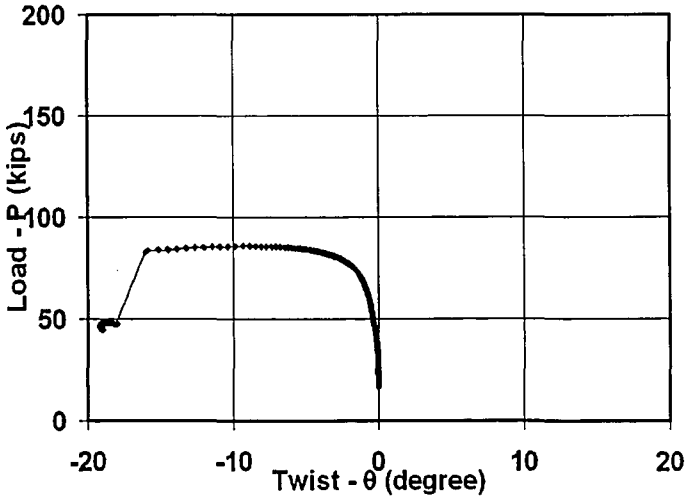

Figure 5.93 DB4 Specimen Load vs. Twist

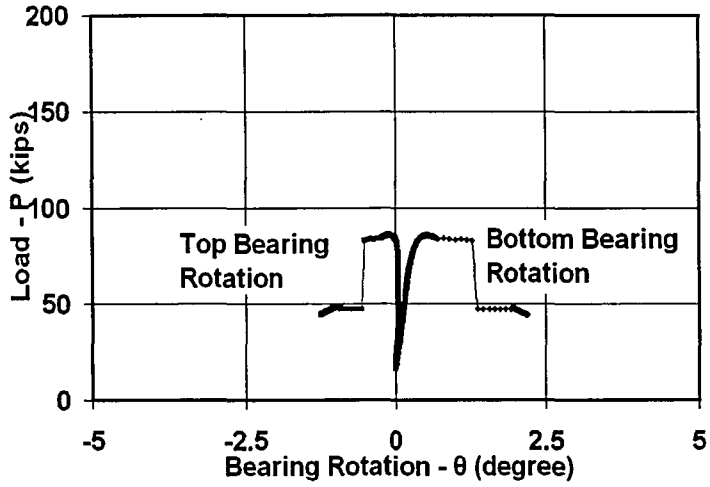

Figure 5.94 DB4 Specimen Load vs. Bearing Rotation

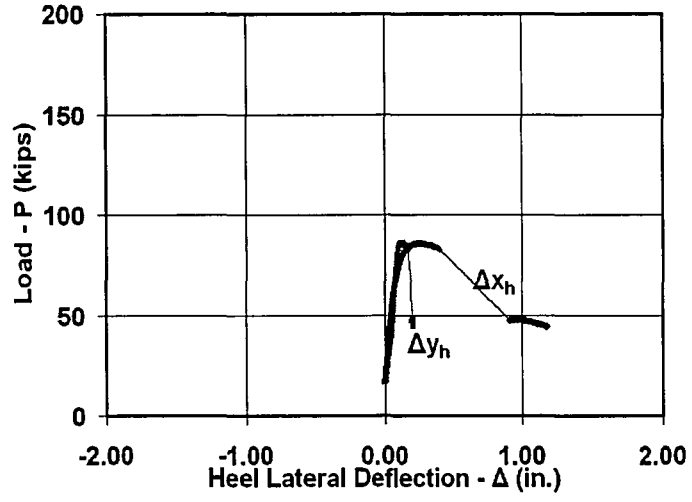

Figure 5.95 DB4 Specimen Load vs. Heel Lateral Deflection

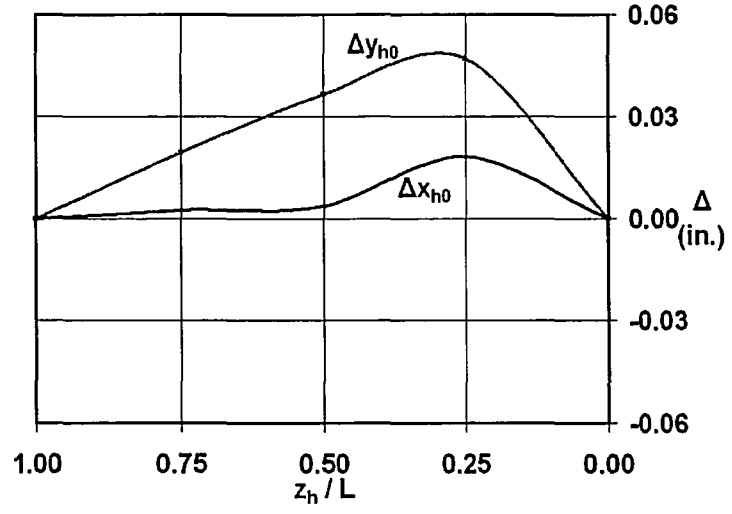

Figure 5.96 DB4 Specimen Initial Out-of-Straightness

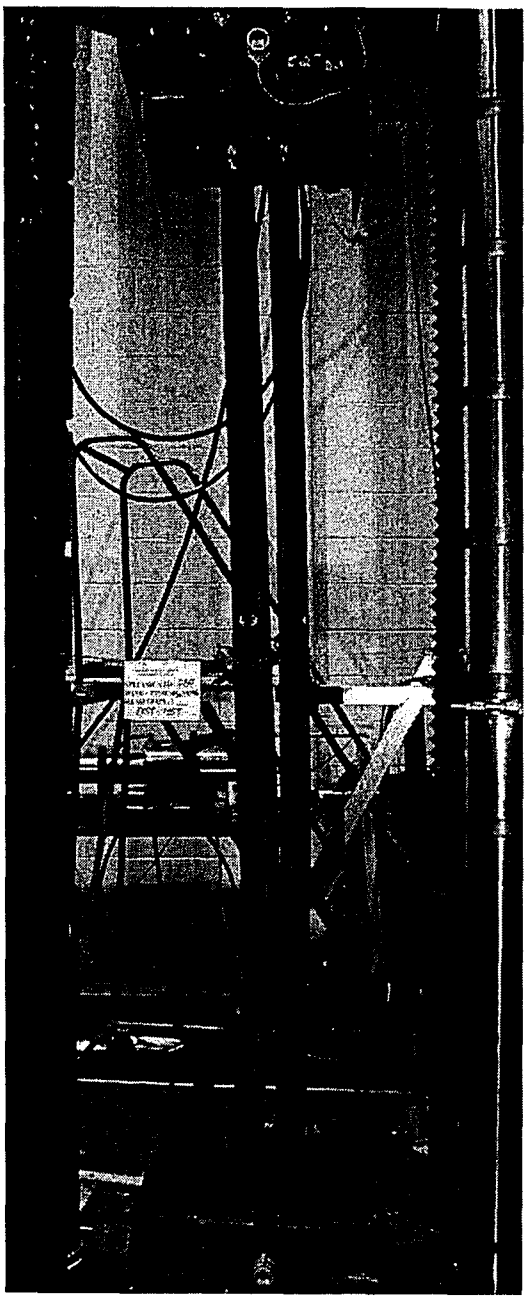

Figure 5.97 Specimen DB4

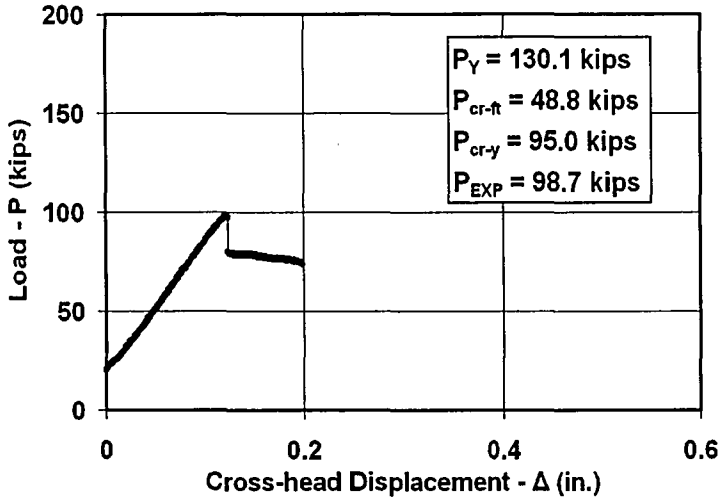

Figure 5.98 DB5 Specimen Load vs. Cross-head Displacement

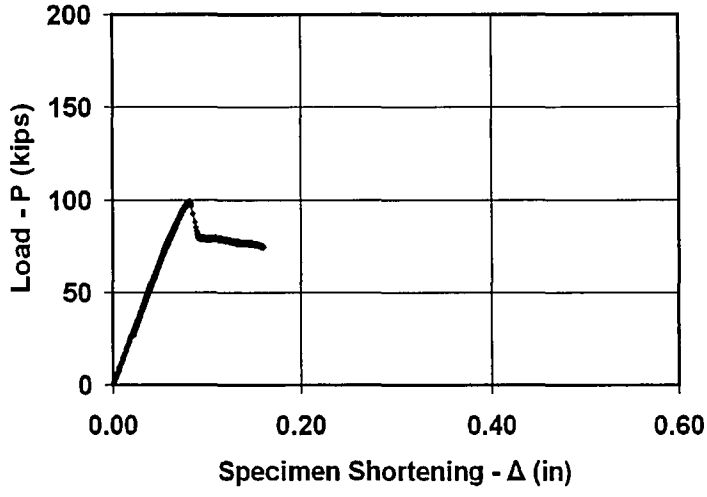

Figure 5.99 DB5 Specimen Load vs. Specimen Shortening

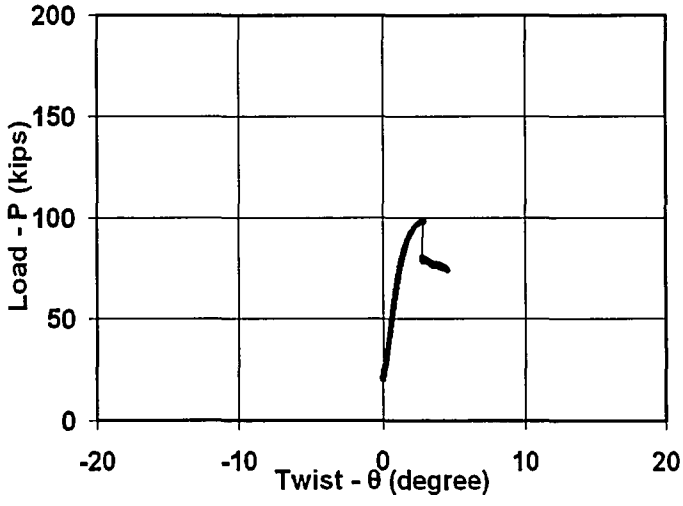

Figure 5.100 DB5 Specimen Load vs. Twist

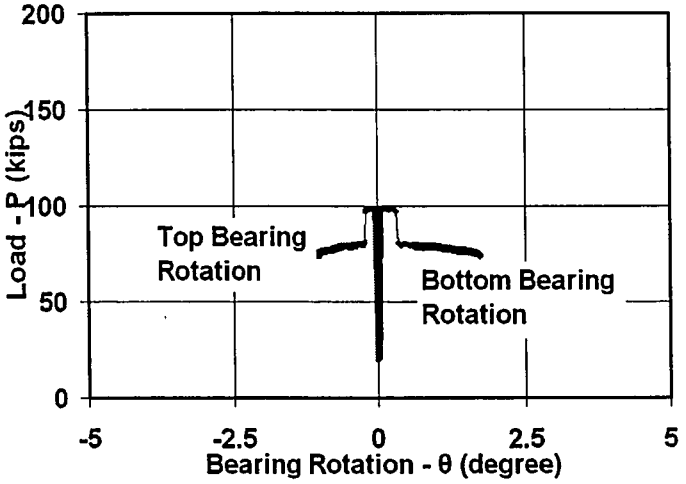

Figure 5.101 DB5 Specimen Load vs. Bearing Rotation

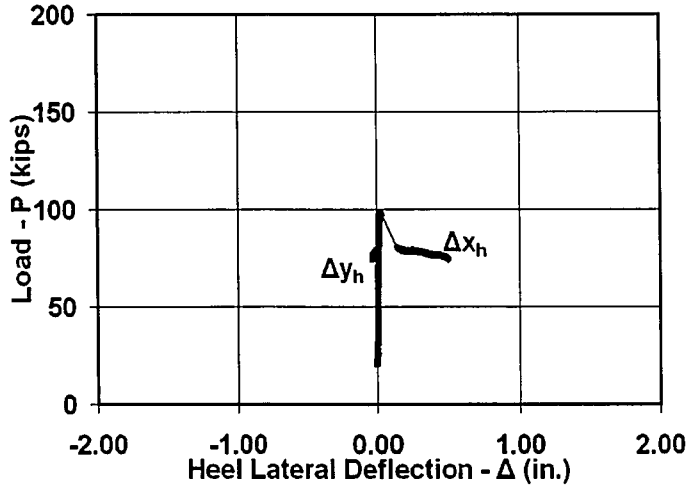

Figure 5.102 DB5 Specimen Load vs. Heel Lateral Deflection

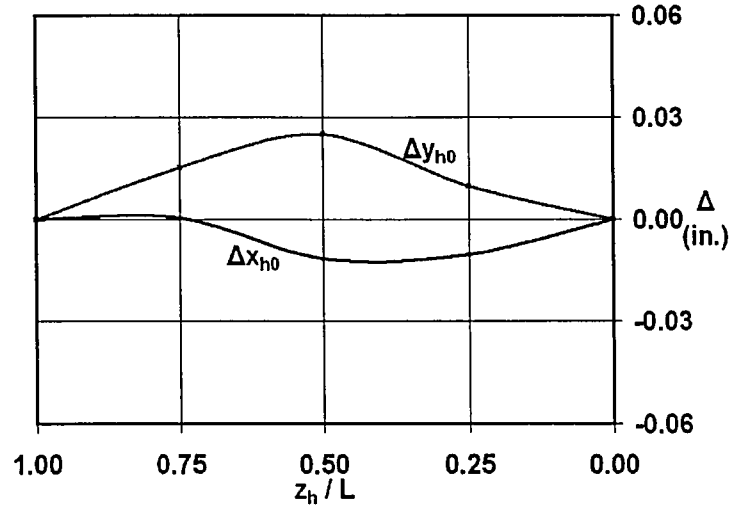

Figure 5.103 DB5 Specimen Initial Out-of-Straightness

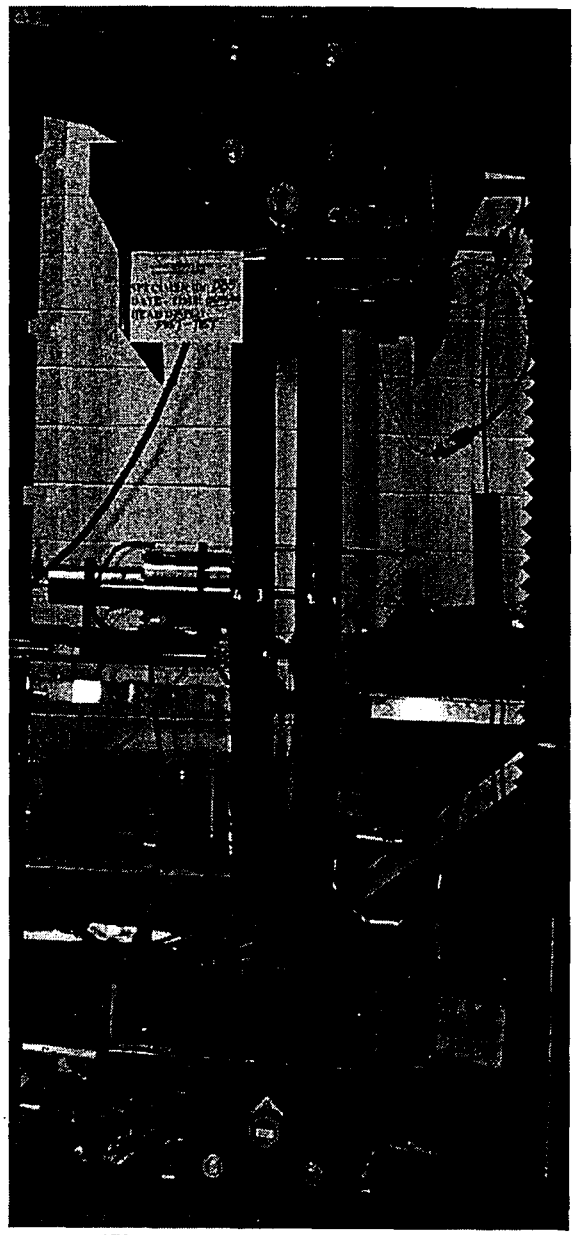

Figure 5.104 Specimen DB5

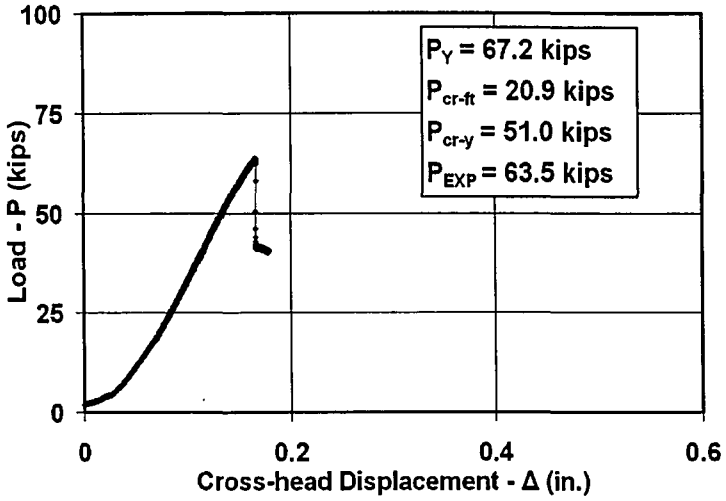

Figure 5.105 DC1 Specimen Load vs. Cross-head Displacement

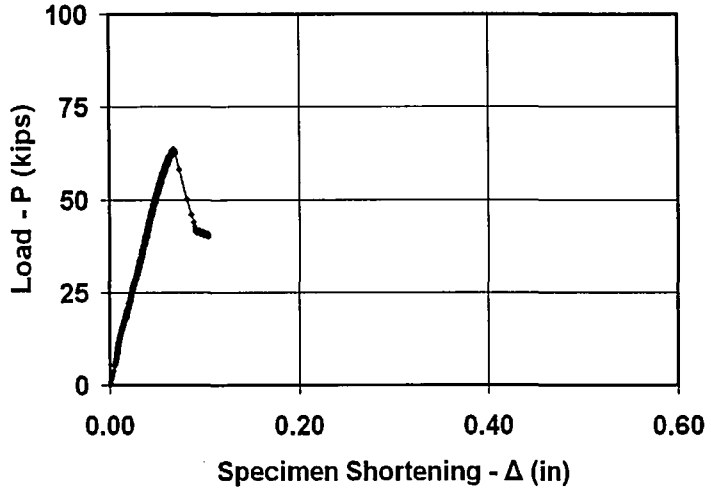

Figure 5.106 DC1 Specimen Load vs. Specimen Shortening

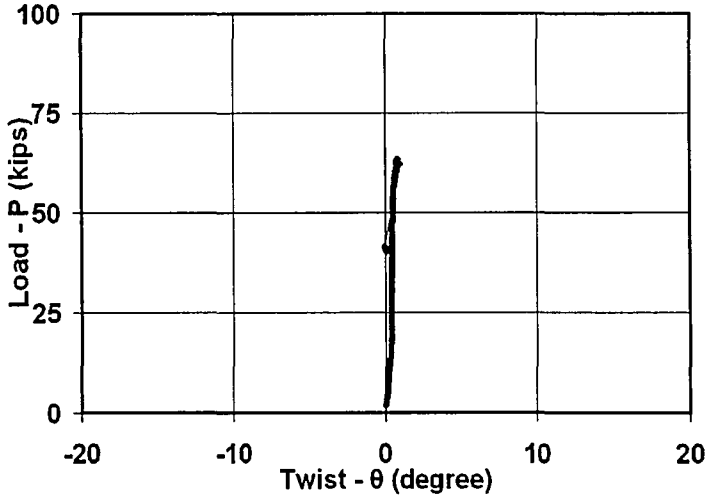

Figure 5.107 DC1 Specimen Load vs. Twist

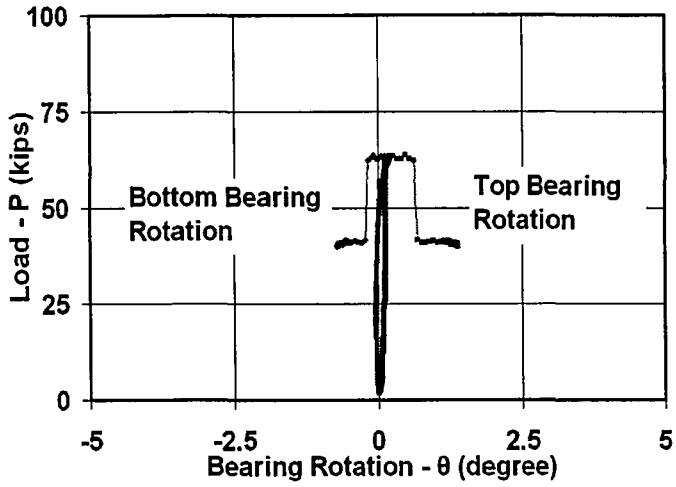

Figure 5.108 DC1 Specimen Load vs. Bearing Rotation

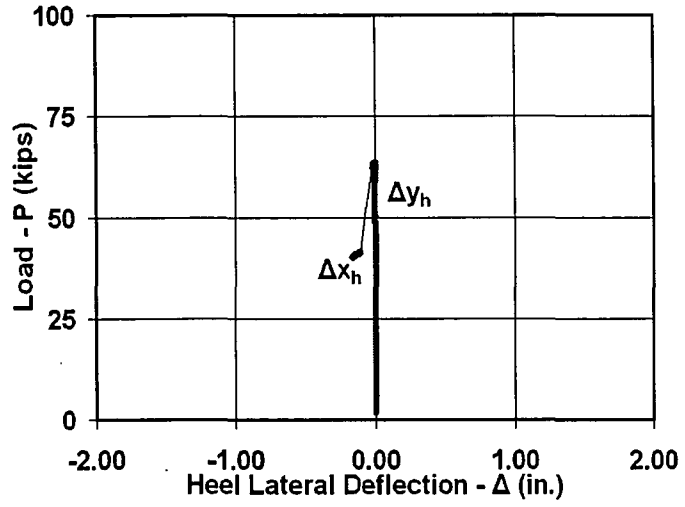

Figure 5.109 DC1 Specimen Load vs. Heel Lateral Deflection

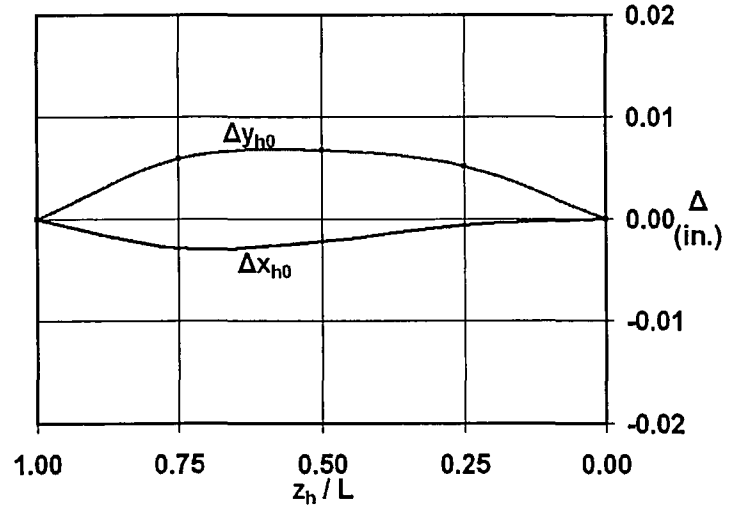

Figure 5.110 DC1 Specimen Initial Out-of-Straightness

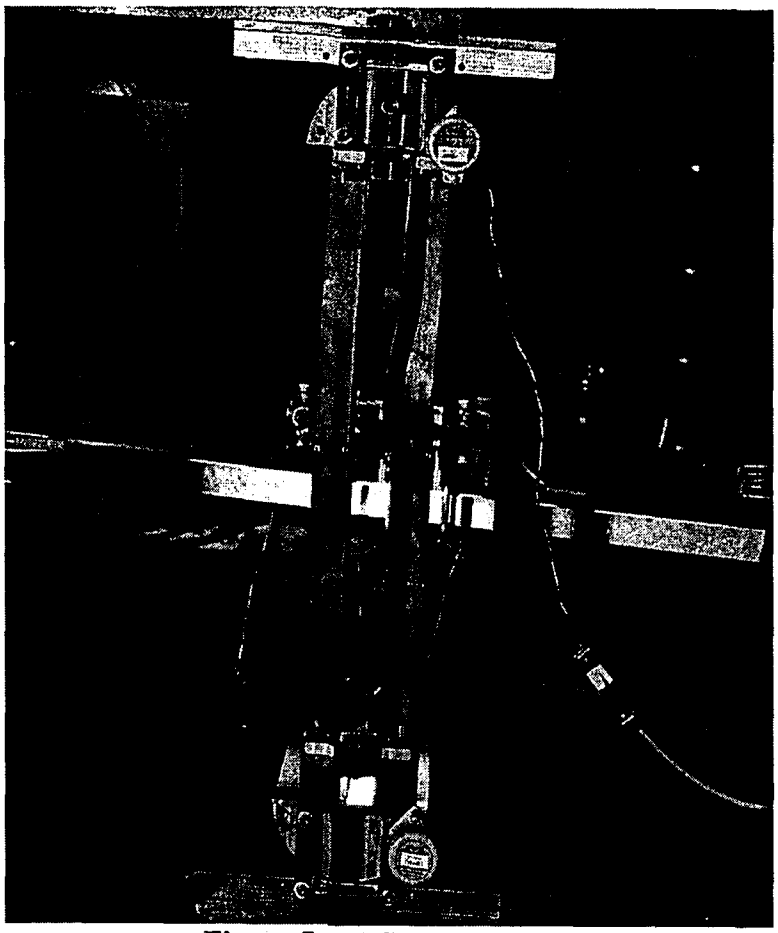

Figure 5.111 Specimen DC1

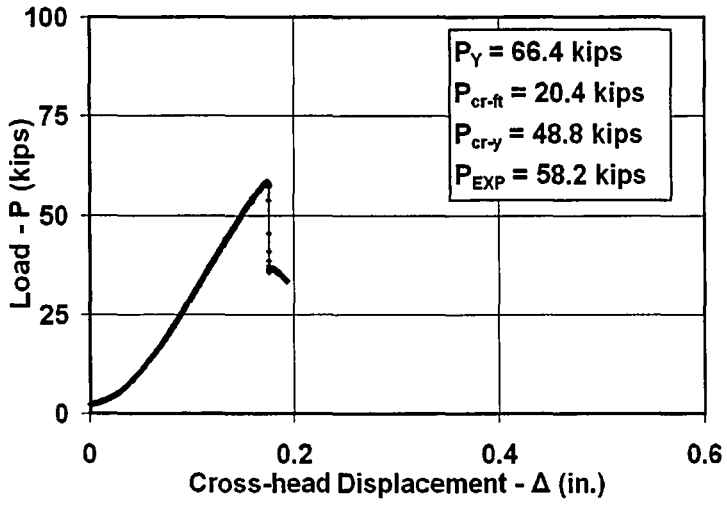

Figure 5.112 DC2 Specimen Load vs. Cross-head Displacement

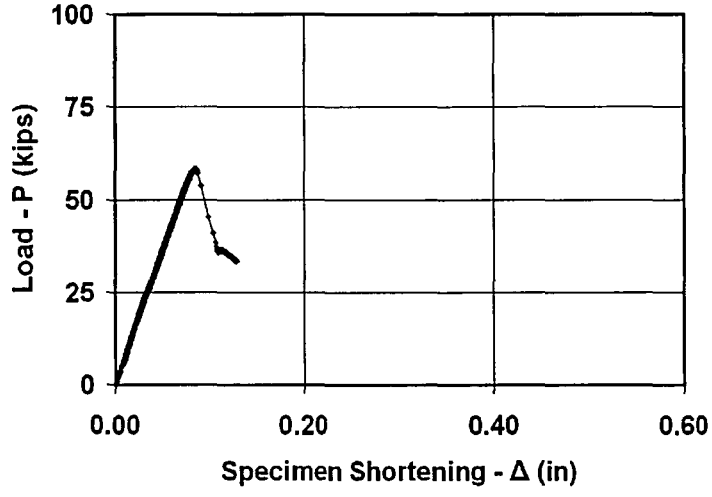

Figure 5.113 DC2 Specimen Load vs. Specimen Shortening

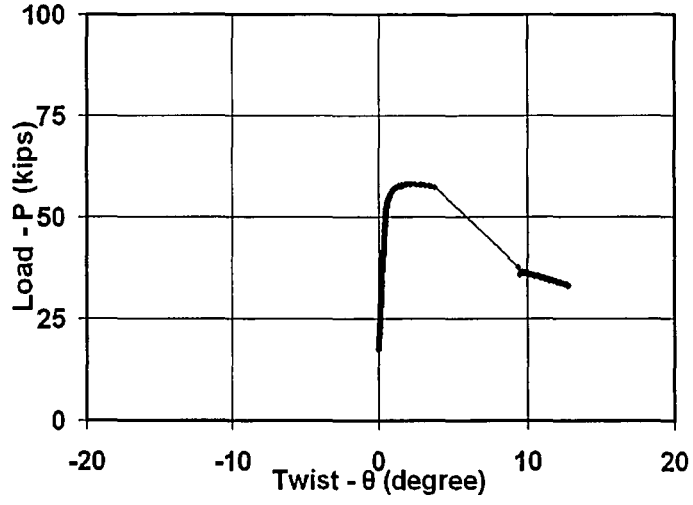

Figure 5.114 DC2 Specimen Load vs. Twist

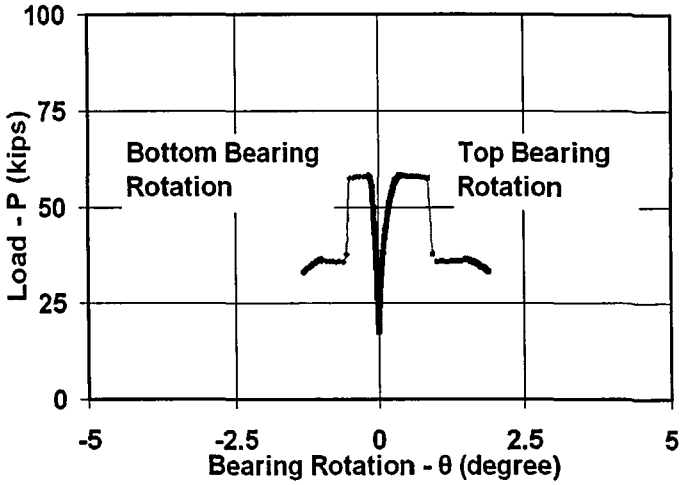

Figure 5.115 DC2 Specimen Load vs. Bearing Rotation

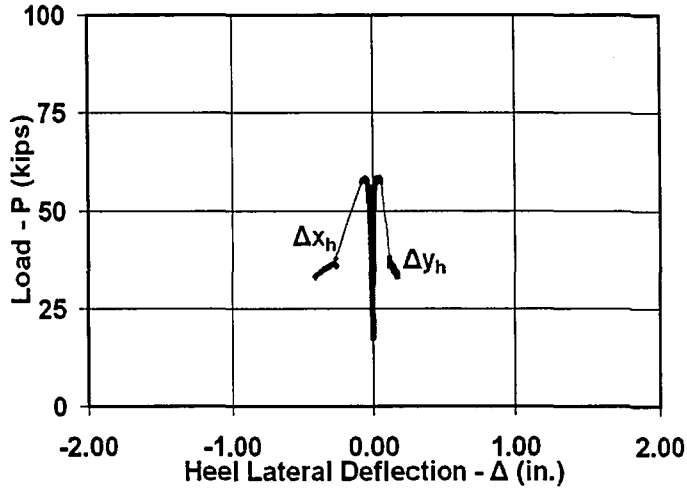

Figure 5.116 DC2 Specimen Load vs. Heel Lateral Deflection

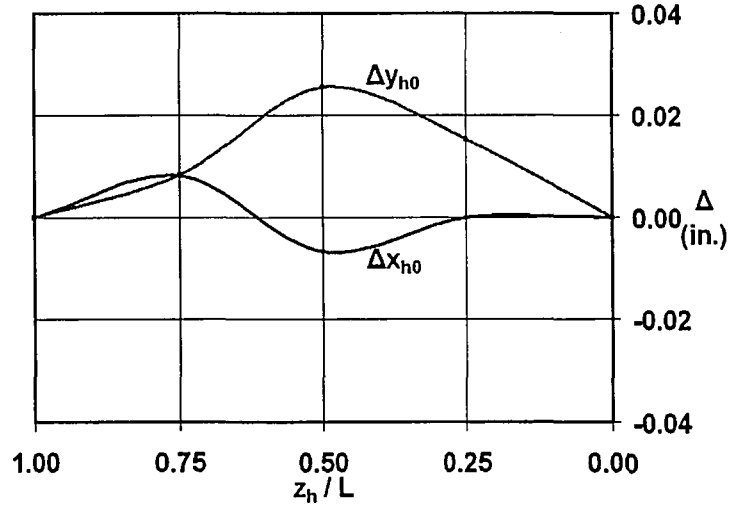

Figure 5.117 DC2 Specimen Initial Out-of-Straightness

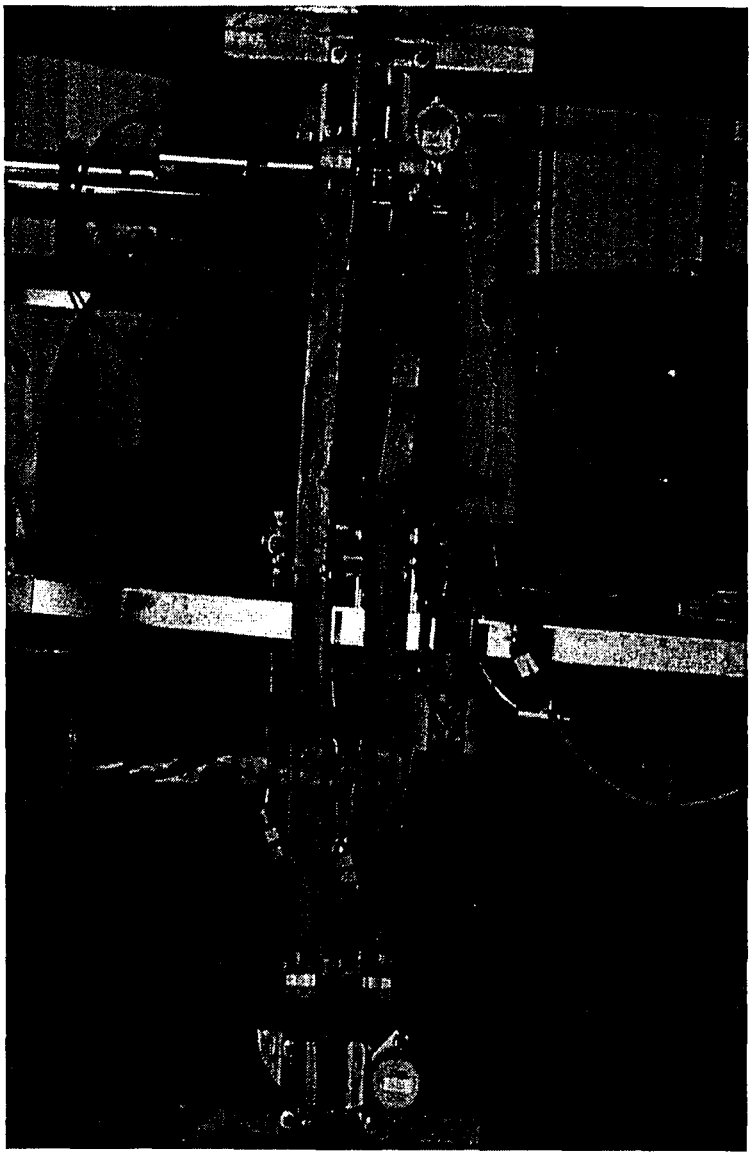

Figure 5.118 Specimen DC2

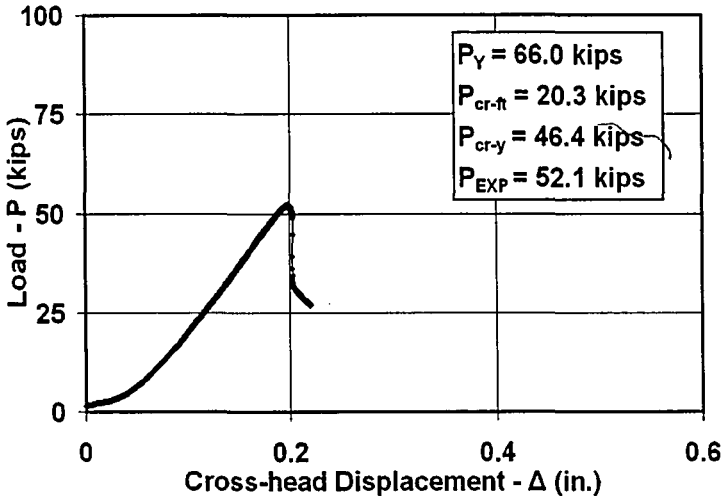

Figure 5.119 DC3 Specimen Load vs. Cross-head Displacement

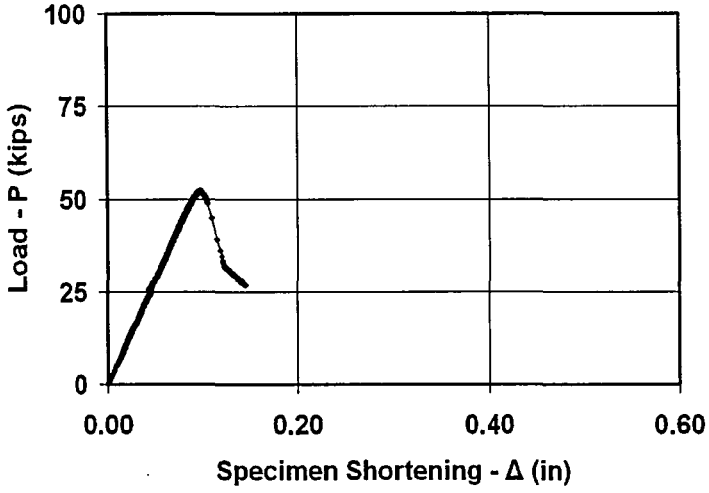

Figure 5.120 DC3 Specimen Load vs. Specimen Shortening

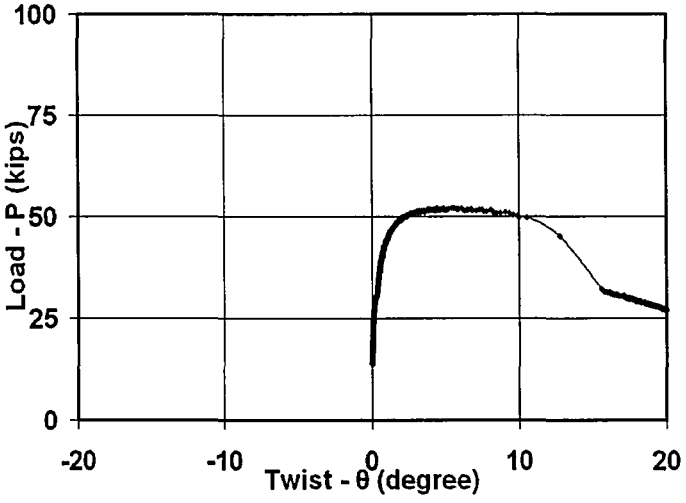

Figure 5.121 DC3 Specimen Load vs. Twist

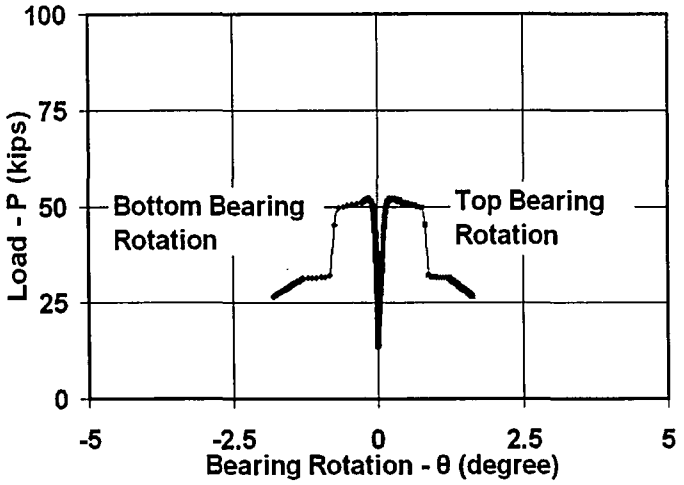

Figure 5.122 DC3 Specimen Load vs. Bearing Rotation

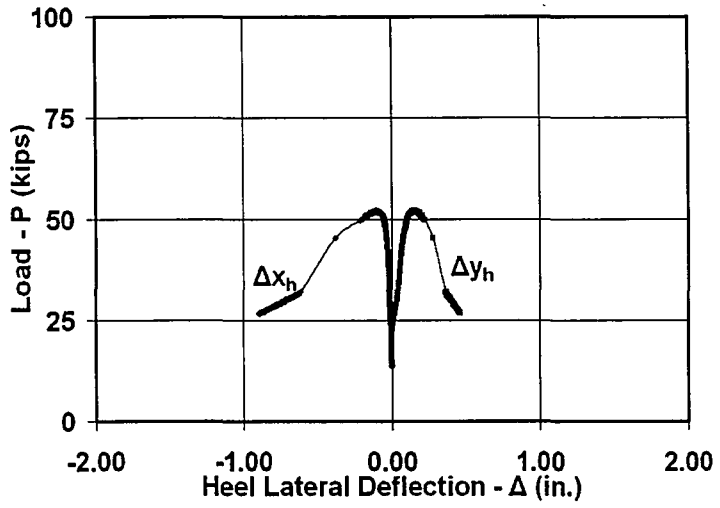

Figure 5.123 DC3 Specimen Load vs. Heel Lateral Deflection

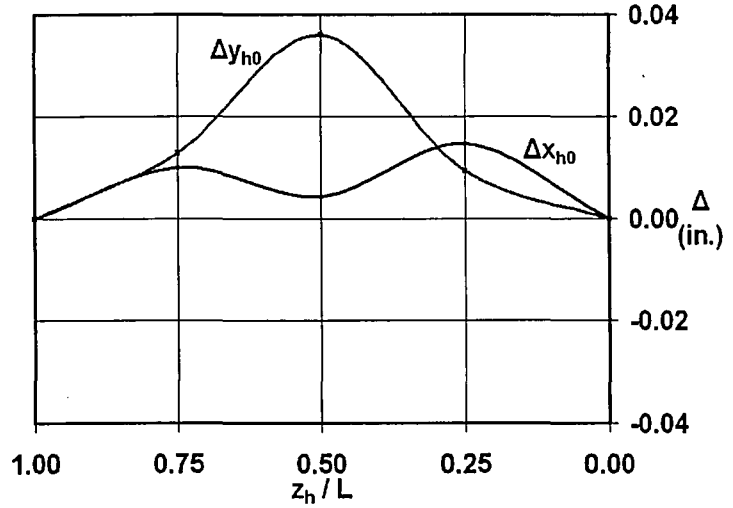

Figure 5.124 DC3 Specimen Initial Out-of-Straightness

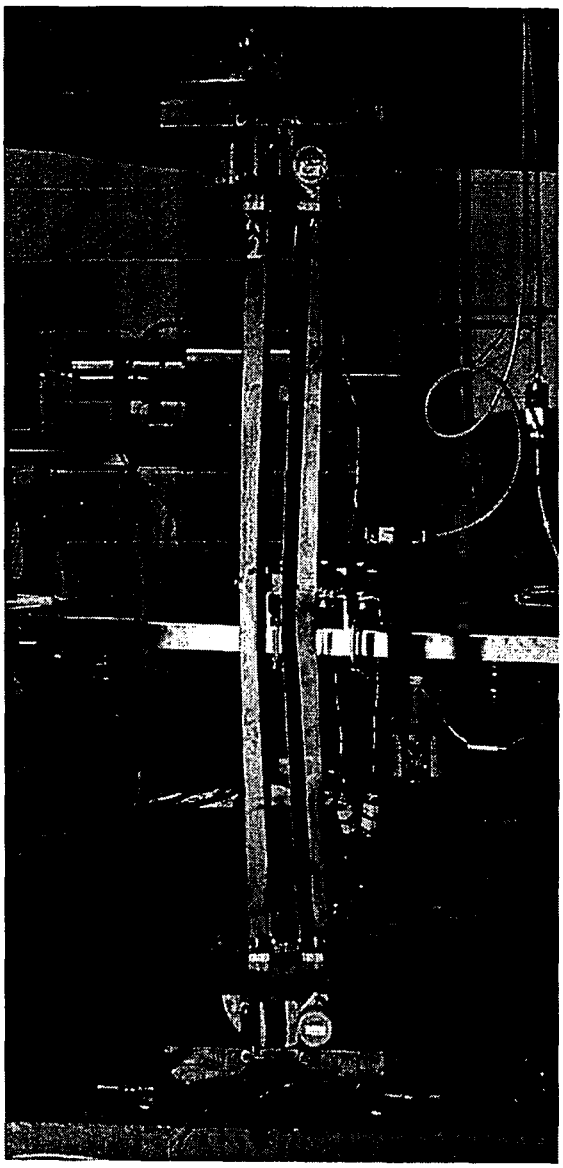

Figure 5.125 Specimen DC3

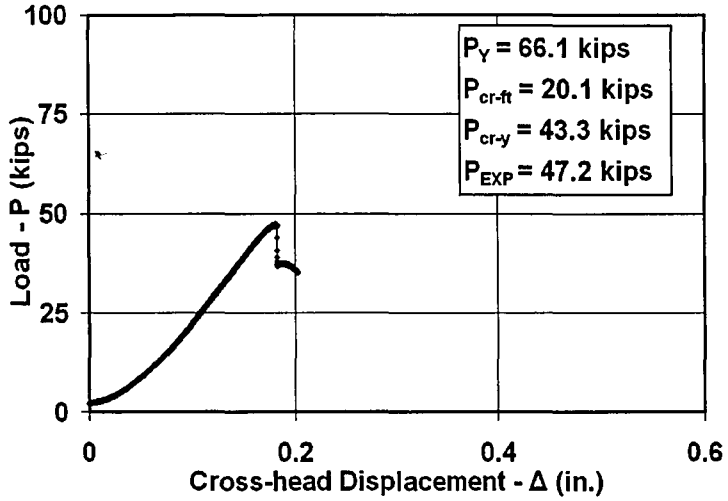

Figure 5.126 DC32 Specimen Load vs. Cross-head Displacement

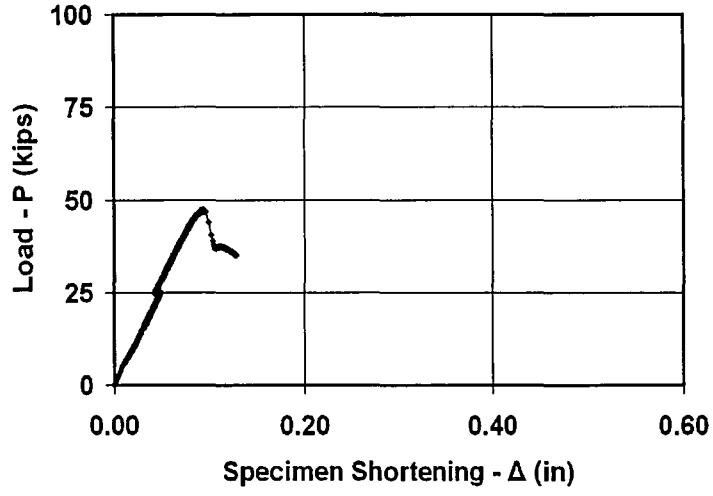

Figure 5.127 DC32 Specimen Load vs. Specimen Shortening

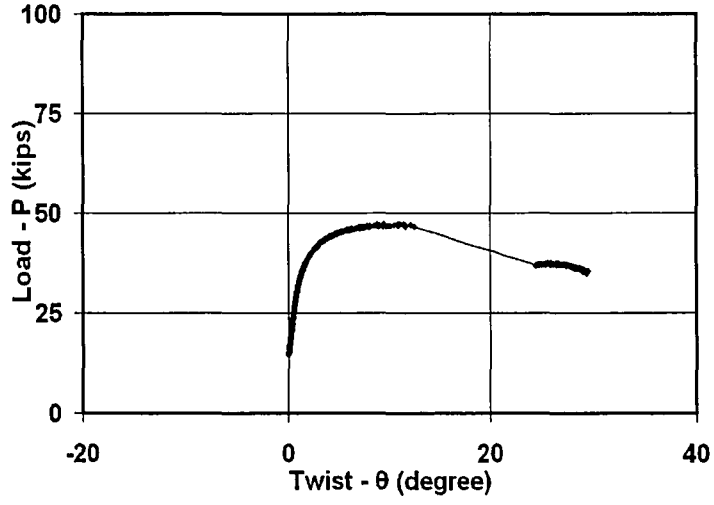

Figure 5.128 DC32 Specimen Load vs. Twist

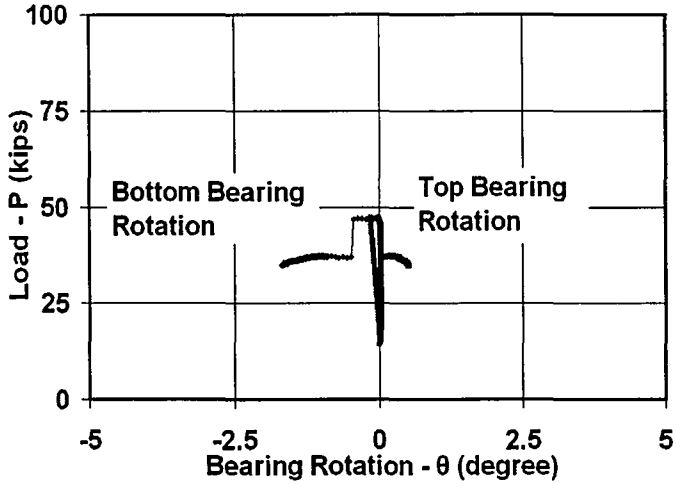

Figure 5.129 DC32 Specimen Load vs. Bearing Rotation

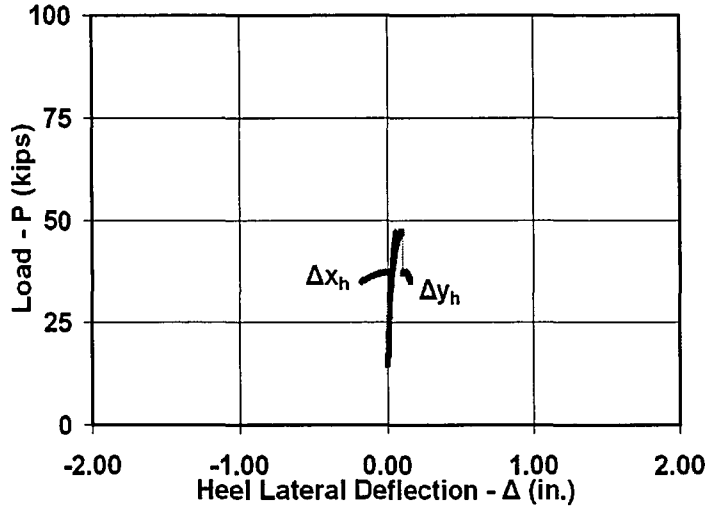

Figure 5.130 DC32 Specimen Load vs. Heel Lateral Deflection

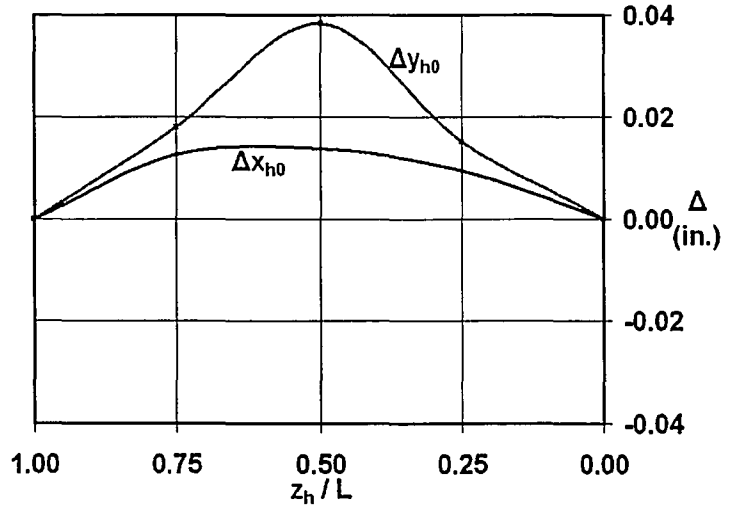

Figure 5.131 DC32 Specimen Initial Out-of-Straightness

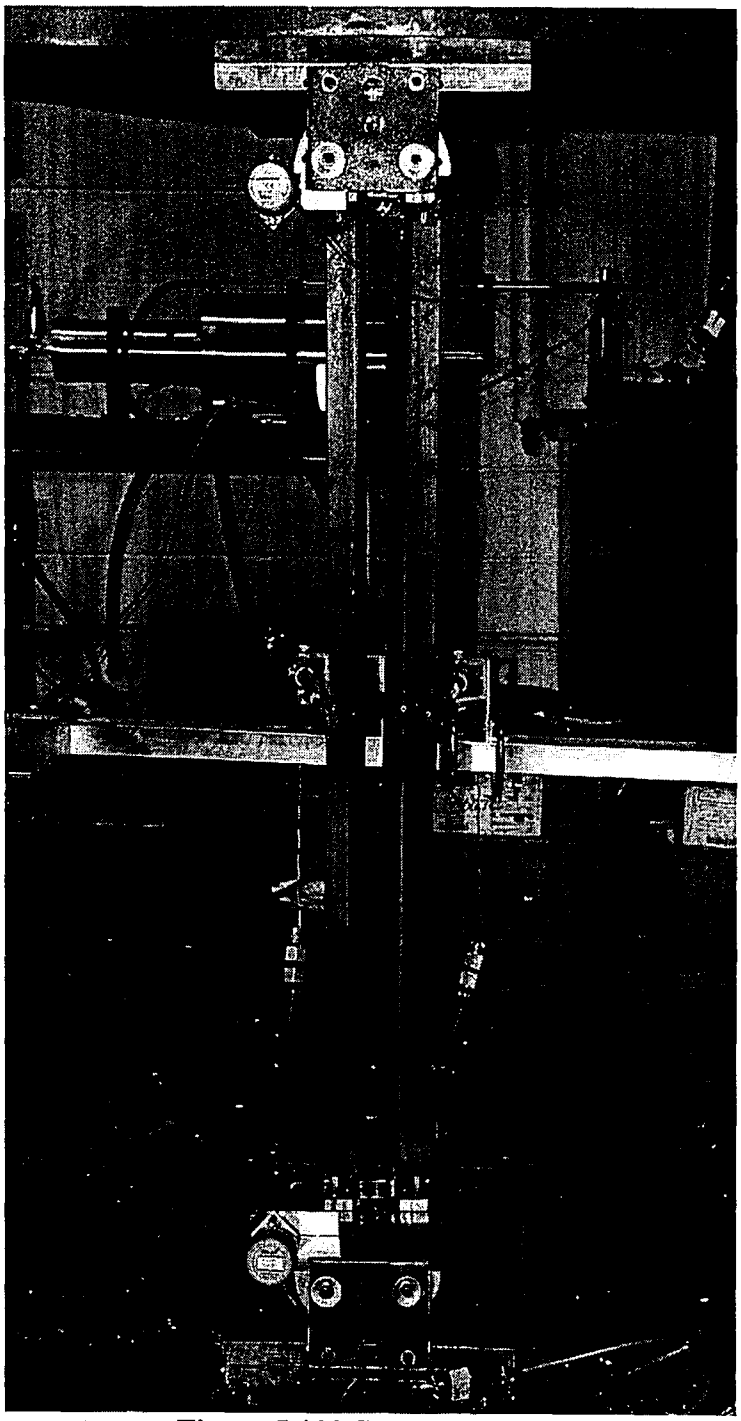

Figure 5.132 Specimen DC32

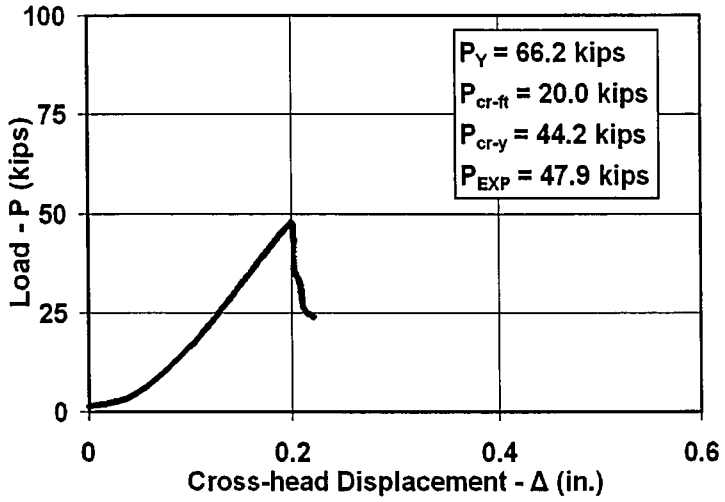

Figure 5.133 DC4 Specimen Load vs. Cross-head Displacement

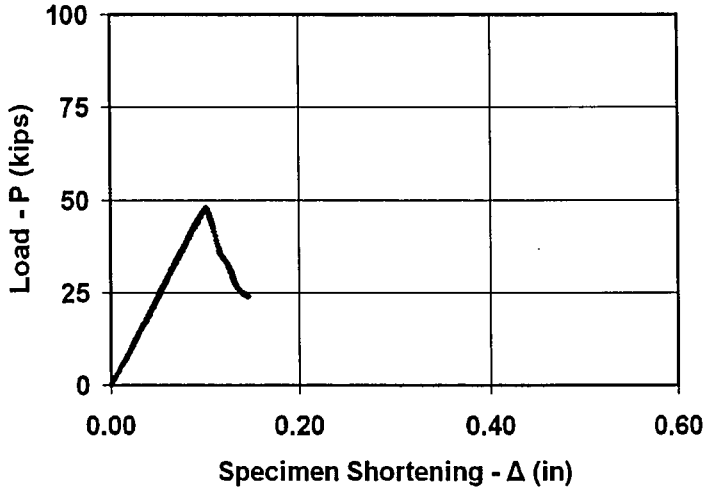

Figure 5.134 DC4 Specimen Load vs. Specimen Shortening

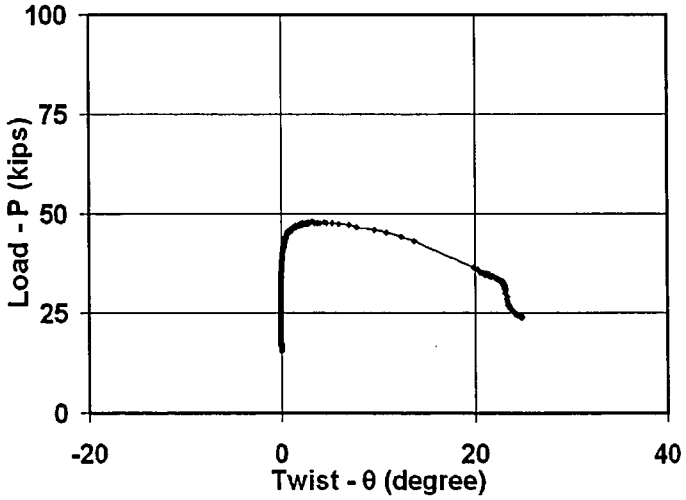

Figure 5.135 DC4 Specimen Load vs. Twist

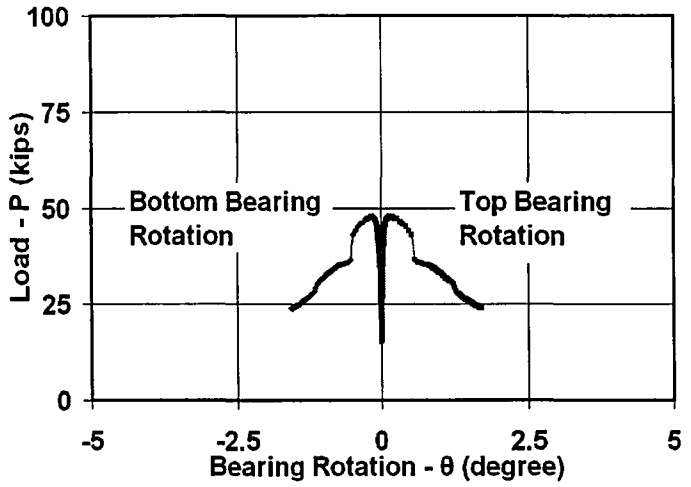

Figure 5.136 DC4 Specimen Load vs. Bearing Rotation

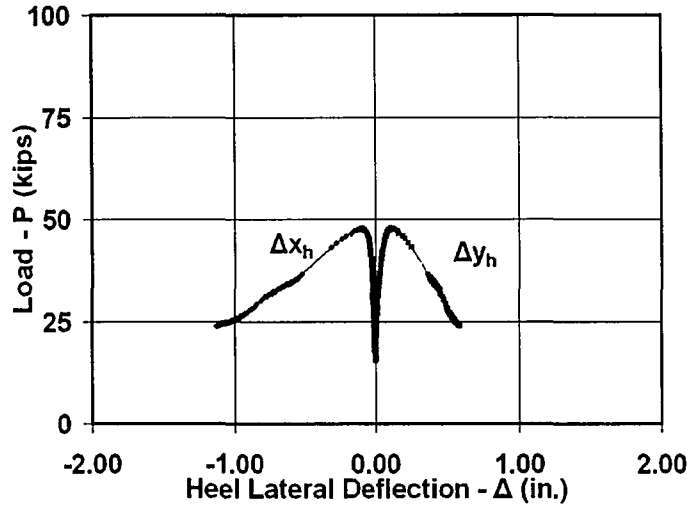

Figure 5.137 DC4 Specimen Load vs. Heel Lateral Deflection

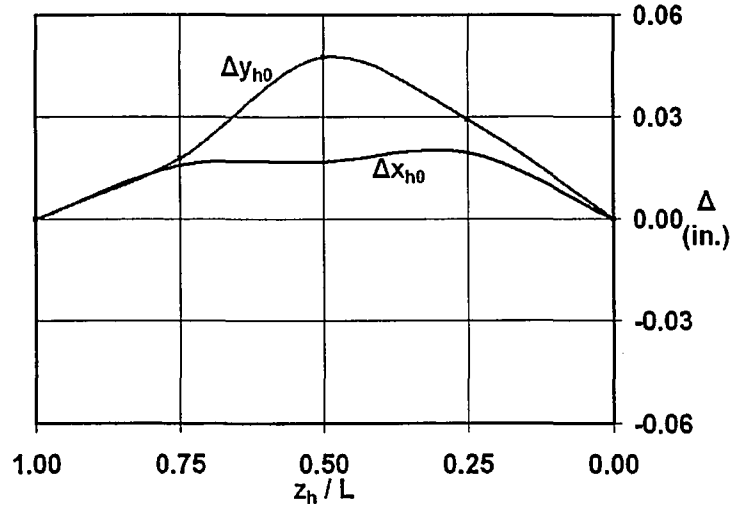

Figure 5.138 DC4 Specimen Initial Out-of-Straightness

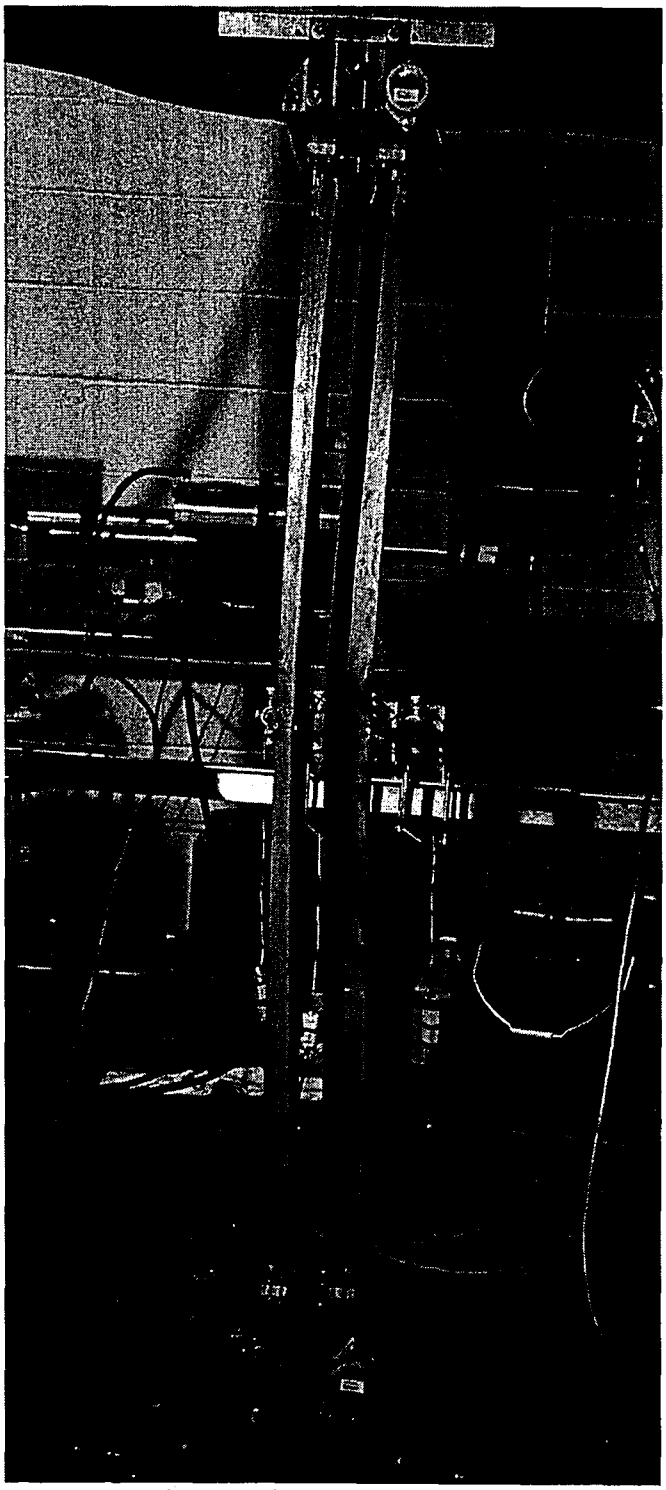

Figure 5.139 Specimen DC4

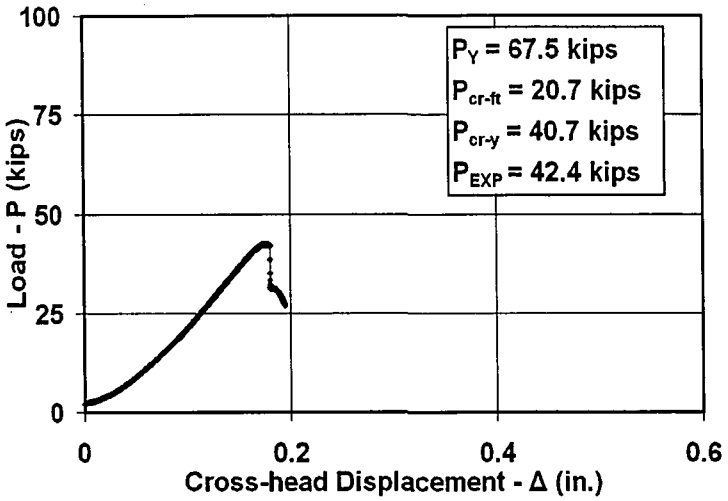

Figure 5.140 DC42 Specimen Load vs. Cross-head Displacement

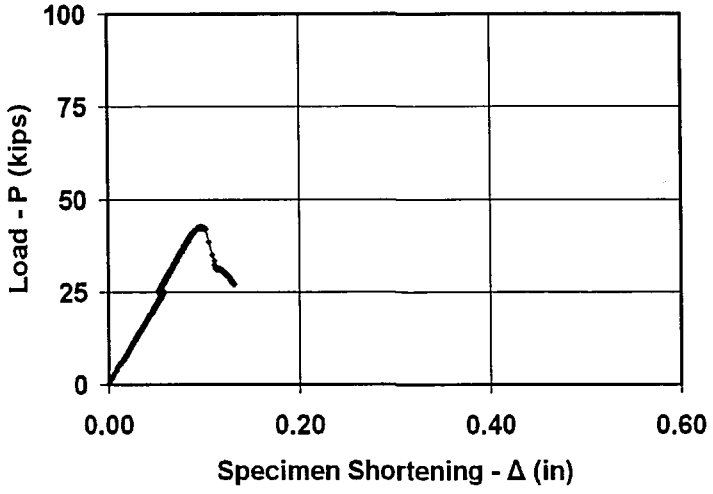

Figure 5.141 DC42 Specimen Load vs. Specimen Shortening

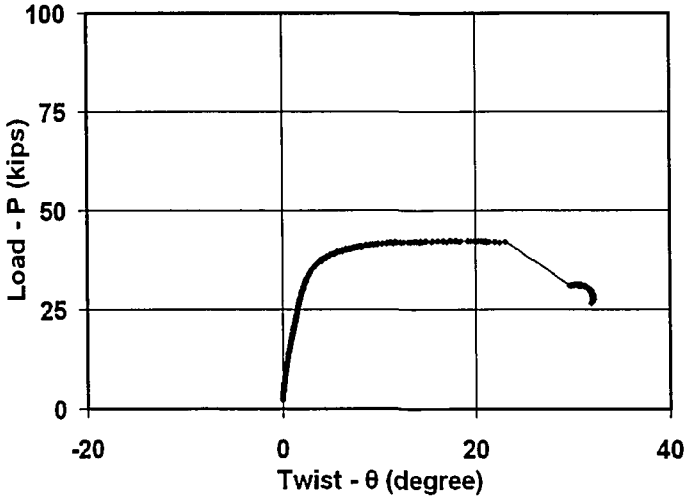

Figure 5.142 DC42 Specimen Load vs. Twist

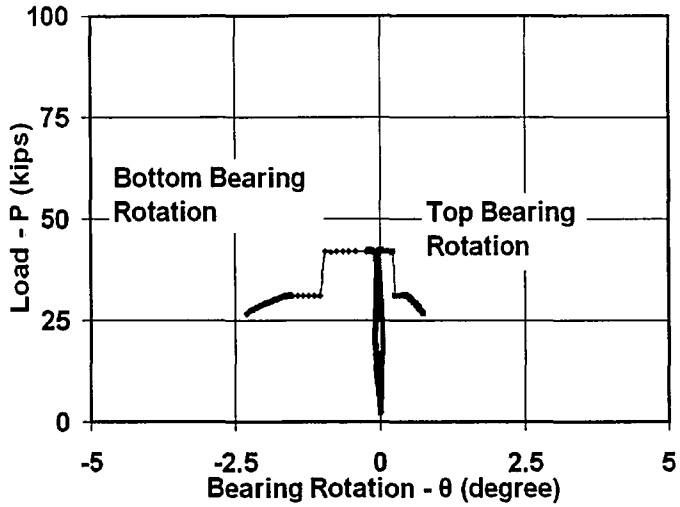

Figure 5.143 DC42 Specimen Load vs. Bearing Rotation

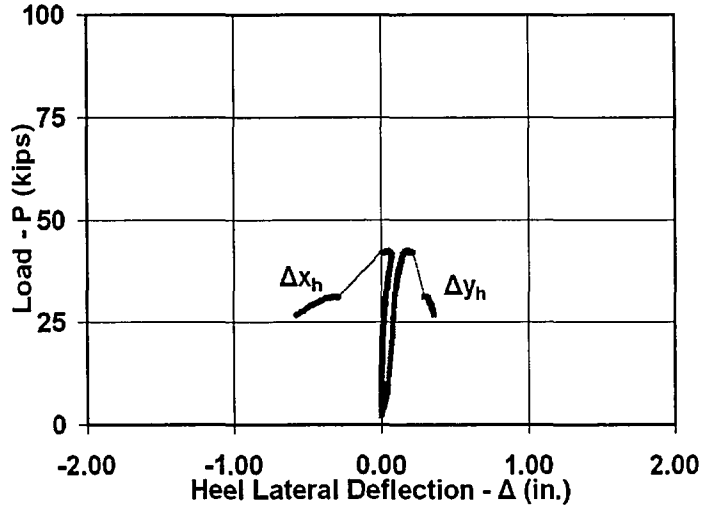

Figure 5.144 DC42 Specimen Load vs. Heel Lateral Deflection

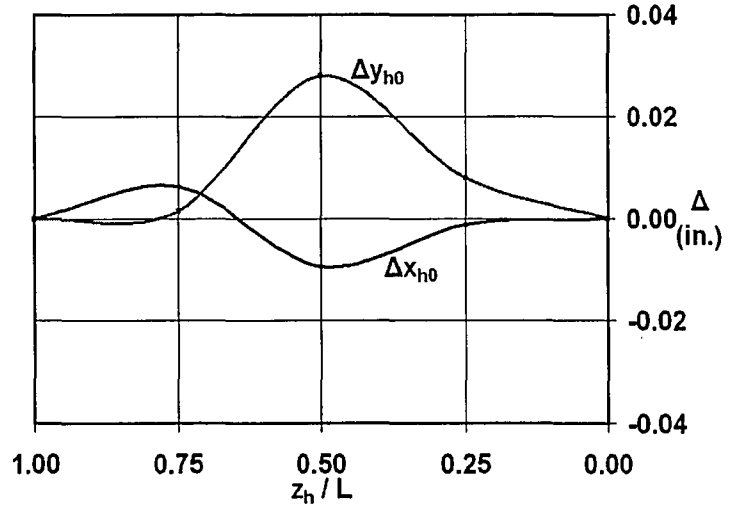

Figure 5.145 DC42 Specimen Initial Out-of-Straightness

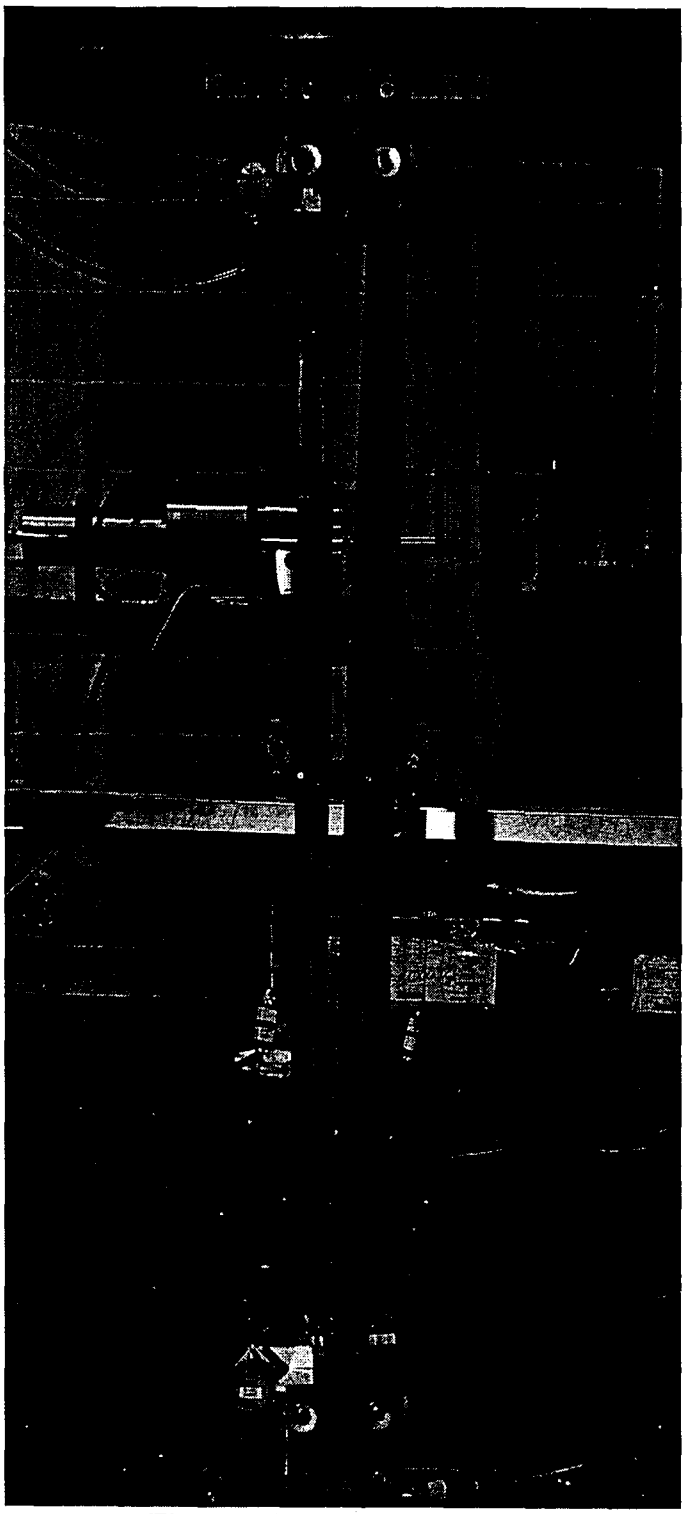

Figure 5.146 Specimen DC42

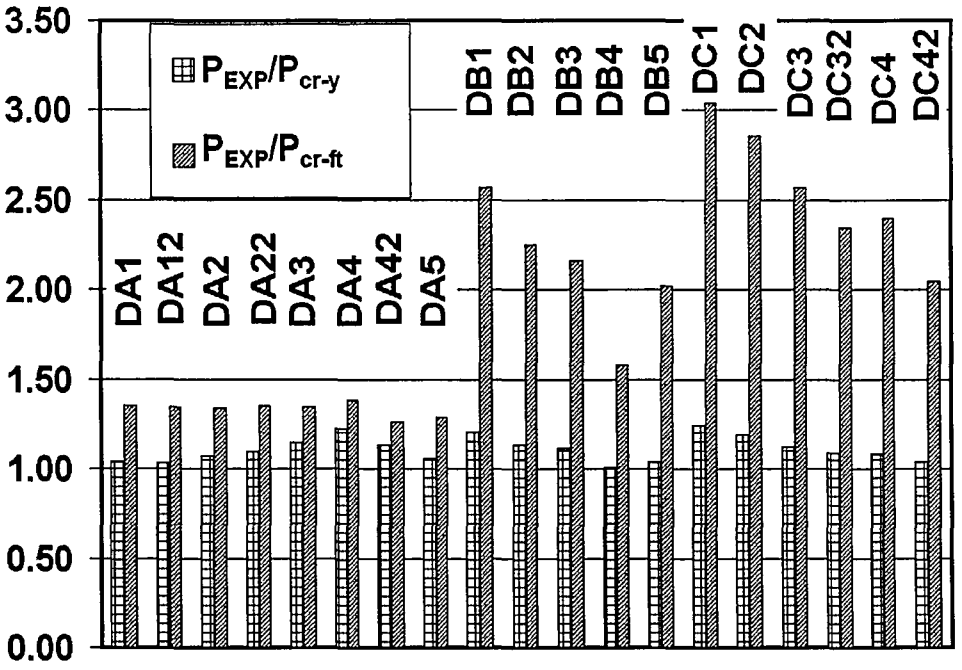

Figure 5.147 Predicted vs. Experimental Results

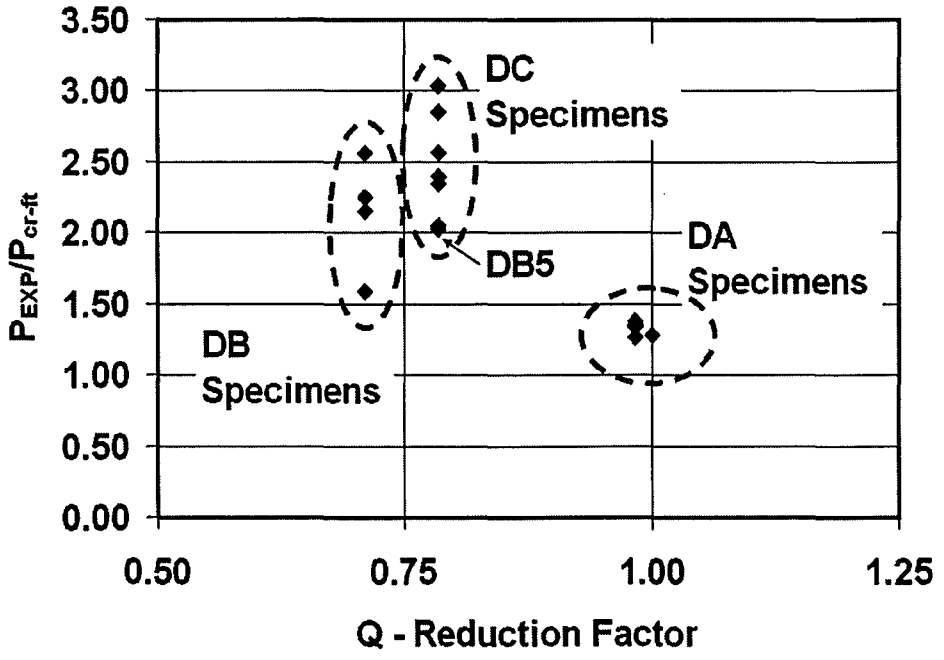

Figure 5.148 Experimental Results vs. Q Reduction Factor

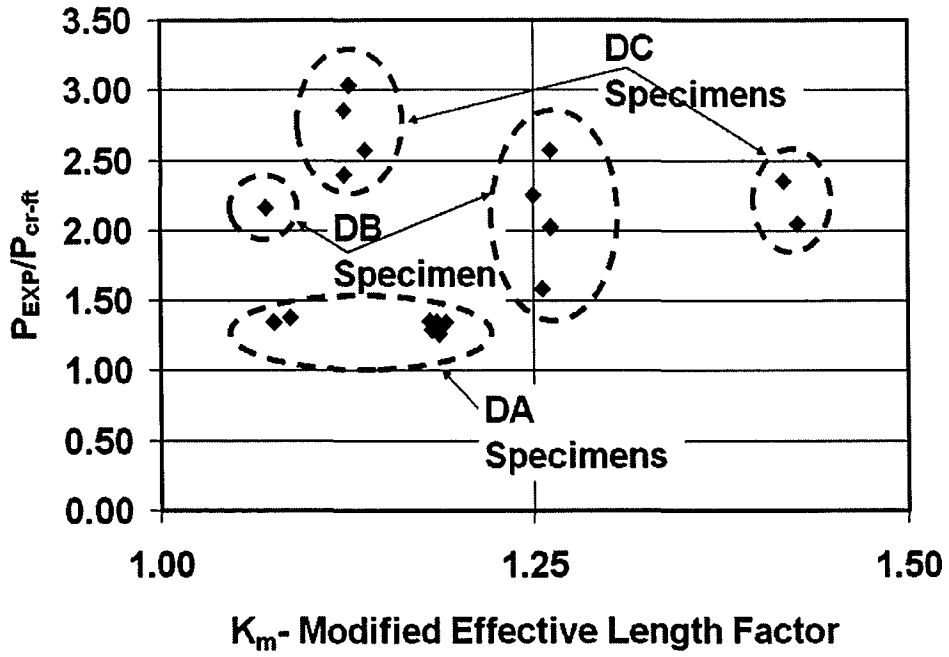

Figure 5.149 Experimental Results vs. K_m Effective Length Factor

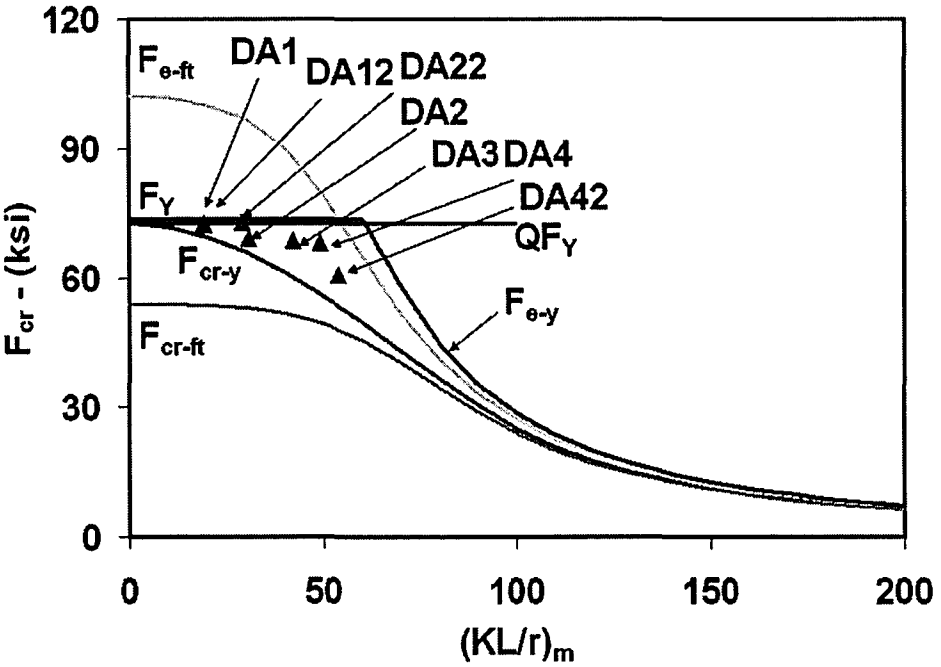

Figure 5.150 Comparison of Experimental Results with Theoretical Results for (Vanadium Steel) DA Specimens

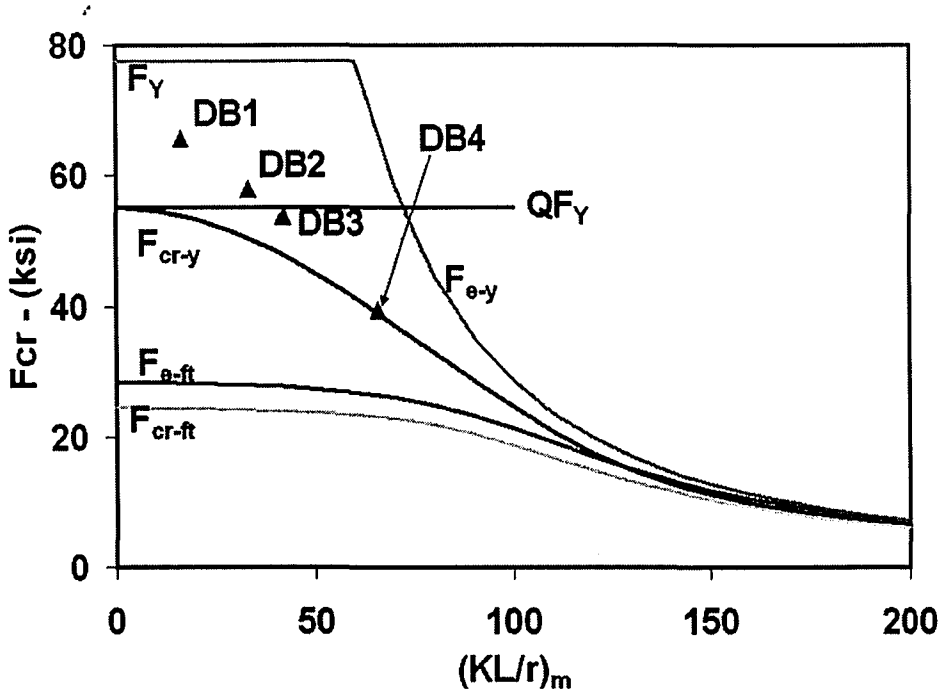

Figure 5.151 Comparison of Experimental Results with Theoretical Results for (Vanadium Steel) DB Specimens

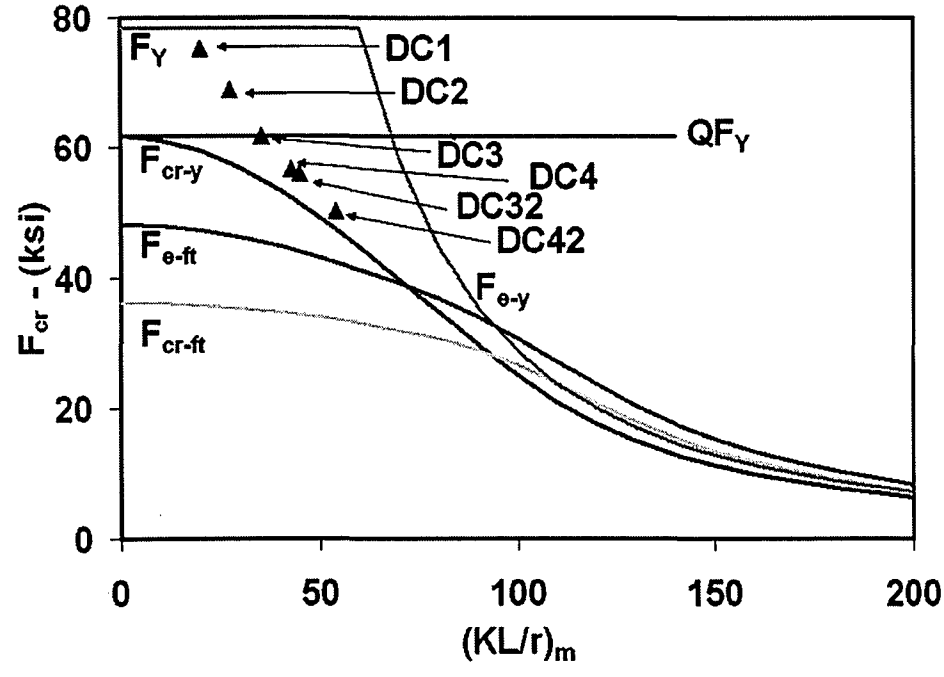

Figure 5.152 Comparison of Experimental Results with Theoretical Results for (Vanadium Steel) DC Specimens

Chapter 6 Buckling Tests of Crimped Single Angle Specimens

6.0 General

This chapter addresses the experiments on crimped single angle specimens. First, the test matrix of specimens is presented. Then, the test set-up and related equipment are discussed. Then, the preparation of the test specimens, the initial out-of-straightness measurements of the specimens, and the instrumentation of the specimens are discussed, along with the test procedure. Then, the theoretical buckling capacities are presented. Finally, the test results are presented and discussed.

6.1 Test Matrix

Crimped single angle compression members are often used as web members in roof and floor joists. Few experiments on these members have been conducted in the past. Crimped single angle web members are shown schemetically in Figure 6.1. As seen in this figure, the ends of web members are crimped where they are attached between the two angles of each chord of the joist. Depending on the length of the crimped zone between the two angles of the chord, two different types of welds can be used. Figure 6.1 shows the two types of welds which are named for their shape: the L-type weld and the U-type weld. Photos of crimped single angle members are shown in Figure 6.2.

The crimped single angle specimens were tested under compressive axial loads in a test setup similar to that used previously for the single angle specimens. Thus, the crimped single angle specimens were aligned and tested vertically in the test setup, as

shown in Figure 6.3. Figure 6.3(a) shows that the crimped angle test specimens included to "chord stubs" to allow the welded end conditions to be included in the test specimen. The specimens were loaded through these chord stubs. Figure 6.3(b) shows further details of the crimped single angle specimens as prepared for testing, which are discussed later.

Figure 6.3(c) shows the types of welds used in the specimens. As seen from this figure, the L-type weld has a larger eccentricity (relative to the centroid of the uncrimped zone of the angle specimen) than the U-type weld. The L-type weld shown in Figure 6.3(c) only represents one end of the crimped angle member where weld is located on the tips of the legs of the angle. The other end of this crimped angle member has weld on the heel in the crimped zone between the angles of the chord stub.

The test specimens are equal leg angles. Even though the AISC (2005) specification do not have specific provisions for the buckling strength of crimped single angle members, the specimens were treated as single angle compression members that would fail in one of the following buckling modes: flexural buckling about the weak axis; or flexural-torsional buckling, involving flexural buckling about the strong axis and torsional buckling. These buckling modes are discussed in Chapter 2. The coordinate systems used to discuss the crimped single angle specimens are presented in Figure 6.4. The expected buckling capacities were calculated according to Chapter E of the AISC (2005) specification.

The test specimens are identified in Table 6.1, along with the steel type and related parameters such as the length of the specimen. The yield stress values are also presented in this table. The yield stress values were determined from tensile coupon tests discussed in Chapter 3. The rated load capacities of the bearings used for these test specimens, and the pattern of the welds between the crimped ends and the chord stubs are also given in Table 6.1.

6.2 Test Setup

6.2.1 Test Machine

The SATEC universal testing machine at the ATLSS Center was used for the compression tests of the crimped single angle specimens, as shown in Figure 6.5. Details about the SATEC machine can be found in Section 4.2.1.

6.2.2 Cylindrical Bearings

In order to create pinned-pinned end conditions, the specimens were tested with cylindrical bearings (the 100 kip bearings) placed at both ends of the specimens, as shown in Figure 6.6(a). The sign convention for rotations of the bearings is presented in Figure 6.6(b). The working principles of these bearings are discussed in Section 4.2.2.

For the crimped single angle specimens in this study, the bearings restrained the rotation of the specimen ends about the weak axis, as shown in Figure 6.4, and rotation about the strong axis was allowed by the bearings.

6.3 Test Preparation, Instrumentation, and Procedure

A procedure on column testing, which is suggested by SSRC (Galambos, 1998), was followed during the tests. This procedure is referred to as Technical Memorandum B4: Procedure for Testing Centrally Loaded Columns (Galambos, 1998). This procedure is the same procedure applied to the single angle and double angle specimens.

6.3.1 Preparation of Test Specimens

The ends of the single angle specimens were crimped and welded to chord stubs by a fabricator. Then the test specimens were shipped to the ATLSS Center at Lehigh University. The outer surfaces of the chord stubs of the test specimens were not parallel and flat for most of the specimens, so hydrostone was used to level the specimen ends. As shown in Figure 6.3(b) and Figure 6.7, 1/2 in. thick steel leveling plates were attached to the outside surfaces of the chord stubs to provide a level, flat surface against the bearings. Hydrostone was placed between the chord stubs and the leveling plates to achieve uniform loading of the chord stubs, as seen in Figure 6.3(b).

Four LVDTs were used for the crimped single angle specimens, as shown in Figure 6.8. For LVDT attachment to the mid-height cross-section, four 1/16 in. diameter holes were drilled at the locations shown in Figure 6.9. The wire of each LVDT goes through one of these holes, and is attached to a small nut on the far side of the angle leg so that the wire stays attached throughout the test.

6.3.2 Initial Out-of-Straightness Measurements

Pretest measurements were made of initial camber and initial sweep along the length of each specimen. Since the centroid of the crimped single angle specimen is not on the legs of the specimen, the camber and sweep were measured at the heel of the cross-section. As shown in Figure 6.10, the pretest measurements were taken at 5 heel locations which are between the two chord stubs.

The pretest measurements of the width and thickness of the specimens are shown in Table 6.2 along with the comparison of width and thickness measurements with the nominal dimension for the specimens. As seen in this table, the measured dimensions are within 3% of the nominal dimensions. the cross-sectional parameters that are found by using the nominal dimensions of the cross-sections are presented in Table 6.3.

A tape measure was used for the pretest measurements, with a precision of 1/64 in. The sweep measurements, Δx_{h0}, and the camber measurements, Δy_{h0}, are reported in Table 6.4. For some of the test specimens, such as SC6, the initial out-of-straightness measurement is zero, as shown in Table 6.4, because the initial out-of-straightness measurement was smaller than the precision of the tape measure.

Bjorhovde (1972) suggests a model for the initial out-of-straightness in the shape of half sine wave over the length of the member, with a maximum initial out-of-straightness value of 1/1470 of the length of the specimen, L.

As seen in Table 6.4, the maximum initial out-of-straightness measurements in the

x_h axis are much higher than L/1470 for specimens SC1, SC4, and SC5, and the maximum initial out-of-straightness measurements in the y_h axis are 4 to 10 times larger than L/1470, because the crimping the ends create large eccentricity at the ends of the crimped members.

6.3.3 Instrumentation

According to the Technical Memorandum B4 (Galambos, 1998), the test data should include the applied load, the lateral deflection, the twist of the critical cross-section, and the axial shortening. The applied load and the cross-head displacement were determined from the SATEC test machine output. The cross-head displacement was used as an indication of axial shortening. Due to uncertainty in the theoretical stiffness and the small linear range of the applied load vs. cross-head displacement curve, the method used for determining axial shortening from cross-head displacement presented in Appendix B was not applied to the crimped single angle specimens.

Four LVDTs were used to measure the lateral deflection at the mid-height cross-section. The twist of the mid-height cross-section, θ_z, was calculated from the LVDT data. The reported lateral deflection measurements represent the lateral deflections of the heel of the crimped single angle specimens (i.e., in the x_h and y_h directions). Figure 6.9 shows the pattern of the LVDTs. As this figure shows, LVDT2 and LVDT3 measured the displacement at 1/8 in. plus the thickness of a leg from the heel of the cross-section. The length of the LVDTs was intentionally made long enough so that the measurements acquired from these two LVDTs can be assumed to be at the heel of

the cross-section.

The lateral deflections were calculated from the data from LVDT2 and LVDT3 by applying the same method used to calculate the lateral deflections for the single angle specimens, presented in Section 4.3.3. As it is shown in Figure 6.6, an inclinometer was placed on each bearing to measure the rotation of the bearing. Table 6.5 indicates a summary of the instrumentation used for the crimped single angle specimens.

6.3.4 Test Procedure

The test procedure for the crimped single angle specimens was the same as the procedure used for the single angle specimens, discussed in Section 4.4.

6.4 Predicted Buckling Capacities of the Crimped Single Angle Specimens

The predicted buckling capacities based on the nominal width and thickness are presented in Table 6.6. The predicted flexural buckling capacity and the predicted flexural-torsional buckling capacity were calculated following the steps presented in Section 4.6.

As seen from Table 6.6, the slenderness values for the principal axes directions are very close to each other. Thus, the predicted flexural buckling capacities about the x axis and the y axis are similar.

As seen from Table 6.4, the initial out-of-straightness in the y axis direction, Δy_{h0}, is much larger than the y axis initial out-of-straightness for the single angle specimens, presented in Table 4.4. Thus, the eccentricity of load is much larger for the crimped single angle specimens which would make these specimens more vulnerable to flexural buckling about the weak axis (i.e., x axis) than the single angle specimens. This larger eccentricity of load was not considered in the buckling capacity calculations. The calculation of the buckling capacities also treated the whole length of the specimen as uncrimped, neglecting the varying cross-sectional properties at the crimped ends. The crimped ends have a great reduced stiffness about the y axis.

The closeness of the flexural buckling capacities in the principle axes directions and the large initial out-of-straightness in the y axis direction suggest that the flexural buckling about the weak axis (i.e., x axis) might control the crimped single angle specimen behavior.

As seen in Table 6.6 the predicted flexural-torsional buckling capacity is smaller than either the predicted flexural buckling capacity about the weak axis (x axis) or the predicted flexural buckling capacity about the strong axis (y axis). As a result, the crimped angle specimens are expected to buckle in the flexural-torsional buckling mode.

6.5 Test Results

6.5.1 Specimen SC1

The load vs. the cross-head displacement is shown in Figure 6.11. The maximum experimental load, P_{EXP}, is lower than both the predicted flexural-torsional buckling capacity, $P_{cr\text{-}ft}$, and the predicted flexural buckling capacity about the strong axis, $P_{cr\text{-}y}$. As seen from Figure 6.11, at approximately 20 kips, the load stays constant while a small increase in the cross-head displacement is observed. Then load continues to grow until the peak load. A rapid drop in the load is observed after the peak load is reached.

The load vs. the twist of the mid-height cross-section is shown in Figure 6.12. Before approximately 20 kips of load is reached, there is a very little torsional deformation observed. After this load level is reached, there is a noticeable increase in torsional deformation observed before the peak load level. Figure 6.13 shows the load vs. the bearing rotation. There are noticeable rotations in both bearings observed before the peak load level. Figure 6.14 shows that the x_h axis lateral deflection at the mid-height cross-section before the peak load is much larger than the y_h axis lateral deflection. Very little y_h axis lateral deflection occurs, as shown in this figure.

The initial out-of-straightness along the length of the specimen is shown in Figure 6.15. The maximum initial out-of-straightness in the x_h axis direction is observed near the mid-height cross-section.

The twist and the lateral deflection in the x_h axis direction both grow simultaneously before the peak load level which is an indication of the flexural-torsional buckling mode. Figure 6.16 shows the specimen after peak load. As seen from this figure, there is no apparent local buckling of the angle legs observed along the length of the specimen. The specimen failed with significant flexural deformation in the crimped zone near the bottom end of the specimen.

6.5.2 Specimen SC2

The load vs. the cross-head displacement is shown in Figure 6.17. The maximum experimental load, P_{EXP}, is lower than both the predicted flexural-torsional buckling capacity, $P_{cr\text{-}ft}$, and the predicted flexural buckling capacity about the strong axis, $P_{cr\text{-}y}$.

The load vs. the twist of the mid-height cross-section is shown in Figure 6.18. As seen from this figure, there is noticeable torsional deformation observed before the peak load, and the deformation continues to grow in the post-peak region. Figure 6.19 shows the load vs. the bearing rotation. The bearings begin to rotate early in the test at low levels of load. The top bearing rotation is much larger than the bottom bearing rotation throughout the test. Figure 6.20 shows that there is observable lateral deflection in the x_h axis and the y_h axis directions before the peak load is reached. After the peak load, the x_h axis lateral deflection continues to grow and becomes much larger than the y_h axis lateral deflection.

The initial out-of-straightness along the length of the specimen is shown in Figure 6.21. This figure shows that the measured initial out-of-straightness in the x_h axis

direction is quite small along the length of the specimen.

Both the torsional deformation and the lateral deflection in the x_h axis direction grow simultaneously throughout the test which is an indication of the flexural-torsional buckling mode. There is no apparent local buckling of the angle legs observed along the length of the specimen. However, flexural deformation in the crimped zone near the top of the specimen can be seen in Figure 6.22.

6.5.3 Specimen SC4

The load vs. the cross-head displacement is shown in Figure 6.23. The maximum experimental load, P_{EXP}, is higher than the predicted flexural-torsional buckling capacity, $P_{cr\text{-}ft}$, and is lower than the predicted flexural buckling capacity about the strong axis, $P_{cr\text{-}y}$. A rapid drop in load is observed after the peak load is reached.

The load vs. the twist of the mid-height cross-section is shown in Figure 6.24. Before the peak load level, there is noticeable torsional deformation observed at the mid-height cross-section. This torsional deformation continues to grow in the post-peak region. Figure 6.25 shows the load vs. the bearing rotation. There are observable rotations in both bearings before the peak load level, and these rotations continue to grow in the post-peak region. The top bearing rotation is larger than the bottom bearing. As seen in Figure 6.26, both the x_h axis and the y_h axis lateral deflections at the mid-height cross-section are observable before the peak load is reached. The x_h axis lateral deflection is larger than the y_h axis lateral deflection in the post-peak region.

The initial out-of-straightness along the length of the specimen is shown in Figure 6.27. The maximum initial out-of-straightness in the x_h axis direction is at a cross-section other than the mid-height cross-section and the magnitude of this initial out-of-straightness exceeds the value of L/1470 used in the model by Bjorhovde (1972), as shown in Table 6.4. The maximum y_h axis initial out-of-straightness is at mid-height cross-section and is much larger than the x_h axis initial out-of-straightness.

The torsional deformation and the lateral deflection in the x_h axis direction grow simultaneously throughout the test which is an indication of the flexural-torsional buckling mode. There is no apparent local buckling of the angle legs observed along the length of the specimen. Figure 6.28 shows the specimen after the peak load is reached. Figure 6.28 indicates that the specimen failed with some flexural deformation in both the top and bottom crimped zones.

6.5.4 Specimen SC5

The load vs. the cross-head displacement is shown in Figure 6.29. The maximum experimental load, P_{EXP}, is lower than both the predicted flexural-torsional buckling capacity, $P_{cr\text{-}ft}$, and the predicted flexural buckling capacity about the strong axis, $P_{cr\text{-}y}$.

The load vs. the twist of the mid-height cross-section is shown in Figure 6.30. As seen in this figure, there is observable torsional deformation as soon as the load was applied to the specimen. Then, very little torsional deformation is observed before the peak load level. The torsional deformation continues to grow in the post-peak region. Figure 6.31 shows the load vs. the bearing rotation. Initial rotations of the bearings

grow throughout the test. Before the peak load there are noticeable rotations in both bearings. Figure 6.32 shows that very little y_h axis lateral deflection is observed in the test. As seen in this figure, there is observable lateral deflection in the x_h axis direction as soon as the initial load is applied and this deflection continue to develop after the peak load is reached.

The initial out-of-straightness along the length of the specimen is shown in Figure 6.33. The initial out-of-straightness in the x_h axis direction exceeds the value of L/1470, while the value in the y_h axis direction is much larger (Table 6.4).

Both the twist and the lateral deflection in the x_h axis direction at the mid-height cross-section grow simultaneously in the post-peak region which is an indication of the flexural-torsional buckling mode. There is no apparent local buckling of the angle legs observed along the length of the specimen. The specimen after the peak load is shown in Figure 6.34. Figure 6.34 shows significant flexural deformation in the crimped zone near the bottom end of the specimen.

6.5.5 Specimen SC6

The load vs. the cross-head displacement is shown in Figure 6.35. The maximum experimental load, P_{EXP}, is lower than both the predicted flexural-torsional buckling capacity, $P_{cr\text{-}ft}$, and the predicted flexural buckling capacity about the strong axis, $P_{cr\text{-}y}$.

The load vs. the twist of the mid-height cross-section is shown in Figure 6.36. As seen from this figure, there is some torsional deformation observed before the peak load is reached, which continues to grow after the peak load. Figure 6.37 shows the

load vs. the bearing rotation. There is no apparent rotation in the bottom bearing before the peak load level. On the other hand, the top bearing has noticeable rotation which further grows in the post-peak region and is much larger than the bottom bearing rotation. Figure 6.38 indicates that there is noticeable lateral deflection in both axis directions before the peak load level. The x_h axis lateral deflection grows after the peak load is reached and is much larger than the y_h axis lateral deflection.

The initial out-of-straightness along the length of the specimen is shown in Figure 6.39. For the x_h axis, the initial out-of-straightness is smaller than the precision of the measurement device. The y_h axis initial out-of-straightness is substantial.

The torsional deformation and the lateral deflection in the x_h axis direction grow simultaneously in the post-peak region which is an indication of the flexural-torsional buckling mode. There is no observable local buckling of the angle legs observed along the length of the specimen. Figure 6.40 shows the specimen after the peak load is reached. Figure 6.40 shows significant flexural deformation in the crimped region near the top of the specimen.

6.5.6 Specimen SD1

The load vs. the cross-head displacement is shown in Figure 6.41. The maximum experimental load, P_{EXP}, is lower than both the predicted flexural-torsional buckling capacity, $P_{cr\text{-}ft}$, and the predicted flexural buckling capacity about the strong axis, $P_{cr\text{-}y}$.

The load vs. the twist of the mid-height cross-section is shown in Figure 6.42. As seen from this figure, twist starts early in the test and grows throughout the test. Figure

6.43 shows the load vs. the bearing rotation. As seen from this figure, there are rotations of the bearings before the peak load level. The top bearing rotation in the post-peak region is larger than the bottom bearing rotation. Figure 6.44 indicates that there are noticeable lateral deflections in both directions at the mid-height cross-section before the peak load level. The lateral deflection in the x_h axis direction developed very quickly as soon as the initial load was applied and then there is no more apparent deflection observed until the peak load is reached. The x_h axis lateral deflection continues to grow and is much larger than the y_h axis lateral deflection in the post-peak region.

The initial out-of-straightness along the length of the specimen is shown in Figure 6.45. The x_h axis initial out-of-straightness is smaller than the precision of the measurement device. The y_h axis initial out-of-straightness is large.

The torsional deformation and the lateral deflection in the x_h axis direction both grow simultaneously in the post-peak region which is an indication of the flexural-torsional buckling mode. There is no apparent local buckling of the angle legs observed along the length of the specimen. Figure 6.46 shows the specimen after the peak load is reached. Figure 6.46 shows that the specimen failed with significant flexural deformation in both the top and bottom crimped zones.

6.5.7 Specimen SD2

The load vs. the cross-head displacement is shown in Figure 6.47. The maximum experimental load, P_{EXP}, is higher than both the predicted flexural-torsional buckling

capacity, $P_{cr\text{-}ft}$, and the predicted flexural buckling capacity about the strong axis, $P_{cr\text{-}y}$.

The load vs. the twist of the mid-height cross-section is shown in Figure 6.48. As seen from this figure, there is some twist observed before the peak load level and very large twist after the peak load. Figure 6.49 shows the load vs. the bearing rotation. There is very little rotation in either bearing observed before the peak load level. As seen in Figure 6.50, there is no apparent lateral deflection in the x_h axis direction before the peak load level. On the other hand, there is y_h axis lateral deflection before the peak load level which grows after the peak load. The x_h axis lateral deflection also grows in the post-peak region.

The initial out-of-straightness along the length of the specimen is shown in Figure 6.51. The x_h axis initial out-of-straightness is smaller than the precision of the measurement device. The y_h axis initial out-of-straightness is substantial.

The torsional deformation and the lateral deflection in the x_h axis direction both grow simultaneously in the post-peak region which is an indication of the flexural-torsional buckling mode. The lateral deflection in the y_h axis direction at the mid-height cross-section suggests that flexural buckling occurred. There is local bending of the angle legs occurred near the mid-height cross-section, as shown in Figure 6.52, which shows the the specimen after the peak load. As seen in this figure, there is not much flexural deformation in either of the crimped ends.

6.6 Discussion of Results

The isolated tests of the crimped single angle specimens simulated the behavior of crimped end web members in joists. The compressive strength of such members can be calculated easily if the eccentricity caused by crimping and the welded connections to the chord are neglected. Thus, to calculate the buckling capacities of the crimped single angle specimens in this study, it was assumed that the specimens are subjected to only axial load (i.e., the bending effects caused by the load eccentricity is neglected in the calculations of the predicted buckling capacities).

The deformed shapes of the specimens after the peak load vary between the specimens, depending on the slenderness of the test specimen. In general, it is observed that all the crimped single angle specimens have both lateral deflection and twist at the mid-height cross-section in the post-peak region, and many specimens exhibited these deformations throughout the entire test. The more slender specimens, in particular, had a noticeable amount of twist at the mid-height cross-section before the peak load level. However, it is also noted that significant flexural deformation was observed in the crimped regions near the ends of the specimen, especially for the less slender test specimens. There was no consistency about which end failed initially. Except for specimens SC4 and SD2, all other test specimens failed before reaching the predicted load capacity. It appears that flexural deformations in the crimped zones influence the buckling capacity.

Specimens SC2 and SC4 are identical specimens, except that their weld patterns differ. Specimens SC2 has L-type weld, whereas, specimen SC4 has U-type weld. As seen from Table 6.7, specimen SC4 has an approximately 25% higher experimental test result than specimen SC2. Both of the specimens have appeared to fail in the expected flexural-torsional buckling accompanying large flexural deformations in one of their crimped zones. Due to the profile of L-type weld, for the case when tips of legs of the angle are welded, the heel of the angle is not restrained as much as the restraint established in the U-type weld. The higher restraint introduced by the U-type weld in the crimped zone increases the flexural stiffness of the crimped end of the angle member. This might increase the flexural capacity of the crimped ends that would affect the experimental capacity of the member as compared for these two specimens.

The flexural deformations in the crimped zones increase the effective length of the test specimens. In the tests, the bearings restrained the rotation about the weak axis, but rotation about the strong axis was unrestrained. Thus, the effective length factors were assumed to be K_x equal to 0.5 and K_y equal to 1.0. The significant flexural deformations in the crimped zones could be considered by using a larger value of K_y.

The test results are compared to the predicted buckling capacities in Table 6.7 and Figure 6.53. The table and figure show that the experimental buckling capacities, P_{EXP}, are generally smaller than both the predicted strong axis flexural buckling capacity, P_{cr-y}, and the predicted flexural-torsional buckling capacity, P_{cr-ft}, except for specimens SC4 and SD2. For specimen SC4, P_{EXP} is higher than P_{cr-ft}, but is lower than P_{cr-y}. For specimen SD2, P_{EXP} is higher than both P_{cr-ft} and P_{cr-y}.

As shown in Table 6.7, the average ratio of P_{EXP} to P_{cr-y} was found to be 0.75 with a standard deviation of 0.15, while the average ratio of P_{EXP} to P_{cr-ft} is 0.89 with a standard deviation of 0.18.

The ratio of P_{EXP} to P_{cr-ft} vs. the Q reduction factor is shown in Figure 6.54. It can be seen from this figure that as the Q reduction factor is smaller; the P_{EXP}/P_{cr-ft} ratio is slightly larger, but the effect is not as pronounced as for the single angle specimens.

In Figure 6.55 and Figure 6.56, the test results are compared with the predicted buckling stresses F_{cr-y} and F_{cr-ft} for the Vanadium steel specimens, in addition to the yield stress, F_Y, the yield stress multiplied by the Q reduction factor, QF_Y, and the elastic flexural-torsional buckling stress, F_{e-ft}. The two figures show that the flexural-torsional buckling capacity is expected to control the buckling capacity, however, the test results generally fall below the flexural-torsional curve for the crimped single angle specimens. A comparison of P_{EXP} vs. the axial yield strength, P_Y, the yield capacity multiplied by the Q reduction factor, QP_Y, and the elastic flexural-torsional buckling capacity, P_{e-ft}, for each of the specimens is also included in Table 6.7.

Table 6.1 Test Matrix for Crimped Single Angle Specimens

Specimen ID	Steel Type	Specimen Size	Weld Type	Bearing Capacity	Measured Yield Stress	Length
		in.×in.× in.		kips	ksi	in.
SC1	Vanadium	L2x2x3/16	L	100	76.9	30
SC2	Vanadium	L2x2x3/16	L	100	76.9	60
SC4	Vanadium	L2x2x3/16	U	100	76.9	60
SC5	Grade 50	L2x2x3/16	L	100	50.0	30
SC6	Grade 50	L2x2x3/16	L	100	50.0	60
SD1	Vanadium	L1.75x1.75x1/8	L	100	78.5	30
SD2	Vanadium	L1.75x1.75x1/8	L	100	78.5	60

Table 6.2 Comparison of Measured vs. Nominal Dimensions of Width and Thickness

Specimen ID	Measured dimensions[1]				Nominal dimensions[2]				Measured/Nominal			
	b_1	b_2	t_1	t_2	b_1	b_2	t_1	t_2	$b_1^{[1]}/b_1^{[2]}$	$b_2^{[1]}/b_2^{[2]}$	$t_1^{[1]}/t_1^{[2]}$	$t_2^{[1]}/t_2^{[2]}$
SC1	2.001	2.010	0.188	0.185	2	2	0.1875	0.1875	1.00	1.00	1.00	0.99
SC2	2.002	1.996	0.188	0.190	2	2	0.1875	0.1875	1.00	1.00	1.00	1.01
SC4	1.939	1.982	0.188	0.192	2	2	0.1875	0.1875	0.97	0.99	1.00	1.02
SC5	2.017	2.020	0.186	0.185	2	2	0.1875	0.1875	1.01	1.01	0.99	0.99
SC6	2.002	2.010	0.186	0.191	2	2	0.1875	0.1875	1.00	1.00	0.99	1.02
SD1	1.711	1.744	0.124	0.127	1.75	1.75	0.125	0.125	0.98	1.00	0.99	1.01
SD2	1.737	1.715	0.127	0.124	1.75	1.75	0.125	0.125	0.99	0.98	1.01	0.99

Table 6.3 Cross-sectional Properties Based on Nominal Dimensions for Width and Thickness

Specimen ID	b_1	b_2	t_1	t_2	F_y	L	A_g	tan(α)	I_x	I_y	r_x	r_y	r_z	C_w	J	y_o	r_o^2	H
	in.	in.	in.	in.	ksi	in.	in^2		in^4	in^4	in.	in.	in.	in^6	in^4	in.	in^2	
SC1	2.000	2.000	0.1875	0.1875	76.9	30	0.71	1.00	0.11	0.43	0.39	0.78	0.39	0.003	0.008	0.67	1.21	0.628
SC2	2.000	2.000	0.1875	0.1875	76.9	60	0.71	1.00	0.11	0.43	0.39	0.78	0.39	0.003	0.008	0.67	1.21	0.628
SC4	2.000	2.000	0.1875	0.1875	76.9	60	0.71	1.00	0.11	0.43	0.39	0.78	0.39	0.003	0.008	0.67	1.21	0.628
SC5	2.000	2.000	0.1875	0.1875	50.0	30	0.71	1.00	0.11	0.43	0.39	0.78	0.39	0.003	0.008	0.67	1.21	0.628
SC6	2.000	2.000	0.1875	0.1875	50.0	60	0.71	1.00	0.11	0.43	0.39	0.78	0.39	0.003	0.008	0.67	1.21	0.628
SD1	1.750	1.750	0.1250	0.1250	78.5	30	0.42	1.00	0.05	0.20	0.35	0.69	0.35	0.001	0.002	0.60	0.95	0.627
SD2	1.750	1.750	0.1250	0.1250	78.5	60	0.42	1.00	0.05	0.20	0.35	0.69	0.35	0.001	0.002	0.60	0.95	0.627

Table 6.4 Initial Imperfection in Principal Axis Directions

Specimen ID	L/1470	Mid-height out-of-straightness		Maximum out-of-straightness	
		Δx_{h0} (in.)	Δy_{h0} (in.)	Δx_{h0} (in.)	Δy_{h0} (in.)
SC1	0.0204	-0.0625	-0.2135	-0.0625	-0.2135
SC2	0.0408	0	-0.1820	0.0070	-0.1820
SC4	0.0408	0.0313	-0.2470	0.0556	-0.2470
SC5	0.0204	-0.0312	-0.1945	-0.0312	-0.1945
SC6	0.0408	0	-0.2960	0	-0.2960
SD1	0.0204	0	-0.1940	0	-0.1940
SD2	0.0408	0	-0.2385	0	-0.2385

Table 6.5 Instrumentation and Measurements

Data	Unit	Instrumentation	Notes
P	kips	SATEC	Axial load
δ	in	SATEC	Cross-head displacement
Δ_1	in	LVDT	Displacement at mid-height cross-section
Δ_2	in	LVDT	Displacement at mid-height cross-section
Δ_3	in	LVDT	Displacement at mid-height cross-section
Δ_4	in	LVDT	Displacement at mid-height cross-section
θ_1	degree	Inclinometer	Top bearing rotation
θ_2	degree	Inclinometer	Bottom bearing rotation
ε_1	microstrain	Strain Gage	Strain at mid-height cross-section
ε_2	microstrain	Strain Gage	Strain at mid-height cross-section
ε_3	microstrain	Strain Gage	Strain at mid-height cross-section
ε_4	microstrain	Strain Gage	Strain at mid-height cross-section

Table 6.6 Predicted Buckling Capacities

Specimen ID	K_x	K_y	$(KL/r)_x$	$(KL/r)_y$	Q	P_Y	P_{cr-x}	P_{cr-y}	P_{cr-ft}	P_{e-ft}
						kips	kips	kips	kips	kips
SC1	0.5	1.0	38.1	38.5	0.92	54.6	43.6	43.5	35.8	61.2
SC2	0.5	1.0	76.1	77.0	0.92	54.6	27.8	27.4	24.1	28.5
SC4	0.5	1.0	76.1	77.0	0.92	54.6	27.8	27.4	24.1	28.5
SC5	0.5	1.0	38.1	38.5	1.00	35.5	32.1	32.1	28.0	61.2
SC6	0.5	1.0	76.1	77.0	1.00	35.5	23.4	23.2	21.2	28.5
SD1	0.5	1.0	43.2	43.5	0.79	33.0	22.0	22.0	15.9	22.2
SD2	0.5	1.0	86.5	87.1	0.79	33.0	13.3	13.1	10.6	12.1

Table 6.7 Experimental Results vs. Predicted Buckling Capacities

Specimen ID	P_{EXP}	P_{EXP}/P_{cr-y}	P_{EXP}/P_{cr-ft}	P_{EXP}/P_Y	P_{EXP}/QP_Y	P_{EXP}/P_{e-ft}
	kips	kips	kips	kips	kips	kips
SC1	23.9	0.55	0.67	0.44	0.48	0.39
SC2	19.8	0.72	0.82	0.36	0.39	0.69
SC4	24.8	0.91	1.03	0.45	0.49	0.87
SC5	23.7	0.74	0.85	0.67	0.67	0.39
SC6	15.5	0.67	0.73	0.44	0.44	0.54
SD1	13.7	0.62	0.86	0.42	0.53	0.62
SD2	13.3	1.02	1.25	0.40	0.51	1.10
Average		0.75	0.89	0.45	0.50	0.66
Standard Deviation		0.15	0.18	0.09	0.08	0.24

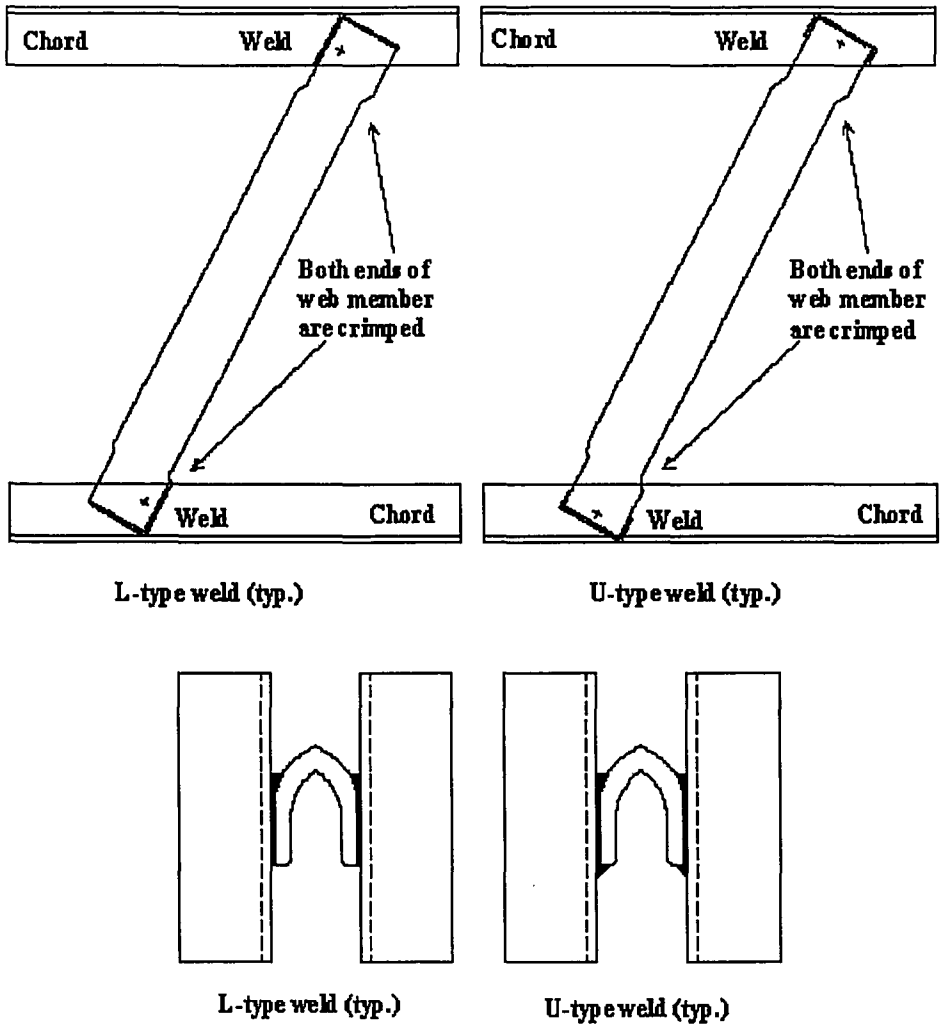

Figure 6.1 Schematic of Crimped Single Angle Web Members

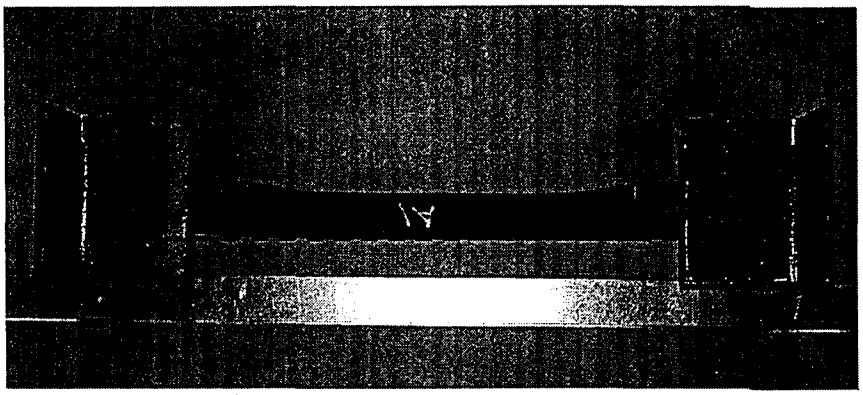

(a) Side View - Specimen SC1

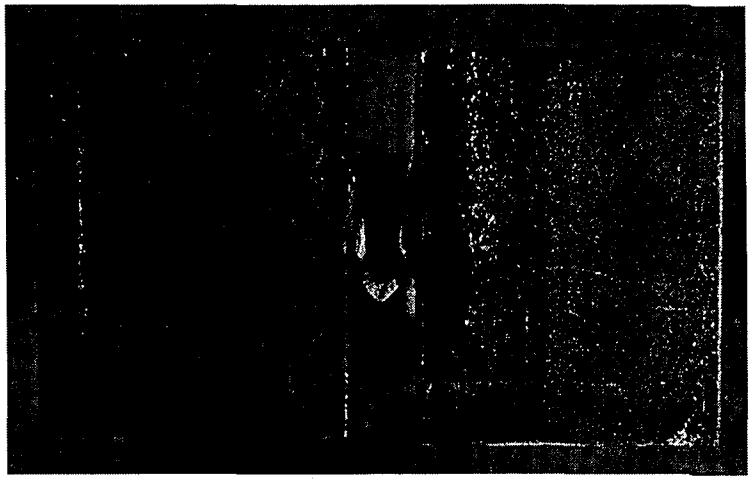

(b) End View - Specimen SC1

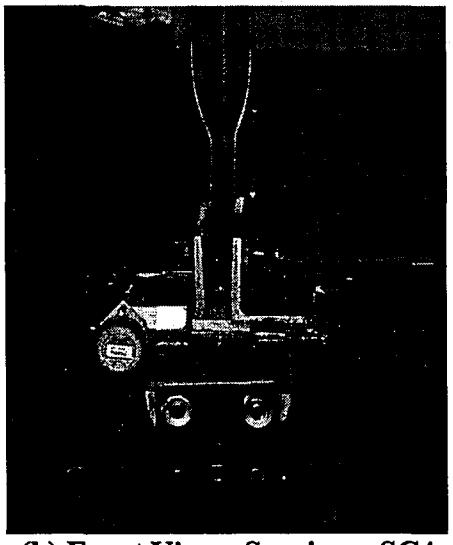

(b) Front View - Specimen SC4

Figure 6.2 Photos of Crimped Single Angle Members

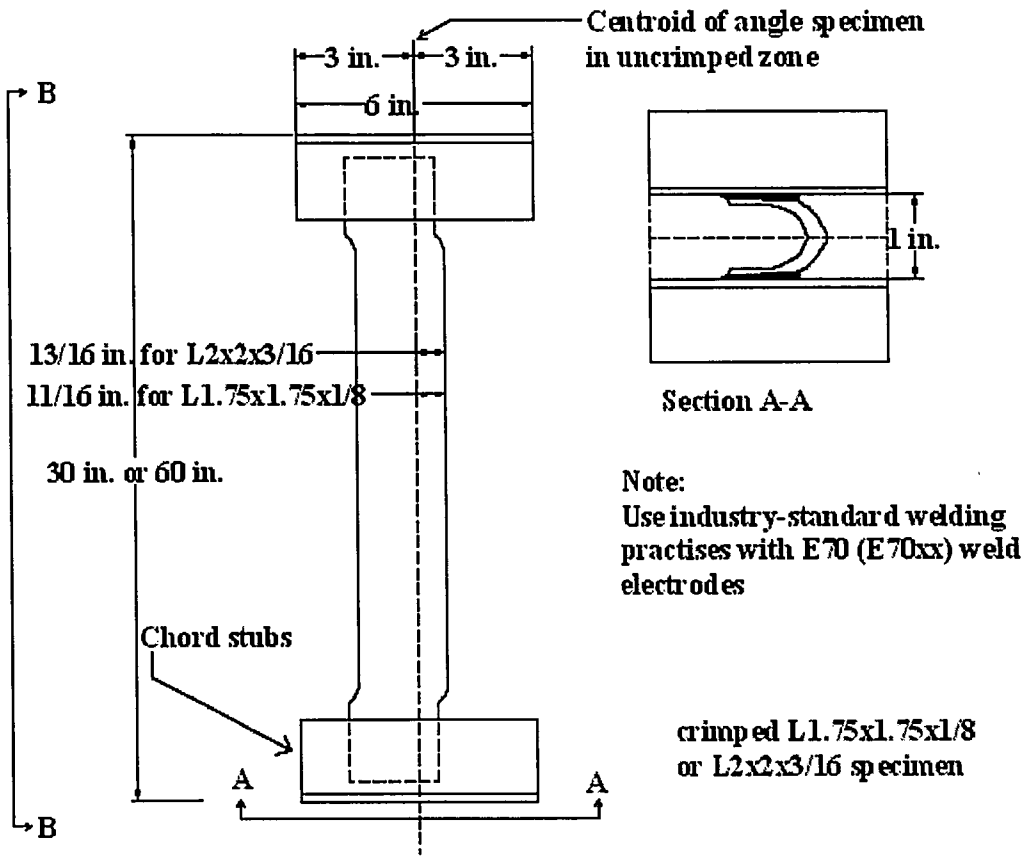

(a) Test Specimen Elevation View

Figure 6.3 Crimped Angle Test Specimens

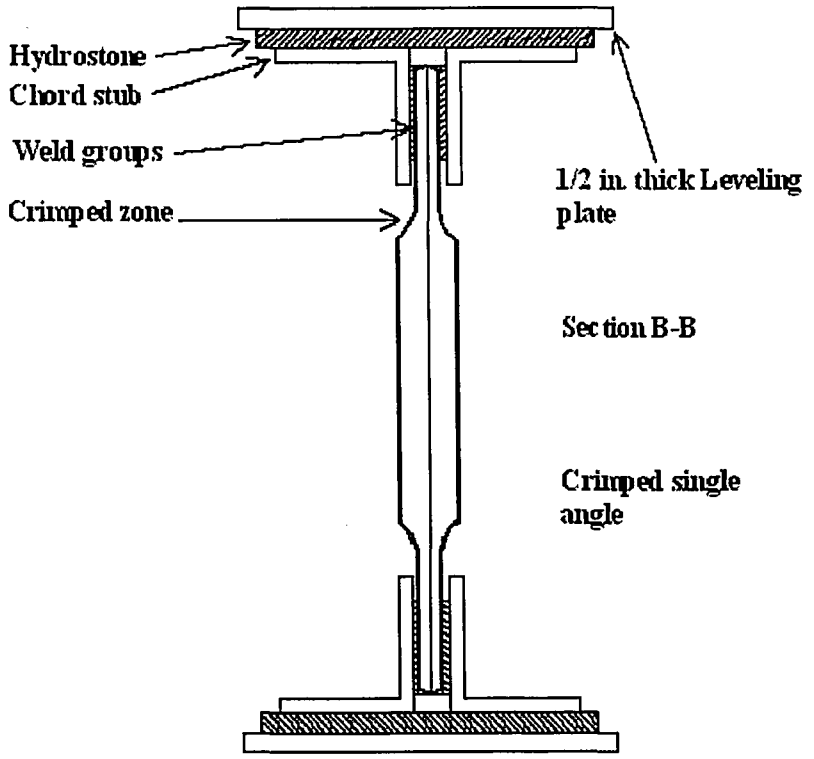

(b) Section View of Specimen with Leveling Plates

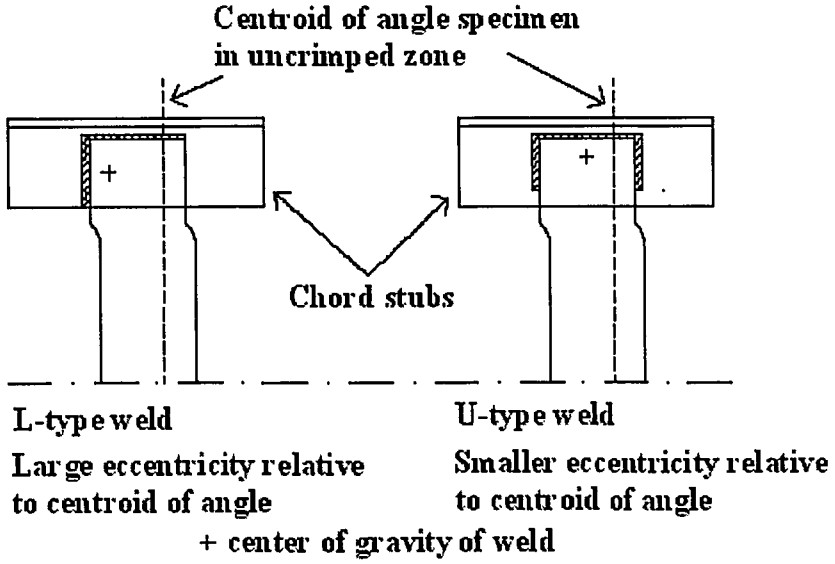

(c) Two Types of Welds at The Crimped Ends of Specimen

Figure 6.3 Crimped Angle Test Specimens (continued)

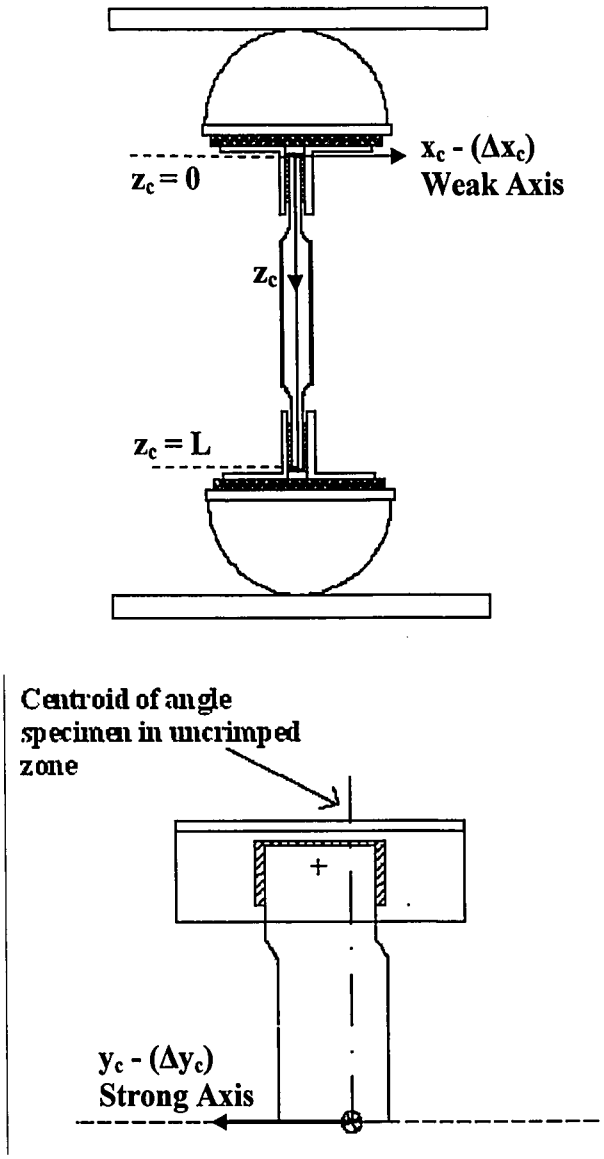

Figure 6.4 Coordinate Axis System

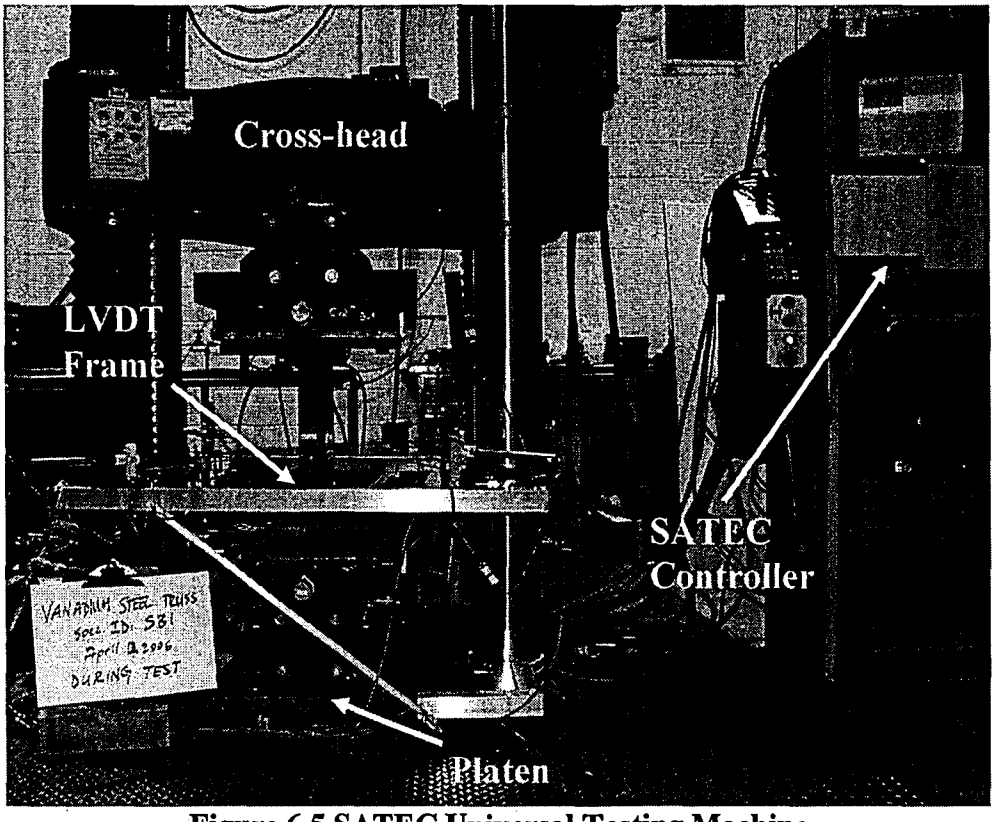

Figure 6.5 SATEC Universal Testing Machine

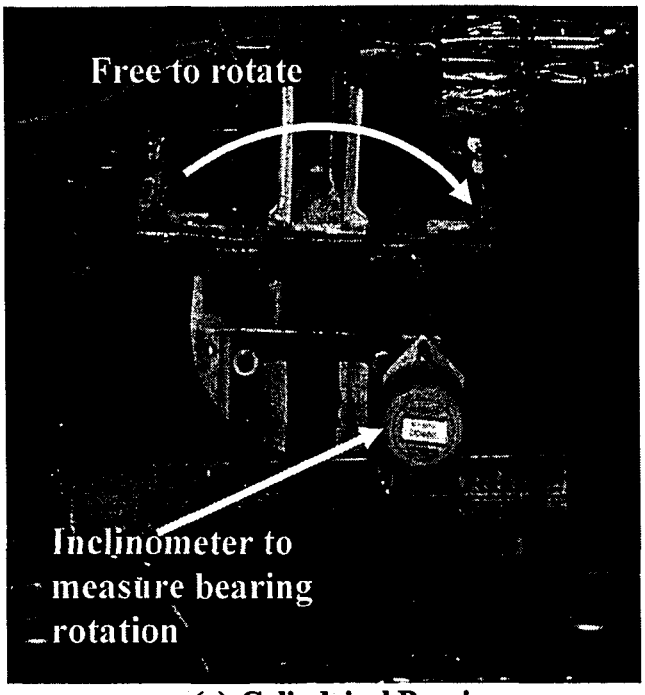

(a) Cylindrical Bearing

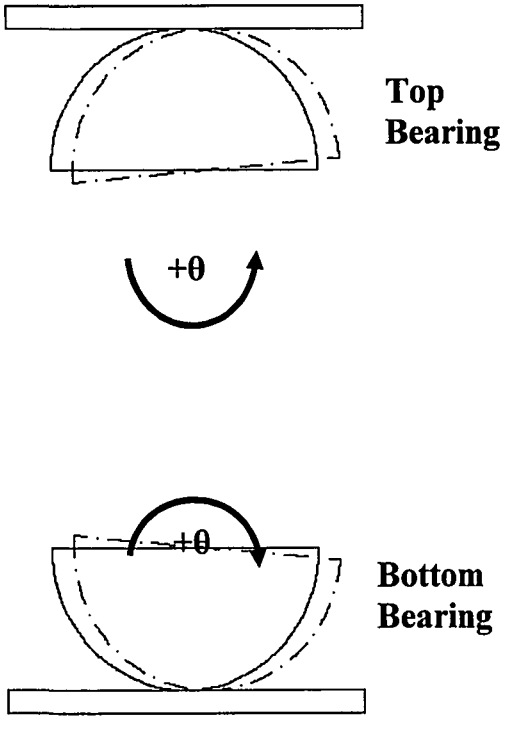

(b) Bearing Sign Convention

Figure 6.6 Cylindrical Bearings and Sign Convention

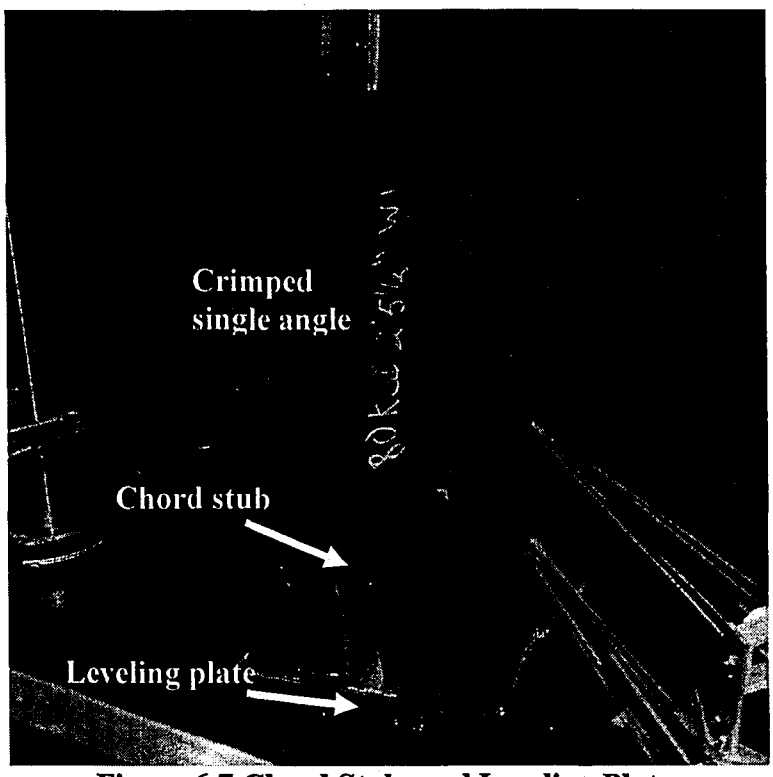

Figure 6.7 Chord Stubs and Leveling Plates

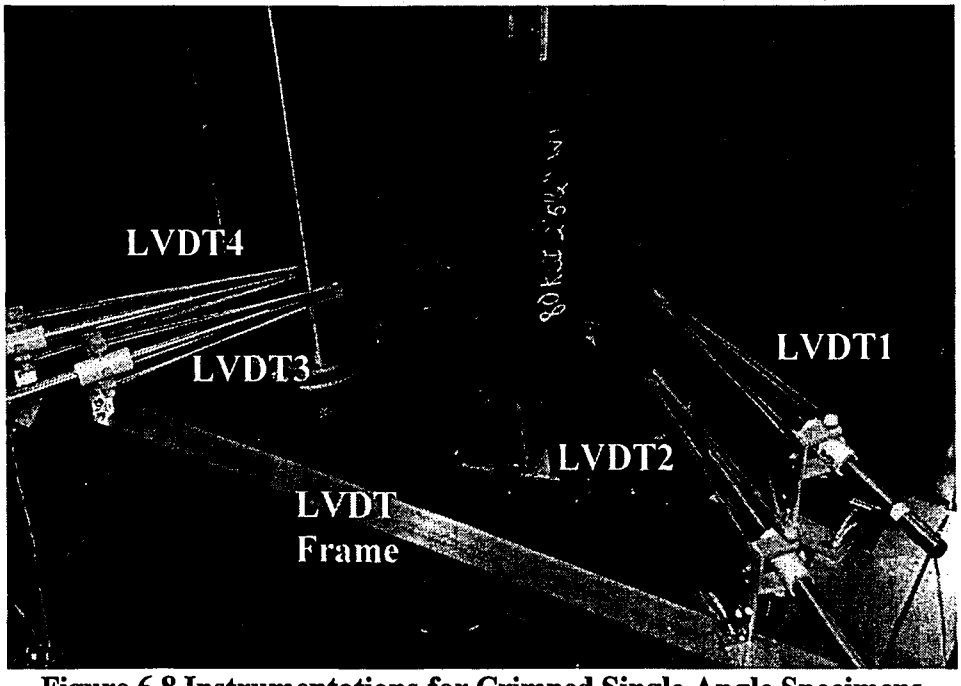

Figure 6.8 Instrumentations for Crimped Single Angle Specimens

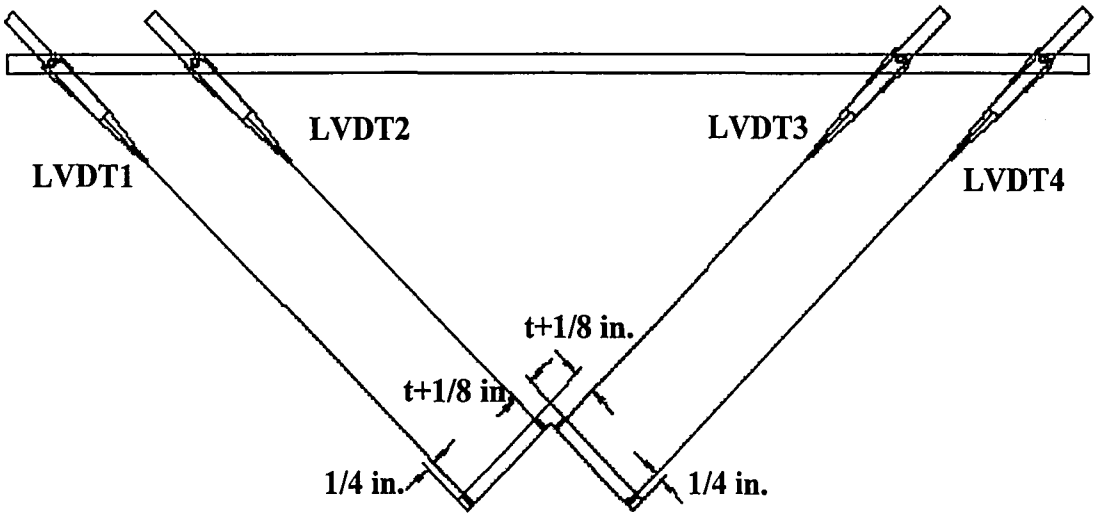

Figure 6.9 LVDT Attachments at Mid-height Cross-section

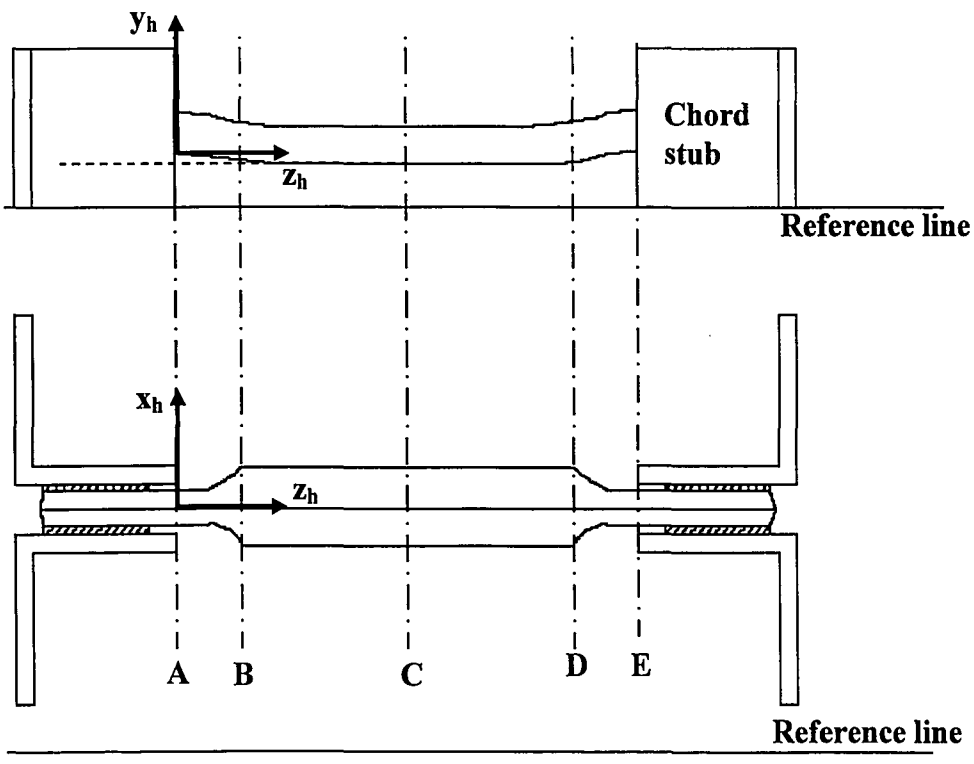

Figure 6.10 Pretest Measurements

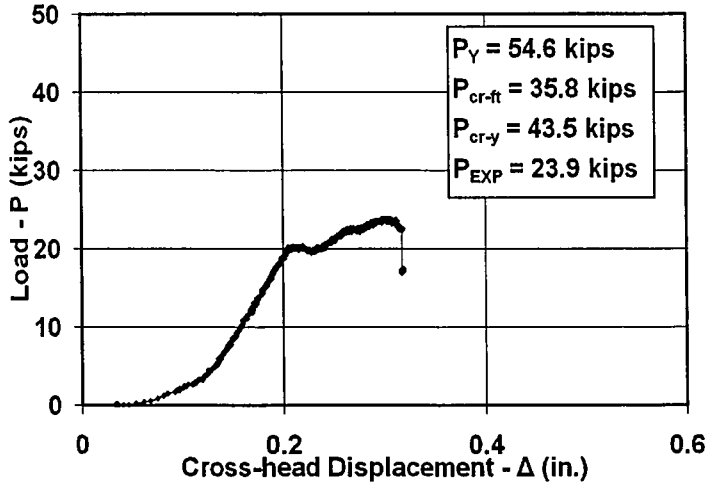

Figure 6.11 SC1 Specimen Load vs. Cross-head Displacement

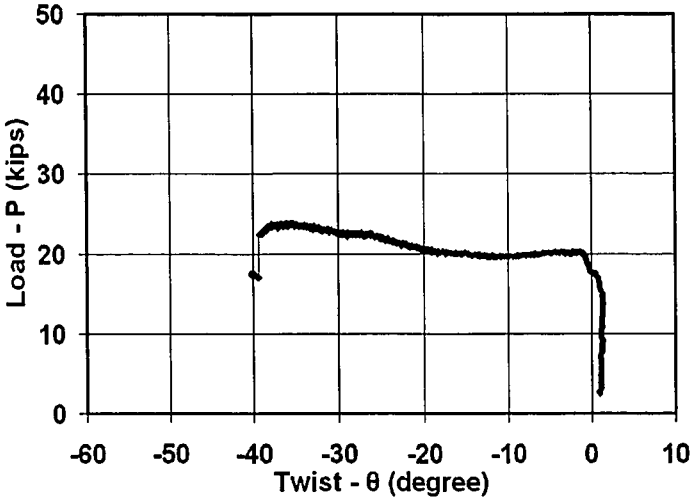

Figure 6.12 SC1 Specimen Load vs. Twist

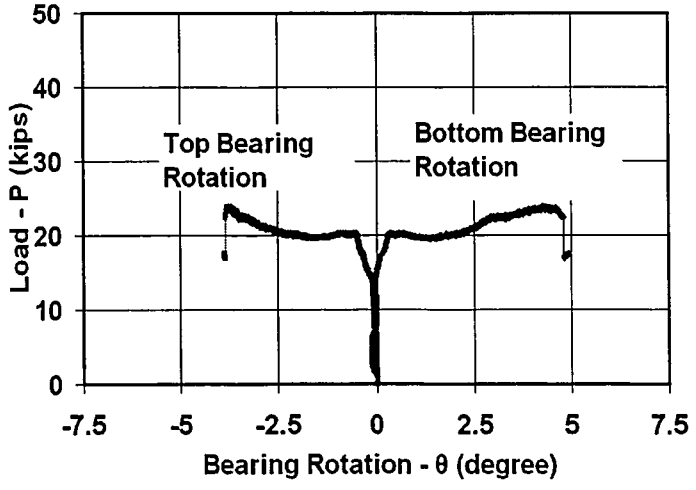

Figure 6.13 SC1 Specimen Load vs. Bearing Rotation

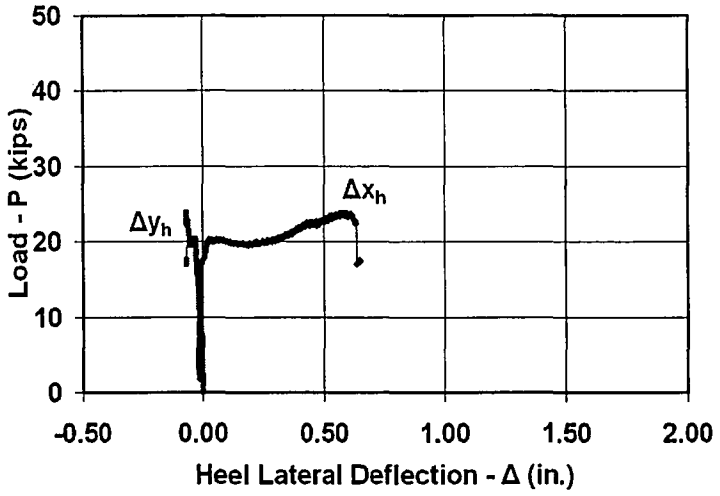

Figure 6.14 SC1 Specimen Load vs. Heel Lateral Deflection

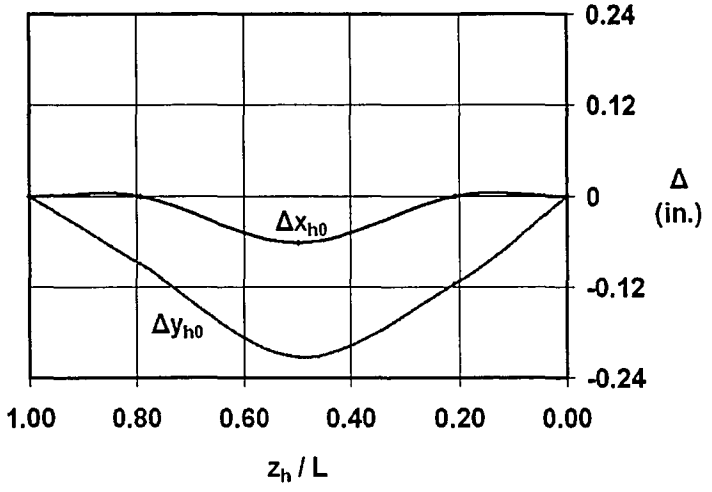

Figure 6.15 SC1 Specimen Initial Out-of-Straightness

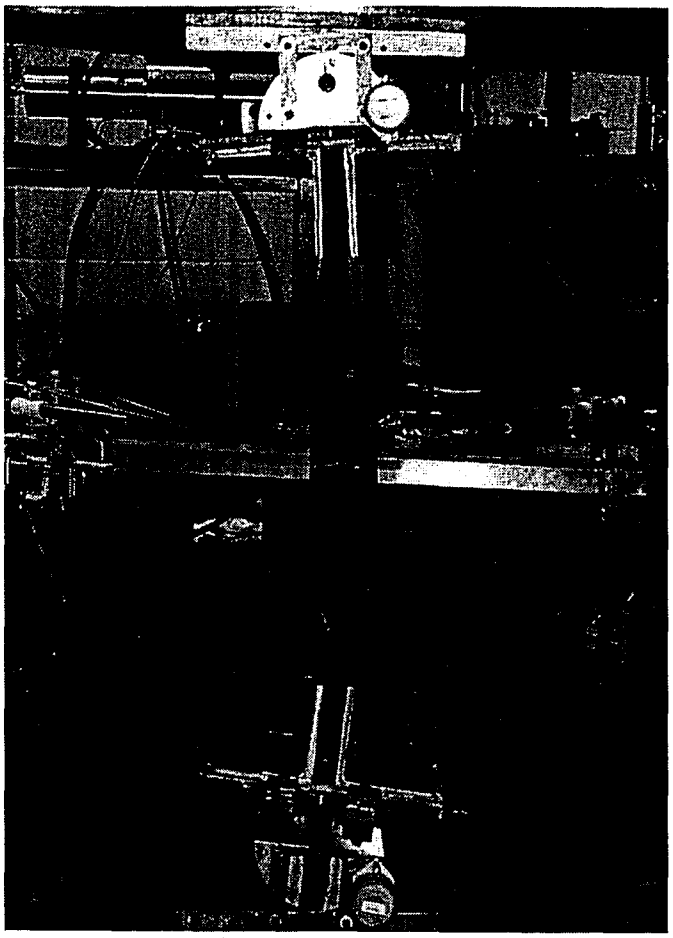

Figure 6.16 Specimen SC1

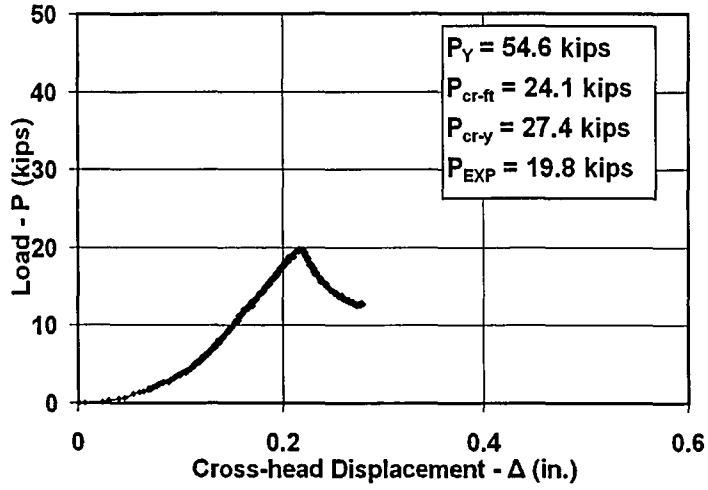

Figure 6.17 SC2 Specimen Load vs. Cross-head Displacement

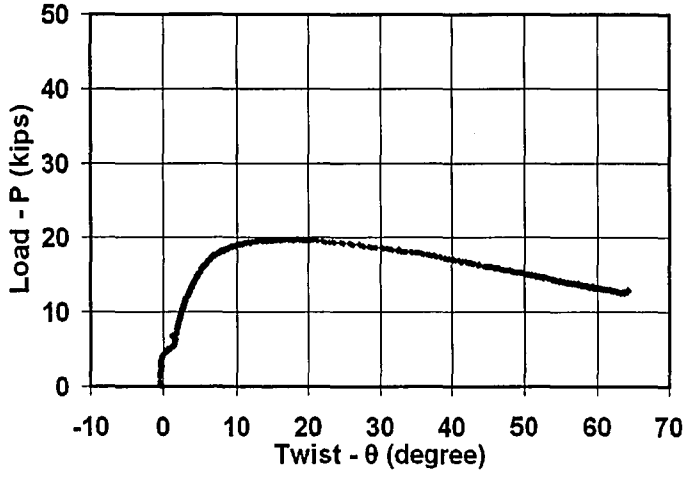

Figure 6.18 SC2 Specimen Load vs. Twist

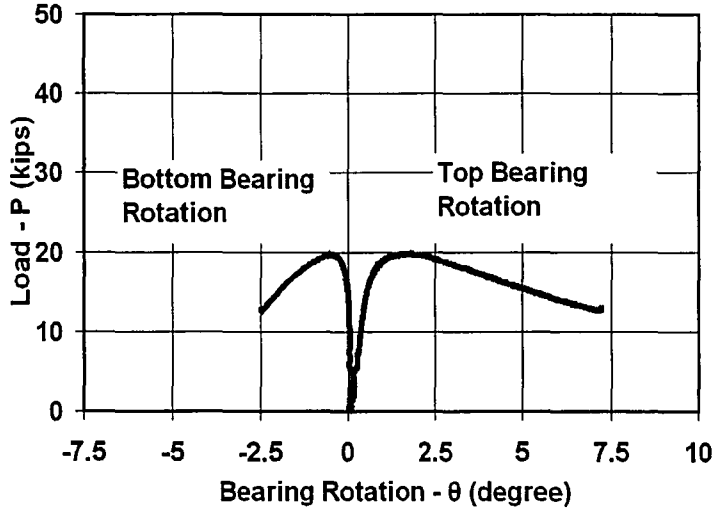

Figure 6.19 SC2 Specimen Load vs. Bearing Rotation

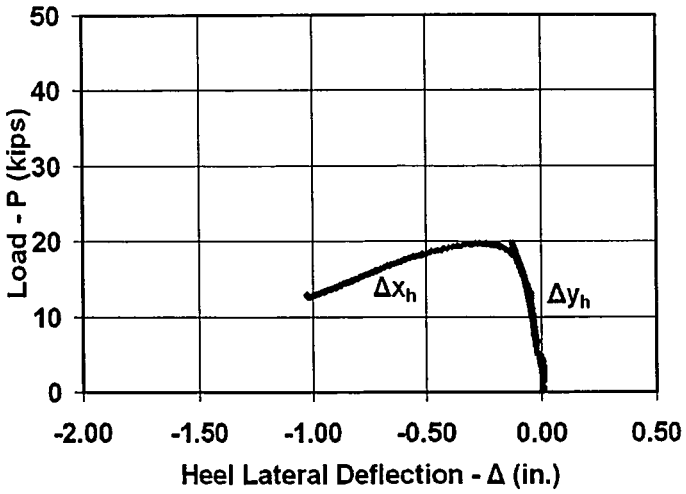

Figure 6.20 SC2 Specimen Load vs. Heel Lateral Deflection

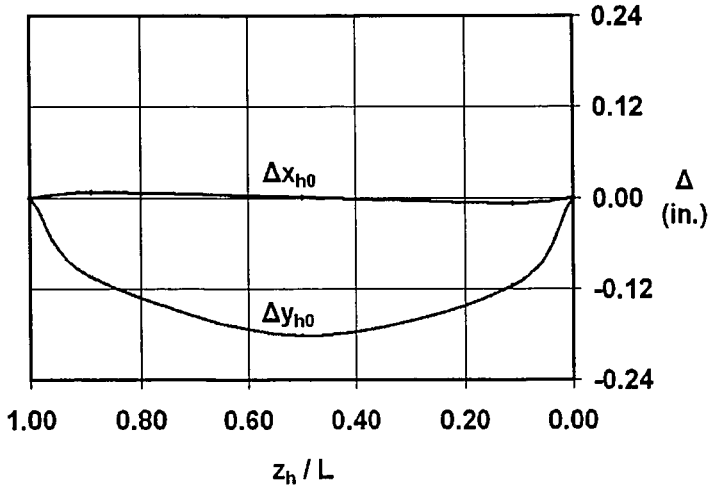

Figure 6.21 SC2 Specimen Initial Out-of-Straightness

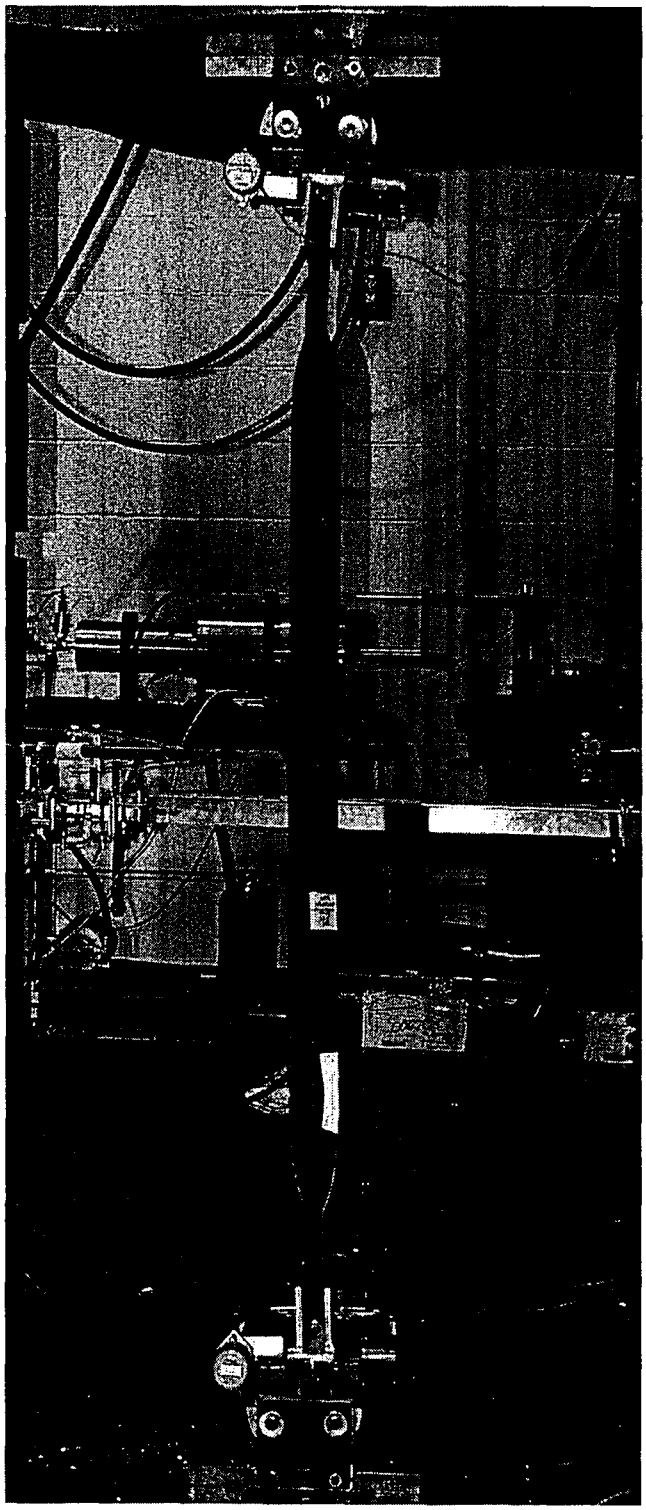

Figure 6.22 Specimen SC2

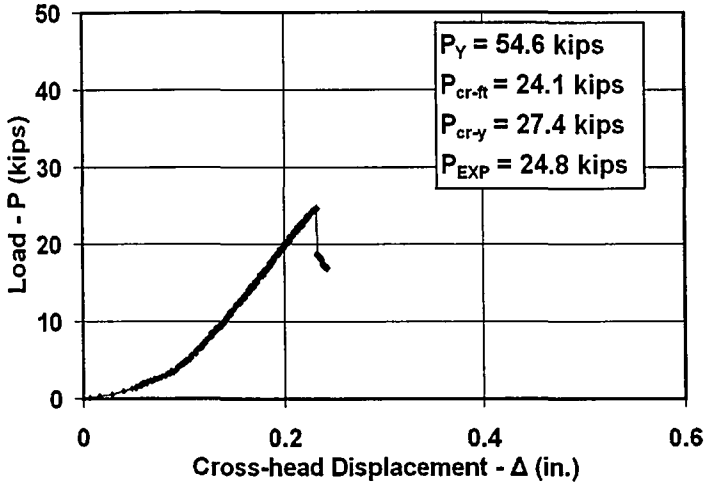

Figure 6.23 SC4 Specimen Load vs. Cross-head Displacement

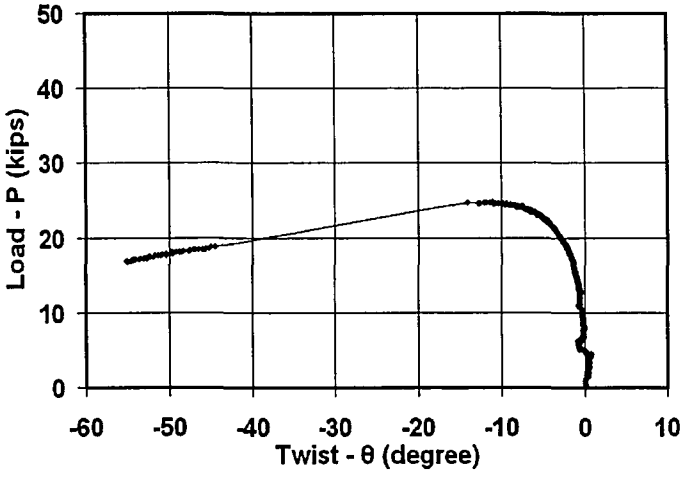

Figure 6.24 SC4 Specimen Load vs. Twist

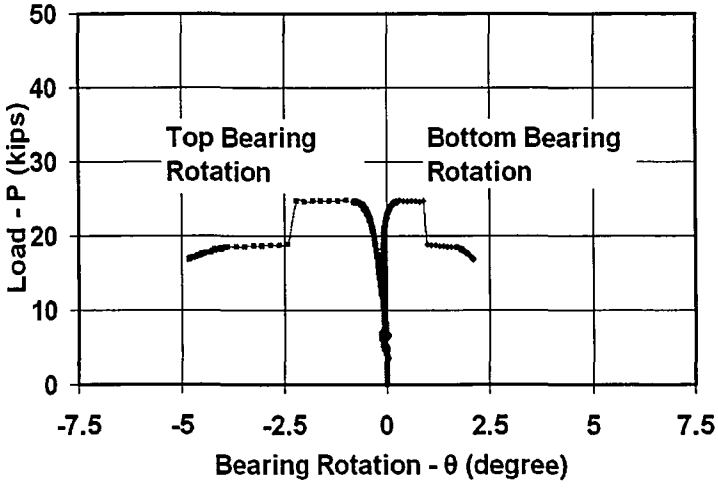

Figure 6.25 SC4 Specimen Load vs. Bearing Rotation

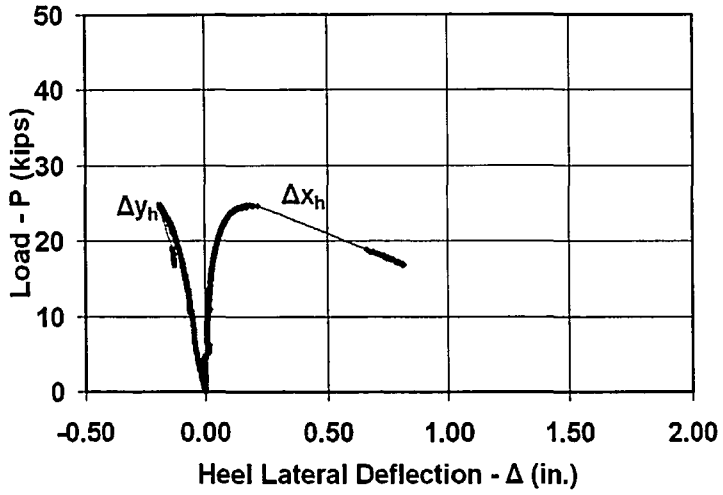

Figure 6.26 SC4 Specimen Load vs. Heel Lateral Deflection

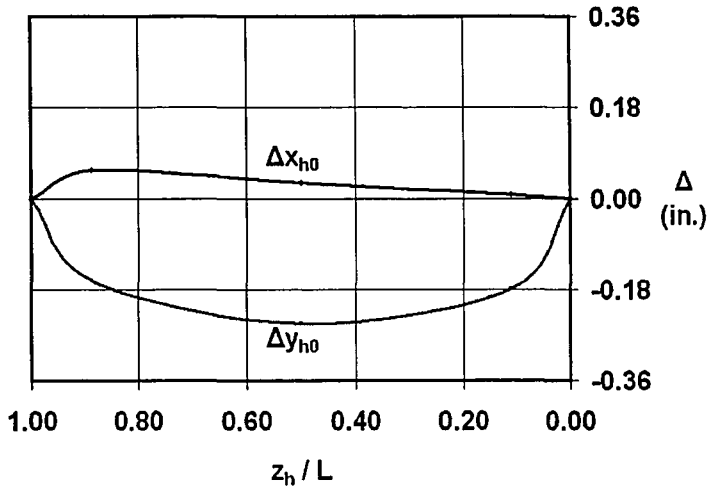

Figure 6.27 SC4 Specimen Initial Out-of-Straightness

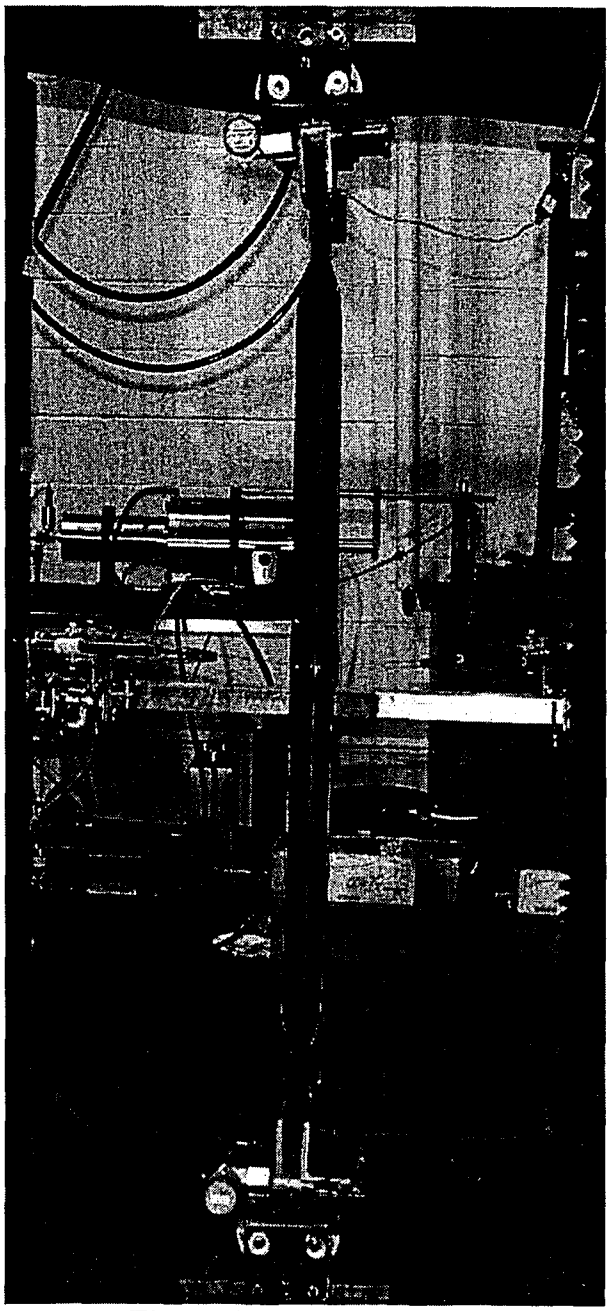

Figure 6.28 Specimen SC4

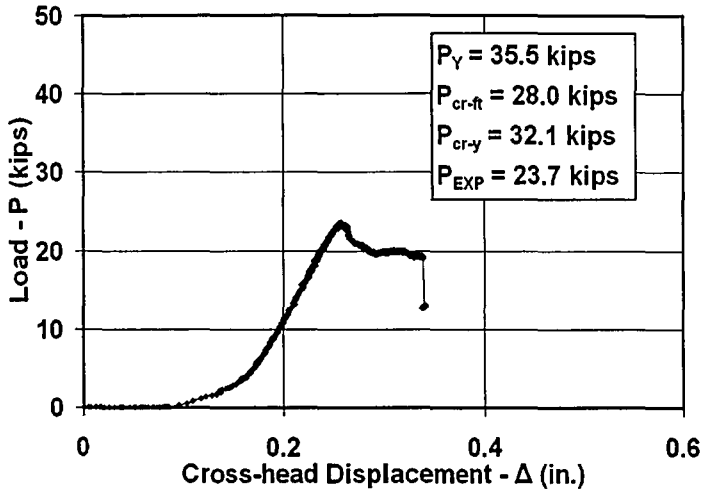

Figure 6.29 SC5 Specimen Load vs. Cross-head Displacement

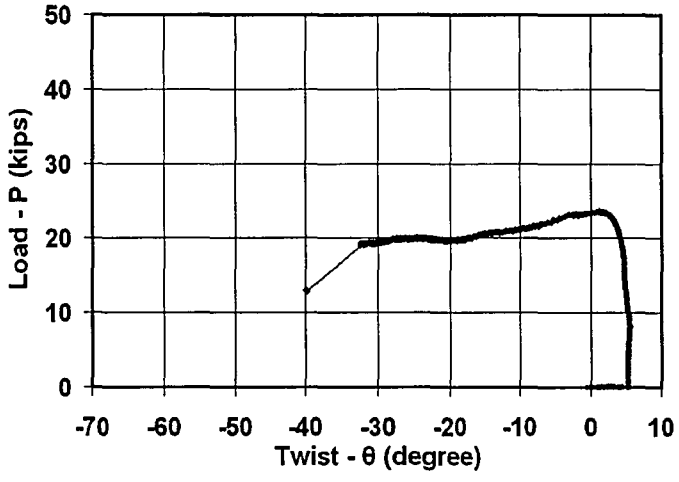

Figure 6.30 SC5 Specimen Load vs. Twist

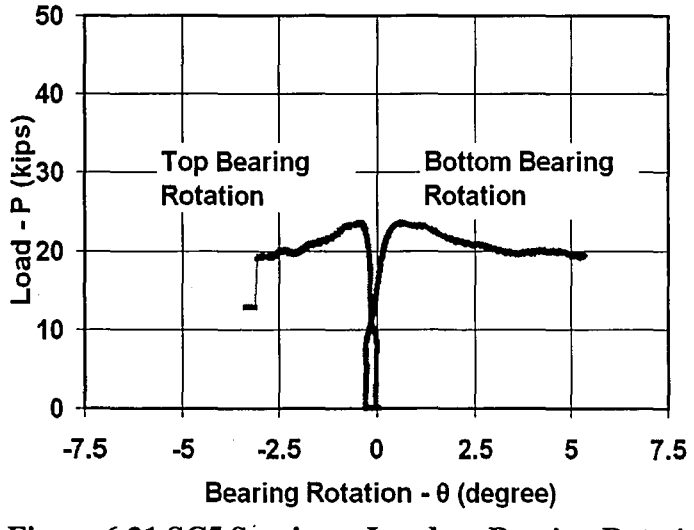

Figure 6.31 SC5 Specimen Load vs. Bearing Rotation

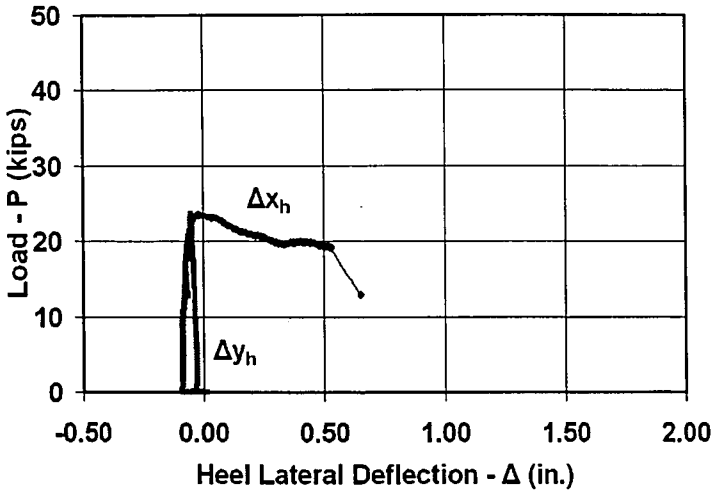

Figure 6.32 SC5 Specimen Load vs. Heel Lateral Deflection

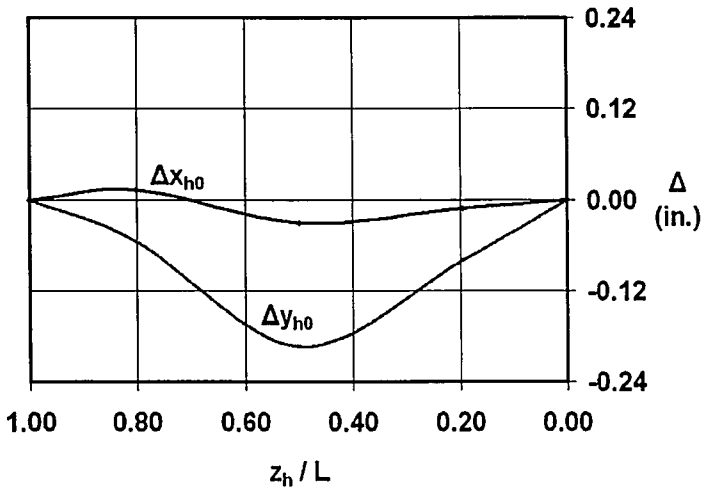

Figure 6.33 SC5 Specimen Initial Out-of-Straightness

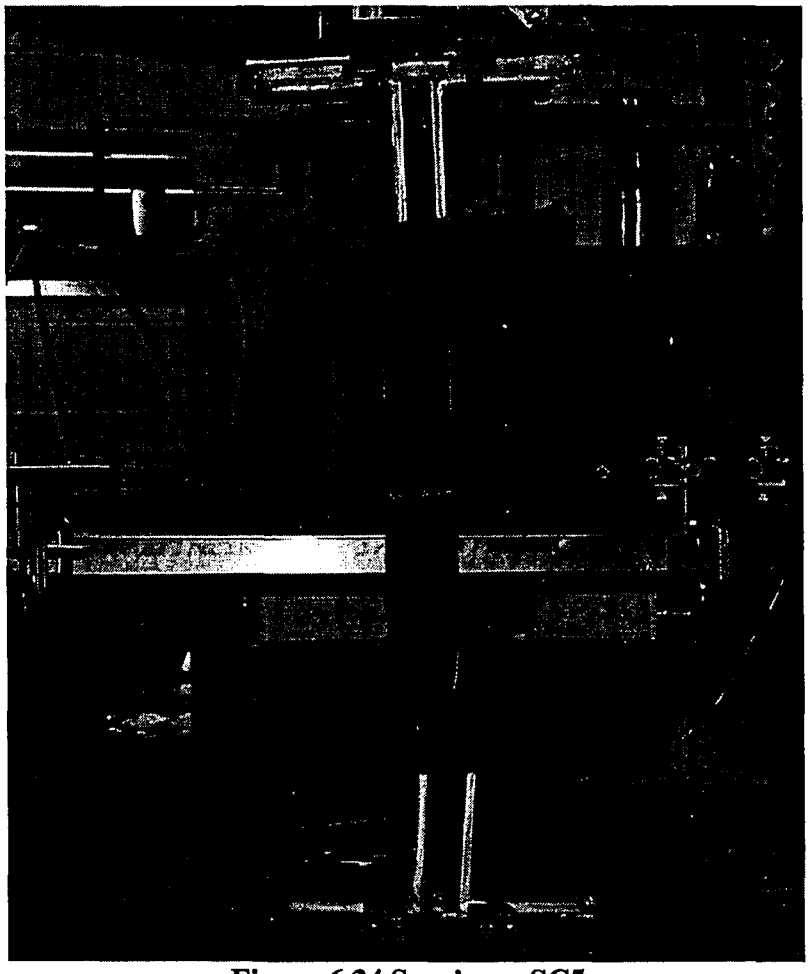

Figure 6.34 Specimen SC5

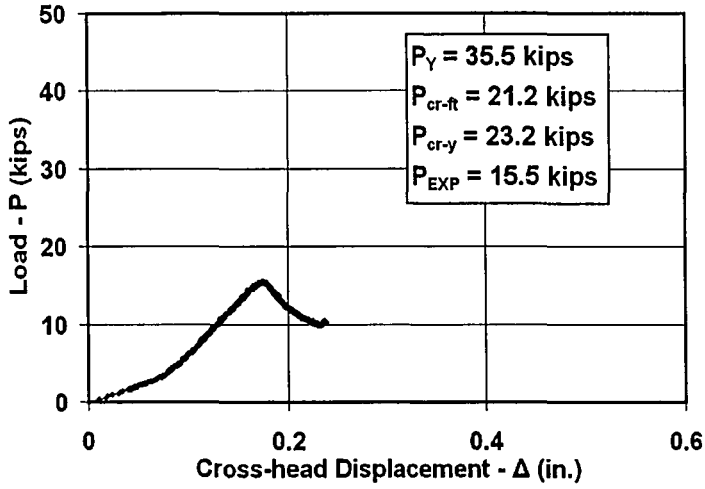

Figure 6.35 SC6 Specimen Load vs. Cross-head Displacement

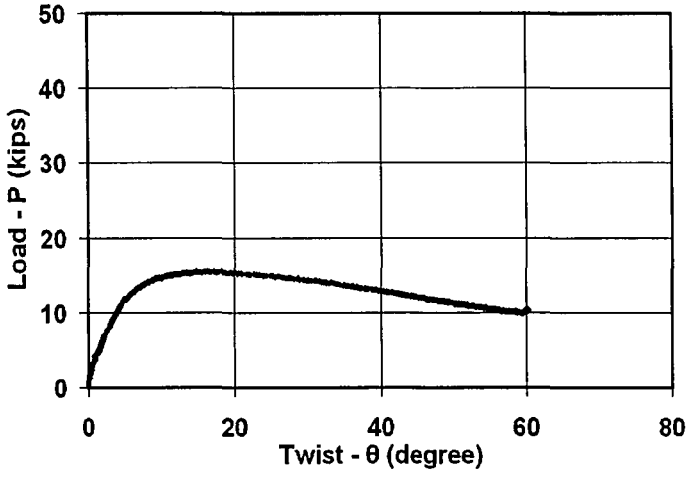

Figure 6.36 SC6 Specimen Load vs. Twist

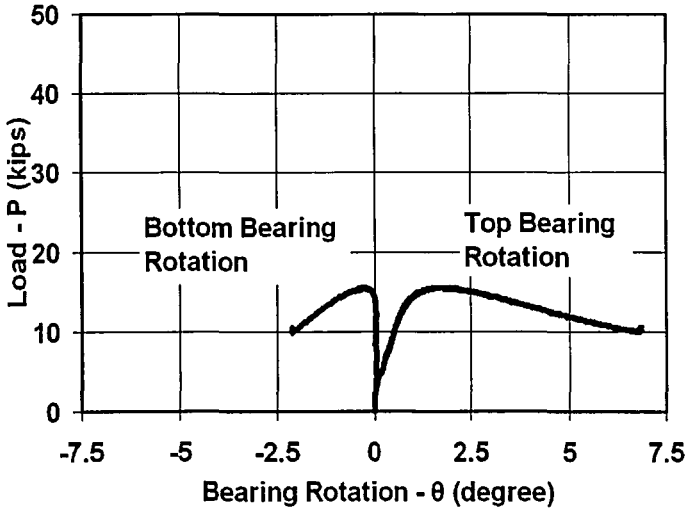

Figure 6.37 SC6 Specimen Load vs. Bearing Rotation

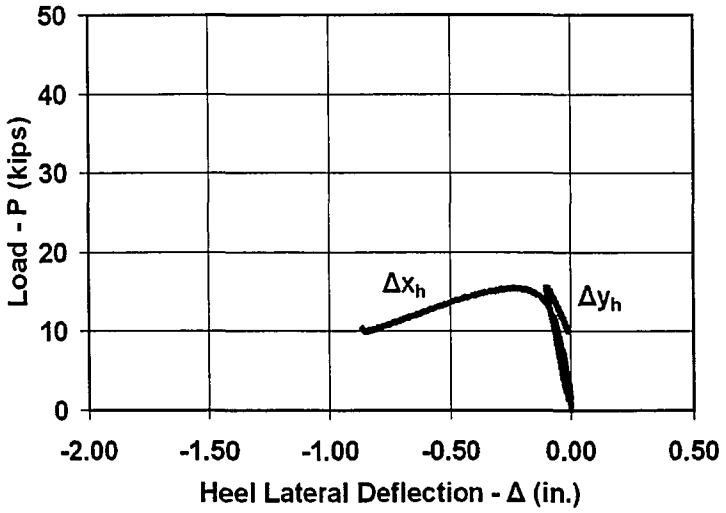

Figure 6.38 SC6 Specimen Load vs. Heel Lateral Deflection

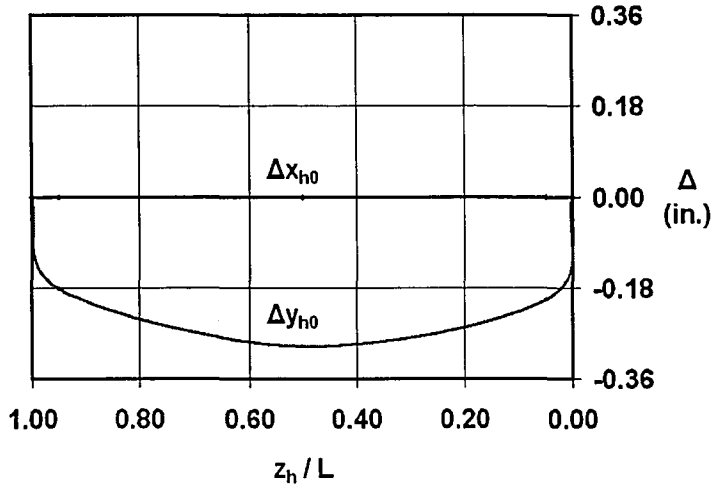

Figure 6.39 SC6 Specimen Initial Out-of-Straightness

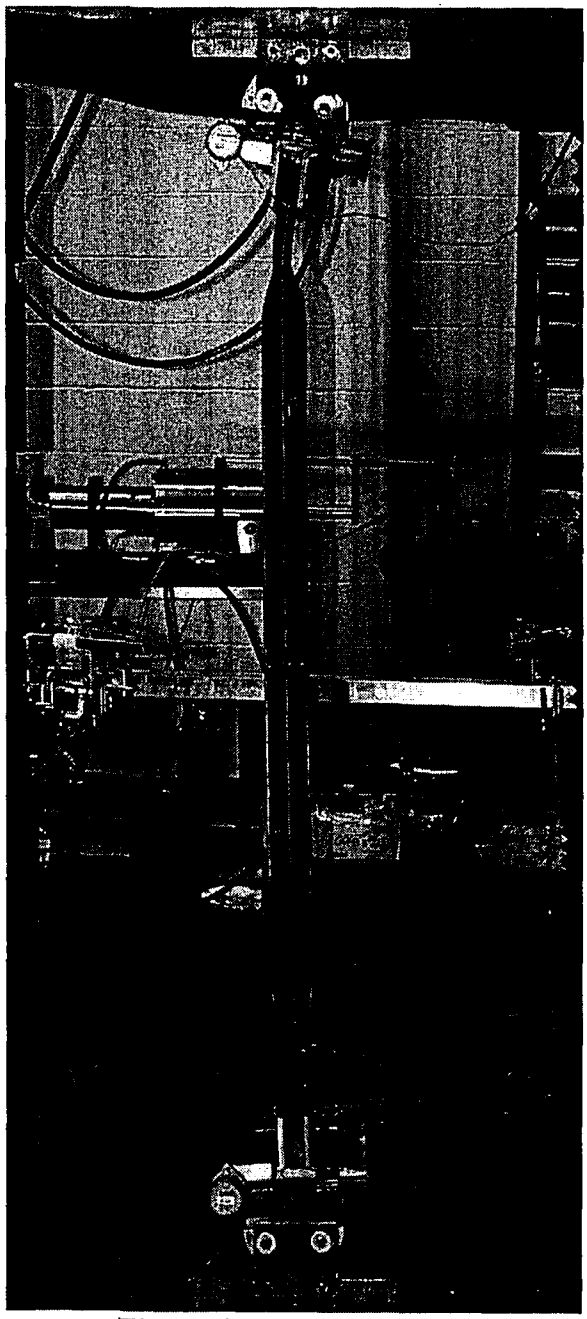

Figure 6.40 Specimen SC6

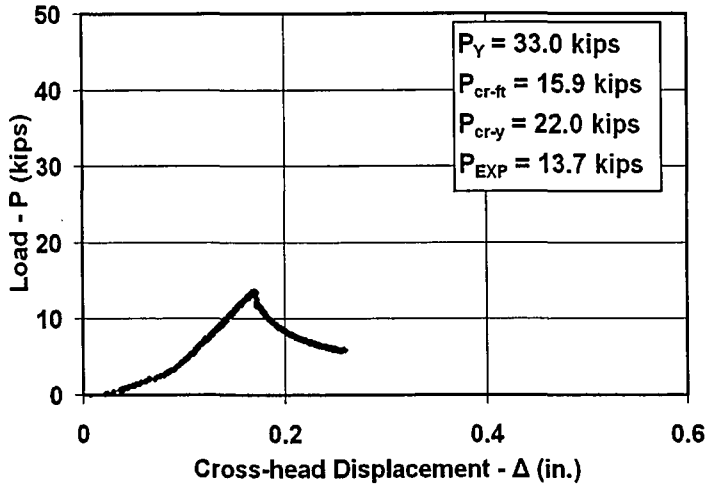

Figure 6.41 SD1 Specimen Load vs. Cross-head Displacement

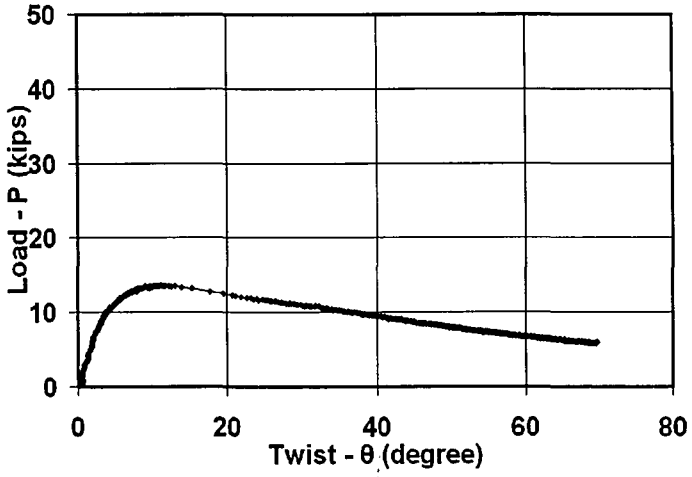

Figure 6.42 SD1 Specimen Load vs. Twist

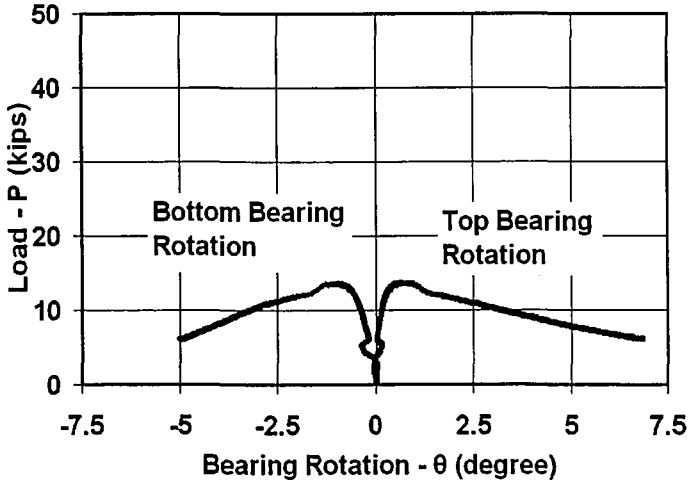

Figure 6.43 SD1 Specimen Load vs. Bearing Rotation

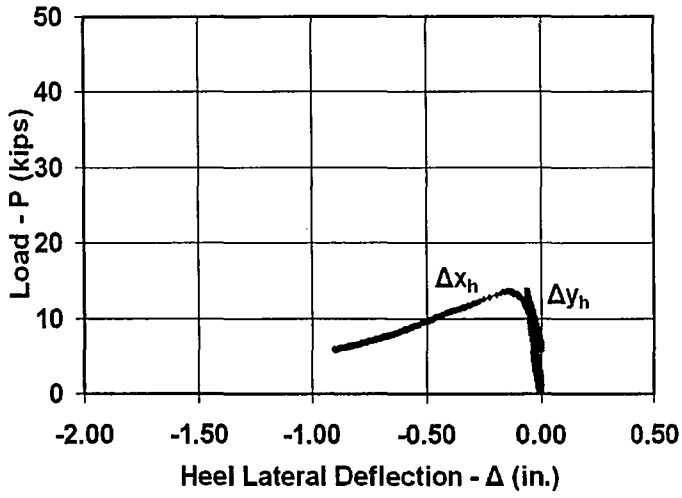

Figure 6.44 SD1 Specimen Load vs. Heel Lateral Deflection

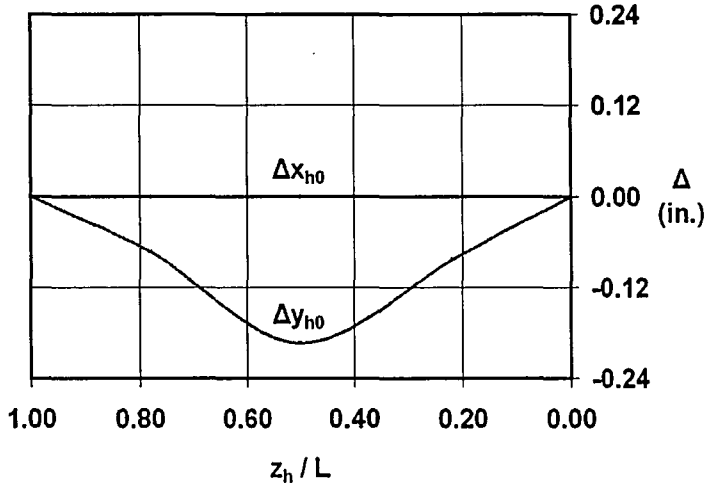

Figure 6.45 SD1 Specimen Initial Out-of-Straightness

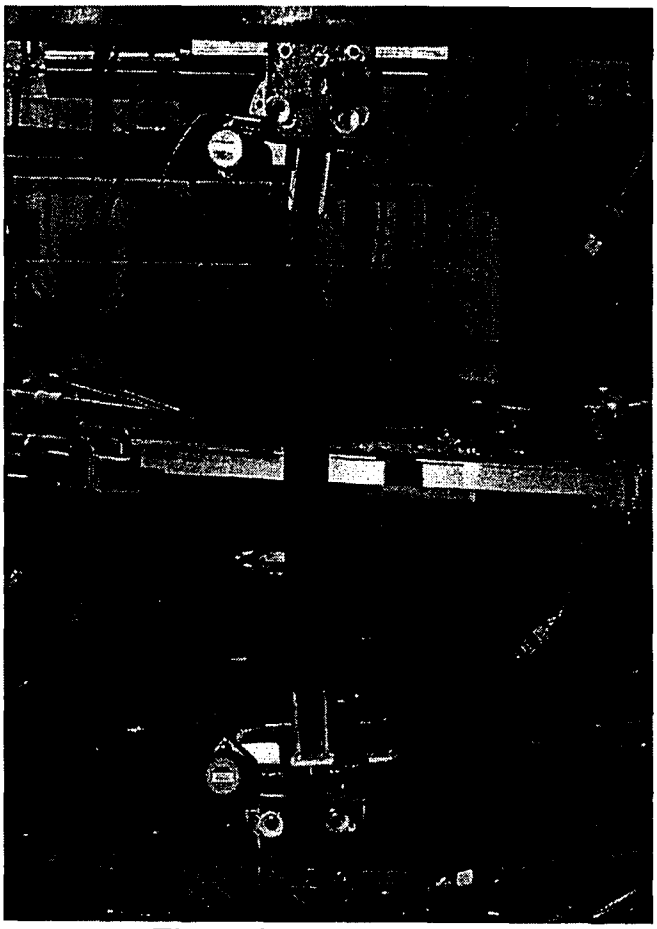

Figure 6.46 Specimen SD1

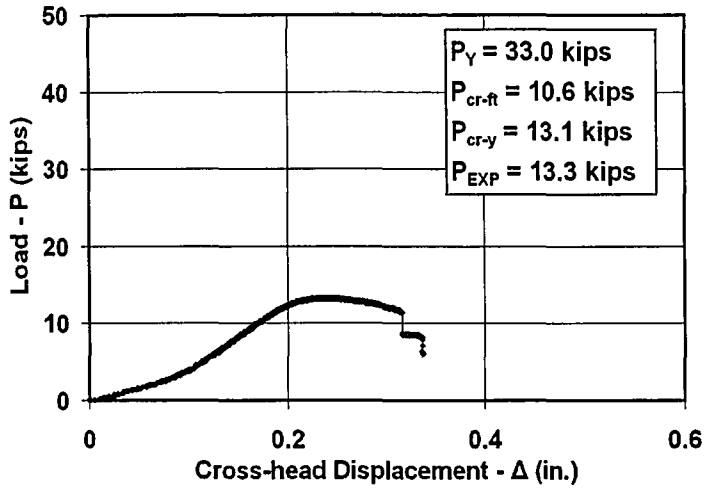

Figure 6.47 SD2 Specimen Load vs. Cross-head Displacement

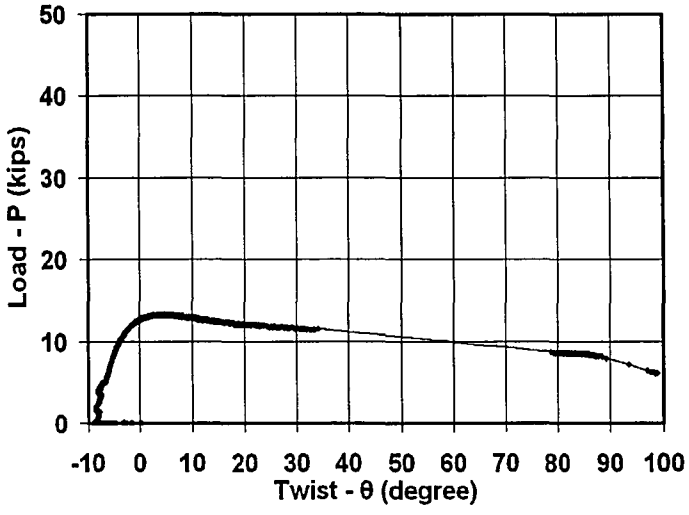

Figure 6.48 SD2 Specimen Load vs. Twist

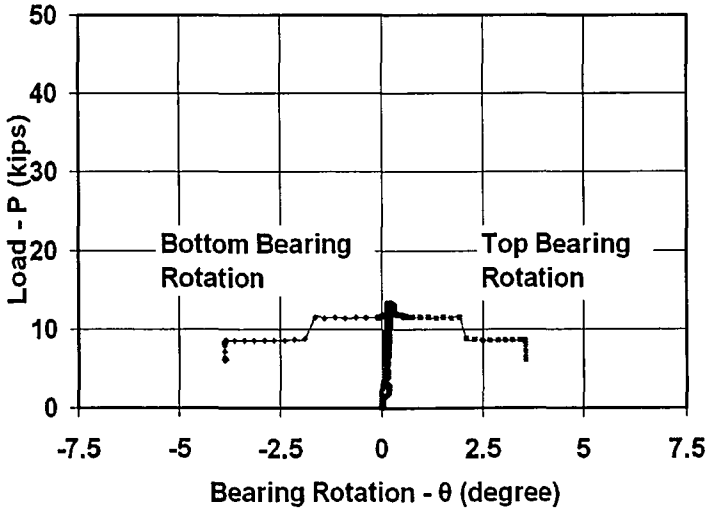

Figure 6.49 SD2 Specimen Load vs. Bearing Rotation

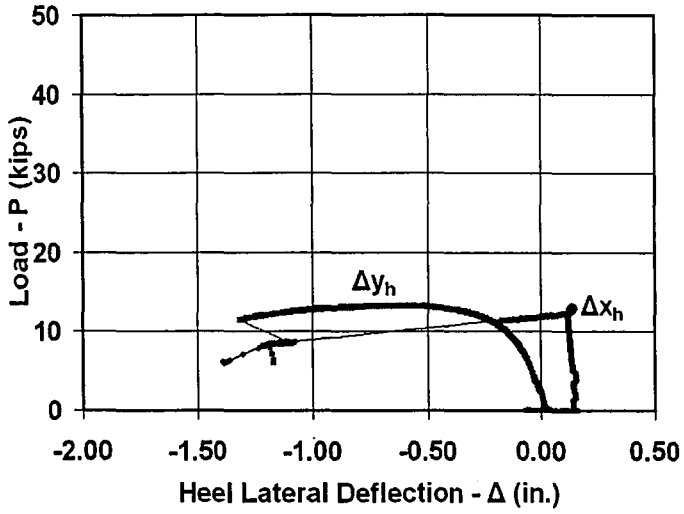

Figure 6.50 SD2 Specimen Load vs. Heel Lateral Deflection

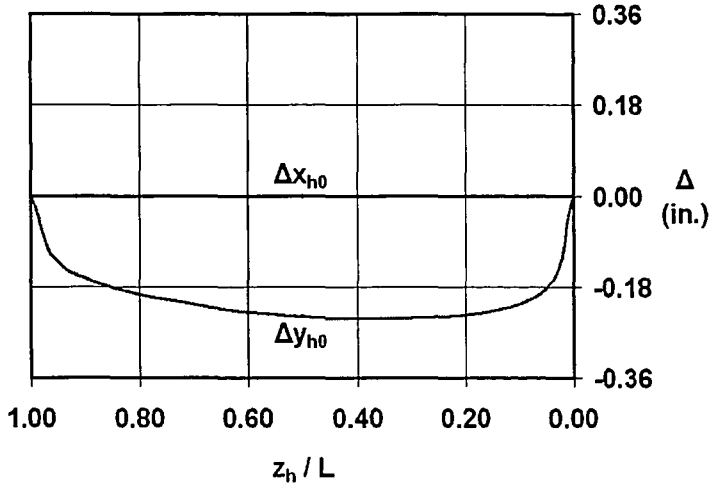

Figure 6.51 SD2 Specimen Initial Out-of-Straightness

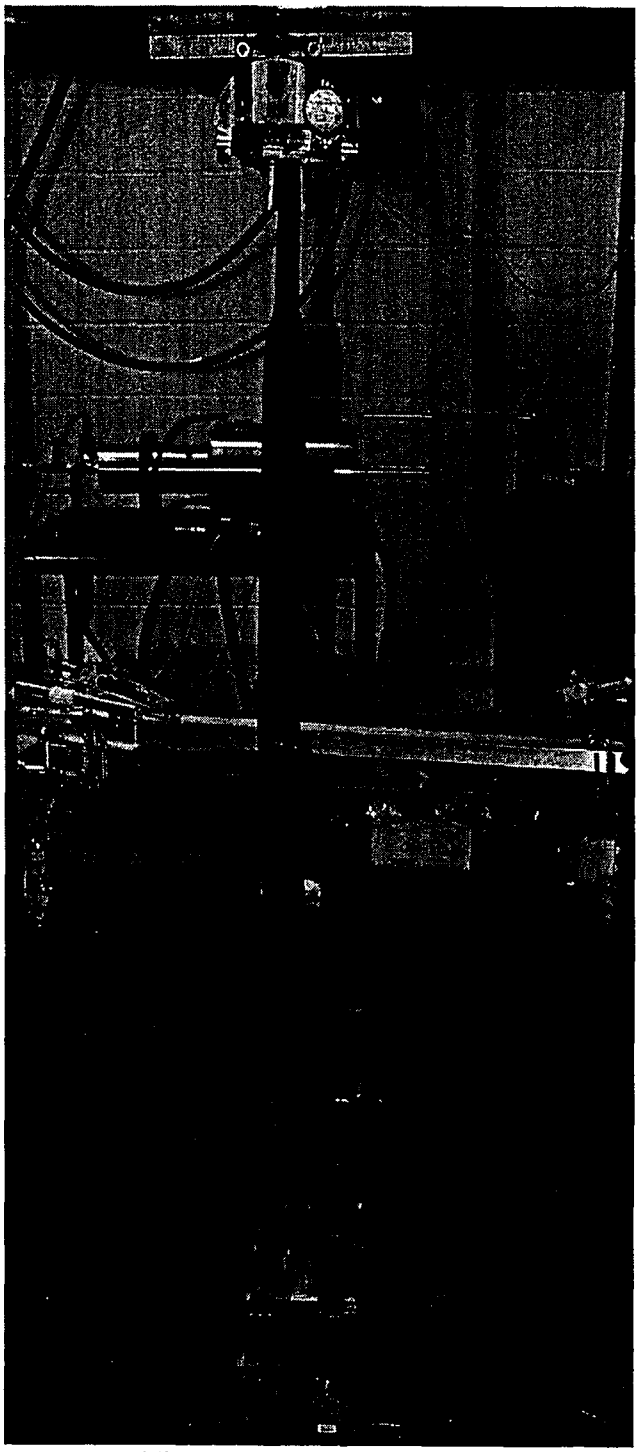

Figure 6.52 Specimen SD2

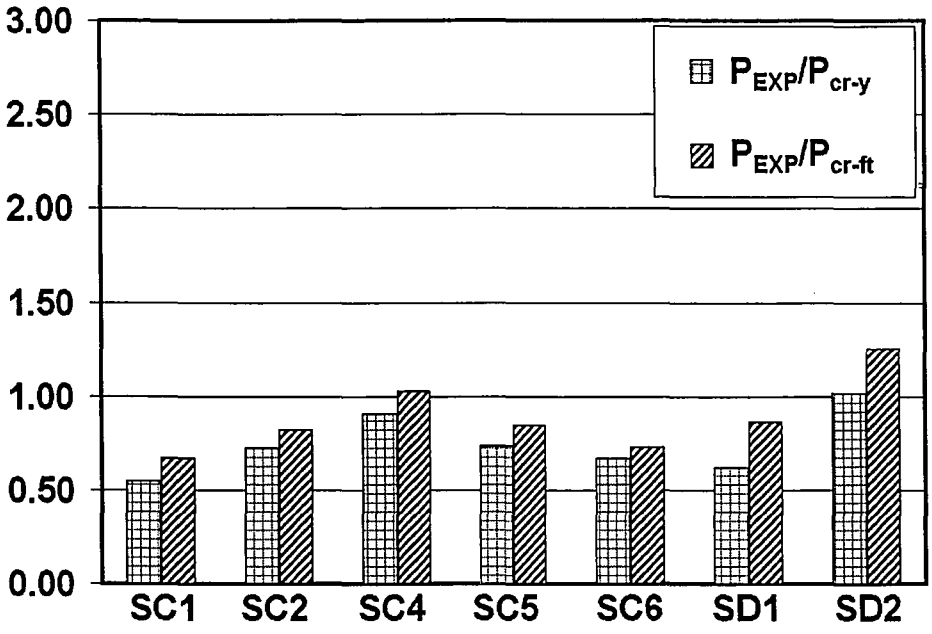

Figure 6.53 Predicted vs. Experimental Results

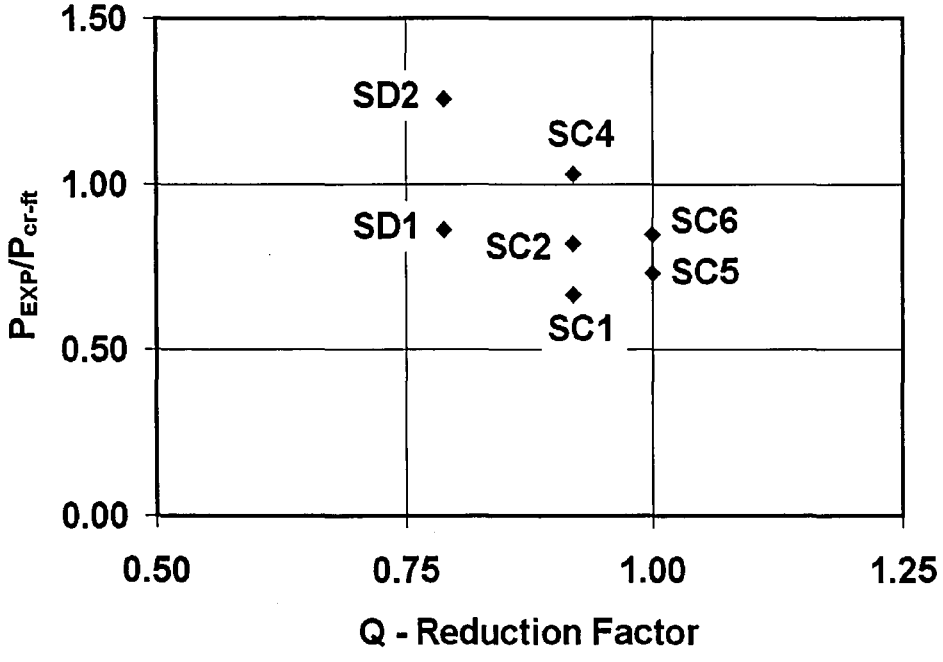

Figure 6.54 Experimental Results vs. Q Reduction Factor

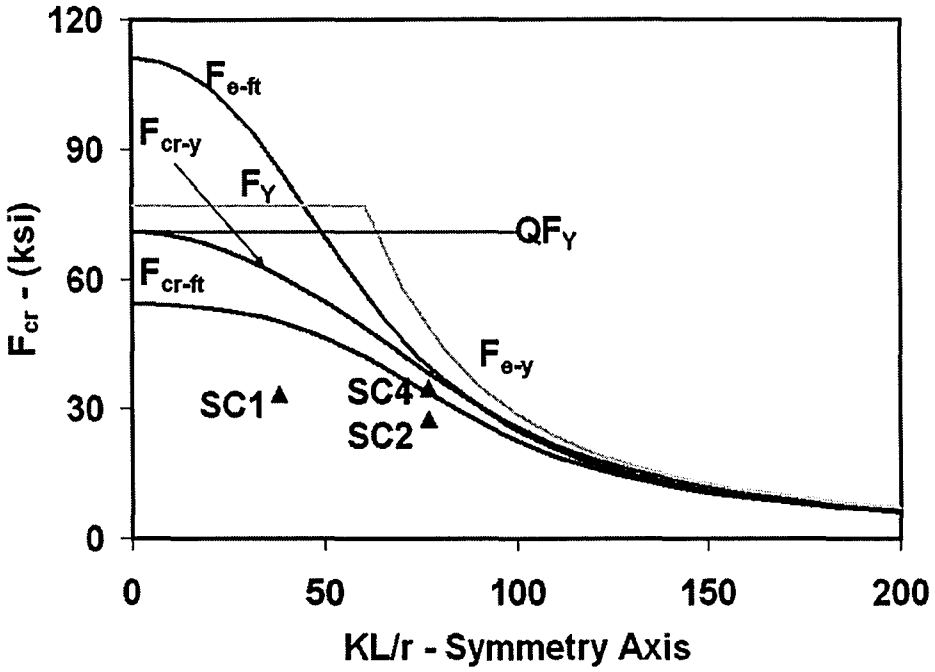

Figure 6.55 Comparison of Experimental Results with Theoretical Results for SC1, SC2, and SC4 (Vanadium Steel) Specimens

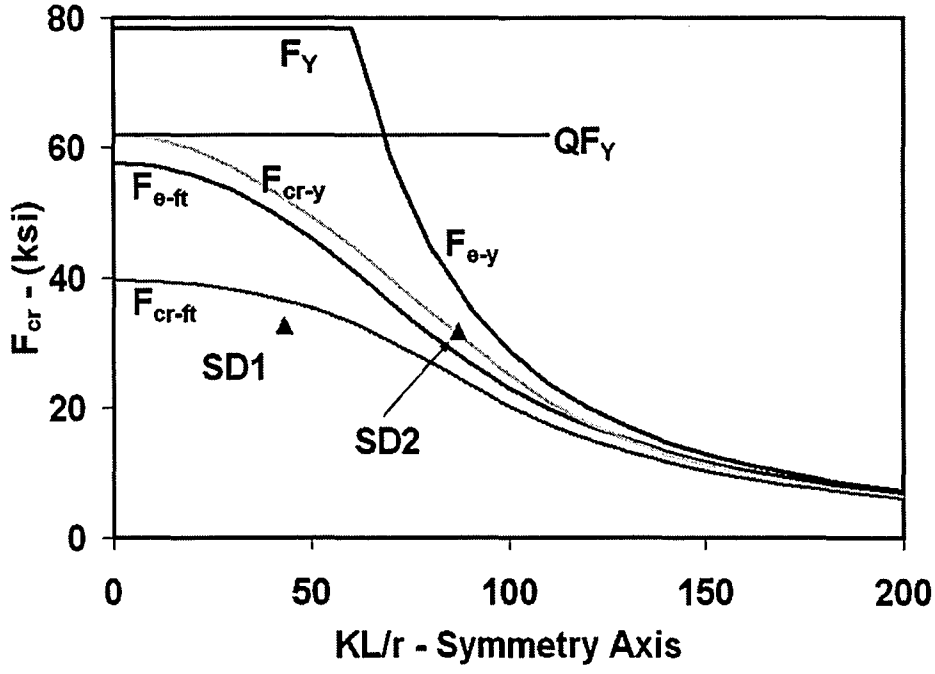

Figure 6.56 Comparison of Experimental Results with Theoretical Results for SD1 and SD2 (Vanadium Steel) Specimens

Chapter 7 Double Angle Truss Subassemblies

7.0 General

The double angle members in the truss subassemblies have end conditions that closely simulate the end conditions seen in real trusses. The angle legs of the double angle members have equal width and thickness. This chapter is organized as follows. First, the test matrix is presented and the purpose of each test specimen is summarized. Then, the test setups are presented. Then, the instrumentation and the test procedures are described. Then, analysis results for the truss specimens are presented. Finally, the test results are presented and discussed.

7.1 Test Matrix

The specimens are identified by the loading pattern used to test them and are either constant moment (CM) specimens or gradient moment (GM) specimens.

The CM truss specimens were tested to evaluate the behavior of Vanadium steel truss compression chord members near the truss mid-span where the overall moment reaches its maximum value and the overall shear is small. A CM truss specimen is shown in Figure 7.1. The web members are designed to carry no force other than the force needed to brace against in-plane buckling of the compression chord members. These test specimens are tested under constant moment to apply constant axial loads to the chords as shown in Figure 7.1.

The GM truss specimens were tested to evaluate the behavior of Vanadium steel truss members when the truss is under combined overall shear and moment. The

diagonal web members are of interest for GM tests. The GM test specimens were designed so that web members C1 and C2, shown in Figure 7.2, would fail. F1 and F2 represent the transverse loads applied to the truss specimen.

As seen in Table 7.1, the test matrix consists of 5 CM and 2 GM test specimens, showing that greater priority was given to the chord members because they account for a greater part of a truss weight than the web members.

As indicated in Table 7.1, specimen C1 is the base case for the CM tests. Figure 7.1 shows specimen C1, where chord and web members are represented by their lines of action. The chords of the truss specimen are identified by the type of loading, for example the west chord in Figure 7.1 is loaded under compression, C, and thus this chord is called the compression chord. The joints between the web members and the chords of the truss are referred to as panel points, and these panel points are numbered P1 through P9 for the CM specimens. In Figure 7.1, the dimensions between these panel points are shown.

In the test of specimen C1, the middle panel of the compression chord between P3 and P5 (Figure 7.1), is expected to fail in the flexural-torsional buckling mode. Thus, displacement in the out-of-plane direction of the truss specimen near panel point P4 is expected. Specimen C2 omits the vertical web members of test specimen C1, and in-plane flexural buckling of the middle panel is expected, with in-plane displacement near panel point P4. Specimen C3 is identical to Specimen C1, except that at the bracing locations of specimen C3, the out-of-plane rotations of the joints (i.e., the

rotations about the transverse in-plane axis of the chord that accompany out-of-plane displacements) were restrained. These out-of-plane rotations were unrestrained for specimen C1. Thus, flexural-torsional buckling is expected in the middle panel, but with a larger load in the compression chord. The bracing locations for each specimen will be discussed later. Specimens C4 and C5 were tested to show the effect of mid-spacers in the chord members on the buckling capacity of the chord members. The mid-spacers between the panel points are of interest for these two test specimens. Specimens C4 and C5 are expected to also fail by flexural-torsional buckling of the middle panel of the compression chord.

In the tests of the GM specimens, the effects of eccentricities introduced at the ends of critical diagonal web members were studied. These eccentricities include the connection eccentricity and the weld eccentricity, as indicated in Table 7.1. Figure 7.2 shows specimen G2. The key locations on the GM truss specimens are: the joints at the ends of the critical diagonal web members, C1 and C2; the mid-length of the critical diagonal web members; and the applied load locations. These locations are numbered P1 through P7 for the GM specimens. In Figure 7.2, the dimensions between the panel points of the GM specimens are shown.

In the test of specimen G2, web members C1 and C2 were expected to fail by flexural-torsional buckling mode. Web member C1 has an eccentric connection with the chords, but web member C2 has a concentric connection. In the eccentric connection, the intersection of the lines of action of the adjacent web members that are

connected at a panel point does not coincide with the line of action of the chord member. The effect of connection eccentricity on the buckling capacity of these web members in trusses was studied in this test specimen.

In the test of specimen G4, web members C1 and C2 were designed to fail at their welds to the chords of the truss specimen. The centroids of the welds at the ends of web member C1 are eccentric with the centroidal axis of the web member. For web member C2, the centroids of the welds at the ends of the web member coincide with the centroidal axis of the web member.

7.2 Test Setups

The test setups for the CM and the GM specimens have many similarities. In the following discussion, the parts of the test setups that are the same in these two setups are described first. Then the parts that differ are discussed.

The overall layout of the CM test setup is shown in Figure 7.3. As shown in this figure, there is a girder at each end of the CM specimen. The one on the left in this figure is the reaction girder. This girder is attached to three columns, which are attached to the lab strong floor to provide fixity. The loading girder, which is on the right in Figure 7.3, is allowed to translate and rotate in-plane with the test specimen.

The CM test setup has two actuators located as shown in Figure 7.3. These actuators are identified by their location in the test setup, for example, the east actuator is on the east of the setup. Figure 7.3 also indicates the other parts of the test setup, which are the pedestal beams, the bracing, and the clevises used at the connections

between the truss and the girders, and also at the connections between the actuators and the girders. The clevises of the actuators are spherical which allows both in-plane and out-of-plane rotations at the ends of the actuators.

The overall layout of the GM test setup is shown in Figure 7.4. Three major differences between the GM test setup and the CM test setup are: (1) the actuators used in the GM tests have a smaller size and load capacity, (2) these actuators located to apply transverse load, and (3) the loading girder is used as the actuator reaction girder as shown in Figure 7.4. The actuators are positioned to load the test specimens in shear. The loading girder used in the CM specimen tests was relocated and fixed such that the actuators could be attached to it, as shown in Figure 7.4. This girder, called the actuator girder, is also attached to three columns, which are attached to lab strong floor to provide fixity. Figure 7.4 also shows the other parts of the GM test setup, such as the clevises.

7.2.1 Loading, Reaction, and Actuator Girders

The CM test setup used the loading girder and the reaction girder. The loading girder displaces with the specimen but the reaction girder is restrained by columns that are fixed to the floor. These girders were centered at the height of the centroid of the chord by using leveling plates and wide flange sections, as shown in Figure 7.5(a). Figure 7.5(a) also shows a cross-section view of the reaction girder and the columns were used to achieve fixity to the lab floor. For the loading girder of the CM test setup, the details of the girder and supporting wide flange sections are the same. However,

the leveling plates are coated with teflon to decrease the friction between the surfaces of the leveling plate and the wide flange sections as the loading girder displaces with the specimen.

The GM specimen tests used the reaction girder and the actuator reaction girder. The reaction girder used for the CM specimen tests was left in place, as shown in Figure 7.4. The actuator reaction girder was the same girder used as the loading girder for the CM specimen tests. However, the actuator reaction girder was attached to columns fixed to the lab strong floor, as shown in Figure 7.5(b).

7.2.2 Actuators

Different actuators were used for the CM specimen tests and the GM specimen tests. For the CM tests, two actuators with 600 kip load capacity were used. Figure 7.3 indicates the positions of the actuators in the test setup. Both ends of the actuators in the CM tests were attached to the girders as shown in Figure 7.5(a).

For the GM tests, two actuators with 110 kip load capacity were used. Figure 7.4 shows the positions of the actuators in the test setup. One end of each actuator in the GM tests was attached to the truss specimens while the other end was attached to the actuator reaction girder. The details of the actuator connections to the truss are shown in Figure 7.6. As shown in Figure 7.6(a), bracing was used at the north actuator connection to the truss. A gusset plate welded between the double angles of the chord extended beyond the outside surface of the chord. This part of the gusset plate had a 3 in. diameter hole for the clevis pin that attaches the clevis at the end of the actuator rod

to the gusset plate. Figure 7.6(b) indicates the south actuator connection to the truss. The bracing details of these actuator connections to the truss specimen will be discussed later.

7.2.3 Pedestal Beams

As seen in Figure 7.7(a), wide flange beams were used underneath the truss specimens. These beams, referred to as pedestal beams, were located under the truss chords. The pedestal beams raised the truss specimens to the proper height and provided a base for the bracing. The pedestal beams were attached to the reaction floor and each other with pairs of channel sections spaced at 5 ft. The channel sections are referred to as attachment beams for the pedestal beams. As Figure 7.7(b) indicates, the two channel sections were placed back-to-back and a steel top plate was attached to the lab strong floor by 3 in. diameter bolts. The attachment beams were welded to the pedestal beams.

7.2.4 Bracing Detail

The test setups had bracing at selected panel points to simulate the bracing effect provided by joist or deck attachments to a truss. There were two types of bracing utilized in the tests.

The first type of bracing (Bracing Type 1) allows out-of-plane rotation at the bracing location. The out-of-plane rotation refers to rotation about an axis transverse to the truss but in the plane of the truss. This rotation is associated with out-of-plane displacement of the chord between the bracing points. A cross-section view of this

type of bracing is shown in Figure 7.8(a).

As seen in Figure 7.8(a), the bracing function is achieved by a top plate, which is referred to as the bracing plate, and a pedestal beam (i.e., the out-of-plane displacement of the chord is restrained by the bracing plate and the pedestal beam). The bracing plate is connected to the pedestal beam by threaded rods passing through tubes which are welded to the side plates of the pedestal beam, or attached to the flange of the pedestal beam.

Figure 7.8(a) shows a 1 in. round steel bar, which is referred to as a dowel, which is welded to the chords of the specimen at the bracing location. At each end of the dowel, two round plates are used. The smaller plate is actually a short section of hollow 1-1/2 in. pipe. The larger plate has a 3 in. diameter. The short pipe was welded to the larger 3 in. round plate, and was used to permit the dowel to rotate out-of-plane, while staying near the center of the 3 in. round plate. The 3 in. diameter steel plate was designed to slide on the bracing plate or the pedestal beam. The sliding surface of the 3 in. diameter plate was coated with teflon to decrease the friction. Small gaps, approximately 1/8 in., were left at the ends of the dowel to allow it to rotate freely. Figure 7.8(b) shows an example of this type of bracing which will be referred to as Bracing Type 1.

The second type of bracing, shown in Figure 7.8(c), restrains the out-of-plane rotation. Compared to the first type of bracing, the second type of bracing omits the round plates and instead uses rectangular plates. The rectangular plates were welded to

the dowel to restrain the out-of-plane rotation. The sliding surfaces of these rectangular plates, which slide on the bracing plate or pedestal beam, were also coated with teflon to decrease the friction. This second type of bracing, called Bracing Type 2, was used only for test specimen C3.

7.2.5 Clevises at the Truss-to-Girder Connections

In the CM and the GM tests, the boundary conditions where the truss ends are attached to the girders were pin-ended connections. These end conditions were achieved by using clevises with pins allowing in-plane rotations of the truss specimens. The parts of a typical clevis are shown in Figure 7.9(a). As seen in this figure, the pins of the clevises pass through shim plates and the gusset plate that extends out from the chord member of the truss.

As seen in Figure 7.1, panel point P1 of the north panel is assumed to occur at a "working point" which is 2 in. from the end cross-section of the chord member. A "working point" is defined as the intersection of the centroidal axes of the web and the chord members. The lengths of the compression chord members are taken as the distance between the working points. However, the pins of the clevises are 7 in. away from the end cross-section of the chord members. The shim plates, shown in Figure 7.9(a), were intended to stiffen the gusset plate which would then restrain the out-of-plane displacement of the gusset plate and restrain the out-of-plane displacement of panel point P1. In the test setup for specimen C1, snug-fitting shim plates were not included at the clevises. During the test of specimen C1, out-of-plane rotation of the

gusset plate permitting out-of-plane displacement of the working point P1. This out-of-plane displacement influenced the test results, as described later, and snug-fitting shim plates were used for the remaining truss tests.

Figure 7.9(b) shows details of the connections at the clevises. As seen from this figure, clevises are bolted with threaded rods to the girders. Figure 7.9(b) shows the shim plates that were welded to the truss gusset plates. The holes for the 3 in. diameter pin were fabricated so that the pin fit tightly.

7.3 Instrumentation and Test Procedures

In this section, the instrumentation and the test procedures for both the CM and the GM tests are presented.

7.3.1 Instrumentation for CM Tests

The intended experimental results included the axial load on the compression and the tension chord, the axial shortening of the compression chord, the in-plane deflection measurements of the panel points, the in-plane and out-of-plane deflection measurements at the mid-length of the panels on the compression chord, and strain measurements. For compression members with symmetric boundary conditions, the mid-length cross-section is the critical section, thus the deflection at the mid-length cross-section of each panel of the compression chord was taken as the deflection of the critical section.

A total of 28 LVDTs, 4 strain gages (SGs), and 2 string pots (SPs) were used to measure the response. Table 7.2 indicates the location of the instruments and the data obtained. LVDTs and SPs were mounted on brackets which were grouped together on separate stands. These stands were positioned near the compression chord of the truss specimens and also near the loading and the reaction girders. Figure 7.10 shows the instrument attachments to the test setup. The LVDTs (and SPs) that were attached to the compression chord were attached to either panel points or the mid-length of the panels of the chord. Figure 7.11 shows more detail of the LVDT (and SP) attachments to the compression chord.

As seen in Table 7.2, instruments measured in-plane displacements at the panel points of the compression chord. Since, the compression chord was expected to buckle out-of-plane, other instruments were used to measure out-of-plane displacements of the compression chord, denoted in Table 7.2 as "in-space" displacements, because displacements in all three coordinate directions were measured. For instance, as shown in Figure 7.11, LVDTs 3, 4, and 5 were positioned such that the out-of-plane displacements could be measured at P2, and LVDT6 and LVDT7 were positioned such that in-plane displacements could be measured at P3. Figure 7.12 shows the instrumentation in place.

The in-plane displacements at the panel points of the compression chord were calculated using a procedure similar to that used to calculate the lateral deflections of the heel of the single angle members in the single angle member compression tests, as

presented in Section 4.3.3. Both calculations made use of the Law of Sines and Law of Cosines, and two LVDTs were utilized. For the truss tests, these two LVDTs were attached to the mid-spacers of the compression chord of the trusses, as shown in Figure 7.12. The detail in Figure 7.13 shows that a small nut was welded to the mid-spacers to attach the LVDT wires.

In order to calculate the displacements at a mid-panel point where 3-dimensional displacements (in-space displacements, as shown in Table 7.2) occur, such as P2, P4, and P6, 3 LVDTs (or SPs) were utilized to take measurements. In Figure 7.13, one LVDT is shown at such a location and it is referred to as LVDT1. The "in-space" displacements of the "heel" of the double angle chord (shown in Figure 5.8) were calculated in 3 directions as follows.

For LVDT1, the direction of the LVDT is projected on the three coordinate directions using the angles between the direction of LVDT1 and each coordinate direction. The coordinate system used for the CM tests is shown in Figure 7.3.

$$\cos(\theta_{X,1}) = \frac{X_h - X_1}{L1 + \Delta 1}$$
$$\cos(\theta_{Y,1}) = \frac{Y_h - Y_1}{L1 + \Delta 1}$$
$$\cos(\theta_{Z,1}) = \frac{Z_h - Z_1}{L1 + \Delta 1} \qquad (7.1)$$

where the cosines of the angles are called the direction cosines and

X_h , Y_h , Z_h : the coordinates of the "heel" at a displaced position

X_1 , Y_1 , Z_1 : the coordinates of LVDT1

$L1$: the initial distance between the attachment points of LVDT1

$\Delta 1$: the length change measured by LVDT1 at a displaced position of the cross-section

$(\theta_{X,1})$, $(\theta_{Y,1})$, $(\theta_{Z,1})$: the angles between the direction of LVDT1 and the coordinate directions at a displaced position of the cross-section

Equation (7.1) shows the direction cosines for LVDT1. Similar equations are written for LVDT2 and LVDT3, which are attached to the same point. Then, the three sets of direction cosines are used in the following equation:

$$\begin{bmatrix} \cos(\theta_{X,1}) & \cos(\theta_{Y,1}) & \cos(\theta_{Z,1}) \\ \cos(\theta_{X,2}) & \cos(\theta_{Y,2}) & \cos(\theta_{Z,2}) \\ \cos(\theta_{X,3}) & \cos(\theta_{Y,3}) & \cos(\theta_{Z,3}) \end{bmatrix} \times \begin{pmatrix} dX_h \\ dY_h \\ dZ_h \end{pmatrix} = \begin{pmatrix} d\Delta 1 \\ d\Delta 2 \\ d\Delta 3 \end{pmatrix} \tag{7.2}$$

where

dX_h , dY_h , dZ_h : the incremental displacements of the "heel" during one step of the data acquisition system

$d\Delta 1$, $d\Delta 2$, $d\Delta 3$: the incremental length changes measured by LVDTs 1, 2, and 3 during one step of the data acquisition system

Equation (7.2) has the form:

$$\underline{A} \times \underline{b} = \underline{x} \tag{7.3}$$

where

$\underline{A}$: the matrix of the direction cosines

$\underline{b}$: the matrix of the incremental displacements of the "heel"

$\underline{x}$: the matrix of the incremental length changes measured by each LVDT

The $\underline{b}$ matrix can be determined for each step as follows:

$$\underline{b} = \underline{A}^{-1} \times \underline{x} \tag{7.4}$$

where $\underline{A}^{-1}$ represents the inverse of the matrix $\underline{A}$.

Equation (7.4) provides the incremental displacements of the "heel" during one step of the data acquisition system. The calculation of the incremental displacements of the "heel" is based on the assumption that the angles that determine the direction cosines for an LVDT do not change during a step of the data acquisition system. After each step, the "heel" position coordinates (X_h, Y_h, Z_h) are updated with the calculated incremental displacements. Then the direction cosines are updated. Finally, the lateral displacements are found by the following equation:

$$\begin{aligned} \Delta X_h &= X_h - X_{h0} \\ \Delta Y_h &= Y_h - Y_{h0} \\ \Delta Z_h &= Z_h - Z_{h0} \end{aligned} \tag{7.5}$$

where

X_{h0} , Y_{h0} , Z_{h0} : the initial coordinates of the "heel"

ΔX_h, ΔY_h, ΔZ_h : the relative lateral displacements of the "heel".

7.3.2 CM Specimen Testing Procedure

The CM specimens were loaded by rotating the loading girder, as shown in Figure 7.14. This rotation was applied by extending the east actuator and retracting the west actuator. The loading was intended to be pure moment, with the total axial load applied to the loading girder being negligible. The east actuator applied a compressive force to the loading girder while the west actuator applied a tensile force to the loading girder. A computer program was written to control the loading by either extending the east actuator or retracting the west actuator in each load step. The program attempted to keep the total axial load on the truss close to zero.

As the compression chord failed in a panel, the loads in the actuators decreased as they continued to be extended or retracted. For specimens C1, C2, and C3, testing was finished when the actuator loads reached to half of their peak values.

For specimens C4 and C5, the testing continued after the failure of compression chord (denoted as Test 1). First, the loads in the actuators were taken to zero load by reversing their direction (i.e., retracting the east actuator and extending the west actuator). Then, a second test of the truss was carried out to fail the east chord in compression (denoted as Test 2). For the second phase of testing (Test 2) the east actuator was retracted and the west actuator was extended (i.e., the loading pattern was reversed while, again, the computer program attempted to keep the total axial load

close to zero). After failure was observed in Test 2, the loads in the actuators decreased as they continued to be extended or retracted. When the actuator loads reached to half of their peak values the test was stopped.

7.3.3 Instrumentation for GM Tests

The LVDT brackets and stands that were used for the CM tests were also used for the GM tests. The critical cross-sections for the GM tests are the mid-length cross-sections of the critical diagonal web members C1 and C2. The instrumentation used for the GM tests are presented in Table 7.3. A total of 18 LVDTs and 8 strain gages were used. The layout of the instrumentation is shown in Figure 7.15.

Strain gages were placed near mid-length cross sections of the critical web members. Two gages were attached each angle of these members on the outstanding legs, as shown in Figure 7.15(b).

As seen in Table 7.3, many of the instruments measured in-plane displacements of either the bracing or the actuator connection locations. The in-plane displacements of these locations were calculated using the procedure developed for the lateral deflections of the heel of the single angle members, presented in Section 4.3.3, as discussed earlier for the CM tests. The LVDTs were attached to dowels at the bracing or the pins at the actuators connection locations.

At the mid-length cross-sections of the critical diagonal web members C1 and C2, 3-dimensional measurements (in-space displacements, as shown in Table 7.3) were acquired. The calculations of these displacements were similar to the calculations for

the "heel" displacements at in-space displacement locations for the CM tests, presented in Section 7.3.1.

Figure 7.16(a) and Figure 7.16(b) show the web members C2 and C1, and the layout of the instrumentation used at their mid-length cross-sections. These figures also show the coordinate axis system for the heel measurements.

7.3.4 GM Specimens Testing Procedure

The GM tests consisted of 3 phases to test the two critical diagonal web members, C1 and C2, as shown in Figure 7.17.

The first phase of testing is shown in Figure 7.17(a) where the north and south actuators were retracted at different rates. The retraction rate of the south actuator was larger than the retraction rate of the north actuator, and as a result, the north actuator applied a compressive force to the truss while the south actuator applied a tensile force. The displacement rates of the actuators were controlled so the forces in the actuators had an approximate 2 to 1 ratio during the linear elastic range of behavior. These forces produced shear in the right panel of the truss, as shown in Figure 7.17(a). After web member C1 failed, the second phase of testing was started.

The second phase of testing is shown in Figure 7.17(b). This phase aimed to decrease the loads in the actuators to zero without damaging any members in the truss specimen other than member C1. Thus, the load in the south actuator was taken to a similar load to the north actuator load by reversing the direction of the south actuator while the displacement of the north actuator was kept constant (i.e., $\Delta_{north} = 0$ while

the south actuator was extending). After similar load levels were observed in both actuators, they were both extended until the loads in the actuators were zero. Then, before moving into the third phase of testing, the pin of the south actuator at its truss connection was disconnected.

The third phase of testing is shown in Figure 7.17(c). At this phase, the north actuator was retracted until web member C2 failed. Then, the actuator continued to retract until the load in the north actuator was reduced to half of the peak load level. Then the test was terminated.

7.4 Analyses of the Truss Specimens

7.4.1 CM Specimens

These analyses determined the relationship between the applied actuator forces and the force on the compression chord. To achieve this purpose the following steps were followed:

1. Compression Chord Capacity Analysis According to the AISC (2005) Specification: This step estimated the buckling capacity of the compression chord. As presented in Section 7.1, the middle panel of the compression chord of the CM test specimens is the critical panel of the chord, because the length of the middle panel is larger than the length of the south and north panels. The chord members of the trusses are double angle cross-sections and the buckling capacity was determined according to the provisions of the AISC (2005) specification, using the procedures presented in Section 5.4.

When Bracing Type 1 was used, the effective length factor, K, was taken as 1.0. In real roof or floor trusses, however, a connection to a steel deck or a transverse joist may provide enough restraint to justify a smaller effective length factor. When Bracing Type 2 was used, K was 1.0 for in-plane buckling and 0.5 for out-of-plane buckling.

2. Overall Static Analysis in Undeformed Condition: This step was determined the required actuator capacities based on the buckling capacity of the compression chord. As shown in Figure 7.18(a), the compression chord buckling capacity, found in step 1 above, was applied to the chords of the truss specimens to determine the corresponding forces in the actuators. The actuator forces were found as follows.

From Figure 7.18(a) the forces in the truss chords were related to the total moment and axial force applied by the actuators on the loading girder:

$$\sum P_X = 0$$
$$P_C - P_T - P_{total} = 0 \tag{7.6}$$

where

P_C : the buckling capacity of the compression chord, found in step 1, applied to the compression chord as an axial load

P_T : the buckling capacity of the compression chord, found in step 1, applied to the tension chord as an axial load (assuming no net axial force

acts on the truss)

P_{total} : the total force applied by the actuators on the loading girder

$$\sum M_{total} = 0$$
$$(-1)\times(P_C + P_T)\times(1.75ft.) + M_{total} = 0 \quad (7.7)$$

where

M_{total} : the total moment applied by the actuators on the loading girder

Then the actuator forces were related to the total moment and axial force using Figure 7.18(b), resulting in the following equations:

$$P_{east} = \left(\frac{M_{total}}{5ft.} + P_{total}\right)\times\frac{1}{2}$$
$$P_{west} = \left(\frac{M_{total}}{5ft.} - P_{total}\right)\times\frac{1}{2} \quad (7.8)$$

M_{total} and P_{total} were determined from Equations (7.6) and (7.7).

For the different CM test specimens, the maximum compression chord buckling capacity was found to be approximately 300 kips in step 1. By utilizing Equations (7.6), (7.7), and (7.8), the required actuator capacity was approximately 100 kips. The actuators used in the CM tests have a 600 kip load capacity.

3. Elastic Analyses: This step estimated the deflections of the panel points and determined the internal forces on the truss members. Using SAP2000

structural analysis software, the truss was analyzed elastically under loads applied to the chords equal to the compression chord buckling capacity found in step 1 (i.e., P_C and P_T defined earlier). The undeformed and the deformed positions of the truss analyzed under these axial loads are presented in Figure 7.19, where P_T and P_C were defined earlier. The resulting elastic deflections were multiplied by a factor of 5 to approximate the inelastic deflections of the truss before and after buckling of the compression chord. These factored deflections were used to plan the bracing and the instrumentation. These deflections were also utilized in the following step.

4. Overall Static Analysis in Deformed Condition: This step determined if a significant error would be introduced if the truss analysis in the undeformed condition were used in the control of the tests and subsequent data analysis. In this analysis, the truss was displaced using the factored elastic deflections determined in step 3.

   a. Figure 7.20(a) shows the chords of the truss and the actuators represented by their lines of action through which the axial load is applied. Pins at the end of each line of action are the actual pins of the clevises which were used at the connections of the truss and the actuators to the girders.

   b. The loading girder was displaced with a rigid body motion according to

the factored elastic deflections, as shown in Figure 7.20(b).

c. The actuator loads that were determined in step 3 were applied in the deformed position, as shown in Figure 7.20(c), and the horizontal components of the actuator loads were found to be negligible. Thus, the error that would be introduced if the truss is analyzed in its undeformed condition is negligible.

5. Relationship Between the Compression Chord Forces and Actuator Forces: This step determined the relationship between the applied actuator forces and the force in the compression chord. Figure 7.21 is similar to Figure 7.18. In this figure, the forces are as follows:

C : the force applied to the compression chord

T : the force applied to the tension chord

P_{east} : the east actuator force

P_{west} : the west actuator force

From Figure 7.21(b):

P_{total} : the total force applied by the actuators on the loading girder

$$P_{total} = P_{east} - P_{west} \tag{7.9}$$

M_{total} : the total moment applied by the actuators on the loading girder

$$M_{total} = -1 \times (P_{east} + P_{west}) \times 5 ft. \tag{7.10}$$

Then, the forces C and T were related to M_{total} and P_{total} using Figure 7.21(a), resulting in the following equations:

$$C = \left(\frac{M_{total}}{1.75 ft.} + P_{total} \right) \times \frac{1}{2}$$
$$T = \left(\frac{M_{total}}{1.75 ft.} - P_{total} \right) \times \frac{1}{2} \quad (7.11)$$

M_{total} and P_{total} were determined from Equations (7.9) and (7.10).

7.4.2 GM Specimens

These analyses determined the relationships between the applied actuator forces and the forces in the critical diagonal web members, C1 and C2. In order to find the applied load on members C1 and C2, the following steps are followed:

1. Critical Member Capacity Analysis According to the AISC (2005) Specification: This step estimated the buckling capacity of the critical members of the GM specimens. Since the diagonal web members C1 and C2 are double angle cross-sections, they were analyzed according to the provisions of the AISC (2005) specification, using the procedures presented in Section 5.4. K was taken as 1.0.

2. Overall Static Analysis in Undeformed Condition: This step determined the actuator capacities, F1 and F2 as shown in Figure 7.2, based on the critical member capacities by using static analysis. The analysis assumed all the connections in the GM trusses are pin connections. Based on these analyses,

the required actuator capacities were found to be 50 kips. The actuators used in the GM tests have a 110 kip load capacity.

3. Elastic Analyses: This step estimated the deflections of the panel points and determined the internal forces in the truss members. Using the SAP2000 software, two models were created as shown in Figure 7.22. One model assumed that all the connections in the GM test specimens are pin-ended, while, the other model assumed that all the connections are fixed. These two cases were chosen to represent the two limiting conditions for the connections. The actuator loads, F1 and F2, determined in step 2 were applied to both models. Then, the forces in the critical web members, C1 and C2, and the lateral deflections of panel points from these two models were compared. It was found that the forces in critical members and the deflections from these two models are within 3% of each other. The deflections were factored by 5 and used to plan the bracing and the instrumentation.

4. Relationship between the Critical Web Member Capacities and the Actuator Loads: As a result of step 3, the pin-ended model was utilized for analyses of the GM test specimens. The forces in the critical web members were related to the applied actuator forces by using the results of these analyses.

7.5 Test Results

7.5.1 Specimen C1

The compression chord was braced at four panel points, P1, P3, P5, and P7, along its length, as shown in Figure 7.23. At P3 and P5, the out-of-plane rotation was unrestrained (Bracing Type 1). The flexural-torsional buckling mode was expected in the middle panel of the compression chord, because the middle panel is longer than the north and south panels (Figure 7.1).

Buckling of the chord was observed in the middle panel as shown in Figure 7.24 with the expected flexural-torsional mode shape. As the loading of the truss continued, buckling occurred in the adjacent north panel of the compression chord member.

In Figure 7.25, the compression chord force vs. the axial shortening for the middle and north panel is shown. The force in the panels of the compression chord equals the compression chord force given by Equation (7.11). The axial shortening data was found by using data from the displacements of the bracing location at the ends of the panels. Figure 7.25 indicates that the north panel of the compression chord was observed to govern the failure behavior of the compression chord of specimen C1.

Figure 7.26 shows the chord force vs. the strain separation data acquired in the south panel. These gages were placed as shown in Figure 7.11. Figure 7.26 indicates that there is a small separation of strain measurements between the back-to-back strain gages, SG 1&2 and SG 3&4, before the peak load level, indicating that some local plate bending initiated in the south panel before the peak load was reached. In Figure

7.27, the chord force vs. the out-of-plane (global Z axis) deflection at the mid-length cross-section of each panel is shown. This figure indicates that there is noticeable deflection occurred at mid-length cross-section of the middle panel as well as the north panel. Figure 7.27 also shows that there is almost no out-of-plane deflection observed at the mid-length cross-section of the south panel.

In test of specimen C1, the peak load of the west actuator was 108 kips, while the peak load was 107 kips for the east actuator. The peak force in the compression chord is calculated to be 308 kips. The predicted flexural buckling capacity about the strong axis for the middle panel is 294 kips, and the predicted flexural-torsional buckling capacity for this panel is 259 kips.

Figure 7.28 shows that near panel point P1, the gusset plate was observed to have a significant out-of-plane rotation and panel point P1 deflected out-of-plane. The rotation of the gusset plate moved the inflection point from the assumed working point at P1 to the pin in the clevis. Thus, the effective length, KL, for this end panel was larger than the actual length of the panel to point P1. As shown in Figure 7.29, the end panels of the compression chord have a 5 ft. length and were intended to have an effective length factor of 1.0. However, due to the gusset plate deformation and subsequent outward movement of the inflection points, as shown in Figure 7.30, the effective length of this end panel became approximately 5 ft. 5 in. Even though the effective length of the north panel is approximately 10% shorter than the middle panel, the compression chord failed in the north panel.

The effect of the gusset plate deformation on moving the inflection point beyond the assumed working point was resolved for other CM test specimens by stiffening the gusset plate by increasing the total thickness of the shim plates, as shown in Figure 7.9(a).

7.5.2 Specimen C2

Specimen C2 has the same layout as specimen C1, but the vertical web members were eliminated in specimen C2 to permit in-plane buckling of the compression chord member to occur. Test specimen C2 is shown in Figure 7.31. Since there were no vertical web members in this specimen, the bracing locations on the tension chord were relocated as shown in this figure.

The compression chord of specimen C2 was vulnerable to in-plane buckling, and the middle panel of the compression chord was considered most critical. The deformed shape of the compression chord is shown in Figure 7.32, where the in-plane deformations can be observed.

Figure 7.33 shows the compression chord force vs. the axial shortening of the south panel. As discussed below, failure of the south panel controlled the behavior of specimen C2. As seen from this figure, after the peak load was reached the axial shortening of the south panel decreased due to problems with the test control although the panel shortening would have increased if the correct commands extending and retracting actuators had been issued. Figure 7.34 shows the chord load vs. the strain separation data acquired in south panel. These gages were placed as shown in Figure

7.11. Figure 7.34 shows a small separation of strain between the back-to-back gages, SG 1&2 and SG 3&4, before the peak load level, indicating some local plate bending. In Figure 7.35, the chord force vs. the in-plane (global Y axis) deflection at the mid-length cross-section of each panel is shown. These in-plane deflections at the mid-length cross-sections are relative to the ends of the panel (i.e., relative to a line connecting the panel points). This figure indicates that the largest in-plane deflection after the peak load was observed in the south end panel indicating that this was the critical panel that caused the chord to unload.

The peak actuator load was 94 kips, and the peak force in the compression chord is calculated to be 268 kips. The predicted flexural buckling capacity about the strong axis for the middle panel is 281 kips. The predicted flexural buckling capacity about the weak axis is 224 kips.

7.5.3 Specimen C3

This specimen is identical to specimen C1 except that Bracing Type 2, shown in Figure 7.8(c), was utilized at bracing locations P3 and P5. The test of this specimen, shown in Figure 7.36, evaluated the effect of the out-of-plane rotational restraint provided by this second type of bracing. The observed buckling mode was similar to what was observed for specimen C1, as shown in Figure 7.37. The buckling of the compression chord occurred in the middle panel.

The compression chord force vs. the axial shortening of the middle panel is shown in Figure 7.38. Comparison of this figure to Figure 7.25 shows that the experimental

capacity of specimen C3 is higher than the capacity of specimen C1, which did not have out-of-plane rotation restrained by the bracing. Figure 7.39 shows the chord force vs. the strain separation data acquired in south panel. These gages were placed as shown in Figure 7.11. Figure 7.39 shows there is no separation of strain between the back-to-back gages, SG 1&2 and SG 3&4, before the peak load was reached. In Figure 7.40, the chord force vs. the out-of-plane (global Z axis) deflection at the mid-length cross-section of each panel is shown. As seen from this figure, the middle panel has the largest out-of-plane deflection in the post-peak region. Throughout the test, there is little out-of-plane deflection observed in the north and south panels.

The peak load of the west actuator was 123 kips, while the peak load was 122 kips for the east actuator. The peak force in the compression chord is calculated to be 350 kips. The capacity of specimen C3 is 14% higher than that observed for specimen C1. The predicted flexural buckling capacity about the strong axis for the middle panel is 338 kips, and the predicted flexural-torsional buckling capacity for this panel is 273 kips.

7.5.4 Specimen C4

This specimen is the same as specimen C1 except that this specimen has fewer mid-spacers in the chord members between the panel points of the truss. Thus, the test of this specimen was intended to evaluate the effect of the number of mid-spacers on the compressive strength of the chord members. Both chord members have the same pattern and number of mid-spacers. The layout of specimen C4 is shown in Figure

7.41. The test specimen C4 was loaded in one direction (Test 1), making the west chord the compression chord, and then loaded in the other direction (Test 2), making the east chord the compression chord.

The experimental results from the two tests of specimen C4 gave similar results in terms of the buckling capacity of the chord member. In both tests, the middle panel buckled as shown in Figures 7.42 and 7.43.

The instrumentation was only on the west chord of specimen C4 which was critical for Test 1. For Test 2, only the chord force is available. Figure 7.44 shows the west chord force vs. the axial shortening of the middle panel of the west chord. As seen in this figure, after the peak chord force was reached in the west chord, the loads in the actuators were taken to zero load by reversing their direction (i.e., retracting the east actuator and extending the west actuator). Then, Test 2 of the truss was carried at to fail the east chord in compression, while the west chord was in tension. Figure 7.44 shows the behavior of the west chord during Test 2, while the west chord is in tension. The figure shows the peak tensile force in the west chord. Equation (7.11) shows that the chord forces, C and T, are equal when the total load, P_{total}, applied to the loading girder is zero. Thus, assuming load levels in the actuators were the same, as intended, then the peak force in the west chord should be equal to the peak force in the east chord, and therefore Figure 7.44 indicates the peak compressive force in the east chord during Test 2.

Figure 7.45 shows the west chord force vs. the strain separation data acquired in

the south panel of west chord. These gages were placed as shown in Figure 7.11. Figure 7.45 shows there is almost no separation of strain between the back-to-back gages, SG 1&2 and SG 3&4, throughout the test of specimen C4. In Figure 7.46, the west chord force vs. the out-of-plane (global Z axis) deflection at the mid-length cross-section of each panel of the west chord is shown. As seen from this figure, the largest out-of-plane deflection occurred in the middle panel of west chord near the peak load of Test 1. In Test 2, the west chord was loaded in tension which straightened this chord, and thus, the out-of-plane deflection at the mid-length cross-section of each panel of the west chord diminished.

In Test 1 of Specimen C4, the peak load of both actuators was 116 kips. The peak force in the compression chord of Test 1 (i.e., the peak force in the west chord) is calculated to be 332 kips. The failure capacity for Test 1 of specimen C4 is 7% higher than that observed for specimen C1. The predicted flexural buckling capacity about the strong axis for the middle panel of the compression chord is 281 kips, and the predicted flexural-torsional buckling capacity for this panel of the compression chord is 252 kips. In Test 2 of Specimen C4, the peak load of the west actuator was 117 kips, and the peak load of the east actuator was 116 kips. The peak force in the compression chord of Test 2 (i.e., the peak force in the east chord) is calculated to be 334 kips. The failure capacity for Test 2 of specimen C4 is within 1% of the failure capacity for Test 1 of specimen C4.

7.5.5 Specimen C5

This specimen is the same as specimen C1 except that this specimen has more mid-spacers in the chord members between the panel points of the truss. Thus, the test of this specimen was intended to evaluate the effect of the number of mid-spacers on the compressive strength of the chord members. Both chord members have the same pattern and number of mid-spacers. The layout of specimen C5 is shown in Figure 7.47. The test specimen C5 was loaded in one direction (Test 1), making the west chord the compression chord, and then loaded in the other direction (Test 2), making the east chord the compression chord.

The experimental results from the two tests of specimen C5 gave similar results in terms of the buckling capacity of the chord member. In both tests, the middle panel buckled as shown in Figures 7.48 and 7.49.

The instrumentation was only on the west chord of specimen C5 which was critical for Test 1. For Test 2, only the chord force is available. Figure 7.50 shows the west chord force vs. the axial shortening of the middle panel of the west chord. As seen in this figure, after the peak chord force was reached in the west chord, the loads in the actuators were taken to zero load by reversing their direction (i.e., retracting the east actuator and extending the west actuator). Then, Test 2 of the truss was carried at to fail the east chord in compression, while the west chord was in tension. Figure 7.50 shows the peak tensile force in the west chord during Test 2. As discussed for specimen C4, the peak compressive force in the east chord during Test 2 can be

surmised from the peak tensile force in the west chord.

Figure 7.51 shows the west chord force vs. the strain separation data acquired in the south panel of west chord. These gages were placed as shown in Figure 7.11. Figure 7.51 shows there is almost no separation of strain between back-to-back gages SG 1&2 throughout the test of specimen C5. This figure shows there is little separation between back-to-back gages SG 3&4 before the peak load, but separation occurs after the peak. The gages then reach their range limit (vertical line in graph). In Figure 7.52, the west chord force vs. the out-of-plane (global Z axis) deflection at the mid-length cross-section of each panel of the west chord is shown. As seen from this figure, the largest out-of-plane deflection occurred at the middle panel of the west chord near the peak load level of Test 1. In Test 2, the west chord was loaded in tension which straightened this chord.

In Test 1 of specimen C5, the peak load of west actuator was 120 kips while the peak load was 118 kips for the east actuator. The peak force in the compression chord of Test 1 (i.e., the peak force in the west chord) is calculated to be 341 kips. The failure capacity for Test 1 of specimen C5 is 11% higher than that observed for specimen C1. The predicted flexural buckling capacity about the strong axis for the middle panel of the compression chord is 296 kips, and the predicted flexural-torsional buckling capacity for this panel of the compression chord is 260 kips. In Test 2 of specimen C5, the peak load of west actuator was 121 kips while the peak load was 123 kips for the east actuator. The peak force in the compression chord in Test 2 (i.e., the

peak force in the east chord) is calculated to be 347 kips. The failure capacity for Test 2 of specimen C5 is within 2% of the failure capacity for Test 1 of specimen C5.

7.5.6 Specimen G2

Specimen G2 was tested to evaluate the effects of connection eccentricities on the compressive strength of diagonal web members. Specimen G2 has two critical diagonal web members, C1 and C2 shown in Figure 7.53, having different connection eccentricities. The centroidal axis of member C2, called the concentric member, coincides with the centroidal axis of both adjacent web members and the chord member that are attached together at the panel point. The centroidal axis of member C1, called eccentric member, intersects the centroidal axis of the adjacent diagonal member with a 2 in. eccentricity from the centroidal axis of the attached chord members.

The gradient moment (GM) tests consist of 3 phases, as discussed earlier and shown in Figure 7.17. The first phase loads the truss until member C1 fails, as shown in Figure 7.54. The third phase loads the truss until member C2 fails, as shown in Figure 7.55.

Figure 7.56 shows the shear force in the right panel of the truss (see Figure 7.17) vs. the axial shortening of member C1. The right panel shear force is equal to the force in the south actuator and represents the shear applied to the part of the truss specimen between the two actuators. There is a significant drop in the panel shear force observed after the peak load. Figure 7.57 shows the right panel shear vs. the strain

separation data for member C1. The gages were placed on member C1 as shown in Figure 7.15(b), and identified as SG5 to SG8. Figure 7.57 shows that there is a noticeable separation between the back-to-back gages, SG 5&6 and SG 7&8, before the peak load. Figure 7.58 shows the panel shear vs. the heel deflection at the mid-length cross-section of member C1. As it is shown in this figure, there is noticeable deflection in both the global Z axis direction (i.e., the out-of-plane direction of the truss, which is the weak axis direction of the double angle web member) and the global Y axis direction (i.e., the in-plane direction of the truss, which is the strong axis direction of the double angle web member) observed before the peak load. The Y axis lateral deflection is much larger than the Z axis lateral deflection in the post-peak region indicating buckling about the Z axis (i.e., buckling about the weak axis).

Figure 7.59 indicates the shear force in the left panel of the truss (see Figure 7.17) vs. the axial shortening of member C2. In the third phase of the test, the left panel shear force is equal to the load in the north actuator and represents the shear applied to the part of the truss specimen between the north actuator and the reaction girder. There is a significant drop in the panel shear force observed after the peak load. As seen from this figure, a very little axial shortening is observed for member C2. Figure 7.60 shows the right panel shear vs. the strain separation data for member C2. The gages were placed on member C2 as shown in Figure 7.15(b), and identified as SG1 to SG4. Figure 7.60 shows that there is a noticeable separation between the back-to-back gages SG 3&4 just before the peak load. Figure 7.61 shows the panel shear vs. the heel

deflection at the mid-length cross-section of member C2. As it is shown in this figure, there is noticeable deflection in both the global Z axis direction (i.e., the out-of-plane direction of the truss) and the global Y axis direction (i.e., the in-plane direction of the truss) observed before the peak load. The Y axis and the Z axis lateral deflections are similar near the peak load and in the post-peak region indicating buckling about both axes.

In the first phase of the test of specimen G2, the peak load in south actuator was 33 kips, while the peak load was 19 kips in north actuator. The corresponding peak force in member C1 is calculated to be 44 kips. The predicted flexural-torsional buckling capacity for member C1 is 20 kips, whereas the predicted flexural buckling capacity about the weak axis is 19 kips. In the third phase of the test of specimen G2, the peak load in north actuator was 32 kips, and the corresponding peak force in member C2 is calculated to be 42 kips. The predicted flexural-torsional buckling capacity for member C2 is 20 kips, whereas the predicted flexural buckling capacity about the weak axis (z_h axis,) is 21 kips. The observed buckling mode for diagonal web member C1 appeared to be flexural buckling about the weak axis. For member C2, the buckling mode appeared to involve both strong axis and weak axis buckling.

7.5.7 Specimen G4

Specimen G4 was tested to evaluate the effect of the eccentricity of the welds at the attachment of the critical web members to the chords on the capacity of these welds.

The test procedure was intended to follow the procedure used for specimen G2. Two diagonal members C1 and C2, as shown in Figure 7.62, were designed so their welds at the ends would fail. C1 member is referred to as "eccentric member" due to the fact that weld geometry at its ends is eccentric with the centroidal axis of this diagonal web member. C2 member is referred to as "concentric member" due to the fact that weld geometry at its ends is coincides with the centroidal axis of this diagonal web member.

To make the welds fail, the critical members were intentionally strengthened by increasing the sizes of the cross sections compared to specimen G2. Member C2 was also stiffened with attached single angle cross-sections since the concentric weld capacity is greater than eccentric weld capacity.

As shown in Figure 7.63, in the first phase of the test, unexpected failures were observed. The mid-spacer at the end of the vertical web member adjacent to member C1 failed and the diagonal web member adjacent to member C1 failed by tensile overload. This overload occurred because the south actuator load reached 69 kips without failing the welds of member C1. These welds were designed to fail when the load in the south actuator was approximately 41. The predicted buckling capacity for member C1 was reached when the south actuator reached 55 kips. Thus, actuator load exceeded the expected load by more than 50%. As it is seen in Figure 7.63, the diagonal web member adjacent to member C1 failed in tension at the end of the first phase. Thus, the test protocol was continued, and the load in the south actuator was

taken to zero to begin the third phase of the test.

In the third phase of the test, the weld at the ends of member C2 were intended to fail at 50 kips of load in the north actuator. The predicted buckling capacity for member C2 was expected to be reached at 67 kips of load in the north actuator. The load in the north actuator exceeded the expected load at weld failure. At approximately 63 kips, a failure of a mid-spacer in the west chord panel between panel points P1 and P2 occurred as shown in Figure 7.64 (a).

The load in the north actuator was then dropped to zero load, and the chord at the failure location was temporarily clamped as shown in Figure 7.64(b). Then the third phase of the test was restarted and the load in the north actuator again passed the expected capacity of the welds. At approximately 80 kips of load in the north actuator, the diagonal web member adjacent to member C2 failed by ductile tensile failure at its connection to the chord. This failure is shown in Figure 7.64 (c). Right after this failure, the vertical web member adjacent to member C2 failed by ductile tensile failure at its connection to the chord as shown in Figure 7.64 (d). Then the loading was stopped and the test was finished.

Even though the load in the north actuator exceeded the load at which the welds were expected to fail by 50%, no failure was observed at the welds or the critical diagonal web members themselves.

7.6 Discussion of Results

In Table 7.4, the slenderness ratios for the principle axes are presented. The predicted buckling capacities, based on the nominal width and thickness measurements along with the Q reduction factor, are presented in Table 7.5, where P_Y is the yield strength of the specimen and $2xP_{cr\text{-}SA}$ column data represent the single angle capacity of the critical members in the trusses.

In Table 7.6, the test results are compared with the predicted flexural buckling capacity about the strong axis, $P_{cr\text{-}y}$, the predicted flexural buckling capacity about the weak axis, $P_{cr\text{-}x}$, and the predicted flexural-torsional buckling capacity, $P_{cr\text{-}ft}$. A comparison of the experimental capacity, P_{EXP}, vs. QP_Y and $P_{e\text{-}ft}$ is also included in Table 7.6. The procedure for calculating the predicted buckling capacities of a double angle cross-section is presented in Section 5.5. The flexural-torsional buckling mode was expected for the CM specimens other than specimen C2, while the weak axis flexural buckling mode was expected for specimen C2. Table 7.6 shows that the predicted flexural-torsional buckling capacities provide conservative results and the test results have better agreement with the predicted flexural buckling capacity about the strong axis. The test results are compared to the predicted flexural and the predicted flexural-torsional buckling capacities in Figure 7.65. This figure shows the test results are always higher than the predicted buckling capacities especially for the critical members of the GM specimens which have a lower Q reduction factor. The conservatism in the predicted capacities show similarities with the conservatism

observed for the isolated double angle test specimens.

The ratio of P_{EXP} to $P_{cr\text{-}ft}$ is plotted against the Q reduction factor in Figure 7.66. It can be seen from this figure that when the Q reduction factor is smaller, the $P_{EXP}/P_{cr\text{-}ft}$ ratio is greater.

The $P_{EXP}/P_{cr\text{-}ft}$ ratio is plotted vs. the modified effective slenderness factor, K_m, in Figure 7.67. It can be seen that the modified effective length factor introduces some conservatism in the predicted buckling capacities for the cases with the large modified effective length factor. The ratio of the experimental results to the predicted buckling capacities for both the isolated double angle specimens and the critical members of trusses suggest that using an effective length of the members is equal to the actual length of the members (i.e., $K = 1.0$) is appropriate.

In Figure 7.68 and Figure 7.69, the test results are compared with buckling capacity curves based on the AISC (2005) specification. It is evident from these figures that the test results are consistently well above the predicted buckling capacities.

Table 7.1 Test Matrix

Specimen ID	Test Type	Critical Member	Critical Details	Expected Failure Mode
C1	CM	cc	Base case	Out-of-plane buckling near P4
C2	CM	cc	No vertical web members	In-plane buckling near P4
C3	CM	cc	Same as C1, except out-of-plane rotation restrained at brace points	Out-of-plane buckling near P4
C4	CM	cc	Same as C1, except fewer chord spacers	Out-of-plane buckling near P4
C5	CM	cc	Same as C1, except more chord spacers	Out-of-plane buckling near P4
G2	GM	dw	Compression web members with different connection eccentricities	Out-of-plane buckling at mid-length of members C1 & C2
G4	GM	dw	Web member welds with different weld eccentricities	Welds at ends of members C1 & C2

CM : Constant Moment cc : Compression Chord
GM : Gradient Moment dw : Diagonal Web

Table 7.2 Instrumentation and Measurements for CM Tests

Instrumentation	Unit	Location	Measurement
P_{east}	kips	-	Load in east actuator
P_{west}	kips	-	Load in west actuator
Δ_{east}	in.	-	Displacement of east actuator
Δ_{west}	in.	-	Displacement of west actuator
LVDT1	in.	At P1	In-plane displacement
LVDT2	in.	At P1	In-plane displacement
LVDT3	in.	At P2	In-space displacement
LVDT4	in.	At P2	In-space displacement
LVDT5	in.	At P2	In-space displacement
LVDT6	in.	At P3	In-plane displacement
LVDT7	in.	At P3	In-plane displacement
LVDT8	in.	At P4	In-space displacement
LVDT9	in.	At P4	In-space displacement
LVDT10	in.	At P4	In-space displacement
LVDT11	in.	At P5	In-plane displacement
SP12	in.	At P5	In-plane displacement
LVDT13	in.	At P6	In-space displacement
LVDT14	in.	At P6	In-space displacement
SP15	in.	At P6	In-plane displacement
LVDT16	in.	At P7	In-plane displacement
LVDT17	in.	At P7	In-plane displacement
LVDT18	in.	At P8	In-plane displacement
LVDT19	in.	At P8	In-plane displacement
LVDT20	in.	At tension chord	Tension chord elongation
LVDT21	in.	At P9	In-plane displacement
LVDT22	in.	At P9	In-plane displacement
LVDT23	in.	At P10	Displacement of girder
LVDT24	in.	At P10	Displacement of girder
LVDT25	in.	At P11	Displacement of girder
LVDT26	in.	At P11	Displacement of girder
LVDT27	in.	At P12	Displacement of girder
LVDT28	in.	At P12	Displacement of girder
LVDT29	in.	At P13	Displacement of girder
LVDT30	in.	At P13	Displacement of girder
SG1	microstrain	At compression chord near P6	Load check on chord
SG2	microstrain	At compression chord near P6	Load check on chord
SG3	microstrain	At compression chord near P6	Load check on chord
SG4	microstrain	At compression chord near P6	Load check on chord

Table 7.3 Instrumentation and Measurements for GM Tests

Instrumentation	Unit	Location	Measurement
P_{north}	kips	-	Load in north actuator
P_{south}	kips	-	Load in south actuator
Δ_{north}	in.	-	Displacement of north actuator
Δ_{south}	in.	-	Displacement of south actuator
LVDT1	in.	At P1	In-plane displacement
LVDT2	in.	At P1	In-plane displacement
LVDT3	in.	At P2	In-plane displacement
LVDT4	in.	At P2	In-plane displacement
LVDT5	in.	At P3	In-plane displacement
LVDT6	in.	At P3	In-plane displacement
LVDT7	in.	At P4	In-plane displacement
LVDT8	in.	At P4	In-plane displacement
LVDT9	in.	At P5	In-space displacement
LVDT10	in.	At P5	In-space displacement
LVDT11	in.	At P5	In-space displacement
LVDT12	in.	At P6	In-space displacement
LVDT13	in.	At P6	In-space displacement
LVDT14	in.	At P6	In-space displacement
LVDT15	in.	At P7	In-plane displacement
LVDT16	in.	At P7	In-plane displacement
LVDT17	in.	North actuator	Actuator displacement
LVDT18	in.	South actuator	Actuator displacement
SG1	microstrain	At C2 near P5	Strain near mid-height cross-section
SG2	microstrain	At C2 near P5	Strain near mid-height cross-section
SG3	microstrain	At C2 near P5	Strain near mid-height cross-section
SG4	microstrain	At C2 near P5	Strain near mid-height cross-section
SG5	microstrain	At C1 near P6	Strain near mid-height cross-section
SG6	microstrain	At C1 near P6	Strain near mid-height cross-section
SG7	microstrain	At C1 near P6	Strain near mid-height cross-section
SG8	microstrain	At C1 near P6	Strain near mid-height cross-section

Table 7.4 Slenderness Ratios Used in the Predicted Buckling Capacity Calculations for Critical Members

Specimen ID	Critical Member Size	K_x	K_y	L_x	L_y	r_x	r_y	$(KL/r)_x$	$(KL/r)_y$	$(KL/r)_M$	K_M
C1	LL3.5 x 3.5 x 3/8	1.0	1.0	36	72	1.07	1.71	33.5	42.2	43.8	1.04
C2	LL3.5 x 3.5 x 3/8	1.0	1.0	72	72	1.07	1.71	67.0	42.2	48.4	1.15
C3	LL3.5 x 3.5 x 3/8	1.0	0.5	36	72	1.07	1.71	33.5	21.1	21.9	1.04
C4test1	LL3.5 x 3.5 x 3/8	1.0	1.0	36	72	1.07	1.71	33.5	42.2	48.4	1.15
C4test2	LL3.5 x 3.5 x 3/8	1.0	1.0	36	72	1.07	1.71	33.5	42.2	48.4	1.15
C5test1	LL3.5 x 3.5 x 3/8	1.0	1.0	36	72	1.07	1.71	33.5	42.2	42.9	1.02
C5test2	LL3.5 x 3.5 x 3/8	1.0	1.0	36	72	1.07	1.71	33.5	42.2	42.9	1.02
G2test1	LL1.75x1.75x1/8	1.0	1.0	58.4	58.4	0.55	1.29	107.0	45.2	63.0	1.39
G2test2	LL1.75x1.75x1/8	1.0	1.0	55.3	55.3	0.55	1.29	101.3	42.8	59.7	1.39

Table 7.5 Predicted Buckling Capacities of Critical Members in Truss Specimens

Specimen ID	Q	P_Y	P_{cr-x}	P_{cr-y}	P_{cr-ft}	P_{e-ft}	$2xP_{cr-SA}$
C1	0.98	368.5	319.4	293.6	258.9	457.9	353.3
C2	0.98	368.5	223.5	280.9	252.3	424.1	269.0
C3	0.98	368.5	319.4	338.2	272.5	542.2	353.3
C4test1	0.98	368.5	319.4	280.9	252.3	424.2	334.5
C4test2	0.98	368.5	319.4	280.9	252.3	424.2	334.5
C5test1	0.98	368.5	319.4	296.0	260.1	463.9	356.9
C5test2	0.98	368.5	319.4	296.0	260.1	463.9	356.9
G2test1	0.79	65.9	18.5	36.4	19.7	22.5	27.5
G2test2	0.79	65.9	20.6	37.8	19.8	22.6	29.3

Table 7.6 Observed Buckling Capacities of Critical Members in Truss Specimens

Specimen ID	Observed Failure Mode	West/North Actuator Load at Failure* (kips)	East/South Actuator Load at Failure* (kips)	P_{EXP}**	P_{EXP}/P_{cr-x}	P_{EXP}/P_{cr-y}	P_{EXP}/P_{cr-ft}	P_{EXP}/P_Y	P_{EXP}/QP_Y	P_{EXP}/P_{e-ft}
C1	FT	108	-107	308	-	1.05	1.19	0.84	0.85	0.67
C2	F_x	94	-94	268	1.20	-	1.06	0.73	0.74	0.63
C3	FT	123	-122	350	-	1.03	1.28	0.95	0.97	0.65
C4test1	FT	116	-116	332	-	1.18	1.32	0.90	0.92	0.78
C4test2	FT	-117	116	334	-	1.19	1.32	0.91	0.92	0.79
C5test1	FT	120	-118	341	-	1.15	1.31	0.93	0.94	0.74
C5test2	FT	-121	123	347	-	1.17	1.33	0.94	0.96	0.75
G2test1	FT	-19	33	44	2.38	-	2.23	0.67	0.85	1.96
G2test2	FT	32	0	42	2.04	-	2.12	0.64	0.81	1.86

* The sign convention for the actuators: (+): Tension and (-): Compression

** Experimental failure capacities shown are found by elastic analysis of trusses under applied actuator loads

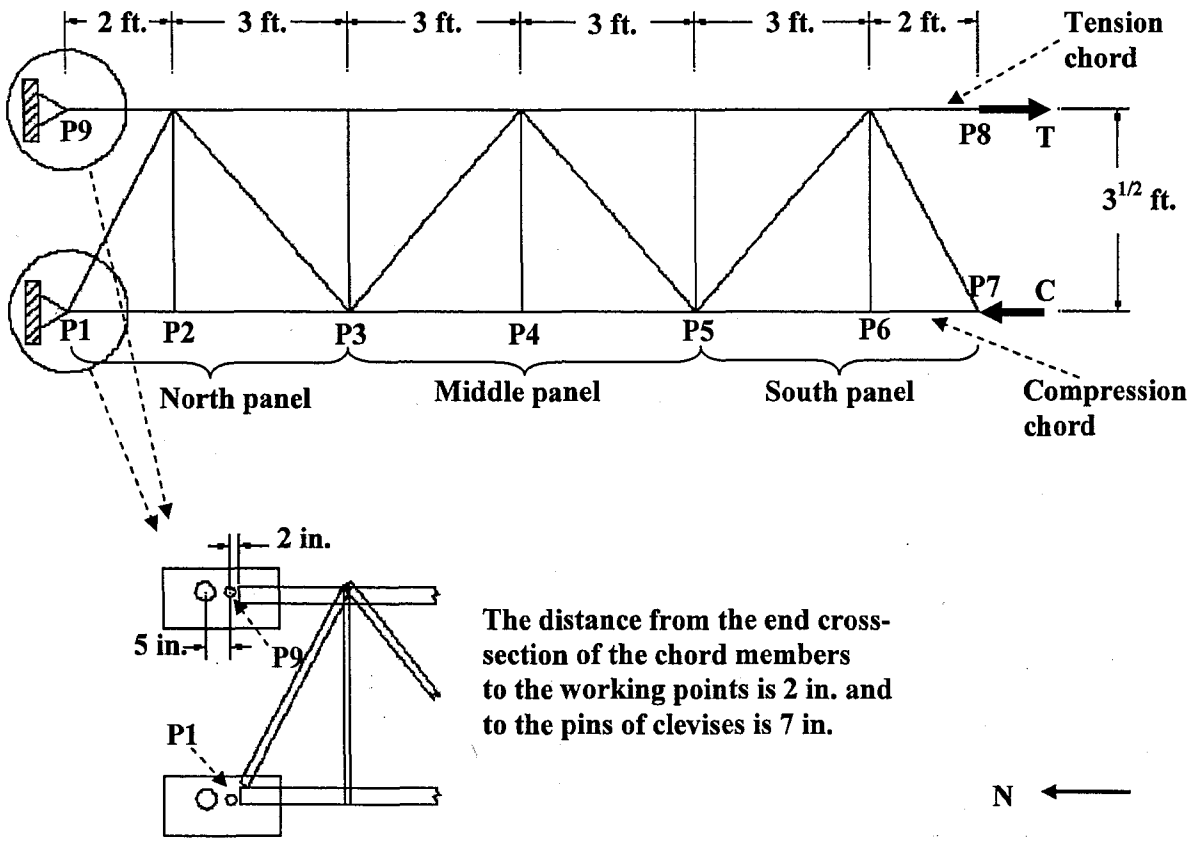

Figure 7.1 Specimen C1

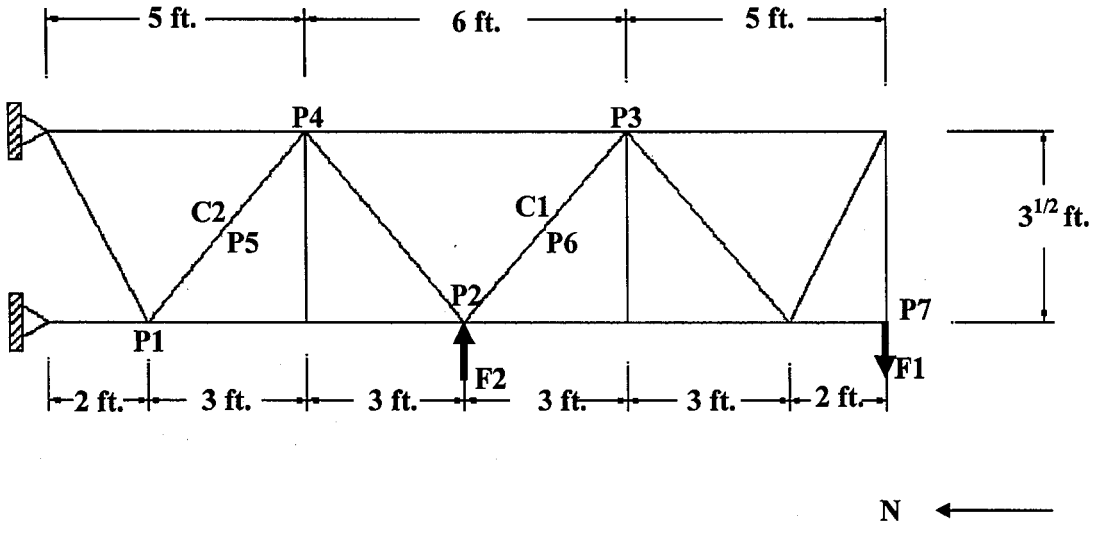

Figure 7.2 Specimen G2

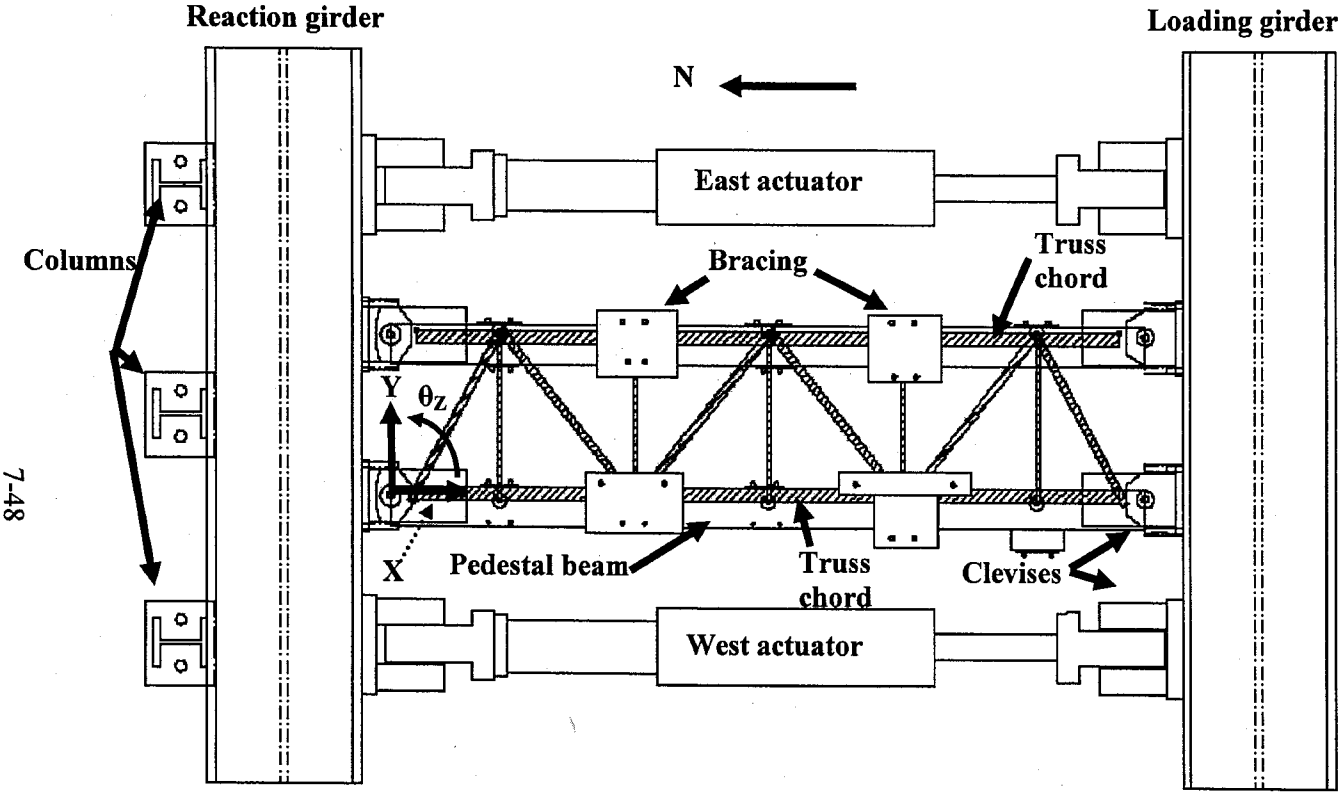

Figure 7.3 Plan View of CM Test Setup

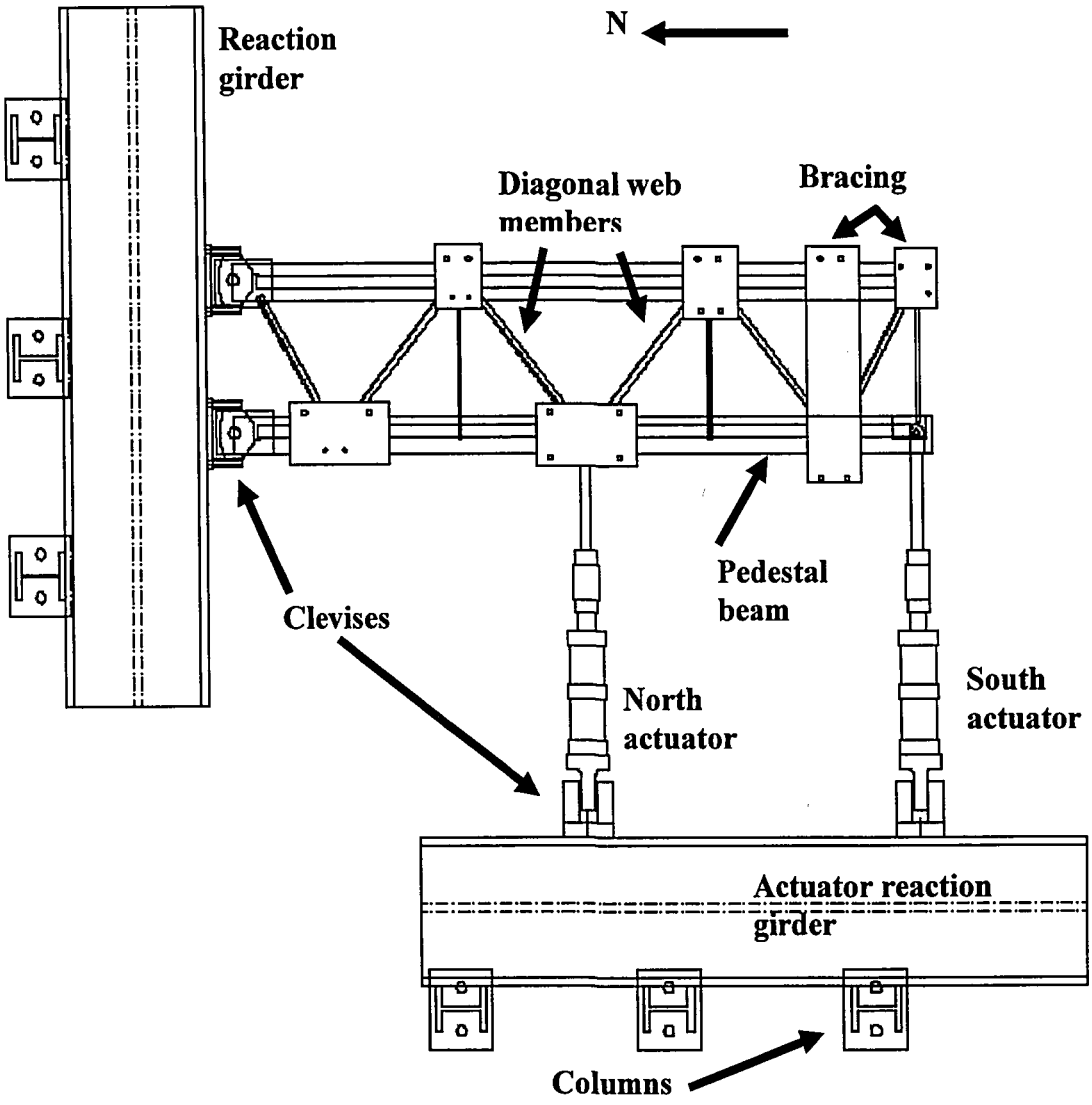

Figure 7.4 Plan View of GM Test Setup

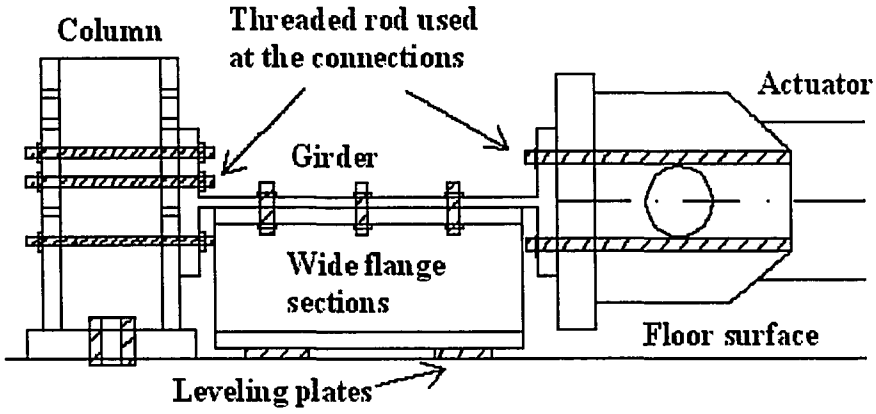

(a) Cross-sectional View of a Reaction Girder

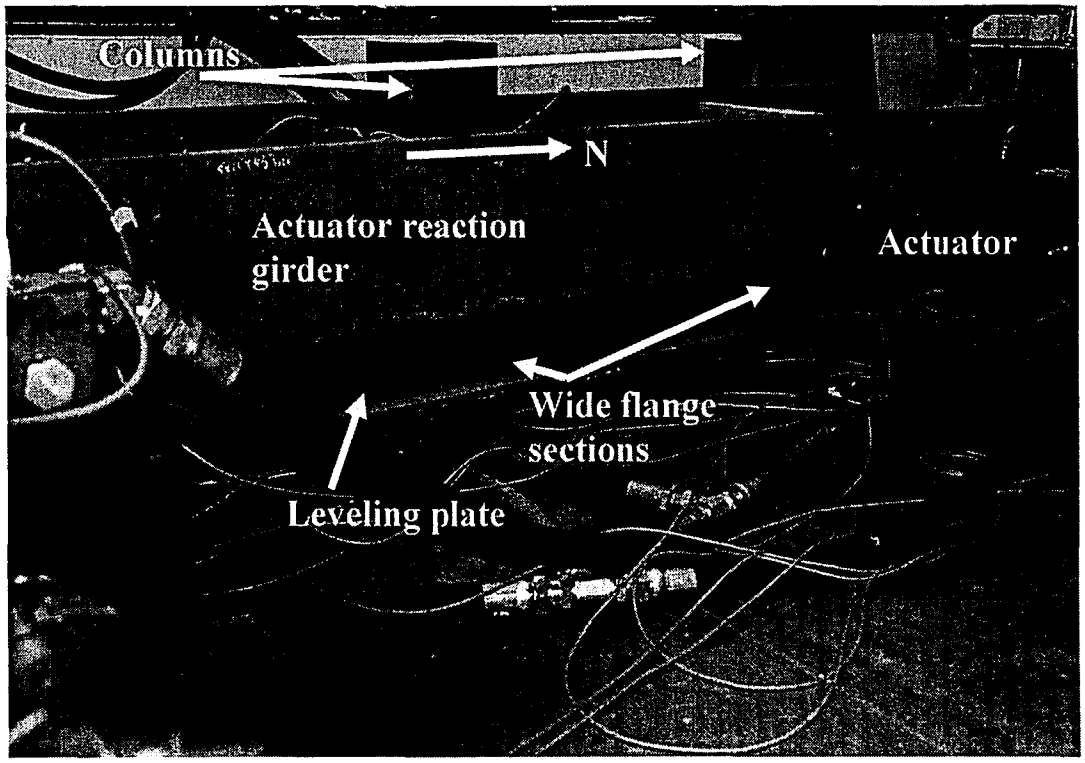

(b) Details of Actuator Reaction Girder

Figure 7.5 Girders Used in Test Setup

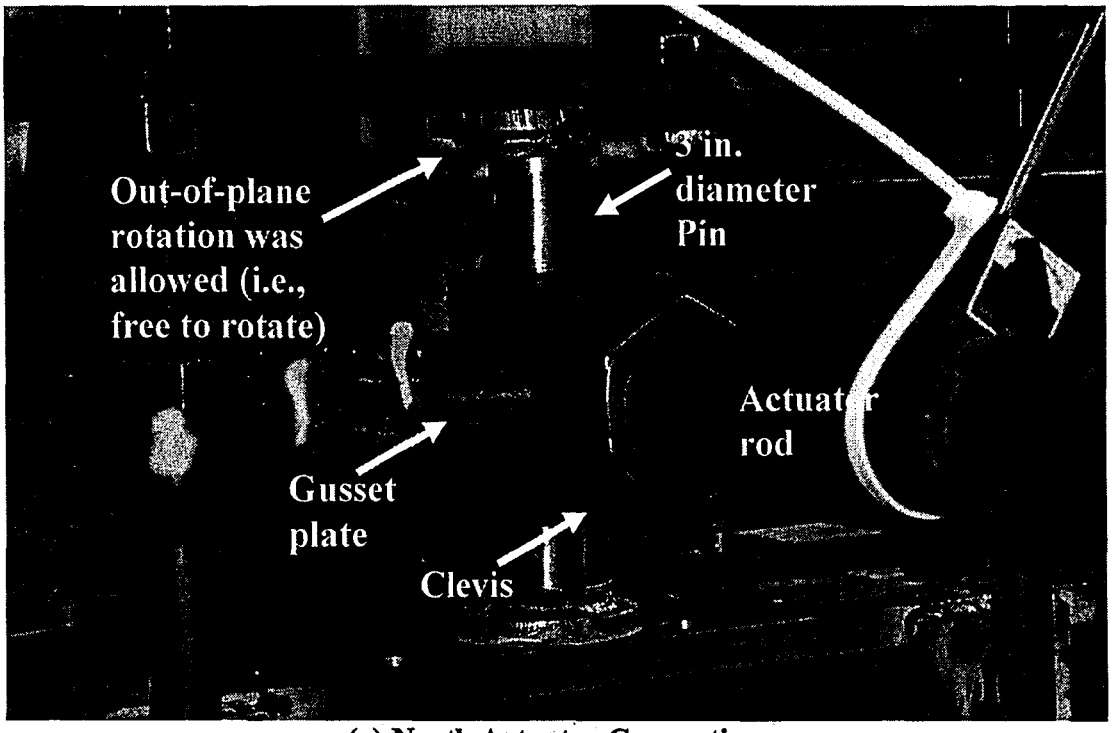

(a) North Actuator Connection

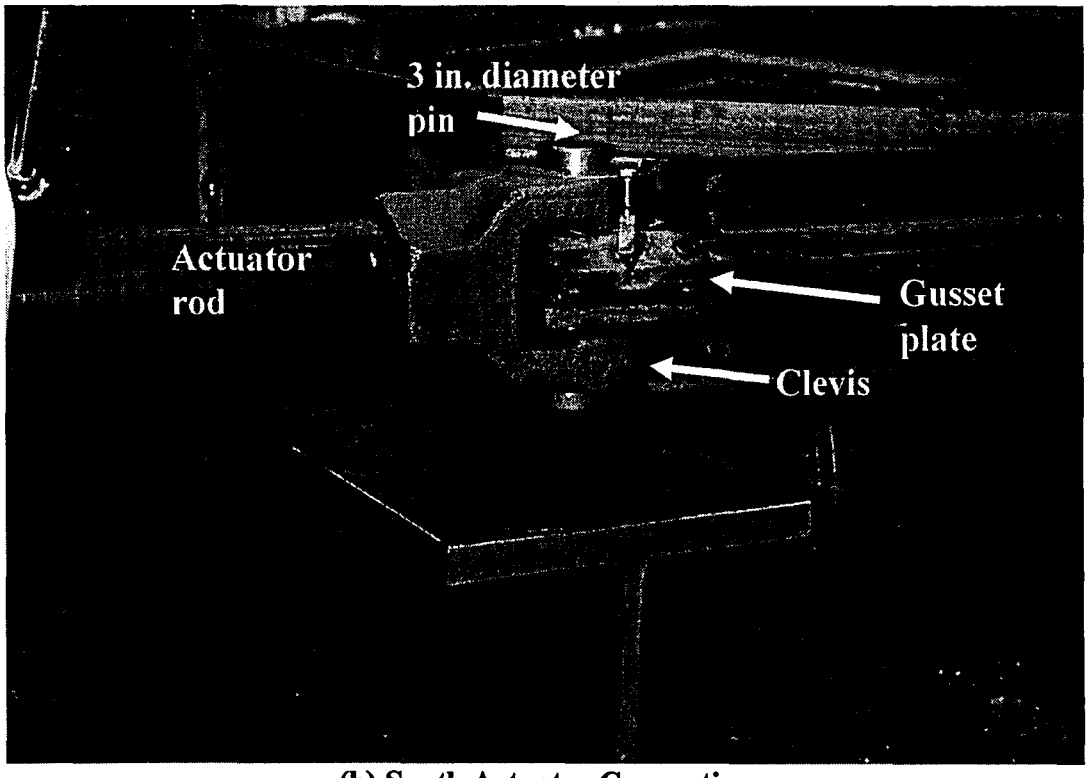

(b) South Actuator Connection

Figure 7.6 Actuator Connections for GM Tests

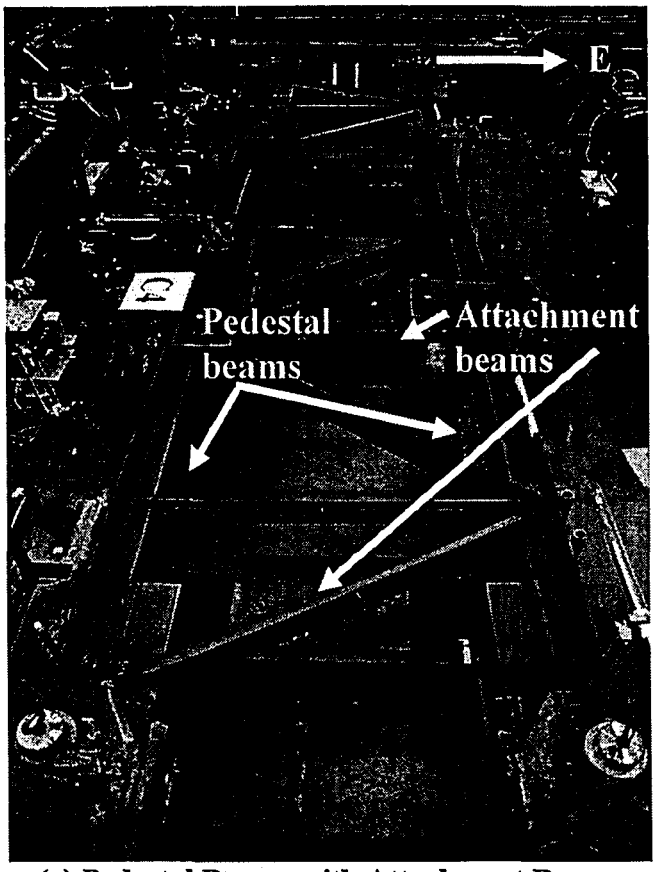

(a) Pedestal Beams with Attachment Beams

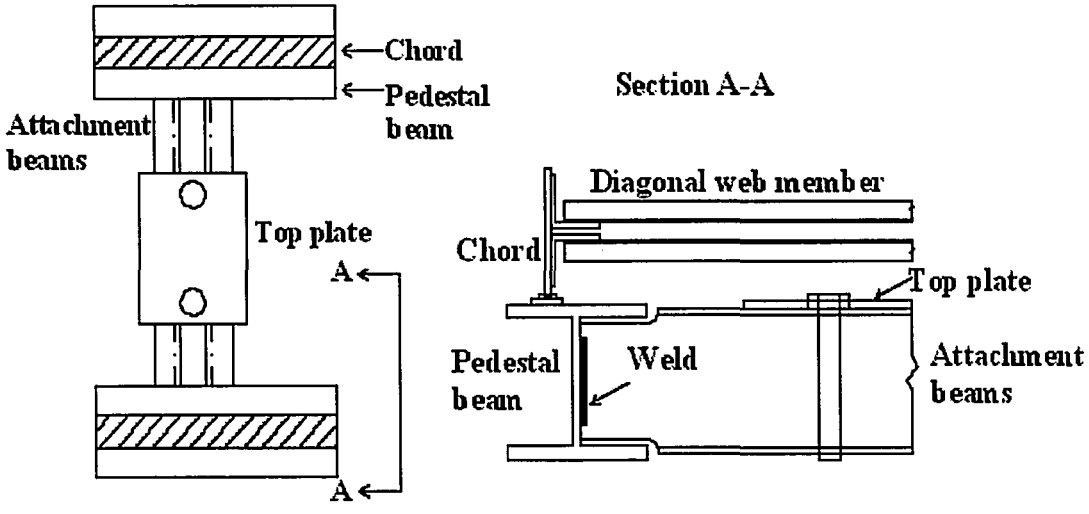

(b) Details of Attachment Beams

Figure 7.7 Pedestal Beams

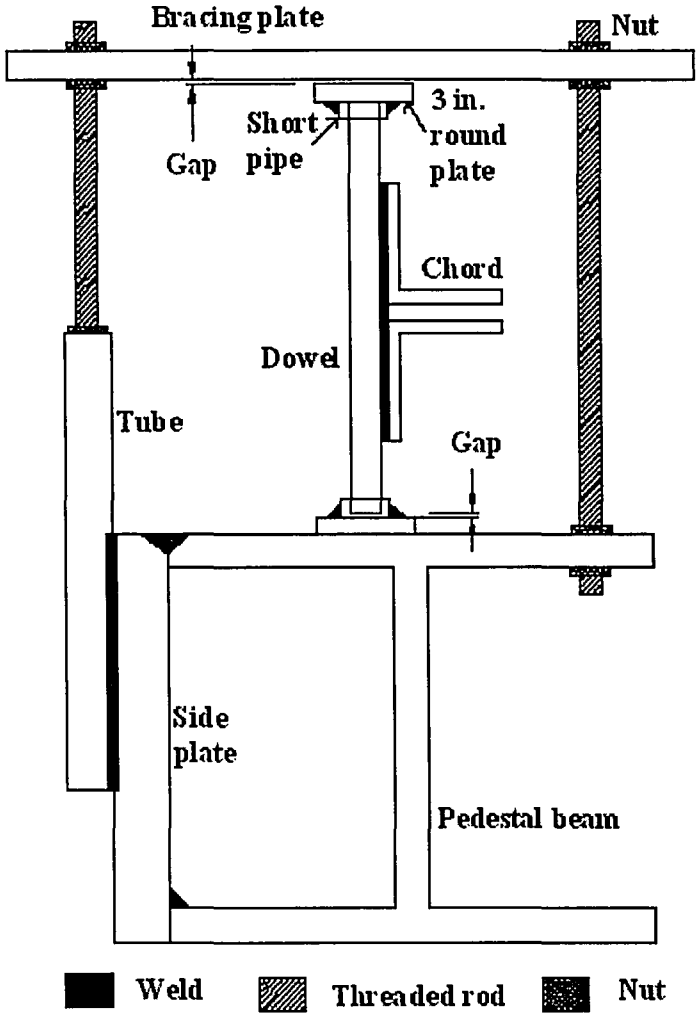

(a) Cross-section View of a Bracing Location

Figure 7.8 Bracing Details

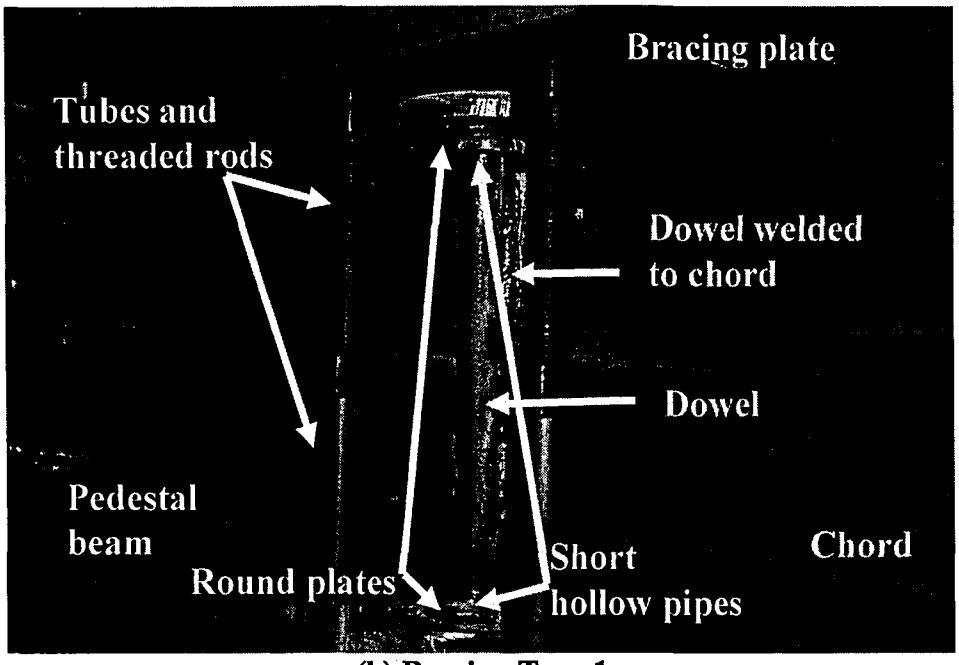

(b) Bracing Type 1

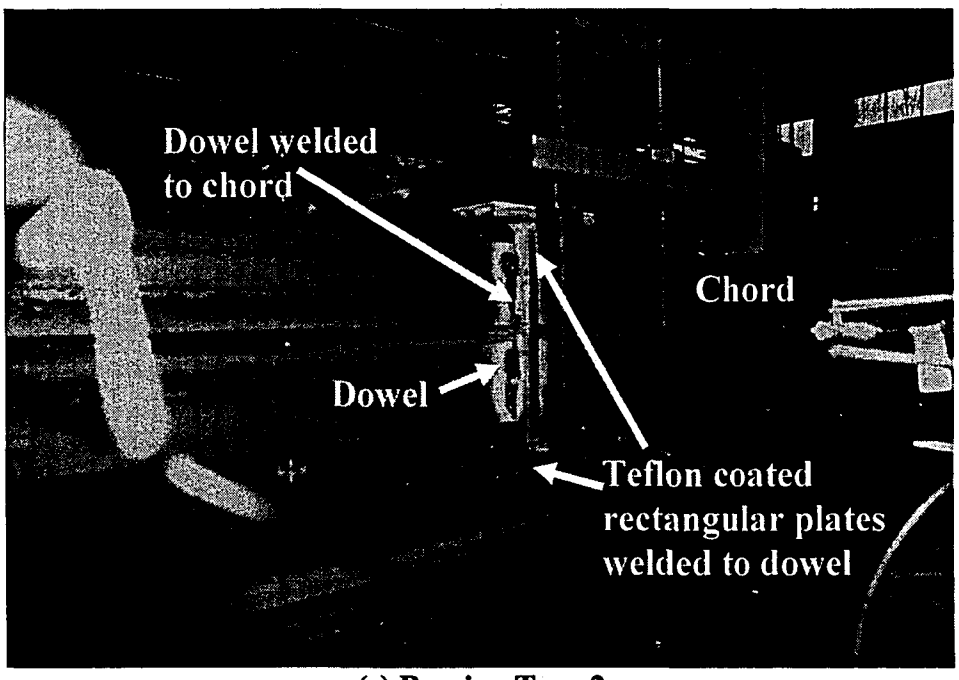

(c) Bracing Type 2

Figure 7.8 Bracing Details (Continued)

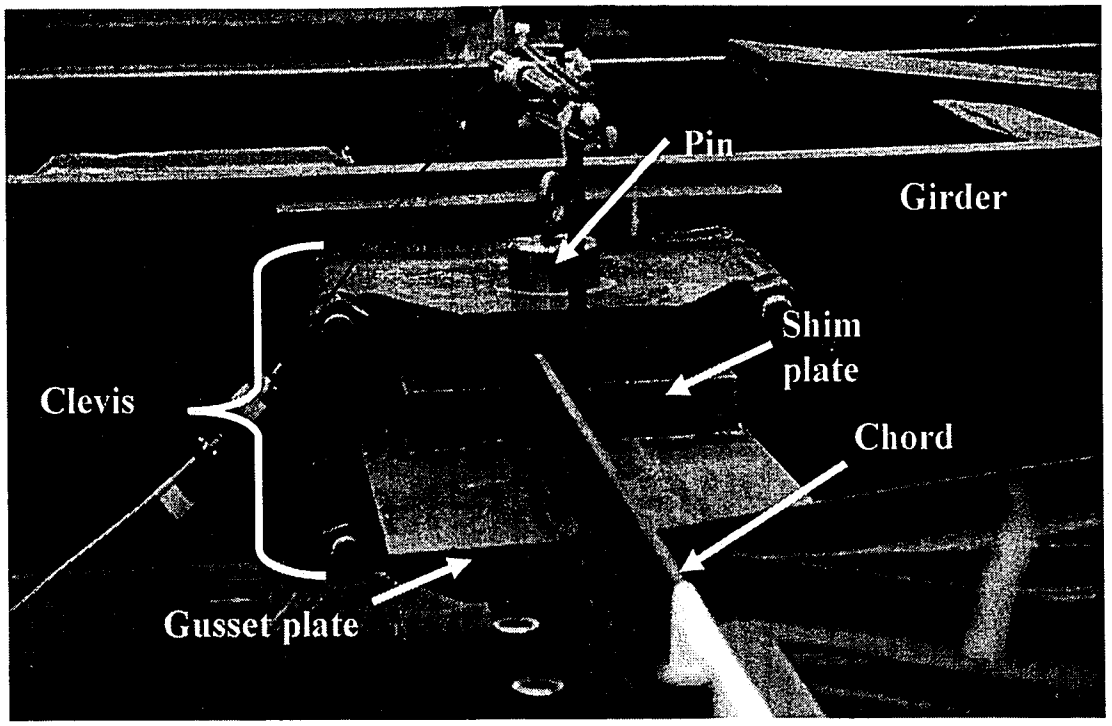

(a) Parts of a Clevis

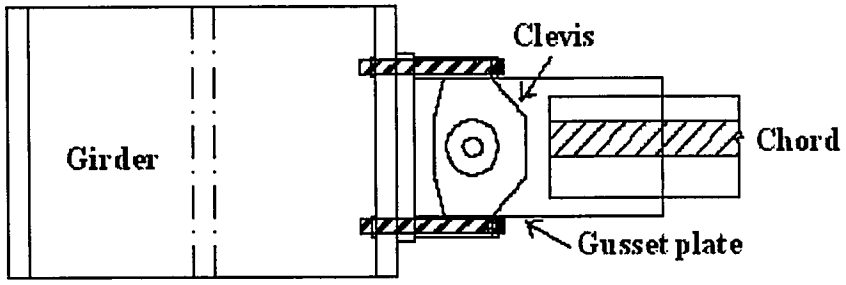

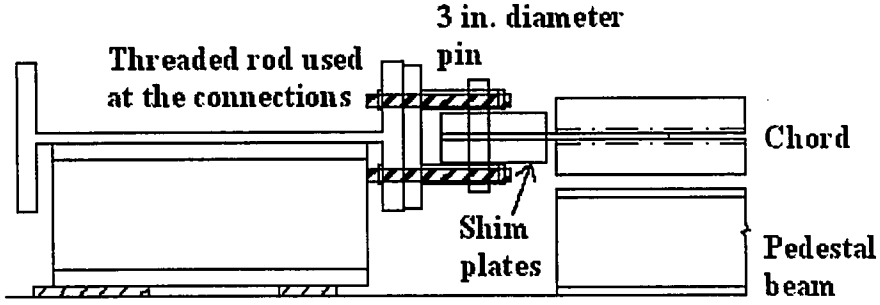

(b) Connection Details of a Clevis

Figure 7.9 Details of Clevises

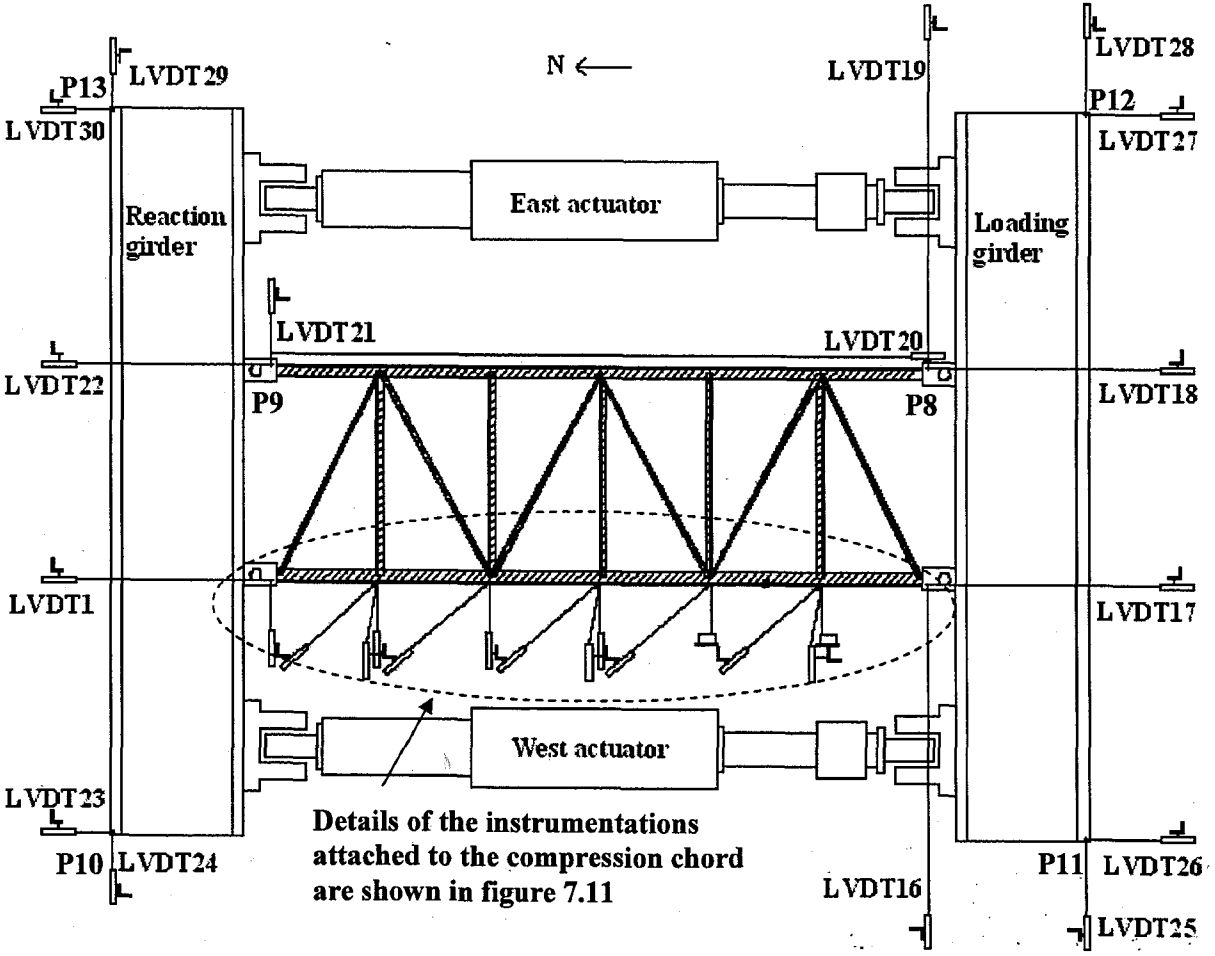

Figure 7.10 Instrumentation for CM Tests

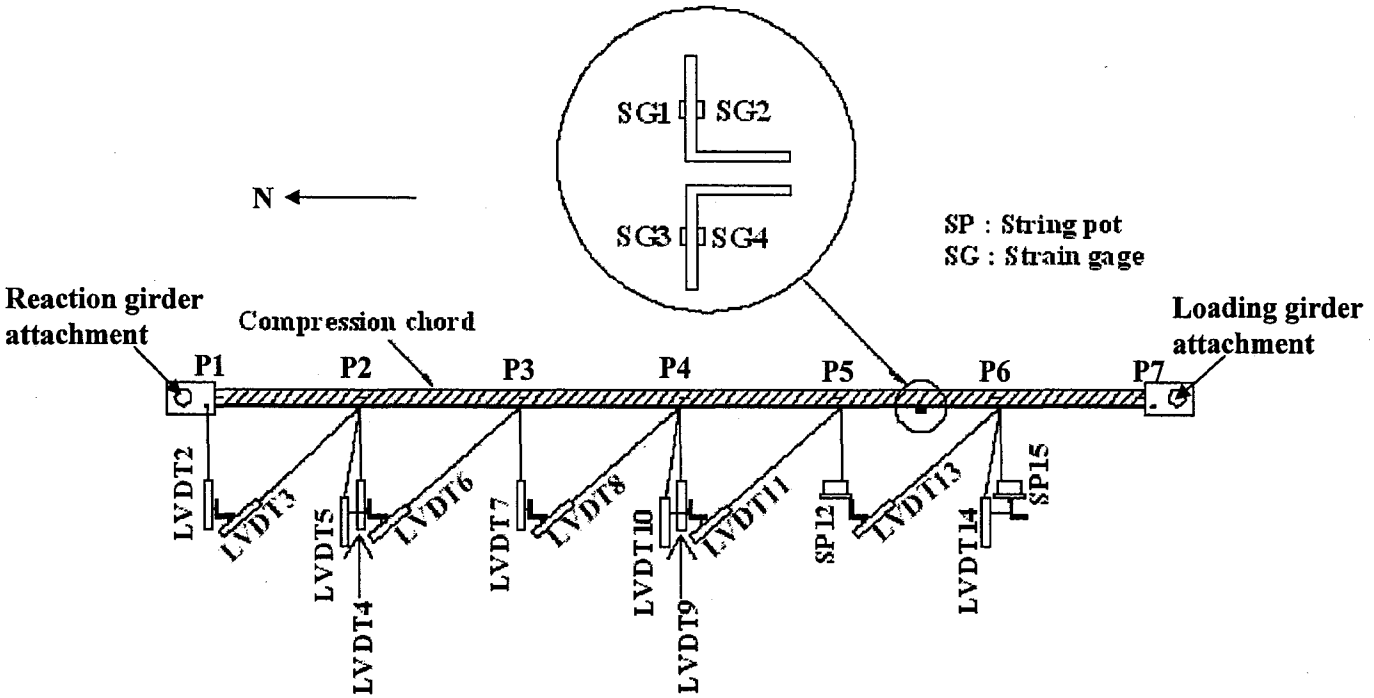

Figure 7.11 Compression Chord Instrumentation Detail for CM Tests

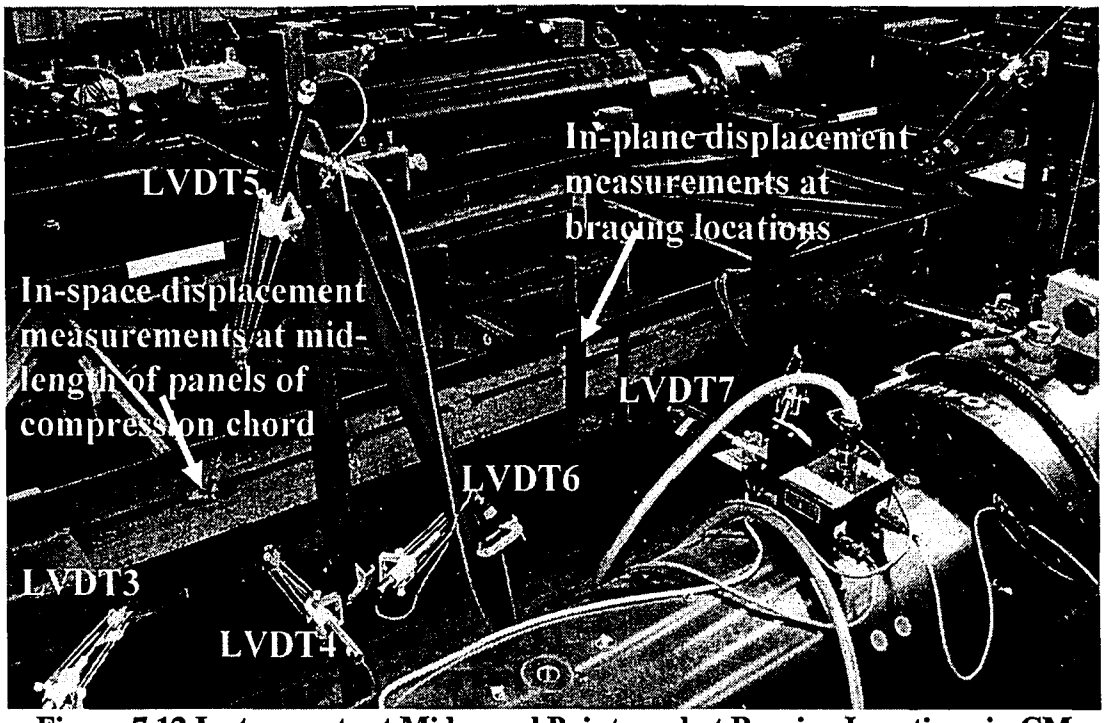

Figure 7.12 Instruments at Mid-panel Points and at Bracing Locations in CM Test Specimens

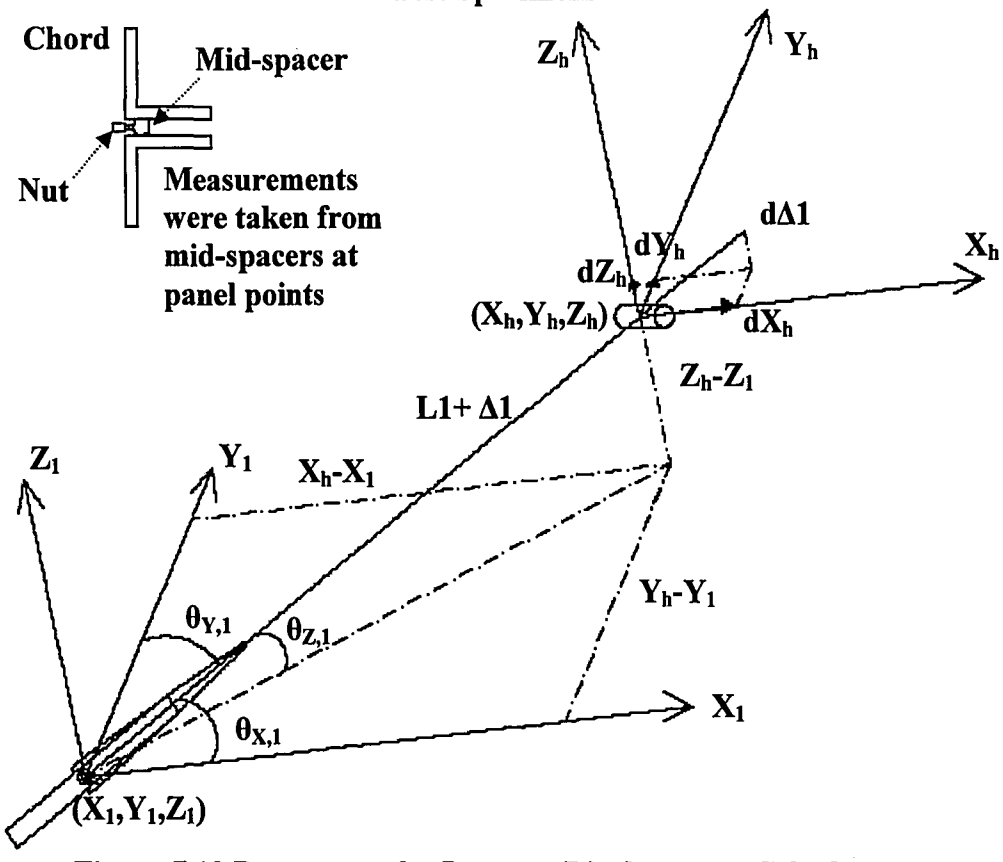

Figure 7.13 Parameters for In-space Displacement Calculations

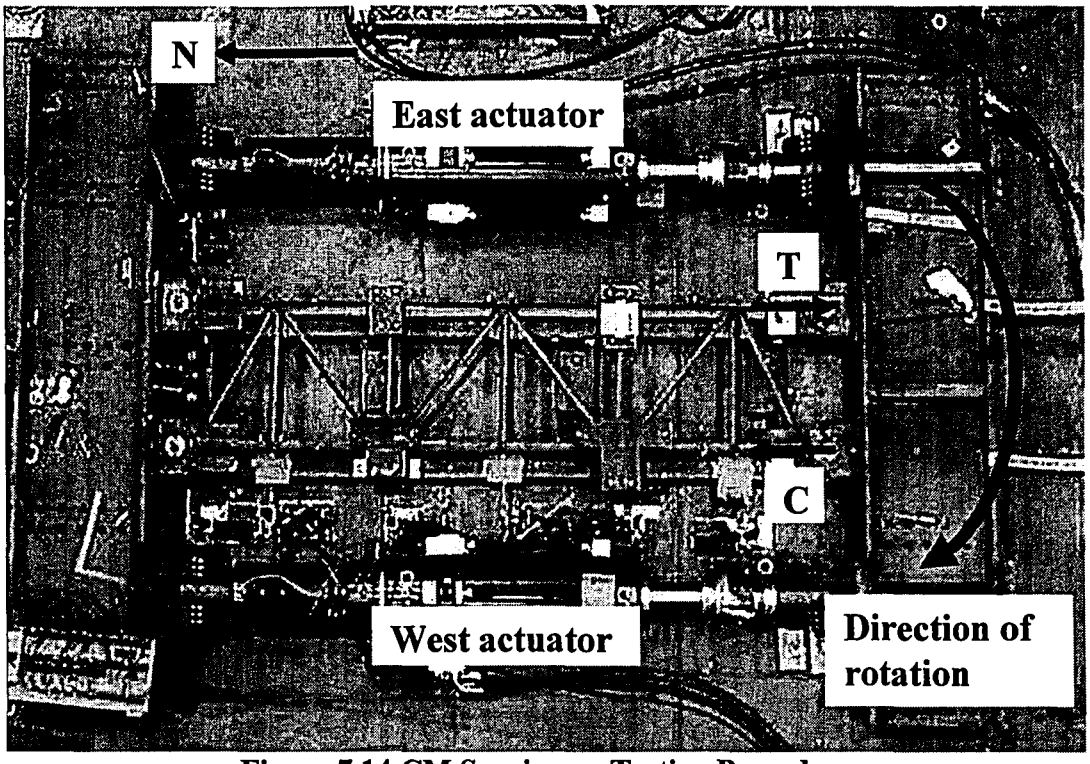

Figure 7.14 CM Specimens Testing Procedure

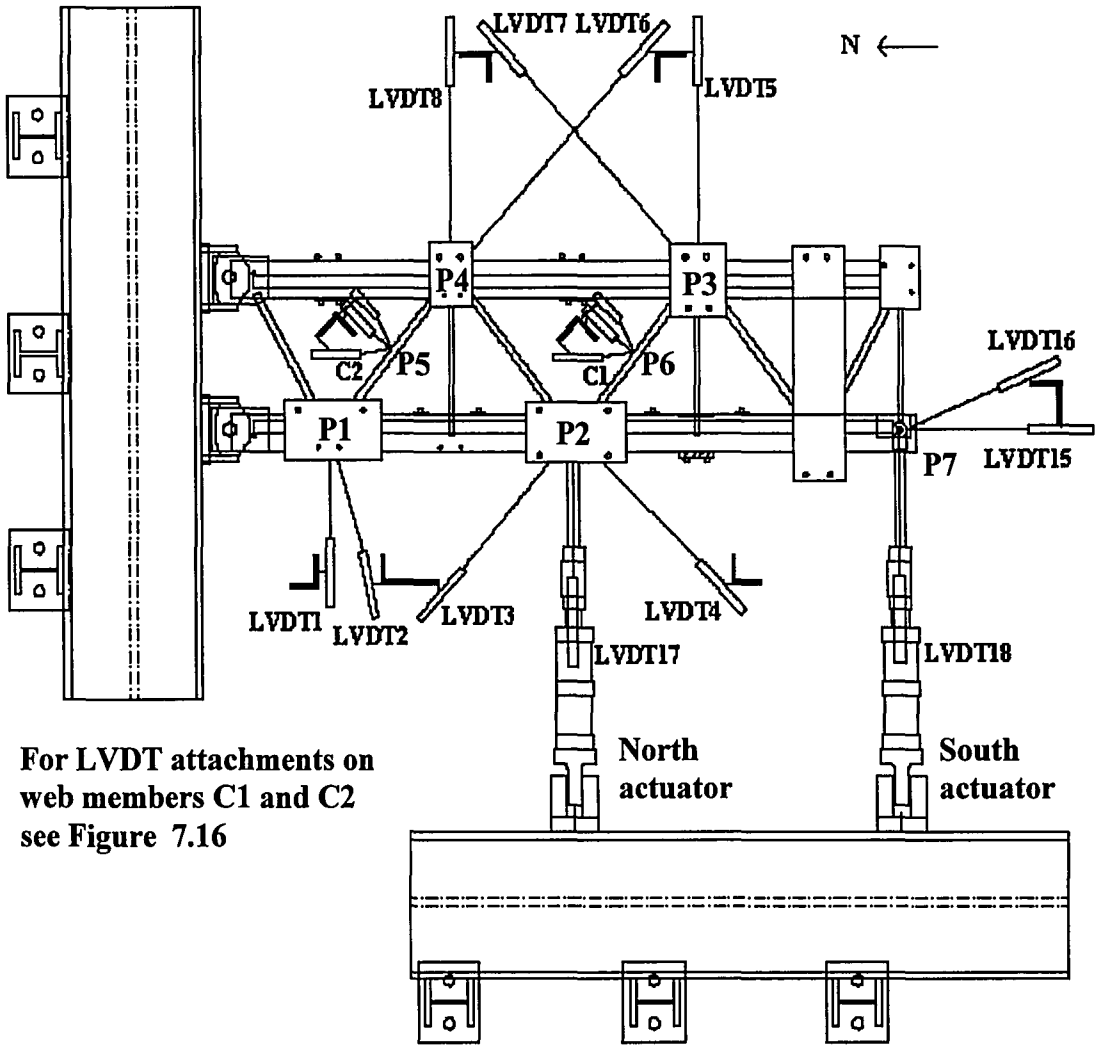

(a) LVDTs

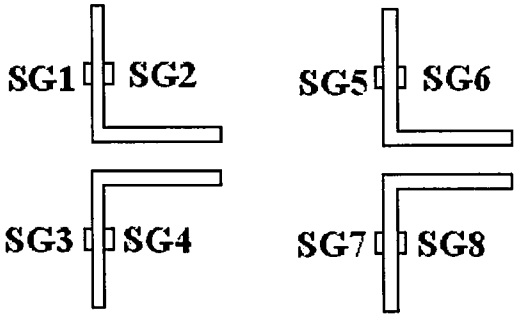

(b) Strain gages

Figure 7.15 Instrumentation for GM Test Specimens

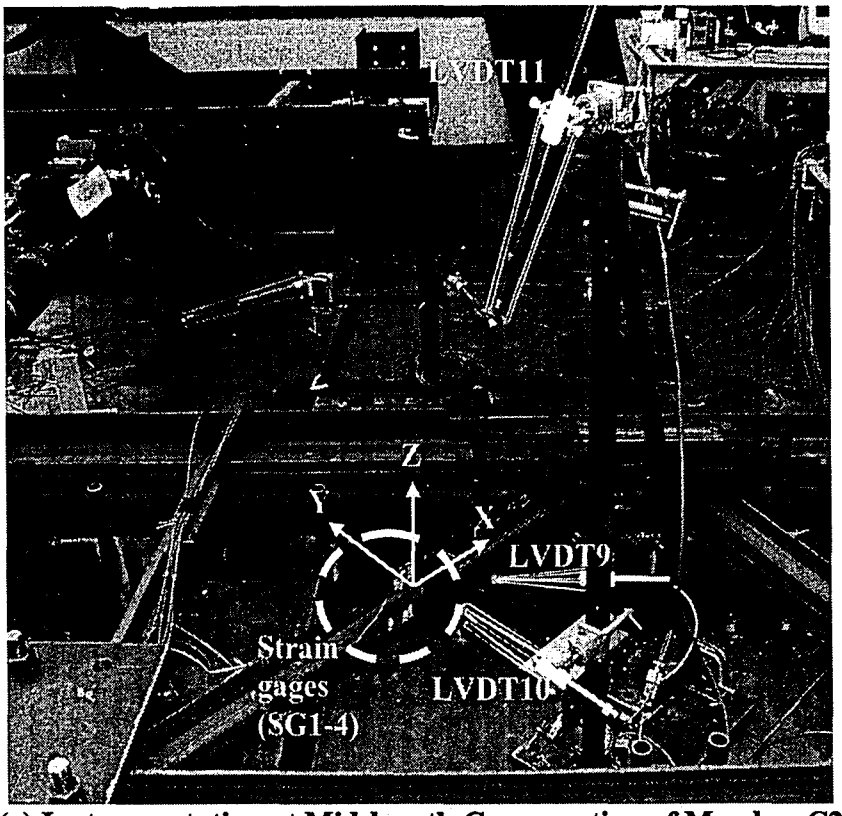

(a) Instrumentation at Mid-length Cross-section of Member C2

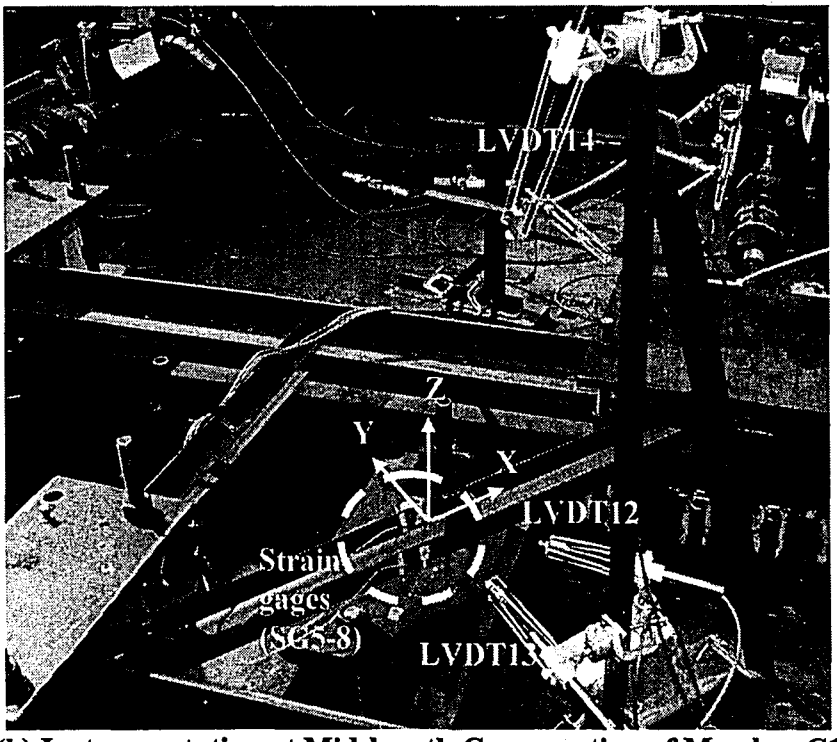

(b) Instrumentation at Mid-length Cross-section of Member C1

Figure 7.16 Instrumentation for GM Test Specimens

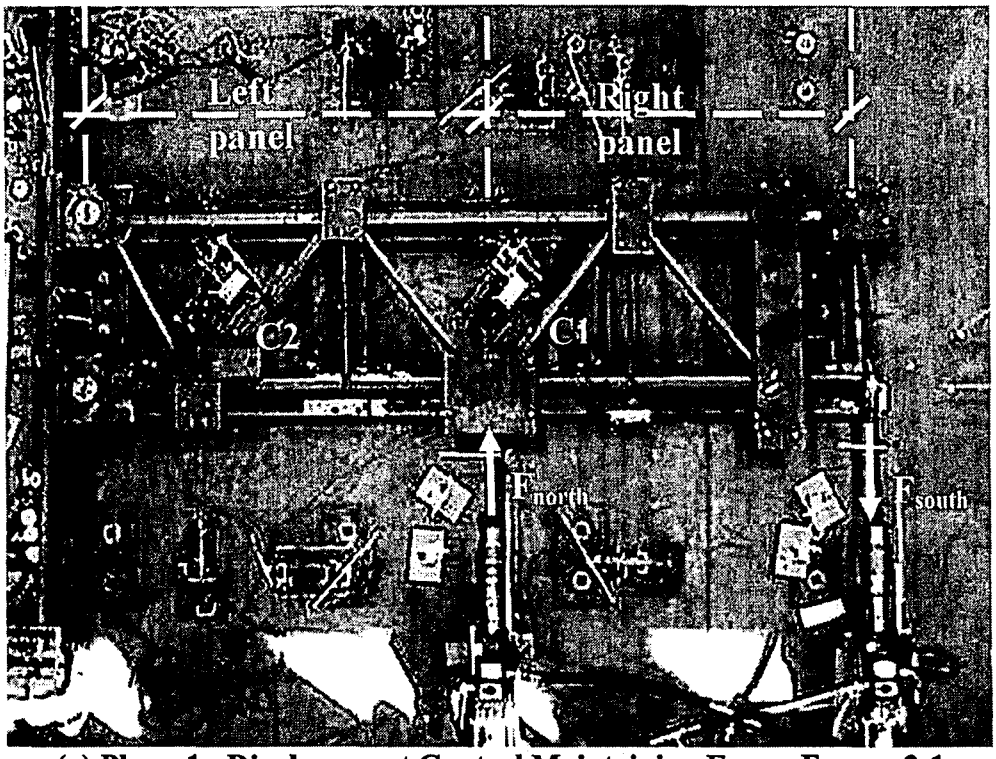

(a) Phase 1 - Displacement Control Maintaining $F_{south} : F_{north} = 2:1$

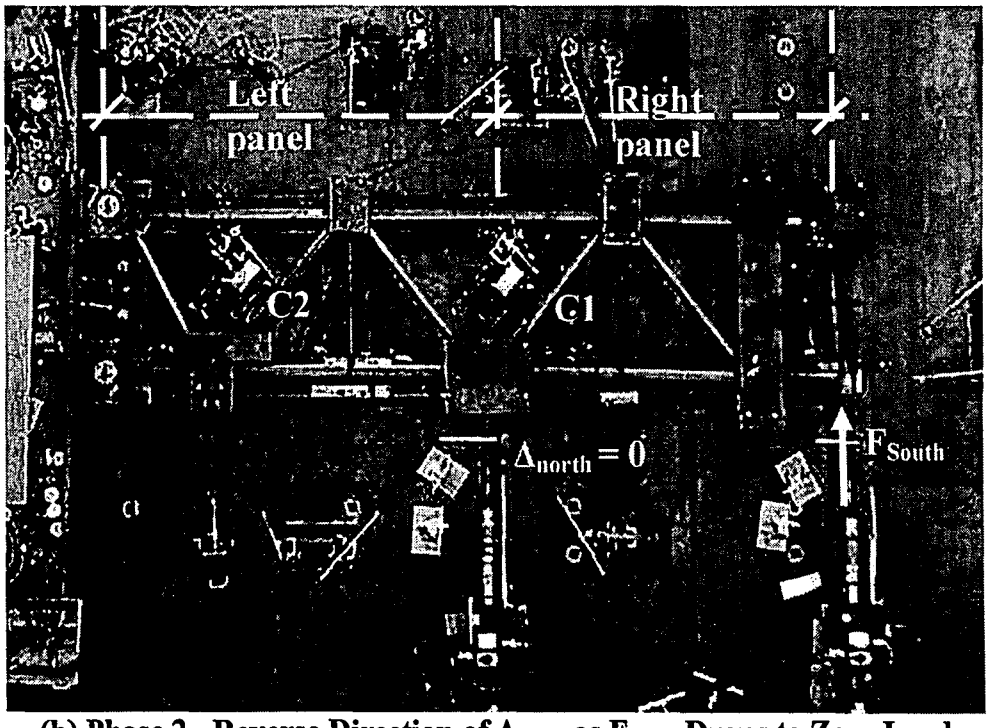

(b) Phase 2 - Reverse Direction of Δ_{south} as F_{south} Drops to Zero Load (while $\Delta_{north} = 0$)

Figure 7.17 GM Specimen Testing Procedure

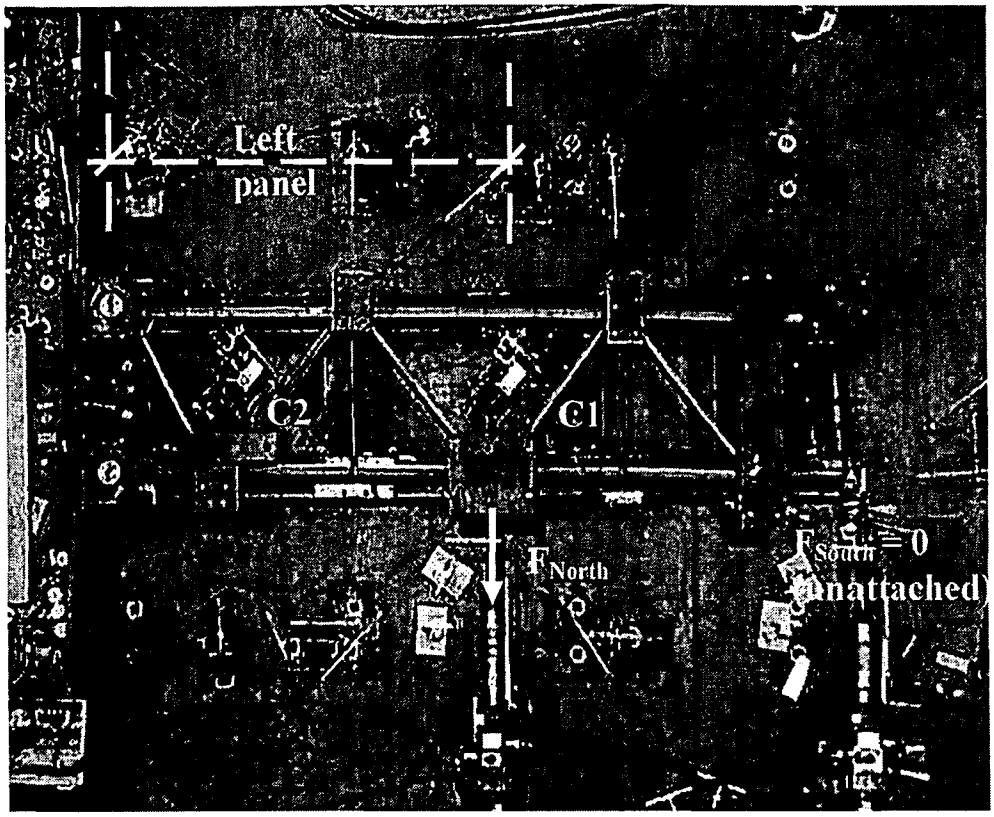

(c) Phase 3 - Displacement Control with Only F_{north} Applied to the Specimen

Figure 7.17 GM Specimen Testing Procedure (continued)

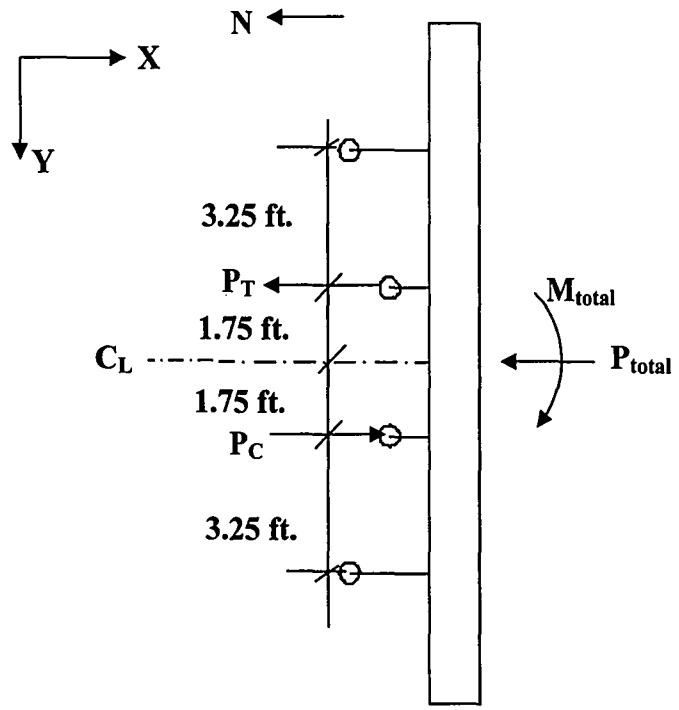

(a) Truss Chord Forces Related to Total Moment and Axial Force

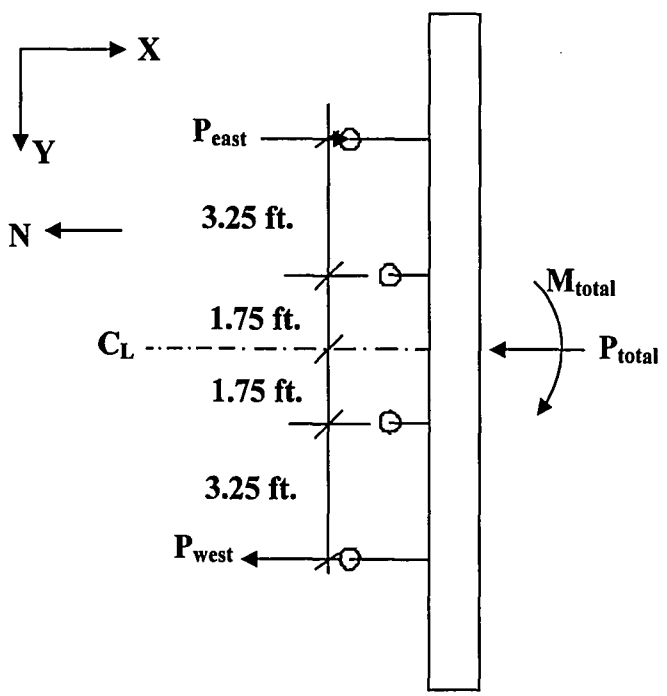

(b) Actuator Forces Related to Total Moment and Axial Force

Figure 7.18 Loading in Undeformed Position

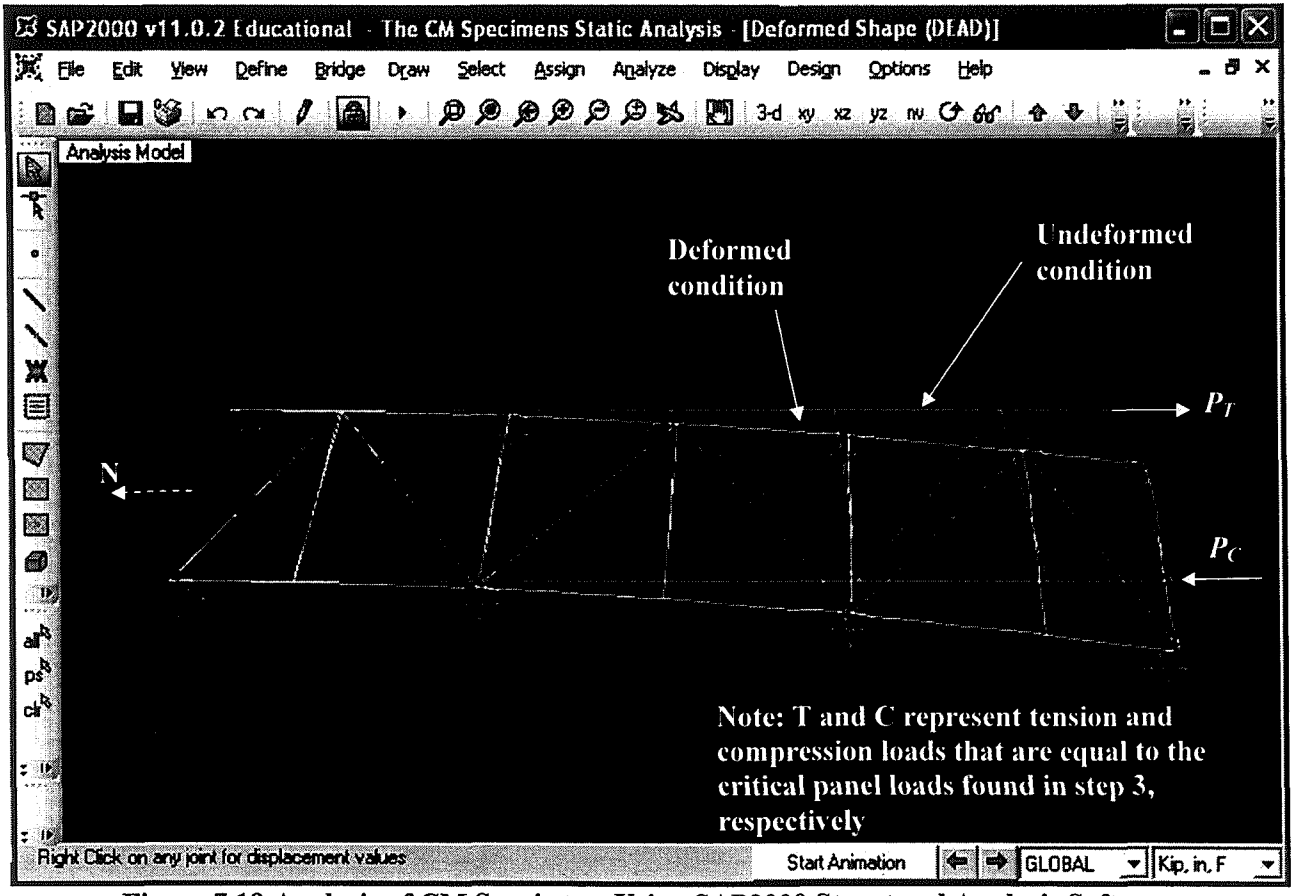

Figure 7.19 Analysis of CM Specimens Using SAP2000 Structural Analysis Software

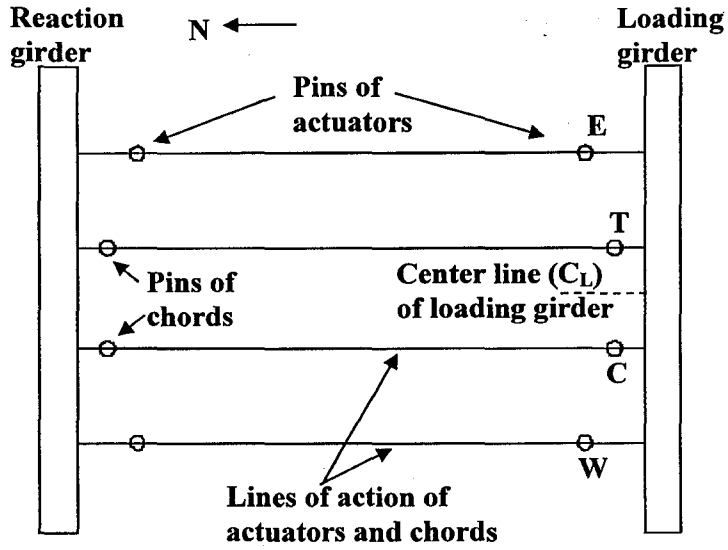

(a) Test Setup in Undeformed Position

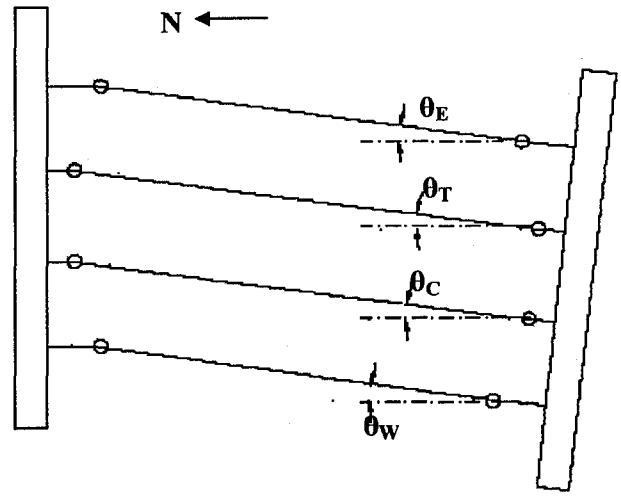

(b) Test Setup in Deformed Position

Figure 7.20 Overall Analysis of CM Specimens in Deformed Condition

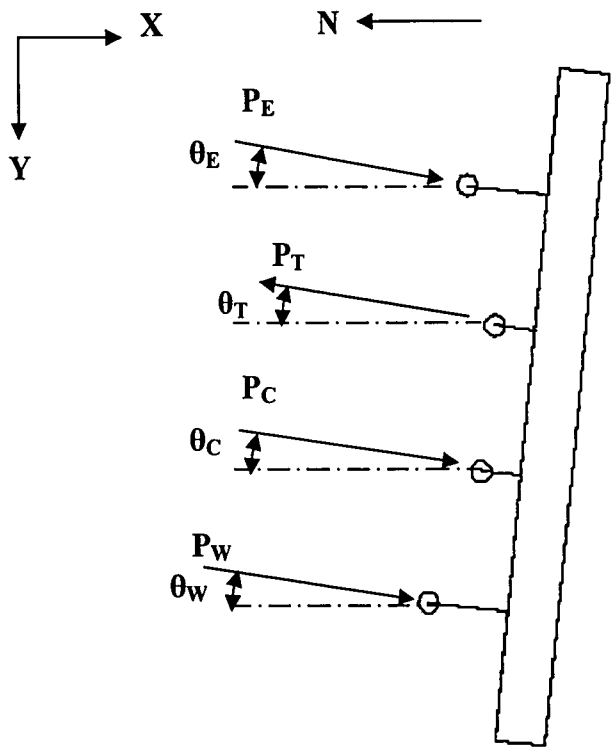

(c) Loading in Deformed Position

Figure 7.20 Overall Analysis of CM Specimens in Deformed Condition (continued)

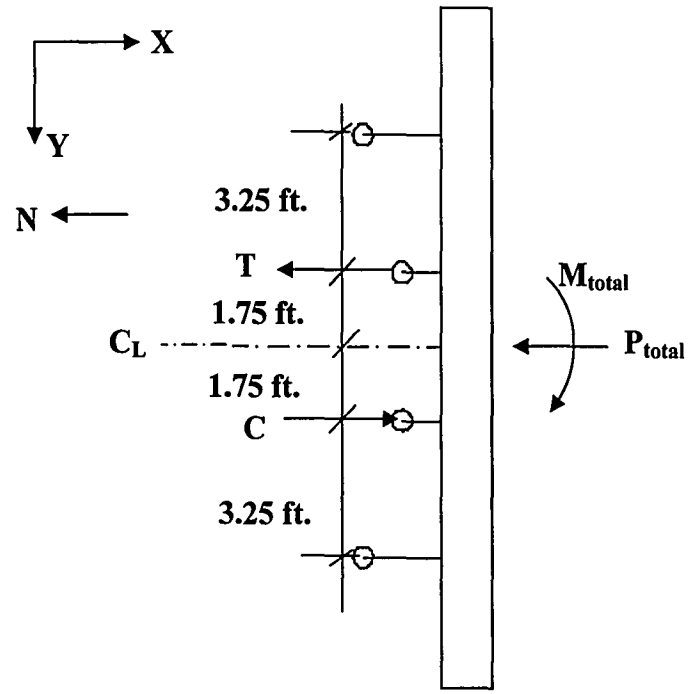

(a) Truss Chord Forces Related to Total Moment and Axial Force

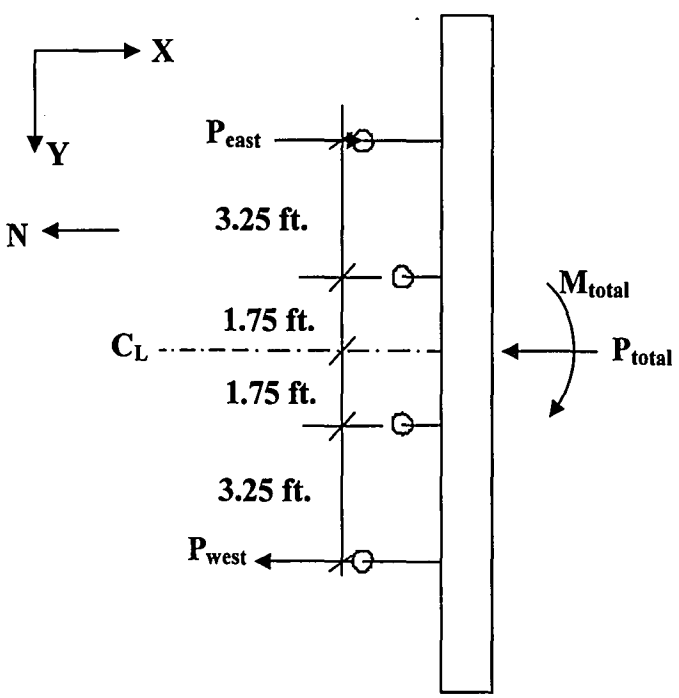

(b) Actuator Forces Related to Total Moment and Axial Force

Figure 7.21 Load Applied to Compression Chord in CM Specimens

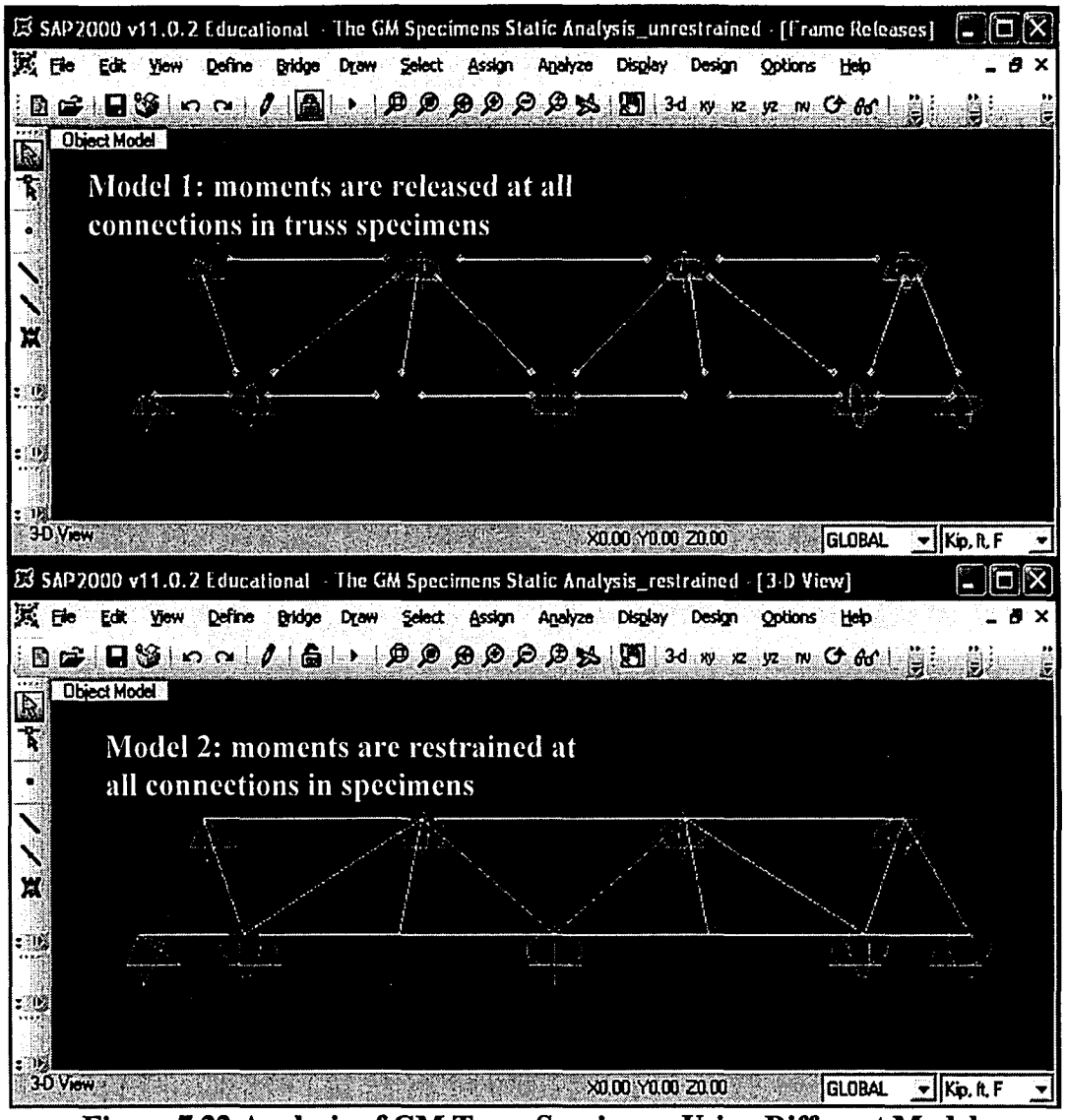

Figure 7.22 Analysis of GM Truss Specimens Using Different Models

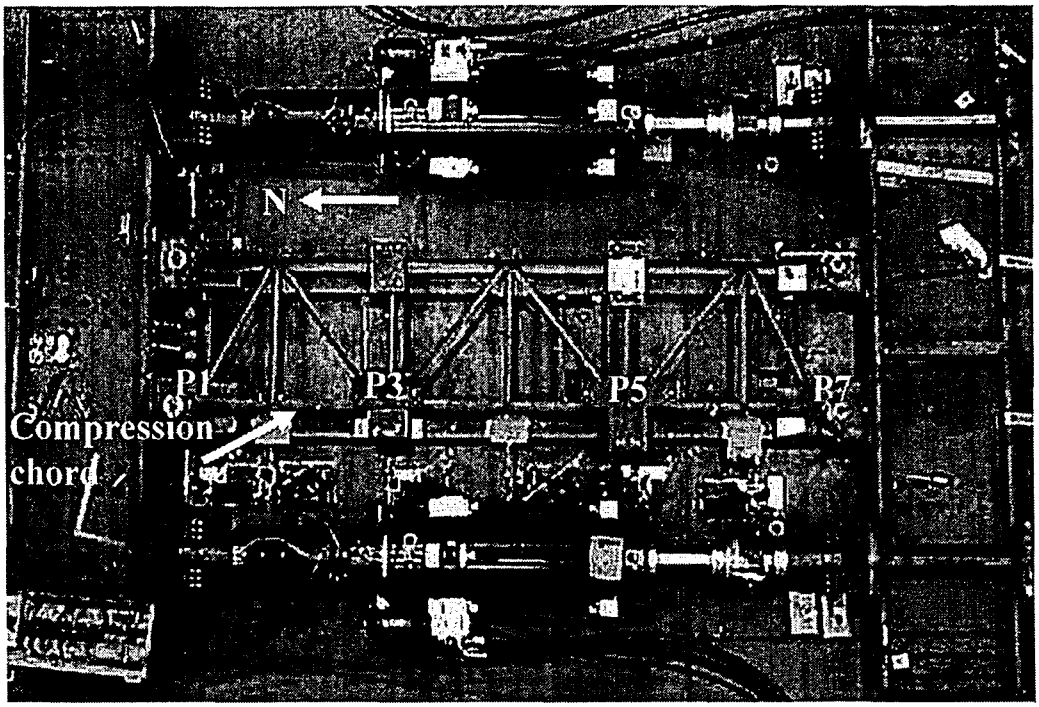

Figure 7.23 Specimen C1

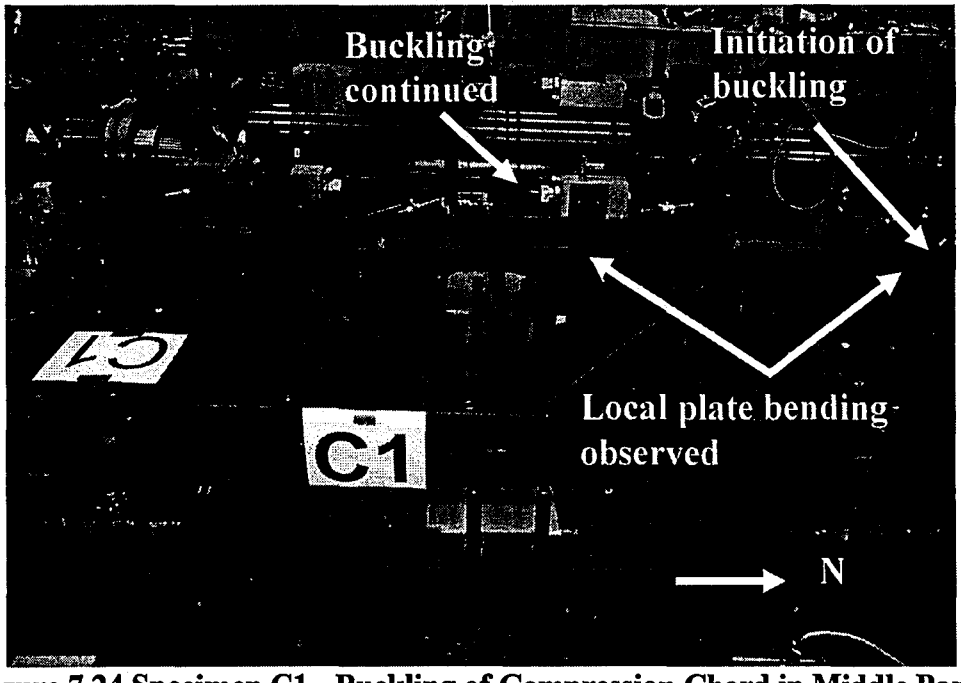

Figure 7.24 Specimen C1 - Buckling of Compression Chord in Middle Panel

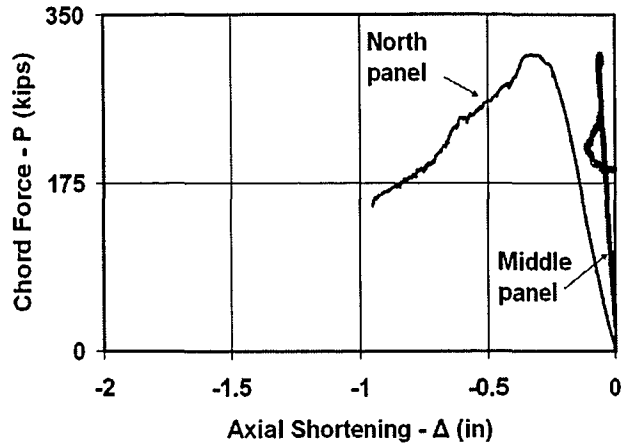

Figure 7.25 Specimen C1 - Compression Chord Force vs. Axial Shortening of the Middle Panel and the North Panel

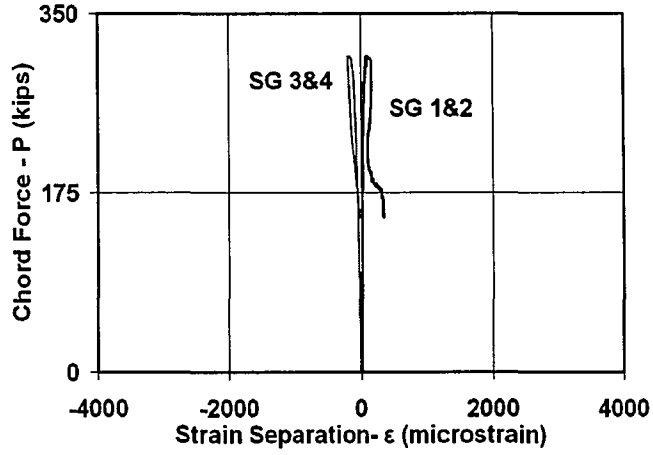

Figure 7.26 Specimen C1 - Compression Chord Force vs. Strain Separation at the South Panel

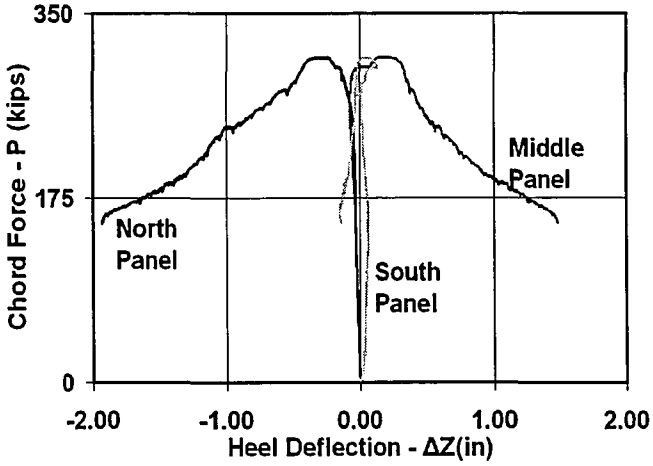

Figure 7.27 Specimen C1 - Compression Chord Force vs. Out-of-plane Deflection at Panel Points

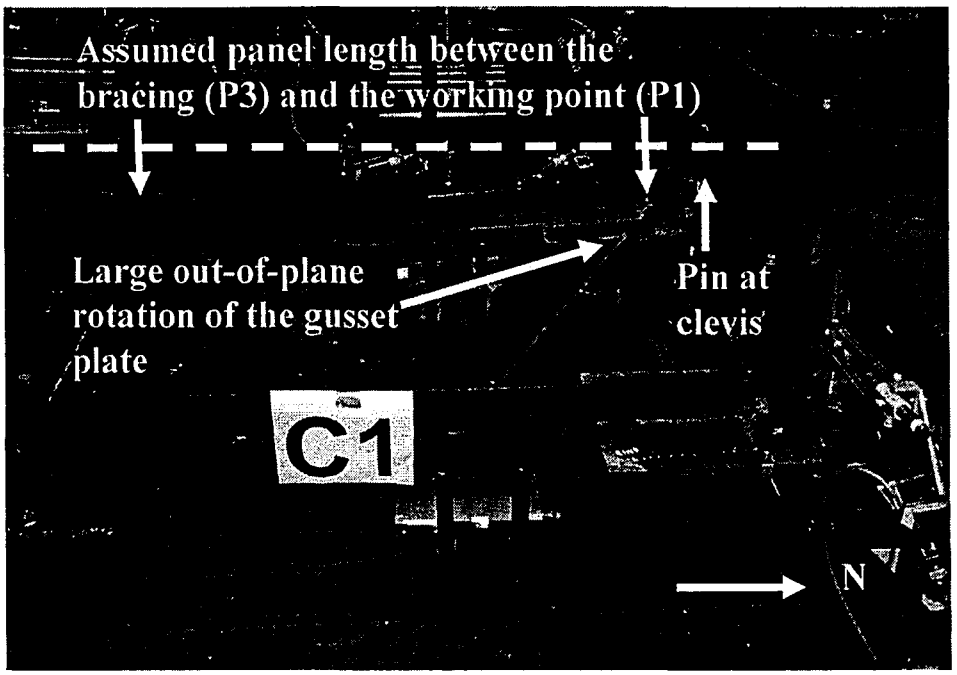

Figure 7.28 Specimen C1 - Large Out-of-plane Rotation is Observed at Fixed End Gusset Plate on Compression Chord

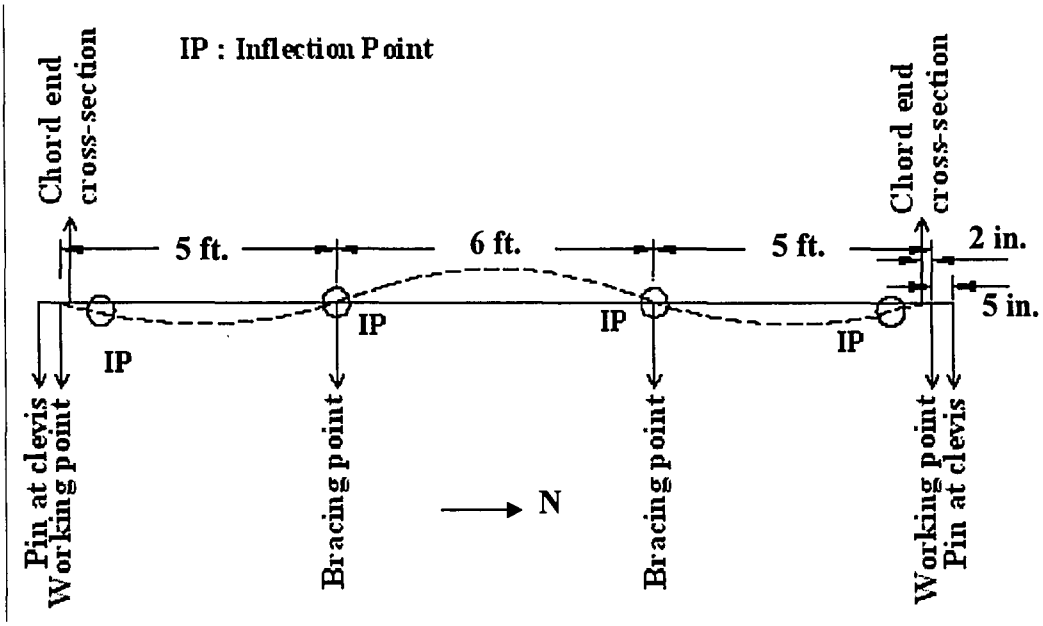

Figure 7.29 Intended Buckling Shape of the Compression Chord of Specimen C1 and Inflection Points along the Length

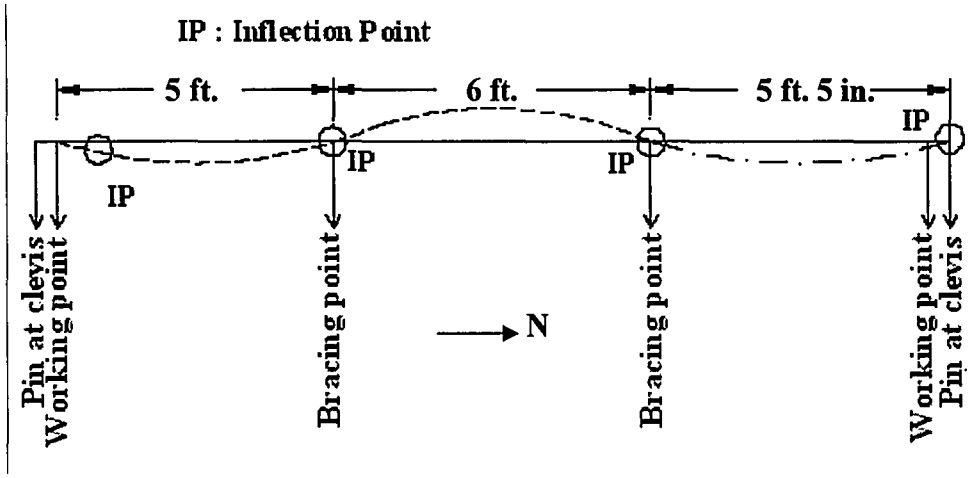

Figure 7.30 Actual Buckling Shape of Compression Chord of Specimen C1, when North End Inflection Point occurred at the Clevis Pin

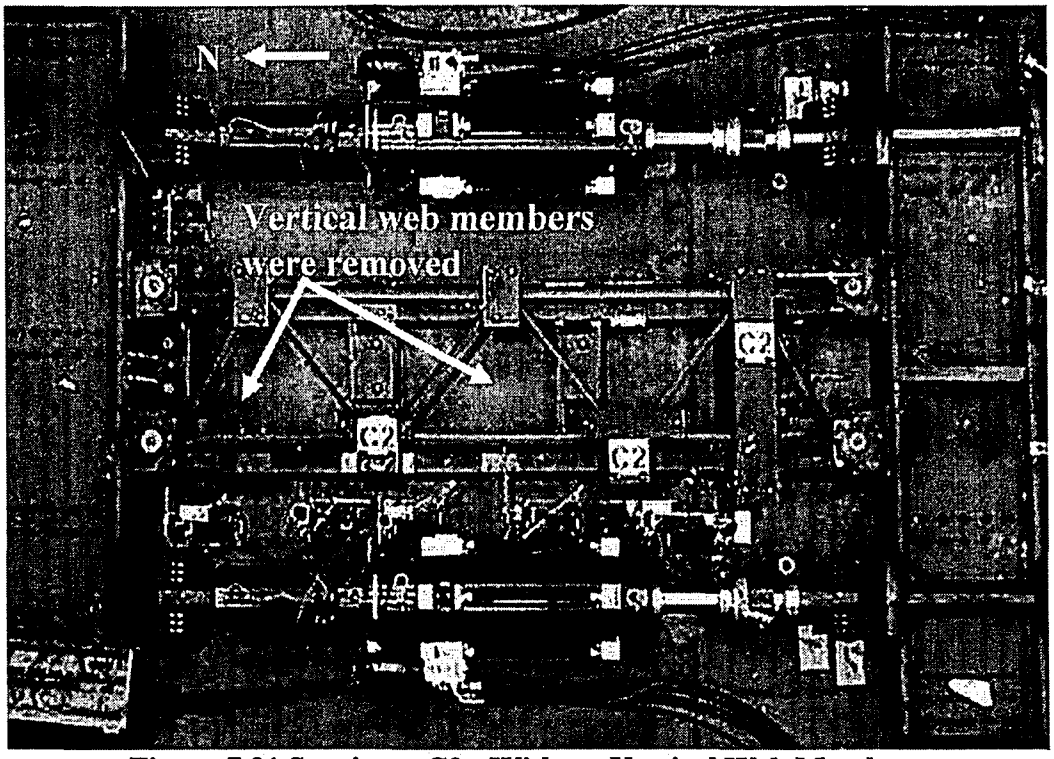

Figure 7.31 Specimen C2 - Without Vertical Web Members

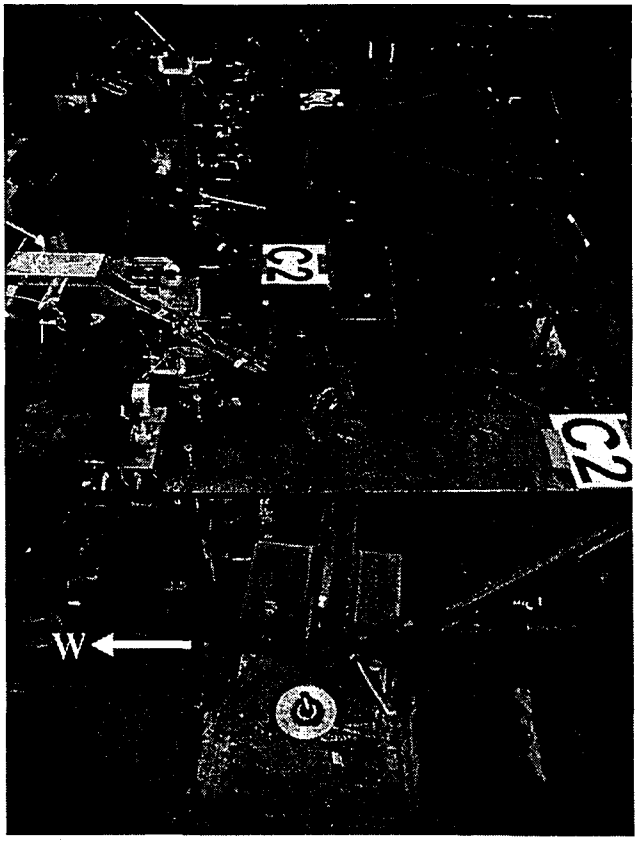

Figure 7.32 Specimen C2 - In-plane Buckling of Specimen C2

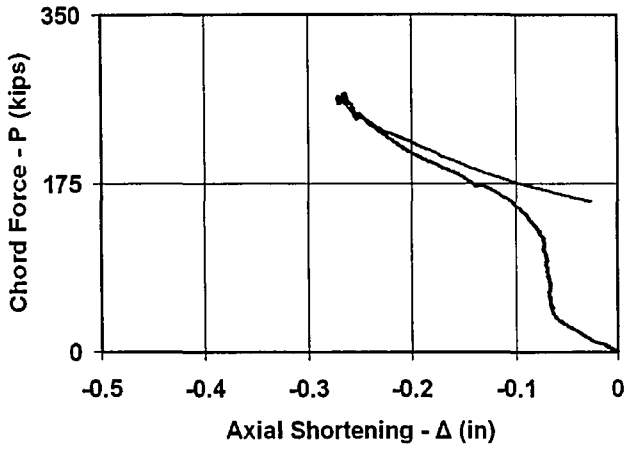

Figure 7.33 Specimen C2 - Compression Chord Force vs. Axial Shortening of the South Panel

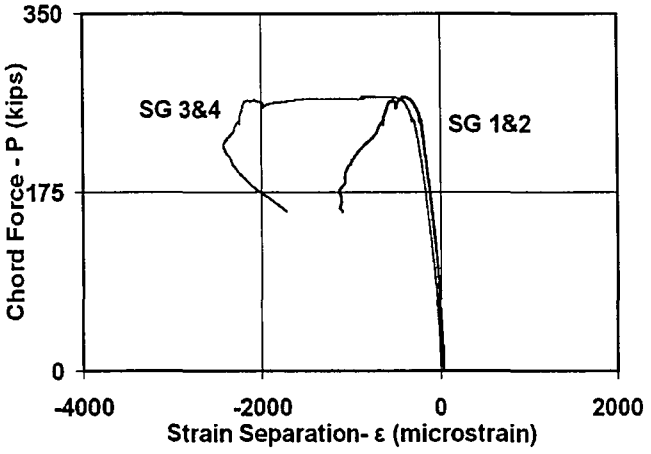

Figure 7.34 Specimen C2 - Compression Chord Force vs. Strain Separation at the South Panel

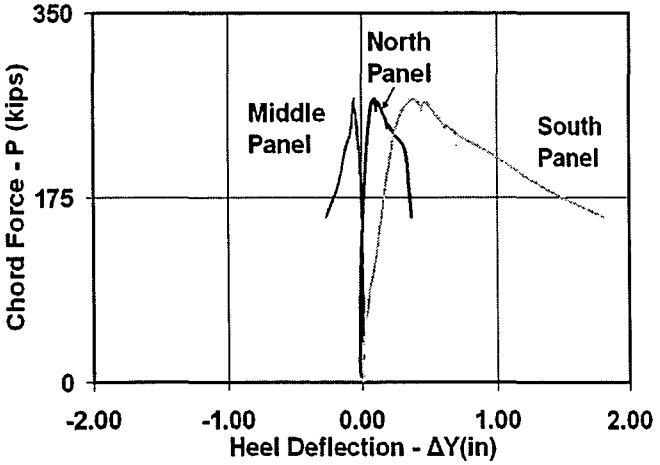

Figure 7.35 Specimen C2 - Compression Chord Force vs. In-plane Deflection at the Mid-length Cross-section

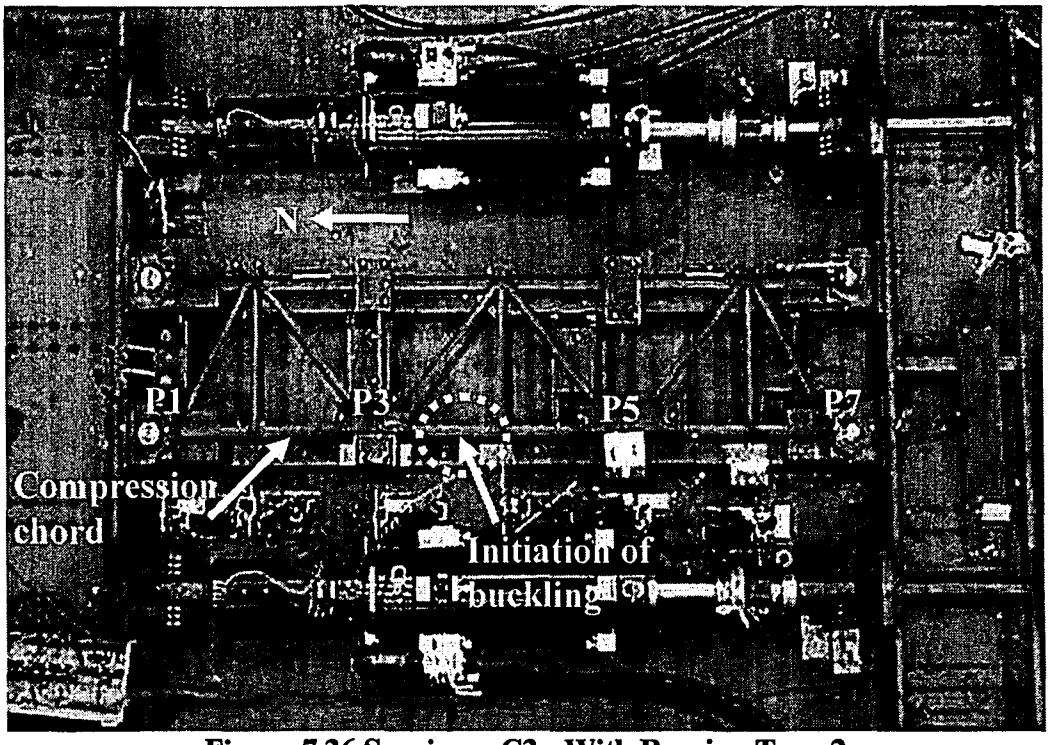

Figure 7.36 Specimen C3 - With Bracing Type 2

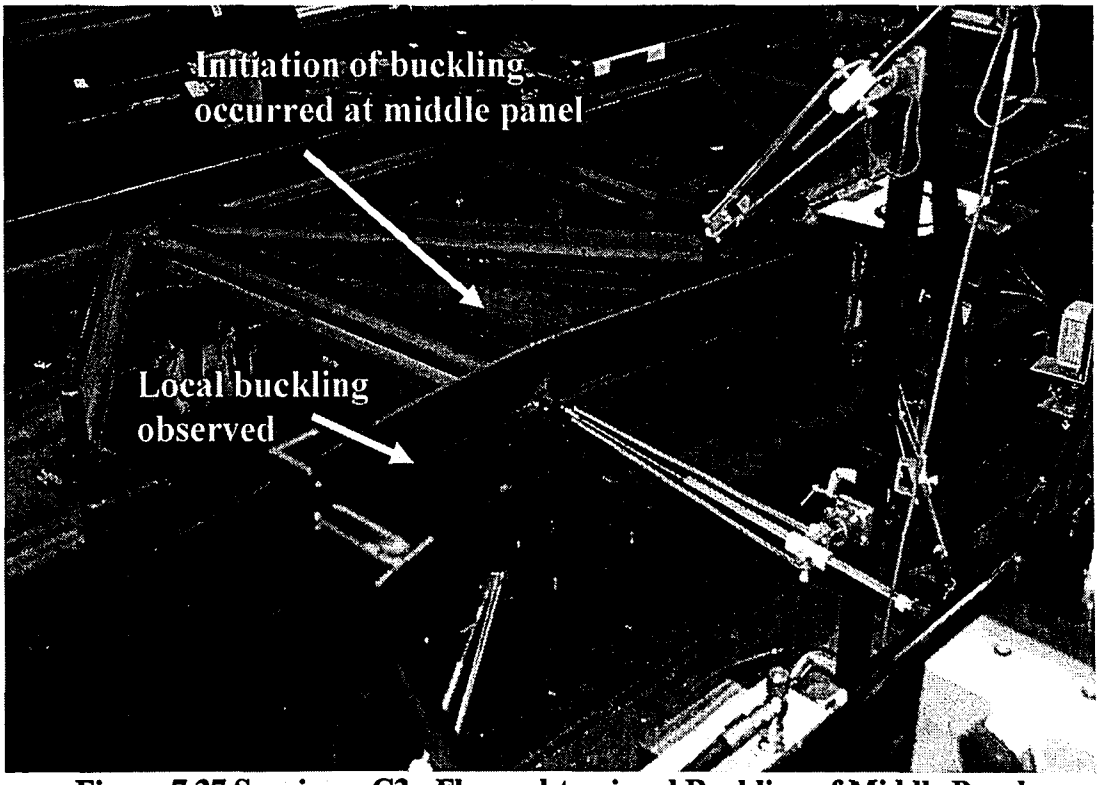

Figure 7.37 Specimen C3 - Flexural-torsional Buckling of Middle Panel

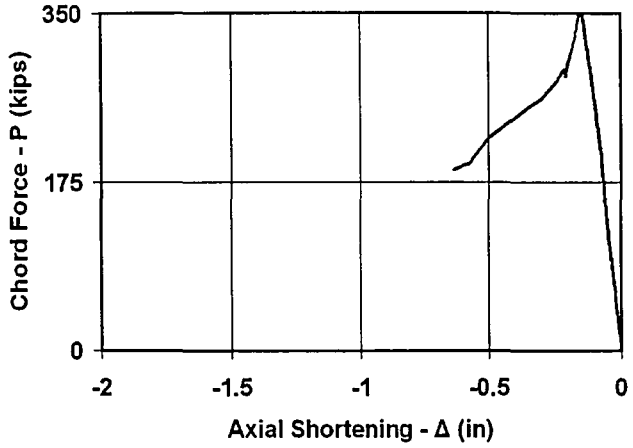

Figure 7.38 Specimen C3 - Compression Chord Force vs. Axial Shortening of the Middle Panel

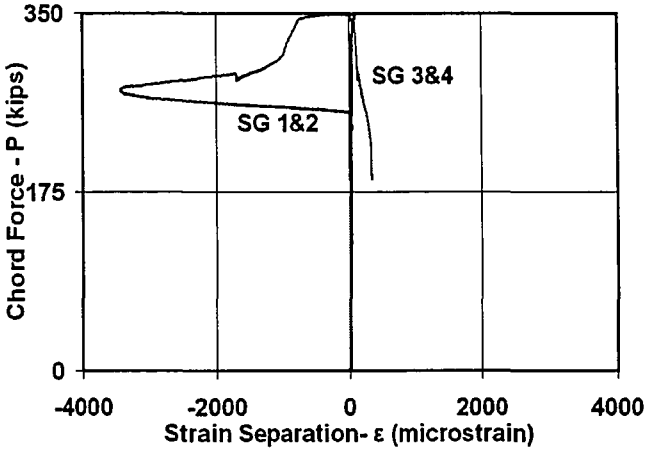

Figure 7.39 Specimen C3 - Compression Chord Force vs. Strain Separation at the South Panel

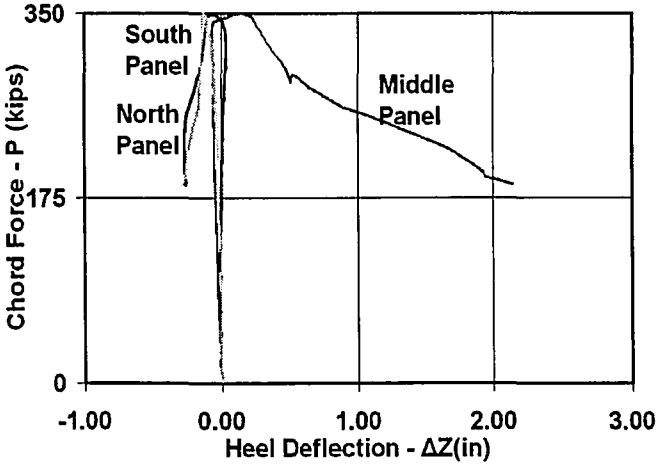

Figure 7.40 Specimen C3 - Compression Chord Force vs. Out-of-plane Deflection at Panel Points

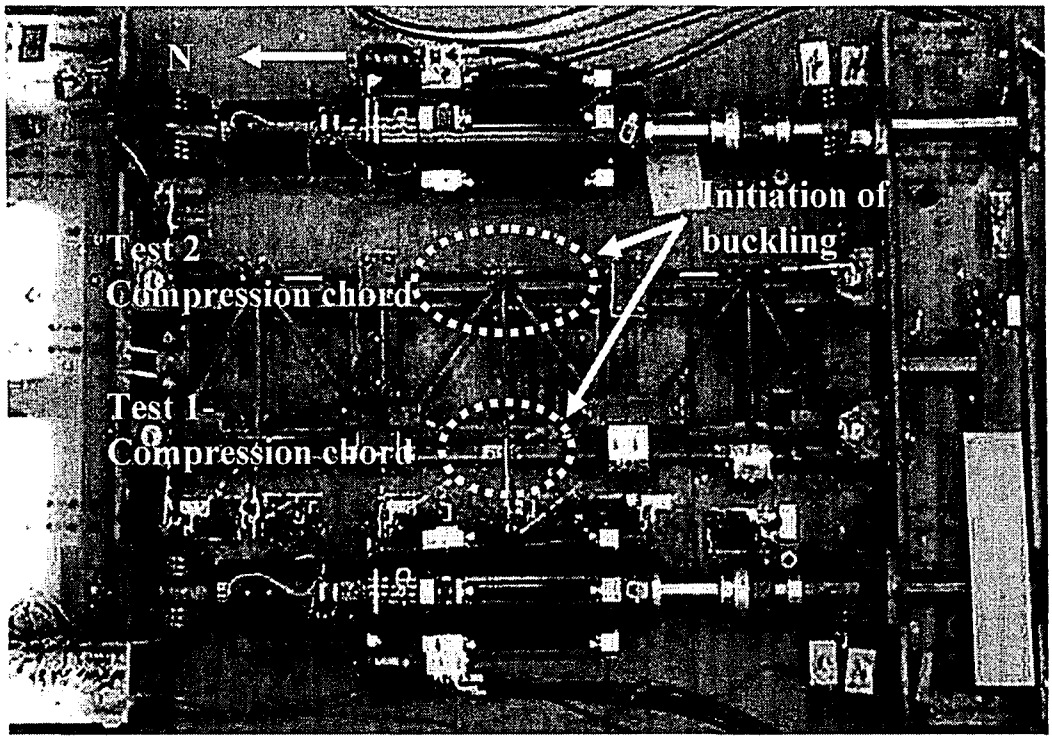

Figure 7.41 Specimen C4 - With Fewer Chord Mid-spacers

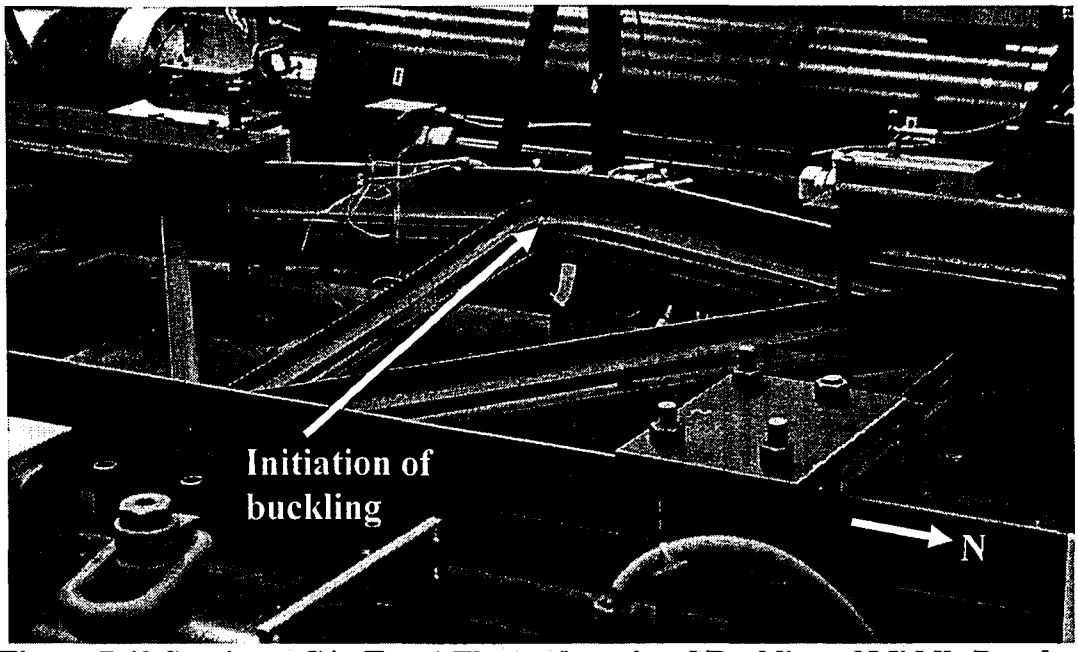

Figure 7.42 Specimen C4 - Test 1 Flexural-torsional Buckling of Middle Panel of West Chord

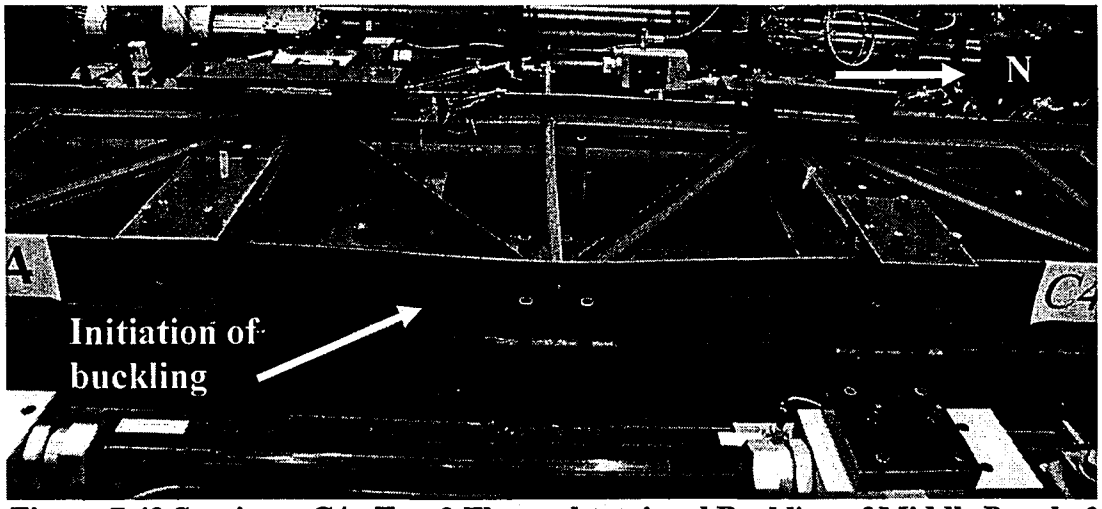

Figure 7.43 Specimen C4 - Test 2 Flexural-torsional Buckling of Middle Panel of East Chord

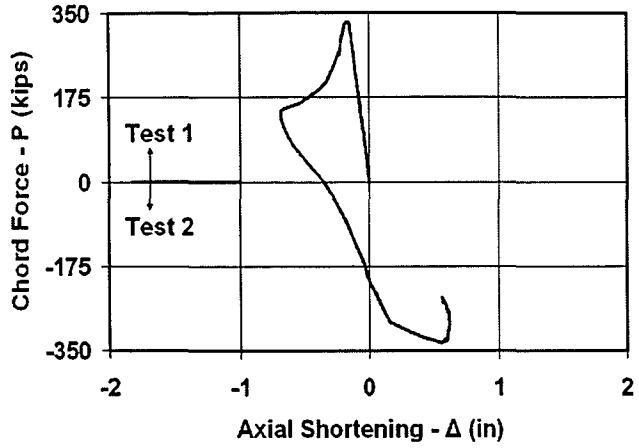

Figure 7.44 Specimen C4 - Chord Force vs. Axial Shortening of the Chord of the Middle Panel of West Chord

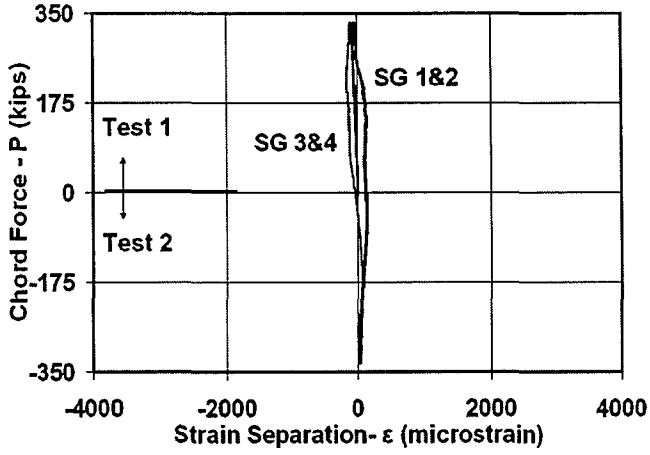

Figure 7.45 Specimen C4 - West Chord Force vs. Strain Separation at the South Panel of West Chord

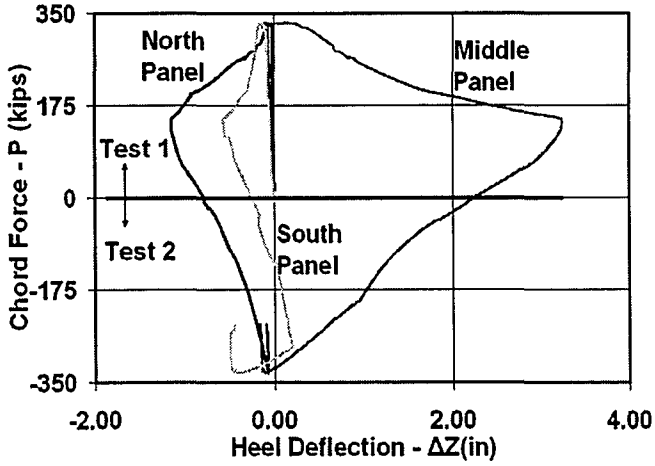

Figure 7.46 Specimen C4 - West Chord Force vs. Out-of-plane Deflection at Panel Points of West Chord

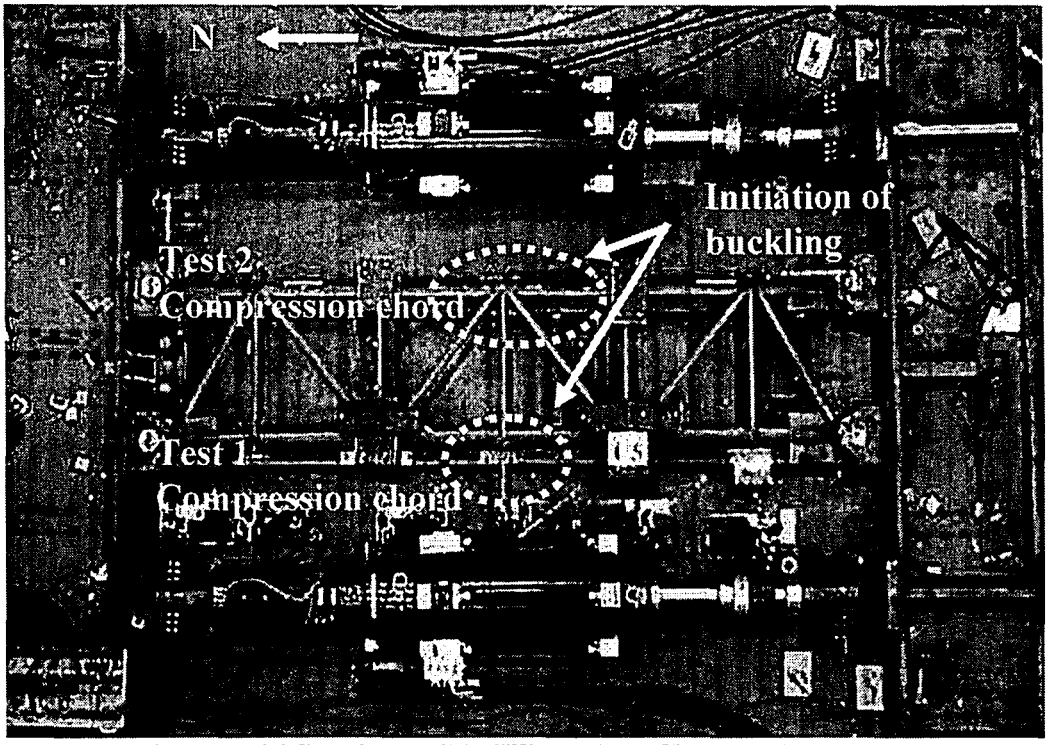

Figure 7.47 Specimen C5 - With More Chord Mid-spacers

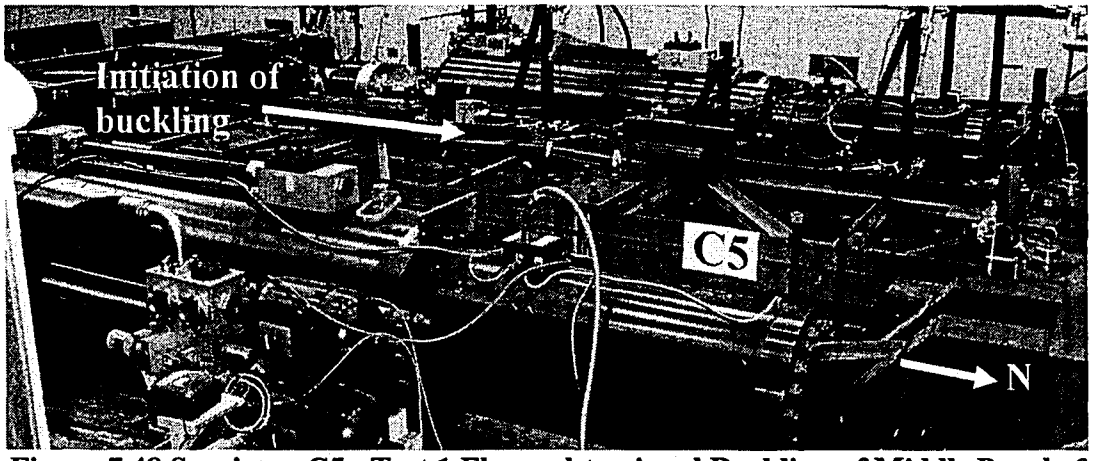

Figure 7.48 Specimen C5 - Test 1 Flexural-torsional Buckling of Middle Panel of West Chord

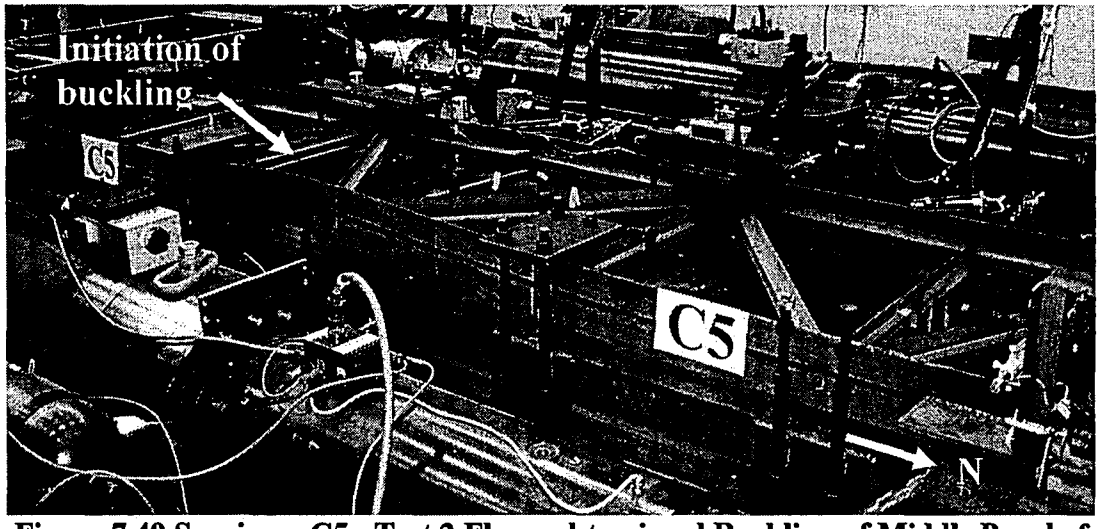

Figure 7.49 Specimen C5 - Test 2 Flexural-torsional Buckling of Middle Panel of East Chord

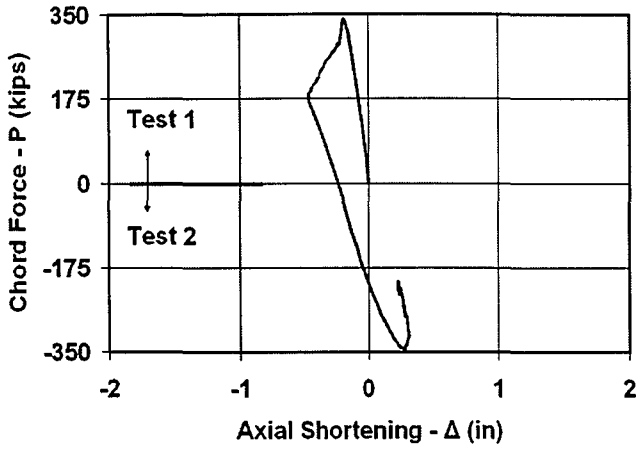

Figure 7.50 Specimen C5 - West Chord Force vs. Axial Shortening of the Middle Panel of West Chord

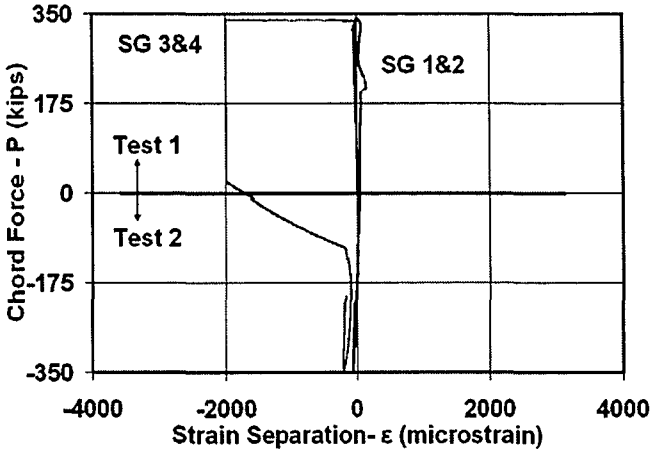

Figure 7.51 Specimen C5 - West Chord Force vs. Strain Separation at the South Panel of West Chord

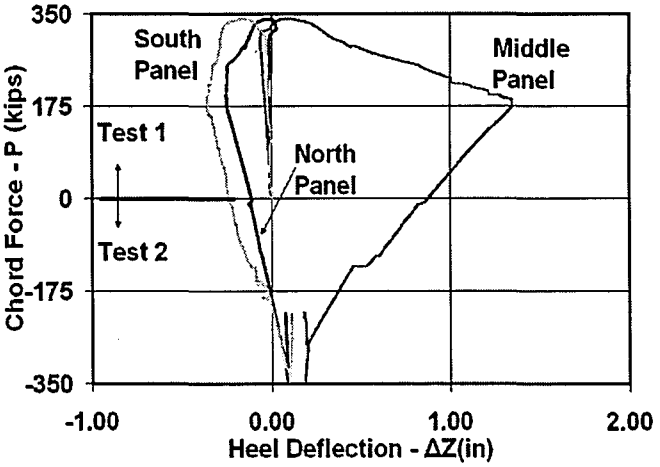

Figure 7.52 Specimen C5 - West Chord Force vs. Out-of-plane Deflection at Panel Points

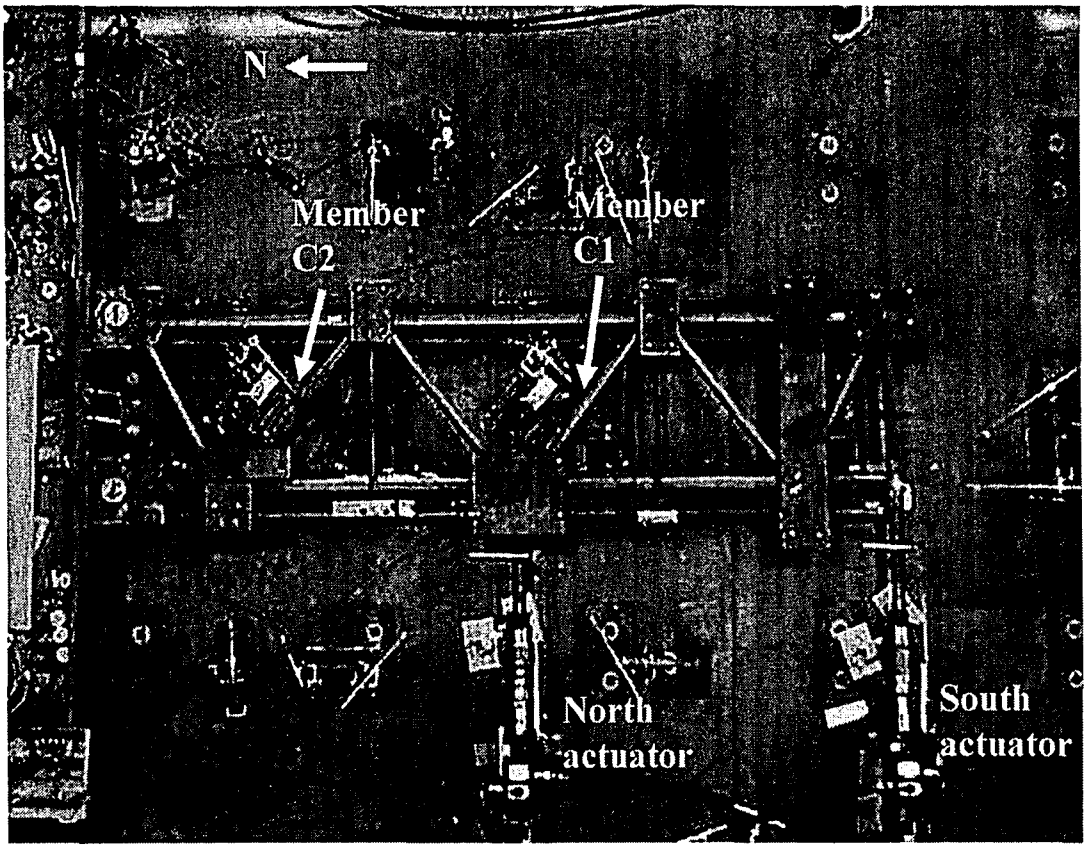

Figure 7.53 Specimen G2

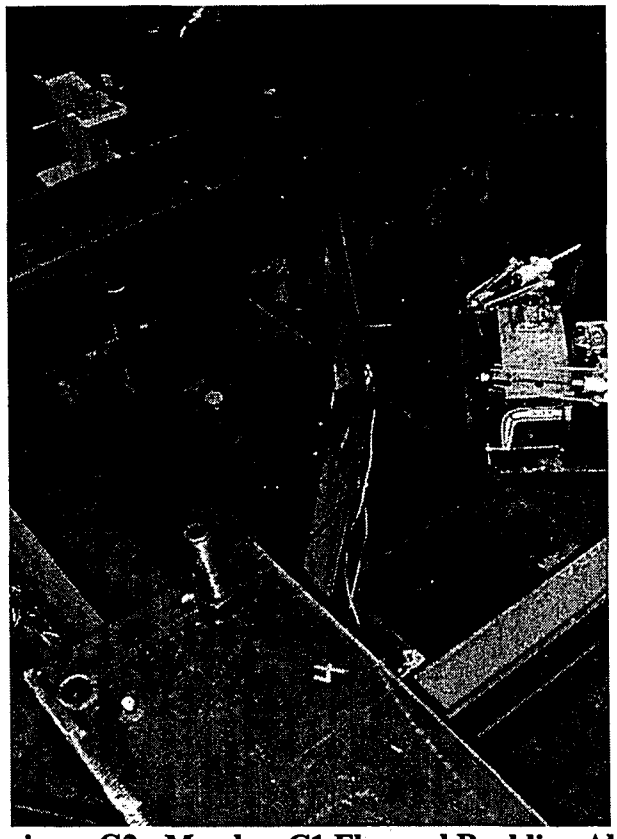

Figure 7.54 Specimen G2 - Member C1 Flexural Buckling About Weak Axis

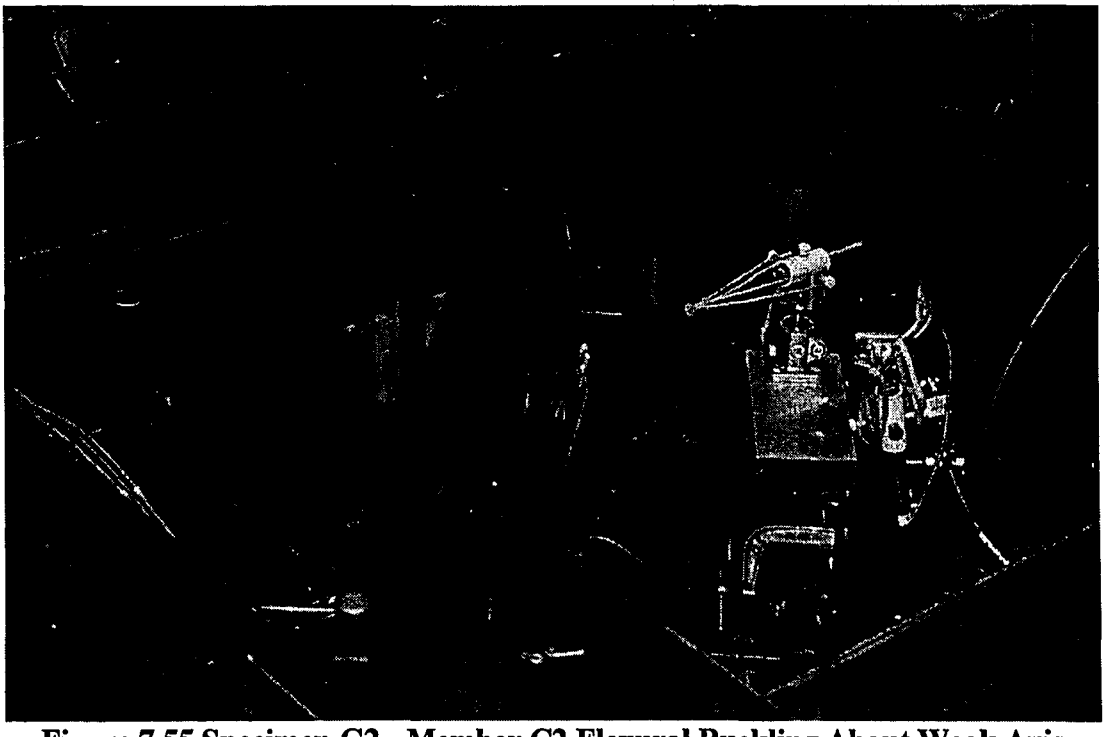

Figure 7.55 Specimen G2 - Member C2 Flexural Buckling About Weak Axis

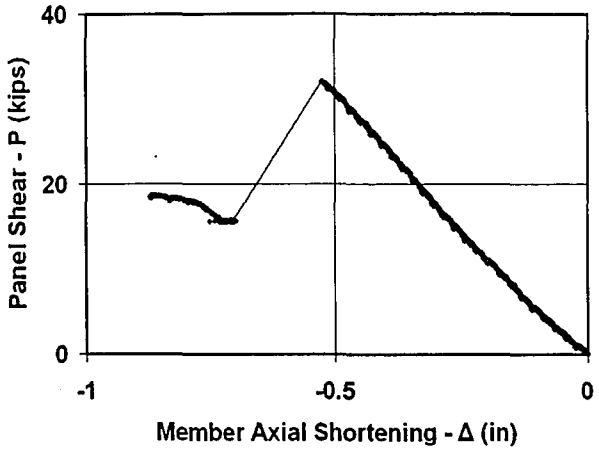

Figure 7.56 Specimen G2 - Right Panel Shear vs. Member C1 Axial Shortening

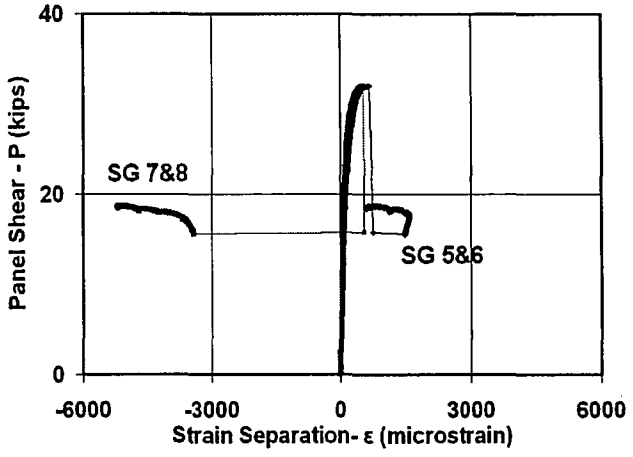

Figure 7.57 Specimen G2 - Right Panel Shear vs. Member C1 Strain Separation

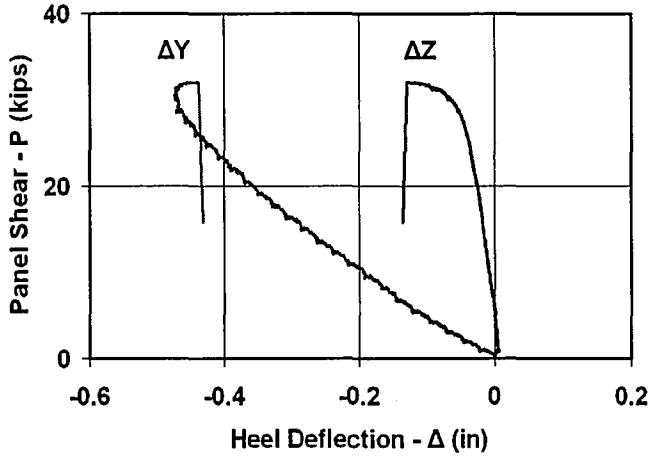

Figure 7.58 Specimen G2 - Right Panel Shear vs. Member C1 Heel Deflection

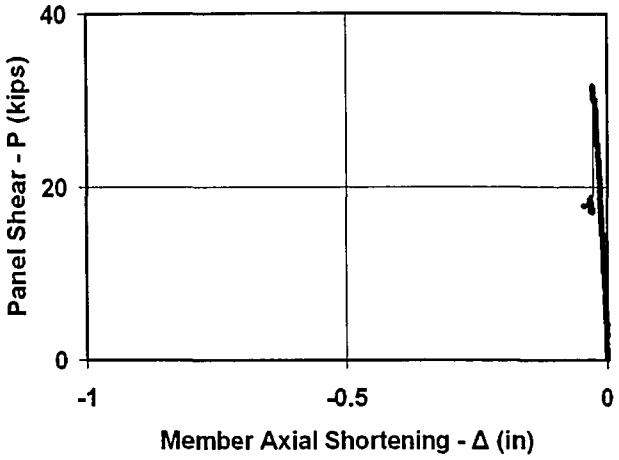

Figure 7.59 Specimen G2 -Left Panel Shear vs. Member C2 Axial Shortening

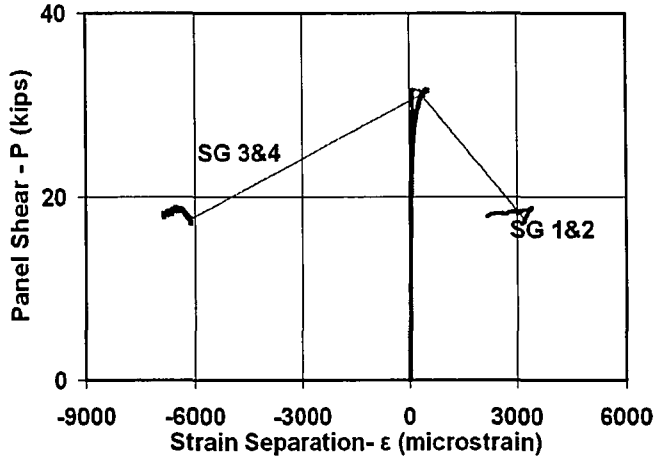

Figure 7.60 Specimen G2 - Left Panel Shear vs. Member C2 Strain Separation

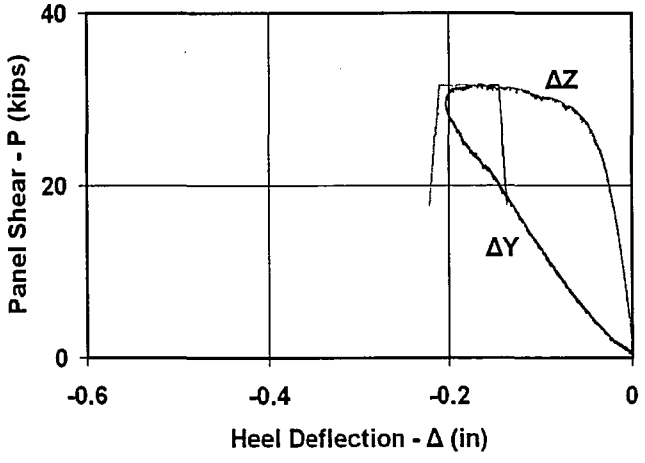

Figure 7.61 Specimen G2 - Left Panel Shear vs. Member C2 Heel Deflection

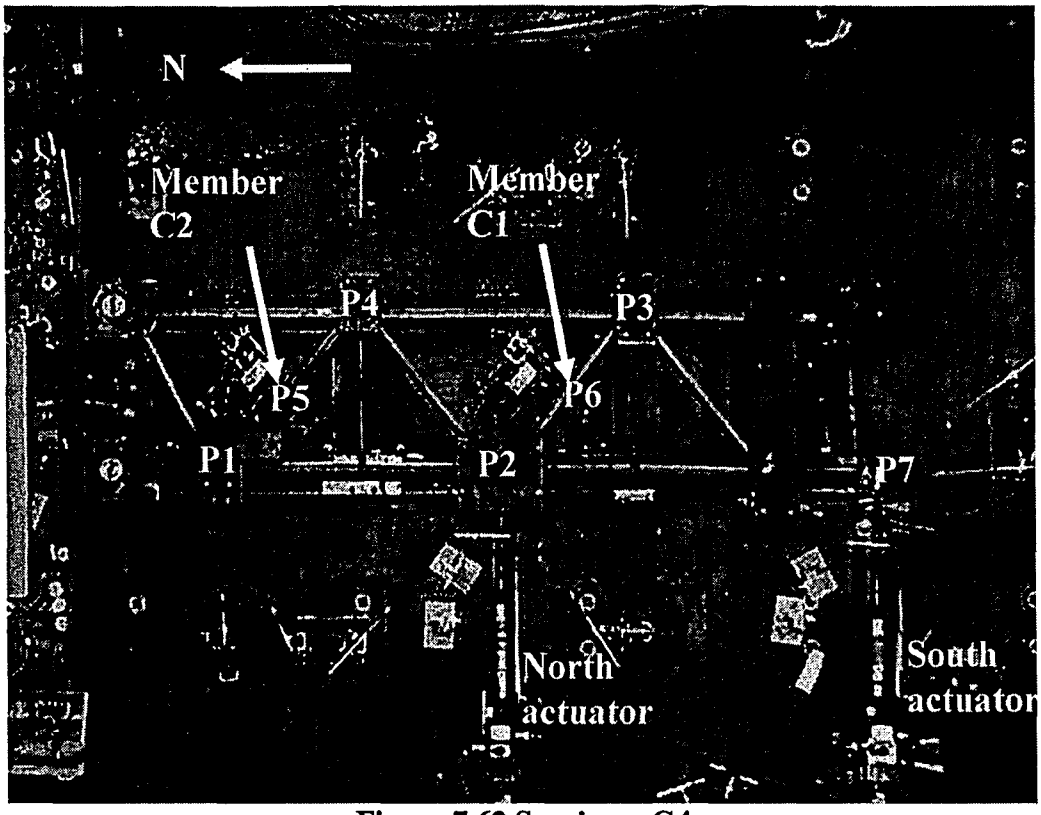

Figure 7.62 Specimen G4

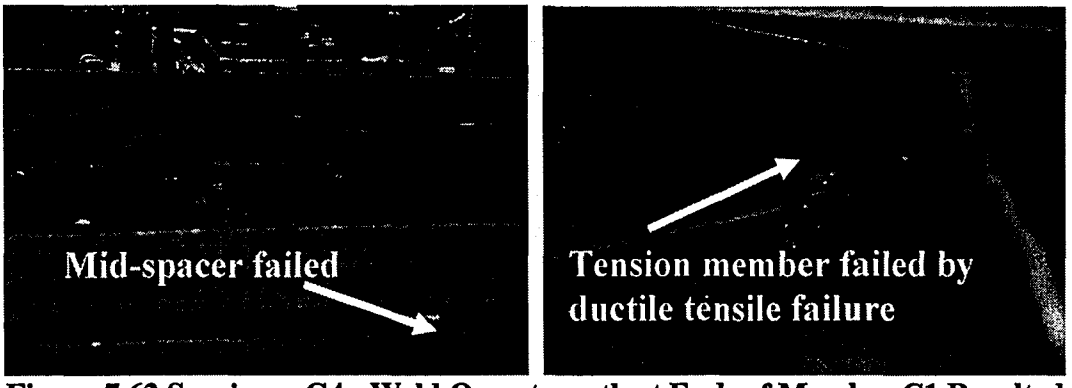

Figure 7.63 Specimen G4 - Weld Overstrength at Ends of Member C1 Resulted in Ductile Tensile Failure of Adjacent Member

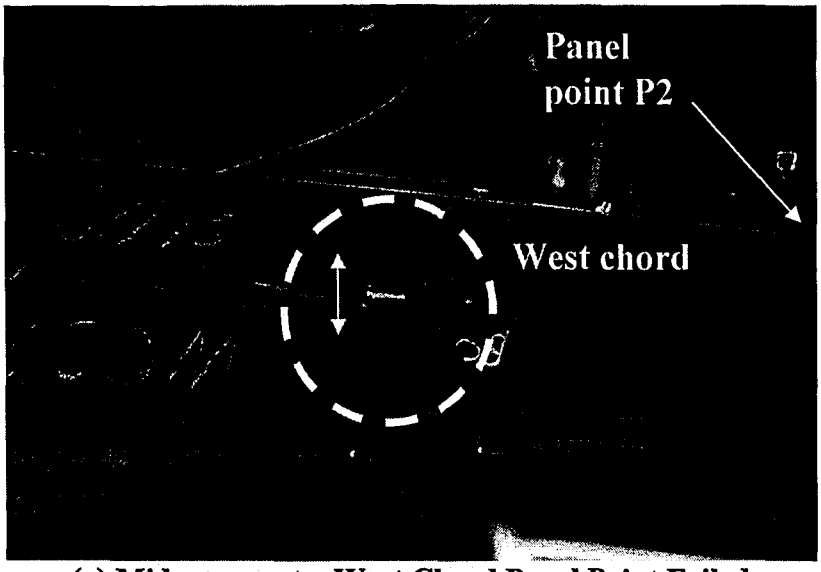

(a) Mid-spacer at a West Chord Panel Point Failed

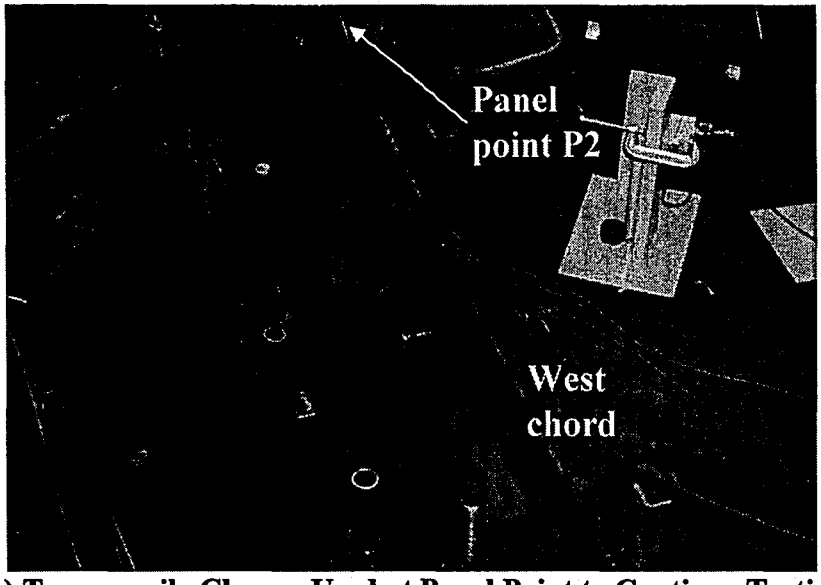

(b) Temporarily Clamps Used at Panel Point to Continue Testing

Figure 7.64 Specimen G4 - Weld Overstrength at Ends of Member C2 Resulted in Ductile Tensile Failure of Adjacent Members

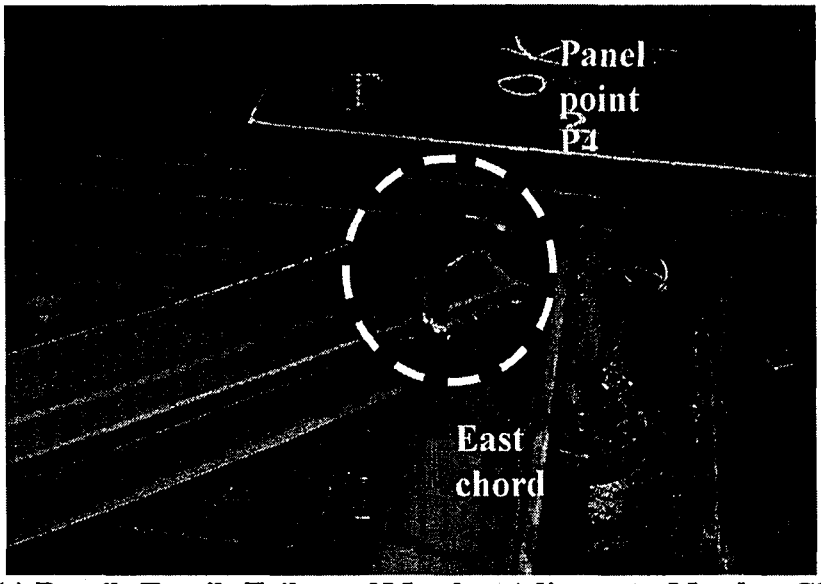

(c) Ductile Tensile Failure of Member Adjacent to Member C2

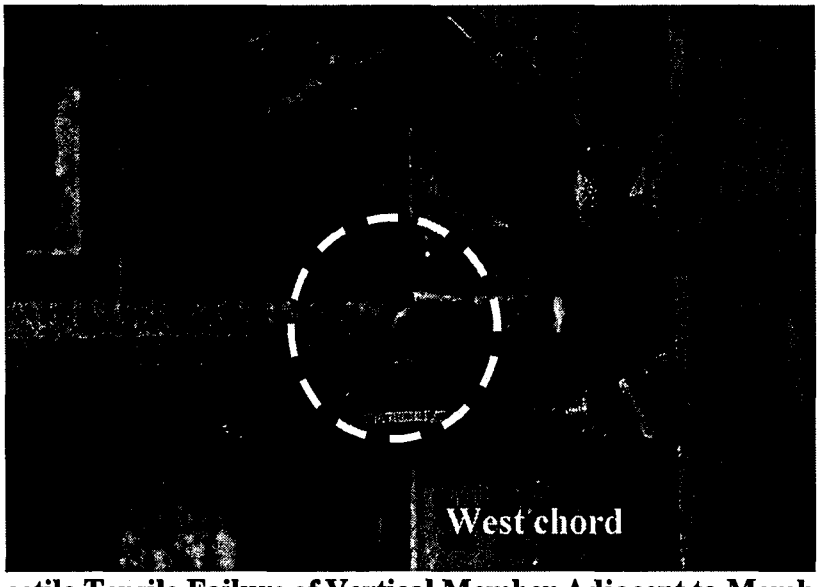

(d) Ductile Tensile Failure of Vertical Member Adjacent to Member C2

Figure 7.64 Specimen G4 - Weld Overstrength at Ends of Member C2 Resulted in Ductile Tensile Failure of Adjacent Members

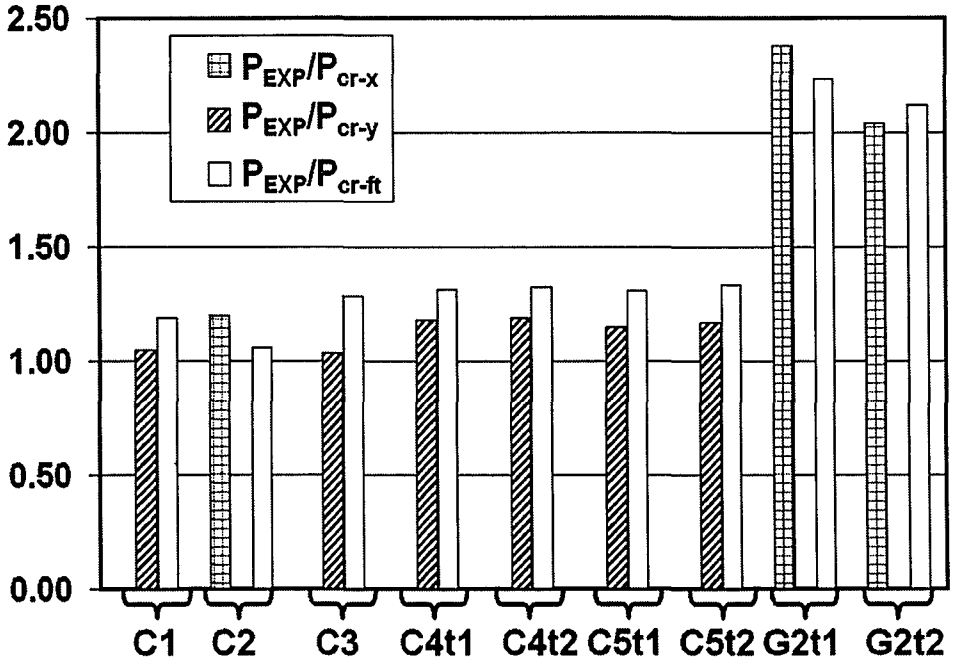

Figure 7.65 Predicted vs. Experimental Results

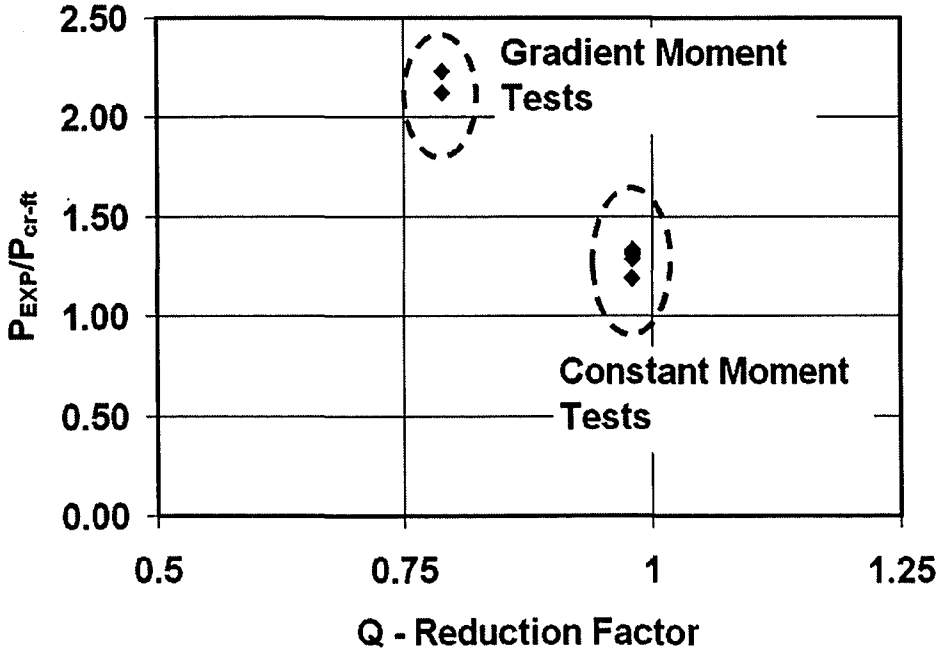

Figure 7.66 Experimental Results vs. Q Reduction Factor

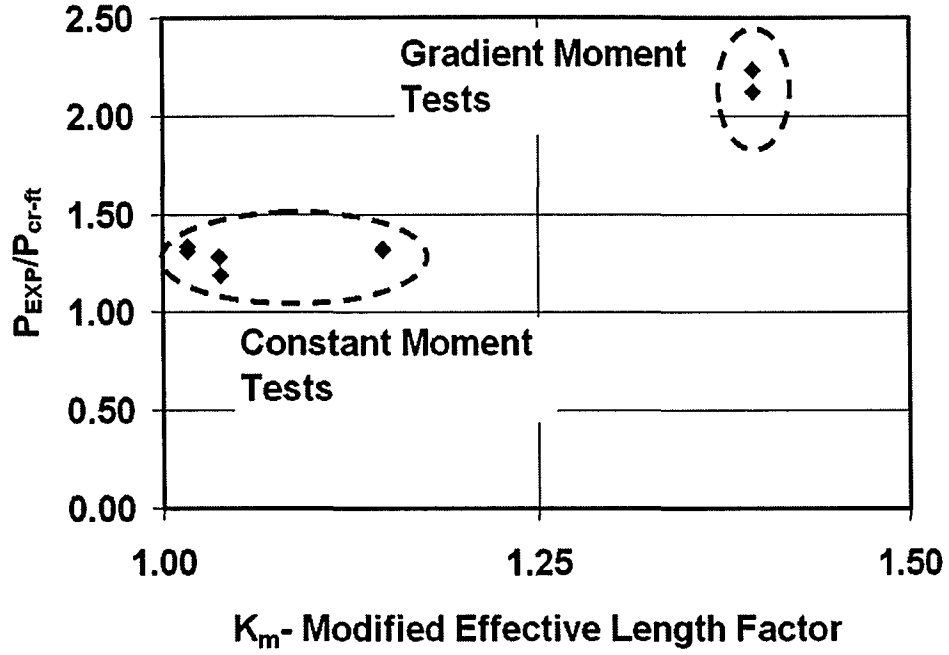

Figure 7.67 Experimental Results vs. K_m Effective Length Factor

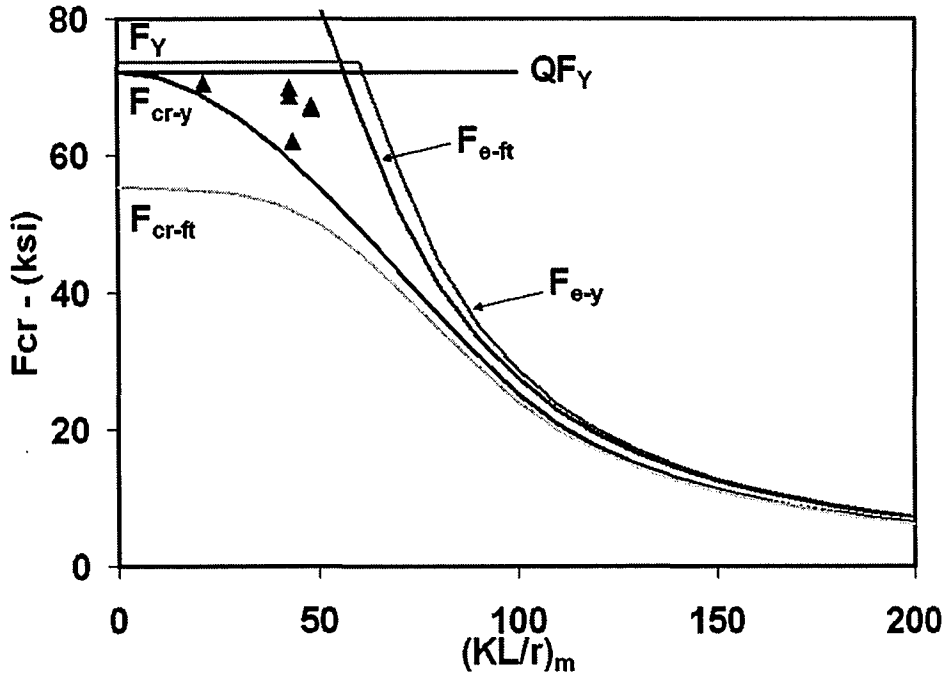

Figure 7.68 Comparison of Experimental Results with Predicted Results for CM Test Specimens, Other Than Specimen C2

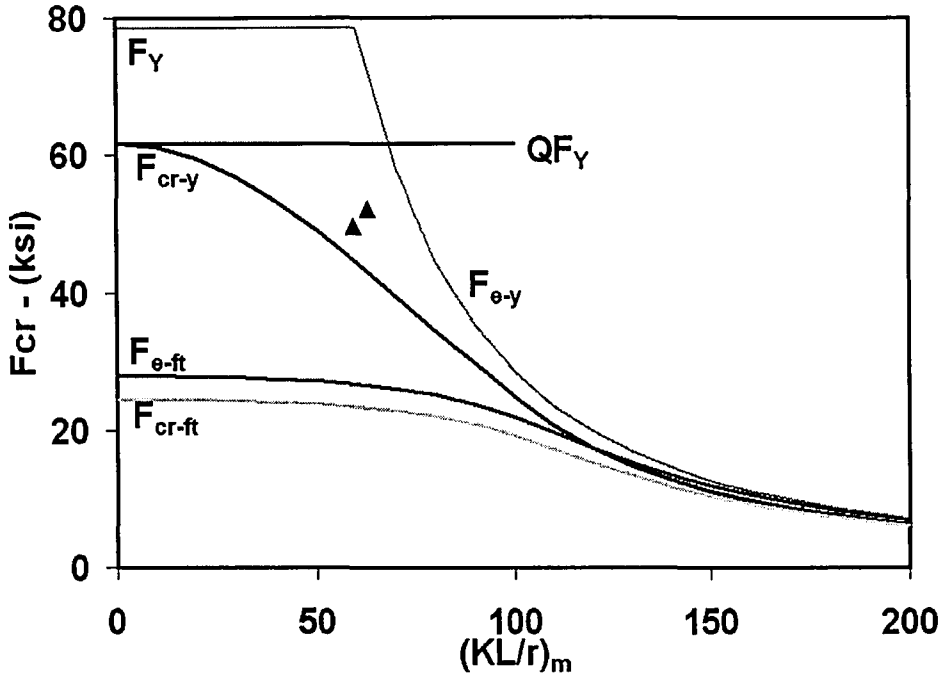

Figure 7.69 Comparison of Experimental Results with Predicted Results for Specimen G2

Chapter 8 Summary, Conclusions, and Recommended Future Work

8.0 Summary

In this experimental research, compression tests were carried out on members with single angle or double angle cross-sections. The experimental study considered isolated compression members and tests of angle members in truss subassemblies. The thesis presents the results of these tests and evaluates them based on comparisons with the AISC (2005) specification.

The compression tests on the isolated member specimens had fixed end conditions for rotation about the weak principal axis direction of the member and pinned end conditions for rotation about the strong principal axis of the member. The members were restrained against twist at the ends. The applied axial load was concentric. The width-to-thickness (b/t) ratios of the legs of the angle cross-sections ranged from slender to nearly non-compact. As a result, the buckling modes of the isolated members were flexural-torsional modes combined with local plate bending and local plate buckling.

The truss subassemblies included only double angle members. In these tests, the double angle members were loaded to failure under conditions closely simulating those found in actual floor and roof trusses.

8.1 Findings

The following findings regarding Vanadium steel angle compression members are determined from the experimental results:

- The tensile tests showed variability in the yield stress values for different cross-section sizes. The yield stress values were consistently smaller than the nominal yield stress value of 80 ksi. The minimum average yield stress was 71.0 ksi for the 4x4x1/2 angles, while, the maximum average value yield stress was 78.5 ksi for the 1.75x1.75x1/8 angles.

- For both the single and double angle compression test specimens the typical failure mode was flexural-torsional buckling with some influence from local plate bending or local plate buckling. The experimental capacity of the specimens were, however, in closer agreement with the predicted flexural buckling capacity about the strong axis (i.e., the y axis) based on the AISC (2005) specification. For both single and double angle test specimens, the AISC (2005) specification suggests that the flexural-torsional buckling mode, which has a capacity less than the flexural buckling capacity about the strong axis, should govern. Thus, the AISC (2005) specification provides conservative estimates of the capacity for both single angle and double angle compression members in the ranges of slenderness and cross-section member slenderness that were studied.

- For the ranges of member and cross-section slenderness that were studied, the AISC (2005) specification suggests that the test specimens should fail in flexural-torsional buckling. Most of the test specimens had lateral deflections in the weak axis direction (i.e., the x axis) that corresponds to strong axis flexure, accompanied by noticeable torsional deformation

which is the indication of the expected flexural-torsional buckling mode. Some of the test specimens had a Q reduction factor close to 1.0, suggesting that the cross-section is nearly compact, while, the rest of them had a Q factor as low as 0.71. For the test specimens with the smaller Q reduction factors, local plate bending is expected, and this behavior was observed. The local plate bending influenced the flexural-torsional buckling capacity, as expected from the AISC (2005) specification. Some of the single and double angle specimens with lower Q reduction factors did not fail in the flexural-torsional buckling mode, but failed by local buckling. For some of the double angle specimens, a single angle buckling failure mode was observed. Thus, the AISC (2005) specification did not always predict the failure mode of the double angle compression members.

- For the single and double angle test specimens with the smaller Q reduction factors, the predicted buckling capacities based on the AISC (2005) specification were far more conservative than for the single angle and the double angle test specimens with the Q reduction factor close to 1.0.

- For the single angle test specimens with crimped ends, the experimental buckling capacities were less than those obtained by using the AISC (2005) specification provisions for single angles without considering the reduced flexural stiffness and strength of the crimped region. Flexural deformations of the crimped regions contributed significantly to the behavior of the

crimped test specimens. A simple application of the AISC (2005) specification provisions for single angles without considering the crimped ends is unconservative, and will overestimate the member capacity in compression.

- The buckling capacities predicted using the AISC (2005) specification were equally conservative for both the isolated double angle test specimens and the double angle members in the truss test specimens. The results suggest that using an effective length (K) factor equal to 1.0 for truss members in compression is appropriate.

8.2 Conclusions

Based on the experimental study presented in this thesis, the following conclusions are drawn:

- The application of the AISC (2005) specification provisions for Vanadium steel compression members with single or double angle cross-sections is conservative. When the width-to-thickness (b/t) ratio of the angle legs is greater and the cross-section is increasingly slender, the AISC (2005) specification provisions became more conservative and tend to underestimate the experimental capacity of the single and double angle members.

- The simple application of the AISC (2005) specification provisions for single angle compression members to single angle members with crimped

ends, without considering the reduced flexural stiffness and strength of the crimped ends, is not conservative and is not recommended.

- Based on the truss subassemblies that were studied, the use of effective length (K) factors equal to 1.0 to predict the compression capacity of double angle Vanadium steel truss members is appropriate.

8.3 Recommended Future Work

In this study, the isolated single angle specimens were tested under only concentrically applied axial load. On the other hand, single angle members are often loaded through one leg which is connected to another member. An experimental study which considers single angle specimens loaded through a connected leg should be undertaken. In addition, a greater number of single angle specimens should be tested to create a statistical database.

In this study, only eight crimped single angle specimens were tested. A large number of crimped single angle specimens should be tested due to importance of crimped single angle members in joists. The effect of the crimped region geometry should be considered and treated as a parameter.

Based on the test results generated in this study, finite element models of single and double angle members can be generated and validated. The models can be extended to represent either actual test conditions, theoretical conditions, or practical conditions. This study would help to create a larger database for the buckling behavior of angle members. Only a few representative specimen lengths and cross-sections

were tested in this study. The finite element study can also be extended to address the effects of the type, number, and relative spacing of mid-spacers on the buckling strength of double angle members.

A future study should establish the pattern and the magnitude of the residual stresses on angle members. These results are needed to create accurate finite element models.

References

AISC (2005), *Steel Construction Manual*, American Institute of Steel Construction, Chicago.

Bjorhovde, R., (1972), *Deterministic and Probabilistic Approaches to the Strength of Steel Columns*, Ph.D. dissertation, Lehigh University, Bethlehem, PA.

Bleich, F., (1952), *Buckling Strength of Metal Structures*, Engineering Societies Monographs, McGraw-Hill, New York, NY.

Estuar, F. R., Tall, L. (1967), "*Testing of Pinned-End Steel Columns*," Test Methods for Compression Members, ASTM STP 419.

Galambos, T. V., (1978), *Structural Members and Frames*, St. Louis, Missouri.

Galambos, T. V., (1991), "*Design of Axially Loaded Compressed Angles*", Proceedings 1991 Annual Technical Session, Structural Stability Council, Chicago, IL, pp.353-367.

Galambos, T. V., (1998), *Guide to Stability Design Criteria for Metal Structures*, Wiley, New York, NY.

Huber, A. W., (1958), "*Fixtures for Testing Pin-Ended Columns*," ASTM Bulletin, No. 234.

Kitipornchai, S. and Lee, H. W., (1986), "*Inelastic Experiments on Angle and Tee Struts*", Journal of Constructional Steel Research 6, pp 219-236.

Madugula, M. K. S., Kennedy, J. B., (1985), Single and Compound Angle Members, Structural Analysis and Design, Elsevier Science Publishing Co., Inc., New York, NY.

Salmon, C. G., Johnson, J. E., (1996), *Steel Structures, Design and Behavior*, Prentice Hall, Upper Saddle River, New Jersey.

Seaburg, P. A., Carter, C.J., (2003), "*Torsional Analysis of Structural Steel Members*", Steel Design Guide Series, 9, AISC, Chicago, IL.

Singer, J., Arbocz, J., Weller, T., (1998), *Buckling Experiments: Experimental Methods in Buckling of Thin-Walled Structures*, Vol. I, Wiley, England.

Vinnakota, S., (2006), *Steel Structures: Behavior and LRFD*, McGraw-Hill, New York, NY.

Yost, J. R., Dinehart, D. W., Gross, S. P., Pote, J.J., Gargan, B., (2004), "*Strength and Design of Open Web Steel Joists with Crimped-End Web Members*", Journal of Structural Engineering, ASCE, pp 715-724.

Appendix A Stress-Strain Diagrams of Coupons

A.1 Sheet-type Coupons

A.1.1 L1.75x1.75x1/8 Series

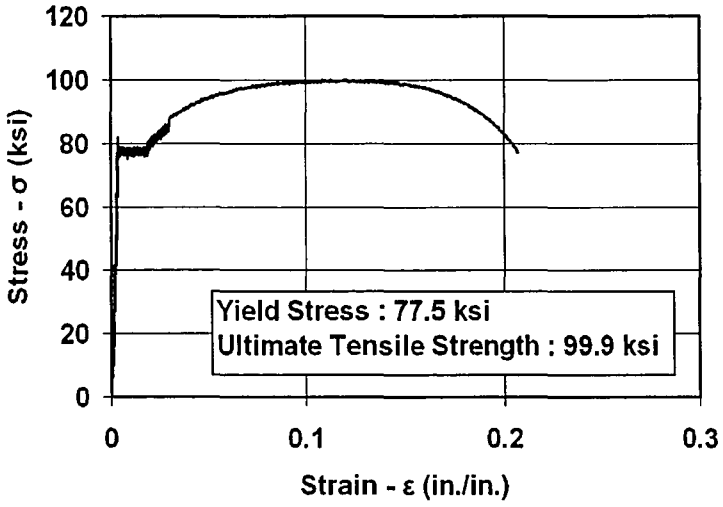

Figure A.1 Coupon 1.75x1.75x1/8-A1

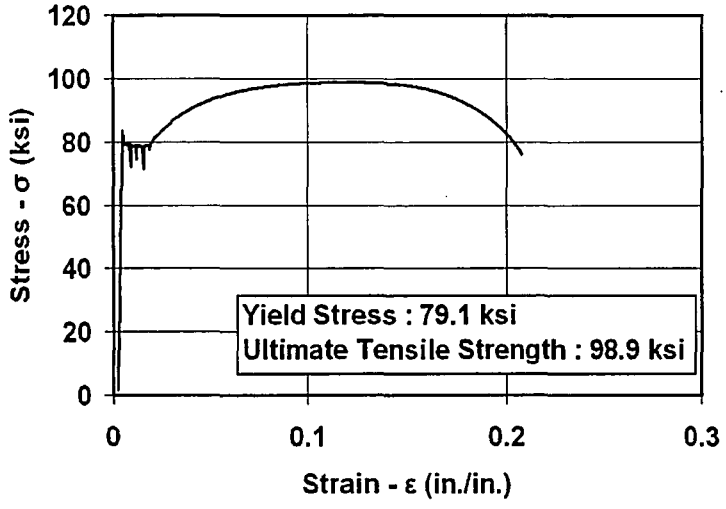

Figure A.2 Coupon 1.75x1.75x1/8-A3

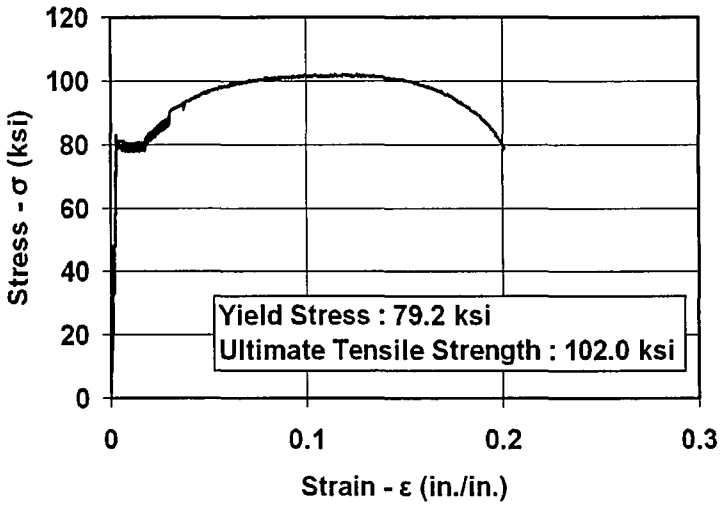

Figure A.3 Coupon 1.75x1.75x1/8-B1

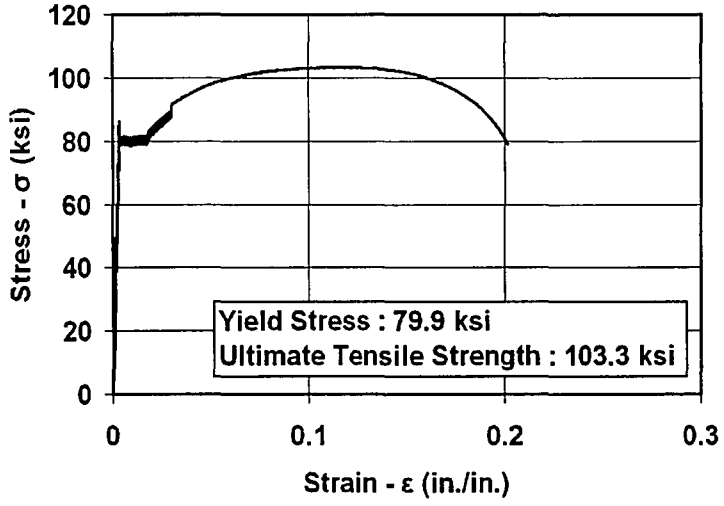

Figure A.4 Coupon 1.75x1.75x1/8-B2

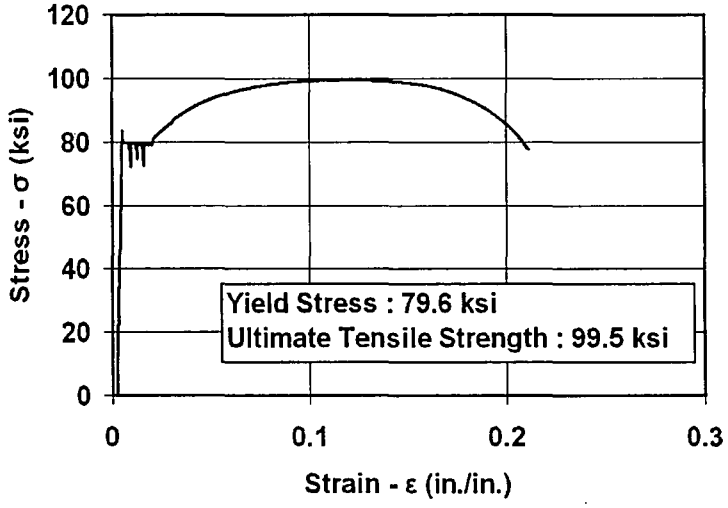

Figure A.5 Coupon 1.75x1.75x1/8-B3

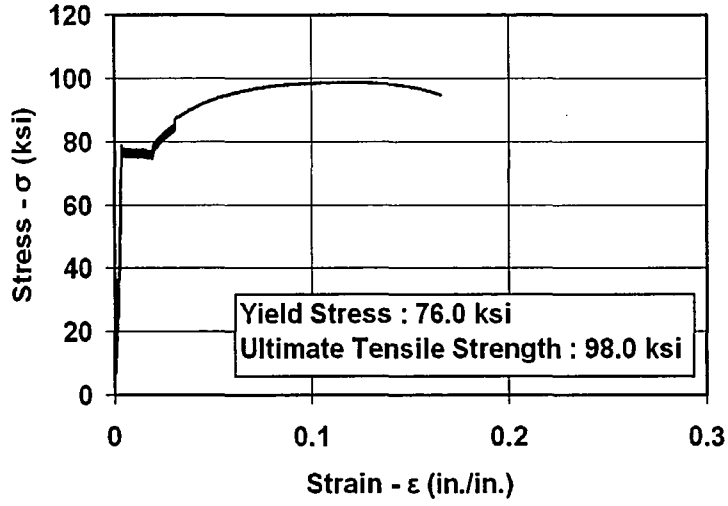

Figure A.6 Coupon 1.75x1.75x1/8-1

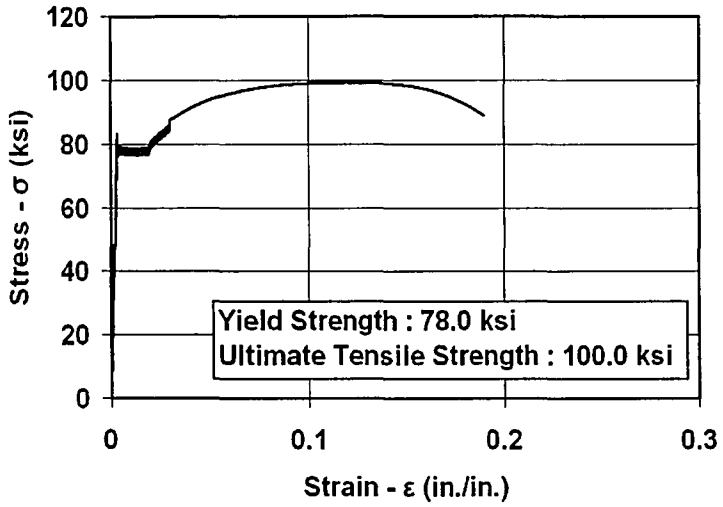

Figure A.7 Coupon 1.75x1.75x1/8-3

A.1.2 L2x2x3/16 Series

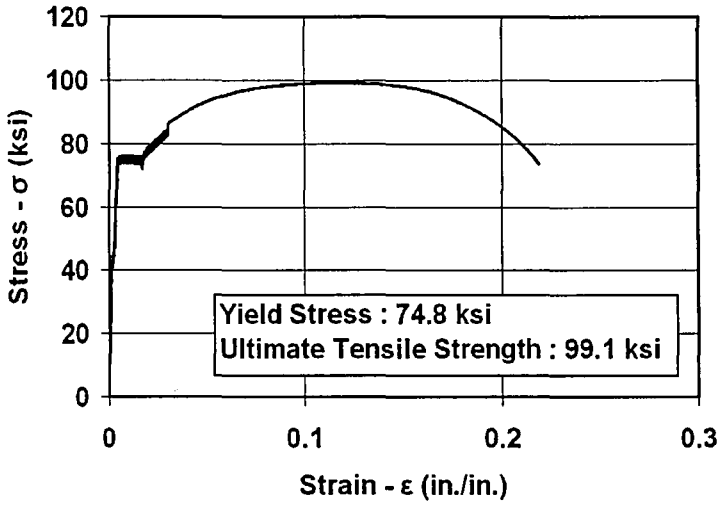

Figure A.8 Coupon 2x2x3/16-A1

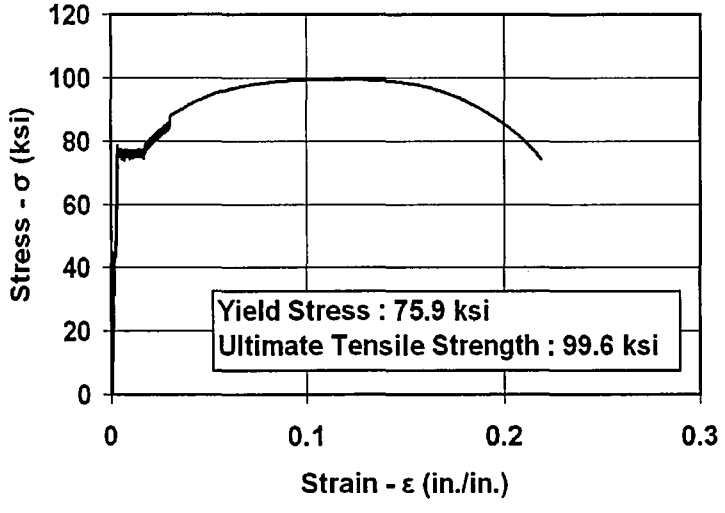

Figure A.9 Coupon 2x2x3/16-A2

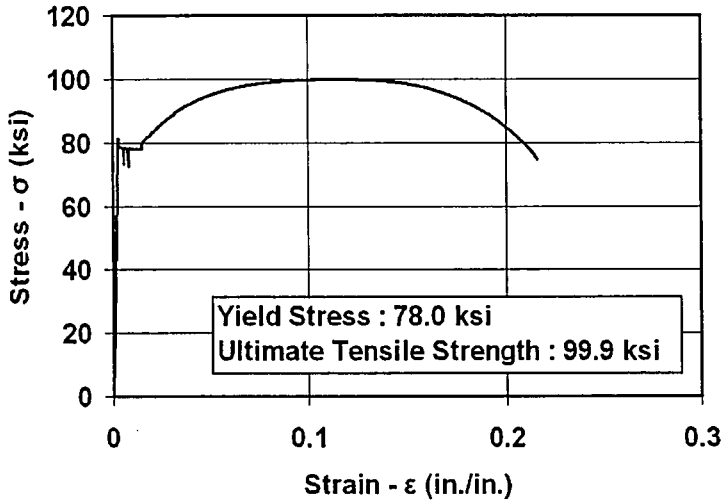

Figure A.10 Coupon 2x2x3/16-A3

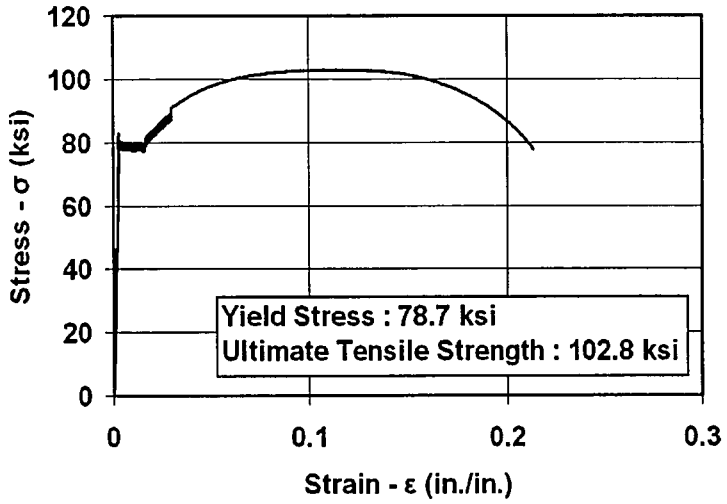

Figure A.11 Coupon 2x2x3/16-B2

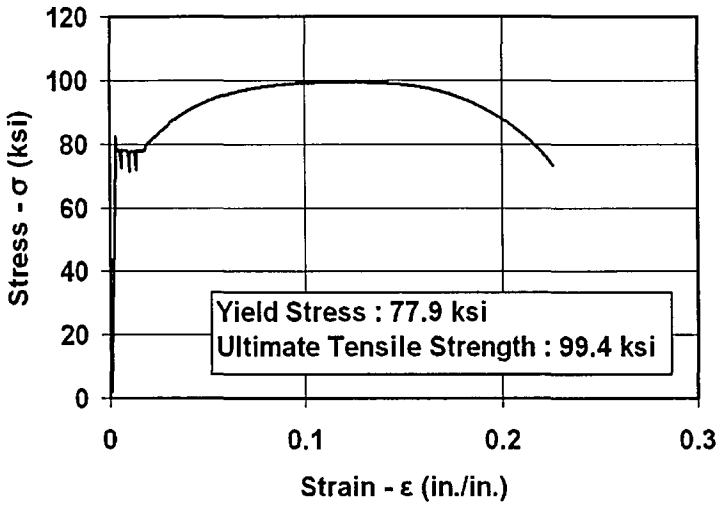

Figure A.12 Coupon 2x2x3/16-B3

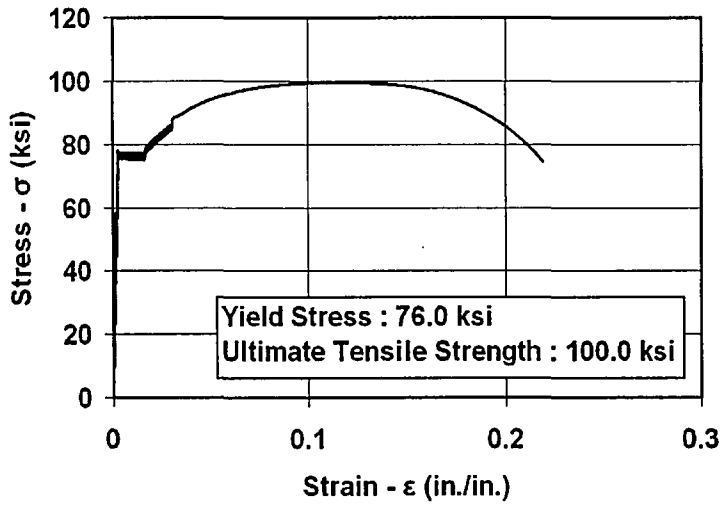

Figure A.13 Coupon 2x2x3/16-3

A.2 Plate-type Coupons

A.2.1 L3x3x3/16 Series

A.2.1.1 Vanadium Steel

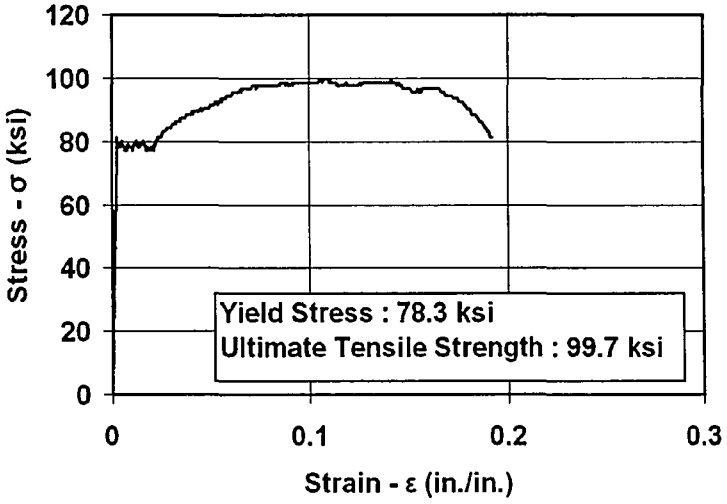

Figure A.14 Coupon 3x3x3/16-A2

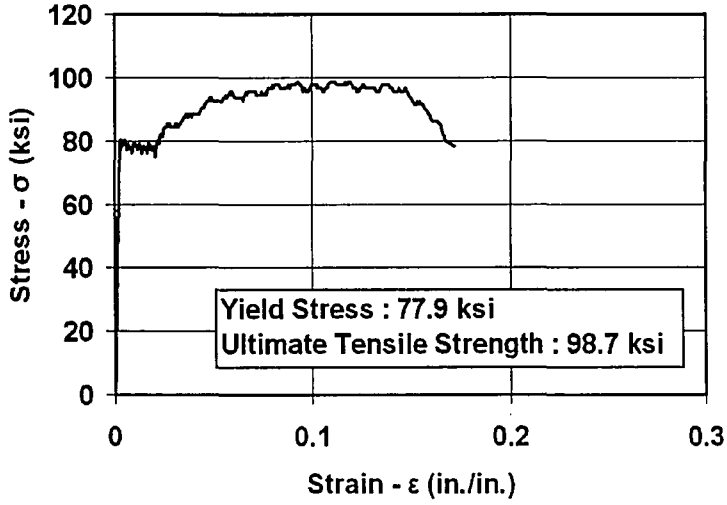

Figure A.15 Coupon 3x3x3/16-A3

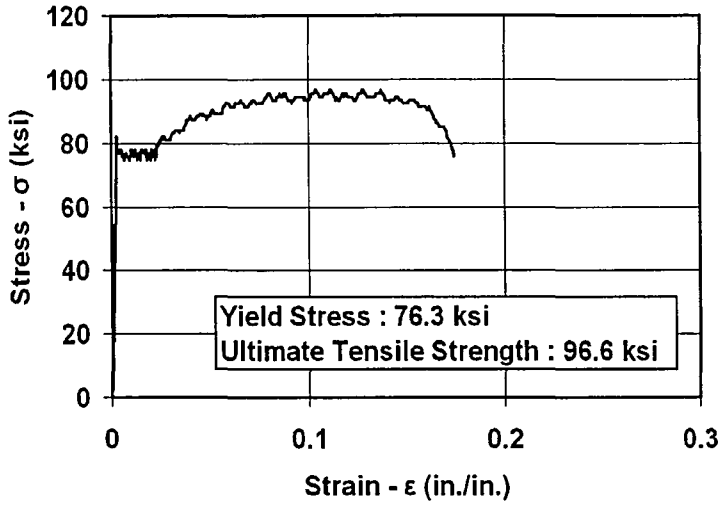

Figure A.16 Coupon 3x3x3/16-B2

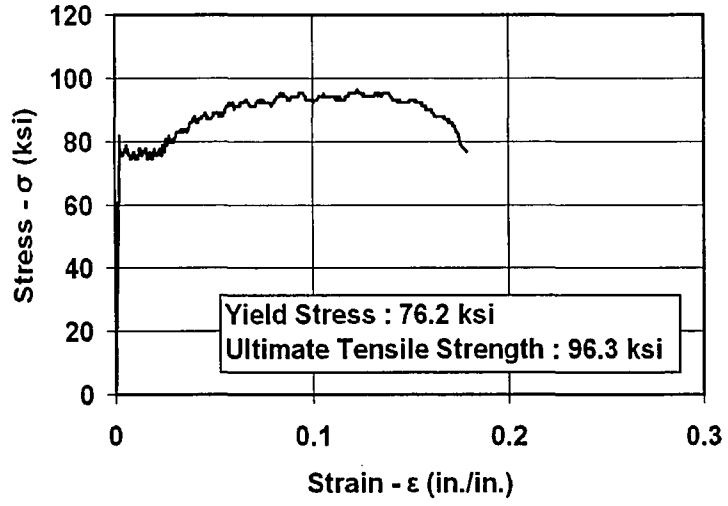

Figure A.17 Coupon 3x3x3/16-B3

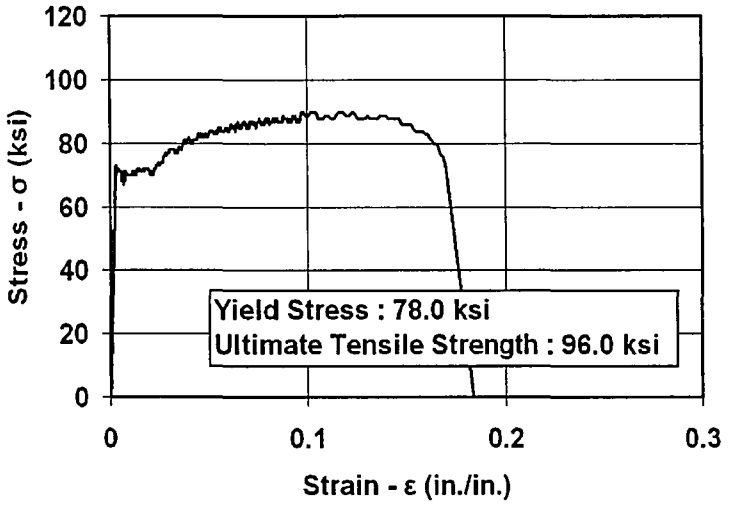

Figure A.18 Coupon 3x3x3/16-1

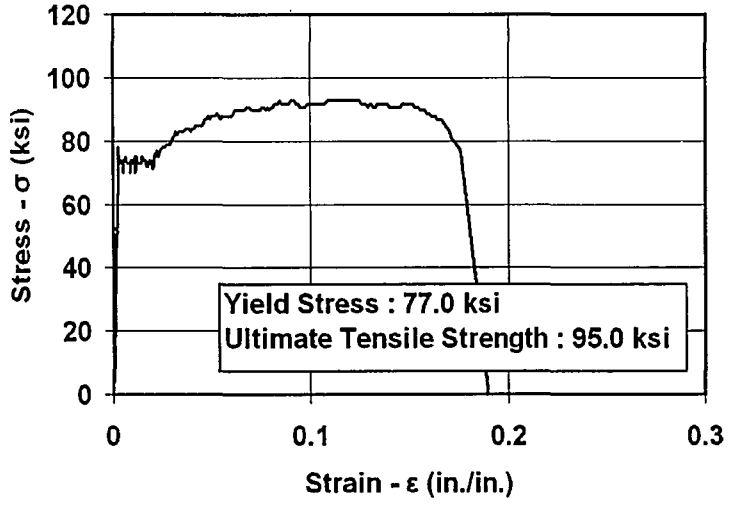

Figure A.19 Coupon 3x3x3/16-2

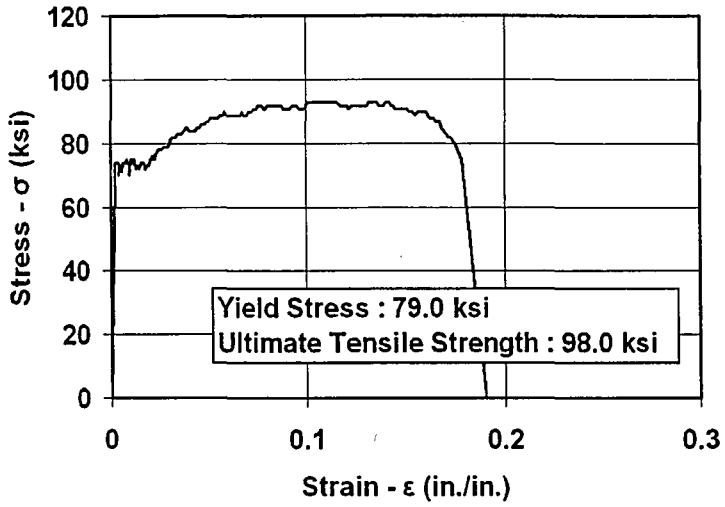

Figure A.20 Coupon 3x3x3/16-3

A.2.1.2 Grade 50 Steel (ASTM A572)

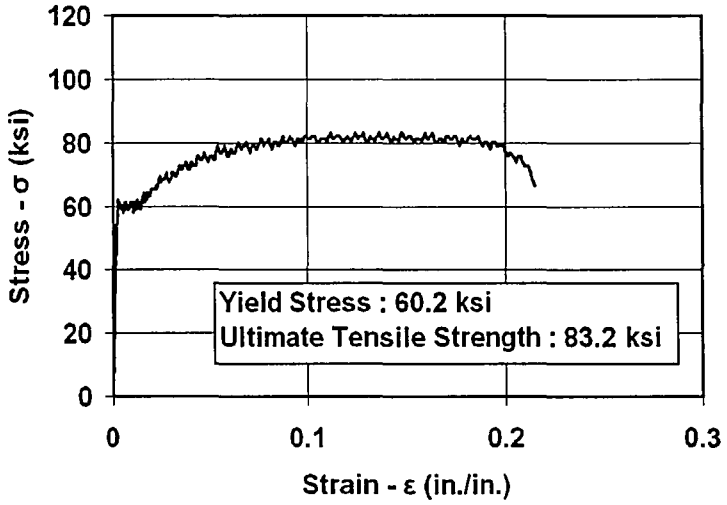

Figure A.21 Grade 50 - Coupon 3x3x3/16-A3

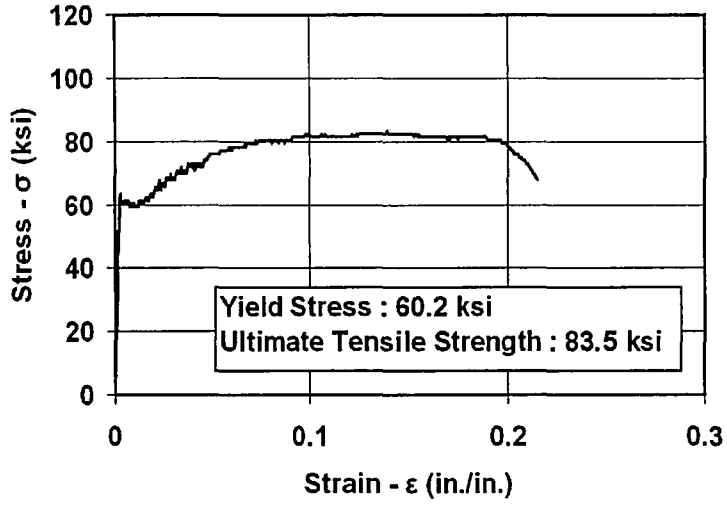

Figure A.22 Grade 50 - Coupon 3x3x3/16-B3

A.2.2 L3.5x3.5x3/8 Series

A.2.2.1 Vanadium Steel

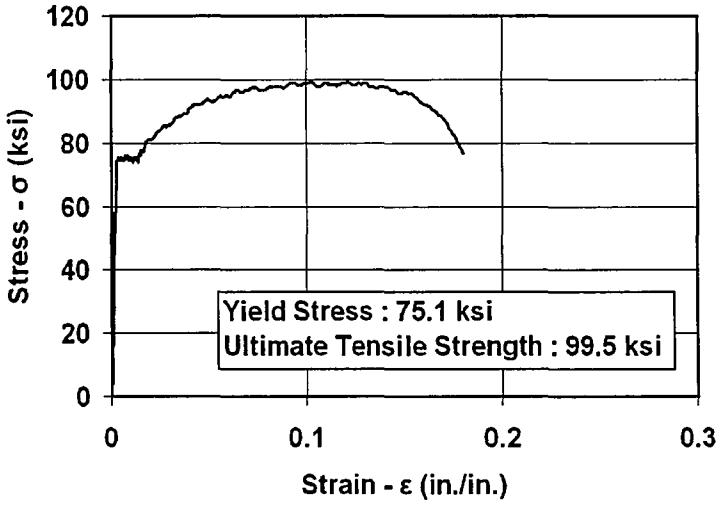

Figure A.23 Coupon 3.5x3.5x3/8-A2

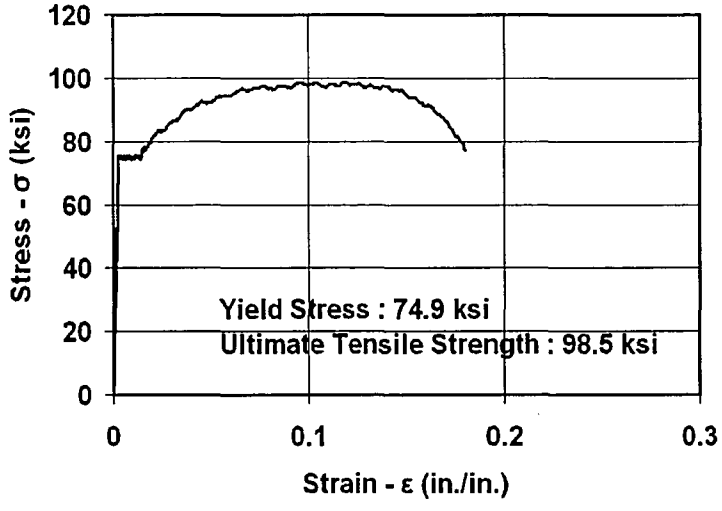

Figure A.24 Coupon 3.5x3.5x3/8-A3

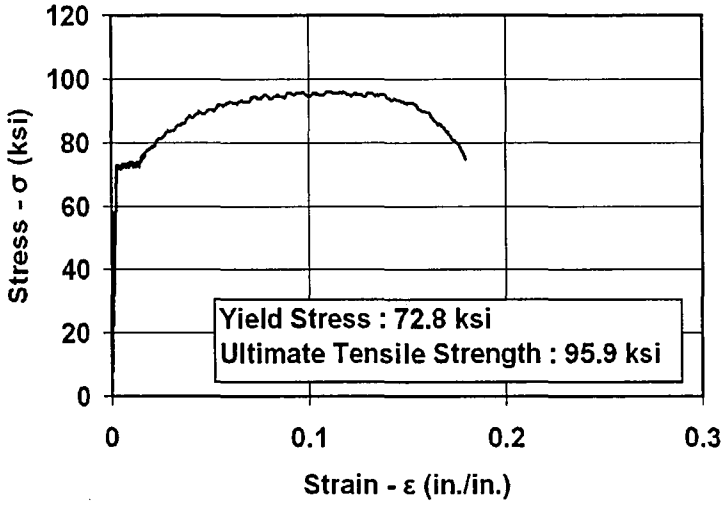

Figure A.25 Coupon 3.5x3.5x3/8-B2

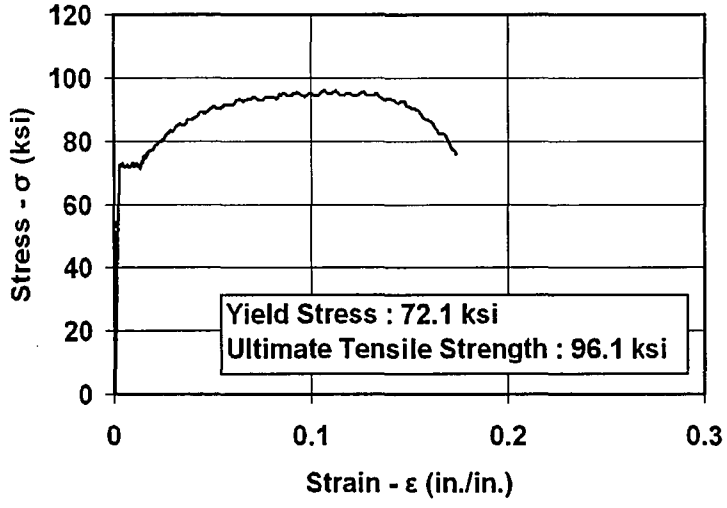

Figure A.26 Coupon 3.5x3.5x3/8-B3

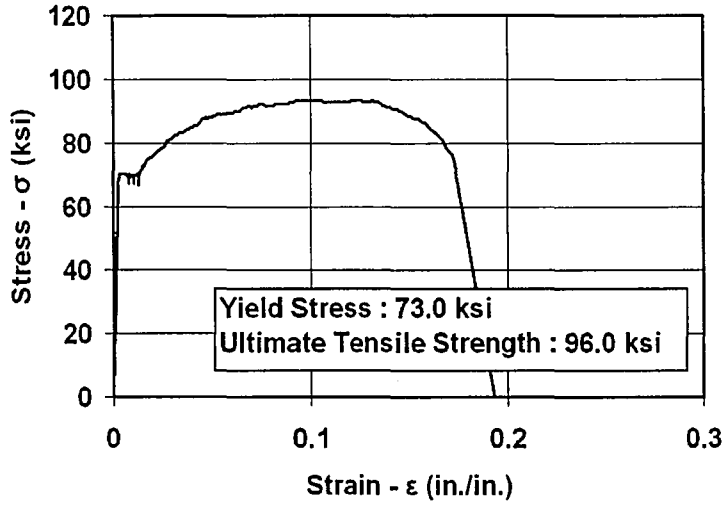

Figure A.27 Coupon 3.5x3.5x3/8-1

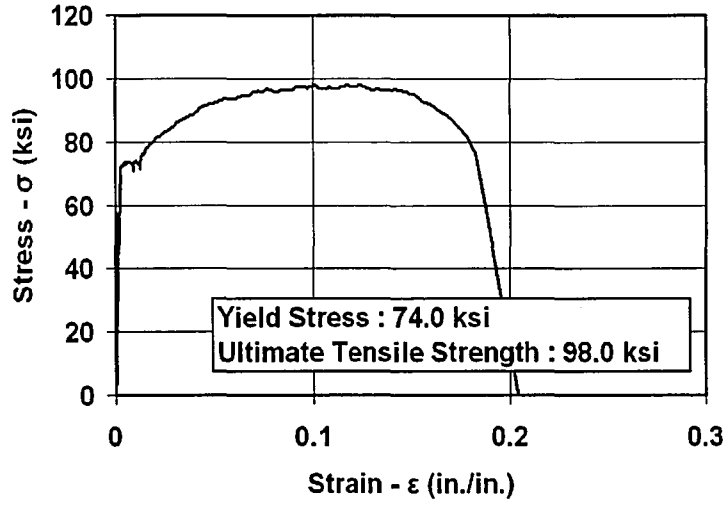

Figure A.28 Coupon 3.5x3.5x3/8-2

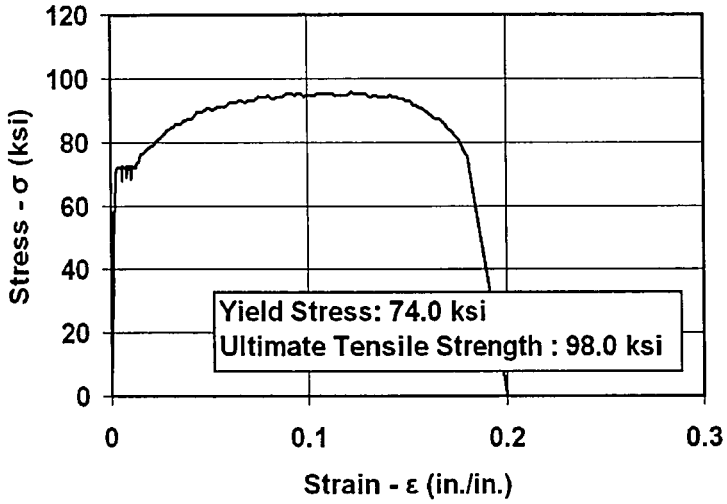

Figure A.29 Coupon 3.5x3.5x3/8-3

A.2.2.2 Grade 50 Steel (ASTM A572)

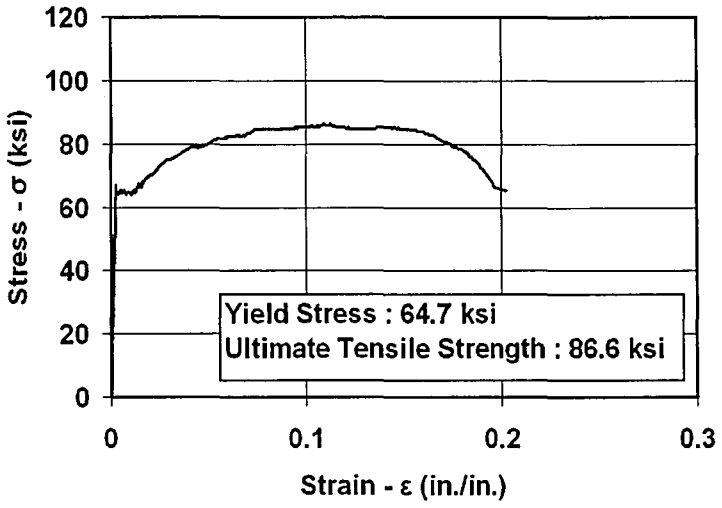

Figure A.30 Grade 50 - Coupon 3.5x3.5x3/8-A3

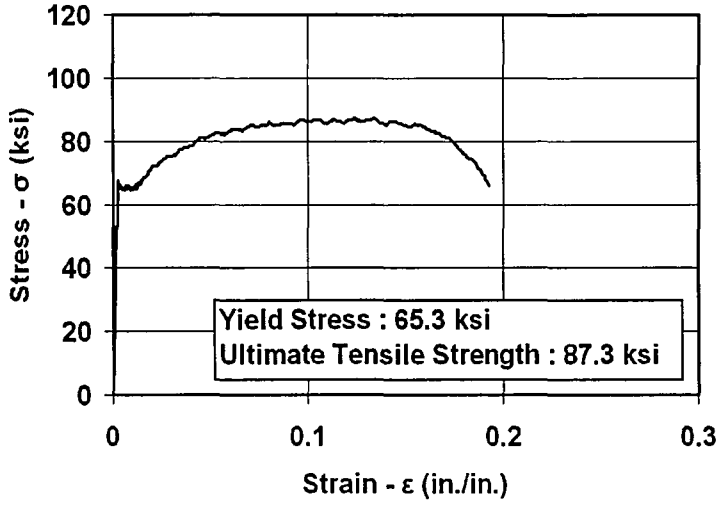

Figure A.31 Grade 50 - Coupon 3.5x3.5x3/8-B3

A.2.3 L4x4x1/2 Series

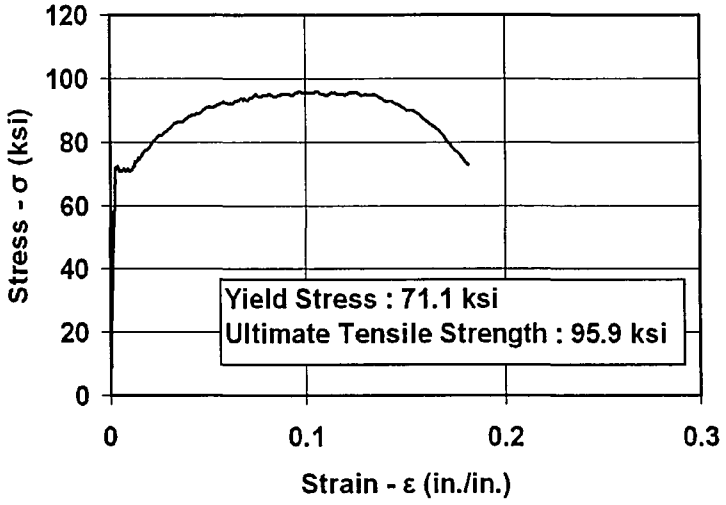

Figure A.32 Coupon 4x4x1/2-A1

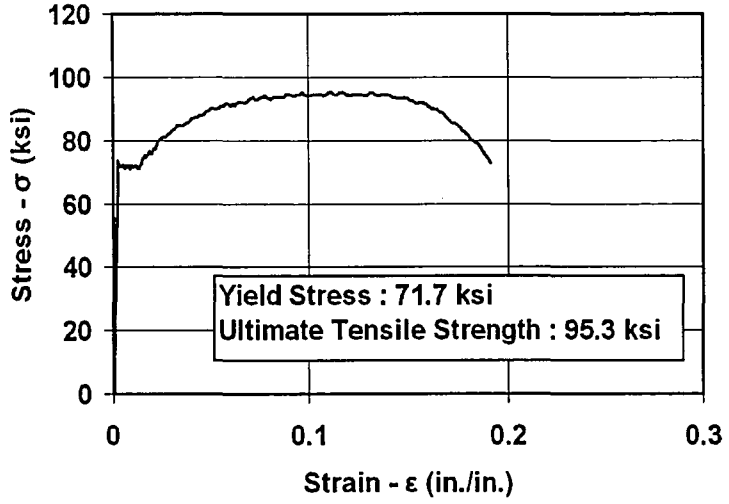

Figure A.33 Coupon 4x4x1/2-A2

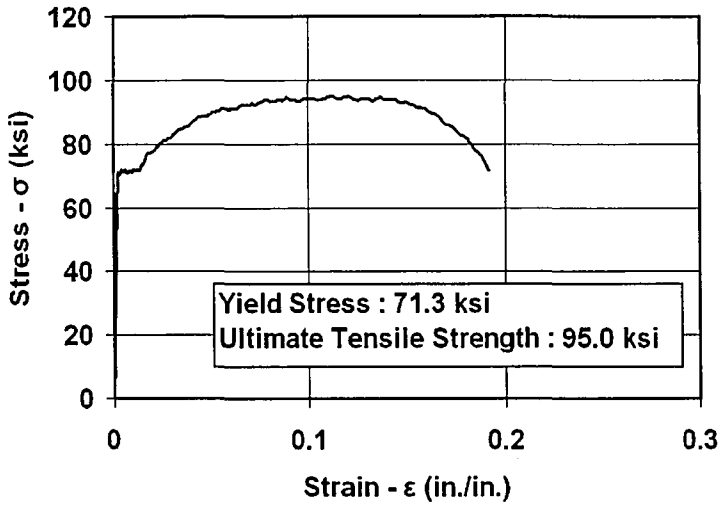

Figure A.34 Coupon 4x4x1/2-B1

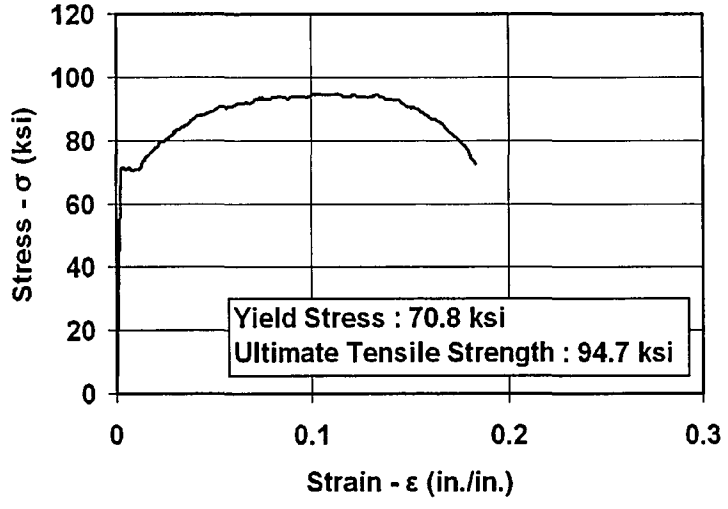

Figure A.35 Coupon 4x4x1/2-B2

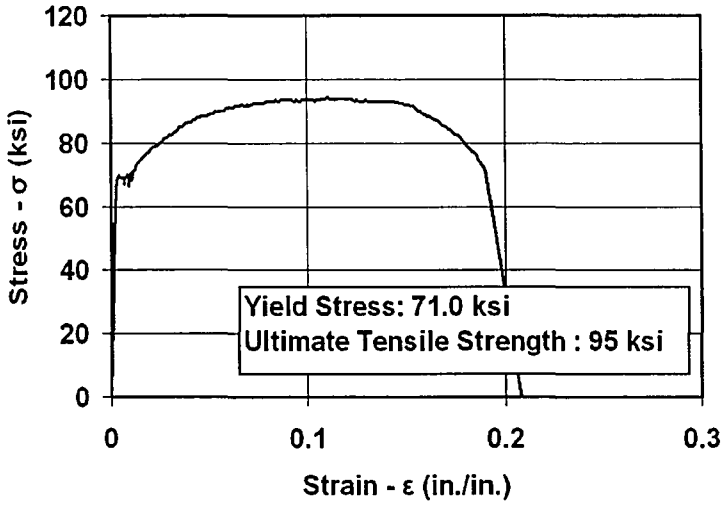

Figure A.36 Coupon 4x4x1/2-1

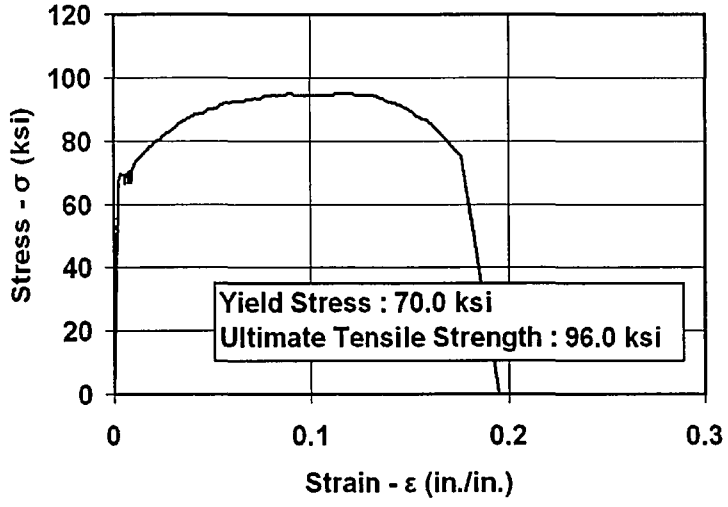

Figure A.37 Coupon 4x4x1/2-2

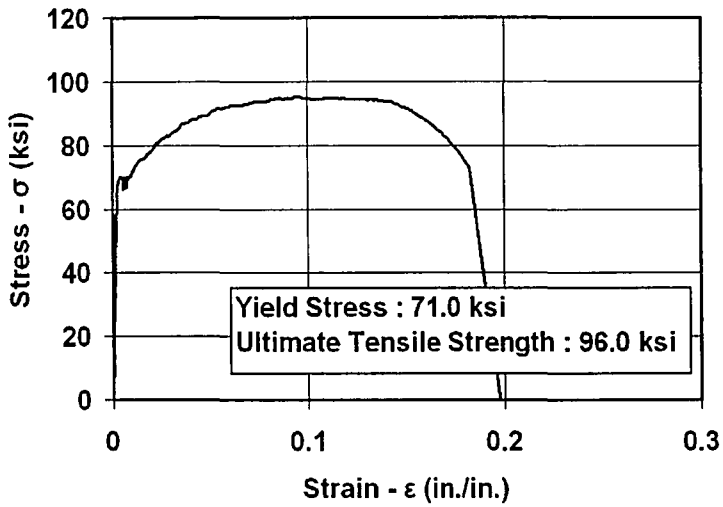

Figure A.38 Coupon 4x4x1/2-3

Appendix B Effects of Test Machine Flexibility on Single and Double Angle Test Results

B.0 Introduction

The instrumentation used during the tests measured the load vs. cross-head displacement behavior. The load vs. specimen shortening (axial deformation) is of greater interest, since the cross-head displacement includes deformations of the test machine components. In this appendix, the deformations of the test machine components during the single angle and double angle tests will be estimated. At the end of the appendix, load vs. specimen shortening graphs for both single angle and double angle tests will be presented.

B.1 Identification of Test Machine Components and Their Flexibility

The components of the test machine are identified in Figure B.1. These components are the cross-head of the machine, the base platen, the bearings, and the columns of the machine. The machine column component is divided into two parts, since length of the machine column between the cross-head and the base platen of machine depends on the length of specimen. These components contribute to the total machine deformation as shown in equation (B.1). As seen in this equation, the height of the bearings (a1 and a2) and the length of the specimen are factors that contribute to the test machine column deformation. As a result, the total machine flexibility is a function of the length of the specimen.

$$\Delta_{machine\_total} = \Delta_{xhead\_platen} + \Delta_{machine\_columns,a1,a2} + \Delta_{machine\_columns,Lspecimen} \quad \textbf{(B.1)}$$

where

$\Delta_{machine\_total}$ = the total deformation of the test machine components

Δ_{xhead_platen} = the deformation of the cross-head, base platen, and bearings

$\Delta_{machine\_columns,Lspecimen}$ = the deformation of the columns of the test machine over the length of the specimen

$\Delta_{machine\_columns,a1,a2}$ = the deformation of the columns of the machine over the length of the bearings

The deformation of some of these components can be estimated as follows:

$$\Delta_{machine\_columns,Lspecimen} = \frac{P}{k_{machine\_columns,Lspecimen}} = \frac{P}{\left(\frac{E \times A_{machine\_columns}}{L_{specimen}}\right)} \quad \textbf{(B.2)}$$

where

$k_{machine\_columns,Lspecimen}$ = the stiffness of the columns of the machine corresponding to the length of the specimen

$A_{machine\_columns}$ = area of the columns of the test machine

$L_{specimen}$ = the length of the specimen

P = the axial load applied to the specimen

$$\Delta_{machine\_columns;a1,a2} = \frac{P}{k_{machine\_columns;a1,a2}} = \frac{P}{\left(\frac{E \times A_{machine\_columns}}{a1 + a2}\right)} \quad \textbf{(B.3)}$$

where

$k_{machine\_columns,a1,a2}$ = the stiffness of the columns of the machine corresponding to the length of bearings

a1+a2 = the total length of the bearings

For a better understanding of the relationships among the flexibilities of the test machine components, the components are modeled as springs that are connected in series as shown in Figure B.2. The deformation of these components results in the total cross-head relative displacement observed in the tests as shown in Figure B.3 for test specimen SA2.

B.2 Relationship of Test Machine Deformation, Specimen Deformation, and Cross-head Displacement

The relationship between the test machine deformations and the cross-head displacement from the experiments is given in equation (B.4a).

$$\Delta_{experimental\_total} = \Delta_{machine\_total} + \Delta_{specimen\_shortening} \quad \textbf{(B.4a)}$$

where

$\Delta_{experimental\_total}$ = the cross-head relative displacement from the experiments

$\Delta_{specimen\_shortening}$ = the shortening of the specimen

Assuming that for the initial part of the test, the specimen exhibits linear elastic behavior, the relationship is given in equation (B4.b)

$$\Delta_{experimental\_total} = \Delta_{machine\_total} + \Delta_{linear\_specimen} \quad \textbf{(B4.b)}$$

where

$$\Delta_{linear\_specimen} = \frac{P}{k_{linear\_specimen}} = \frac{P}{\left(\frac{E \times A_{specimen}}{L_{specimen}}\right)} \quad \textbf{(B.5)}$$

$k_{linear\_specimen}$ = the linear elastic stiffness of the specimen

$A_{specimen}$ = cross-sectional area of the specimen

B.3 Linear Range of Experimental Results

To estimate the flexibility of the test machine components, a linear range of the load versus cross-head displacement data was identified. This linear range is defined by a lower and an upper limit on the applied load P. This linear range is shown for specimen SA2 in Figure B.4.

The lower limit was considered to be end of seating of the specimen that is observed from load vs. cross-head displacement curve. The region of the load vs. cross-head displacement curve where the slope (stiffness) reaches its highest value was also considered in determining the lower limit, because the out of straightness of the specimen, residual stress effects, and the specimen seating all reduce the stiffness. The lower limit P_{LL} is 80 kips.

The upper limit was determined by subtracting an assumed residual stress value of 20 ksi from the theoretical plate local buckling stress value, which is found by utilizing the Q reduction factor described in Section 2.1.4.5.1, and the yield stress determined from tensile coupon tests. The upper limit P_{UL},

$$P_{UL} = (Q \times F_Y - \sigma_r) \times A = 128 \text{ kips} \quad \textbf{(B.6)}$$

where

$Q = 0.97$

$F_Y = 73.7$ ksi

σ_r = an assumed residual stress value = 20 ksi

$A = 2.484$ in^2

B.4 Estimated Specimen Shortening with Linearized Flexibility of Cross-Head, Base Platen, and Bearings Components

The initial analysis of the test machine flexibility provided an estimate of the load vs. specimen shortening behavior assuming that the test machine had a linear elastic behavior. First the total machine deformation $\Delta_{machine\_total}$ was estimated from equation (B.4a). Then Δ_{xhead_platen} was estimated from equation (B.1), assuming that the behavior of the columns of the machine is linear elastic throughout the test. The slope of the load versus Δ_{xhead_platen} in the linear range of the test was used to estimate a stiffness value, k_{xhead_platen}, for each specimen. An average of these stiffness values, called $k_{average\_xhead\_platen}$, was determined. Assuming also that the cross-head, base platen, and bearings are elastic throughout the test with a stiffness $k_{average\_xhead\_platen}$, a modified total test machine deformation was found from equation (B.7).

$$\Delta_{modified\_machine\_total} = \Delta_{average\_xhead\_platen} + \Delta_{machine\_columns,a1,a2} + \Delta_{machine\_columns,Lspecimen} \quad \textbf{(B.7)}$$

$\Delta_{average\_xhead\_platen}$ = the deformation of the cross-head, base platen, and bearings, assuming linear elastic behavior for these components

$$\Delta_{average\_xhead\_platen} = \frac{P}{k_{average\_x-head\_platen}}$$

(B.8)

$k_{average\_xhead\_platen}$ = the average stiffness of the cross-head, the base platen, and the bearings over the linear range of the tests

The modified total test machine deformation from equation (B.7) is then used to estimate the specimen shortening using equation (B.9) which is derived from equation (B.4a)

$$\Delta_{specimen\_shortening} = \Delta_{experiment} + \Delta_{modified\_machine\_total}$$

(B.9)

The results from equation (B.9) for specimen SA2 are shown in Figure B.4. The figure shows that the slope in the linear range of the test agrees with the theoretical stiffness, but the nonlinear behavior due to seating is substantial.

B.5 Evaluation of Nonlinearity before Lower Limit of Load

As it can be seen from the load versus cross-head displacement plots in Chapters 4 and 5, and the load vs. estimated specimen shortening graph in Figure B.4, a nonlinear portion of the curve exists before the lower load limit P_{LL} is reached. This nonlinearity is presumed to be caused by seating of the cross-head, base platen, and bearings that is occurring in this load range. As it is seen in Figure B.2, there are four components that contribute to the total cross-head displacement under applied load. It can be assumed that springs which represents the deformations $\Delta_1 = \Delta_{machine\_columns,a1,a2}$, and $\Delta_2 = \Delta_{machine\_columns,Lspecimen}$ behave linearly throughout the test. The spring which represents the specimen deformation $\Delta_4 = \Delta_{specimen\_shortening}$ can be assumed to be linear

up to the upper load limit P_{UL}. Thus, the spring which represents the cross-head, base platen, and bearing deformations, $\Delta_3 = \Delta_{xhead\_platen}$ is assumed to be nonlinear before reaching to lower load limit P_{LL}.

An improved specimen shortening deformation estimate was generated by determining a polynomial function that fits the nonlinear behavior of the Δ_{xhead_platen}.

First, equation (B.10) was obtained by combining equations (B.1) and (B.4a).

$$\Delta_{xhead\_platen} = \Delta_{experiment\_total} - \Delta_{machine\_columns,a1,a2} - \Delta_{machine\_columns,Lspec} - \Delta_{linear\_specimen} \quad \textbf{(B.10)}$$

Figure B.5a shows the nonlinear Δ_{xhead_platen} data for specimen SA2. The initial negative value of the deformation is due to the assumption of zero cross-head relative displacement at the beginning of the test when there is a small initial load. In equation (B.10), the specimen shortening is represented by its theoretical value, $\Delta_{linear\_specimen}$, which is reasonable for the initial part of the test.

Then, the cross-head, base platen, bearings deformation Δ_{xhead_platen}, is adjusted to have zero displacement at a load level, referred to as $P_{initial}$ (P_i). This adjustment is shown in Figure B.6. Then, the abscissa and ordinate are exchanged in order to be able to fit a polynomial to the deformation as a function of load.

$f(P') = a + bP + cP^2 + dP^3$ is the polynomial function that was applied between P_i and P_{LL} to fit the nonlinear Δ_{xhead_platen} data.

As seen in Figure B.7, the following boundary conditions are applied to solve the constants of the polynomial function

$$f(P'=0)=a=0$$
$$f(P'=P_i=10kips)=\Delta o$$
$$f'(P'=P_i)=f'_i$$
$$f(P'=P_{LL})=\Delta_{LL}+\Delta o$$
$$f'(P'=P_{LL})=\frac{1}{k_{average\_xhead\_platen}}$$

(B.11)

$f'(P')=b+2cP+3dP^2$ is the first derivative of function and Δo is the negative value at intersection of f(P') function with ordinate in Figure B.7 where P_i = 10 kips and P_{LL}=80 kips.

Solving for the coefficients of the polynomial function is repeated for eligible specimens that meet the criteria of having a linear range of data with steepest slope (stiffness). Then coefficients of the function are found by taking the average values of those coefficients find for each test specimen;

$$\Delta o=-0.0101\,\text{in.}$$

$$f(P)=1.081*10^{-3}P+-7.546*10^{-6}P^2+2.783*10^{-8}P^3$$

(B.12)

The data is generated by using this polynomial function, referred to as cubic fit in Figure B.8, and a good fit is observed with cross-head deformation data. This comparison is shown in Figure B.8. Then, original test data is initialized with zero initial cross-head displacement and load (0,0) as shown in Figure B.9. An offset head

travel value is found in order to initialize it and then data between (0,0) and (Δ_{offset} , P_i) are generated.

In order to find offset head travel value, equation (B.13) is used which calculates the total deformation of the machine components at P_i;

$$\Delta_{offset} = \Delta_{machine\_columns,a1,a2}(P_i) + \Delta_{machine\_columns,Lspecimen}(P_i) + \Delta_{specimen\_shortening}(P_i) + \Delta_{x-head\_platen}(P_i) \quad \textbf{(B.13)}$$

B.6 Modified Specimen Shortening using Nonlinear Δ_{xhead_platen}

Firstly, experimental cross-head displacement data is modified with Δ_{offset} as shown in equation (B.14). Then modified specimen shortening data, $\Delta_{modified\_specimen\_shortening}$, are found by equation (B.15);

$$\Delta_{modified\_experimental\_total} = \Delta_{offset} + \Delta_{experimental\_total} \quad \textbf{(B.14)}$$

$$\Delta_{modified\_specimen\_shortening} = \Delta_{modified\_experimental\_total} - \Delta_{xhead\_platen}(P) - \Delta_{machine\_columns,a1,a2} - \Delta_{machine\_columns,Lspecimen} \quad \textbf{(B.15)}$$

where

$$\Delta_{xhead\_platen}(P) = 1.063*10^{-3}P + -7.159*10^{-6}P^2 + 2.556*10^{-8}P^3 \quad \text{for } P<P_{LL}$$

$$\Delta_{xhead\_platen}(P) = \frac{P}{k_{average\_x-head\_platen}} \quad \text{for } P>P_{LL}$$

Load vs. modified specimen shortening graphs are shown in Figure B.11 and Figure B.12 for single and double angle specimens, respectively.

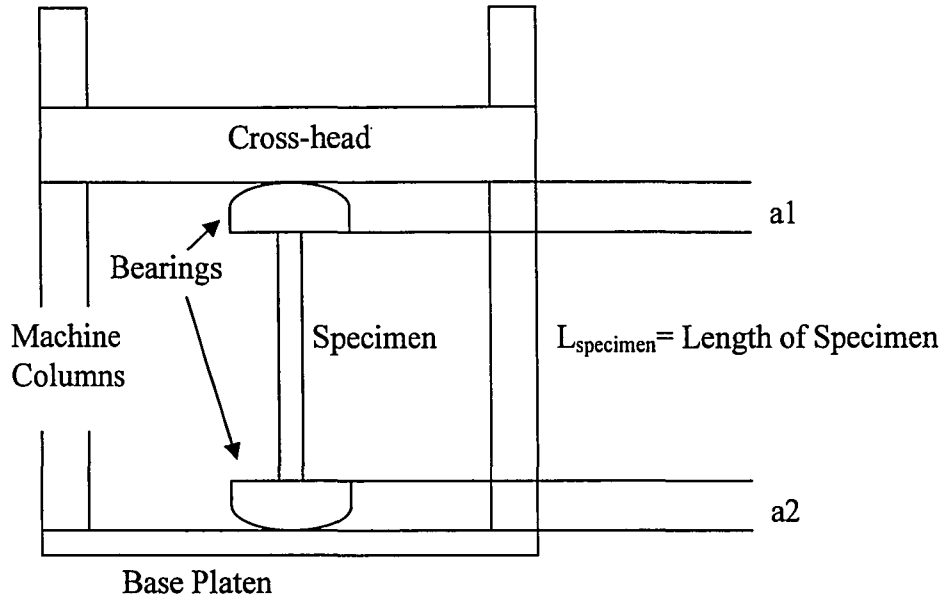

Figure B.1 Schematic of Testing Machine and Test Specimen

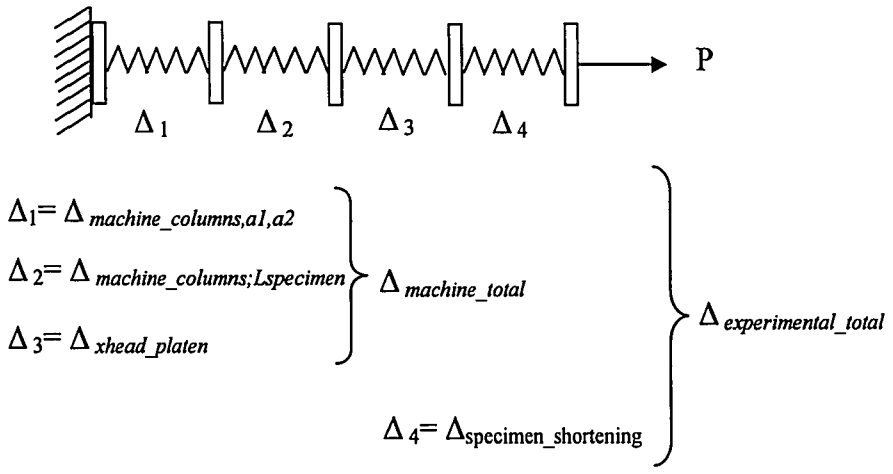

Figure B.2 Components of Test Machine Represented as Individual Springs

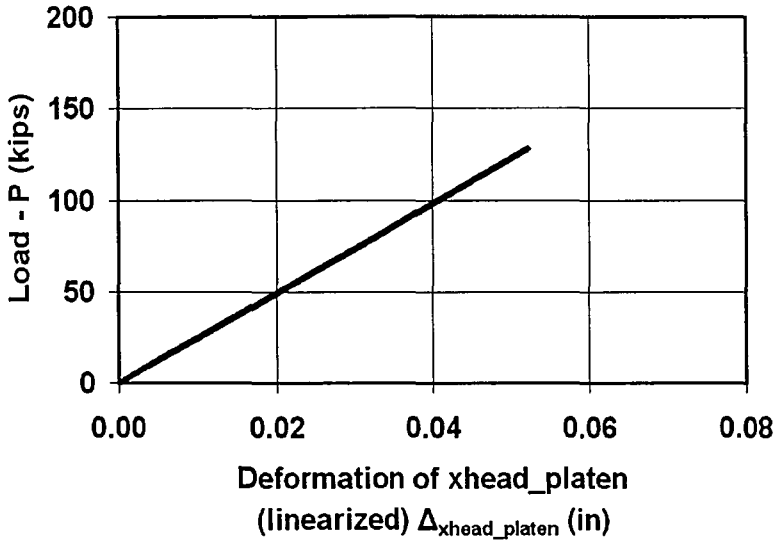

(a) Load vs. (Linearized) Δ_{xhead_platen}

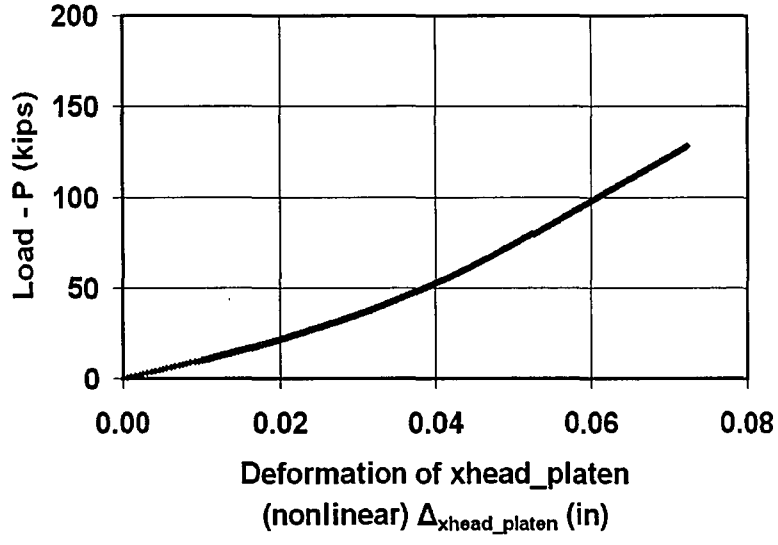

(b) Load vs. (Nonlinear) Δ_{xhead_platen}

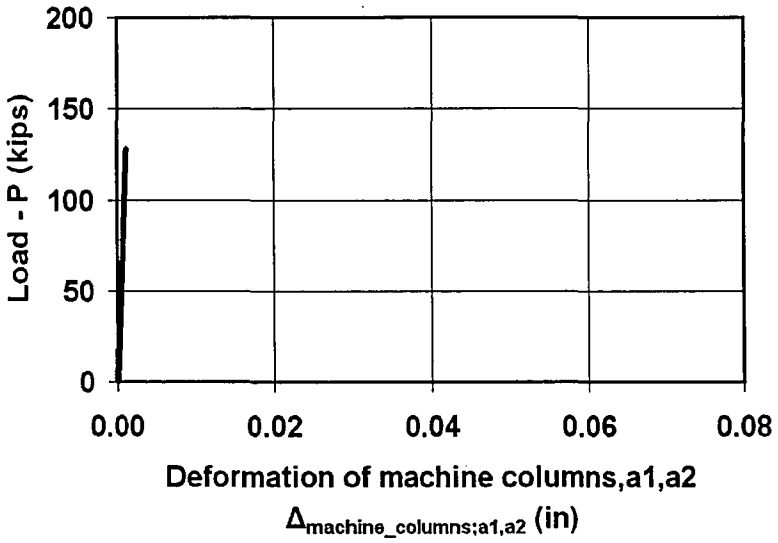

(c) Load vs. $\Delta_{machine\_columns,a1,a2}$

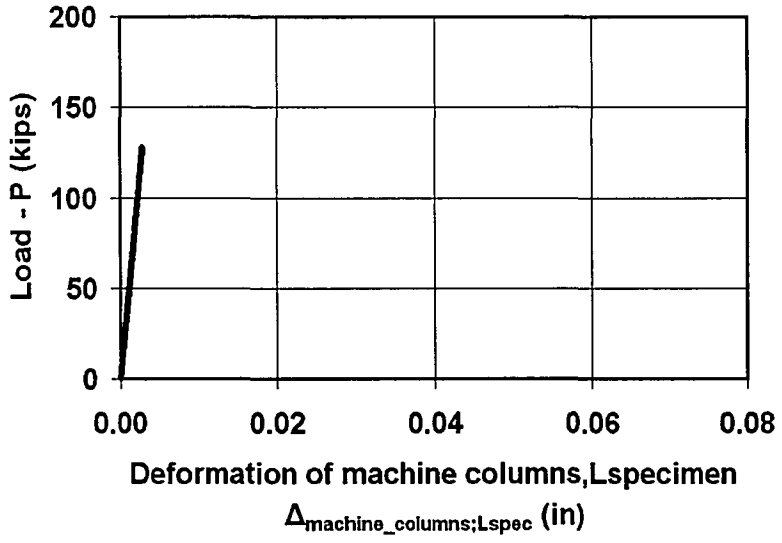

(d) Load vs. $\Delta_{machine\_columns,Lspec}$

Figure B.3 Components of Cross-head Displacement – Specimen SA2

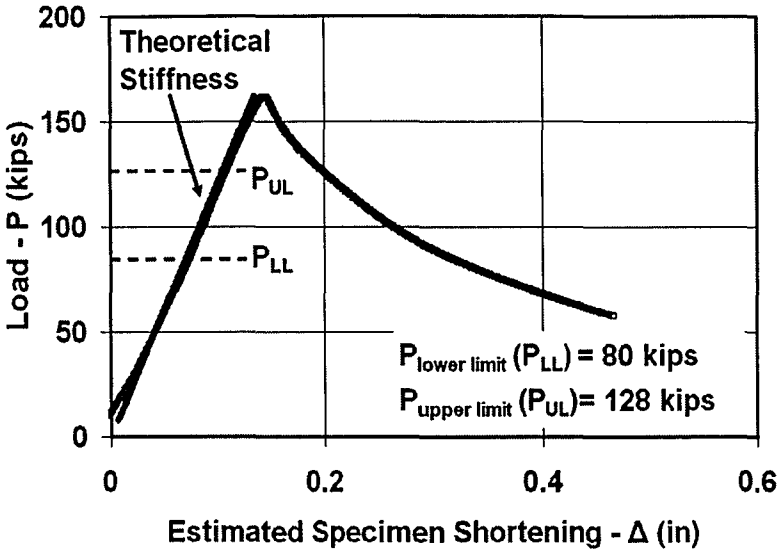

Figure B.4 Load vs. Estimated Specimen Shortening - Specimen SA2

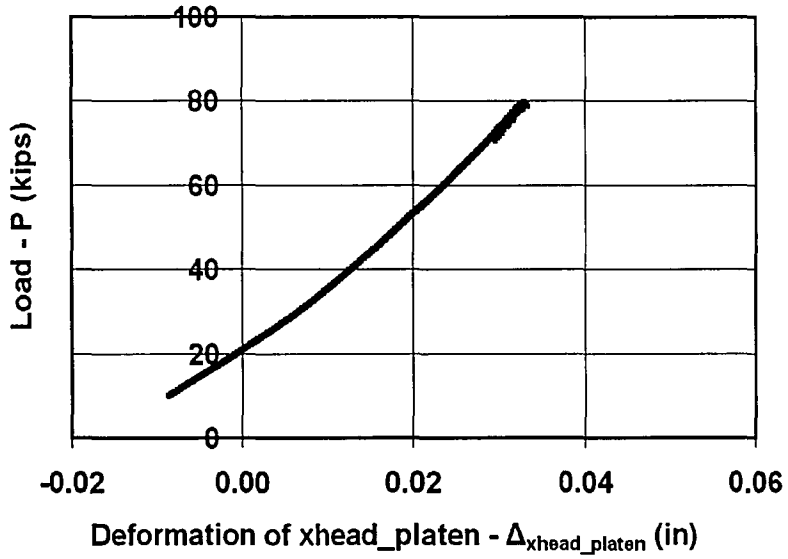

Figure B.5 Cross-Head Behavior under Lower Load Limit – Specimen SA2

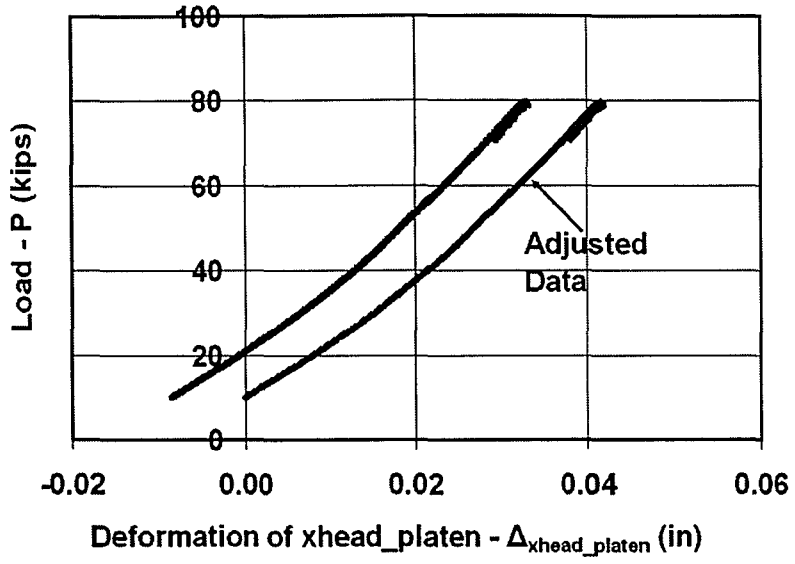

Figure B.6 Cross-Head Data Initialized for Zero Displacement Specimen SA2

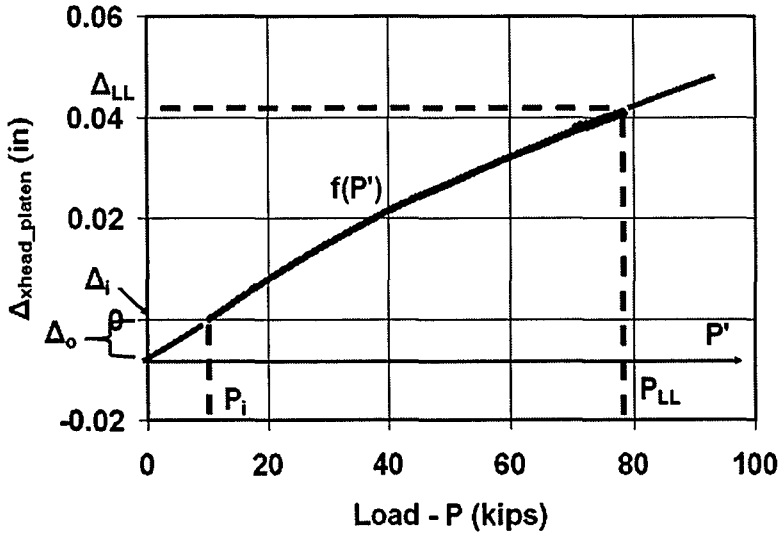

Figure B.7 Polynomial Fit Function shown with Boundary Conditions Specimen SA2

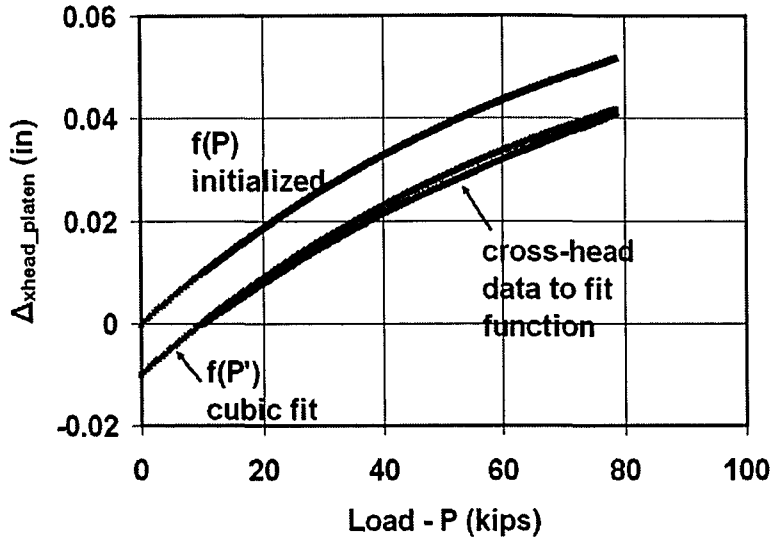

Figure B.8 Initialized Function Data Compared with Original Cross-Head Data Specimen SA2

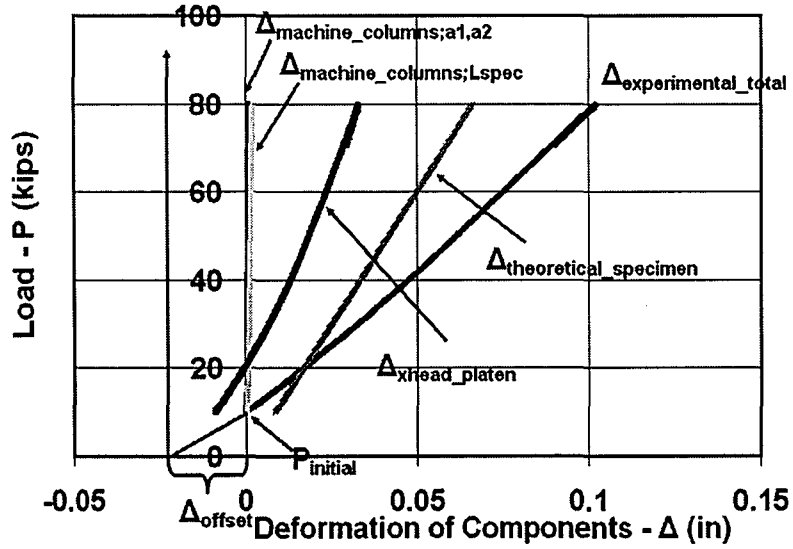

Figure B.9 Original Test Data Components and Generation of Data – Specimen SA2

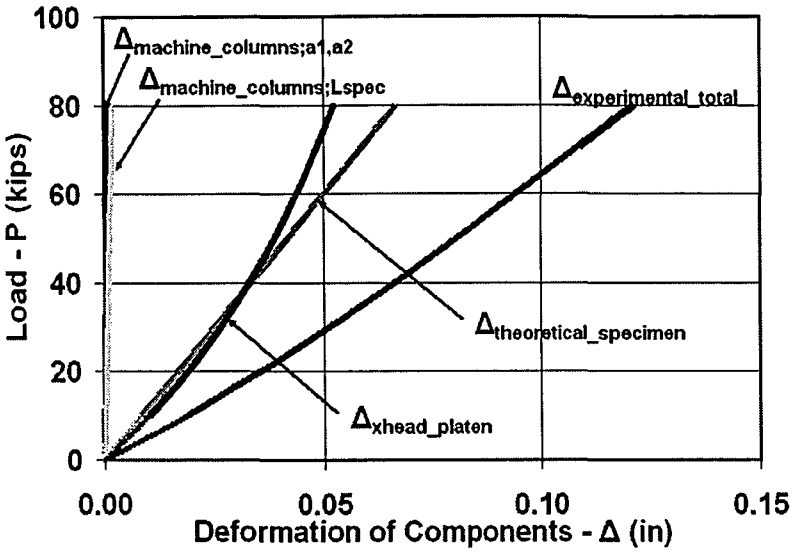

Figure B.10 Initialized Data with Offset – Specimen SA2

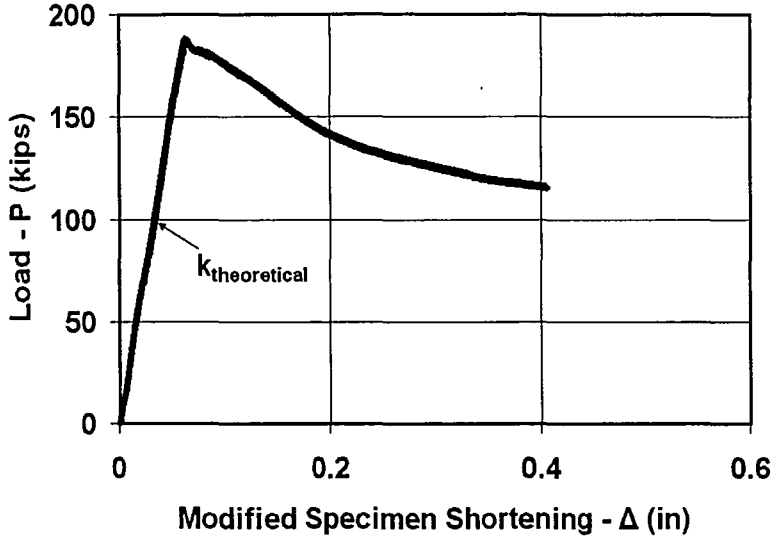

(a) Specimen SA1

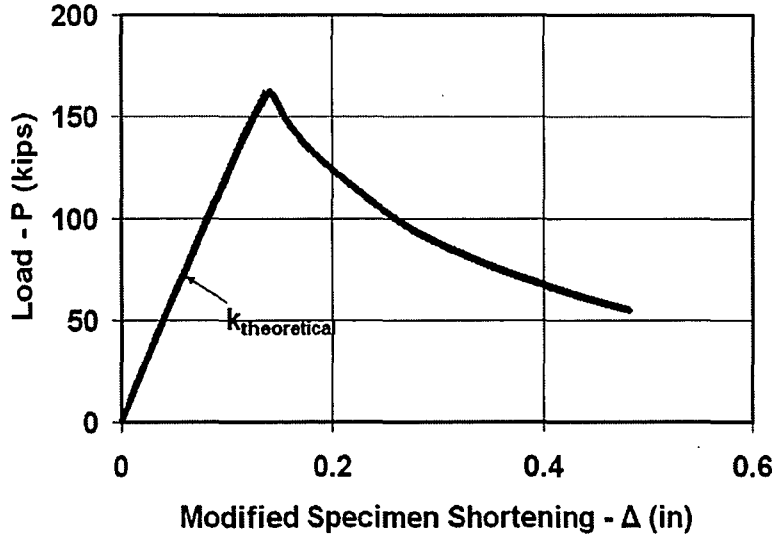

(b) Specimen SA2

Figure B.11 Load vs. Modified Specimen Shortening for Single Angle Specimens

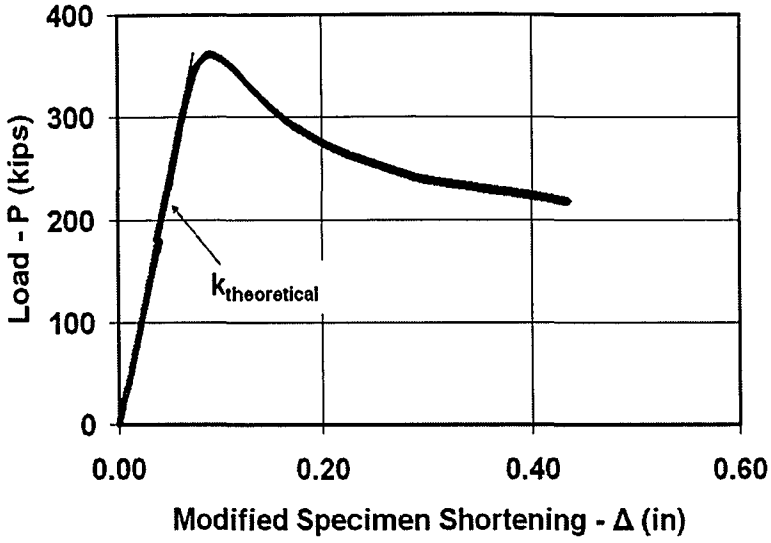

(a) Specimen DA1

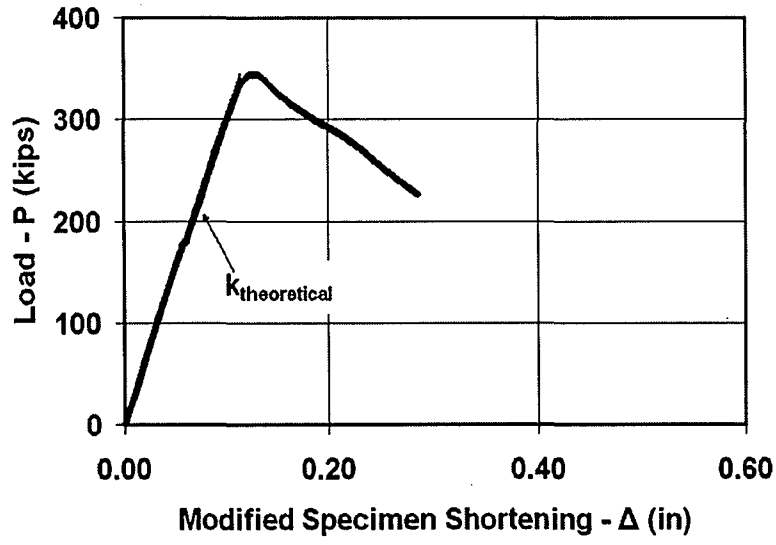

(b) Specimen DA2

Figure B.12 Load vs. Modified Specimen Shortening for Double Angle Specimens

Vita

Ali Bedii CANDAS was born on February 7, 1982 in Manisa, TURKEY. In June 2005 Ali received his Bachelor of Science degree in Civil Engineering from Bogazici University in Istanbul, TURKEY. Ali pursued his Master of Science degree at Lehigh University in Bethlehem, Pennsylvania and worked as a Graduate Research Assistant at Advanced Technology for Large Structural Systems (ATLSS) facility. Ali will receive his degree in July 2007. After graduation, Ali will be working as a structural engineer for Thornton Tomasetti, Inc. in New Jersey.

END OF TITLE